CONF-940627--Vol.2

NASA Conference Publication 3290

Proceedings of the Fourth International Conference and Exhibition: World Congress on Superconductivity

Volume II

Proceedings of a conference and exhibition held at Marriott Orlando World Center, Orlando, Florida, June 27 - July 1, 1994

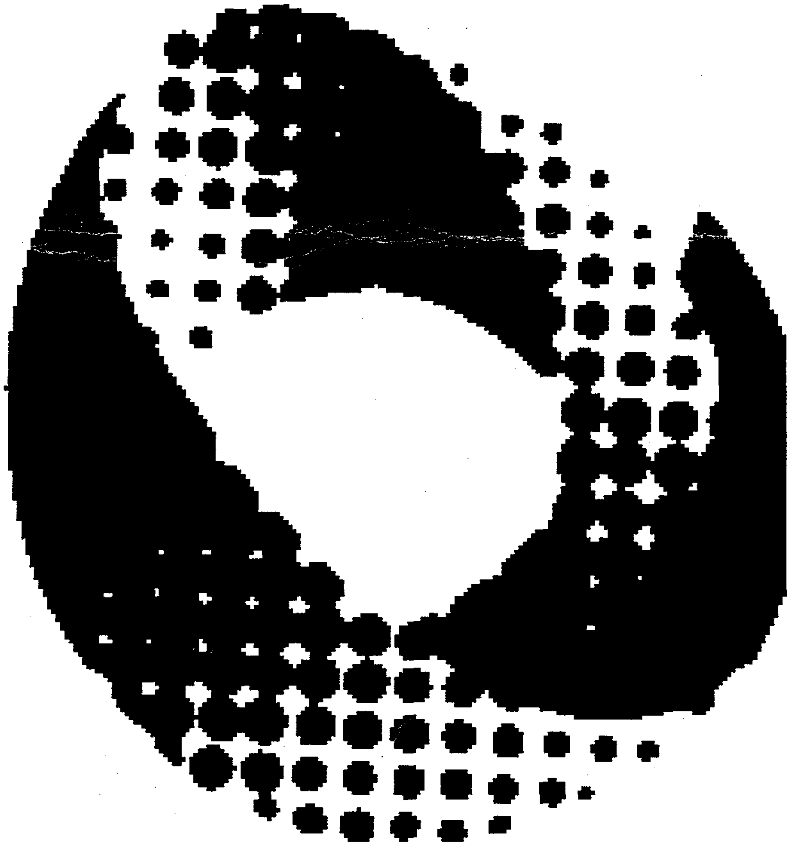

1994

NASA Conference Publication 3290

Proceedings of the Fourth International Conference and Exhibition: World Congress on Superconductivity

Volume II

Kumar Krishen and Calvin Burnham, Editors
Lyndon B. Johnson Space Center
Houston, Texas

Proceedings of a conference and exhibition held at
Marriott Orlando World Center, Orlando, Florida,
June 27 - July 1, 1994

MASTER

1994

DISTRIBUTION OF THIS DOCUMENT IS UNLIMITED

This publication is available from the NASA Center for AeroSpace
Information, 800 Elkridge Landing Road, Linthicum Heights,
MD 21090-2934 (301) 621-0390.

The World Congress on Superconductivity

The World Congress on Superconductivity (WCS) was formed in Houston in 1987 by a group of volunteer engineers and scientists interested in increasing the focus on this emerging technology field of superconductivity. The leadership of the WCS, a non-profit 501(c)3 organization, is comprised of individuals from several major technical societies such as the Engineers Council of Houston, the American Chemical Society, IEEE, etc. This group is augmented by leaders of the international research, academic, science, government and business communities who serve on the Advisory Board or ad hoc committees. Since its inception, the Advisory Board has been global in scope with technologists from such countries as Japan, Russia, Switzerland, etc., actively involved in steering the direction of our programs.

The goals of the WCS have been to establish and foster the development and commercial application of superconductivity technology on a global scale by providing a non-adversarial, non-advocacy forum where scientists, engineers, businessmen and government personnel can freely exchange information and ideas on recent developments and directions for the future of superconductive research.

To date, four international conferences have been completed since 1987. These conferences were attended by over fifteen hundred delegates from thirty-six nations. The success of these conferences is remarkable in light of the fact that the WCS has no staff and must rely on monetary donations from the private sector, foundations and government agencies. In addition, thousands of man-hours have been donated by the WCS volunteer staff in the organizing of this activities. WCS is especially thankful for the assistance of Dr. Kumar Krishen as program chairman and the support from NASA which makes this activity possible.

Because of the unique nature of the WCS and its success, the organization is sanctioned by the United Nations and is a member of the UN's Advance Technology Alert System. The WCS was awarded Leadership Houston's International Corporate award for its Munich conference in 1992.

Plans are currently underway for the 5th International Conference of the World Congress on Superconductivity, which will be held in July 1996 in Budapest, Hungary. This meeting will coincide with the 1,100 year anniversary of Hungary. For more information on this meeting and WCS activities, please contact Calvin Burnham, President, World Congress on Superconductivity, P.O. Box 27805, Houston, TX 77227-7805; telephone 713-895-2500; fax 713-469-5788; e-mail: 70425.501@compuserve.com

VOLUME 1

Session: **PLENARY, ROUNDTABLE AND KEYNOTE**
Session Chair: **Dr. Kumar Krishen**

Session: **ACCELERATOR TECHNOLOGY**
Session Chair: **Dr. Siegfried Wolff**

Session: **POWER AND ENERGY**
Session Chair: **Prof. Istvan Kirschner**

Session: PERSISTENT MAGNETIC FIELDS
Session Chair: Dr. Roy Weinstein

Session: PERFORMANCE CHARACTERIZATION
Session #1 Chair: Dr. R. K. Pandey
Cochair: Dr. U. Varshney

Session #2 Chair: Dr. R. K. Pandey
Cochair: Dr. U. Varshney

Session: PHYSICAL PROPERTIES
Session PP-1 Chair: Prof. Valeri Ozhogin
Cochair: Prof. Evgenii Z. Meilikhov

Session PP-2 Chair: Prof. Valeri Ozhogin
Cochair: D. Brinkman

Session: FABRICATION METHODOLOGY
Session Chair: Dr. U. Balachandran

VOLUME 2

Session: SUPERCONDUCTIVE MAGNETIC ENERGY STORAGE (SMES) UTILITY INTEREST GROUP
Session Chair Dr. Phillip Baumann
SMES1: Technical Session

SMES 2: Technical Session

Session: THIN FILMS
Session Chair: Prof. Tomoji Kawai

Session: HIGH TEMPERATURE MATERIALS
Session #1 Chair: Prof. Mikio Takano

Session #2 Chair: K. Kishio

Session: **DEVICE APPLICATIONS**
Session Chair: **Dr. Yoshifusa Wada**

Session: **WIRE FABRICATION**
Session Chair: **Dr. K. C. Goretta**

AOD

Session: **GRANULAR SUPERCONDUCTORS**
Session Chair: **Prof. Manu S. Multani**

Session: POSTERS

Superconductive Magnetic Energy Storage (SMES) Utility Interest Group

Chair: Dr. Phillip Baumann

POLICY ISSUES INHERENT IN ADVANCED TECHNOLOGY DEVELOPMENT

Philip D. Baumann
InterFact, Inc.

In the development of advanced technologies, there are several forces which are involved in the success of the development of those technologies. In the overall development of new technologies, a sufficient number of these forces must be present and working in order to have a successful opportunity at developing, introducing and integrating into the marketplace a new technology.

This paper discusses some of these forces and how they enter into the equation for success in advanced technology research, development, demonstration, commercialization and deployment. This paper limits itself to programs which are generally governmental funded, which in essence represent most of the technology development efforts that provide defense, energy and environmental technological products. Along with the identification of these forces are some suggestions as to how changes may be brought about to better ensure success in a long term to attempt to minimize time and financial losses.

- **Need for Consistency in the Administration's Direction**

  Priorities within the Administration change regularly. These changes can occur either from a transition from one Administration to another, or within one Administration itself which has difficulty in planning well and staying with a plan which is working. Shifts in policies and thus priorities as they relate to generalities and then filter down to technology development can severely limit and destroy essentially effective technology development programs. For example, changes in policy from defense to health care cause significant shifts to occur in the overall make-up of the President's Budget. This shift can quickly rift through various programs and either weaken them through sufficient budget cuts or cancel them altogether. The effects on these programs is seldom, if ever, realized by the powers to be. Worse, some programs are turned on and off repeatedly over through the years, to where they are so fragmented in purpose, their effectiveness in delivering technology to the marketplace is next to zero.

- **Need for an Administration Mentor**

  Many technologies have been under development in various programs within the Department of Energy, Defense and Commerce. Most, if not all of these technologies, require programs of a multiple year nature. Typically, programs range from two to five years, with a five to ten year program not being unusual in nature. Certain examples of long term programs in the energy area are fusion, MHD and accelerator technologies. Large programs having adequate momentum tend to go toward completion, and do so with an Administration "Mentor." This mentor typically has a personal interest in the technology, whether based upon pure personal interest or interest as a stepping stone to further opportunities upon successfully completing the program efforts. This mentor shepherds the technology through the various levels of development and ensures that the program has continuity from start to finish.

Many governmental programs are absent a shepherd. These programs generally do not experience the same success rate as mentored projects. The downfalls of these projects include lack of technical continuity, lack of periodic project review meetings for support gathering, lack of foresight to out-year funding needs, lack of direction to the contractors involved to ensure quality outcomes, and lack of attention to schedule. In the end, these projects very often resemble make-work projects in retrospect. Whether the supporters of these projects are Congressional, industry or consumer, the difficulty degree for success is the highest in the absence of an Administration mentor.

- **Need for Consistency in Congress**

  This may very well be the most potentially detrimental situation in a technology's developmental life cycle. There are several patterns, and lack of patterns, within the Congress which can have both chronic and acute effects on a technology's development. Inconsistency from year to year in funding on a program can severely affect the quality of continuity in a developing technology. For whatever reasons, Congress often chooses to delay funding for a program, or kills a program only to resume it a year or years later. The effects on the success of the overall program is significantly affected when this occurs. Other difficulties arise when major shifts on monies are required, such as with natural disasters, where large blocks of funding are removed from programs, the effects of which to the specific technology programs and the general welfare of the country are not measured or even know for years or perhaps never.

  Increase awareness on the part of the Congress in applying major shifts in funding priorities or the shifting of major programs may reduce this problem, however, because of the sheer size of the system and the diversified interest levels involved, much success is not likely to be achieved.

- **Need for a Congressional Mentor**

  Programs for the development of advanced technologies virtually always require a Congressional mentor in the beginning in order to have the initial funding power in Congress. The extent to which this mentor is committed can range from merely providing some effort on behalf of a constituent, or can be so strong by personal conviction that support remains intact throughout the term of the program effort in the absence of any parochial interest. In any event, a Congressional mentor, to some extent, is necessary.

- **Enroll all of Your Project Participants into a Solidified Team**

  Ensure that all of the participants on the project team, no matter how small or insignificant they may appear with regard to the whole picture, are fully enrolled into the project. Make sure that anyone with the capability to influence the program, either positively or negatively, is made an important component in the program, and feels like a contributing player in some capacity.

- **Full Development of Economic Merits of the Technology's Existence**

  Oftentimes, a technology will be funded for development, in the absence of an economic cost/benefit study. Later, a study of this nature is a much needed commodity in order to justify either Administration or Congressional support. Instead of assuming the value of a technology as is the situation in so many cases, a cost/benefit assessment is a small price to pay to be able to produce such a document at a strategic point in time.

- **Need for Broad Interest Base and Consensus of Technology's Value**

  The broader the consensus of the interest base and value of a particular technology, the greater the success rate will be for commercial success. When supporters come from different viewpoints and angles as to the merit of a technology, the greater the perceived breadth of applicability the technology will have. Demonstration of such will be significantly helpful in gaining Administration and Congressional support.

- **Consuming Industry's Support in Technology Direction and Development**

  Many industries are reasonably aggressive in maintaining a status of what technologies are under development for their respective industry. Some industries are not particularly aggressive in exploring what technologies are under development or available to them. The absence of an industry, or a sector of an industry, to operate in a manner that allows them to maintain the latest information on developing technologies, can often result in that particular technology not coming to fruition for the industry. Oftentimes, a technology of significant importance and economic merit may not reach commercial availability because a large enough support base to ensure its continued funding does not exist. It costs an industry precious little to provide a base of enthusiasm, which in many cases is all that is required to maintain the ongoing viability of a program. The absence of supporters for a technology at key times of Congressional inquiry as to the level of support spells almost certain death for the program.

POLICY ISSUES INHERENT IN ADVANCED TECHNOLOGY DEVELOPMENT

Philip D. Baumann

InterFact, Inc.

- Need for Consistency in the Administration's Direction
- Need for an Administration Mentor
- Need for Consistency in Congress
- Need for a Congressional Mentor
- Enroll all of Your Project Participants into a Solidified Team
- Full Development of Economic Merits of the Technology's Existence
- Need for Broad Interest Base and Consensus of Technology's Value
- Consuming Industry's Support in Technology Direction and Development
- Technology Developer's Responsibility to Educate Their Future Consumers
- Competition-based Self Defeat of Common Goals

- **Technology Developer's Responsibility to Educate Their Future Consumers**

  Many programs which are developed by technology developers to fill an identified potential market niche are often not of presence to the potential consumer. In efforts to develop a technology, a developing vendor may spend the majority of their efforts directly on the development of the technology under some reasonably tested assumptions that the market will be present.

  When the time arrives to again work with the Administration and the Congress to maintain funding levels for out-years, often the developing vendor is unable to demonstrate hard facts to support a bonafide market. This often results in either significantly politically forced situations to bring about out-year funding or the loss of support for any funding within the Administration and Congress, resulting the closure of programs which may have significantly high merit to the ultimate consumer.

  Better education by technology developers to their potential customers may result in a broader base from which to demonstrate support and maintain the viability of a technology development program through to commercial availability.

- **Competition-based Self Defeat of Common Goals**

  Oftentimes in the development of a technology, governmental program will employ two or more teams in the early stages to develop competing designs. This often ensure the government, and consumers with the best design, as competition can often produce better products and the best components of each of the designs can be combined into one if applicable.

  Because of the oftentimes diversity of approach and philosophy of competitors to their technology's development and deployment, the Administration and Congress may hear different messages. While it is not the intent of vendors to create an atmosphere of confusion or misreading, multiple messages can sometimes produce the appearances of an non-united front for the development of a technology. While it is never the intent of a vendor to potentially jeopardize a program, discontinuity produces confusion, and confusion produces doubt. Even the fiercest of competitive environments, competitors should work together to ensure that there are at least the appearances of a common thread in the overall efforts of a program.

These ten typical issues are indicative of issues inherently present in a majority of programs. The consideration and incorporation of these simple concepts into any technology development program requiring governmental support and involvement can significantly increase the probability that the program will be successful.

Financial Options Methodology
for
Analyzing Investments in New Technology

presented June 29, 1994, at the
4th International Conference and Exhibition of the World Congress on Superconductivity, Orlando, Florida

B.D. Wenning

Texas Utilities Services Inc.
Skyway Tower
Dallas, Texas 75201

ABSTRACT

The evaluation of investments in longer term research and development in emerging technologies, because of the nature of such subjects, must address inherent uncertainties. Most notably, future cash flow forecasts include substantial uncertainties. Conventional present value methodology, when applied to emerging technologies severely penalizes cash flow forecasts, and strategic investment opportunities are at risk of being neglected.

Use of options valuation methodology adapted from the financial arena has been introduced as having applicability in such technology evaluations. Indeed, characteristics of superconducting magnetic energy storage technology suggest that it is a candidate for the use of options methodology when investment decisions are being contemplated.

INTRODUCTION

Conventional financial analysis utilizing present value methodology (i.e., discounted payback period; net present value; internal rate of return, profitability index) is often applied to engineering problems in order to more optimally allocate resources. The use of such familiar techniques satisfies the requirement for a structured approach to perform such analyses as well as provides a common basis for communicating economic justification to financial managers. Present value methodology, however, may not be suitable for analysis of research and development investments — those which may not yield significant results until many years in the future, hence cash flow forecasts are uncertain — since the benefit stream from the investment is severely discounted.

Near term investments in research and development are typically modest in comparison to near-commercial project capital requirements. Research and development expenditures often times buy the investor early rights to later larger and preferential pre-commercial positions. In essence, the early research and development investments give the investor the right, but not the obligation, to purchase a more substantive position in the technology in the future. By definition, the investor is purchasing a call option contract — a call option gives the purchaser the right to purchase shares of an enterprise at an exercise price on a certain future date.

Options methodology and option pricing valuation are techniques well-established in the financial arena which can be borrowed to more appropriately value investments in research and development. The recognition that research and development expenditures maintain the strategic option for the corporation can provide a perspective which may offset present institutional bias toward both short-term evaluation tools and short-term results.[1]

OPTIONS METHODOLOGY

The most well known and commonly used technique for valuing options is the Black-Scholes option pricing model (OPM).[2] This model's introduction roughly coincided with the opening of the Chicago Board of Trade in 1973 and has been accepted for valuing call options. The model consists of two elements to assess the value of a contemplated option purchase. The first element in the model accounts for the benefit stream anticipated from the exercise of the option. The second element accounts for the estimate of the striking price or exercise price at maturity of the option. The exercise of this option will be necessary to enable the benefits to be realized at some future date.

Stated in equation form:

$$V_0 = P_0[N(d_1)] - Ee^{-rt}[N(d_2)]$$

where

V_0 = the value of the option

P_0 = the current price of the investment

$[N(d_i)]$ = probability that a deviation less than d_i will occur in a standard normal distribution. The value of a cumulative normal density function.

E = the exercise price

e = exponential constant, 2.71828

r = risk-free interest rate

t = time until option is exercised

$d_1 = \dfrac{\ln(P/E) + [r + 0.5(\sigma^2)]t}{\sigma\sqrt{t}}$

$d_2 = d_1 - \sigma\sqrt{t}$

σ^2 = variance of the rate of return on the investment

Assumptions used in the Black-Scholes OPM are:

1. The call option can only be exercised on its maturity date (known as a European option).
2. No dividends, taxes, or transaction costs are associated with the option over the life of the option.
3. The short-term interest rate is known and constant during the life of the option.
4. No short sales restrictions exist.
5. The price moves randomly in continuous time.

A more detailed description of the model can be found in a number of financial textbooks. Its use rather than its derivation are important here.

---

[1] Mitchell, G.R. and Hamilton, W.F. "Managing R&D as a Strategic Option." *Research and Technology Management* (May-June 198), 15-22.

[2] Black, F. and Scholes, M. "The Pricing of Options and Corporate Liabilities." *Journal of Political Economy,* 81 (May-June 1973), 637-654.

The factors in the OPM can be illustrated on a timeline as shown in Figure 1, below.

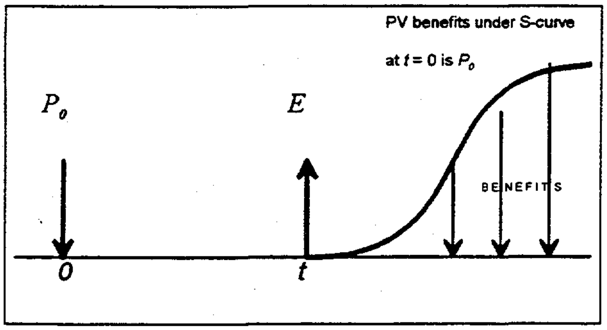

Figure 1

The interpretation of the Black-Scholes OPM equation is rather simple. The first element, $P_0[N(d_1)]$, represents the current value of the investment adjusted by a factor which represents the variability one expects in this value. Mathematically, the adjustment is the probability that a deviation less than d_1 will occur in the standard normal distribution. In normal stock options, the first element represents the present value of the stock. The second element, $Ee^{-rt}[N(d_2)]$, represents the value of the exercise price at time of maturity, t, discounted by the risk-free rate of return. The exercise price also is adjusted for the probability that it will actually occur as expected.

APPLICATION TO RESEARCH & DEVELOPMENT

Observation of investments in research and development suggest that the call option model can be applied to research and development or new technology investments in certain circumstances. OPM is not applicable to those projects which are near-term and involve capital investments to achieve final commerciality — traditional present value techniques may readily and perhaps most appropriately be used to analyze such near-term investments. On the other hand, those projects which require an up-front investment (i.e., the option purchase price) to reserve future rights and whose benefit stream is conditioned on some future capitalization (i.e., the exercise price) indeed represent a typical call option situation which can be adopted from the financial arena. For situations such as this, Black-Scholes OPM can be used.

In dealing with stock options, the exercise price, E, is the additional capital the investor can chose to expend at the maturity of the option. In research and development, this exercise price is the additional start-up capital required for commercialization just prior to initial benefits being realized. This may appear to the investor as the cost for, for instance, pilot manufacturing facilities to achieve the first batch of benefits from the new technology. The exercise price is discounted by the riskless rate of return, r, continuously compounded over the duration of the option, t, and adjusted by $[N(d_2)]$ for the probability that the cost will actually occur as estimated.

Again dealing with stock options, the current investment price, P_0, is the present value of the expected dividends to be returned from the investment. In research and development, P_0 is correspondingly the present value of the expected yield from the project. The adjustment to this element in the model, $[N(d_1)]$, accounts for the variance of the investment price, P_0.

Most of the factors in the OPM model can be reasonably estimated for option investment analysis. The riskless rate of return, r, is usually taken as the current U.S. treasury bill or treasury note rate. Time, t, is the time before the investment of additional capital, E, is necessary.

The anticipated benefit stream can be reduced to a present value, P_0. Estimating the variance, however, can be problematic.

As a proxy for the variance associated with new drug development, the pharmaceutical company Merck uses the annual standard deviation of returns for typical biotechnology stocks in their application of OPM.[3] Conservatively, Merck uses between 40% to 60% for project volatility.

Pharmaceutical development is confined within the same industry and past performance may provide some prognosis for future results. However, typically, new technologies and research and development deal with issues without a historical pattern from which to draw.

The model appropriately is sensitive to the variance factor. Common sense would dictate that predictions of actual results are subjective and variance will be an important parameter in the analysis. Experienced judgment must, therefore, be utilized to generate a reasonable model input.

Two factors in the analysis deserve special attention: (1) the time to maturity and (2) the variance of the estimates. In contrast to present value techniques, OPM suggests *greater* value is associated with longer term projects. That is, with longer times to maturity of the exercisable option, the greater the opportunity for the value of the investment to rise. Consequently, OPM imputes greater value to long-term projects than perhaps traditional present value techniques which exponentially discount and penalize future benefit streams.

Using options methodology also ascribes greater value to projects whose outcome may be uncertain. The variance of longer term projects increases the probability of larger than expected yields, increasing the value of the option. The probability of *smaller* than expected results is not as detrimental. Downside loss is limited to be no greater than the option purchase cost. Longer term projects which have lengthy periods before they become commercial and which have uncertain yields do, in fact, *increase* the value of the option in stark contrast with how such projects would be viewed using present value methodology.

What the Black-Scholes OPM provides is a credible tool for the analysis of certain new technology investments which provide the investor meaningful insight into the value of, especially, projects with long term results.

POTENTIAL APPLICATION OF OPTIONS METHODOLOGY TO SMES

Superconducting Magnetic Energy Storage (SMES) has characteristics which suggest that OPM may be useful to analyze decisions regarding investment in research and development of the technology. The need for SMES technology exists today. Utility and customer requirements for energy storage range from small kilowatt-second storage devices for power quality up through the large, multi-megawatt-hour, bulk power devices for utility spinning reserve and/or load leveling. The smaller one megawatt-for-one-second SMES systems are commercially available. One would not find Black-Scholes OPM too useful in analyzing a commercial hardware purchase decision.[4] Conventional present value techniques would apply.

---

[3] Nichols, Nancy. "Scientific management at Merck: An Interview with CFO Judy Lewent." *Harvard Business Review* (Jan-Feb 1994) 88-99.

However, research and development investments in intermediate- and large-sized SMES systems *could* be analyzed using OPM. Such investments in research, development, and even demonstration are analogous to option purchases. The future commercial start-up investments necessary to take the technology to market are analogous to the option's exercise price.

Market analyses for utility and customer use of SMES devices includes uncertainties. If one were to use present value methods to analyze the early research and development investments, depending on the discounting applied to the analysis, such investments may not be justified. Despite potential extraordinarily huge benefits from the SMES technology and the relatively small investment in research and development, the technology may not get off the ground without proper analysis of early investments.

Since the early research and development costs are likened to the option purchase, the use of Black-Scholes OPM may yield sufficient incentive to pursue research and development.

IDENTIFIED NEED

To utilize Black-Scholes OPM, one must be able to estimate the various factors involved in the model. Further examination of the variability of estimates of (1) follow-up investment needs, and (2) benefit streams, from new technology research and development is necessary to better judge the appropriate statistical parameter, d_i. Unlike stock options which can be valued based on the stock's historical variability or like pharmaceutical research and development which has a database of drug development statistics, new technologies often confound existing paradigms and, therefore, defy simple analysis.

CONCLUSION

Use of options methodology such as the Black-Scholes option pricing model has particular relevance to the analysis of early expenditures for research and development in emerging technologies. Financial managers should recognize that the usefulness of conventional present value methodology diminishes as the framework for the project departs from near-term commercial likelihood. OPM may provide a useful approach to the analysis of such longer term technologies as SMES, not only being a more appropriate analysis tool but one which financial managers will already have familiarity.

---

[4] One might, however, find OPM useful if one were evaluating investment in a start-up company marketing such devices.

SMES: Redefining the Path to Commercial Demonstration

W.G. Bingham and R.W. Lighthipe[1]
Bechtel, San Francisco, California, U.S.A.
[1] San Diego Gas & Electric, San Diego, California, U.S.A.

SMES (Superconducting Magnetic Energy Storage) is an emerging technology offering tremendous potential benefits to the utility industry. San Diego Gas & Electric (SDG&E) and Bechtel are leading a team of companies and national laboratories working towards design and construction of the world's first demonstration facility for large, commercial SMES for enhancing transmission stability in the Southwestern United States.

Environmental, economic, and regulatory forces are reshaping the way utilities generate, transport, and distribute electricity. Electric power has always been available on instant demand with a high degree of reliability, flexibility, and control. On the other hand, it has never been easily stored in large quantities. Environmental limits on generation and the advent of renewables, deregulation and competition, and the increasing complexity of transmission systems, all point towards the need for a reliable and cost-effective means to store and retrieve electric power.

In SMES, electric energy is stored by circulating a current in a superconducting coil, or inductor. Because no conversion of energy to other forms is involved (e.g., mechanical or chemical), round-trip efficiency is very high, upwards of 90%. SMES can respond very rapidly to dump or absorb power from the grid, limited only by the switching time of the solid-state components connecting the coil to the grid. SMES can typically respond to a grid transient and achieve full power in about 100 ms (or six cycles).

SMES was initially conceived as a load-leveling device to store energy in bulk to reduce a utility's daily peak demand. In that sense, SMES would fill the same market niche as pumped-hydro, batteries and compressed air energy storage (CAES). Because of its fast response, SMES can provide benefit to a utility not just as a load-leveling device, but also by enhancing transmission line stability and power quality. SMES can be viewed as a Flexible AC Transmission System (FACTS), with the added dimension that it can insert real power into the grid. Such capability can significantly improve transmission line dynamics, allowing for higher load transfer without compromising grid stability. Line stabilization will be the utility application leading to the first commercial demonstration of SMES.

Since the technology of low-temperature superconducting (LTS) wire is fully mature, early SMES units will be based on LTS. This will ensure timely demonstration of the integrated technology, and the development of a SMES market. High-temperature superconductors (HTS) can then be introduced as that technology matures in order to further reduce costs and increase the operating efficiency.

For the past six years, Bechtel has led a team of companies and national laboratories in the development and testing of a new and economical design leading to the world's first commercial demonstration SMES unit. This report describes the recent design breakthroughs, and the current efforts by San Diego Gas & Electric and the Bechtel Team to proceed with a utility demonstration of the technology: SMES-1.

PRINCIPLES OF OPERATION

As an energy storage device, SMES is a relatively simple concept. It stores electric energy in the magnetic field generated by DC current flowing through a coiled wire (see Figure 1). If the coil were wound using a conventional wire such as copper, the magnetic energy would be dissipated as heat due to the wire's resistance to the flow of current. However, if the wire is superconducting (no resistance), then energy can be stored in a "persistent" mode, virtually indefinitely, until required.

The coil is cooled to liquid helium temperature to achieve superconductivity. The superconductor of choice for this application is a niobium-titanium alloy. When the coil is energized, it is subject to outwardly radial electromagnetic forces (Lorentz loads) that need to be restrained.

The coil is a DC device, yet charge and discharge are usually accomplished through an AC utility grid, so that a power conditioning system (PCS) is required as the interface. The PCS can use a standard solid-state DC/AC converter to transfer power back between the superconducting coil and the grid/load.

HISTORY OF SMES DEVELOPMENT

Although superconductivity was not discovered until 1911, the idea of storing energy in the magnetic field of a coil is over a hundred years old, going back to the time of Nicola Tesla. Superconducting magnets as energy storage devices were proposed in the early 1960s. The use of SMES for a utility application (load-leveling) was first proposed in the late 1960s in France. In the U.S., research on SMES started in the early 1970s at the University of Wisconsin, and soon after at Los Alamos National Laboratory (LANL). A joint effort between LANL and Bonneville Power Administration (BPA) led to the design, construction, and testing of a 30 MJ (8.3 kWh)/10 MW SMES unit used on the Pacific Intertie transmission line operated by BPA to rid the line of unwanted sub-synchronous oscillations. The SMES unit built, by General Atomics, operated successfully for a year between 1983 and 1984. The BPA unit demonstrated the feasibility of the SMES concept for utility application. Industrial participation in the development of SMES started in the early 1980s, when Bechtel became involved with the technology through work with the Electric Power Research Institute (EPRI) and LANL.

In 1987, the Department of Defense (DOD) selected SMES as the only feasible power supply option for the ground-based free electron laser, which was under development as part of the Strategic Defense Initiative. The DOD launched the SMES Engineering Test Model (ETM) program to demonstrate the feasibility of the technology for the dual purpose of a power supply for military applications and energy storage for the utility industry. The SMES-ETM was designed to store 20 MWh (72 GJ), and deliver up to 400 MW.

Between 1987 and 1990 DOD, through the Defense Nuclear Agency (DNA), funded a design competition to develop a conceptual design for the SMES-ETM. Two design teams, one of which was led by Bechtel, were awarded contracts of approximately $15 million each over a 2.5 year period. When the SDI's free electron laser project was terminated the SMES-ETM program was halted. However, after a 2-year hiatus, DOD resumed the SMES development competition and awarded a total of $30 million as part of a program to reduce risks of the conceptual designs and to better define costs (the latter with EPRI support). Under DNA's sponsorship, the Bechtel Team recently completed this successful risk reduction program through component development and testing. As a result of this work, the Bechtel Team design has broken with prevailing thinking, and moved from using the earth to contain the electromagnetic forces to a self-supporting coil concept. The tremendous advantages of self-supported SMES are apparent in Figure 2. The result of this paradigm shift is a more reliable, affordable, marketable product, and a new path to technology demonstration.

DNA also conducted a Utility Application seminar to determine the ranges of energy and power for different applications. The results of this workshop are summarized in Figure 3. To assure low risk technology, DNA formed a Technical Review Committee (TRC) consisting of EPRI and recognized experts on superconductivity applications and chartered them with reviewing the design. In addition to reviewing the underground earth supported design, the TRC also conducted an in-depth review of Bechtel's above-ground self supporting coil design described in the next section.

SELF-SUPPORTING SMES DESIGN

The major elements comprising a self-supported SMES plant are shown in Figure 4. The proportions shown are for a 1 MWh/500 MW unit. The centerpiece is the superconducting coil, enclosed in a vacuum vessel to minimize heat loads to the helium cryogen. The power conditioning building houses the power conditioning system equipment required to interface between the electric power grid (and switchyard) and the coil. The switchyard is also part of this system. The cryogenics building houses the major components of the cryogenic and vacuum pumping systems that cool the coil, and the administration building houses offices and the control room.

All the magnetic forces to which the coil is subjected are reacted to by the coil structure itself, so that the system can be built above ground. Initially it was believed that large-scale SMES would only be economical with earth (warm) support. The present design, however, uses a strong cable-in-conduit conductor which allows for an efficient support structure. In this concept, a self-supporting coil is substantially cheaper than its earth-supported counterpart for stored energies up to 3,000 MWh. This is a major departure from prevailing thinking.

The added cost for coil material (alloy aluminum) in the self-supporting design are more than offset by cost savings through simplification and enhanced constructibility. Major systems and components are eliminated: trench, cold-to-warm supports, shield penetrations, coil attachments, associated instrumentation and parts, etc. The simplified self-supporting system is shown in Figure 5.

The self-supported design is also easier to construct, leading to cost reductions through shortened schedule and reduced risk. There are fewer parts to install and keep track of, construction is above grade, and the thermal shield system (a labor intensive item) is much easier to install due to less demanding tolerances and absence of complicated penetrations. The end result is a 30% cost reduction and a 25% reduction in construction schedule.

In addition to lower capital costs, the elimination of conduction losses through the cold-to-warm supports also reduces operating costs. As the coil is above ground, siting flexibility is excellent because soil conditions and water table considerations are completely removed.

The self-supporting SMES system is not only lower in risk, it is also very scalable. By changing the size of the conductor, the aluminum dump shunt/support, and pultrusion support/insulation member, the same basic design can be adapted for coils storing from 1 MWh to 1,000 MWh and more (see Figure 6). This scalability, and the reduced cost and risk of the self-supporting design define a new path for the demonstration and commercialization of SMES.

THE NEXT STEP: SMES-1

While the key components have been successfully manufactured and tested, demonstration of SMES technology as an integrated system is a prerequisite to broad acceptance and application by the utility industry. In addition to demonstrating SMES technical performance, it would provide the cost and schedule information needed to back future investment decisions by the utilities.

SDG&E and Bechtel are presently actively pursuing the formation of a consortium to design, construct, and operate a demonstration unit. The mission is to stimulate the development of a domestic SMES industry through a government, utility, and industry cost-sharing demonstration (SMES-1 prototype) program while simultaneously enhancing utility asset efficiency in the Southwest United States. Although still in its definition phase, SMES-1 is envisioned as a 1 to 3 MWh device, with a power capability of 500 MW, and connected to the grid in a transmission stabilization mode (the dimensions shown in Figure 4 roughly correspond to a 1 MWh coil and a 500 MW PCS). SMES-1 will be located at SDG&E's Blythe, California site and would increase simultaneous load-transfer operating limits by 8% for import of power to Southern California. The experience gained with this plant would advance SMES technology for other utility applications, providing such benefits as increased transmission capacity, voltage control, SSR damping, tie line control, spinning reserve, frequency control, energy storage (renewables), underfrequency load shedding reduction, and black start. The SMES-1 plan is fully responsive to DOE's national energy strategy which calls for the utility industry to meet the challenges of accommodating increased transmission system access, resulting in greatly increased complexity of control and protection without compromising reliability of service; accommodating the need to increase asset utilization while minimizing new capital investment through modernization and plant life extension and reliability-centered maintenance; automation of the energy delivery system for expanded customer services and full adoption of integrated resource/delivery planning and operation; integrating distributed generating resources that may not be utility-owned or -controlled; increasing the power transmission capability of existing right-of-way corridors to offset difficulties in siting new corridors; and incorporating energy storage technologies as a viable option.

Modular Transportable Superconducting Magnetic Energy Systems

Dennis Lieurance, Foster Kimball, and Craig Rix
Martin Marietta / Space Magnetics, San Diego, California

***Abstract*-Design and cost studies were performed for the magnet components of mid-size (1-5 MWh), cold supported SMES systems using alternative configurations. The configurations studied included solenoid magnets, which required onsite assembly of the magnet system, and toroid and racetrack configurations which consisted of factory assembled modules. For each configuration, design concepts and cost information were developed for the major features of the magnet system including the conductor, electrical insulation, and structure. These studies showed that for mid-size systems, the costs of solenoid and toroid magnet configurations are comparable and that the specific configuration to be used for a given application should be based upon customer requirements such as limiting stray fields or minimizing risks in development or construction.**

INTRODUCTION

Designs for superconducting magnetic energy storage systems have been under development for several decades as a means for providing efficient electric energy storage. Potential applications for these systems have ranged from small systems, similar in size to current laboratory magnets, providing power quality control to massive systems designed for diurnal load leveling capable of storing several thousand megawatt-hours. Until recently, the major focus for large scale design studies has been on low aspect ratio solenoids that have depended upon earth (or warm) support systems to react the radial Lorentz loads. This was because it has long been advocated that large-scale SMES can only be economical with earth (or warm) support [1]. This belief has driven the design of large scale systems and demonstrating earth supported systems was considered essential for engineering test models intended to demonstrate SMES technologies. However, recent cost studies have shown that the economical cross-over point for cold and warm supported designs is much higher than previously believed and that cold supported designs will be less expensive than warm supported designs for any application likely to be built in the foreseeable future. These cost studies have been based upon systems incorporating design and technology advancements made by Martin Marietta during the SMES-ETM program and have been confirmed using both parametric studies and point designs of systems designed for energy storage capabilities from 1 to 1,000 MWh [2].

The realization that demonstrating earth supported systems is not necessary, greatly increases the design flexibility and opportunities for cost savings on mid-size (1-5 MWh) SMES systems. For systems in this size range, magnet costs are driven more by fabrication and assembly operations than by material costs. Therefore, designs which can minimize labor costs and construction schedules through the use of standardized, factory assembled modules have the potential to become competitive with systems that are assembled in-situ. Design and cost studies were performed for the magnet components of mid-size (1-5 MWh), cold supported SMES systems using three alternative configurations. The configurations studied included solenoid magnets, which required on-site assembly of the magnet system, and toroid and racetrack configurations which consisted of factory assembled modules.

DESIGN REQUIREMENTS

The requirements for the SMES magnet system were based upon the data generated and lessons learned from the SMES-ETM program and from input from potential customers in the government and electric utility industry. These requirements were divided into two categories, system requirements and coil pack requirements. The system requirements included general system level objectives necessary to ensure that the design met technology and cost objectives. These requirements included demonstrating critical technologies for SMES, minimizing costs and risks, and developing a system that provides siting flexibility.

The coil pack requirements were more specific and included design criteria and constraints developed during the SMES-ETM program that directly affected the design of the magnet components. These requirements included the use of a high current (100 kA) cable-in-conduit conductor operating at 1.8 K and the use of a coil pack design which is self supporting and which is capable of absorbing the stored energy during an energy dump.

CONFIGURATION OPTIONS

The configurations studied included solenoid magnets, which required on-site assembly of the magnet system, and toroid and racetrack configurations which consisted of factory assembled modules. For each configuration, preliminary designs were prepared for various size coils ranging from 1 to 10 MWh of energy storage capability. A comparison between these configurations for a 1 MWh system is shown in Figure 1.

Solenoid Coil Description The solenoid coil pack consists of a two radial layer, helically wound coil as shown in Figure 2. The major components of the coil pack assembly include the conductor, dump shunt, and electrical insulation system. The dump shunt consists of an aluminum extrusion which provides the thermal mass necessary to absorb the stored energy during an energy dump and also provides the structural support for the axial and radial Lorentz loads. For a mid-size SMES, the cross-sectional area of the dump shunt is governed by the width required to install bolts at the field assembly joints. This results in the structure being oversized between joints so that structural stresses are relatively low. The area required for thermal mass purposes is lower than that required for structural purposes so there is a large thermal margin in the system as well.

The electrical insulation system serves to electrically insulate the conductor turns from each other and the ground. The primary insulation consists of a layer of Kapton tape wrapped around the assembled conductor and dump shunt. A layer of pre-impregnated fiberglass tape is wrapped over the Kapton to protect the Kapton from tears or abrasion. An outer case, consisting of precured and formed fiberglass components, serves to hold the layers of the coil pack together and also provides additional redundancy for electrical insulation purposes.

Each of the major components (conductor, dump shunt, and electrical insulation segments) is fabricated offsite and assembled into the coil onsite using field assembly joints and splices. This minimizes material usage but results in extensive onsite labor and inspection procedures.

Toroid Coil Description The toroid coil pack consists of 36 oval shaped modules approximately 14 feet wide by 47 feet long arranged in a circular configuration as shown in Figure 3. Each module consists of 16 conductor turns arranged in two layers. The primary electrical insulation consists of a layer of Kapton tape wrapped around the conductor turns. A layer of fiberglass tape is wrapped over the Kapton to protect the Kapton from tears or abrasion. This assembly is then vacuum pressure impregnated to form the conductor assembly.

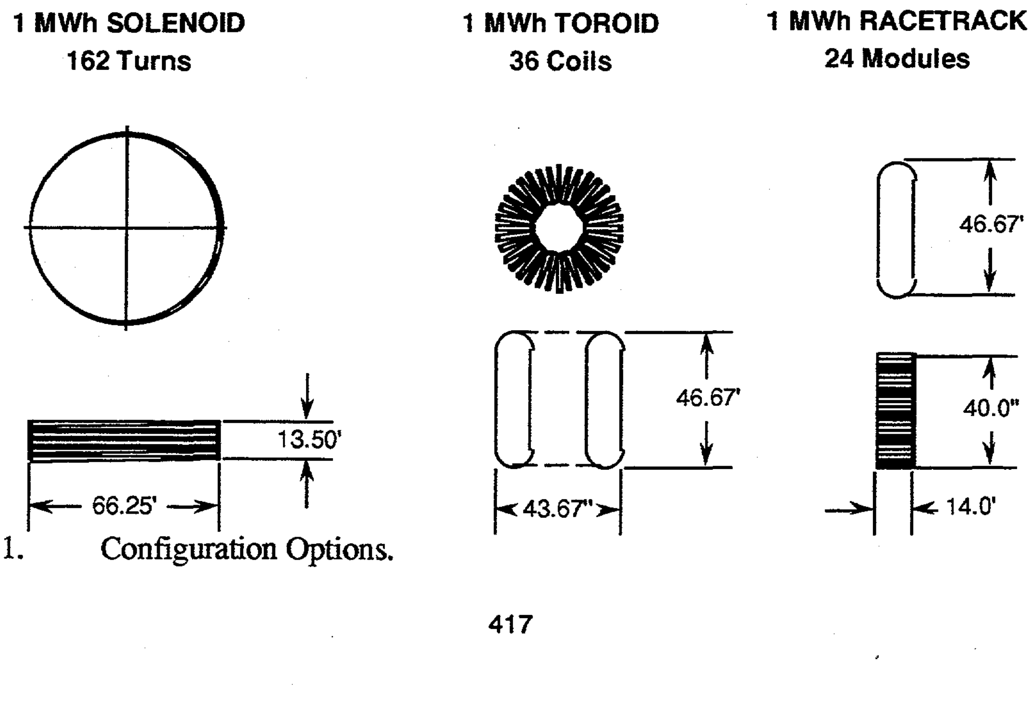

Figure 1. Configuration Options.

This conductor assembly is then placed into a structural case. The case consists of inner and outer leg segments. The inner leg case wall is designed to be wedged together with adjacent modules to form a bucking cylinder to react the inward Lorentz loads from the toroid. Tension straps running from the inner leg to the outer leg are used to react the outward Lorentz loads on the outer leg.

Each module is designed to be fabricated in a factory and then shipped to the site. Fabricating modules in the factory provides for a cleaner and more controlled environment for conductor and insulation fabrication, allows for the use of rate tooling and trained and experienced technicians, and improves quality assurance, including the capability for testing of the completed modules prior to shipping, when compared to the field assembly operations required for the solenoid.

Race Track Coil Description The race track coil pack consists of 24 racetrack modules approximately 14 feet wide by 47 feet long stacked on top of each other as shown in Figure 4. These modules are similar to the modules used for the toroid with modifications to the case walls to react the different Lorentz Loads.

COIL COMPARISON SUMMARY

The design studies demonstrated that all of the configuration operations were technically viable and were capable of satisfying the design requirements of demonstrating critical technologies for SMES, minimizing costs and risks, and developing a system that provides siting flexibility.

The critical superconducting magnet technologies for cost effective large SMES systems include high current cable-in-conduit conductors, 1.8 K helium operation, high voltage electrical insulation, and quench protection systems capable of handling the large amounts of stored energy. All of the configurations studied demonstrate these technologies. The major differences are in the design of the structure required to react the loading conditions which are unique to each configuration. However, the structural behavior of the materials and design configurations are well understood and are predictable using currently available technologies.

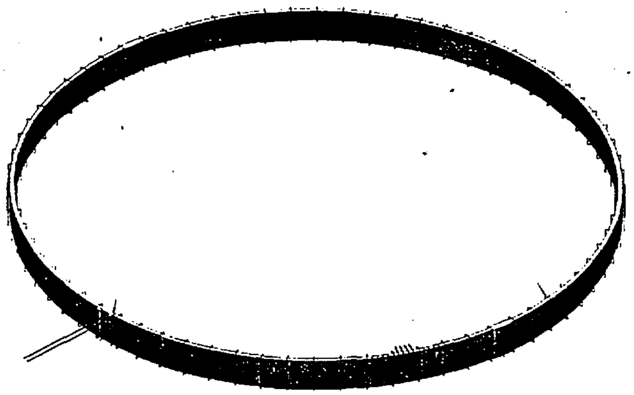

Figure 2. Solenoid Coil Configuration.

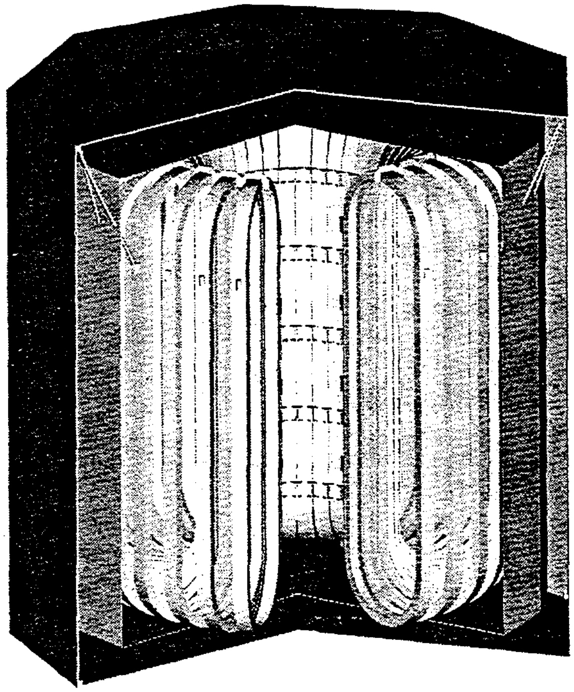

Figure 3. Toroid Coil Configuration.

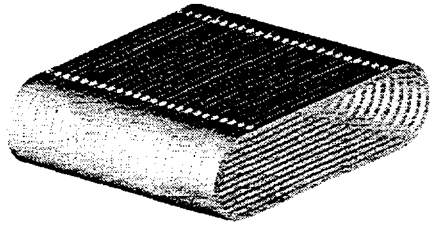

Figure 4. Race Track Coil Configuration.

Although the risks for any configuration are considered to be reasonable, the toroid and race track configurations offer advantages in several key areas. The first advantage is in technology demonstration. For a solenoid system, technology demonstration is limited to the component level and system verification requires a full scale unit. For a modular system, technology demonstration can be performed on full scale modules allowing critical design and manufacturing technologies to be fully verified before committing to a full-up system. The toroid magnets also utilize technologies which are common to other ongoing large superconducting magnet programs such as ITER and TPX. Developments in coil winding and electrical insulation technologies could be shared with those programs. The final difference in risk minimization is in the repairability of a production unit. The repair of a faulty section of a solenoid would require the removal and replacement of a large section which is essentially integral with adjacent components. The toroid and racetrack designs are based upon interchangeable modules which are only connected at a few carefully selected field assembly points

All of the configurations offer considerable siting flexibility in that they are free standing systems that do not require special soil conditions to react the magnetic loads. The major differences are in the stray field effects due to the magnet configurations. The solenoid and race track generate a field that requires a circle approximately 230 feet in radius before the 10 gauss limit is reached. the toroid generates almost no stray field and the 10 gauss limit is contained within the vacuum vessel.

The results of an analysis of the direct manufacturing costs of the different coil configurations are shown in Table 1. The costs ranged from $6.4M for the solenoid to $14.1M for the toroid. Additional analysis, which includes the effects of the reduced onsite construction time for the race track and solenoid and incorporates learning curve effects for multiple SMES units, is in the process of being performed. This analysis is expected to show that the total system cost difference is less than that shown when only magnet manufacturing costs are included. When compared to the total system cost, which is in the range of $60M-$70M, the differences in the costs between the solenoid and toroid magnets should not be the major factor in choosing the magnet configuration.

Table 1. 1 MWh Coil Cost Comparison.

	Solenoid	Solenoid RaceTrack	Toroid
Field Labor			
Cost	$1.4 M	$0.2 M	$0.3 M
Time	12 mo	3 mo	3 mo
Factory Labor	-	$2.0 M	$3.2 M
Material	$3.1 M	$6.1 M	$ 7.0 M
Conductor			
Cost	$1.9 M	$2.3 M	$ 3.6 M
Length	33,400'	40,600'	60,900'
TOTAL	$6.4 M	$10.6 M	$14.1 M

CONCLUSIONS

The study concluded that transportable, modular coils can be cost effective when considered as part of an ongoing business for SMES devices around 1 MWh. They are also effective in incrementally demonstrating the technologies required in larger scale devices. They offer the possibility of a lower risk demonstration device due to the ability to test single modules individually at cryogenic temperatures, prior to the entire array.

On the other hand, truck transportable modules are not particularly cost effective for constructing devices larger than 5 MWh, unless the transportation limits can be significantly increased by either exceeding normal truck/rail sizes or by limiting applications to barge accessible locations.

This study was funded by Martin Marietta.

REFERENCES

1 Verga, R.L., "SMES and other large-scale SDI cryogenic applications", Adv. Cryo. Eng., 1990, 35A.

2 Rix, C., et al, "A Self-Supporting Superconducting Magnetic Energy System (SMES) Concept", presented at the 15th International Cryogenic Engineering Conference.

Thin Films

Chair: Prof. Tomoji Kawai

Optimization of the Deposition Conditions and Structural Characterization of $Y_1Ba_2Cu_3O_{7-x}$ Thin Superconducting Films.

J. Chrzanowski, S. Meng-Burany, W. B. Xing, A.E. Curzon, B. Heinrich and J.C. Irwin, *Department of Physics, Simon Fraser University, Burnaby, B. C., Canada V5A 1S6.*

R. A. Cragg, H. Zhou, F. Habib, V. Angus and A. A. Fife, *CTF Systems, Inc., 15-1750 McLean Ave., Port Coquitlam, B.C., Canada V3C 1M9.*

ABSTRACT

Two series of $Y_1Ba_2Cu_3O_z$ thin films deposited on (001) $LaAlO_3$ single crystals by excimer laser ablation under two different protocols have been investigated. The research has yielded well defined deposition conditions in terms of oxygen partial pressure $p(O_2)$ and substrate temperature of the deposition process T_h, for the growth of high quality epitaxial films of YBCO. The films grown under conditions close to optimal for both j_c and T_c exhibited $T_c \geq 91$ K and $j_c \geq 4 \times 10^6$ A/cm^2, at 77 K. Close correlations between the structural quality of the film, the growth parameters ($p(O_2)$, T_h) and j_c and T_c have been found.

1. Introduction.

There are several technological difficulties which occur in the growth of high-T_c films regardless of the deposition technique. These involve optimization of the oxygen partial pressure, the substrate temperature, the substrate surface preparation, the laser beam energy density, cooling procedure, etc. Moreover the deposition of superconducting oxides is further complicated because of the multielemental structure of the compounds and their sensitivity to film cation-composition [1] and oxygenation [2] which substantially influence both the superconducting properties and morphology of the film [1, 2]. These observations clearly manifest the importance of a precise and reliable control of the growth parameters of copper oxide superconducting films.

To investigate the many growth parameters the precise control of the oxygen pressure, $p(O_2)$, and substrate temperature, T_h, must be identified first. The aim of the present research was thus twofold: 1) Optimization of the deposition conditions for the growth of epitaxial films with the highest j_c and T_c, exhibiting simultaneously the best morphology. 2) Structural characterization of the film and a search for correlations between the structural and superconducting properties of the film.

2. Experimental.

Thin films of YBCO were prepared by laser deposition using a YBCO target and pulsed excimer laser. The substrates used were $LaAlO_3$ (001) single crystals which possess a lattice spacing a = 3.79 Å, which is closely matched to the a-b plane spacing of YBCO. A Lambda Physik LPX 2051 excimer laser with $\lambda = 248$ nm (KFr) operated at a repetition rate of 5-10 Hz, and at a fluence of 1.5 J/cm^2 was used. The illuminated area was 4 x 2 mm^2, and the laser was equipped with special electrodes to improve the beam profile uniformity. Two similar systems were used to obtain films fabricated under the two different protocols. In protocol 1 (film series 1), a constant temperature of the substrate heater was maintained (T_h = 820 °C) while the oxygen partial pressure in the deposition chamber was variable ($50 < p(O_2) < 300$ mTorr). In protocol 2 (film series 2), a constant pressure of oxygen was maintained ($p(O_2) = 200$ mTorr), while the temperature of the heater was variable ($740 < T_h < 820^o$ C).

For protocol 1 the target holder was a Kurt J. Lesker Co, Polygun system which holds up to six 2.5 cm diameter targets in a hexagonal carousel rotated under computer control synchronized with the laser firing. In protocol 2, a single YBCO target was rotated around the axis normal to the target face. In both systems the separation between the target and the substrate was the same; s = 5 cm.

After deposition using either protocol the films were cooled slowly (5^o C/min) down to room temperature in 600 mTorr of oxygen. The resulting film thickness was 3000 Å. The films were very smooth exhibiting a mirror-like appearance. Microscopic observations, however revealed the existence of numerous pinholes (of sub-micron size) which apparently did not affect j_c and T_c in the films.

Application of the two different deposition protocols enabled us to explore regions in the $p(O_2)$ vs. 1/T phase diagram of YBCO situated close to the YBCO stability line, Fig. 1, which according to previous reports [3-5] represent the most promising regime for the growth of high quality YBCO films.

To obtain the best conditions for the film growth in terms of the oxygen pressure and the substrate temperature during the film deposition, the phase diagrams $p(O_2)$ versus 1/T for YBCO by Bormann, Hammond and Noelting (B-H-N) [3,4] and by Beyers and Ahn [5] were used for a starting point in the studies presented in this paper. However, one has to remember that the specific conditions for film growth may vary between different systems and methods of film deposition.

In Fig. 1 the continuous dark line denotes the most recent [5] thermodynamical stability line for tetragonal YBCO, while the discontinuous one represents a previous stability line [3,4] and is shown only for comparison. We will discuss our results with regard to the new stability line. The critical current density, j_c, and the critical temperature, T_c, were determined by an inductive method [6]. The width of the superconducting phase transition was $\Delta T_c \sim 0.5K$.

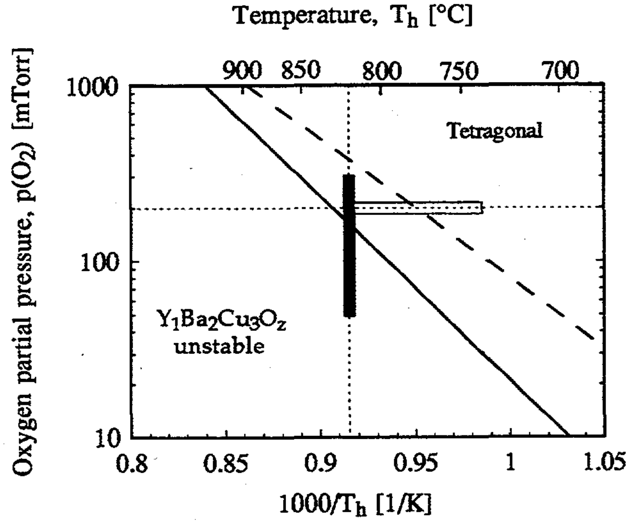

Fig. 1. Graph of oxygen partial pressure $p(O_2)$ versus temperature T showing the critical stability line for tetragonal $Y_1Ba_2Cu_3O_z$ ($z = 6.0$), according to recent data (Ref. 5); continuous line. The old stability line published by Bormann, Hammond and Noelting (Ref. 3 and 4) is also shown for comparison as a broken line. The black and white areas denote the p-T phase space where series 1 and 2 were grown, respectively.

3. Results and discussion.

3.1. Optimization of the growth conditions.

The measurements of T_c and j_c as a function of the oxygen partial pressure $p(O_2)$ and the substrate temperature T_h are presented in Figs. 2 and 3. It is interesting to note that while the critical temperature appears to be a monotonic function of $p(O_2)$ and T_h, the critical current density j_c in the films in both series exhibits a distinct maximum as a function of $p(O_2)$ or T_h. The highest T_c was 90 K in series 1 (variable oxygen pressure), and 92 K, in series 2 ($p(O_2) = 200$ mTorr), while maxima of j_c were 3.4 and 4.5 x 10^6 A/cm^2, respectively. On average both parameters, T_c and j_c, were somewhat higher in series 2, though the differences in j_c remained practically within the limits of experimental errors of j_c (± 10%). As can be seen in Figs. 2a and 3a, the critical temperature T_c was observed to rise with an increasing oxygen partial pressure $p(O_2)$, approaching a saturation value of 90 K for $p(O_2) > 200$ mTorr. However when the substrate temperature T_h was increased from 740 to 820 °C, at $p(O_2) = 200$ mTorr, a systematic decrease in T_c from 92 to ~88 K was observed. In both film series $p(O_2)$ and T_h moved in the phase diagram in the directions above and to the right of the stability line.

Figures 2 and 3 showed that the highest values of T_c and j_c do not occur under the same deposition conditions. Note that the highest values of j_c (Figures 2b and 3b) occur in the vicinity of the stability line of tetragonal YBCO where less perfect crystalline structure can be expected.

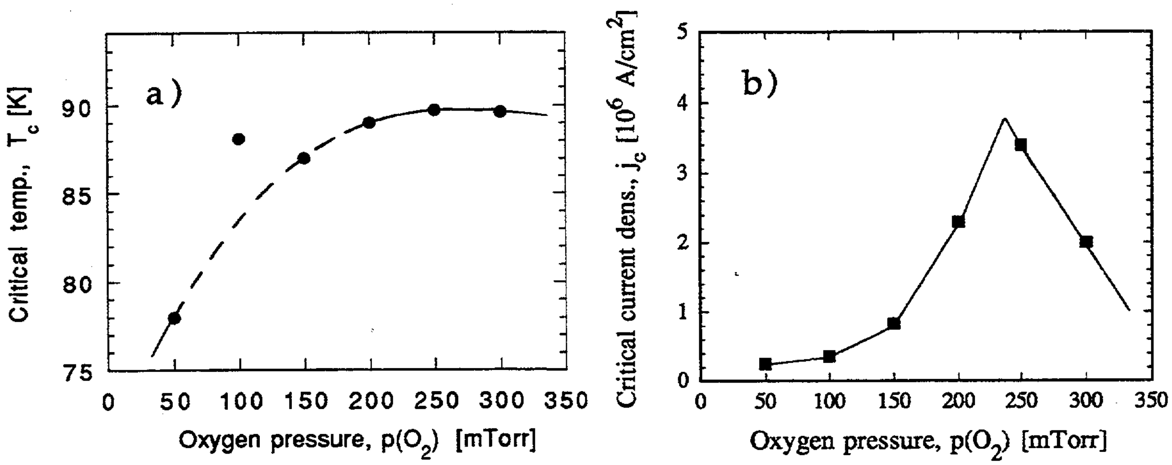

Fig. 2. Critical temperature T_c (a) and critical current density j_c (b) as functions of the oxygen pressure during film deposition (protocol 1).

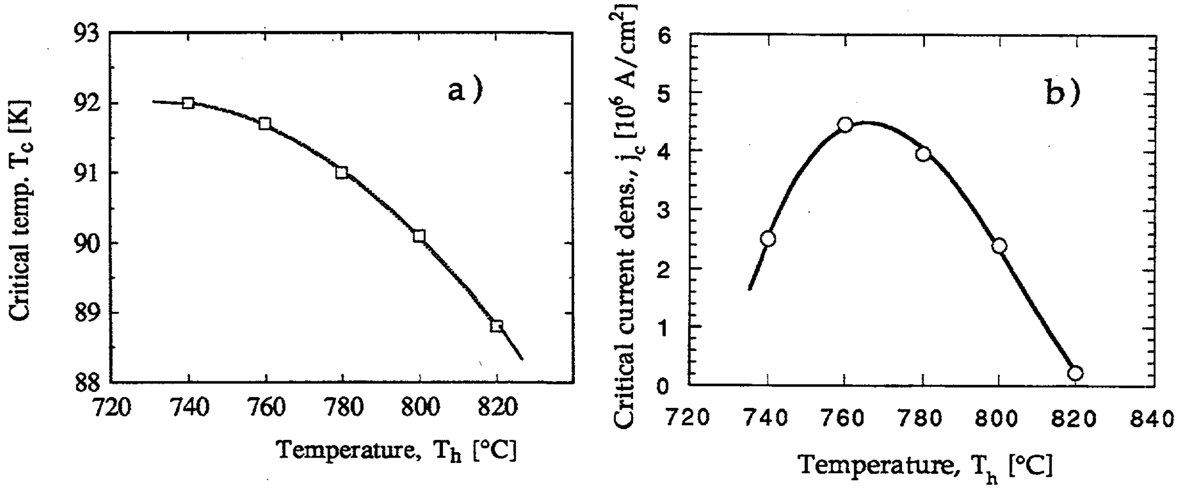

Fig. 3. Critical temperature T_c (a) and critical current density j_c (b) as functions of the film deposition temperatutre T_h (protocol 2).

3.2 Structural Characterization of Films.

Structural characterization of film series 1 and 2 have been carried out employing X-ray diffraction (XRD), scanning elecron microscopy (SEM), energy dispersive analysis of X-rays (EDAX) and Raman spectroscopy.

A typical X-ray pattern of a YBCO film belonging to series 2 is presented in Fig. 4. It is evident that only (00ℓ) Bragg reflections are present indicating a highly c-axis oriented texture. The (00ℓ) lines behaved in a similar manner and therefore only the changes in the (005) line were used to characterize the films. The intensity ratio of the (005) X-ray peaks with respect to the background, for the films deposited under conditions close to optimal, was in excess of 2000. When the ratio of the count rate I(005)/background increased above ~1000, it was possible to observe the splitting of the $K\alpha_1$ and $K\alpha_2$ Copper X-ray doublet. The peak half-width for an individual $K\alpha$-line reflection was observed to be $\Delta(2\theta) = 0.07^\circ$, which indicates excellent crystallinity in the film. A corroboration of the structural perfection was provided also by measurements of the mosaic spread and electron channeling patterns. The in-plane epitaxy, was also investigated by using Raman spectroscopy [7]. The Raman measurements showed that the degree of the epitaxial growth occured over 82 to 95% of the sampled area.

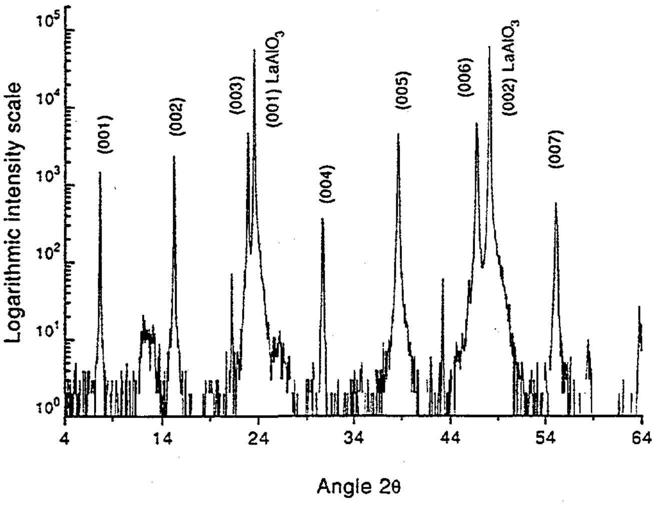

Fig. 4. A typical x-ray pattern for a film from series 1. $T_c = 89.6$ K, $j_c = 2 \times 10^6$ A/cm^2.

The elemental composition of the films determined from EDAX measurements was approximately constant and the average metal content was in the ratio Y : Ba : Cu = 1.14 : 1.57 : 3.00, indicating that Ba-deficient films were grown.

Rocking curve measurements of the (005) peaks performed for both series of films showed that their half-widths did not exceed $\Delta\omega = 0.6^o$. The best films exhibited a small mosaic spread, $\Delta\omega \sim 0.20^o$ [8]. In Fig. 5 the dependence of $\Delta\omega$ as a function of $p(O_2)$ is shown. Clearly a rapid narrowing in the line-width occurs when the oxygen pressure rises above ~150 mTorr. This behaviour indicates a sensitivity of the film structure to the oxygen partial pressure and very likely corresponds to the isotherm $T_h = 820\ ^oC$ crossing the stability line in the YBCO phase diagram [5], see also Fig. 1. For $p > 200$ mTorr, the mosaic spread in the films was roughly constant.

The growth carried out above the stability line results in a marked improvement of the superconducting parameters. While the changes in T_c are small (~2 K), the critical current density rises almost by a factor of 3 with an increase of the oxygen pressure from 150 to 200 mTorr. A further increase of the oxygen pressure to 300 mTorr leads to added improvement of the film structure ($\Delta\omega = 0.22°$), but simultaneously the decrease of critical current, apparently due to a reduction of the number of flux pinning sites.

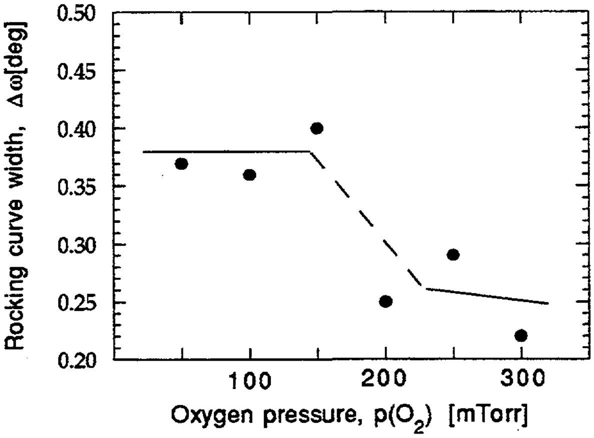

Fig. 5. Rocking curve width of the (005) x-ray reflections plotted against oxygen pressure in the deposition system during film growth, $T_h = 820°C$.

In series 2 the mosaic spread was constant at $\Delta\omega = 0.25° \pm 0.03°$. This value is very close to that observed in film series 1 which were grown above the stability line ($p(O_2) > 150$ mTorr). The maximum in j_c for film series 2 appeared at $T_h = 760\text{-}770\ °C$, see Fig. 3. Since the mosaic spread was nearly constant in series 2, one can argue that the variations in j_c were caused by changes in the film cation-composition. The critical current density j_c has been found to be a very sensitive function of the film-cation composition [1]. Very small variations ($\pm$ 0.01-0.02) in the Cu content (metallic fraction Cu/(Y + Ba + Cu)) resulted in a 5 fold decrease of j_c [1]. Our EDAX measurements for the films of series 2 showed, in fact, small systematic variations in the Cu/(Y + Ba + Cu) and Ba/Y ratios. They were found to change from 0.51 to 0.54 and from 1.32 to 1.41, respectively. It is therefore possible that variations in the measured cation concentrations may account for a constant width of the rocking curves and for the simultaneous occurence of a maximum in j_c at 760-770°C, Fig. 2. Contrary to the behaviour of j_c the critical temperature is a much weaker function of the Cu content [1]. A more extensive discussion of the effect of changes in metal composition on the structural and superconducting properties of YBCO films will be presented elsewhere [9].

In film series 1 the c-axis length was observed to correlate directly with the oxygen partial pressure, indicating a linear shortening of the c-axis with increasing oxygen partial pressure. It changes from c=11.75 Å (at 50 mTorr) to 11.66 ± 0.01 Å, (at 200 mTorr), Fig. 6. For pressures $p > 200$ mTorr the c-axis length remains approximately constant.

In film series 2, changes in T_h had a rather limited effect on the c-axis length up to 800°C. As can be seen in Fig. 7 a small shortening of the c-axis length (~0.02 Å) occured in the temperature range from 740 to 800°C. The Raman measurements on films of series 2 showed that the O(4) vibration frequency changed very little from 500 cm^{-1} (at 740 °C) to 503-504 cm^{-1} (at 780-800°C). These results also indicate that varying T_h from 740 to 800K changes the oxygenation of the films insignificantly [10]. The frequency range of the O(4) vibrations (≥ 500 cm^{-1}) indicates that the films grown below 800°C were practically fully oxygenated, that is the oxygen content was ≥ 6.9 [10]. Above 800 °C, an elongation of the c-axis length seems to occur, likely because of a smaller oxygen uptake at this temperature and this pressure (in the vicinity of the stability line). Indeed Raman measurements showed a small decrease of the O(4) vibration frequency from ~504 cm^{-1} in films grown at 780°C to 500 cm^{-1} in those grown at 820°C, which may indicate some

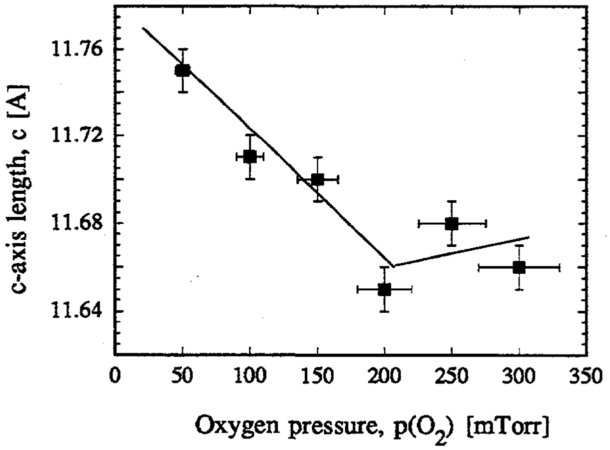

Fig. 6. C-axis parameter, c_0, as a function of the oxygen pressure during film deposition.

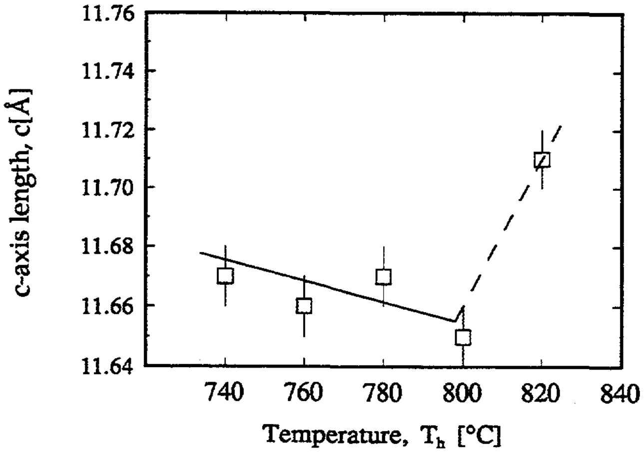

Fig. 7. C-axis parameter, c_0, as a function of the temperature of the film deposition, T_h.

oxygen loss. Fig. 8 shows that at a constant oxygen pressure of 200 mTorr, the c-axis length reaches its minimum for T_h close to 780°C (± 20°C) yielding $c = 11.66 \pm 0.01$ Å.

Close correlations have also been observed between the c-axis length and the T_c and j_c parameters in the films grown in series 1 and 2. Maxima in both T_c and j_c appear when the lattice parameter $c_0 = 11.66$-11.68 Å, see Fig. 8 and 9. In film series 1 (variable oxygen pressure) T_c apparently passes through a maximum as a function of c_0 whose value changes due to the change in oxygen content. A decrease of T_c by ~1K seems to occur for the highest pressure (300 mTorr). This observation seems to be in agreement with other reports [11], showing that the maximum of T_c in $Y_1Ba_2Cu_3O_z$ takes place for the oxygen content $z = 6.93$ (±0.02), not $z = 7.00$. The dependence of T_c versus c-axis length presented in Fig. 9 can be approximated by a quadratic function, which is very similar to

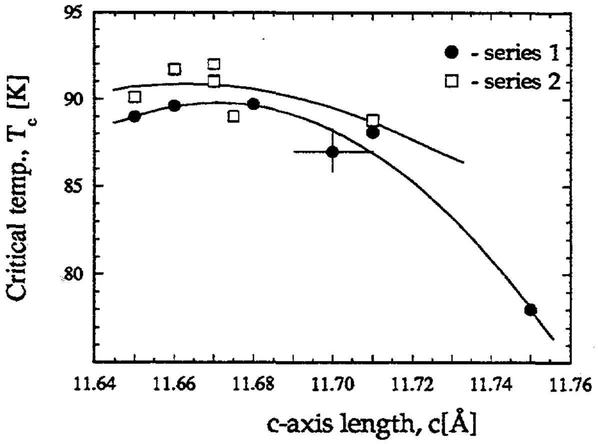

Fig. 8. Critical temperature T_c of the YBCO films grown at a constant oxygen pressure (open squares) and constant temperature (black circles) as a function of the lattice parameter c_0.

that illustrating the dependence of T_c on hole concentration (h+) per CuO_2 plane, induced either by chemical substitutions [12] or the oxygen content [13, 14].

The films from series 2 (variable T_h) exhibited relatively small changes in c_0 which is consistent with small variations in T_c (~2K), see Fig.8. These changes in T_c due to variations in c_0 are very likely caused by small systematic changes in the film cation composition as discussed above. However, the critical current density is very sensitive even those small changes in c_0, see Fig.9. This observation is in agreement with other reports [1] and will be discussed in detail elsewhere [9].

The EDAX measurements showed that the shortest c_0 occurred for Ba-deficient, but Y-rich films. The highest values of T_c and j_c were observed in off-stoichiometric (Ba-deficient, Y rich) films ($Y_{1+x}Ba_{2-y}Cu_3O_z$; x = 0.11-0.18, y = 0.32-0.43). This observation is in good agreement with a Stanford group report [15], where the Ba/Y ratio for the highest T_c was observed to be about 1.4. This value is almost identical with that found in our EDAX measurements (Ba/Y = 1.61/1.15 = 1.4). The Stanford group [15] also found that a large number of Y for Ba substitutions resulted in a significant presence of point defects which act as effective flux pinning centres [16]. Also Y for Ba substitutions may lead to some shortening of the c-axis length. In our fully oxygenated films, the c-axis length is 11.66 Å, as compared to the ideal value of 11.6802 Å [13].

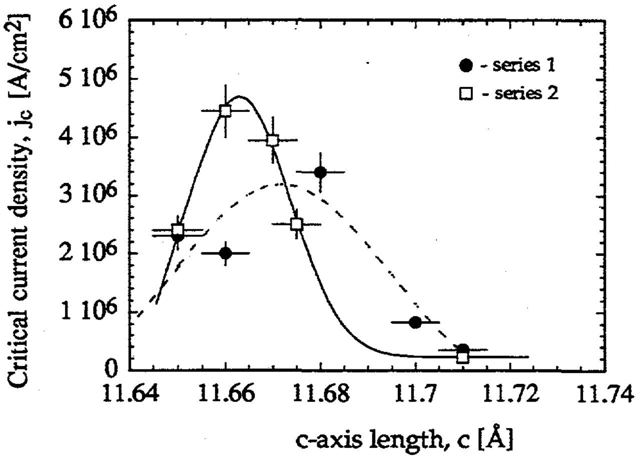

Fig. 9. Critical current density j_c in the YBCO films grown at a constant oxygen pressure (open squares) and constant temperature (black circles) as a function of the lattice parameter c_0.

4. Conclusions

Application of two different deposition protocols enabled us to explore regions in the phase diagram (oxygen pressure $p(O_2)$ vs. growth temperature (T_h) of YBCO films situated close to its stability line. The films with the best structure were grown above and to the right of the stability line, i.e. toward the interior of the stability region for YBCO, and those films also exhibited the highest critical temperature T_C. In contrast the highest j_C (up to 4.5 x 10^6 A/cm^2) occured in films grown in the vicinity of the stability line, where T_C was 1-2 K lower than the maximum value observed in this work. These results indicate that our best epitaxial films approach the structural quality of single crystals where the critical current density is low because of reduced density of flux pinning sites.

It is thus clear that the best conditions for optimum T_c do not result in samples with the highest j_c. The fabrication of films with both high T_c and j_c therefore requires some sort of compromise between structural perfection (high T_c) and the presence of crystallographic defects (high j_c).

Acknowledgments

The financial support of National Science and Engineering Council of Canada (NSERC), Industry Canada (STP-AIM Program), BC Ministry of Employment and Investment, and Furukawa Electric Co., is gratefully acknowledged.

References

[1] N.G. Chew, S.W. Goodyear, J.A. Edwards, J.S. Satchell, S.E. Blenkinsop, and R.G. Humphreys, Appl. Phys. Lett. **57**, 2016(1990).
[2] R. Feenstra, T.B. Lindemer, J.D. Budai, and M.D. Galloway, J. Appl. Phys. **69**, 6569(1991).
[3]. R. Bormann and J. Noelting, Appl. Phys. Lett., **54**, 2150(1989).
[4] R.Hammond and R. Bormann, Physica C **162-164**, 703(1989).
[5] R. Beyers and B.T. Ahn, Annu. Rev. Mater. Sci. **21**, 335(1991)
[6] W.B. Xing, B. Heinrich, J. Chrzanowski, J.C. Irwin, H. Zhou, A. Cragg and A.A. Fife, Physica C **205**, 311(1993).
[7] C. Thomsen, and R. Wegerer, H.-U. Habermeier and M. Cardona, Sol. St. Commun. **83**, 199(1992).
[8] J. Chrzanowski et al, this conference.
[9] J. Chrzanowski et al., to be published.
[10] R. M. Macfarlane, H.J. Rosen, E.M. Engler, R.D. Jacowitz, and V.Y. Lee, Phys. Rev. B **38**, 284(1988).
[11] A. Altendorf, X.K. Chen, J.C. Irwin, R. Liang and W.N. Hardy, Phys. Rev. B **47**, 8140(1993).
[12] J. J. Neumeier and H. A. Zimmermann, Phys. Rev. B **47**, 8385(1993).
[13] J.D. Jorgensen, B.W. Veal, A.P. Paulikas, L.J. Nowicki, G.W. Crabtree, H. Claus, and W.K. Kwok, Phys. Rev. B **41**, 1863(1990).
[14] e.g.J.L. Tallon and G.V.M. Williams, J. Less- Common. Metals **164 & 165**, 70(1990), and references cited therein.
[15] V. Matijasevic, P. Rosenthal, K. Shinohara, A.F. Marshal, R.H. Hammond, and M.R. Beasley, J. Mater. Res. **6**, 682(1991).
[16] T.L. Hylton, and M.R. Beasley, Phys. Rev. B **41**, 11669(1990).

GROWTH AND ANALYSIS OF HIGHLY ORIENTED (11n) BCSCO FILMS FOR DEVICE RESEARCH

K. K. Raina and R. K. Pandey, Center for Electronic Materials, Electrical Engineering Department, Texas A&M University, College Station, TX 77843-3128, U.S.A

ABSTRACT

Films of BCSCO superconductor of the type $Bi_2CaSr_2Cu_2O_x$ have been grown by liquid phase epitaxy method (LPE), using a partially closed growth chamber. The films were grown on (001) and (110) $NdGaO_3$ substrates by slow cooling process in an optimized temperature range below the peritectic melting point (880 ^{0}C) of $Bi_2CaSr_2Cu_2O_8$. Optimization of parameters, such as seed rotation, soak of initial growth temperature and growth period results in the formation of 2122 phase BCSCO films. The films grown at rotation rates of less than 30 and more than 70 rpm are observed to be associated with the second phase of Sr-Ca-Cu-O system. Higher growth temperatures (>860 °C) also encourage to the formation of this phase. XRD measurements show that the films grown on (110) $NdGaO_3$ have a preferred (11n)-orientation. It is pertinent to mention here that in our earlier results [1] published elsewhere we obtained c-axis oriented $Bi_2CaSr_2Cu_2O_8$ phase films on (001) $NdGaO_3$ substrate. Critical current density is found to be higher for the films grown on (110) than (001) $NdGaO_3$ substrate orientation. The best values of zero resistance (T_{co}) and critical current density obtained are 87 K and 10^5 A/cm^2, respectively.

INTRODUCTION

Various growth techniques have been reported for Bi-Ca-Sr-Cu-O superconducting films. Most of these investigations deal with the growth of high quality c-axis oriented epitaxially grown films [1-5]. The intrinsic anisotropic properties of Bi-Ca-Sr-Cu-O superconducting system (i.e. the coherence length of about 2 °A along the c-axis and 24 °A in the a-b plane) leads to the growth kinetics resulting in the formation of (00n)-orientated films. However, a film with (00n)-orientation is unsuitable for the fabrication of Josephson tunneling junctions. It is because of the fact that coherence length along c-axis is too short to obtain a Josephson effect. For this reason it is important to grow (11n)-oriented high-T_c superconducting films. Furthermore, the epitaxial nature of these LPE grown films make them attractive for many other devices including IR photodetectors, microwave resonators and integrated structured devices.

Recently, (11n)-oriented superconducting BCSCO films have been grown by the MBE [6] and MOVCD [7-8] techniques. MgO [7] and $SrTiO_3$ [6,8] have been used to grow such films. However, there has been no attempt made to grow (11n)-oriented BCSCO films by the LPE method. Also there has been no report so far on the (11n)-oriented film of BCSCO using $NdGaO_3$ substrate although it has been used to grow (11n)-oriented YBCO (123) epitaxial films [9].

In this paper we report the growth of (11n)-oriented $Bi_2CaSr_2Cu_2O_8$ films on (110) $NdGaO_3$ substrate. Optimization of various growth conditions which lead to the formation of 2122 phase are described and discussed. Formation of the second phase observed during the process of optimization is also described.

EXPERIMENTAL

The experimental arrangement of the LPE apparatus consists of a resistively heated furnace having facility for translation and rotation of seed. A partially closed growth chamber in the form of a platinum crucible embedded in an alumina blanket and further placed in an alumina crucible is used for the growth of BCSCO films. The alumina crucible is covered at the top by an alumina plate with a central hole of about 1 cm. for passing through the seed rod. The details about charge preparation of BCSCO and the method of film preparation are same as reported by us [1].

Transport resistivity and critical current density measurements were made by standard four-probe method using gold electrodes. Electrodes were made by sputtering gold and silver epoxy was used to embed the silver wires on the samples. A 10 μV/mm electric field criterion was used to measure the critical current density.

RESULTS AND DISCUSSION

Table 1 illustrates the optimization of the growth conditions for single 2122 phase of BCSCO films. It is well known that on melting (885 °C) $Bi_2CaSr_2Cu_2O_8$ splits into sub-

Table 1. Growth parameters leading to single and mixed phase formation of 2122 BCSCO films.

Growth parameters	1st soak		2nd soak		Seed rotation rpm	Growth temp °C	Charge preparation of BCSCO	Remarks
	Time hrs	Temp °C	Time hrs	Temp °C				
Optimized growth parameters for 2122 phase formation	12	925	4-5	855-860	50-70	855-835	900 °C for 1 hr	DF(5)* CF(15)**

*DF(5) = Discontinuous film for the growth time of 5 hours
**CF(15) = Continuous film for the growth time of 15 hours

phases. Therefore, in order to form a single phase 2122-BCSCO and to avoid intergrowth of sub-phases various growth parameters as described in table 1 have to be optimized. It is observed that seed rotation of more than 70 and less than 30 rpm encourage the formation of secondary phases in the film. Similarly, the second soak of about 4-5 hours is necessary to allow maximum reformation of 2122 phase in the molten solution. It is important that the second soak be carried out below the peritectic melting point of $Bi_2CaSr_2Cu_2O_8$ phase. Charge preparation of BCSCO also plays a crucial role in the formation of 2122 phase films. Fig.1 shows resistivity versus temperature relationship of films grown from different charge preparations. Judging by the T_{co} at 85 K, it is observed that the charge preparation at 900 °C for one hour is conducive for the growth of 2122 films. The best supersaturation conditions leading to the formation of 2122 phase and elimination of second phase are found in the temperature range of 855-835 °C. This fact is demonstrated in graph of resistivity versus temperature shown in Fig.2. The T_{co} for the film grown under supersaturated conditions is 87 K; whereas for the one grown in undersaturated conditions it is about 70 K. The same inference is derived from the Fig.3 (J_c versus temperature) where J_c is observed to be almost 3 times higher for the film grown under supersaturated conditions than the film grown in undersaturated conditions.

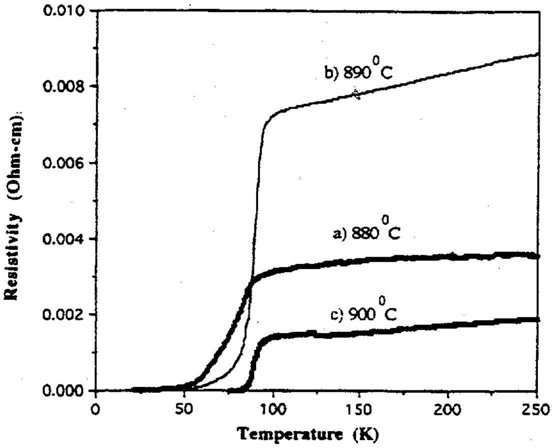

Fig.1. Resistivity versus temperature of BCSCO films under different charge preparation conditions.

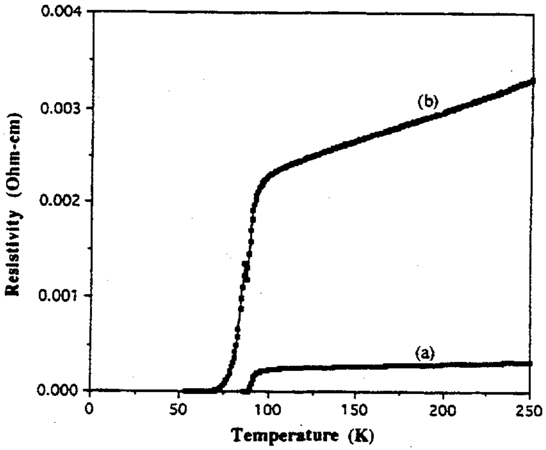

Fig.2. Resistivity versus temperature of BCSCO films grown between a) 855-835 °C and b) 845-825 °C for 15 hours growth period.

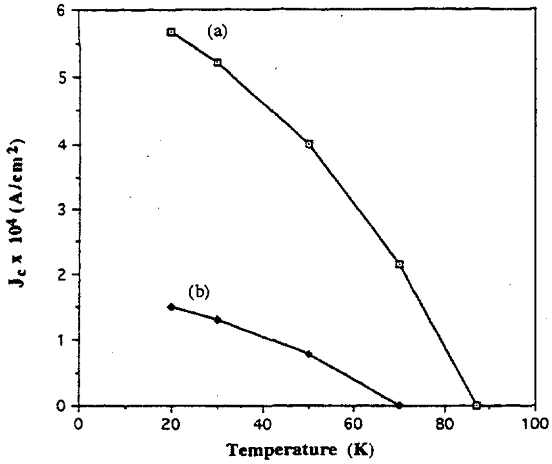

Fig.3. J_c versus temperature relationship of 2122 film grown between a) 855-835 °C and b) 845-825 °C for 15 hours growth period.

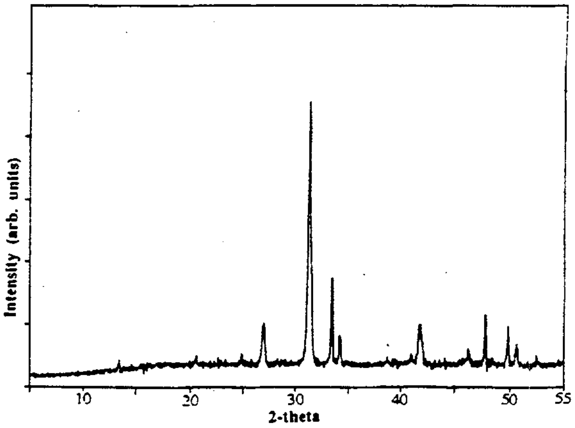

Fig.4. XRD pattern of the needle crystals belonging to the family of $(Ca_{1-y}Sr_y)_{1-x}CuO_{2-z}$ system.

As mentioned above the second phase of BCSCO is formed under certain growth conditions. Fig.4 shows an XRD graph of such a phase. This phase is observed to be associated with $(Ca_{1-y}Sr_y)_{1-x}CuO_{2-z}$ [10] family of infinite layer superconductors which exhibit superconductivity only under high pressure and for a specific composition. The EDAX analysis of this phase confirms the presence of Ca, Sr, Cu and O elements. This phase grows on the $NdGaO_3$ substrate as well as along the walls of the platinum crucible with different morphologies. Fig.5 shows a scanning electron micrograph of this phase grown in the form of needle crystals. The resistivity of one of these needles shows a semiconducting behavior which is in agreement with the reported literature[11]. The resistivity of these needles below 50 K almost becomes insulating in nature. These needles have a thickness between 10-50 micron and get cleaved easily. Fig.6 illustrates the same phase grown on (110) $NdGaO_3$ substrate. Here the morphology is in the form of clusters. The difference in the morphology can be understood by the fact that the nucleation takes place at two different surfaces i.e. platinum wall for needle shape crystals and a smooth surface of substrate for cluster type formation.

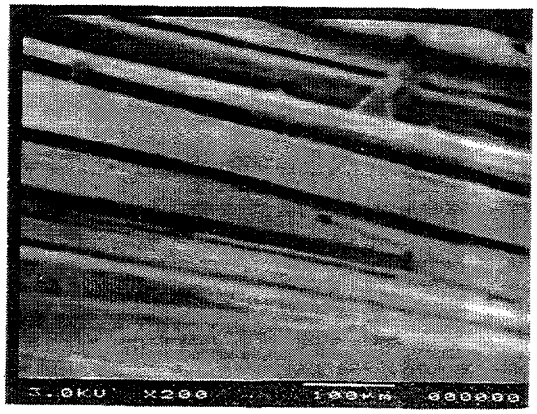

Fig.5. SEM showing the needle morphology of the crystals of $(Ca_{1-y}Sr_y)_{1-x}CuO_{2-z}$ system.

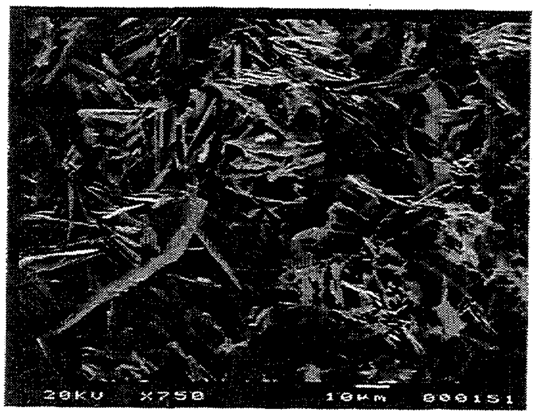

Fig.6. SEM showing cluster type morphology of the Bi-Ca-Sr-Cu-O sub-phase grown on (110) $NdGaO_3$.

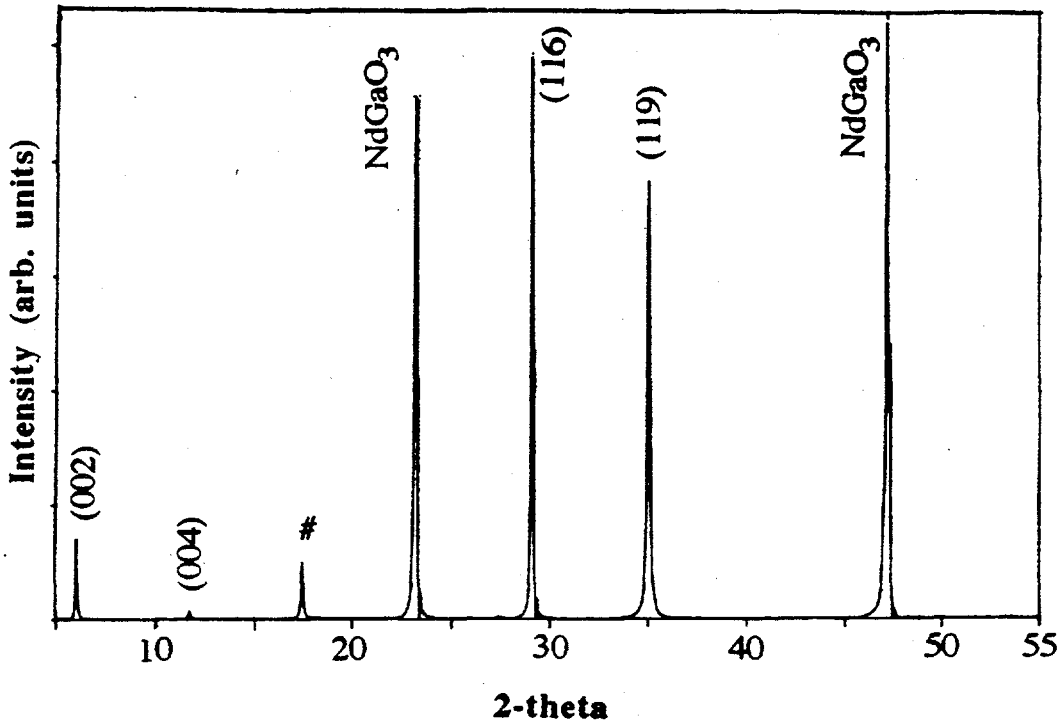

Fig.7. X-ray powder diffraction graph of 2122 phase BCSCO film grown on (110) $NdGaO_3$ substrate. The symbol # stands for unidentified.

Fig.7 shows an XRD pattern of a BCSCO film grown on (110) $NdGaO_3$ substrate. The figure shows the strong presence of (116) and (119) plane orientations. Assuming the well established values of lattice constants i.e. a=5.40, b=5.42 and c=30.81, the theoretical value of (119) orientation comes out to be 2.551 ('d' value) which is very close to the experimental value of 2.558. Similarly, the theoretical and experimental values for (116) orientation are 3.067 and 3.065, respectively. There is the possibility that (116) plane may be mistaken due to its proximity to (0010) orientation. But analyzing on the basis of authentic lattice constants reported in the literature, the closest possible match in terms of 'd' spacing is in favor of (116) orientation only. Moreover, by comparing with our earlier results [1] of c-axis oriented LPE films of BCSCO, it is clear that the major peaks in the Fig.7 can be attributed to (116) and (119) orientations. So far, (110) [7], (117), (118) and (119) [6,8,12] orientations have been reported in the literature for 2122 phase of BCSCO superconducting films using MgO and $SrTiO_3$, respectively. As indicated in Fig.7 there are two major peaks due to $NdGaO_3$ substrate. Two smaller peaks of (002) and (004) are also present. While the (11n)-orientations are influenced by epitaxy of (110) $NdGaO_3$ substrate, the (00n) planes result due to the anisotropic growth kinetics of the Bi-oxide superconducting system. Fig.8 is a backscattered SEM of (11n)-oriented grown 2122 phase film of BCSCO. The texture of the film is observed to be smooth. The particles in the figure are those of KCl flux. Fig.9 shows the relationship between critical current density (J_c) and temperature for the films grown on (001) and (110) orientations of the $NdGaO_3$ substrates. The value of J_c at 20 K for the film grown on (110) substrate orientation is about 1.5 times of the film grown on (001) substrate. The higher value of J_c for the film having (11n) preferred orientation may be because of the depairing mechanism (of J_c) where shorter coherence length of the c-axis contributes to higher critical current

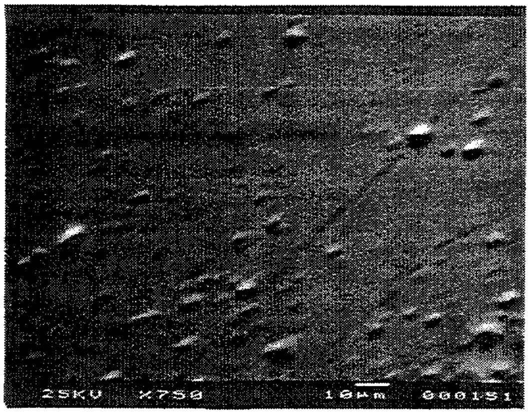

Fig.8. Backscattered SEM picture of a smooth 2122 phase film grown on (110) $NdGaO_3$ substrate.

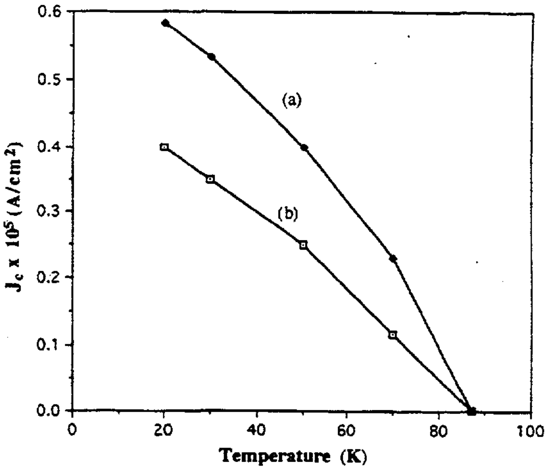

Fig.9. J_c versus temperature relationship of 2122 films grown on a) (110) and b) (001) $NdGaO_3$ substrate in the temperature range of 855-835 °C.

density. The critical current density reported here should be around 10^5 A/cm^2 at 4.2 K, although we were unable to measure it due to temperature limitation in our cryogenic system. This value is less than the values that have been reported for laser ablated, MOCVD and MBE grown epitaxial films of BCSCO. This may be because of the limitations of the LPE grown films where at higher temperatures, a slight misorientation of the seed and lattice and thermal expansion coefficient mismatch (between substrate and the grown material) can result in the introduction of dislocations. These dislocations (low angle grain boundaries) can become the source of weak-links which are known to reduce the current density of the superconducting materials. The other limitation associated in our films is the presence of microcracks which might be formed due to fast cooling of the $NdGaO_3$ substrate. The fast cooling of the substrate is, however, necessary to prevent the diffusion of Ga from $NdGaO_3$ substrate into the film.

CONCLUSIONS

In conclusion, a preferential orientation of (11n) of the $Bi_2CaSr_2Cu_2O_8$-phase deposited on (110) $NdGaO_3$, has been obtained by the LPE method. Besides (11n) orientation, smaller peaks in XRD pattern (Fig.7) attributed to (00n) planes are also observed. Presence of these (00n) orientations is due to the high anisotropic properties of BCSCO superconducting system. Under certain growth conditions a phase belonging to the family of $(Ca_{1-y}Sr_y)_{1-x}CuO_{2-z}$ infinite layered superconductor is observed. Critical current is observed to be higher for the films grown on (110) than on (001) orientation of $NdGaO_3$ substrate. The highest critical current density and the zero resistance temperature (T_{co}) obtained are 10^5 A/cm^2 and 87 K, respectively. The films can be grown on both vertical as well as horizontally mounted substrates.

Acknowledgments

The sponsorship of NASA-Center for Space Power (Grant No. NAGW-1194) of this reserch is highly appreciated. Authors are especially thankful to Dr. Frank Little of

STRUCTURAL, TRANSPORT AND MICROWAVE PROPERTIES OF 123/SAPPHIRE FILMS: THICKNESS EFFECT

M.R.PREDTECHENSKY, A.N.SMAL', Yu.D.VARLAMOV, S.M.VATNIK, O.M.TUKHTO
Institute of Thermophysics, Novosibirsk, 630090, Russia
I.G.VASIL'EVA
Institute of Inorganic Chemistry, Novosibirsk, 630090, Russia

ABSTRACT. The effect of thickness and growth conditions on the structure and microwave properties has been investigated for the 123/sapphire films. It has been shown that in the conditions of epitaxial growth the Al atoms do not diffuse from substrate into the film and the films with thickness up to 100nm exhibit the excellent DC properties. The increase of thickness of GdBaCuO films causes the formation of extended line-mesh defects and the increase of the surface resistance (R_s). The low value of surface resistance R_s(75GHz,77K)=20 mOhm has been obtained for the two layer YBaCuO/CdBaCuO/sapphire films.

1. Introduction

High temperature superconducting (HTSC) thin films are currently of interest for microwave applications [1]. The HTSC films for microwave devices would have to be uniform over several inches, smooth, with high density of critical current and low value of microwave losses. Moreover, the film substrates should have a small dielectric constant and low-loss tangent.

In our previous works (see, f.e., [2,3]) we have reported on the epitaxial films of 123 system on sapphire substrates without buffer layer with $j_c(78K) \approx 10^7 A/sm^2$, and also the films on Al_2O_3 substrates with 100 mm diameter, which have been fabricated by the laser deposition technique. However, such high transport properties have been obtained for the films of thickness less 100 nm, i.e. less the penetration depth λ [4]. Smallest values of the surface resistance of HTSC films have been obtained for such thicknesses D which are comparable with λ, $D \approx 300$ nm.

In this report the effect of the thickness and growth conditions of the films on the crystalline structure, transport and microwave properties has been investigated. Two step deposition allowed us to obtain the relatively low surface resistance of the films, R_s(78K,75GHz) ≈ 20 mOhm.

CSP for his consistent support and encouragement to this program. We are also thankful to Dr. C. D. Brandle of AT&T Bell Laboratories, NJ and Mr. David E. Witter of Texas Instruments Inc., Dallas, TX for valuable technical discussions. We also thank our friends (especially to Narayanan Solayappan) in the Center for Electronic Materials for their help.

REFERENCES

1. K. K. Raina, S. Narayanan and R. K. Pandey: J. Mater. Res. **7**, (1992) 2303.
2. K K. Endo, H. Yamasaki, S. Misawa, S. Yosida and K. Kajimura: Nature **355**, (1992) 327.
3. G. Balestrino, V. Foglietti, M. Marinelli, E. Milani, A. Paoletti and P. Paroli: IEEE Transactions on Magnetics **27**, (1991) 1589.
4. M. Fukutomi, J. Machida, Y. Tanaka, T. Asano, T. Yamamoto and H. Maeda: Jpn. J. Appl. Phys. **27**, (1988) L1484.
5. D. B. Schlom, A. F. Marshall, J. T. Sizemore, Z. J. Chen, J. N. Eckstein, I. Bozovic, K. E. Von Dossonneck, J. S. Harris Jr. and J. C. Bravmann: J. Cryst. Growth **55**, (1989) 702.
6. Y. Ishizuka and T. Miura: J. Cryst. Growth **123** (1992) 357.
7. N. Kubota, T. Sugimoto, Y. Shiohara and S. Tanaka: J. Mater. Res. **8**, (1993) 978.
8. T. Sugimoto, N. Kubota, Y. Shiohara and S. Tanaka: Appl. Phys. Lett. **60,** (1992) 1387.
9. N. Homma, S. Okayama, H.Takahashi, I. Yoshida, T. Morishita, S. Tanaka, T. Haga and K. Yamaya: Appl. Phys. Lett. **59**, (1991) 1383.
10. Z. Hiroi, M. Azuma, M. Takano and Y. Takedo: Physica C, **208,** (1993) 286
11. K. Shigematsu, I. Higashi, K. Hoshino, H. Tahahara and M. Aono: Jpn. J. Appl. Phys. **28,** (1989) 1442.
12. K. Kuroda, K. Kojima, O. Wada, M. Tanioku, K. Yokoyama and K. Hamanaka: Jpn. J. Appl. Phys. Lett. **29,** (1990) L1816.

2. Experimental

As it has been described in details in our previous reports [3,5], for the films deposition it have been used the irradiation of a pulse laser (1.06μm) with energy density 8 J/sm^2 and the stoichiometric targets of YBaCuO and GdBaCuO systems. The pressure of ambient oxygen at the deposition was about 0.5 Torr. As the substrates it has been used the sapphire (1012).

In order to better verify the quality of the films the following experimental techniques and equipment were used. The oriental properties [6], crystalline structure and morphology of films were tested by X-ray, Raman spectroscopy and SEM.

The chemical and phase composition of films were tested by differential dissolution (DD) method. This is a new method for characterization of multiphase inorganic materials (chemical method of phase analysis) [7,8]. This method can be shortly described as following.

The film sample under study is placed in reactor, with the time-variated concentration solvent flowing over the film. The solution obtained goes to the detector-analyzer (ICP). Time-variated masses of dissolved elements (except the oxygen) are determined. The regime of dissolution is fixed up such a way that the phases consisting the sample are dissolved differentially (one after another) due to irregularity of their chemical potentials of dissolution. The information obtained is used for stoichiograms construction (set of time- variated molar relations of elements) to interpret the composition and the relative amount of each phase. In this work DD method was used, in particular, to study the interaction character between materials of film and substrate [8].

The transport and superconducting properties of films were investigated by the standard four probe technique and the measurement of DC current-voltage characteristics. For these measurements the film microbridges and meander structures have been patterned by lithography or scribing with acute diamond tool. The Ag or Au contacts to the film samples have been fabricated by the laser deposition technique. The DC critical current of samples was determined by criteria 1μV.

The surface resistance R_S of HTSC films has been measured by the technique [9] of replacing one end wall of a copper cylindrical cavity ⌀6.7mm·2.75mm which resonates at frequency of 75.2 GHz in H_{011} circular mode.

3. Results and discussion

In our previous report [2,3] it has been shown that the growth conditions and, correspondently, the quality of laser deposed films depend on a number of technological parameters such as the substrate temperature, characteristics of the laser beam, target-substrate distance, oxygen pressure and the crystalline structure and surface orientation of the substrate materials, too.

Optimal values of the parameters are connected in a such a way that the exchange of one of them can be compensated by correction of other ones. So the exchange of film properties can be obtained by the variation of any of these parameters.

In this work we used the variation of substrate temperature (T_S) to change the film quality and to highlight the correlation of structure, chemical composition and superconducting properties of films.

The kinetic dependences of the dissolution by DD method for two YBaCuO films fabricated at the different T_S are shown on Fig.1. As an example, consider the process of dissolution for the sample deposited at T_S=800°C (Fig.1b). It is seen the impurity phases localized near to the surface layers of the film are dissolved at first. It is also seen that the large content of aluminum atoms is registered that is the consequence of aluminum diffusion from substrate. The following peak on the plot characterizes the dissolution of 123 phase and the impurity phases dispersed in one. And, it is the last, the dissolution of impurity phases localized in the film-substrate region is observed.

The picture of the dissolution of film sample deposited at T_S=780°C (Fig.1a) is distinguished by the absence of aluminum in the surface layer and the smaller concentration of localized and dispersed impurity phases.

The kinetic dependences of dissolution of film samples deposited at other T_S values are like that on Fig.1b.

The orientation characteristics, phase composition and superconducting properties of the films of 80 nm thickness deposited at different T_S are shown in the Table 1. It is seen that the sample deposited at T_S=780°C has the best oriental properties, highest value of critical current density and contains the smallest amount of the impurity phases. In addition, as it has been shown above the not aluminum atoms are registered in the surface film layer.

The next conclusion may be drawn from these results. In the case of optimal growth conditions the epitaxial layers with perfect structure are formed at the initial stage of the film growth. These increased above 100 nm, the structural defects are accumulated in the film in such a way that the influence of substrate orientation is lost and the external layers of thick films have the polycrystalline structure.

One of the reasons of such behavior can be the variation of growth conditions for top film layers at the increasing film thickness. Actually, if the first film layers are deposited on sapphire surface that is the heteroepitaxy occur but the following layers grow as homoepitaxial. So, the optimal deposition conditions must be differed for initial and following film layers.

The investigation of the thickness dependence on surface resistance in this work has been made for the GdBaCuO films. Using the GdBaCuO system allowed us to obtain the thick epitaxial films. The orientation characteristics of top and near substrate-film interface layers of GdBaCuO and YBaCuO thick films to be compared are shown in the Table 2. This result was obtained by Raman spectroscopy technique described f.e. in Ref.[2].

Table 2. The orientation properties of the surface (top) layers and the film layers near the substrate-film interface (bottom layer) of YBaCuO and GdBaCuO films with thickness of 300 nm. Results of Raman spectroscopy investigations.

Material of film	Top layer	Bottom layer
YBaCuO	pollycrystalline	epitaxial
GdBaCuO	epitaxial	epitaxial

The GdBaCuO films with thickness up to 100 nm exhibited the exellent DC properties. In particular, the values of critical current density ($j_c(77K)\sim10^6-10^7$ A/cm^2) and the transition temperature (T_c=90-91K) were reproduced for the microbridges with the the width 1-10 µm and the length up to 10 cm indicating the high quality of films. But the measurement values of surface resistance were approximately 70 mOhm.

However, at the increasing film thickness the superconducting properties are changed though the orientation properties were high. For the films with thickness about 200 nm the effective value of the critical current density dropped about two times but the surface resistance value was smaller then for the 80 nm thickness films (see Table 3). At the further increasing film thickness to 300 nm the abrupt drop of the critical current density and the increasing of the surface resistance had been observed.

The reason of such degradation of superconducting and microwave properties was the formation of the extended defects in the films. This were the low visible in optical microscope thin lines forming the regularly shaped mesh. The preferred directions of lines correlated with the orientation of a,b-axes of film. The average size of the regions between the mesh lines was up to 10-40 μm. It should be noted that the line defects observed in optical microscope are not registered by SEM.

To visualize the film structure with line defects the films were heated by pulse laser irradiation with the energy density 0.5 J/cm^2. The photography of the surface of thick epitaxial film after irradiation treatment is shown on Fig. 3a. It is seen that the film cracking along the directions of line defects occurs. Unexpectedly, such films after irradiation treatment conserve the superconducting properties but the value of critical current density drops from 10^4 to $10^2 A/cm^2$. It should be noted that at the analogously treatment the cracking thick YBaCuO films take place, too. But the directions of the cracks have the casual character (see the Fig.3b).

The formation of line defects have been registered after the standard post deposition cooling in the oxygen with the pressure of 1 atm at a cool rate of 10 °C/min. This procedure is used in order to optimize the oxygen content in the film. At the decreasing of cool rate up to 0.5°C/min the formation of defects take place, too. This effect disappeared only in the case when the film samples were cooled at the low oxygen pressure of about 1 Torr. The defects appeared, too at the repeat heating and cooling of the samples at the oxygen pressure of 1 atm.

From this result it may be concluded the effect of line defect formation is bound up with film deformations at the ortho-tetra phase transition which occurs for the oxide superconductors of 123 systems. In our work [2,3] it has been found that the structural mismatching of sapphire and oxide superconductors cause the deformation of film and, correspondingly, changing their structural and superconducting properties. It may be assumed that the increasing film thickness increases the magnitude of deformations at the phase transition and, as result the formation of defects takes place. In the case of YBaCuO films with the polycrystall top layer the visible defects are no formed, because the small size of grains and the large quantity of intergrain boundaries reduce the effect of deformations.

To depress this effect in the thick epitaxial films we used the two layers deposition. The first layer of 60 nm thickness was deposited from GdBaCuO target, and then the following thick layer was deposited from YBaCuO target. Both layers were deposited at substrate temperature of 780°C.

The concept of such two layer deposition consisted of using the difference of the growth rate of yttrium and gadolinium based oxide superconductors. The anisotropy of the growth rates along c-axis and in a,b-plane is smaller for yttrium system then for gadolinium one. So, the size of the monocrystalline regions in the yttrium based films is assumed be smaller then for the gadolinium based films.

Actually, using the two layer deposition allows us to fabricate the films without visible defects and with relatively low surface resistance. It seems likely that at two layer deposition the amount of boundaries between monocrystalline regions are increased in the yttrium based film layer and these defects accumulate the film deformations. But these changes of the film structure should be lowered the effective value of critical current density, that is observed in experiments.

Table 3. The properties of GdBaCuO films versus the film thickness

Film thickness, nm	Critical current density (77K), A/cm^2	Surface resistance (75.2 GHz, 77K), mOhm
80	$8*10^6$	70
200	$3*10^6$	60
300-400 (with defects)	10^4_10^5	$\geqslant$300
300 (two layer deposition)	$6*10^6$	20

In Table 3 the transport and microwave characteristics of HTSC films with different thickness, including two layer samples are shown. It is seen the best result has been obtained for the two layer deposited film.

However, it is not correctly to conclude from here that the two layer deposition is the only way to obtain the good microwave properties for the films on sapphire substrates. We guess that by optimization of growth conditions the films with low surface resistance can be fabricated using the only one target. The our further investigations will be continued in this direction.

4. Conclusions

We have shown that in the 123/sapphire films of thickness more than 100 nm it can occur the formations of extended line defects with regular structure at ortho-tetra phase transition. The films without such defects and with the low value of the surface resistance have been obtained by using the technique of two layer deposition.

This work was supported in part by Committee of HTSC problems (grant 91091) and in part by International Science Foundation.

5. References

1. Proc. 3rd.Int.conf.:World Congress on Superconductivity, Munich, Germany, Sept.15-18,1992, Appl.Superconductivity 1 (1993).
2. M.R.Predtechensky, Proc. NATO ASI: Multicomponent and Multilayered Thin film for Advanced Microelectronics: Techniques, Fundamentals and Devices, Bad Windsheim, Germany, Sept.21-Oct.2, 1992, Series E: Appl.Sciences, 234 (1993) 357.
3. M.R.Predtechensky, A.N.Smal', Yu.D.Varlamov, V.Yu.Davidov, Superconductivity: Phys.Chem.Techn. 5 (1992) 2126.
4. B.W.Langley, S.M.Anlage, R.F.W.Pease,M.R.Beasley, Rev.Sci.Instrum. 62 (1991) 1801.
5. Yu.D.Varlamov, V.F.Vratskikh, M.R.Predtechensky et al, Pis'ma v JTF 2 (1988) 2068.
6. Yu.D.Varlamov, V.F.Vratskikh, M.R.Predtechensky et al,Superconductivity: Phys.Chem.Techn. 3 (1990) 2328.
7. I.G.Vasil'eva, A.A.Vlasov, Ya.I.Gibner, V.V.Malahov, DAN RAN, 324 (1992) 596.
8. M.R.Predtechensky, A.N.Smal' ,I.G.Vasil'eva, Z.L.Akkerman, A.A.Vlasov, V.V.Malahov, Superconductivity:Phys.Chem.Techn. (to be published).
9. H.S.Newman, A.K.Singh, K.Sadanada and M.A.Imam, Appl.Phys.Lett., 54 (1989) 389

Scanning micro-Hall probe mapping of magnetic flux distributions and current densities in $YBa_2Cu_3O_7$ thin films

W. Xing,[a] B. Heinrich,[a] Hu Zhou,[b] A.A. Fife,[b] A.R. Cragg,[b] and P.D. Grant[c]

[a] Department of Physics, Simon Fraser University, Burnaby, B.C. Canada V5A 1S6
[b] CTF Systems Inc., 15-1750 McLean Avenue, Port Coquitlam, B.C. Canada V3C 1M9
[c] National Research Council of Canada, Ottawa, Canada K1A 0R6

Mapping of the magnetic flux density B_z (perpendicular to the film plane) for a $YBa_2Cu_3O_7$ thin-film sample was carried out using a scanning micro-Hall probe. The sheet magnetization and sheet current densities were calculated from the B_z distributions. From the known sheet magnetization, the tangential ($B_{x,y}$) and normal components of the flux density **B** were calculated in the vicinity of the film. It was found that the sheet current density was mostly determined by $2B_{x,y}/d$, where d is the film thickness. The evolution of flux penetration as a function of applied field will be shown.

PACS numbers: 74.60.Jg, 74.75.+t

I. Introduction

Stationary and scanning Hall probes have been used for evaluation of high temperature superconducting (HTS) thin films.[1-4] The magnetic flux density B_z normal to the film surface is usually measured. Algorithms were developed[4-7] to calculate the sheet current density **J** from the measured field above the sample (inverse problem). In our previous paper,[4] the inverse problem was converted to a magnetostatic calculation using

$$\mathbf{J} = \nabla \times \mathbf{M} = \left(J_x, J_y\right) = \left(\frac{\partial M}{\partial y}, -\frac{\partial M}{\partial x}\right). \tag{1}$$

where the sheet magnetization M is normal to the film plane (parallel to z-axis).

The flux density B_z at the point (m,n,z) is given by[8]

$$B_z = \sum_{i,j=1}^{N1,N2} \frac{\mu_0}{4\pi} M(i,j) \int_{S_{i,j}} \frac{3z^2 - r^2}{r^5} dx'\, dy' = \sum_{i,j=1}^{N1,N2} M(i,j) G(m,n,i,j,z) \tag{2}$$

where r is the distance between the local sheet magnetization M(i,j) and the field point (m,n,z). N1 and N2 are the total number of scanning steps in the x and y directions, respectively. The integral in (2) is over the area of the grid cell (i,j). Equation (2) can be written in matrix notation[4]

$$\mathbf{B_z} = \mathbf{G} \cdot \mathbf{M}. \tag{3}$$

where G is a matrix of order of $N_1^2 \times N_2^2$ and M and B_z are column vectors of dimensions N1 × N2. Equation (3) states that the sheet magnetization is uniquely determined by the measured $B_z(x,y)$. The sheet magnetization M(i,j) allows one to calculate the flux density **B** anywhere around the film including the tangential components $B_{x,y}$ of **B**, which are not obtainable directly from our scanning Hall Probe measurements. That way one can obtain a full picture of the flux penetration. This is a forward problem which does not require the time consuming solutions of inverse matrixes.

The contributions to **J** from the gradient of B and from the curvature of **B** were compared. The purpose of this paper is to illustrate graphically the evolution of flux penetration into a zero-field-cooled $YBa_2Cu_3O_7$ (YBCO) thin-film sample.

Ideal film: saturation remanent state

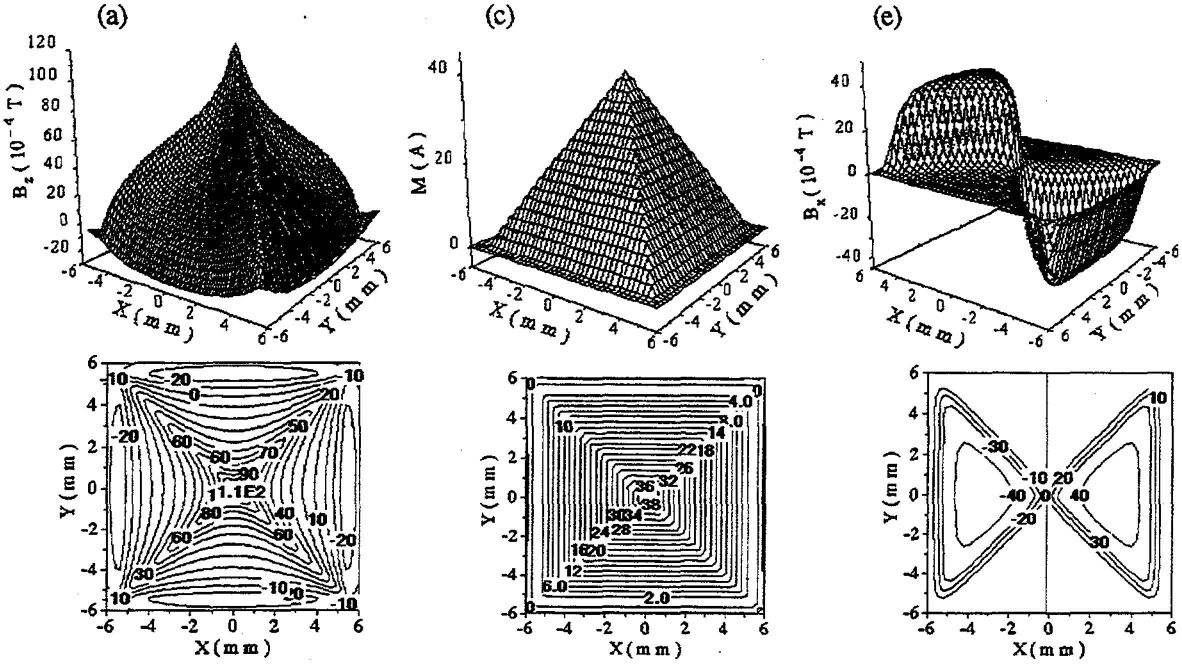

YBCO film (Y259): saturation remanent state

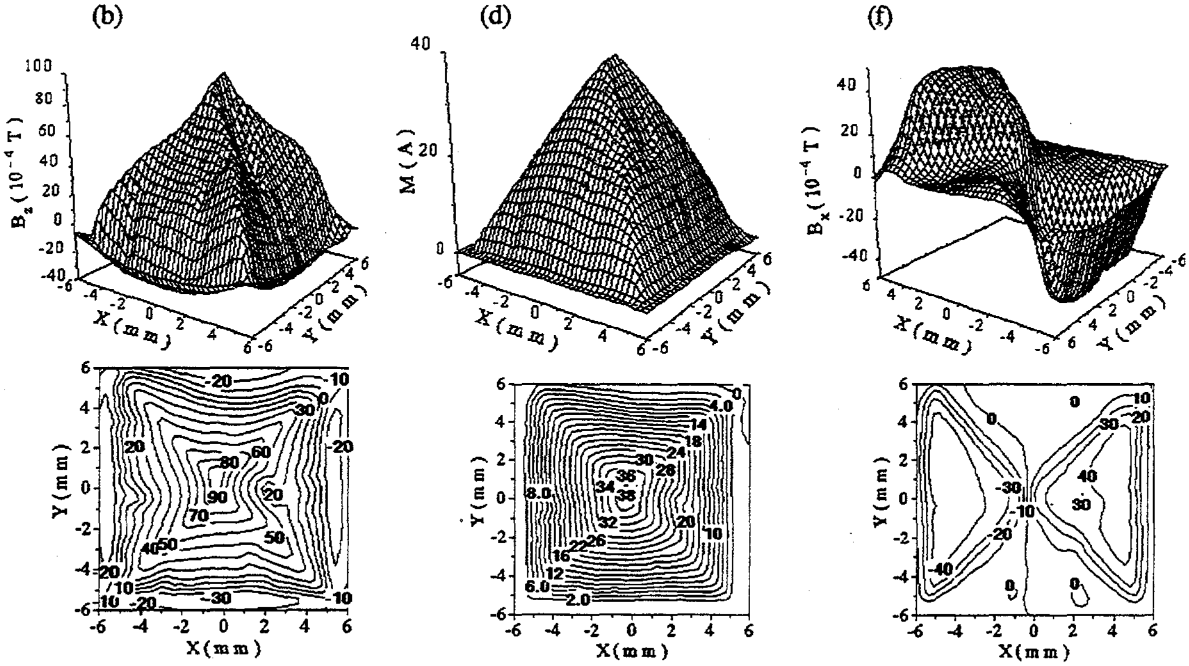

Fig. 1. (a) and (b) B_Z, (c) and (d) M, and (e) and (f) B_x distributions in the remanent state for an ideal film with uniform current distributions and for a YBCO thin film (sample Y259), respectively.

II. Experimental

The micro-Hall probe was patterned from a GaAs quantum-well heterostructure thin film (University of Bath). Its active area is 25 × 25 μm. The scanning micro-Hall probe system is a customized commercial device developed by Quantum Technology Corp.[9] in collaboration with the participants from Simon Fraser University. Epitaxial quality YBCO thin-film samples were prepared on $LaAlO_3$ substrates by pulsed excimer laser ablation from a stoichiometric target of YBCO. We present the data for one of the YBCO films (Y259) in this paper. Sample Y259 had a critical temperature of 90 K, and lateral dimensions ≈ 1.08 × 1.08 cm, and thickness d ≈ 300 nm. The Hall probe was maintained at a constant height of z ≈ 250 μm above the film surface while taking the lateral scans. The lateral scanning step was 0.3 mm. The experimental details can be found in Ref. 4.

III. Results and discussion

Fig. 1 compares the theoretical calculations for an ideal film (uniformly distributed currents flowing in concentric square paths) with the measurement results for the YBCO (Y259) thin film. Figs. 1(a) and 1(b) show the B_z distributions for the ideal film and for the YBCO film, respectively. An external field H_a ($\mu_0 H_a \approx 30$ mT) perpendicular to the film plane was applied to the YBCO film (zero-field-cooled), and then H_a was switched off. The mapping of B_z was carried out with the film in a remanent state. The applied flux B_a penetrated fully into the film. The ideal film was chosen to have the same size as that of sample Y259. The sheet current for the ideal sample, j (= J/d) = 2.5 × 10^6 A/cm^2, was chosen to bring the overall dependence of B_z close to that of the YBCO sample. The distribution of M(x,y) was obtained by solving the matrix equations (2).[4] The results are shown in Figs. 1(c) and 1(d). Fig. 1(d) demonstrates that the YBCO sample was in the saturated state. The contour lines of M(x,y) represent the current stream lines, and the separation between stream lines is inversely proportional to the value of the sheet current density [Eq. (1)].

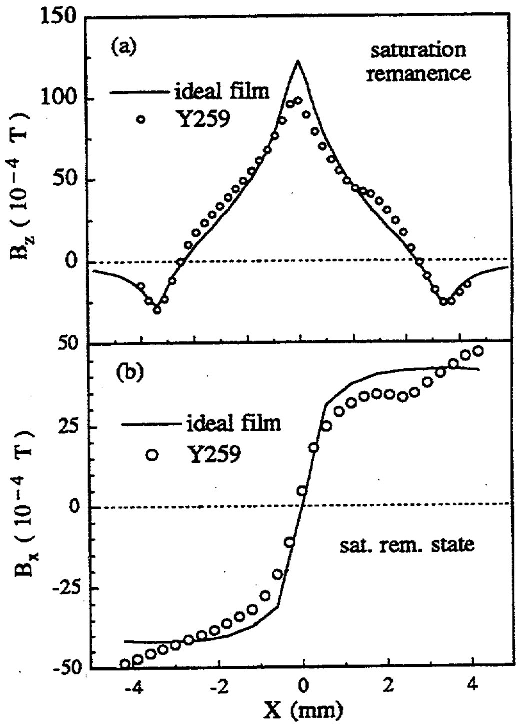

Fig. 2. (a) $B_z(x)$ and (b) $B_x(x)$ for y = 0 in the saturation remanent state; the open circles are $B_{x,z}$ values for the YBCO film and the solid lines for the ideal film.

B_x and B_y at point (m,n,z) are given by

$$B_{x,y} = \sum_{i,j=1}^{N1,N2} \frac{\mu_0}{4\pi} M(i,j) \cdot \int_{S_{i,j}} \frac{3x(\text{or } y)z}{r^5} dx'\, dy' . \tag{4}$$

Figs. 1(e) and 1(f) show that $B_x(x,y)$ is distributed over two opposing triangles. The sample symmetry requires that the component B_y is distributed in two other triangles. In each triangular region, there are either $B_{x,z}$ or $B_{y,z}$ components of $\mathbf{B}$. B_x and B_y vanish along the film diagonals.

The distributions of B_x, B_z, and M for the YBCO film are very similar to those of the ideal film. However there are noticeable deviations of the flux distribution from the four-fold symmetry pattern which are caused by defects in the YBCO sample, see Figs. 1 and 2.

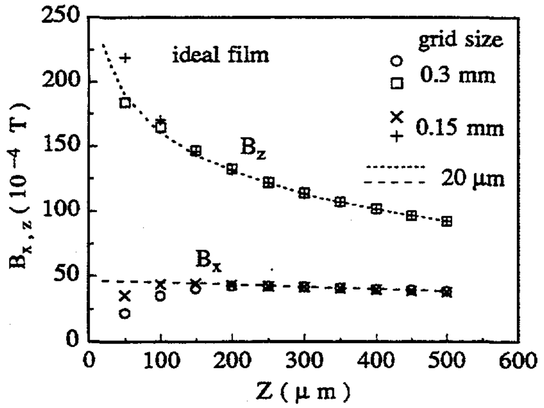

Fig. 3. Calculated $B_{x,z}$ values versus z for the ideal film for different grid size of the sheet magnetization M(x,y).

The calculations in Fig. 3 were used to demonstrate the dependence of B_x and B_z on the grid size, w, of the sheet magnetization M(x,y). B_z was calculated at the film center. B_x was calculated at midway between the center and the edge of the film. The calculated values of B_x are correct if the distance above the sample surface $z \geq w$. B_x decreases for $z < w$ and reaches zero when $z \rightarrow 0$. This is an artifact of the finite grid size. In an ideal sample B_x should reach a constant value by approaching the film surface (Ampere's law). The decrease in B_x for $z < w$ is due to the change of the sign of B_x across the mid-plane of the film. The calculated values of B_z support that view. B_z is continuous across the film thickness and the calculated B_z show no noticeable dependence on w.

The application of Ampere's Law

$$\oint \mathbf{B} \cdot d\mathbf{l} = \mu_0 I \tag{5}$$

to a path in x-z plane shown in Fig. 4 leads to

$$\frac{\Delta B_x}{d} + \frac{\Delta B_z}{\ell}\frac{t}{d} = \mu_0 j_y, \tag{6}$$

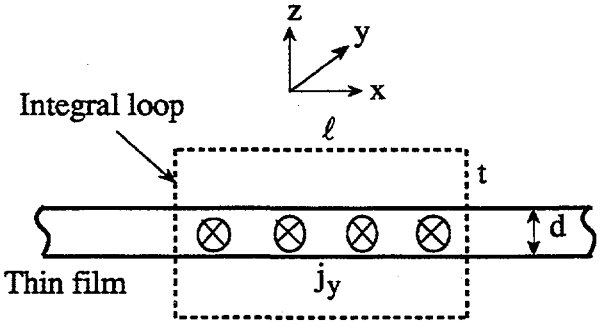

Fig. 4. Schematic diagram of the integral path for the application of Ampere's law.

where ℓ and t are the integral paths along the x and z directions and ΔB_z is the difference in the B_z components which are separated laterally by ℓ. ΔB_x is the difference between the B_x components above and below the film, see Fig. 4. Since d is comparable to 2λ, where λ is the London penetration depth, j is considered uniform over the film thickness. (Otherwise, j is the average value over the film thickness.) The first term in (6) is due to the curvature of **B**, ($B\nabla \times \hat{\mathbf{B}}$, where $\hat{\mathbf{B}}$ is the unit vector along $\mathbf{B} = B\hat{\mathbf{B}}$) and the second term is due to the gradient of B, ($\nabla B \times \hat{\mathbf{B}}$).[10] Since B_x and B_z are comparable and t can be close to d, the flux gradient term is much smaller (by approximately three orders of magnitude) than the flux curvature term. In other words, j is mostly determined by the curvature term,

$$\frac{\Delta B_{x,y}}{d} = \frac{2B_{x,y}}{d} = \mu_0 \left| j_{y,x} \right|. \tag{7}$$

This observation is in agreement with the theoretical analysis of Clem.[10] From Eq. (7) and from the local sheet current $j_c = 3 \times 10^6$ A/cm^2 corresponding to x ≈ -5 mm in Fig. 2, it can be shown that the calculated value of B_x (for z=250 μm) is 13% smaller than that obtained from Eq. (7). In fact, the profile of the $B_x(x)$ curve in Fig. 2(b) is very similar to that of $j_y(x)$ for the YBCO film.[4] This shows clearly that the local current density in superconducting thin films determines the parallel components of **B** in the vicinity of the film. Fig 2(b) shows that B_x does not reach the saturated value as in the case of an ideal sample. The observed slope of B_x in Fig. 2(b) is a consequence of the dependence of j_c on the local B_z, see Ref. 4.

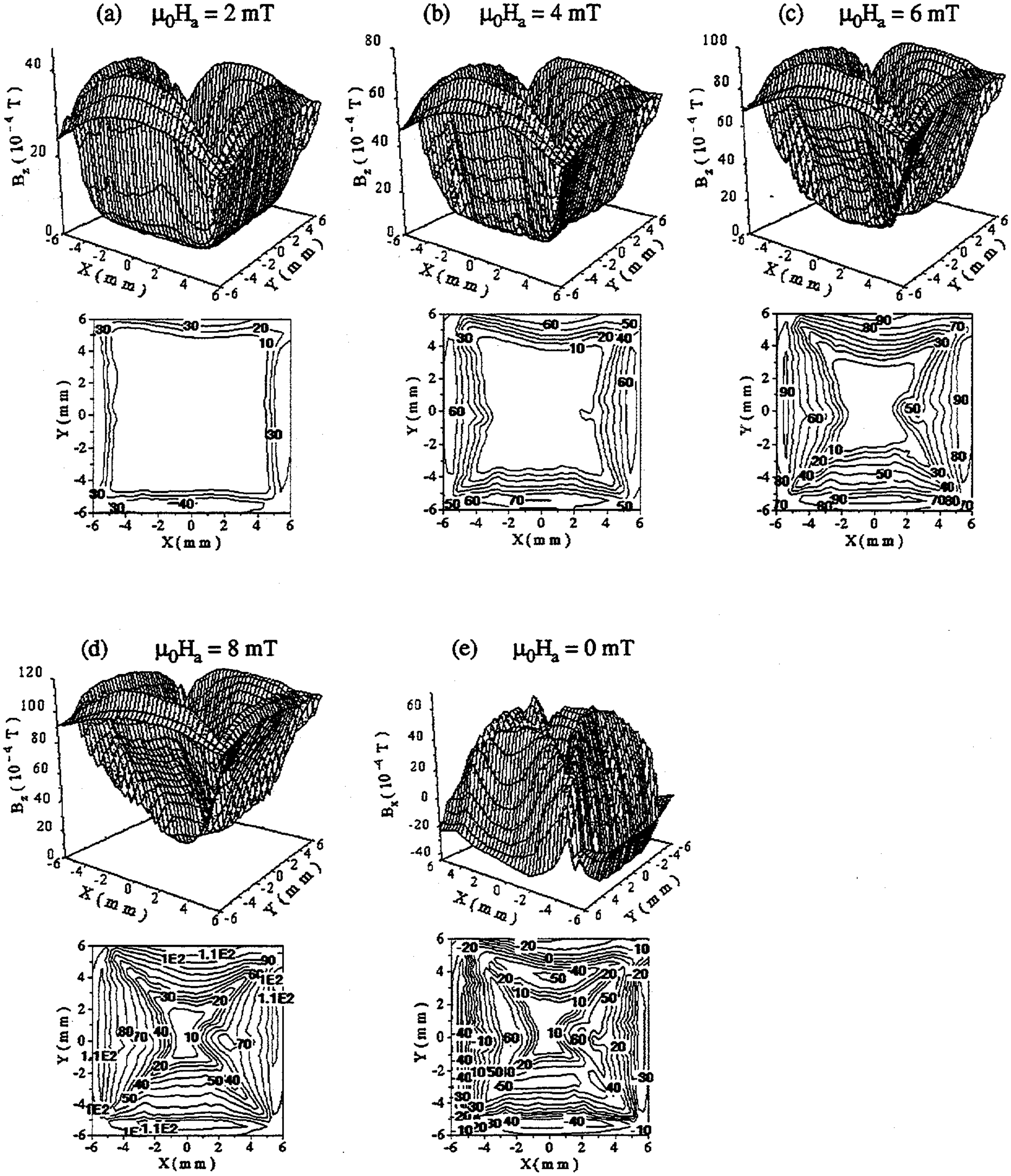

Fig. 5. Measured B_z of the YBCO film for μ_0H_a = (a) 2 mT, (b) 4 mT, (c) 6 mT, (d) 8 mT, and (e) 0 mT.

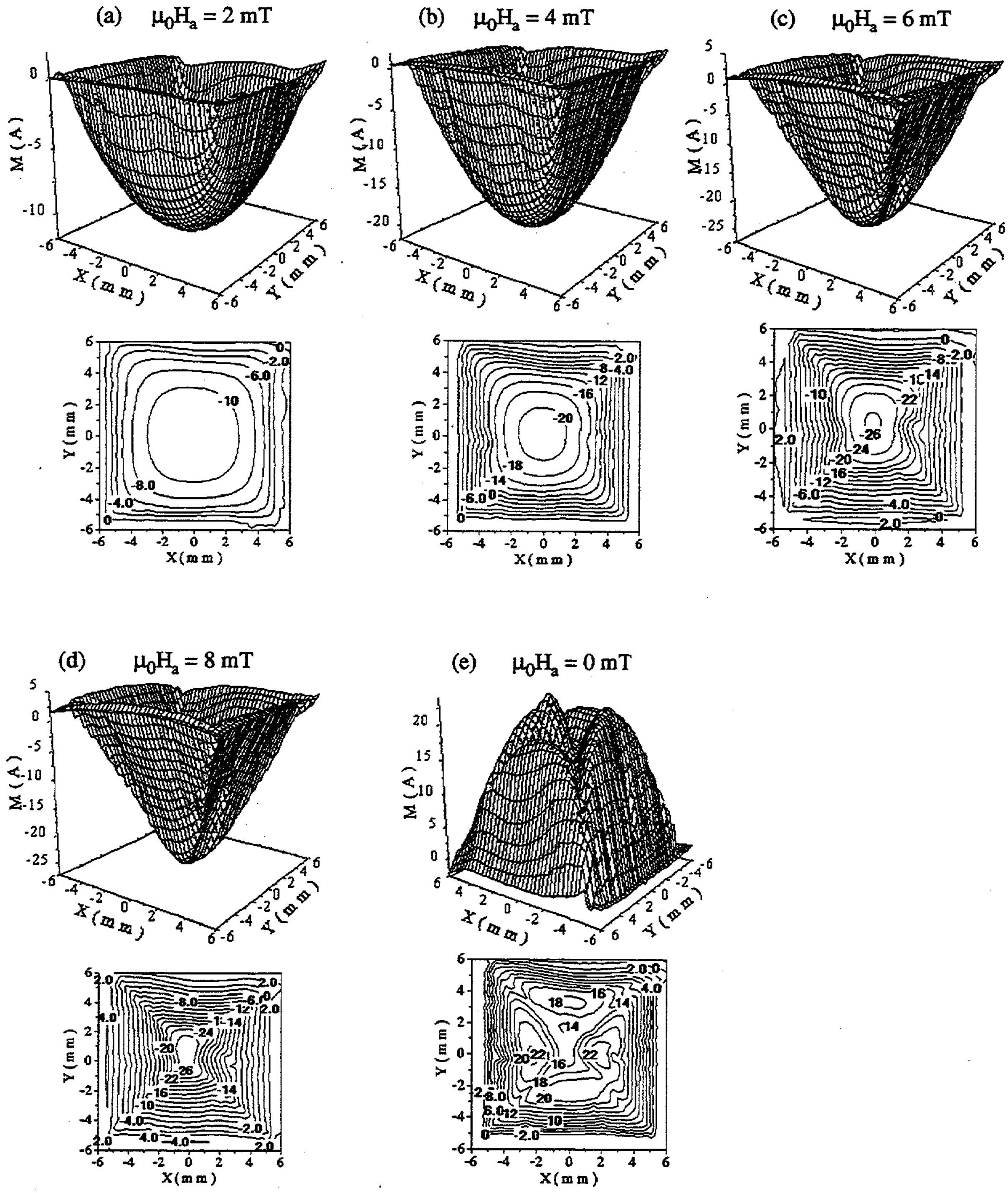

(a) $\mu_0 H_a = 2$ mT

(b) $\mu_0 H_a = 4$ mT

(c) $\mu_0 H_a = 6$ mT

(d) $\mu_0 H_a = 8$ mT

(e) $\mu_0 H_a = 0$ mT

Fig. 6. The sheet magnetization M of the YBCO film for $\mu_0 H_a$ = (a) 2 mT, (b) 4 mT, (c) 6 mT, (d) 8 mT, and (e) zero mT.

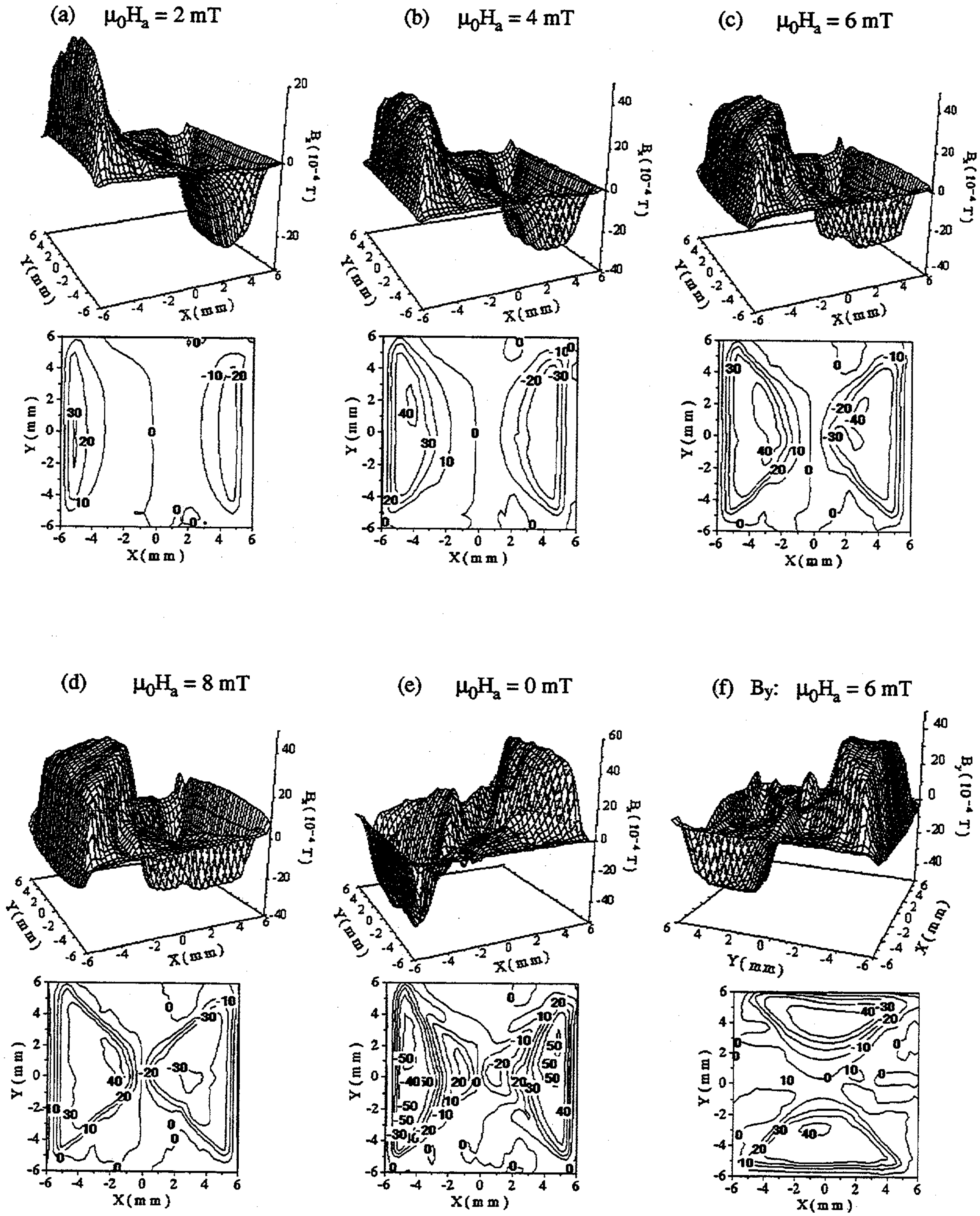
(a) $\mu_0H_a = 2$ mT
(b) $\mu_0H_a = 4$ mT
(c) $\mu_0H_a = 6$ mT
(d) $\mu_0H_a = 8$ mT
(e) $\mu_0H_a = 0$ mT
(f) By: $\mu_0H_a = 6$ mT

Fig. 7. B_x of the YBCO film for μ_0H_a = (a) 2 mT, (b) 4 mT, (c) 6 mT, (d) 8 mT, and (e) 0 mT; (f) B_y for μ_0H_a = 6 mT.

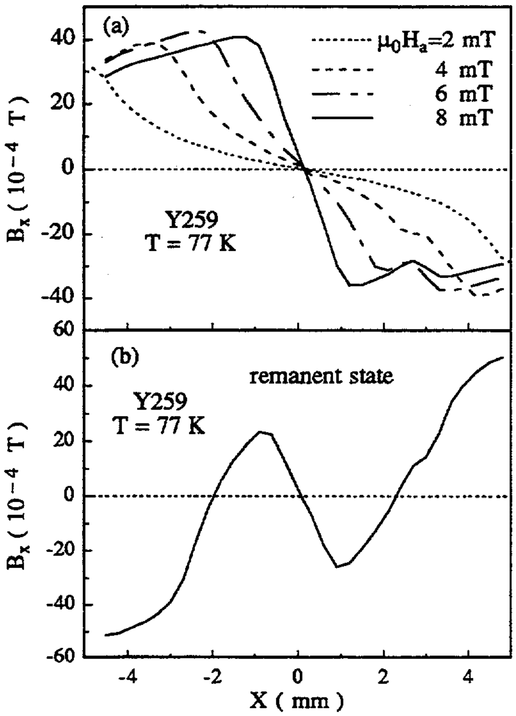

Fig. 8. B_x versus x for the YBCO film (a) in different applied fields (b) in a remanent state.

Figs. 5-8 show B_z, M, and B_x distributions for sequentially applied external fields. Fig. 9 shows vector field plots of the total flux density **B** in the x-z plane at y = 0 for various final states, described in the figure caption. The evolution of flux penetration and the corresponding current distributions can be best viewed by the combination of Figs. 5-9.

Fig. 7(f) shows the non-zero values of B_y over the region where B_x should dominate. This non-symmetrical flux distribution is due to the presence of a defect which is centered around x=3, y=0, see Fig. 5(c). Fig. 5(c) shows that the sheet current path curves around this defect and that causes a simultaneous presence of the B_x and B_y components in that region.

Figs. 9(a) and 9(b) show the saturation remanent flux distributions for the ideal and the YBCO films, respectively. The return flux (pointing in $-\hat{z}$ direction) results in the demagnetizing field around the film edge. The magnitude of **B** decreases rapidly away from the film surface.

Figs. 5-9 show that for relatively low applied fields (e.g. $\mu_0H_a = 2$ mT), the induced supercurrents effectively shield the interior of the film from the external flux B_a. However, the tangential components $B_{x,y}$ are present over the entire film surface. The exclusion of B_z requires screening currents across the whole film surface,[4] and the presence of $B_{x,y}$ in vortex-free region is a consequence of Ampere's law. However note that the values of $B_{x,y}$ in the vortex-free region are smaller than those in the vortex-penetrated regions [corresponding to the plateaus in $B_x(x,y)$ in Fig. (7)] where the supercurrent reached its critical value, see Fig. 8.

Fig. 9(c) shows a noticeable bending of the flux lines over the film surface. The Lorentz force density $\mathbf{F} = \mathbf{j} \times \mathbf{B}$ has two components. The tangential component (due to B_z) points inwards and is responsible for moving the flux lines; this force density is balanced by the pinning force density. The perpendicular component (due to $B_{x,y}$) points downwards at the top and upwards at the bottom of the film. This part of the Lorentz force density causes the tilting of vortex lines.

It is interesting to note that the distortion of the applied flux is clearly visible only for $z \leq 5$ mm, see Fig. 9(c), which is approximately equal to the half length of the film edge.

As the applied field progressively increases, the flux penetrates deeper into the film and the region in which flux lines appreciably deviate from the external flux is more and more confined to the center of the film, see Figs. 9(d)-9(f);

Fig. 9(g) shows the flux line patterns in the remanent state after the applied field $\mu_0H_a = 8$ mT was switched off. The trapped flux shows four hilltops, see Fig. 5(e). It is worthwhile to point out that at the hilltops (maxima of B_z) both $B_{x,y}$ and J are zero [Figs. 8, 9(b), and 9(g)]. The induced currents flow in closed loops under each hilltop and enclose the hilltops along the sample edges [Fig. 6(e)]. This multiply-connected current distribution can be reconstructed using a linear superposition principle with appropriate "virgin" states[11,4].

(a) ideal film: sat. rem. state

(b) YBCO film: sat. rem. state

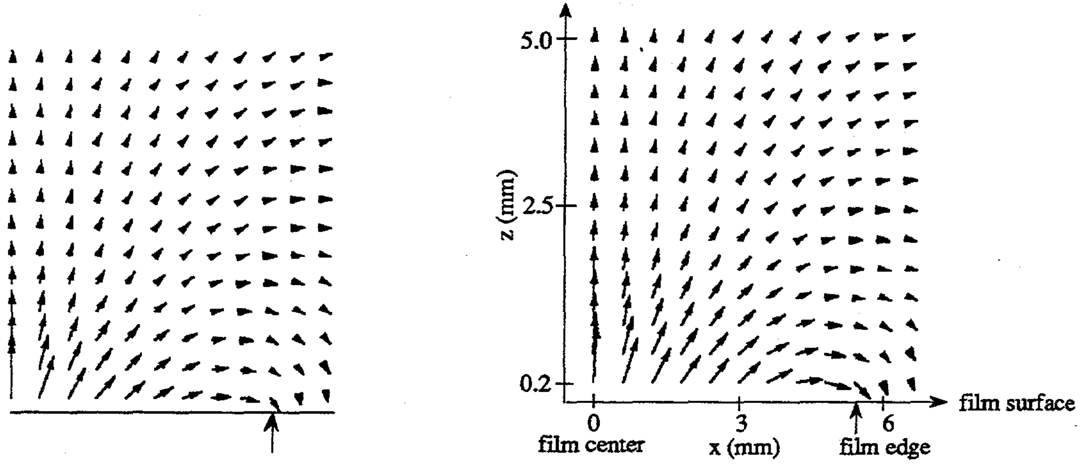

(c) $\mu_0 H_a = 2$ mT

(d) $\mu_0 H_a = 4$ mT

(e) $\mu_0 H_a = 6$ mT

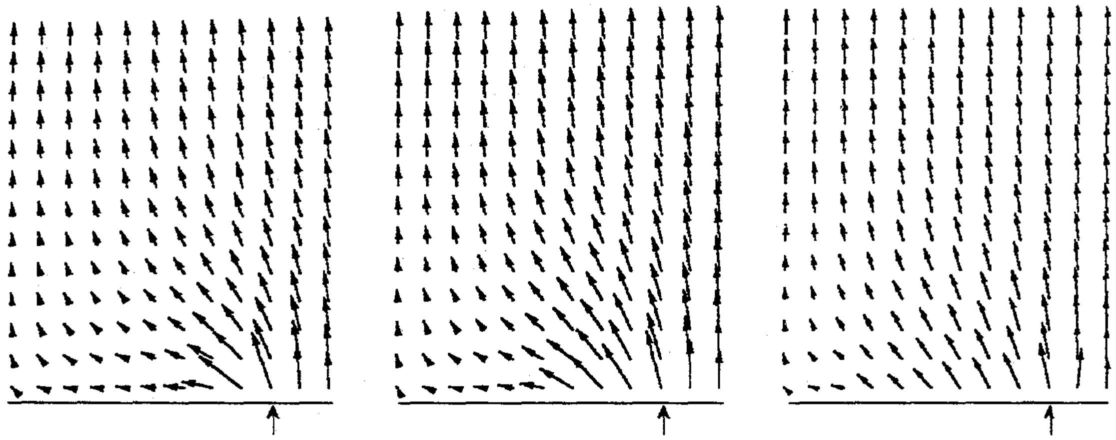

(f) $\mu_0 H_a = 8$ mT

(g) $\mu_0 H_a = 0$ mT

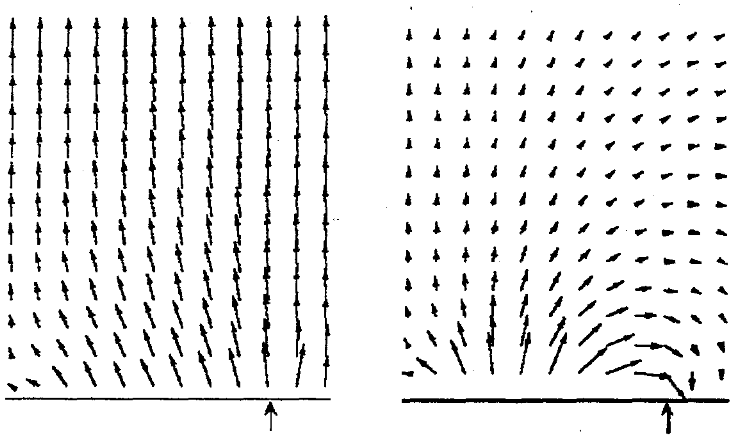

Fig. 9. Vector field plots of the flux density B in x-z plane (a) and (b) for the ideal and the YBCO films in the saturation remanent state, and for the YBCO film for $\mu_0 H_a$ = (c) 2 mT, (d) 4 mT, (e) 6 mT, (f) 8 mT, and (g) 0 mT.

IV. Conclusion

The mapping of B_z near the superconducting film surface is shown here to include complete and detailed information of the current distributions in the film, and the flux density in the film vicinity. The tangential components $B_{x,y}$ of the flux density $\mathbf{B}$ were calculated from the sheet magnetization M which was determined from the normal component of $\mathbf{B}$, B_z. B_z was measured by a scanning micro-Hall probe. The minimum height at which the tangential components $B_{x,y}$ can be evaluated is determined by the scan step size. The application of Ampere's law indicates that the induced supercurrents in the YBCO thin-film sample are nearly entirely determined by $2B_{x,y}/d$, which is due to the curvature of $\mathbf{B}$.

The Lorentz force has two components, one due to B_z, the other due to $B_{x,y}$. In the stationary state, the Lorentz force caused by B_z is compensated by the restoring force of pinning sites and the Lorentz force caused by the tangential flux densities $B_{x,y}$ is responsible for the tilting of flux lines. The calculation of $\mathbf{B}$ in the vicinity of the film revealed several interesting features: (a) the extent of screening by supercurrents in the vertical direction is comparable to that in the horizontal direction. With an increasing applied field, the flux penetrates deeper into the film and the region in which flux lines appreciably deviate from the external field is more and more confined to the center of the films; (b) in the remanent state, the areas with a maximum trapped flux density have no supercurrents; (c) the tangential components B_x and B_y are mostly present in separate and mutually perpendicular triangular regions. A significant presence of B_x and B_y in the same region, is a consequence of local defects; (d) the tangential flux densities B_x, B_y are nearly zero along the film diagonals.

Acknowledgments

We thank P.H. Brown and S. Govorkov for assistance in testing and assembling the measuring system. The assistance of S. Bending of University of Bath in providing the custom Hall probe is gratefully acknowledged.

This work was supported by the Natural Sciences and Engineering Research Council of Canada, Industry Canada (STP-AIM program), and the BC Ministry of Employment and Investment.

References

[1] M.J. Scharen, A.H. Cardona, J.Z. Sun, L.C. Bourne, and J.R. Schrieffer, Jpn. J. Appl. Phys., 30, L15 (1991).

[2] P. Brüll, D. Kirchgässner, and P. Leiderer, Physica C 182, 339 (1991).

[3] W. Rauch, H. Behner, and E. Gornik, Physica C 201, 179 (1992).

[4] W. Xing, B. Heinrich, Hu Zhou, A.A. Fife, and A.R. Cragg, submitted to J. of Appl. Phys., 1994.

[5] G.M. Asher, J.T. Williams, C.R. Walters, H. Joyce and R.J.A. Paul, IEEE Trans. Magn. 18, 540 (1982).

[6] B.J. Roth, N.G. Sepulveda, and J.P. Wikswo, J. Appl. Phys. 65, 361 (1989).

[7] P.D. Grant, M.W. Denhoff, W. Xing, P.H. Brown, S. Govorkov, I. Entin, J.C. Irwin, B. Heinrich, H. Zhou, A.A. Fife, and A.R. Cragg, submitted to Physica C, 1994.

[8] J. D. Jackson, Classical Electrodynamics, (Wiley, New York, 1975), Chap. 5.

[9] Quantum Technology Corp., 1370 Alpha Lake Road, Unit 15, Whistler, B.C. Canada V0N 1B1, Telephone: (604) 938-0030.

[10] John R. Clem, to be published in the Proc. of the 7th int. workshop on critical currents in superconductors, Jan. 24-27, 1994, Alpbach, Austria.

[11] E.H. Brandt, M. Indenbom, and A. Forkl, Europhys. Lett. 20, 735 (1993).

Angular Dependence of Critical Current Density and Magnetoresistance of Sputtered High-T_c-Films

A. Geerkens[a], M. Meven[b], H.-J. Frenck[a], S. Ewert[a]

[a] Institute of Physics, Technical University of Cottbus,
P.O. Box 10 13 44, D-03013 Cottbus, Germany

[b] 2nd Physical Institute, RWTH Aachen,
Templergraben 55, D-52056 Aachen, Germany

Abstract

The angular dependence of the critical current density and the magnetoresistance of high-T_c-films in high and low magnetic fields and for different temperatures were measured to investigate the flux pinning and the superconducting properties. A comparison of the results for the different superconductors shows their inrcreasing dependence on the angle Θ between the magnetic field and the *c*-axis of the film due to the anisotropy of the chosen superconductor. Furthermore the influence of the current direction to the Θ-rotation plane is discussed.

1. INTRODUCTION

Although the high-T_c-superconductors (HTSC) are used in many various applications, the mechanisms of many effects these materials show are not very well understood until now. To study the flux line lattice by the intrinsic pinning the magnetoresistance and the critical current density are measured as a function of the angle between the magnetic field and the HTSC thin film. Besides other criterions of characterization the quality of the HTSC films can be determined by measuring the angular dependence of the dissipation mechanism.

2. EXPERIMENTAL

The DC-sputtered films with a thickness between 70 nm and 250 nm are highly oriented with the *c*-axis perpendicular to the surface of the $SrTiO_3$ single crystal substrate. SEM pictures show that the films are without any outgrowths larger 1 µm. Especially the $YBa_2Cu_3O_{7-\delta}$ films with a T_c up to 90 K and a transition width of 1-2 K determined by measuring the AC-susceptibility reach critical current densities about $9x10^6$ A/cm^2 at 77 K. The as grown $Bi_2Sr_2CaCu_2O_{8+x}$ films show a T_c about 75 K. The critical current densities yield values about $5x10^5$ A/cm^2 at 50 K.

The angular dependence of the critical current density and the magnetoresistance were measured with a pulsed current method to avoid warming up of the bonded gold wire contacts on the structured film. Conduction paths of 20 μm width and 2 mm length were prepared by wet chemical etching.

The used sample holder allows to vary the angle between the magnetic field and the *c*-axis of the film (angle Θ) as well as the angle between the current direction and the Θ–rotation plane. The accuracy of the tilt angle is better than 0.05°. An offset of 1° can occur due to inaccurate adjustment. The temperature was varied between 4.2 K and 77 K and magnetic fields between 10 mT and 8 T were used.

3. RESULTS AND DISCUSSION

To study the pinning of the HTSC films they were investigated by measuring the critical current density and the magnetoresistance dependent on the temperature and the strength and the angle of the magnetic field. Furthermore current-voltage-curves were taken. The results for $YBa_2Cu_3O_{7-\delta}$ and $Bi_2Sr_2CaCu_2O_{8+x}$ films are compared due to the anisotropy of the chosen superconductor.

3.1. Critical Current Density

3.1.1. $YBa_2Cu_3O_{7-\delta}$

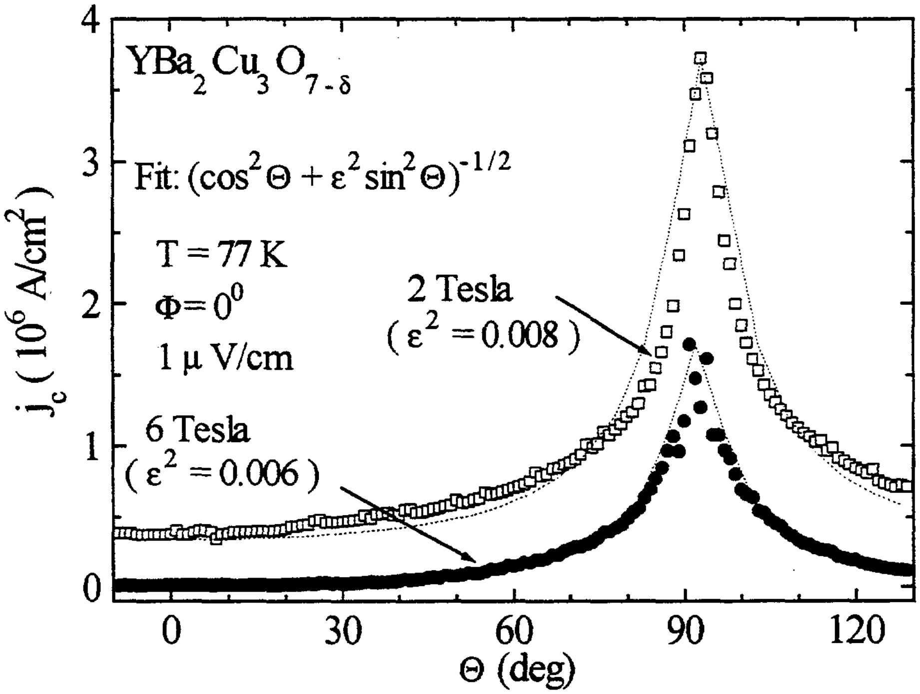

Figure 1. Critical current density $j_c(\Theta)$ in high magnetic fields.

Figure 1 shows some typical results of an investigated $YBa_2Cu_3O_{7-\delta}$ film. These measurements of the angular dependence of the critical current density were made in high magnetic fields and at a temperature of 77 K. As criterion for the critical current density a voltage of 1 μV/cm was chosen. At $\Theta = 0^\circ$ the *c*-axis of the $YBa_2Cu_3O_{7-\delta}$ film is parallel to the magnetic field *B* and at $\Theta = 90^\circ$ the *c*-axis is perpendicular to the magnetic field. Due to the layered structure of this superconductor the critical current density $j_c(\Theta)$ reaches its maximum at $\Theta = 90^\circ$ when the magnetic field is parallel to the CuO_2 planes [1]. This indicates the strong pinning at this angle where the flux lines are located by extrinsic pinning centers. The minimum of $j_c(\Theta)$ appears for the magnetic field being parallel to the *c*-axis of the film ($\Theta = 0^\circ$).

The fits of the data were made using the function $j_c(\Theta) \sim (\cos^2\Theta + \varepsilon^2\sin^2\Theta)^{-1/2}$. For this fit the effective magnetic field is reduced to $B_{eff} = B(0^\circ)(\cos^2\Theta + \varepsilon^2\sin^2\Theta)^{1/2}$ with ε being the anisotropy parameter [2]. For $\varepsilon^2 = 0.008$ at two Tesla and $\varepsilon^2 = 0.006$ at six Tesla this function fits the data quite well. The small value for ε, which decreases with increasing the magnetic field, shows the very anisotropic behaviour of the $YBa_2Cu_3O_{7-\delta}$ film in high magnetic fields.

In Figure 2 the corresponding results of $j_c(\Theta)$ in low magnetic fields are presented. In low magnetic fields the same function as used for the high fields fits the results, but the dependence on the angle Θ is less pronounced, which can be observed in the higher values of the anisotropy parameter between $\varepsilon^2 = 0.14$ and $\varepsilon^2 = 0.25$.

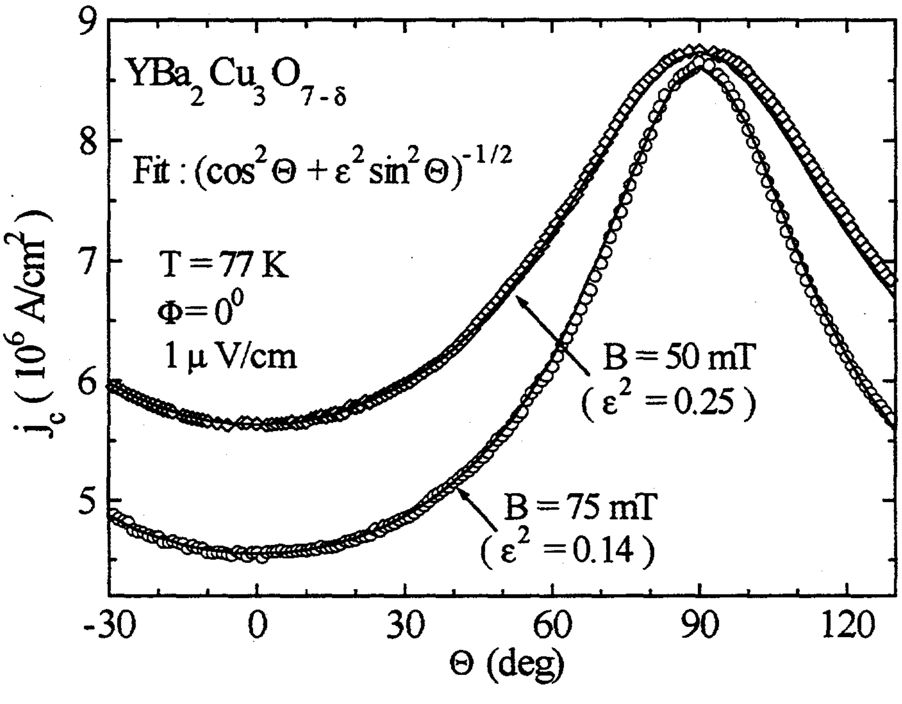

Figure 2. Critical current density $j_c(\Theta)$ in low magnetic fields.

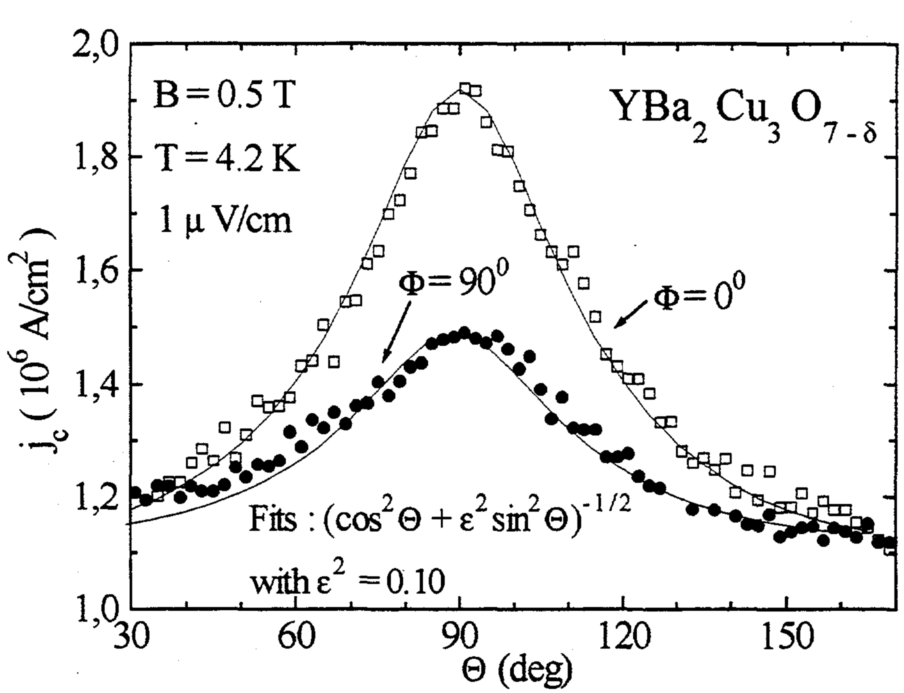

Figure 3. Critical current density $j_c(\Theta)$ for different angles Φ.

In Figure 3 a typical example of the different results of $j_c(\Theta)$ for the current direction parallel ($\Phi = 0^\circ$) or perpendicular ($\Phi = 90^\circ$) to the Θ-rotation plane (*cB*-plane of the film) is presented. Although both curves fit the theory quite well with the same anisotropy parameter, the curves differ from each other, especially for the tilt angle Θ near 90°. For $\Phi = 90^\circ$ the difference between the maximum and the minimum of the critical current density is only half as big as for $\Phi = 0^\circ$. For the angles $\Theta = 90^\circ$ and $\Phi = 90^\circ$ the *c*-axis of the film is perpendicular to the external magnetic field *B* and the current flows perpendicular to *B*. So this effect may be caused by a strong Lorentz force acting on a segment of the flux lines parallel to the layers [3]. This would also explain that the curves for angles Θ near 0° or 180° lie one upon another because for the *c*-axis parallel to the magnetic field there is no difference in the measuring geometry wether the angle Φ is 0° or 90°. This difference between $\Phi = 0^\circ$ and $\Phi = 90^\circ$ disappears for high quality films with high critical current densities, for which the intrinsic pinning is strong enough to cover the Φ-dependent part of the dissipation. So these measurements could be used as a criterion of film quality.

3.1.2. $Bi_2Sr_2CaCu_2O_{8+x}$

Besides measurements on $YBa_2Cu_3O_{7-\delta}$ thin films sputtered $Bi_2Sr_2CaCu_2O_{8+x}$ films were investigated, too.

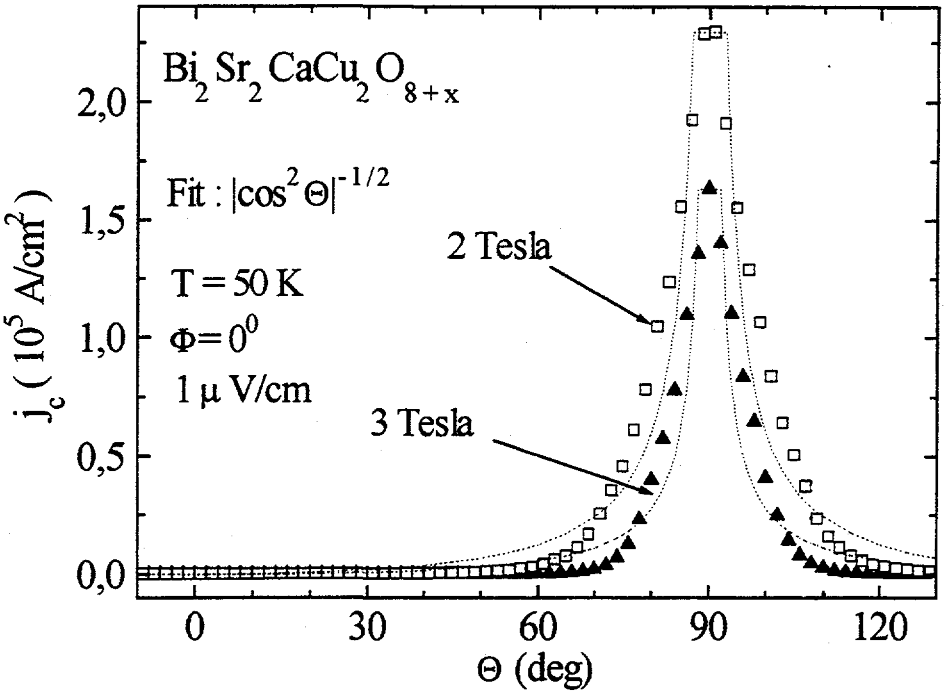

Figure 4. Critical current density $j_c(\Theta)$ in high magnetic fields.

In Figure 4 the results of the angular dependence of the critical current density $j_c(\Theta)$ for a $Bi_2Sr_2CaCu_2O_{8+x}$ film in high magnetic fields are presented. The sharpened maxima of the critical current densities compared to the results for $YBa_2Cu_3O_{7-\delta}$ films seem to be related to the stronger anistropy of the layered structure of these films. For the nearly two dimensional behaviour of this superconductor in high magnetic fields the function $j_c(\Theta) \sim |\cos^2\Theta|^{-1/2}$ is best fitting [3]. But also the function used for the $YBa_2Cu_3O_{7-\delta}$ results with a very small anisotropy parameter fits the $Bi_2Sr_2CaCu_2O_{8+x}$ measurements quite well.

A typical result for $j_c(\Theta)$ in a low magnetic field is shown in Figure 5. Corresponding to the measurements on the $YBa_2Cu_3O_{7-\delta}$ films the anisotropic behaviour of the film decreases with decreasing the magnetic field. For an external magnetic field of 50 mT the function $j_c(\Theta) \sim (\cos^2\Theta + \varepsilon^2\sin^2\Theta)^{-1/2}$ is best fitting. But whereas the anisotropy parameter ε for the $YBa_2Cu_3O_{7-\delta}$ film for this magnetic field is around $\varepsilon^2 = 0.25$, this parameter is for the $Bi_2Sr_2CaCu_2O_{8+x}$ film with $\varepsilon^2 = 0.08$ only about 1/3 of this value due to the stronger anisotropy of the $Bi_2Sr_2CaCu_2O_{8+x}$ superconductor.

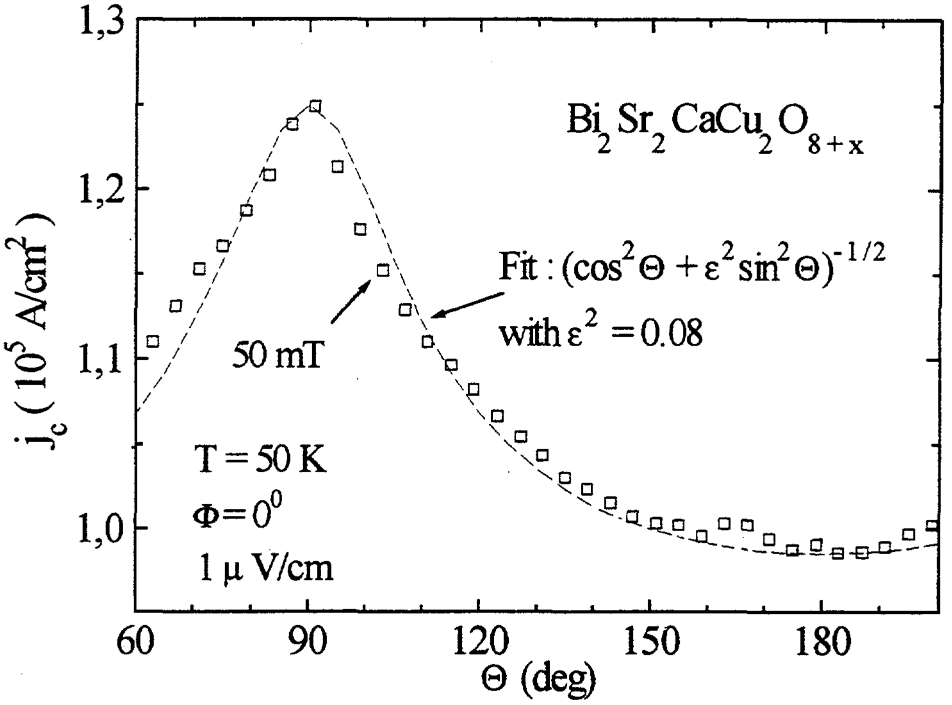

Figure 5. Critical current density $j_c(\Theta)$ in a low magnetic field.

3.2. Magnetoresistance

Besides investigations of the angular dependence of the critical current density $j_c(\Theta)$, the magnetoresistance $\rho(\Theta)$ was measured in high and low magnetic fields.

3.2.1. High magnetic fields

Figure 6 shows a typical result of the angular dependence of the magnetoresistance $\rho(\Theta)$ in high magnetic fields at a temperature of 4.2 K for a $YBa_2Cu_3O_{7-\delta}$ film. The measurements were made for high current densities due to the superconductor being in the mixed state. As expected the magnetoresistance reaches its minimum at $\Theta = 90^\circ$, which means that the *c*-axis of the film is perpendicular to the magnetic field *B*. The maximum of $\rho(\Theta)$ appears at $\Theta = 0^\circ$ where the *c*-axis is parallel to *B*. As in the corresponding measurements of the critical current density the magnetoresistance in high magnetic fields reveals the strong anisotropy of these superconductors because of the layered structure of these films [4]. The function $\rho(\Theta) \sim |\cos^2\Theta|^{1/2}$ for nearly two dimensional behaviour of the film fits as well as $\rho(\Theta) \sim (\cos^2\Theta + \varepsilon^2\sin^2\Theta)^{1/2}$ with $\varepsilon^2 \leq 0.01$. So this also supports the assumption that for the magnetic field parallel to the CuO_2 planes the pinning is very strong and the flux lines are located by extrinsic pinning centers.

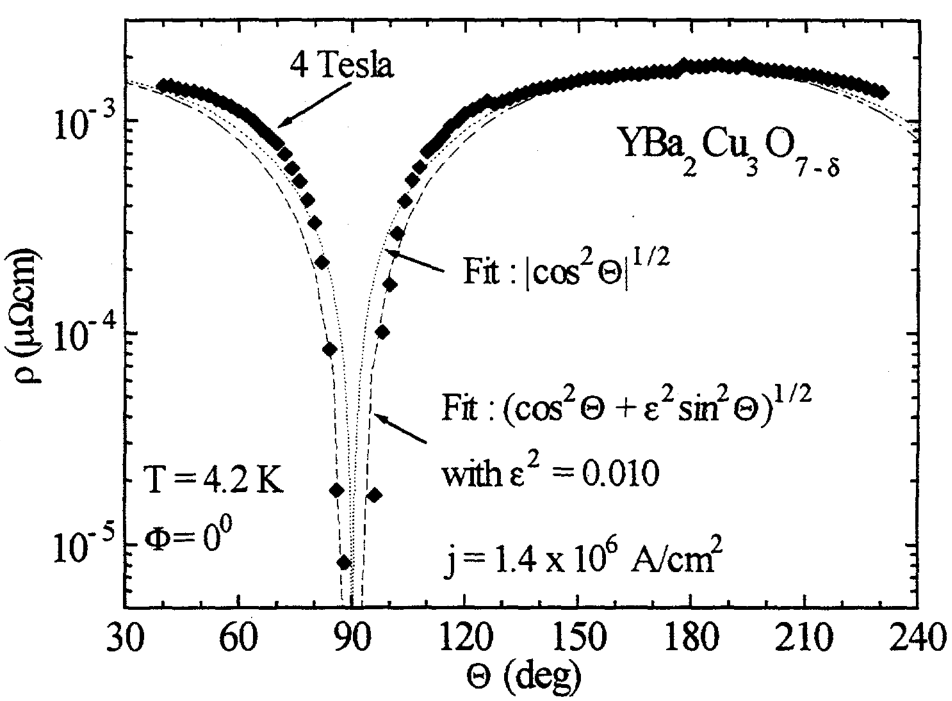

Figure 6. Magnetoresistance $\rho(\Theta)$ in a high magnetic field.

For the measurements of the magnetoresistance $\rho(\Theta)$, as presented in Figure 7, the angle Φ between the current direction and the cB-plane (Θ-rotation plane) of the film was 90°, which means that for $\Theta = 90^\circ$ the current direction was perpendicular to the magnetic field B. The amplitude of the magnetoresistance is smaller for $\Phi = 90^\circ$, but the minima are sharpened. These results correspond to the measurements of the angular dependence of the critical current density $j_c(\Theta)$ as far as for $\rho(\Theta)$ there is a Φ-dependent part of the dissipation probably caused by the Lorentz force acting on the flux lines, too. The logarithmical $\rho(\Theta)$ curves are similar to the inverted $j_c(\Theta)$ curves.

At six Tesla there is a local minimum for $\Theta = 0^\circ$ or 180° independent of the angle Φ. This form of the curves appears only in high magnetic fields and not all measured films show this effect. We attribute these extra pinning of the flux lines to the pinning at twin boundaries [5,6].

In high magnetic fields and at $\Phi = 90^\circ$ the function $\rho(\Theta) \sim |\cos^2\Theta|^{1/2}$ is best fitting due to the nearly two dimensional behaviour of the $YBa_2Cu_3O_{7-\delta}$ film. For the results obtained in a magnetic field of 0.5 Tesla the function $\rho(\Theta) \sim (\cos^2\Theta + \varepsilon^2\sin^2\Theta)^{1/2}$ is used because of the decreasing anisotropy with decreasing the magnetic field.

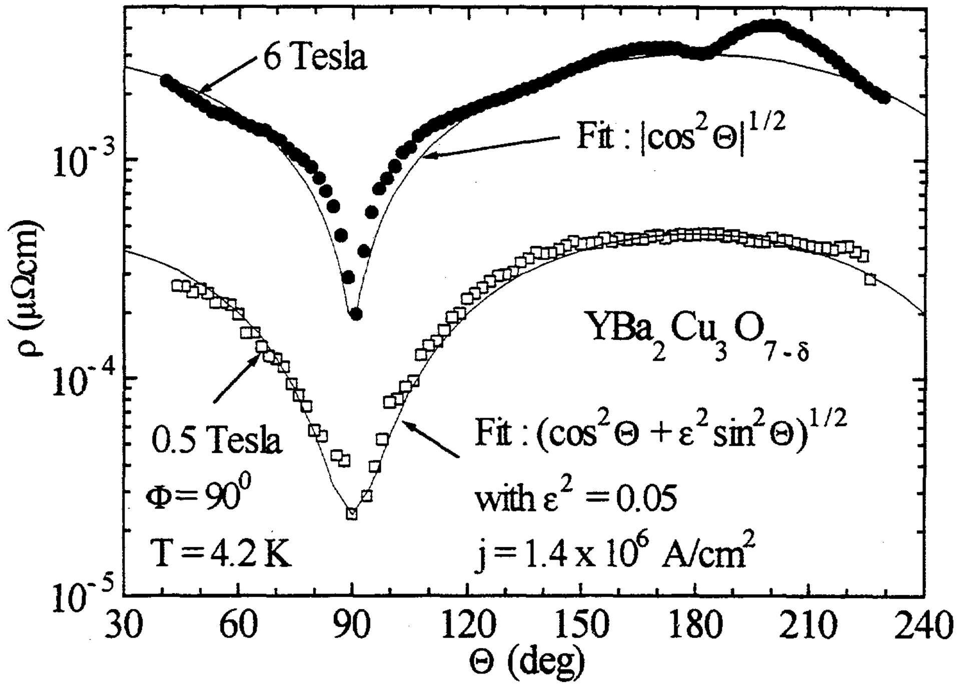

Figure 7. Magnetoresistance $\rho(\Theta)$ for $\Phi = 90^\circ$.

3.2.2. Low magnetic fields

While for high magnetic fields the value of the external magnetic field is the same as for the internal field, the external field may differ from the field in the sample in very low magnetic fields. Probably because of this in low magnetic fields phenomena are seen, which are related to some hysteretical effects.

In Figure 8 the magnetoresistance $\rho(\Theta)$ in a magnetic field of 25 mT at a temperature of 4.2 K is presented. Whereas the dashed curve was measured with a constant magnetic field between the angle Θ-steps, the solid line shows the $\rho(\Theta)$ curve with no magnetic field between the Θ-steps. If the external magnetic field is switched off before every Θ-step, the minimum of the magnetoresistance appears at $\Theta = 90^\circ$ as expected. But if it is continously operated during the angle Θ movement from 30° to 240°, the minima of $\rho(\Theta)$ are shifted and asymmetrical. The drop of the magnetoresistance is sharpened, whereas the increase of $\rho(\Theta)$ is broadened. If the angle Θ is tilt in the opposite direction, the shift changes its direction, too [7].

This hysteretical effect is not seen for high quality films or at higher temperatures above the irreversibility line. It seems to be related with penetrating and trapping of flux, if the sputtered HTSC film consists of several granular parts. The change of the effective external field, which depends on the tilt angle Θ, influences the internal field in the sample due to a motion of vortices. Therefore the flux seems to penetrate and to be trapped for a constantly applied magnetic field [8], which means that the vortices are pinned due to the macroscopic inhomogeneity of the pinning potentials in the sample [9]. If the magnetic field is switched off before every Θ-step, the flux is expelled from the sample. For corresponding critical current measurements on these films we got similar results. The appearance of this effect could be a further criterion of the quality for the HTSC films.

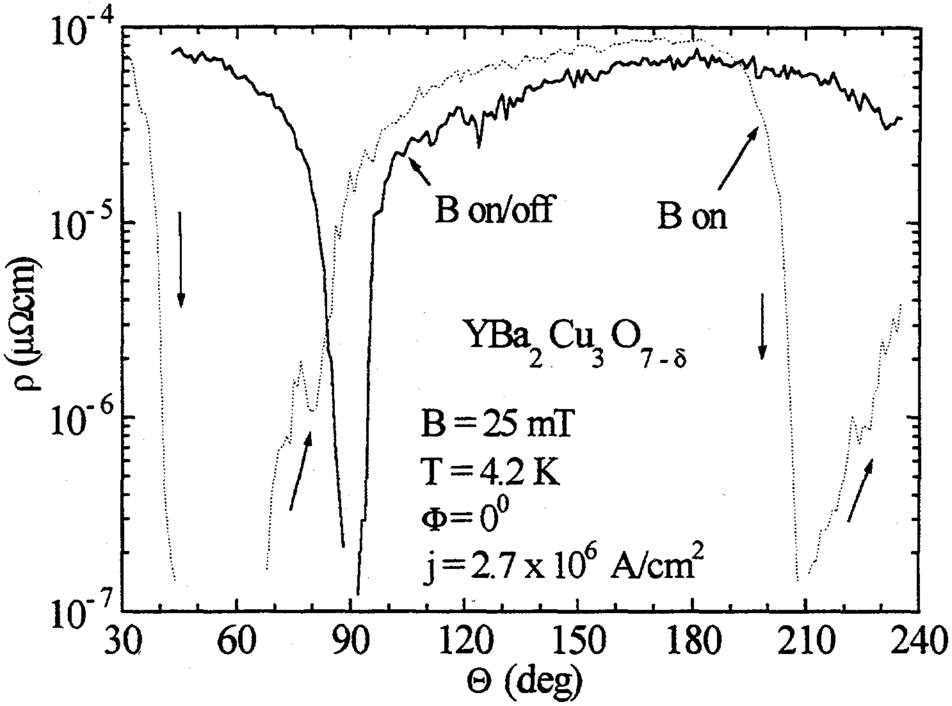

Figure 8. Magnetoresistance ρ(Θ) in a low magnetic field.

The dependence of the magnetoresistance on the strength of the external magnetic field B for low magnetic fields at a constant angle $\Theta = 0^\circ$ is shown in Figure 9. The results reveal a $\rho(B) \sim B^{1/2}$ dependence, which indicates a more three dimensional behaviour of the $YBa_2Cu_3O_{7-\delta}$ films for low magnetic fields due to the theory [10,11]. For measurements of the critical current density dependent on the strength of the magnetic field B, we got a $j_c(B) \sim 1/B$ dependence for very low magnetic fields, which also indicates the small anisotropy of these films for low magnetic fields. This is in agreement with our other results, which show the anisotropic character of the investigated $YBa_2Cu_3O_{7-\delta}$ and $Bi_2Sr_2CaCu_2O_{8+x}$ films increasing with increasing the magnetic field.

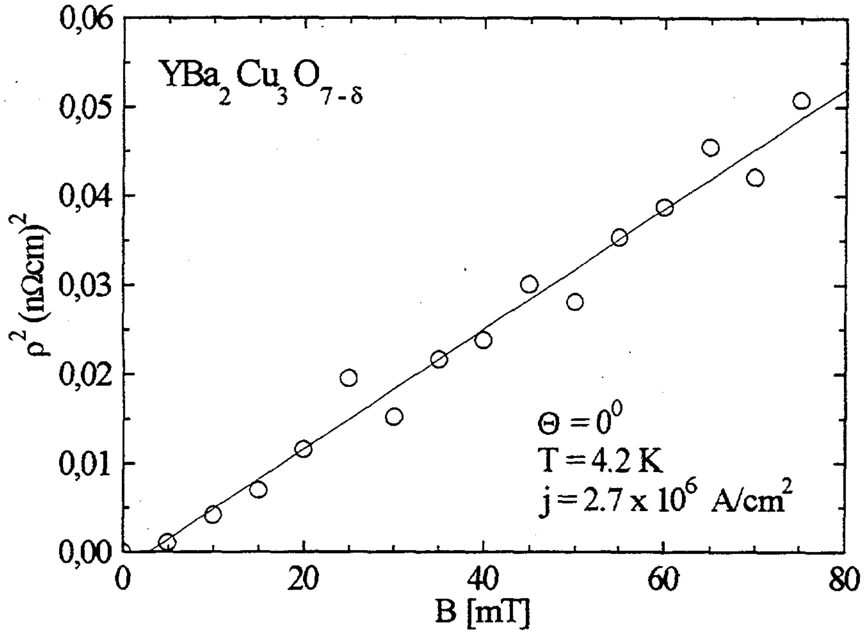

Figure 9. $\rho^2(B)$ curve for low magnetic fields.

Acknowledgement

This work was supported by the BMFT (FKZ : 13N5487/5).

REFERENCES

1. P. H. Kes, J. Aarts, V. M. Vinokur, and C. J. van der Beek, Phys. Rev. Lett. 64 (1990) 1063.
2. G. Blatter, V. B. Geshkenbein and A. I. Larkin, Phys. Rev. Lett. 68 (1992) 1626.
3. M. Tachiki, S. Takahashi, Solid State Commun. 72 (1989) 1083.
4. Y. Iye, A. Fukushima, T. Tamegai, T. Terashima, Y. Bando, Physica C 185-189 (1991) 297.
5. B. Roas and L. Schultz, G. Saemann-Ischenko, Phys. Rev. Lett. 64 (1990) 479.
6. Y. Iye, T. Terashima and Y. Bando, Physica C 177 (1991) 393.
7. A. Geerkens, R. Scholtes, F. Stellmach, M. Brakmann, S. Ewert and Yu. B. Lyanda-Geller, J. Alloys Comp. 195 (1993) 435.
8. J. E. Evetts, B. A. Glowacki, Cryogenics 28 (1988) 641.
9. E. H. Brandt, Inst. J. Mod. Phys. B5 (1991) 751.
10. B. L. Altshuler and A. G. Aronov, "Electron Electron Interaction in Disordered Systems", A. L. Efros and M. Pollak (Ed.), North Holland (1985).
11. A. Kawabata, Solid State Commun. 34 (1980) 431.

Correlations Between Critical Current Density, j_c, Critical Temperature, T_c, and Structural Quality of $Y_1B_2Cu_3O_{7-x}$ Thin Superconducting Films.

J. Chrzanowski, W. B. Xing, D. Atlan, J. C. Irwin and B. Heinrich, *Department of Physics, Simon Fraser University, Burnaby, B.C., Canada V5A 1S6.*

R. A. Cragg, H. Zhou, V. Angus, F. Habib and A. A. Fife, *CTF Systems, Inc., 15-1750 McLean Ave., Port Coquitlam, B.C., Canada V3C 1M9.*

ABSTRACT

Correlations between critical current density (j_c) critical temperature (T_c) and the density of edge dislocations and nonuniform strain have been observed in YBCO thin films deposited by pulsed laser ablation on (001) $LaAlO_3$ single crystals. Distinct maxima in j_c as a function of the linewidths of the (00ℓ) Bragg reflections and as a function of the mosaic spread have been found in the epitaxial films. These maxima in j_c indicate that the magnetic flux lines, in films of structural quality approaching that of single crystals, are insufficiently pinned which results in a decreased critical current density. T_c increased monotonically with improving crystalline quality and approached a value characteristic of a pure single crystal. A strong correlation between j_c and the density of edge dislocations N_D was found. At the maximum of the critical current density the density of edge dislocations was estimated to be $N_D \sim 1\text{-}2 \times 10^9 /cm^2$.

1. Introduction.

Researchers involved with high-T_c film growth have focussed their efforts on optimizing deposition and annealing parameters to achieve the highest critical current density (j_c) and critical temperature (T_c) [1]. The highest j_c and T_c values have been reported for epitaxially grown films of YBCO, deposited on closely matched lattices such as the (001) faces of $SrTiO_3$ and $LaAlO_3$ single crystals [2]. It is usually assumed that the ultimate values of T_c and j_c in films with a defect-free crystalline structure. However, Siegel et al [3] showed recently that an excellent YBCO film structure may have a relatively low critical current density, close to that of bulk single crystals.

In this paper we present direct evidence that improvement of a film structural quality beyond a specific limit is detrimental for the critical current density in YBCO thin films. Our results indicate that a certain density of structural defects is required for effective pinning of flux lines. Distinct maxima in j_c as a function of $\Delta\omega$ (linewidths of the rocking curves) and as a function of $\Delta(2\theta)$ (linewidths of the (00ℓ) Bragg reflections) have been found in epitaxial films. The dependence on $\Delta\omega$ implies the importance of edge dislocations in the flux pinning. The dependence of j_c on $\Delta(2\theta)$ indicates that the flux pinning is affected by structural defects responsible for variations in the c-axis length.

2. Film deposition.

The YBCO films investigated here were deposited by pulsed laser deposition from a YBCO target onto the (001) faces of $LaAlO_3$ single crystals (1 x 1 cm^2) using a KrF excimer laser (248 nm). The resulting film thicknesses were about 3000 Å. The details concerning film deposition, annealing and structural characterization are described elsewhere [4]. The films studied exhibited a smooth, lustrous appearance and were free of any visible defects. The critical temperature and the critical current density (at 77 K) were determined by an inductive method [5].

3. Methods of structure characterization.

X-ray structure investigation of the films was carried out on a Siemens D-5000 diffractometer with filtered (Ni) CuK_α radiation. The studies presented in this paper were carried out using θ–2θ X-ray scans and X-ray rocking curves. A brief description of these techniques is presented below.

The Bragg line broadening $\Delta(2\theta)$ is known to arise both from the instrumental resolution as well as from structural properties of the specimen under investigation [6-8]. In our case, the instrumental broadening has been observed to be negligibly small ($\Delta(2\theta)_{instr} = 0.02^o$). Over and above this instrumental broadening the line width is usually increased by such factors as small crystallite size and lattice distortions caused by a nonuniform strain in the film due to the presence of edge dislocations, cation substitutions, vacancies, interstitial atoms, etc. [6-8]. In fine-grain polycrystalline samples, the main contribution to $\Delta(2\theta)$ is due to small grain size. In epitaxial films such a contribution is negligible. Thus the major source of the variation in the linewidth $\Delta(2\theta)$ appears to be caused by variations of the c-axis length within the film.

The measured linewidth, $\Delta(2\theta)$, of Bragg reflections exhibiting a Gaussian line-shape can be expressed as [6,7]:

$$[\Delta(2\theta)]^2 = [k\,\lambda/g\,\cos\theta]^2 + [2\Delta d/d]^2\,\tan^2\theta + [\Delta(2\theta)]^2_{instr}, \qquad (1)$$

where; θ is the Bragg angle of a (00ℓ) reflection, k is a constant (= 0.9), λ is the wavelength of the x-ray radiation (here Cu_{K_α}), g is the average structural coherence length along the c-axis, d is the lattice spacing in the direction normal to the film surface, and Δd is the variation from the average lattice spacing. $\Delta(2\theta)_{instr}$ is the instrumental broadening. For epitaxial and polycrystalline films consisting of large grains ($g \geq 1000$ Å) the major contribution to the line broadening comes from the second term [7] and thus the above formula reduces to

$$\Delta(2\theta) = 2\,(\Delta d/d)\,\tan\theta. \qquad (2)$$

For a given Bragg reflection (the (005) reflection was used in this work), $\tan\theta$ = constant, so that $\Delta(2\theta) \sim \Delta d/d = \varepsilon$, where ε is the lattice nonuniform strain [7,8].

It is known that even high quality single crystals consist of sub-micron (~1000 Å) blocks (sub-grains), which scatter x-ray radiation coherently [6-8]. These blocks, forming a *mosaic structure*, are separated by arrays of edge dislocations which are polygonized to form small angle boundaries during the high temperature annealing of the film [9].

Regardless of the film growth mechanism, the merging growth spirals or islands produce planar arrays of edge dislocations which separate mosaic blocks. YBCO films grown by laser ablation usually contain many screw dislocations which were also observed in our films (Fig. 1.).

Fig.1. STM image of a laser ablated YBCO film grown on $LaAlO_3$ (100) showing growth spirals. The image covers area of 1.6 x 1.6 μm^2.

HREM studies of YBCO films [10] have shown numerous edge dislocations which occur most likely at the sites where the growth spirals merge, thus creating dislocation walls. These dislocations accommodate the misorientation of the adjacent domains, and are seen as the termination points of the lattice extra half-planes [10].

The density of the edge dislocations can easily be estimated [11]. Assuming that the boundary between two blocks (or islands) consists of a sheet of parallel edge dislocations of the same sign (whose lines are parallel to the a- or b-axis of the film) and if the misorientations of the neighbouring domains exhibit a Gaussian distribution, than the relationship between the measured rocking curve linewidth, $\Delta\omega$, and the density of edge dislocations N_D, is given by [11]:

$$N_D = (\Delta\omega)^2/9b^2, \tag{3}$$

where b is magnitude of the Burgers vector of the edge dislocations. This method is sensitive to dislocations extending at right angles to the crystal surface and compares well with the method relying on etch pit counting [11].

3. Results.

To investigate the influence of structural quality on T_c and j_c, we have studied the mosaic spread in the YBCO films by measuring the widths of the (005) X-ray lines rocking curves. In Fig. 2. the critical current density, j_c, measured in the YBCO films is plotted as a function of $\Delta\omega$, the half-width of the (005) X-ray peak rocking curve. It is evident from Fig. 2, that there is a distinct maximum in j_c vs. $\Delta\omega$ dependence. The maximum is around $\Delta\omega = 0.28^o$. The density N_D can be estimated here from equation (3) using the Burgers vectors of edge dislocations in YBCO reported by Mannhart et al [12], b[100] and b[010]. For $\Delta\omega = 0.28^o$, the corresponding values are 1×10^9 cm^{-2} and 2×10^9 cm^{-2} respectively. It is worth noting here that these values are very close to the density of screw dislocations reported in Ref. 12. For a small mosaic spread (< 0.3°) one edge dislocation is needed to define a single coherent domain, thus the density of edge dislocations should roughly be equal to that of screw dislocations.

For either larger or smaller mosaic spread than $\Delta\omega = 0.28°$, the measured j_c rapidly decreases. While low values of j_c for broad rocking curves, $\Delta\omega > 0.5°$, can easily be accepted, a decrease in j_c for a small mosaic spread is not as obvious. However this result

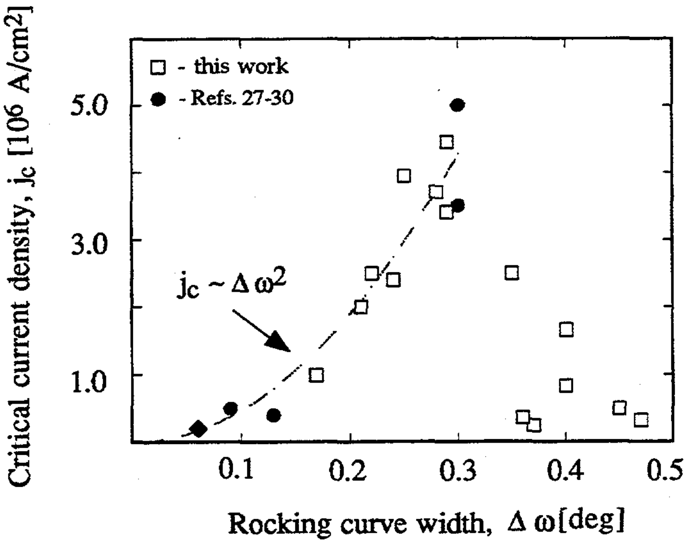

Fig. 2. Critical current density j_c plotted as a function of the half-width of the (005) peak rocking curve, $\Delta\omega$. j_c data for YBCO single crystals (diamond) [18] and a few high quality YBCO films reported in literature [27-30] (full circles) are also shown for comparison.

can be understood if one accepts that an improvement of the film structure, which involves lowering of the density of the edge dislocations, leads simultaneously to substantially weaker pinning of the flux lines. It has been observed [17,18] that YBCO single crystals exhibit j_c values 10-100 times lower than those found in YBCO epitaxial films. As a rule, such single crystals also exhibit very narrow x-ray lines.

All the films investigated exhibited exclusively (00ℓ) reflections of the YBCO compound indicative of a highly c-axis oriented texture. However the full width at half-maximum (FWHM) of the (00ℓ) Bragg reflections varied between films. A similar behaviour in the observed dependence of j_c on $\Delta\omega$ was found in the j_c vs. $\Delta(2\theta)$ diagram, see Fig.3. A plot of j_c vs. $\Delta(2\theta)$, for the (005) peak shows (Fig. 3) a distinct exponential-like decrease in j_c in the range $0.12^o < \Delta(2\theta) < 0.50^o$, with a maximum appearing close to $\Delta(2\theta) = 0.12^o$. The critical current density measured in the films exhibiting narrower Bragg peaks ($\Delta(2\theta) = 0.07\text{-}0.10^o$), and thus clearly of a better structural quality, was smaller by a factor of 2-3.

Fig. 3 shows clearly that the lattice strain ε has indeed a substantial effect on the superconductivity in YBCO films, which is in agreement with other observations [13]. Such an effect was also observed for laser ablated and RF sputtered Tl-2212 films as shown in Fig. 3.

4. Interpretation and Conclusions.

Although there is no consensus regarding the role of screw dislocations on flux pinning, a change in the dislocation density leads to substantial changes in j_c [12]. We will show here that it is the edge dislocation arrays situated around perimeters of the growth spirals (or islands) which most likely create the centres necessary for the effective pinning of flux lines in YBCO films.

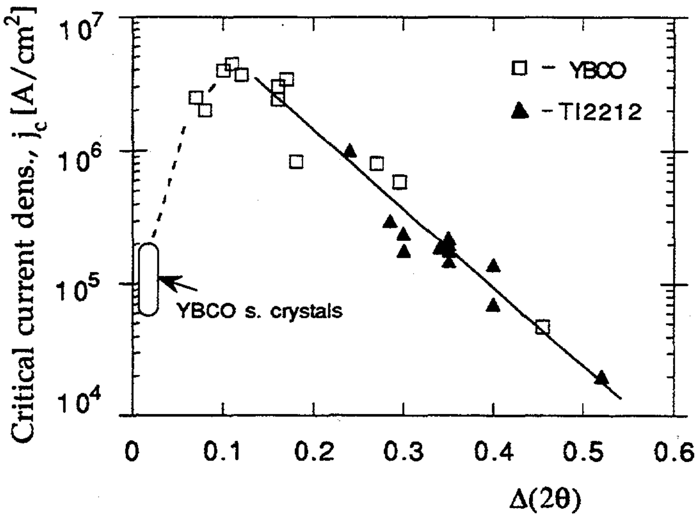

Fig. 3. Critical current density j_c plotted versus half-width ot the (005) Bragg reflection, $\Delta(2\theta)$. For comparison some points obtained for the Tl-2212 films (full triangles) are also presented.

The observed dependence of j_c on $\Delta\omega$ may be explained as follows. Initially, for a large mosaic spread ($\Delta\omega > 0.5^o$), the dislocation arrays reduce the critical current density relative to the value within the coherent domains by acting either as a partial barrier to the supercurrent flow or as weak flux pinning sites. However, this latter effect has been ruled out by careful analysis of the I-V characteristics of the grain boundaries exposed to microwave radiation [14].

For smaller $\Delta\omega$ ($< 0.5^o$), the tunneling barrier becomes narrower and a high current density can be transported between the domains. Such an effect should exhibit an exponential-type dependence on barrier thickness since the tunneling current is likely to vary as $j_c \sim \exp(-2a/\xi_b)$, where 2a is an effective width of the barrier between two adjacent blocks, and ξ_b is the coherence length within the barrier [15]. The array of edge dislocations acts as an effective SNS junction. Assuming a direct proportionality between the pinning potential and the critical current density [16] one can express j_c, as a function of the mosaic spread by

$$j_c \sim U_{eff}[(\Delta\omega)^2/b^2]\cdot\exp(-2a/\xi_b)], \qquad (4)$$

where U_{eff} is an effective pinning energy of the edge dislocation. The first term in (4) corresponds to the flux pinning effect due to the interaction between the edge dislocations and the fluxoids, and the second term represents the attenuation of tunneling current as discussed above. For two mosaic blocks of size $L > 1000$ Å and with $\Delta\omega < 0.3^o$ the largest width of the tunneling barrier does not exceed $2a = 5$ Å $(2a < \xi_{ab} = 15$ Å$)$, which indicates that a high critical current can flow through the edge dislocation wall almost unperturbed. However for higher dislocation densities, the barrier thickness increases as $2a = \Delta\omega\, L$, and becomes comparable with ξ_{ab}. Hence the tunneling current density falls off rapidly. This behavior is evidenced in Fig. 2 for $\Delta\omega > 0.3^o$.

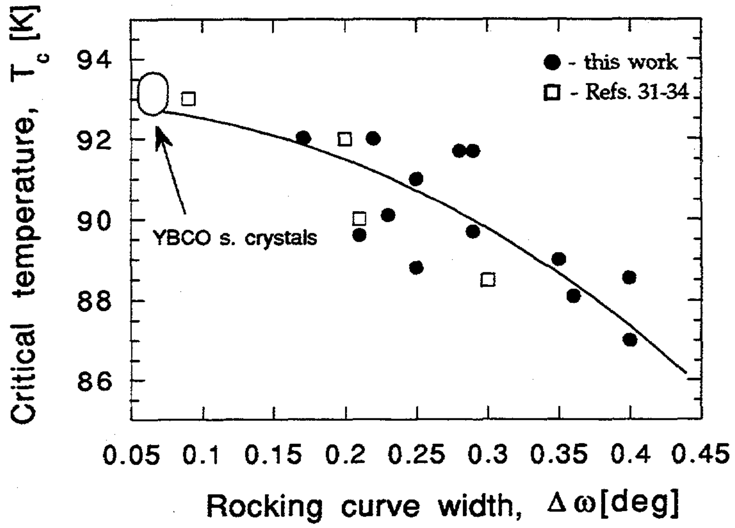

Fig. 4. Ctitical temperature T_c, plotted as a function of the mosaic spread, $\Delta\omega$. As in Fig. 2, the data reported for YBCO single crystals [18] and some of YBCO epitaxial films reported in literature [31-34] are shown (open squares).

The observed increase of j_c in the region of small mosaic spread is proportional to $(\Delta\omega)^2$, see Fig. 2. It is interesting to note that the density of edge dislocations, N_D, is also proportional to $(\Delta\omega)^2$. We suggest that this behaviour is a manifestation of a strong relationship between the critical current density and density of the edge dislocations in the YBCO thin films. We would like to suggest that the initial increase of the critical current density scales with the density of edge dislocations.

It has already been shown for classical superconductors that the strain field of the edge dislocation is an important factor for the pinning effect [19]. The large local distortion of atomic positions can change electronic properties of the film, creating local inhomogeneities in its superconducting properties. Moreover the dangling bonds of edge dislocations create substantial local electric pertubations in the film, leading to charged grain boundaries. It has been recently postulated that such charged grain boundaries in high-T_c materials should be very effective pinning centres which can attract vortices to the grain boundary more effectively than in classical superconductors [20]. The regions of higher dislocation density act as very attractive sites for flux lines [19, 20].

The presence of dislocation networks (edge and spiral dislocations) creates a nonuniform distribution of the lattice strain which leads to a broadening of $\Delta(2\theta)$ diffraction lines in the films. Therefore it is not surprising that a local maximum in j_c was also found in the dependence of j_c on $\Delta(2\theta)$. A contribution to the scattering/pinning effect from isolated point defects [21] as well as of local aggregations of point defects in the vicinity of dislocation (Cottrell atmospheres) [19], and coherent intergrowths [22], can also be significant.

The role of twin boundaries acting as vortex pinning sites has been recently questioned on the grounds that: 1) the measurements of j_c on the same twinned and detwinned YBCO single crystals showed a negligible role of twin boundaries on flux pinning at low temperatures [23]; 2) in YBCO thin films, observed differences in the twin spacing did not result in changes in the volume pinning force. The microstructure of the twin boundaries did not affect the vortex-pinning behaviour of the film [24]. Moreover, the highest critical currents in YBCO layers were observed in twin-free YBCO/$(Nd,Ce)_2CuO_x$ multilayers [25].

The critical current density exhibits a maximum in j_c as a function of the edge dislocation density, while the critical temperature T_c improves constantly with increasing perfection of the film. Fig. 4 shows that $T_c = T_{max}[1 - k(\Delta\omega)^2]$, where k is a constant. One can argue that T_c decreases monotically with an increasing density of edge dislocations, ($N_D \sim (\Delta\omega)^2$). Such a dependence ($T_c = T_c(N_D)$) suggests that edge dislocations are strong scattering centres, whose elimination enhances the critical temperature. This is contrary to the behavior of j_c which requires the presence of lattice defects which act as pinning centres.

This type of behaviour has recently been demonstrated by the introduction of point defects into a high quality superconducting matrix [26]. A few per cent substitution of Pr atoms for Y in YBCO, resulted in a decrease of T_c by about ~2 K, but simultaneously enhanced the critical current density by a factor of 2-3.

Acknowledgements.

The financial support of National Science and Engineering Council of Canada (NSERC), Industry Canada (STP-AIM Program), BC Ministry of Employment and Investment, and Furukawa Electric Co., is gratefully acknowledged.

References.

1. See e.g. R. Feenstra, T.B. Linderberg, J.D. Budai and M.D. Galloway, J. Appl. Phys. **69**, 6569(1991), and references cited therein.
2. U. Poppe, N. Klein, U. Daehne, H. Soltner, C.L. Jia, B. Kabius, K. Urban, A. Lubig, K.Schmidt, S. Hensen, S. Orbach, G. Mueller, and H. Piel, J. Appl. Phys. **71**, 5572(1992).
3. M.P. Siegel, J.M. Phillips, A.F. Hebard, R.B. van Dover, R.C. Fanow, T.H. Tiefeland J. Marshal, J. Appl. Phys, **70**, 4982(1991).
4. J. Chrzanowski, M.X. Burany, W.B. Xing, A.E. Curzon, J.C. Irwin, B. Heinrich, A. Cragg, V. Angus, F.Habbib, H. Zhou and A. Fife, this conference.
5. W.B. Xing, B. Heinrich, J. Chrzanowski, J.C. Irwin, H. Zhou, A. Cragg and A.A. Fife, .Physica C **205**, 311(1993).
6. Elements of X-ray Diffraction, 2nd ed., D.B. Cullity, Addison-Wesley, 1978.
7. Elements of X-ray Crystallography, L.A. Azaroff, McGrow-Hill, 1968.
8. X-ray Diffraction Procedures, H.P. Klug and L.E. Alexander, Wiley & Sons, 1966.
9. Dislocations and Plastic flow in crystals, A.H. Cottrell, Clarendon Press, 1965.
10. R. Ramesh, D.M. Hwang, J.B. Barner, L. Nazar, T.S. Ravi, A. Inam, B. Dutta, X.D. Wu, and T. Venkatesan, J. Mat. Res. **5**, 704(1990).
11. A.D. Kurtz, S.A. Kulin and B.L. Averbach, Phys. Rev. **101**, 1285(1956).
12. J. Manhart, D. Ansemetti, J.G. Bednorz, A. Catana, Ch. Gerber, K. A. Mueller, and D.G. Schlom, Z. Phys. B **86**, 177(1992).
13. M.F. Chisholm and S.J.Pennycook, Nature **351**, 47(1991).
14. D. Dimos, P. Chaudhari and J. Manhart, Phys. Rev. B **41**, 4038(1990).
15. J. Clarke, Proc. Roy. Soc. A **308**, 447(1969).
16. T.T. Palstra, B. Batlogg, R.B. van Dover, L.F. Schneemeyer, and J.V. Waszczak, Phys. Rev. B **41**, 6621(1990).
17. A. Umezawa, G.W. Crabtree, J.Z. Liu, H.W. Weber, W.K. Kwok, L.H. Nunez, T.J. Moran, C.H.Sowers and H. Claus, Phys. Rev. B **36**, 7151(1987);
    M.D. Lan, J.Z. Liu, R.N. Shelton, H.B. Radouski, B.W. Veal and J.W. Downey, Phys. Rev. B **46**, 11919(1992).
18. W.N. Hardy et al. private communication.
19. F.R.N. Nabarro in: Dislocations in Solids, vol. 5, ch. 21, North-Holland, 1980.

20. B.Ya. Shapiro and I.B. Khalfin, Physica C **219**, 465(1994).
21. T.L. Hylton and M.R. Beasley, Phys. Rev. B **41**, 11669(1990).
22. T.I Selinger, U. Helmersson, Z. Han, J.-E. Sundgren, H. Sjostrom and L.R. Wallenberg, Physica C **202**, 69(1992).
23. L.J. Schwartzendruber, D.L. Kaiser, F.W. Gayle, L.H. Bennet and A. Roytburd, Appl. Phys. Lett. **58**, 1566(1991).
24. B.M. Lairson, S.K. Streiffer, and J.C. Bravman, Phys. Rev. B 42, 10067(1990).
25. R. Gross, A. Gupta, E. Olsen, A. Segemueller, and G. Koren, Appl. Phys. Lett. **57**, 203(1990).
26. H. Ren, K.N.R. Taylor, Y.J. Chen, J.A. Xia, and H. Quing, Physica C **216**, 447(1993).
27. D.H. Lienberg, P.C. McIntyre, H.J. Cima and T.L. Francavilla, Cryogenics **37**, 1066(1992).
28. S.N. Barilo, G.I Bychkov, A.V. Zubets, N.S. Orlova, V.I. Gatalskaya, D.I. Zhigunov, L.A. Kurnewich, M.N. Olekhnovich and A.V. Pushkariev, IEEE Trans. Appl. Supercond. **3**, 1074(1993).
29. B. Kabius, K. Urban, A. Lubig, K. Schmidt, S. Hensen, S. Orbach, G. Mueller and H. Piel, J. Appl. Phys. **71**, 5572(1992).
30. W. Schauer, V. Windte, J. Reiner, G. Linker, J. Greek, X.X. Xi and W.K. Schomburg, Proc. ICMC '90 Topical Conference on Mat. Asp. High-Tc Supercond., May 1990, Garmisch-Partenkirchen, FRG.
31. T. Nagashi, H. Itozaki, S. Tanaka, T. Mansura, N. Ota, N. Fujimori and S. Yazu, J. J. Appl. Phys. **30**, L718(1991).
32. S.G. Lee, G. Koren, A. Gupta, A. Segemueller and C. Chi, Appl. Phys. Lett. **55**, 1261(1989).
33. C.T. Rogers, A. Inam, J.B. Barner, R. Ramesh and T. Venkatesan, Proc. ICMC '90 Topical Conference on Mat. Asp. High-Tc Supercond., May 1990, Garmisch-Partenkirchen, FRG.
34. A. Gladun, N. Cherpak, A. Gippus, S. Hensen, M. Lenkens, G. Mueller. S. Orbach and H. Piel, Cryogenics 32, 1071(1992).

THIS PAGE INTENTIONALLY LEFT BLANK

THIS PAGE INTENTIONALLY LEFT BLANK

High Temperature Materials

Session 1 Chair: Prof. Mikio Takano

The Oxygen Content of the High-Temperature Superconducting Compound $Bi_{2+x}Sr_{3-y}CayCu_2O_{8+d}$ with Respect to Varying Ca and Bi Contents

P. Majewski, H.-L. Su, F. Aldinger

Max-Planck-Institut für Metallforschung, Heisenbergstr. 5, D-70569 Stuttgart, FRG

Abstract

The oxygen content of $Bi_{2+x}Sr_{3-y}Ca_yCu_2O_{8+d}$ (2212 phase) has been determined as a function of its cation concentration. With increasing Ca and Bi content the oxygen content increases and T_c decreases. The oxygen content of Ca rich 2212 phase increases with decreasing annealing temperatures. The study shows that the T_c of the 2212 phase primarilly is controlled by its cation concentration.

1. Introduction

The oxygen content of the 2212 phase with respect to varying cation concentrations of the phase has not yet been determined in detail, although the phase exhibits an extended single phase region which allows considerable deviations from the ideal formula $Bi_2Sr_2CaCu_2O_8$ [1,2]. In addition, the T_c of the phase obviousely is a function of the Sr, Ca and Bi content [1,3]. The question arises, whether the T_c is controlled by the oxygen content directly or by the cation concentration which of course influence the oxygen content of the phase.

2. Experimental

Samples were prepared along the concentration range $Bi_{2.18}Sr_{3-y}Ca_yCu_2O_z$ with y = 0.8, 0.9, 1.1, 1.3, 1.45, 1.5 and 1.7. A second batch of samples were prepared with varying Bi contents refering $Bi_{2+x}Sr_2CaCu_2O_z$ with $x = 0.125$, 0.18, 0.2 and 0.3. The samples were sintered for 24 hours at 820 °C in air. Subsequently, the samples were regrinded, pressed, sintered at the same temperature for 60 hours and furnace cooled. Finally, the samples were annealed at 670 °C in flowing nitrogen for 15 hours in order to reach high T_c values. Phase identification has been performed using a Scanning Electron Microscope with EDX (Cambridge Instruments S 200), X-ray diffraction (Philips PW 1050, CuK) and optical microscopy (Zeiss Axiomat) using polarized light. The oxygen content has been measured by carrier gas hot extrusion using the Leco Inst. N/O-analysator TC 436. The CO_2 content of the prepared samples were measured using the Rosemount carbon/hydrogen analysator 5003. The critical temperatures have been determind by AC susceptibility measurements. The standard deviation of the CO_2 analysis is about 0.005 weight percent and that of the T_c measurements ± 1 K.

3. Results

The prepared samples consist at least of about 95 volume percent 2212 phase. Second phases are Ca_2CuO_3, $Sr_{14}Cu_{24}O_{41-x}$ and CuO. The oxygen content of the prepared samples increases with increasing Ca and Bi content (Fig. 1 and 2). The accuracy of the d-value obviousely depends on the second phase content of the samples. The samples having a great deviation of the d-value (e.g. samples with the y-value of 0.9 and 1.7 in Fig. 1) have a second phase content of about 5 percent. Whereas single phase samples (e.g. y-value 1.1 in Fig. 1) exhibit a very narrow deviation of the d-value. However, even with respect to the deviation of the d-value the trend of the d-value with increasing Ca and Bi content of the 2212 phase is clearly seen.

In agreement with the literature data, the T_c of the prepared samples decreases with increasing Ca and Bi content. The CO_2 content of a Sr rich ($Bi_{2.18}Sr_{2.1}Ca_{0.9}Cu_2O_{8+d}$) and a Ca rich ($Bi_{2.18}Sr_{1.5}Ca_{1.5}Cu_2O_{8+d}$) sample have been determined to be 0.06 weight percent. The thermogravimetry measurements reveal that the oxygen content of the 2212 phase increases with

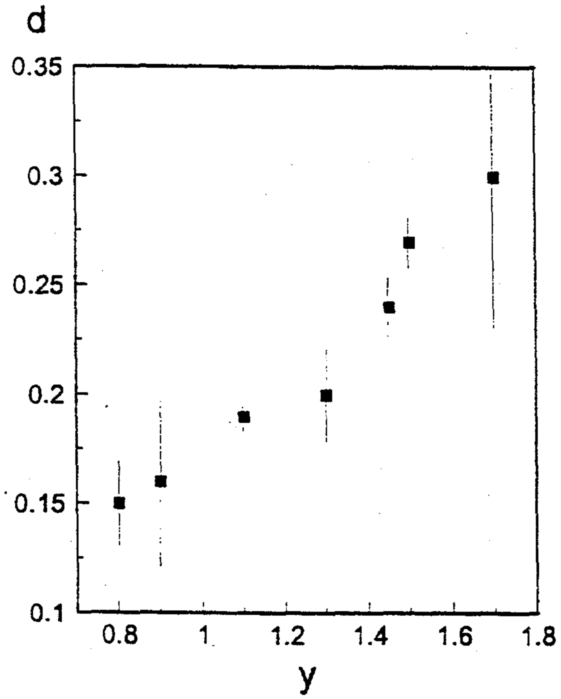

Fig. 1: The oxygen index d vs. the Ca content. y-values ref. $Bi_{2.18}Sr_{3-y}Ca_yCu_2O_{8+d}$.

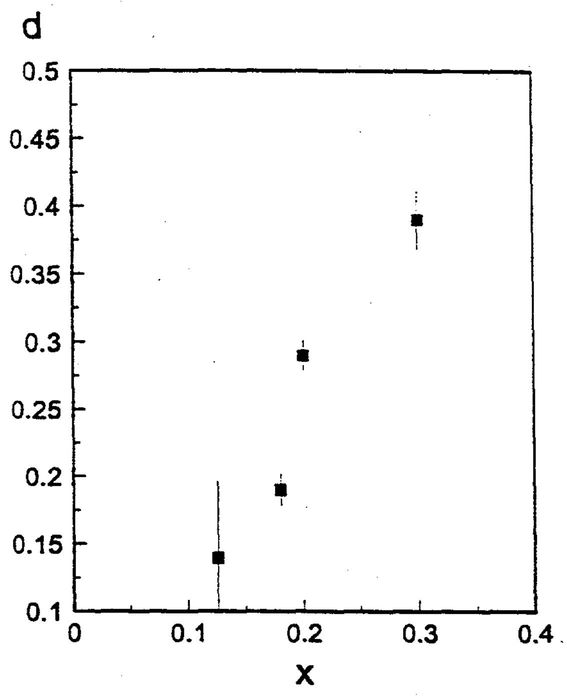

Fig. 2: The oxygen index d vs. the Bi content. x-values ref. $Bi_{2+x}Sr_2CaCu_2O_{8+d}$.

decreasing temperature (Fig. 3), which agrees with the results of [4]. In addition, Fig. 3 clearly shows that this increase is a function of the Ca content of the phase and reaches highest values at Ca rich compositions. Simultaneousely, with decreasing annealing temperature the T_c of the 2212 phase decreases (Fig. 4). However, the decrease of T_c of Ca rich ($\Delta T_c \approx 10$ K) 2212 phase is much more pronounced than that of Sr rich one ($\Delta T_c \approx 2$ K).

4. Discussion

With respect to the deviation of the d-value due to the second phase content of the samples, the observed increase of the oxygen content of the 2212 phase is obviousely caused by an increased oxygen solubility of the Ca and Bi rich 2212 phase compared to $Bi_2Sr_2CaCu_2O_{8+d}$. The identical CO_2 contents of the Sr and Ca rich samples give evidence that the observed increase of the oxygen content is not an artefact, i.e. due to unreacted $CaCO_3$ in the Ca rich samples.

The enhanced oxygen content of the Bi rich samples is possibly due to the fact, that the Bi ions, which substitute the Ca^{2+} and Sr^{2+} ions, are three valent. The resulting excess of the positiv charge supposedly is totaly or partly balanced by the observed increase of the oxygen content of the phase. However, the increase of the oxygen content with increasing Ca content of the phase can not be explained by that model, because both Ca and Sr are two valent.

Fig. 5 shows the T_C values vs. the oxygen index d, published by [5] and the T_C values and oxygen indices d of the prepared samples with varying Sr:Ca ratios. It is clearly seen that the samples with intermediate Sr:Ca ratios (Sr:Ca ≈ 1.7:1.3 to 1.5:1.5) exhibit moderate T_C values of about 80 K, although they have oxygen contents, which should yield high T_C values of about 90 K. The reason for this discrepancy supposedly is that the T_C of the phase is primarily controlled by the cation concentration, especially by the Ca content of the phase. However, considering the prepared samples with enhanced Bi content this effect is not or less pronounced compared to the samples with varying Sr:Ca ratios (Fig. 6). At decreasing temperatures the oxygen content of the 2212 phase was found to

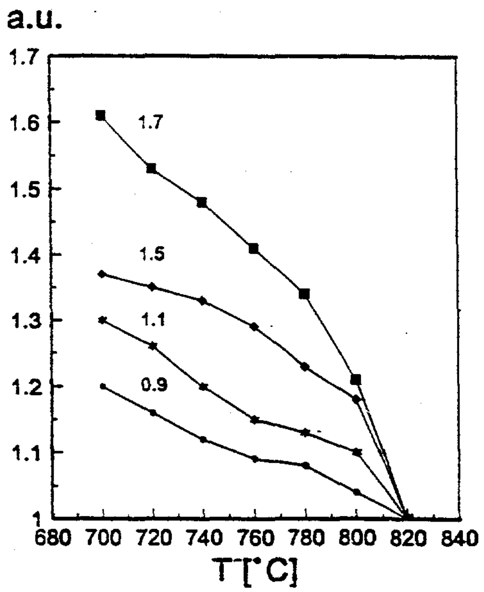

Fig. 3: Oxygen content of the 2212 phase determined by thermo gravimetry measurements vs. temperature. Values are y-values ref. $Bi_{2.18}Sr_{3-y}Ca_yCu_2O_{8+d}$.

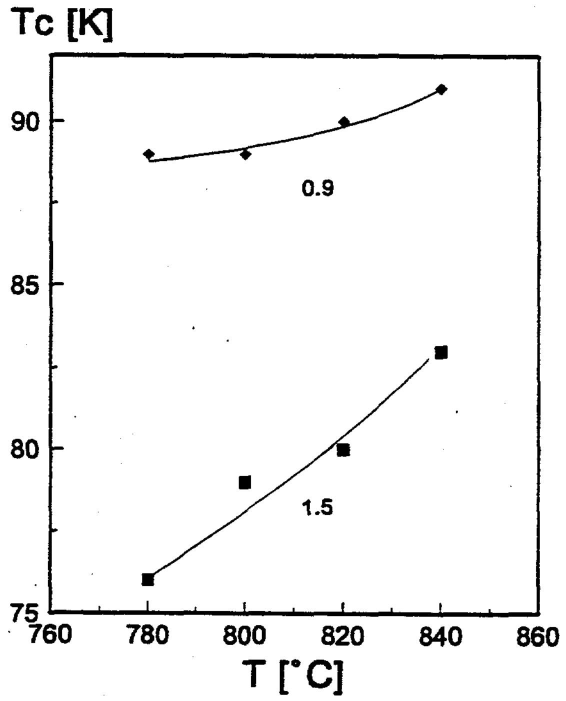

Fig. 4: The T_c of the 2212 phase vs. temperature. The values are y-values ref. $Bi_{2.18}Sr_{3-y}Ca_yCu_2O_{8+d}$.

increase and T_c was found to decrease which agrees with the results of [4]. Considering Ca rich 2212 phase, the increase of the oxygen content and the corresponding decrease of T_c is much more pronounced than that of the Sr rich 2212 phase which clearly shows that at constant cation concentration the oxygen content of the 2212 phase significantly influences the T_c.

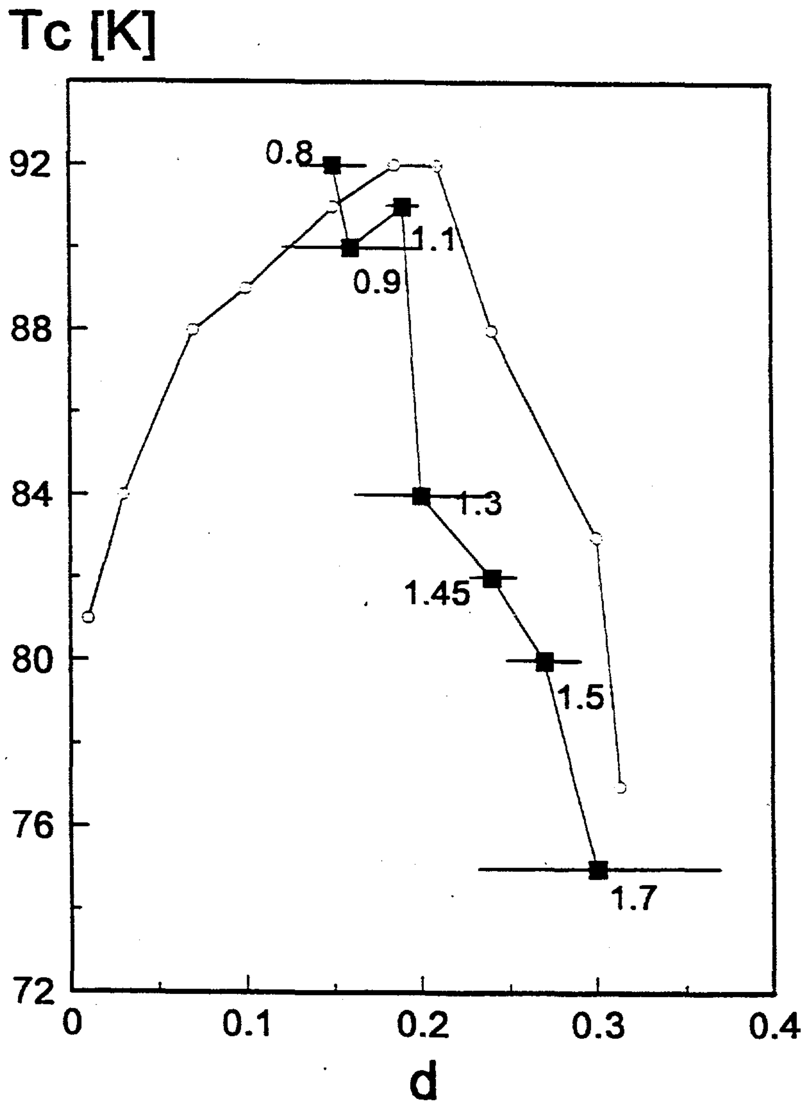

Fig. 5: The T_c vs. the oxygen index d of samples with varying Sr:Ca ratios (black squares: this work; grey points: [5]). The values at the squares are the y-values refering $Bi_{2.18}Sr_{3-y}Ca_yCu_2O_{8+d}$.

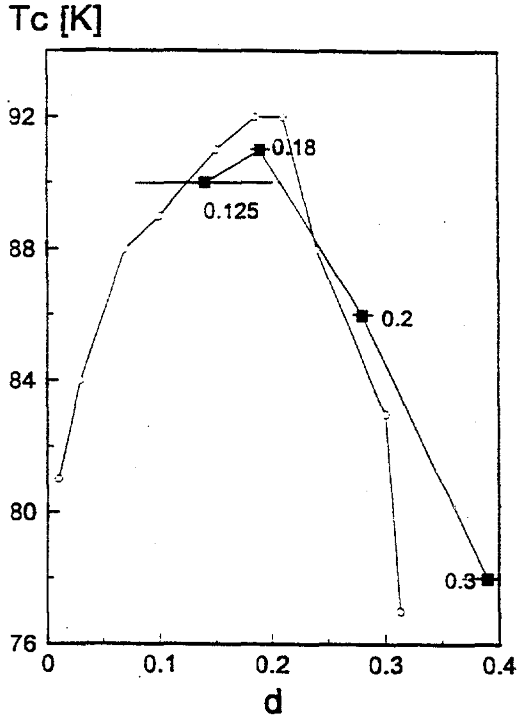

Fig. 6: The T_c vs. the oxygen index d of samples with varying Bi contents (black squares: this work; grey points: [5]). The values at the squares are the x-values refering $Bi_{2+x}Sr_2CaCu_2O_{8+d}$.

6. References

[1] P. Majewski, H.-L. Su, B. Hettich, Adv. Mat., **4** (1992), 508.

[2] R. Müller, Th. Schweizer, P. Bohac, R.O. Suzuki, L.J. Gauckler, Physica C, **203** (1992), 299.

[3] P. Majewski, B. Hettich, N. Rüffer, F. Aldinger, J. Elec. Mater., **22** (1993), 1259.

[4] T. Schweizer, R. Müller, P. Bohac, L.J. Gauckler, Proc. of the Third Conf. Europ. Ceram. Soc, Madrid, 1993, Editors: P. Duran, J.F. Fernandez, Elsevier, London, 1993, 611.

[5] J. Bock, E. Preisler, High-Temperature Superconductors - Materials Aspects, Editors: H.C. Freyhardt, R. Flükiger, M. Peuckert, DGM, Oberursel, FRG, 1991, 215.

Pb Solubility of the High-temperature Superconducting Phase $Bi_2Sr_2Ca_2Cu_3O_{10+d}$

Stefanie Kaesche, Peter Majewski, Fritz Aldinger
Max-Planck-Institut für Metallforschung, Institut für Wekstoffwissenschaften, Pulvermetallurgisches Laboratorium, Heisenbergstraße 5, D-70569 Stuttgart

Abstract

For the nominal composition of $Bi_{2.27-x}Pb_xSr_2Ca_2Cu_3O_{10+d}$ the lead content was varied from x=0.05 to 0.45. The compositions were examined between 830°C and 890°C which is supposed to be the temperature range over which the so-called 2223 phase ($Bi_2Sr_2Ca_2Cu_3O_{10+d}$) is stable.

Only compositions between x=0.18 to 0.36 could be synthezised in a single phase state. For x>0.36 a lead containing phase with a stoichiometry of $Pb_4(Sr,Ca)_5CuO_d$ is formed, for x<0.18 mainly $Bi_2Sr_2CaCu_2O_{8+d}$ and cuprates are the equilibrium phases.

The temperature range for the 2223 phase was found to be 830°C to 890°C but the 2223 phase has extremely varying cation ratios over this temperature range. Former single phase 2223 samples turn to multi phase samples when annealed at slightly higher or lower temperatures. A decrease in the Pb solubility with increasing temperature was found for the 2223 phase.

1. Introduction

In the system BiO-SrO-CaO-CuO three superconducting phases are known: $Bi_2Sr_2CuO_6$ (2201), $Bi_2Sr_2Ca\ Cu_2O_8$(2212) and $Bi_2Sr_2Ca_2Cu_3O_{10}$ (2223). 2212 is easily prepared over a large composition range with different T_c's. But $Bi_2Sr_2Ca_2Cu_3O_{10}$ which is of special interest due to its high critical temperature of 110 K is still very difficult to prepare in a single phase state though Majewski et al. [1] reported a way . They prepared samples containing up to 90 to 95 vol. % 2223 phase with a starting composition significantly Bi-richer than the exact 2223 composition, but at much higher sintering temperatures than recommended for leaded compositions. It is fairly well-known that the 2223 phase formation is promoted by partial substitution of Bi by Pb [2]. But there still exist major problems for single phase material preparation. Numerous attempts have been made to synthesize the lead substituted 2223 phase in a single phase state [3 to 7] but most of the time it was done in an empirical way to find out the best starting composition, temperature, pressure and atmosphere. But this is not very satisfactory since many disagreements exist between the authors.

For the lead free system Majewski et al. [8] and more recently R. Müller et al. [9] presented the phase equilibria in the BiO-SrO-CaO-CuO system at different temperatures in air with special regard to the single phase region of the 2212 and 2201 phase. In [9] the single phase regions of 2212 and 2201 are very precisely worked out for 830°C.

In [8] the single phase region of 2212 for various temperatures and the associated T_c's are reported.

In contrast to the very exact knowledge of the homogeneity range of the 2212 phase only few informations of the homogeneity range of the 2223 phase are found in the literature. This lack of information may be due to the extremely complicated circumstances. Only a few attempts have been made to examine the phase equilibria and to find a single phase region for the 2223 phase. Endo et al. [3] studied the region in the vicinity of the ideal stoichiometry 2223 and found remarkably differences in the phase formation and small differences in T_c. They found that $T_c(0)$ is affected by small composition variations, and if Ca and Cu is in excess to the ideal stoichiometry T_c may be lowered to around 95 K.

A more detailed study is given by Strobel et al. [10] who considered a temperature-concentration cut through the system along the composition line $Bi_{1.6}Pb_{0.4}Sr_2Ca_{n-1}Cu_nO_{2n+4+x}$ from 825 to 1100°C under the assumption that Pb forms no phases independent on Bi.

They say that the 2223 phase exists, as a dominant phase between around 835°C and 875°C for $3 < n < 4$. The presence of Pb lowers the transition lines of the superconducting phases to about 10 to 15°C. None of these studies provides a complete discription of the single phase region of 2223 and of the dependence on Pb content.

Knowing the homogeneity range in dependence on temperature and lead content would be very helpful for preparation of high-quality material. There is still no explanation why partial substitution of Bi by Pb helps to prepare the 2223 phase. The positive effect of Pb might be due to a widening of the homogeneity range or a stabilization of the 2223 phase. To get more insight in the complicated circumstances the lead content was systematically varied starting from the nominal composition of $Bi_{1.91}Pb_{0.36}Sr_2Ca_2Cu_3O_{10+d}$. This composition with a common substitution degree was found to be relatively easily prepared in a single phase state.

2. Experimental

Samples were prepared by the conventional solid state synthesis route starting from 99.9 % pure oxides (Bi_2O_3, PbO, CuO) and carbonates ($CaCO_3$, $SrCO_3$). The powders were weighed and intimately mixed in an agate mortar. The calcination was performed in three steps: 12 h at 750°C, 24 h at 780°C and 12 h at 800°C. After calcination the powders were again grind, pressed into small cylindrical rods and sintered for 60 h in air at 850°C. The sintering step was four times repeated after an intermediate grinding and pressing step resulting in a total sintering time of 300 h. These long reaction times in connection with intermediate grinding and pressing are necessary to assure the completeness of the reaction. After this 300 h reaction time all compositions were annealed at 830 for 200 h, at 860°C, 865°C , 870°C for 60 h, at 880°C 12 h and at 890°C for 2 h. The increasing amount of liquid with increasing temperature makes it necessary to decrease the annealing time since the liquid reacts very easily with the alumina crucible. But this decrease in reaction time with increasing temperature is no drawback for the examinations since all samples were first five times reacted at 850°C to make sure that

the most limiting step for reaching the equilibrium state, the 2223 formation, is completed before annealing at various temperatures.
Starting from the nominal composition of $Bi_{2.27-x}Pb_xSr_2Ca_2Cu_3O_{10+d}$ samples with x=0.05, 0.18, 0.27, 0.36 and 0.45 were prepared.
Phase identification was performed by optical microscopy, X-ray diffraction using Cu-K_α and EDX analyses.
For the composition $Bi_2Pb_{0.27}Sr_2Ca_2Cu_3O_{10+d}$ representing a composition in the middle of the homogeneity range the lead content of the 2223 crystallites was measured at all considered temperatures. Microprobe analysis was necessary to accurately monitor the Pb content.

3. Results

3.1. Homogeneity Range

In Table 1 all found phase equilibria are listed in connection with a symbol corresponding to a certain region in Fig. 1. Figure 1 shows the homogeneity region and existence regions for 2223 in the section under consideration. For the sake of clarity only regions are drawn, no real phase diagram is constructed due to the enormous complexity of five component systems.
Between x=0.18 and 0.36 a single phase region of 2223 is found. Figure 2 shows a Scanning Electron Microscope photograph (BSE) of a sample with the nominal composition of $Bi_2Pb_{0.27}Sr_2Ca_2Cu_3O_{10+d}$. The sample is located in the middle of the single phase region and no other phase than 2223 is detected.

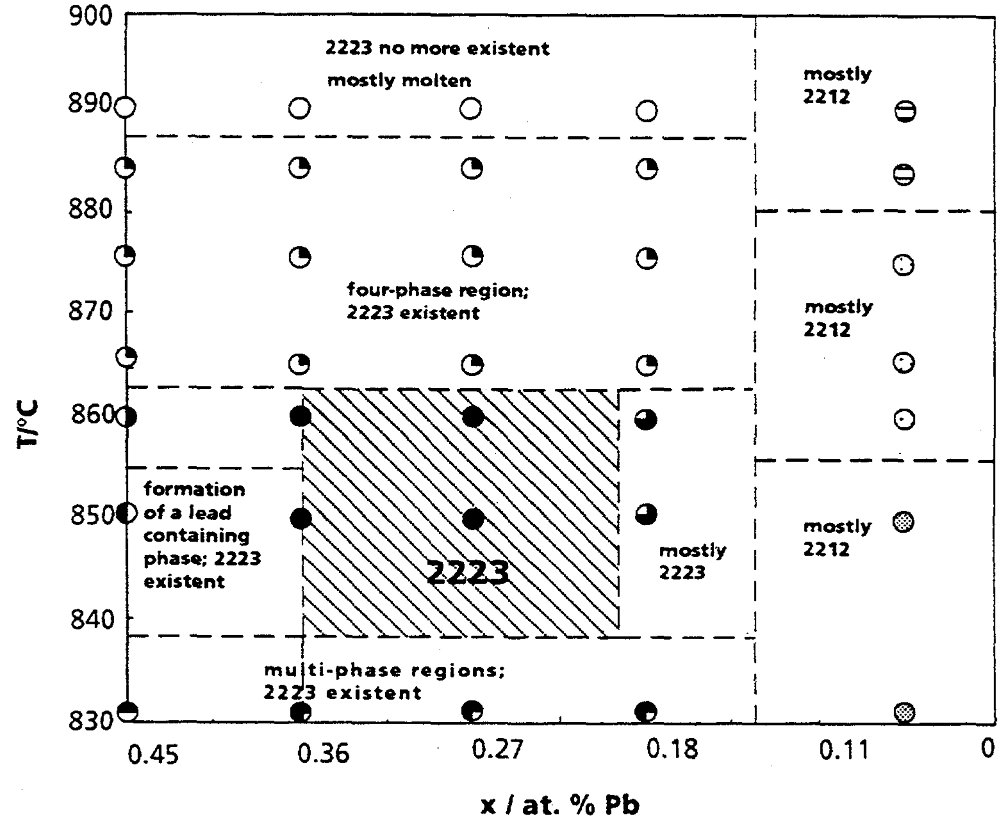

$Bi_{2.27-x}Pb_xSr_2Ca_2Cu_3O_{10+d}$

Fig. 1. Homogeneity region and existence regions of 2223

● single phase 2223

◓ $Pb_4(Sr,Ca)_5CuO_d$ + 2212 + 2223 + CuO

◕ CuO + 2223 +2212

◍ 2212 + $(Sr,Ca)_{14}Cu_{24}O_{41-x}$+ Ca_2CuO_3 + CuO

◐ $Pb_4(Sr,Ca)_5CuO_d$ + $(Sr,Ca)_{14}Cu_{24}O_{41-x}$ + 2223 + liquid + CuO

◕ CuO + 2223 +2212

◑ $Pb_4(Sr,Ca)_5CuO_d$ + $(Sr,Ca)_{14}Cu_{24}O_{41-x}$ + 2223 + liquid

⊙ 2212 + $(Sr,Ca)_{14}Cu_{24}O_{41-x}$+ Ca_2CuO_3 +2223

◔ 2223 + $(Sr,Ca)_{14}Cu_{24}O_{41-x}$ + Ca_2CuO_3 + liquid

⊖ 2212 + $(Sr,Ca)_{14}Cu_{24}O_{41-x}$+ Ca_2CuO_3 +2223 + liquid

○ $(Sr,Ca)_{14}Cu_{24}O_{41-x}$ + Ca_2CuO_3 + 2212 + liquid

Table 1. All analysed phases with symbols corresponding to Fig.1

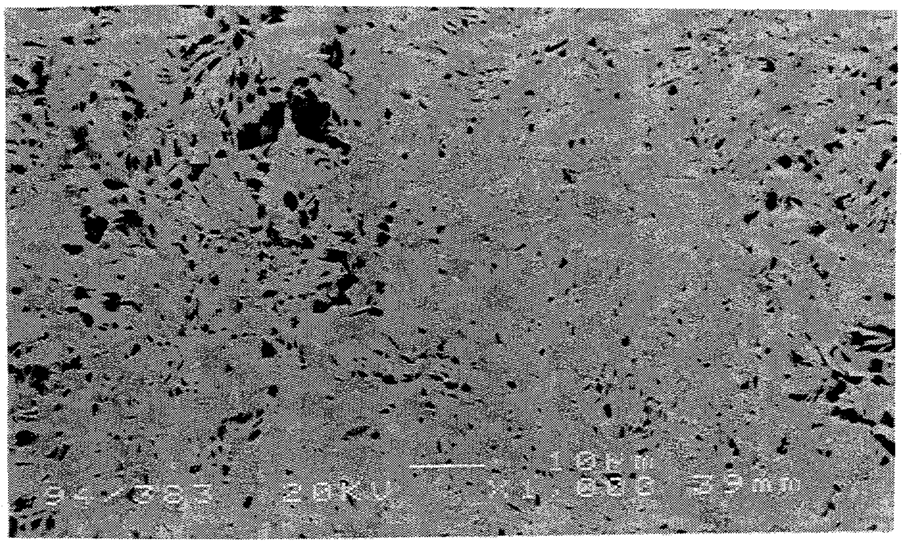

Fig. 2. BSE image of $Bi_2Pb_{0.27}Sr_2Ca_2Cu_3O_{10+d}$ at 850°C

For x>0.36 2223 is in equilibrium with numerous other phases among which a lead containing phase ($Pb_4(Sr,Ca)_5CuO_d$) indicates that the maximum Pb-solubility is exceeded. For x<0.18 only small amounts of 2223 are detected. Phase equilibria with predominantely 2212 are stable over the whole temperature range.

Annealing of samples at temperatures between 865 and 885°C results in no differences concerning the phase equlilibria for x=0.45 to 0.18 all compositions are located within a four phase region (Table 1).Figure 3 shows a BSE image of a sample at 880°C lying in the four-phase region.

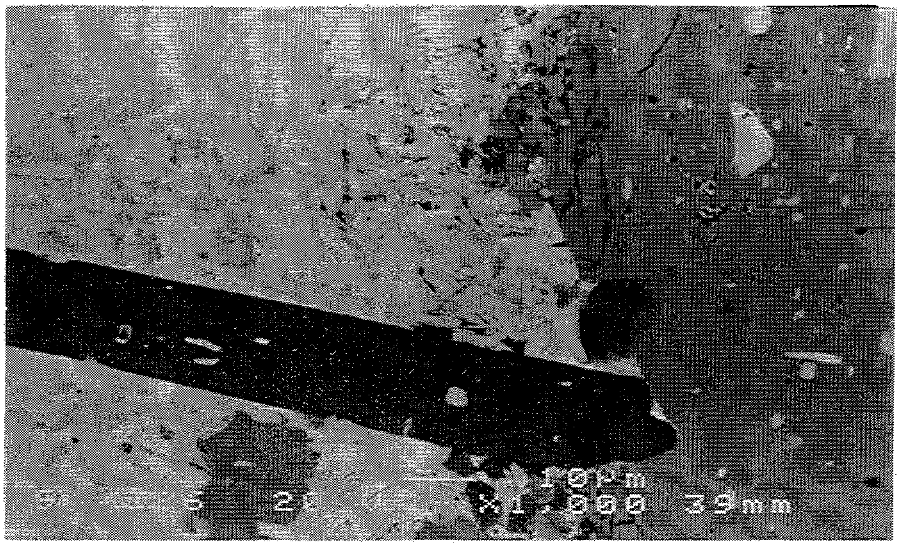

Fig. 3. BSE image of $Bi_2Pb_{0.27}Sr_2Ca_2Cu_3O_{10+d}$ at 880°C (white: liquid, light grey: 2223, grey: Ca_2CuO_3, dark grey: $(Sr,Ca)_{14}Cu_{24}O_{41-x}$)

Samples with x=0.45 to 0.18 contain no 2223 at temperatures higher than 890 °C. We can state the following reaction scheme:

$$2223 \xrightarrow{T>865°C} 2223 \text{ (Ca-/Pb-deficient)} + Ca_2CuO_3 + (Sr,Ca)_{14}Cu_{24}O_{41-x} + \text{liquid}$$

$$\xrightarrow{T>890°C} 2212 + Ca_2CuO_3 + (Sr,Ca)_{14}Cu_{24}O_{41-x} + \text{liquid}$$

The 2223 compositions formed with increasing temperature have no more a stoichiometry of $(Bi,Pb)_{2.27}Sr_2Ca_2Cu_3O_{10+d}$ and are located outside the plane under consideration. With increasing temperature the Sr content goes up and the Ca content down, moreover the Cu to (Bi,Sr,Ca,Pb) ratio goes up indicating a cation deficiency for higher temperatures.

Up to 890°C no significant changes in phase equlilibria were found (Fig. 1). The decomposition of the 2223 phase happens within a temperature range of about 5 degrees. At 885°C 2223 is still detected whereas at 890°C there is no more 2223. No difference between compositions with differing Pb content could be found.

Samples with x<0.18 show a completely different behavior. Over the whole temperature range 2212 is the predominating phase with small amounts of cuprates and liquid (at temperatures higher than 875°C) (Fig. 1 and Table 1). At 890°C significantly less liquid compared to compositions with x>0.18 is formed indicating the transition to another phase region.

3.2. Lead Content

Microprobe analyses were performed for a composition with x=0.27 to document the changes in cation stoichiometry with temperature. This composition is located in the center of the homogeneity region.

850°C analysis results in the nominal composition since the sample is single phase. With increasing temperature the 2223 crystallites become Pb- and Ca-deficient.

Figure 4 shows the lead solubility of the 2223 crystallites in dependence of temperature represented by the ratio Bi/(Bi+Pb).

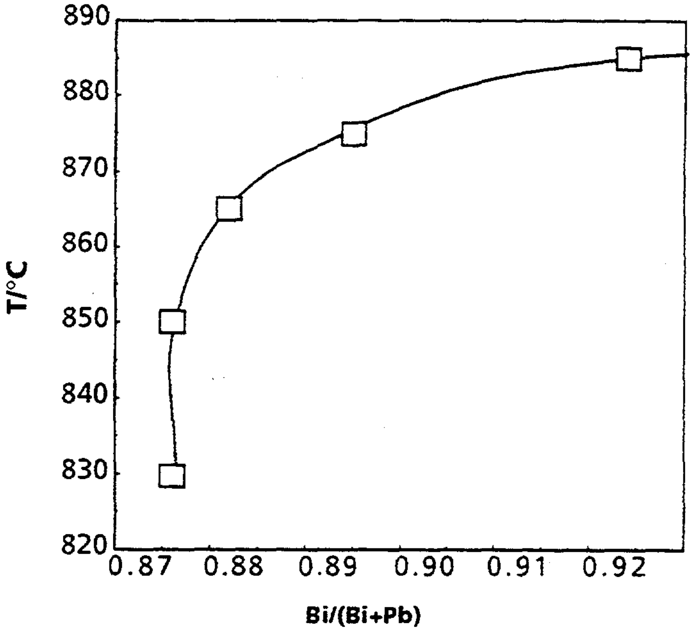

Figure 4. Pb-solubility of 2223 in dependence of temperature

4. Discussion

Regarding the homogeneity for a nominal composition of $Bi_{2.27-x}Pb_xSr_2Ca_2Cu_3O_{10+d}$ it is remarkable that there is no lead free composition for this (Bi+Pb) content. This suggests a widening of the homogeneity range of 2223 by lead substitution. In fact, this is in accordance with the results for the lead free system where no 2223 in the vicinity of the idealized stoichiometry 2223 is found but compositions of about 2.5 223 gave high volume percentages of 2223 [1]. Thus we can regard the here presented homogeneity region as a section through the whole homogeneity region having the connection to the lead free system at Bi=2.5, i.e. out of the plane under consideration.

More experiments are necessary to assure this assumption. Nevertheless the results imply a widening of the homogeneity range to Bi-poorer compositions, compared to the lead free system with increasing Pb content.

In the considered section for compositions with x<0.18 the borderline of the homogeneity range is crossed and the compositions are in a different phase region.

The fact that the sample with $x=0.05$ shows almost no 2223 and significantly less liquid than all other compositions up to 890°C indicates a location of the sample in a different phase region. If one would assume that the compositions with $x<0.18$ are confronted with a higher kinetic barrier for 2223 formation due to less Pb than such with $x>0.18$, this barrier should be partly overcome with increasing temperature indicated by a growing 2223 content. At 890°C the samples should have comparable amounts of liquid as the compositions with $x>0.18$ since there is no kinetic barrier for liquid formation.

From these results it is possible to say that there is no continuous Pb substitution from $x=0$ to 0.36 possible for a (Bi,Pb) content of 2.27. Also for other 2223 compositions phase formation may depend on proper Pb content corresponding to a certain substitution degree. For the determination of the complete homogeneity range experiments with (Bi+Pb) content variations are in progress.

Since the lead content is also a function of temperature the 2223 preparation gets even more complicated. One has to establish for every temperature the homogeneity range as a function of Bi substitution.

5. Literature

1. P. Majewski; B. Hettich; K. Schulze; G. Petzow: Adv. Mater. 3(10)(1991)488.
2. B.W. Statt; Z.Wang; M.J.G. Lee; J.V. Yakomie; P.C. de Camargo; J.F. Maya; J.W. Rutter: Physica C 157(1988)251.
3. U. Endo; S. Koyama; T. Kawai: Jap. J. Appl. Phys. 28(1989)L190.
4. H. Sasakura; S. Minamigawa; K. Nakahigashi; M. Kogachi; S. Nakanishi; N. Fukuoka; M. Yoshikawa; S. Naguchi; K. Okuda; A. Yanase: Jap. J. Appl. Phys. 28(1989)L1163.
5. Y.L. Chen; R. Stevens: J. Am. Ceram. Soc. 75(1992)1142.
6. Y.L. Chen; R. Stevens: J. Am. Ceram. Soc. 75(1992)1150.
7. Y.L. Chen; R. Stevens: J. Am. Ceram. Soc. 75(1992)1160.

Superconductivity Theory Applied to the Periodic Table of the Elements

Thomas Lee Elifritz
Director of Research

Formation Inc.
The Information Corporation
5901 Milwaukee Street
Madison, Wisconsin 53704
(608) 249-8100

Abstract

The modern theory of superconductivity, based upon the BCS to Bose-Einstein transition, is applied to the periodic table of the elements, in order to isolate the essential features of high temperature superconductivity and to predict its occurrence within the periodic table. It is predicted that Sodium-Ammonia, Sodium Zinc Phosphide and Bismuth (I) Iodide are promising materials for experimental explorations of high temperature superconductivity.

Introduction

The purpose of this talk is to bring to the attention of the experimental community some recent theoretical results of modern superconductivity theory, in a manner which is understandable to those not well versed in the mathematical and physical machinery of this modern day theory. I will begin by explaining in simple, rather naive terms, the essential nature of the modern theory of high temperature superconductivity, which is regarded as a crossover transition theory between the BCS theory of the cooperative Cooper pairing of high-density, weakly-coupled, wide-band electrons, and the formation and Bose-Einstein condensation of low-density, strongly-coupled, narrow-band bipolarons, which is now commonly referred to as the Ogg-Schafroth theory of superconductivity [1-4]. I will then describe to the experimentalist what this new theory predicts concerning the properties of a typical high temperature superconductor, and I will present several likely candidates for materials which are predicted to satisfy those requirements. I will also present a brief but thorough reference list to the theoretical and experimental literature, for those who may wish to pursue an endeavor which I believe will ultimately lead to practical and efficient high and/or near room temperature superconductivity, at the device and product levels.

8. P. Majewski; B. Hettich: in: Proc. MRS Spring Meeting, San Francisco (1992)

9. R. Müller; Th. Schweizer; P. Bohac; R.O. Suzuki; L.J. Gauckler: Physica C 203(1992)299.

10. P. Strobel;J.C. Toledano; D. Morin; J. Schneck; G. Vacquier; O. Monnereau; J. Primot; T. Fournier: Physica C 201(1992)27.

There is nothing mysterious about high temperature superconductors. The only mysterious thing about theories of high temperature superconductivity are the theorists themselves. It has been said, and not unkindly, that there are as many theories of high temperature superconductivity as there are theorists, that superconductivity theorists do not read one another's papers, that they don't perform experiments and that they never make predictions. Fortunately, they do occasionally publish papers, and many of them are quite good reading. I think the major problem with these theories of high temperature superconductivity is that, as with the theorist, they are usually over-specialized. What we need then, is to identify the most general theory of high temperature superconductivity, which contains the many other theories as special cases, so as not to refute any one theory, thereby offending the theorist. This is precisely what I have done, and in doing so I have obtained a very good theory of high temperature superconductivity, not my own, which is evidently capable of making predictions, which are, ***in theory***, experimentally verifiable.

This new theory of superconductivity is the BCS to Bose-Einstein transition theory and the high temperature superconductivity appears in the crossover regime between these two extremes of this spectrum. The ultimate predictions we would like to make with this theory, are the specific compounds and crystal structures which would ideally demonstrate this wonderful and interesting phenomenon of high temperature superconductivity. If the realization of room temperature superconductivity is ever to come about, we must move beyond the notion that the heavy metal/alkaline earth/copper oxide/layers are the ultimate manifestation of the concept of high temperature superconductivity. We must think boldly. It does not suffice to perform endless experiments with no theoretical understanding of the basic phenomena, nor does it make sense to create individual theories which are incapable of making predictions, and are not experimentally verifiable. To truly know about high temperature superconductivity, we must be at one with the periodic table of the elements.

The appeal of the BCS to Bose-Einstein transition theory lies in its simplicity and elegance, and also its ability to give exact results in the BCS and Bose-Einstein extremes, as well as meaningful results in the crossover regime. It also pays tribute to its predecessor in that it lends credibility to the original Ogg-Schafroth theory of superconductivity, yet the generalization of the BCS wavefunction is still equally valid in both extreme limits. It is only in this crossover regime, dominated by fluctuations, and ultimately, phase separation, where the application of Migdal's theorem becomes invalid [5], and the bipolaronic effects become dominant. This is precisely the regime we are interested in, where charge, spin and mass degrees of freedom couple in extraordinary ways, producing the enhanced electron lattice interactions, creating what we now know as high temperature superconductivity. The ability of this theory to yield useful predictions lies in the fact that, while this theory encompasses a ***continuum*** of models from one extreme to the other, we now know that the occurrence of superconductivity in the crossover regime involves only electron pairs, and thus the application of this theory to the periodic table of the elements in this regime, requires that the model be ***discrete*** within the ionic lattice, up to the correlation length. As we shall see, this implies that severe constraints exist on the geometry and composition of the lattice, and thus, this greatly simplifies the choosing of the elements for the optimum superconducting effect. By process of elimination then, we quickly arrive at the results.

Results

The experimental results which verified the BCS to Bose-Einstein transition theory as the correct approximation of the thermodynamic description of superconductivity was the now famous Uemura plot [6]. It was well known at that time that these materials were extreme type II superconductors with extremely short correlation lengths, and by this time the early theoretical results were in place [7-11], but it was the Uemura group's elegant measurements of the energy scales and penetration depths, and the graphical interpretation of those results, that had such a profound impact on the theoretical work in the crossover regime [12-21], and even they were able to correctly point in the right direction at that time [22,32]. The model of this theory has evolved to such a high degree of simplicity in the one-dimensional form, that it is nothing less than beautiful [23-29]. We now have even a more vivid confirmation of the essential enhancement of the electron lattice interaction in the crossover regime, in the form of the simple and elegant simulations done by the Egami group [30-31], and they also are pointing again in the right direction. If there ever was a smoking gun, then this is it. There is no question that the BCS to Bose-Einstein transition theory is the approximate thermodynamic description of superconductivity, independent of any specific pairing interactions, and the enhancement of the electron-lattice interaction by the strong electron/ion correlations within the crossover regime is the essential mechanism responsible for the phenomenon of high temperature superconductivity, as we know it.

The crossover regime is less amenable to theoretical treatment than the extremes, however, and to gain a useful understanding we must again revert to our models, which ultimately have to be verified by experiment. The models come in a variety of forms, but one of the most easily understood forms is the boson-fermion model [32-36], which is also referred to as the bipolaronic two-component model, and the induced pairing model. The motivation for this model is rather simple. Although the continuum theory, for which the one dimensional example is exact, predicts a continuous transition from the fermionic BCS extreme through the bosonic Bose-Einstein extreme, within the crossover regime it is paradoxical, because we must consider the discreteness of the constituent electron pairs. Thus, the only way to satisfy this discreteness condition is to acknowledge that both pair breaking and pair formation interactions are in direct competition with each other. It is precisely this knowledge, coupled with the short correlation lengths and modified energy scales, which allows us to make useful predictions, for not only are the individual electron pairs discrete, but so are the ions which comprise the lattice. Thus, we are able to use the theory as a useful guide in measuring the electron-lattice interaction and coupling strength, and furthermore, we can use dimensionality considerations as a guide to crystal structure.

The theory itself is exact in one dimension [29], and we are now finding that the theory is, in certain respects, analytic in the limit of infinite dimensions [37-44], and these results also apply to the various models. Of course, the dimensions of interest are 2 and 3, [45-47] and these dimensions may be regarded as analogous to the crossover regime. The analysis will be restricted, however, to the one dimensional case, as this is the simplest, but more to the point, we can construct higher dimensions from the lower dimensional cases, and we know the essential BCS singularity is ***not*** unique to the two-dimensional case [24].

The modeling of the BCS to Bose-Einstein transition theory in one dimension is straightforward [29]. The essential parameters here are simply the correlation length of the pairs, and the average interparticle separation, determined by the number density. It is the ratio of the correlation length to the average interparticle spacing, which determines the energy value of the coupling constant, and when this ratio approaches unity, we can then apply the discreteness condition, and derive the strength of the electron-lattice interaction in relative (dimensionless) units. If critical transition temperature correlates directly with the electron-lattice interaction strength, then the only parameters of the problem are the correlation length and number density, and these are obviously discrete in the crossover. The only further complication (or restriction) to this problem, is in the crossover regime. By definition, there are two components, bosons and fermions, each presumably with their own correlation lengths and number densities. But since the ratio of the correlation length to the interparticle spacing is close to unity, then these values are related by the coupling strength, which scales proportional to that ratio. Thus, the complication is a simplification and it is then rather easy to derive a finite number of discrete possible configurations, determined by the relative electron-lattice interaction strength, which also scales discretely in the crossover. In real (bipolaronic) systems these will correspond to on-site, inter-site, and next-nearest-neighbor interactions, also referred to as the microscopic coherence cells.

It is the discreteness of the ionic lattice which simplifies the problem and makes the analysis possible. Since the electrons are nearly localized, then either they are localized, and thus correlated, or they are not localized, but have a finite correlation length, which is measured in units of the lattice constant. Either way, there are only a finite number of possibilities, when the correlation length is short. Thus, it is easy to see that the crossover transition, corresponding to a ratio of exactly unity, represents the maximum density that a bosonic system can remain purely bosonic, and the minimum density that a fermionic system can remain purely fermionic, and that this density is directly proportional to the interaction strength [14], and clearly favors the symmetric formation and/or dissociation of electron pairs, over the units of the lattice constant. The only other parameter is density, and this is what Uemura has been telling us all along. There is nothing mysterious about it.

Therefore, since crossover transition is equivalent to Bose-Einstein condensation, then density of the electron pairs is the primary enhancer of critical transition temperature. In order to increase this density, we must reduce the correlation length, and enhance the electron-lattice interaction, whatever the cost. The cost is great for higher and higher T_c's. As we might expect, the restrictions implied by the discreteness of the ionic lattice also imply that the critical transition temperatures will also scale discretely, and the number of compounds and crystal structures which are able to satisfy the severe constraints implied by the discreteness condition will become fewer and fewer as T_c's climb higher and higher. In fact, unless the charge carrier concentration varies continuously across the transition, we would expect that tripling and doubling behavior of the T_c's would be observed in the crossover region, and this is what is observed. Ultimately, at the maximum theoretical T_c, competition from charge, spin and mass density fluctuations would become so extreme, that the ability of the superconducting ground state to overcome these fluctuations would finally fail, leading to density disproportionation and/or a liquid-gas phase separation [48].

Conclusions

We can now proceed with the application of the BCS to Bose-Einstein transition theory of superconductivity, to the periodic table of the elements, to enable us to predict the nature and occurrence of high temperature superconductivity within the periodic table. As I have stated earlier, we proceed initially by process of elimination, as we already know a great deal about most of the elements and compounds comprising the periodic table. We will use previous experimental evidence in the literature as our guide, but we now know that what we are looking for is something very new, or something previously overlooked, otherwise the cuprates are indeed the final word on high temperature superconductivity, and this exercise will have been in vain. We must understand that, since these materials are in the fluctuation regime when they are in the crossover region, and that the density is the fundamental parameter, then any element or compound may be forced into this behavior, merely by expanding or contracting the lattice [49]. What we are looking for, are materials which induce the largest reorganization of charge, spin or mass, with the smallest variation of the lattice density, that is, materials with the largest electron-lattice interaction strength, which is still less than, or equal to, the disproportionation energy of the lattice [50-52].

The first thing we realize is that most of the existing forms of high temperature superconductivity are not exactly on the crossover transition, because their correlation lengths are several times their interparticle spacing, or their interparticle spacing is several times their interatomic spacing, and they need to be doped into superconductivity. Thus, there is ***some*** room for improvement. It is also obvious that the cuprates are on the BCS side of the transition, that is, the boson/fermion ratio is asymmetric in favor of fermions, and the bismuthates are clearly on the Bose-Einstein side of the transition, asymmetric in favor of the bosons. We observe that the cuprates favor two-dimensional spin fluctuations, and that the bismuthates favor three-dimensional charge fluctuations. Given the fact that, other than T_c, the superconducting properties of the cuprates are poor, and except for T_c, the superconducting properties of the bismuthates are excellent, while their density of states at the fermi level is rather low, then it is obvious that the bismuthates need to be examined much more closely, for possible T_c improvement, and this is what I have done.

We understand that when a material is exactly on the crossover transition, then it is either an antiferromagnetic insulator, if it is linear, or it is a spin singlet superconductor. Another possibility, which has been previously overlooked, is that it may be a diamagnetic insulator, if it is disproportionated, but not actually phase separated. An example of this would be the mixed-valance compounds. In fact, as we now consider the ions within the same theory as the electrons, then a variety of situations emerge, most of which involve ionic pairing states and the geometry of the lattice. Thus, we would expect that, within the crossover regime, pairing states would be extremely sensitive to geometry of the lattice, and that the optimum (extreme) fluctuation states, exactly at crossover transition, would occur when the lattice geometry is metastable, but constrained, by the conditions imposed upon it. Since these pairing states are indeed fluctuating, then the geometry ***must*** be linear. And, in fact, we do observe that the highest critical transition temperatures are obtained, when the cuprate layers are exactly flat, and when the bismuthate lattice is precisely cubic.

We also observe that high temperature superconductivity is often associated with lattice phase transitions, and that these phase transitions occur, not in the superconducting phases, but at their boundaries. It would be easy to imagine that these phase transitions have no relationship at all with the superconducting phases, but the evidence now suggests that these transitions occur at the boundaries of the superconducting phases, precisely because the effect of the superconductivity is to defeat or frustrate these phase transitions. Thus, the theory predicts that at the exact point of crossover transition, at the maximum theoretical T_c, a phase transition from a diamagnetic or antiferromagnetic insulating state, directly into the singlet superconducting state would be observed, independent of doping, and that this transition would be strongly dependent upon density. Thus, the condition of maximum theoretical T_c is a cusp-like phenomenon, and we would expect that, although every element or compound within the periodic table is intrinsically capable of entering the maximum fluctuating state, only one compound is capable of sustaining that state as the highest temperature superconducting state, for any configuration of bosons and fermions.

High temperature superconductivity is a two-component phenomenon involving pairs of electrons and ions within a discrete lattice. When we approach the periodic table of the elements in search of new and better forms of high temperature superconductivity, we can immediately rule out the vast areas inhabited by the metals and intermetallic alloys, because they display the traditional BCS form of superconductivity. Likewise, we can also disregard low density materials, as their critical transition temperatures are much too low. This includes the semiconductor materials which exist along the diagonal metalloid band. The BCS to Bose-Einstein transition theory of superconductivity distinctly predicts that ***anionic metals,*** which are on the borderline between ionic, metallic and covalent bonding, are the best possible choices for investigation. We can precisely predict, with this simple theory, that the materials most favorable for this behavior would be multi-valent or mixed valence metal-anion compounds of the highest possible density, which span the metalloid band, perpendicular to it but not on it. The experimental community has so far investigated the metal oxides, sulfides, fullerides and borides. The only part of the periodic table which has not been previously considered viable material for high temperature superconductivity, are alkali-metal and group V-halide salts, and these are precisely the type of materials and compounds which this theory actually predicts, as having the optimum high T_c properties.

There are also only a handful of distinct and discrete methods of moving across the metal-insulator transition occurring at the crossover transition, at maximum theoretical T_c. One method would be to take a high density fermionic metal and then continuously reduce the density, until the pairing interaction at the crossover transition sets in. There is now no question that this is precisely what occurs in Sodium-Ammonia solutions, and this was the original motivation for Ogg's experimental investigations of this system. Another method would be to take a low density bosonic insulator, and continuously increase the density of the bosons, until metallic behavior sets in at the crossover transition. It is my fundamental thesis that this occurs in the bismuth iodide system, and since we are dealing with discrete bosons at the outset, the theory predicts that the exact nature of the transformation is from the diamagnetic insulating state, to the singlet superconducting state, which is necessarily manifested by a polymeric mixed-valance to f.c.c. Bismuth (I) Iodide phase transition [64].

The metal ammonia solutions have been around for a long time, and like the high temperature superconductors, they have been extremely resistant to theoretical description within the crossover regime [53-57]. The relationship between bismuth iodide and sodium ammonia solutions, on the other hand, has been previously overlooked, even though the molten salt chemists have known that there are many similarities in their behavior, and the Russians have been for many years predicting that this system would exhibit precisely this type of behavior [58-61]. If the sodium-ammonia is regarded as a continuous, low density fermionic system and the bismuth-iodide is seen as a discrete, high density bosonic system, then theory predicts that, at maximum theoretical T_c, we would expect to find an optimum mixed boson-fermion system, which would scale across the metal insulator transition in a discrete and continuous manner midway between sodium-ammonia and bismuth (I) iodide. And, in fact, we find that the Russians are again observing that zinc phosphide appears to display these same bosonic pairing states [60-61]. It is only necessary to add fermions to this system, in order to induce this material into the crossover regime, and alkali metal is obviously an ideal way to do this. ***Sodium Zinc Phosphide*** is thus an entirely new system.

As we move away from the metal insulator transition and maximum theoretical T_c, which occurs along the metalloid band within the periodic table, more ionic configurations become possible, and this is where I believe the well known exotic superconductors reside. At maximum theoretical T_c, it is the phase separation and disproportionation of the ionic lattice which must be overcome to produce the high temperature superconductivity. As this temperature decreases, it is expected that less extreme methods of disproportionation would occur and I expect that the organization of the cuprates into two-dimensional layers is one example of this behavior. On the other hand, as this temperature increases, then extreme methods of control must be imposed upon the lattice to prevent phase separation, and force these materials into the high temperature superconducting state. I believe that selective chemical oxidation is one method of accomplishing this, and that reports of high temperature, high current conductivity in oxidized polypropylene and sodium-ammonia are a demonstration of this phenomenon. In fact, if the role of oxygen and hydrogen is seen as the primary mechanism of oxidation and reduction reactions, and the concept of metallic, superfluid hydrogen is considered valid, then it is only a small step to controlled oxidation and reduction reactions in a superconducting environment, at quantum unit efficiency, and a superconducting, sodium-based Castner dry cell might be one result of this technique.

I will conclude by giving a vision of things to come. I have learned a great deal by the application of this BCS to Bose-Einstein transition theory of superconductivity to the periodic table of the elements, much more than I could describe in this short presentation. I believe we are on the verge of a revolution in solid state and condensed matter physics, and that this theory unequivocally predicts the existence of an entirely new class of high temperature superconductors - the inorganic ***metal-salt*** solutions. I also believe that these materials are much more than simply better high temperature superconductors. There are deep relationships between the physics and chemistry of these materials, and the periodic table, and the existence of the liquid-gas phase separations and non-linear interactions, indicating that these materials are more efficient and environmentally friendly alternatives to the traditional physical, chemical and mechanical devices which now dominate our lives.

I openly admit that there is no new science in this report. I have only made an unbiased and common sense application of what appears to be a very good theory of superconductivity, to the periodic table of the elements, based upon the totality of the theoretical and experimental evidence. In this respect, my references are incomplete, thus, I apologize for any omissions from the list. Since it is presently beyond my ***immediate*** capability to carry through the experimental chemistry required to confirm or refute these results, the purpose of this report is to inform those of you who may wish to pursue this endeavor. It is now up to the experimental community to attempt to confirm or refute the specific predictions this theory is able to make. If this theory is correct, and I have yet to uncover any clear evidence to the contrary, while the competing models have all been shown to be generalizable by this theory [62-64], the results should truly be spectacular.

Acknowledgments

I would like to personally and publicly thank the scientists and staff, past and present, of the Caribbean Marine Research Center at Lee Stocking Island, Exuma, Bahamas, for their intellectual and logistical support throughout this endeavor. Thank-you.

References

[1] J. Bardeen, L.N. Cooper and J.R. Schrieffer, Phys. Rev. **108**, 1175 (1957)

[2] R.A. Ogg, Jr., Phys. Rev. **69**, 243 (1946); ibid. **69**, 668 (1946); ibid. **70**, 93 (1946)

[3] R.M. Schafroth, Phys. Rev. **100**, 463 (1955)

[4] Z. Li-yuan and Z. Yun-song, Physica C **198**, 378 (1992)

[5] M.A. Ikeda, A. Ogasawara and M. Shugihara, Phys. Lett. A **170**, 319 (1992)

[6] Y.J. Uemura *et al.*, Phys. Rev. B **38**, 909 (1988);
Phys. Rev. Lett. **62**, 2317 (1989); ibid. **66**, 2665 (1991)

[7] D.M. Eagles, Phys. Rev. **164**, 489 (1967); ibid. **186**, 456 (1969);
Sol. St. Comm. **80**, 823, 831 (1991); Physica C **211**, 319 (1993)

[8] A.J. Leggett, In : *Modern Trends in Condensed Matter Physics,*
A. Pekalski and J. Przystawa, Eds., (Springer Verlag, Berlin, 1980);
J. de Phys. Supp. **41-C7**, 19 (1980)

[9] K. Miyake, Prog. Theor. Phys. **69**, 1794 (1983)

[10] P. Nozieres and S. Schmitt-Rink, J. Low Temp. Phys. **59**, 195 (1985)

[11] K. Nasu, Phys. Rev. B **35**, 1748 (1987); ibid. **37**, 5075 (1988)

[12] M. Randeria, J. Duan and L. Shieh,
Phys. Rev. Lett. **62**, 981 (1989); Phys. Rev. B **41**, 327 (1990)

[13] M. Dreschler and W. Zwerger, Ann. Phys. **1**, 15, (1992)

[14] A. Tokumitu, K. Miyake and K. Yamada, Phys. Rev. B **47**, 11988 (1993)

[15] R. Haussmann, Z. Phys. B **91**, 291 (1993)

[16] C.A.R. Sa de Melo, M. Randeria and J.R. Englebrecht,
Phys. Rev. Lett. **71**, 3202 (1993)

[17] L. Belkhir and M. Randeria, Phys. Rev. B **45**, 5087 (1992); ibid. **49**, 6829 (1994)
[18] J.O. Sofo, C.A. Balseiro and H.E. Castillo, Phys. Rev. B **45**, 9860 (1992)
[19] T. Kostryko and R. Micnas, Phys. Rev. B **46**, 11025 (1992)
[20] A.S. Alexandrov and A.B. Krebs, Sov. Phys. - Usp. **35**, 345 (1992)
[21] A.S. Alexandrov and S.G. Rubin, Phys. Rev. B, **47**, 5141 (1993)
[22] R. Micnas, J. Ranninger and S. Robaszkiewicz, Rev. Mod. Phys. **62**, 113 (1990)
[23] M. Casas, C. Esebbag, A. Extremera, J.M. Getino, M. de Llano, A. Plastino and H. Rubio, Phys. Rev. A **44**, 4915 (1991)
[24] C. Esebbag, J.M. Getino, M. de Llano, S.A. Moszowski, U. Oseguera, A. Plastino and H. Rubio, J. Math. Phys. **33**, 1221 (1992)
[25] V.C. Aquilera-Navarro, M. de Llano and A. Plastino,
In : *Condensed Matter Theories*, Vol. 6,
S. Fantoni and S. Rosati, Eds., (Plenum, New York, 1991)
[26] V.C. Aquilera-Navarro and M. de Llano,
In : *Condensed Matter Theories*, Vol. 7,
A.N. Proto and J.L. Aliaga, Eds., (Plenum, New York, 1992)
[27] C. Esebbag, M. de Llano and R.M. Carter (Quick)
In : *Condensed Matter Theories*, Vol. 8,
L. Blum and F.B. Malik, Eds., (Plenum, New York 1993)
[28] R.M. Quick, C. Esebbag and M. de Llano, Phys. Rev. B **47**, 11512 (1993)
[29] V.C. Aguilera-Navarro and M. de Llano, Rev. Mex. de Fis. **40**, 167 (1994)
[30] T. Egami, S. Ishihara and M. Tachiki, Science **261**, 1307 (1993)
[31] S. Ishihara, T. Egami and M. Tachiki, Phys. Rev. B **49**, 8944 (1994)
[32] R. Friedberg and T.D. Lee,
Phys. Lett. A **138**, 423 (1989); Phys. Rev. B **40**, 6745 (1989)
[33] R. Friedberg, T.D. Lee and H.C. Ren, Phys. Rev. B **42**, 4122 (1990);
Phys. Lett. A **152**, 417 (1991); ibid. **152**, 423 (1991)
[34] F.H.L. Essler, V.E. Korepin and K. Schoutens,
Phys. Rev. Lett. **67**, 3848 (1991); ibid. **68**, 2960 (1992); ibid. **70**, 73 (1993);
Nucl. Phys. B **372**, 559 (1992); ibid. **384**, 431 (1992)
[35] A. Montorsi and M. Rasetti, Phys. Rev. Lett. **72**, 1730 (1994)
[36] S. Nettel, Phys. Rev. B **48**, 13709 (1993)
[37] W. Metzner and D. Vollhardt, Phys. Rev. Lett. **62**, 324 (1989)
[38] E. Muller-Hartmann, Z. Phys. B **74**, 507 (1989); ibid. **76**, 211 (1989)
[39] B. Menge and E. Muller-Hartmann, Z. Phys. B **82**, 237 (1991)
[40] A. Georges and G. Kotliar, Phys. Rev. B **45**, 6479 (1992)
[41] A. Georges, G. Kotliar and W. Krauth, Z. Phys. B **92**, 313 (1993)
[42] F.J. Ohkawa, Phys. Rev. B **46**, 9016 (1992); ibid. **46** (1992)
[43] J.K. Freericks, M. Jarrell and D.J. Scalopino,
Phys. Rev. B, **48**, 6302 (1993); Europhys. Lett. **25**, 37 (1994)
[44] S. Ciuchi, F. de Pasquale, C. Masciovecchio and D. Feinberg,
Europhys. Lett. **24**, 575 (1993)

[45] F. Mila and X. Zotos, Europhys. Lett. **24**, 133 (1993)
[46] K. Penc and F. Mila, Phys. Rev. B **49**, 9670 (1994)
[47] P.G.J. van Dongen, Phys. Rev. B **49**, 7904 (1994)
[48] E. Dagatto, J. Riera, Y.C. Chen, A. Moreo, A. Nazarenko, F. Alcaraz and F. Ortolani, Phys. Rev. B **49**, 3548 (1994)
[49] J.P. Perdew, R.G. Parr, M. Levy and J.L. Balduz, Jr., Phys. Rev. Lett. **49**, 1691 (1982)
[50] K. Moulopoulos and N.W. Ashcroft, Phys. Rev. A **43**, 1685 (1991); Phys. Rev. B **41**, 6500 (1990); ibid. **42**, 7855 (1990); ibid. **45**, 11518 (1992); Phys. Rev. Lett. **66**, 2915 (1991); ibid. **69**, 2555 (1992)
[51] A.R. Denton and N.W. Ashcroft, Phys. Rev. A **42**, 7312 (1990); ibid. **43**, 3161 (1991)
[52] N.W. Ashcroft, Phil. Trans. R. Soc. Lon. A **334**, 407 (1991); J. Non-Cryst. Sol. **156-158**, 621 (1993); Z. Phys. Chem. **156**, 41 (1988);
[53] *International Conference on the Metal - Insulator Transitions*, Rev. Mod. Phys. **40**, 673 (1968)
[54] M.H. Morrel and J.C. Thompson, Adv. Phys. **17**, 857 (1973)
[55] J.C. Thompson, *Electrons In Liquid Ammonia*, (Clarendon, Oxford, 1976)
[56] Colloque Weyl I, *Metal Ammonia Solutions*,
G. Lepoutre and M.J. Sienko, Eds., (W.A. Benjamin, New York, 1964)
Colloque Weyl II, *Metal Ammonia Solutions*,
J.J. Lagowski and M.J. Sienko, Eds., (Butterworths, London, 1970)
Colloque Weyl III, *Electrons in Fluids*,
J. Jortner and N.R. Kestner, Eds., (Springer Verlag, New York, 1973)
Colloque Weyl IV, J. Phys. Chem. **79**, 2789 (1975)
Colloque Weyl V, J. Phys. Chem. **84**, 1065, (1980)
Colloque Weyl VI, J. Phys. Chem. **88**, 3699 (1984)
Colloque Weyl VII, J. de Phys. IV, **1**, C5 Conf. (1991)
[57] *Physics and Chemistry of Electrons and Ions in Condensed Matter*, J.V. Acrivos, N.F. Mott and A.D. Yoffe, Eds., (D. Reidel, Dordrecht, 1984)
[58] V.A. Kovarskii and A.A. Golub, Sov. Phys. - Sol. St. **16**, 405 (1974)
[59] R.I. Shekhmamet'ev and N.V. Starostin, Phys. Stat. Sol. B **154**, K51 (1989)
[60] G.T. Petrovskii and N.V. Starostin, Sov. Phys. - Doklady **37**, 364 (1992)
[61] B. Bektashov and R.I. Shekhmamet'ev, Sov. Phys. - Sol. St. **34**, 1290 (1992)
[62] M.D. Nunez Regueiro and A.A. Aligia, Phys. Rev. Lett. **61**, 1889 (1988)
[63] A.A. Aligia and M. Balina, Phys. Rev. B **47**, 14380 (1993)
[64] T.L. Elifritz, Spec. Sci. Tech. **17**, 85 (1994)

Thomas Lee Elifritz,
Lansing Cay, c/o Farmer's Cay
Via M/V Lady Francis
Exuma, Bahamas

Chemical Stabilization and High Pressure Synthesis of Ba-free Hg-based Superconductors, $(Hg,M)Sr_2Ca_{n-1}Cu_nO_y$ (n=1~3)

K. Kishio[1,2], J. Shimoyama[1], S. Hahakura[1], K. Kitazawa[1],
K. Yamaura[2], Ź. Hiroi[2] and M. Takano[2]

(1)*Department of Applied Chemistry, University of Tokyo, Bunkyo-ku, Tokyo 113, Japan*
(2)*Institute for Chemical Research, Kyoto University, Uji, Kyoto-fu 611, Japan*

Abstract

A homologous series of new Hg-based HTSC compounds, $(Hg,M)Sr_2Ca_{n-1}Cu_nO_y$ with n=1 to 3, have been synthesized. The stabilization of the pure phases have been accomplished by chemical doping of third elements such as M=Cr, Mo and Re. While the Hg1201(n=1) phase was readily obtained in this way, it was necessary to simultaneously dope Y into the Ca site to stabilize the Hg1212(n=2) phase. On the other hand, single-phase Y-free Hg1212(n=2) and Hg1223 (n=3) samples were synthesized only under a high pressure of 6 GPa. In sharp contrast to the Ba-containing compounds, all the samples prepared in the present study have been quite stable during the synthesis and no deterioration in air has been observed after the preparation.

1. Introduction

Recent successive discoveries of the homologous series of $HgBa_2Ca_{n-1}Cu_nO_y$ (n=1,2,3,4) [1-4], have stimulated again the further search of new high-T_c superconductors, as this Hg-based family established the record-high T_c of 134 K and over 160 K under ambient and high pressures, respectively. However, these materials have been found to be sensitive to carbon dioxide or humidity so that they are chemically rather unstable under ambient air. The present authors speculated that substitution of Sr for Ba would be effective to chemically stabilize these samples and have successfully synthesized recently a Ba-free Hg-based superconductor, $(Hg,Cr)Sr_2CuO_y$ [5]. While its T_c, approximately 60 K, was relative lower than that of its Ba-based analogue, $HgBa_2CuO_4$, this Sr-based compound was found to be quite stable under open air.

As it is well recognized, an increase in the number of CuO_2 sheets in the unit cell structure of layered cuprates is a promising way to enhance T_c. After the discovery of the $(Hg,Cr)Sr_2CuO_y$, we have immediately tried synthesis of similarly Cr-doped $HgSr_2Ca_{n-1}Cu_nO_y$ (n=2,3). However, this attempt was unsuccessful, resulting in the formation of the Hg1201 phase plus impurity phases only, without any trace of the intended Hg1212 or Hg1223 phase. At the same time, we searched for other metal elements by which the Ba-free Hg1201, Hg1212 and Hg1223 structures could be structurally stabilized.

In this paper, we report synthesis and superconducting properties of new barium-free mercury-based superconducting systems, $HgSr_2(Ca,Y)_{n-1}Cu_nO_y$ (n=1,2) by chemical doping of Cr, Mo, or Re into the Hg (or Cu) sites. We have also adopted a high-pressure synthesis technique, by which Hg1233 (n=3) could be successfully obtained as a single phase sample. Values of T_C of the prepared samples were approximately 60~70 K and 90~100 K for 1201 and 1212 compounds, respectively. On the other hand, our Hg1223 showed only T_C ~59 K. We believe that, in terms of the carrier doping, this sample is still in the under-doping state with the preparation conditions we have so far examined.

2. Experimental

Samples were synthesized by using the two-step solid state reaction technique. Mo-Sr-(Ca,Y)-Cu-O and Re-Sr-(Ca,Y)-Cu-O precursors were prepared by calcining mixed powders of $SrCO_3$, $CaCO_3$, CuO, MoO_3, ReO_3 and Y_2O_3 at 950°C for 24h in air. The obtained precursors were then mixed together with HgO and pressed into pellets of 10 mm$\phi \times$ 1 mm in dimension. All these procedures have been followed under an open air. Subsequently, each pellet was sealed in an evacuated quartz ampoule, sintered at 860~940°C for 10~40h and finally quenched to room temperature. For the high-pressure synthesis, the mixed powder of the precursor and HgO was loaded into a gold capsule and reacted at 1000°C for 30 min under a pressure of 6 GPa using a cubic-anvil type high-pressure apparatus [6].

Crystal structure was analyzed by the standard powder X-ray diffractometer with Cu-$K\alpha$ radiation. Superconducting properties were studied via DC susceptibility and resistivity measurements. Susceptibility was measured using a SQUID susceptometer (HOXAN HSM-2000X) under an applied field of 10 Oe. Resistivity measurements were performed by the conventional d.c. four-probe method.

3. Results

3.1. Hg(Sr)1201 compounds

Powder X-ray diffraction analysis revealed that samples with nominal composition of $(Hg_{1-x}Mo_x)Sr_2CuO_y$ with x=0.3~0.5 were almost single phase of Hg1201 structure. A powder X-ray diffraction pattern of the sample with x=0.3 is shown in Fig. 1. Diffraction peak indices with the tetragonal unit cell are also displayed in the figure. Samples with x=0.1 and 0.2 contained $SrHgO_2$ as an impurity phase as we observed in the case of $(Hg_{1-x}Cr_x)Sr_2CuO_y$ [5]. In the samples with x≥0.7, $SrCuO_2$ and $SrMoO_4$ phases appeared dominantly and their amounts increased with an increase of x. Lattice parameters, a_0 and c_0, of the tetragonal unit cell were calculated to be 3.80 Å and 8.86 Å, respectively, being almost independent of x. The c_0 value was a little larger than that of $(Hg_{1-x}Cr_x)Sr_2CuO_y$, c_0=8.64~8.71 Å (0.3≤x≤0.7) [5].

Diamagnetism due to the superconductivity was observed for the Mo-doped samples in the x

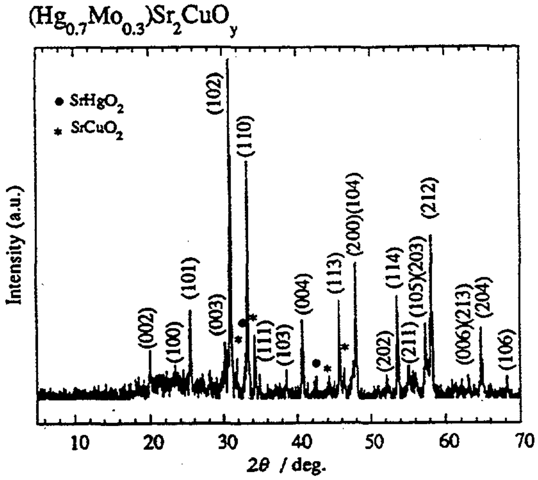

Fig. 1 : Powder X-ray diffraction patterns of $(Hg_{0.7}Mo_{0.3})Sr_2CuO_y$ sample. Diffraction peaks of Hg(Sr)1201 phase are shown with their tetragonal (h, k, l) indices.

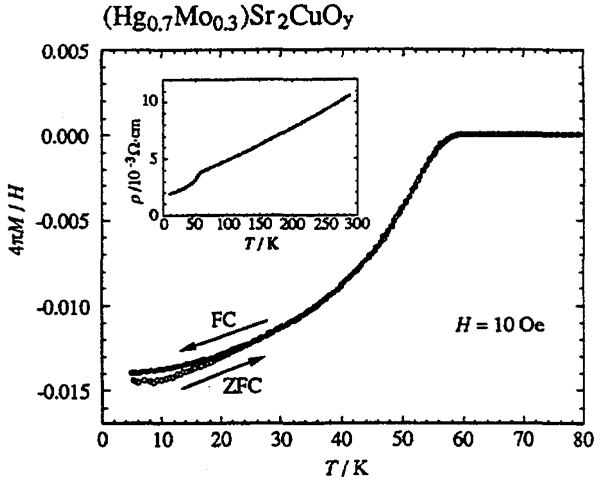

Fig. 2 : Susceptibility and resistivity (inset) curves of $(Hg_{0.7}Mo_{0.3})Sr_2CuO_y$ sample.

range of $0.1 \leq x \leq 0.7$. $T_{c(onset)}$ was found to depend on x and increased from 52 K for x=0.1 to 72 K for x=0.7. Figure. 2 shows the zero-field-cooled (ZFC) and field-cooled (FC) susceptibility curves taken under a magnetic field of 10 Oe for $(Hg_{0.7}Mo_{0.3})Sr_2CuO_y$ and the temperature dependence of its resistivity is shown in the inset. The ZFC and FC magnetization curves lie close to each other and the superconducting volume fraction at 5 K estimated from the ZFC curve was 1.5 %. The resistivity curve showed a metallic behavior with a small drop at 58 K corresponding to the $T_{c(onset)}$ in the magnetic measurement, but the zero resistance was not observed down to 4.2 K. These results and the X-ray diffraction pattern (Fig. 1) indicate that the superconducting coupling between the crystal grains is rather weak in this sample. This behavior is quite different from the $(Hg_{1-x}Cr_x)Sr_2CuO_y$ system with x=0.3 which showed the perfect diamagnetism at low temperatures and the zero resistance with a sharp transition at 58 K [5].

The effect of Re substitution for stabilizing the Hg1201 phase was observed at a lower doping level, x, than Cr or Mo doping. Samples composed of Hg1201 as the major phase were obtained with the $0.05 \leq x \leq 0.2$ in both samples with nominal compositions, $(Hg_{1-x}Re_x)Sr_2CuO_y$ and $HgSr_2(Cu_{1-x}Re_x)O_y$. Figures. 3(a) and (b) show powder X-ray diffraction patterns of $(Hg_{0.9}Re_{0.1})Sr_2CuO_y$ and $HgSr_2(Cu_{0.9}Re_{0.1})O_y$. Both patterns are similar to each other only slightly differing in the amount of impurity phases. However, a larger amount of impurity phases such as $SrHgO_2$ was compared to the case of the Cr or Mo-substitution. Lattice parameters, a_0 and c_0, were almost same for the both samples; 3.783 Å and 8.883 Å, respectively.

Superconducting transition was observed with x up to 0.5 in these sample series. T_c was approximately 70K independent of x(0.05~0.2). Figure. 4 shows the ZFC and FC susceptibility curves taken under a magnetic field of 10 Oe for $HgSr_2(Cu_{0.9}Re_{0.1})O_y$, and the resistivity curve is

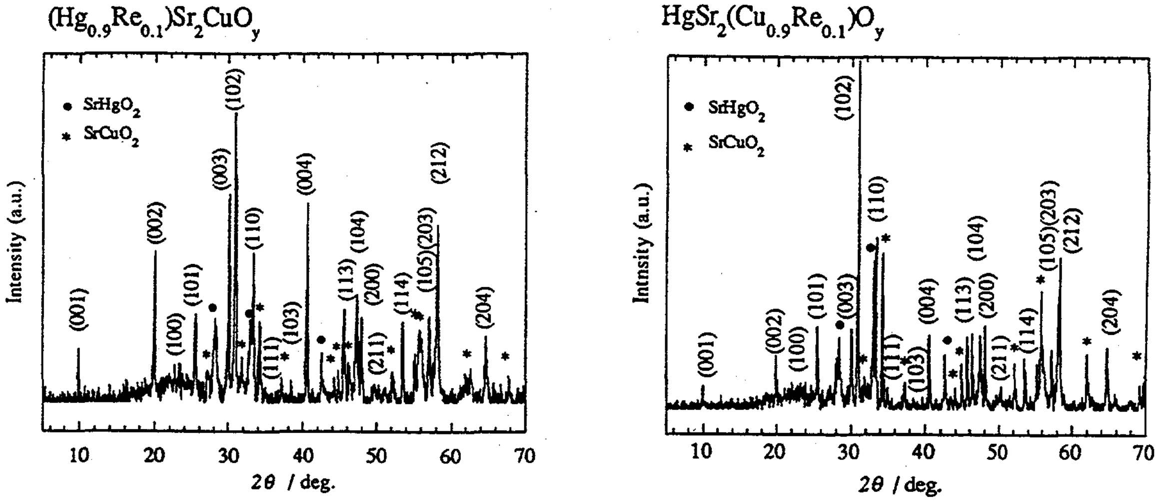

Fig. 3 : Powder X-ray diffraction patterns of $(Hg_{0.9}Re_{0.1})$ Sr_2CuO_y (a) and $HgSr_2(Cu_{0.9}Re_{0.1})O_y$ (b).

shown in the inset. The superconducting volume fractions at 5 K estimated from the ZFC curve were 1.8% and 9.5% for $(Hg_{0.9}Re_{0.1})Sr_2CuO_y$ and $HgSr_2(Cu_{0.9}Re_{0.1})O_y$, respectively. Corresponding to this low superconducting volume fraction, resistivity showed only a small drop at 70 K and did not show zero resistivity down to 4.2 K for the both samples, as was in the case of the Mo-substituted system.

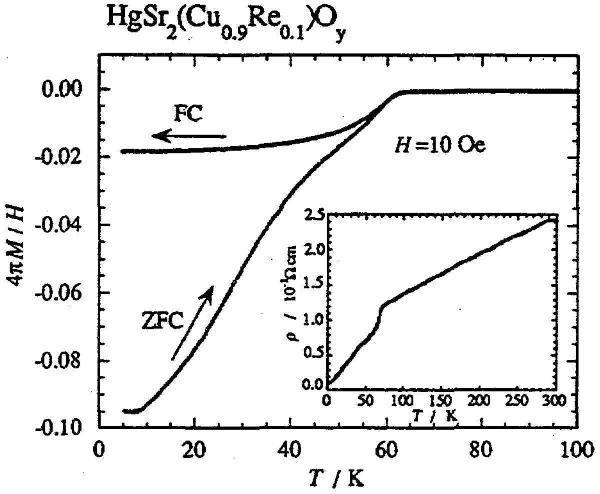

Fig. 4 : Susceptibility and resistivity curves of $HgSr_2(Cu_{0.9}Re_{0.1})O_y$.

3.2 Hg(Sr)1212 compounds

It was found that the simultaneous Y substitution of the Ca site was necessary to stabilize the Cr- or Mo-doped 1212. Figure. 5 shows x ray diffraction patterns of $(Hg_{0.7}M_{0.3})Sr_2(Ca_{1-x}Y_x)$ Cu_2O_y for x= 0~1.0. While the Y-free sample (x=0) did not contain any trace, the amount of the Hg1212 phase increased with increasing x up to 0.3 and the samples in the x range of $0.3 \leq x \leq 0.7$ were found to be of nearly single phase. Variations of lattice parameters, a_0 and c_0, with x are shown in Fig. 6. In the x range of $x \leq 0.7$, a_0 increases while c_0 decreases with increasing x.

Samples with x=0.1~0.9 showed superconductivity in the ZFC susceptibility measurements as shown in Fig. 7. The inset shows its blow-up around T_c. The variation of $T_{c(onset)}$, and superconducting volume fraction at 5 K estimated from the ZFC magnetization with x are summarized in Fig. 8. The highest $T_{c(onset)}$, 96K, was observed for the sample with x=0.3, and decreased with increasing x. Only the sample with x=0.3 exhibited almost the full volume fraction at

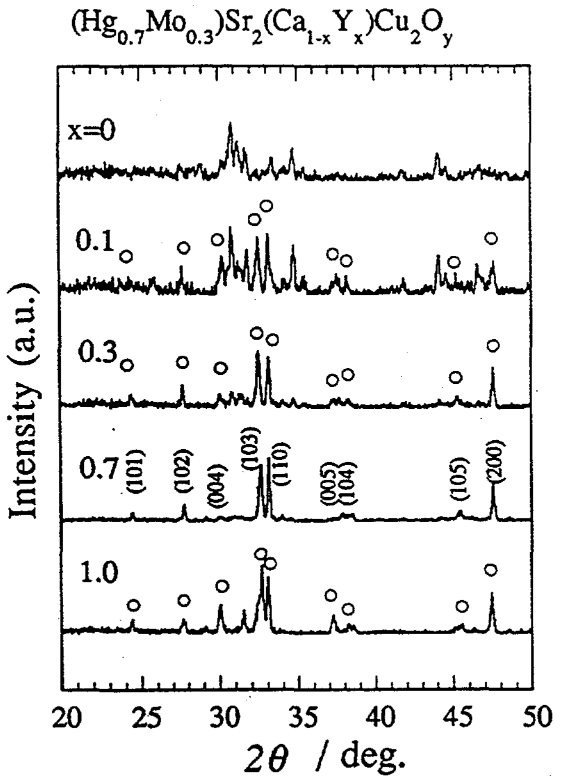

Fig. 5 : Powder X-ray diffraction patterns of $(Hg_{0.7}Mo_{0.3})Sr_2(Ca_{1-x}Y_x)Cu_2O_y$ as a function of Y content x. Open circles indicate diffraction peaks of the main phase with the Hg1212 structure.

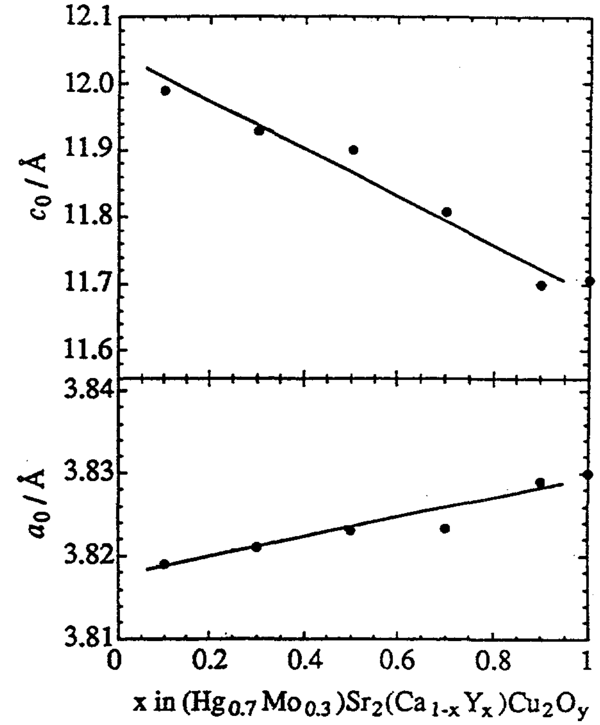

Fig. 6 : Variation in tetragonal lattice parameters of $(Hg_{0.7}Mo_{0.3})Sr_2(Ca_{1-x}Y_x)Cu_2O_y$ as a function of Y doping.

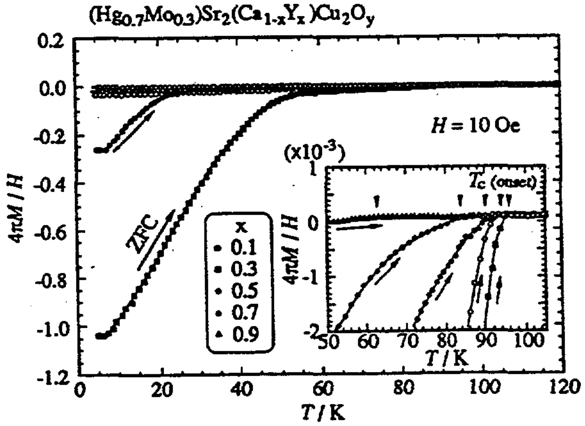

Fig. 7 : ZFC susceptibility curves of $(Hg_{0.7}Mo_{0.3})Sr_2(Ca_{1-x}Y_x)Cu_2O_y$ taken under H=10 Oe.

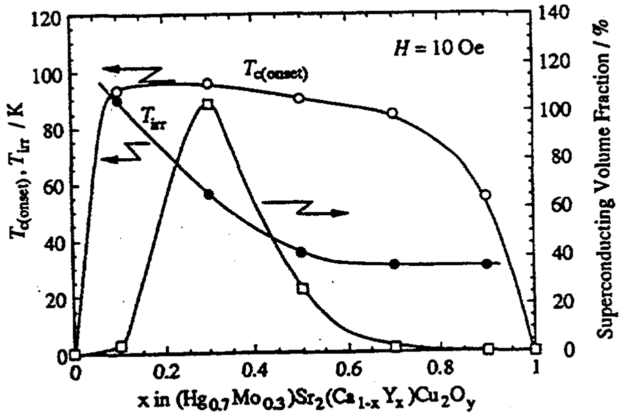

Fig. 8 : $T_{c(onset)}$, superconducting volume fraction and irreversible temperature (H=10 Oe) of $(Hg_{0.7}Mo_{0.3})Sr_2(Ca_{1-x}Y_x)Cu_2O_y$.

5 K, while other samples showed weaker diamagnetism. In the resistivity measurement, this sample with x=0.3 showed $T_{c(onset)}$ at 95 K and zero resistance at 73 K.

In Fig. 8, we also plot the irreversible temperature, T_{irr}, determined from the splitting point

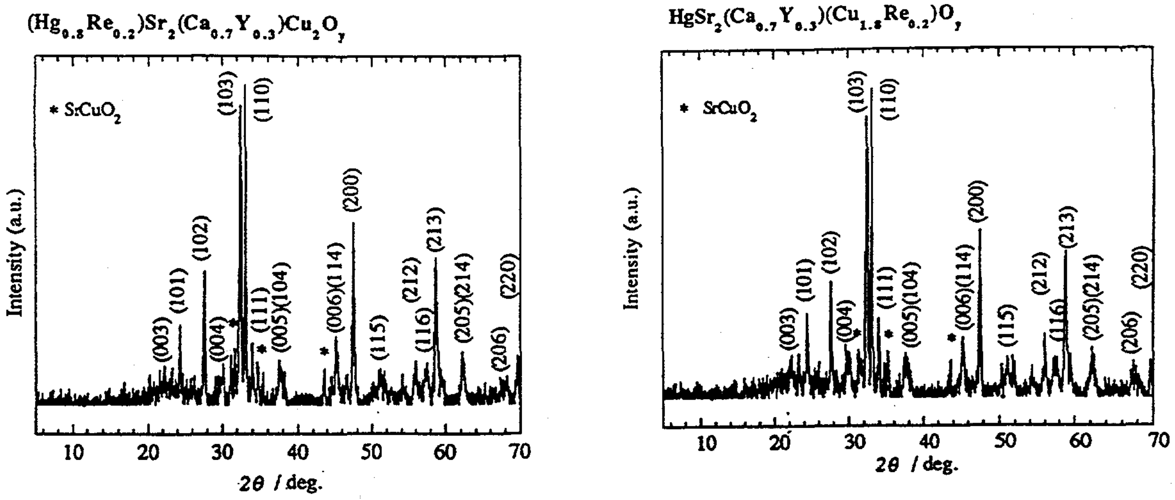

Fig. 9 : Powder X-ray diffraction patterns of Re-doped Hg1212 samples. Hg-site substitution (a) and Cu-site substitution (b).

of ZFC and FC curves taken under the magnetic field of H=10 Oe. It is noteworthy that T_{irr} drastically decreases with increasing x. In the case of the Bi2212 superconductor, it has been recently shown that T_{irr} varies strongly as a function of carrier doping, namely, T_{irr} is lower as the sample is less hole-carrier doped [7]. By analogy, it is considered that the samples with x>0.3 are in the underdoping state, because the Y substitution for Ca is expected to result in a decrease in the hole carrier concentration. The variations of lattice parameters a_0 and c_0 with x are quite consistent with this picture.

The simultaneous Re and Y substitutions were also found to be effective to stabilize the Hg1212-structure in both $(Hg_{1-x}Re_x)Sr_2(Ca_{1-x'}Y_{x'})Cu_2O_y$ and $HgSr_2(Ca_{1-x'}Y_{x'})(Cu_{2-x}Re_x)O_y$. A Y-free sample, x'=0, was composed of mixed phases of Hg1212, Hg1201 and other impurity phases. On the other hand, samples with x=0.2 and x'≥0.3 were obtained as Hg1212 single phase, as shown in Figs. 9(a) and (b). Lattice parameters, a_0 and c_0, were 3.818Å and 11.879Å, nearly same in these two samples. Their temperature dependence of resistivity are shown in Fig. 10. Both show $T_{c(onset)}$'s at approximately 100 K and zero resistance at about 83 K. In contrast, the Y-free sample (x'=0) did not show zero resistivity down to 4.2 K.

3.3 Hg(Sr)1223 compounds

By using the conventional quartz ampoule method, we have tried to synthesize a number of samples with nominal compositions of Hg1223 and 1234 with and without chemical doping. However, we have not been successful to detect any diffraction peaks for these phases. Alternatively, we have recently started high pressure synthesis using a cubic-anvil type apparatus. Figure 11 shows the x-ray diffraction pattern for one of the successfully prepared samples, $(Hg_{0.7}Cr_{0.3})Sr_2Ca_2Cu_3O_y$. The calculated lattice parameters were a_0=3.859 Å and c_0=15.069 Å, clearly exhibiting the formation of almost pure Hg1223 phase. The ZFC susceptibility signal reached over 150% (due to

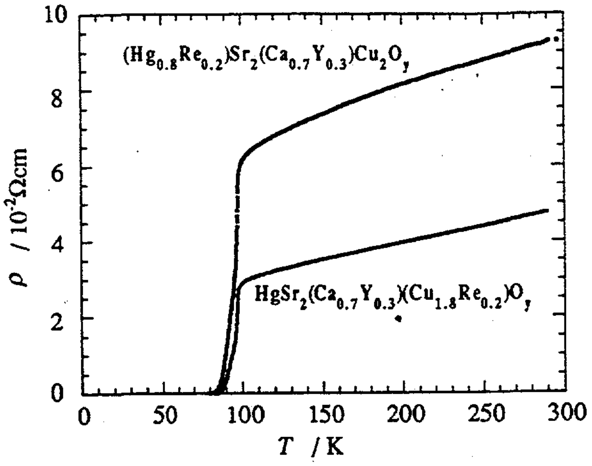

Fig. 10 : Resistivity curves of Re-doped Hg1212 samples.

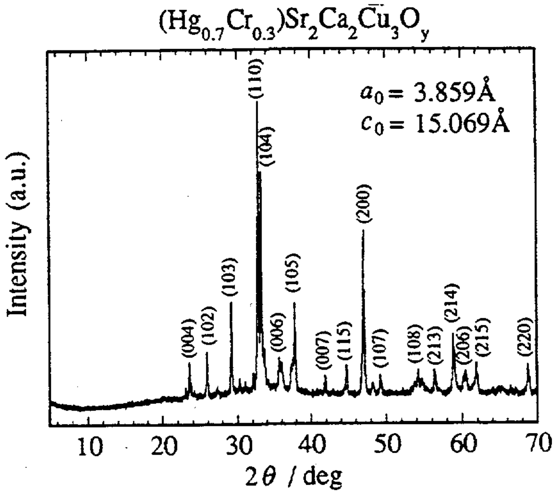

Fig. 11 : X-ray diffraction pattern of high-pressure synthesized $(Hg_{0.7}Cr_{0.3})Sr_2Ca_2Cu_3O_y$.

the demagnetization effect). However, T_c of this sample was only 59 K.

In Fig. 12, the lattice parameters of $(Hg_{0.7}Cr_{0.3})Sr_2Ca_{n-1}Cu_nO_y$ for n=1~3, are plotted as a function of *n*. It must be noted that the 1201 sample was synthesized by the quartz ampoule method, while the 1212 and 1223 samples could be prepared only under high pressure. The increase of c_0, in unit of ~3.2 Å, corresponds well to the thickness of $CaCuO_2$ layer. On the other hand, we have found that a_0 is slightly increasing with *n*. This is rather inconsistent with the behavior in the $HgBa_2Ca_{n-1}Cu_nO_y$ system [1-4] where the decrease of a_0 with *n* has been reported. We interpret the tendency in Fig.12 is due to the low carrier doping state of our samples prepared by high pressure technique and this has lead to the observed unexpectedly low T_c of our 1223 compound.

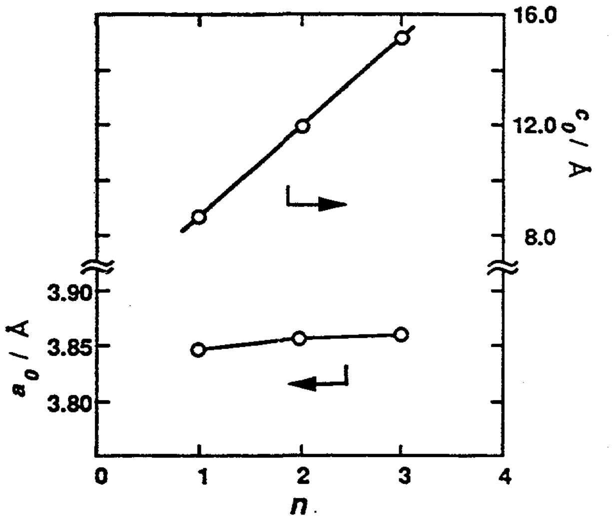

Fig. 12 : Variation of lattice parameters as a function of n in $(Hg_{0.7}Cr_{0.3})Sr_2Ca_{n-1}Cu_nO_y$.

4. Discussion

Table 1 summarizes a list of the newly discovered Hg(Sr)-based compounds in the present study, including Hg(Cr)1201 reported in the previous publication [5]. The optimum range of the doping composition, x, and T_c should be regarded as approximate values, since we have not

Table 1: List of Ba-free Hg-based superconductors discovered in the present study and in the previous publication [5].

composition	optimal range	T_c /K
$(Hg_{1-x}Cr_x)Sr_2CuO_y$	$0.3 \le x \le 0.4$	~60
$(Hg_{1-x}Mo_x)Sr_2CuO_y$	$0.1 \le x \le 0.7$	~60
$HgSr_2(Cu_{1-x}Re_x)O_y$	$0.05 \le x' \le 1.0$	~70
$(Hg_{0.7}Cr_{0.3})Sr_2(Ca_{1-x'}Y_{x'})Cu_2O_y$	$0.5 \le x' \le 1.0$	n.s.
$(Hg_{0.7}Mo_{0.3})Sr_2(Ca_{1-x'}Y_{x'})Cu_2O_y$	$0.5 \le x' \le 1.0$	~95
$HgSr_2(Ca_{1-x'}Y_{x'})(Cu_{1.8}Re_{0.2})O_y$	$0.5 \le x' \le 1.0$	~100
$(Hg_{0.7}Cr_{0.3})Sr_2Ca_2Cu_3O_y$	-	~59

attempted the post-annealing effect of these samples under various conditions. In addition, many samples have not shown the zero resistivity and full diamagnetism at the present stage. However, it is evident that, irrespective of the dopant M, the optimized 1201 compounds exhibit T_c at around 60~70 K and the 1212 compounds show T_c at 95~100 K. We also believe that T_c of the 1223 compounds should exceed well over 100 K. These observations support again the universal feature of the layered cuprate superconductors in that the number of the CuO_2 sheets in the unit cell is the most important parameter in determining the maximum attainable T_c of a given family of HTSC compounds.

Regarding the site selection of the dopants, it is quite clear from the X-ray analysis that Cr and Mo can be substituted on the Hg site. However, the Re substitution site in both 1201 and 1212 samples is not clear yet. The relatively lower doping composition of Re for effective stabilization of the structure as well as the smaller ionic radius of the Re ion compared to Cr and Mo suggest that the substitution site of Re is the Cu site. Further optimization of the superconducting properties and identification of the doping site and detailed structural analysis using neutron diffraction are under progress.

In summary, we have synthesized 70 K and 100 K-class new Ba-free Hg-based supercondctors; $(Hg,M)Sr_2CuO_y$ and $(Hg,M)Sr_2(Ca,Y)Cu_2O_y$ (M=Cr, Mo or Re). Cr- and Mo-doping for the Hg site and Y-doping for the Ca site were found to be effective to stabilize the Hg(Sr)1201 and 1212 crystal structures. We also found that the Re-doping was effective in stabilization at the lower doping level, while the Re substitution site has not been identified. Finally, Cr-stabilized 1223 compound, $(Hg_{0.7}Cr_{0.3})Sr_2Ca_2Cu_3O_y$, has been obtained as a single phase sample by the high-pressure technique, although T_c (=59 K) of the 1223 phase has not been fully optimized.

References

[1] S.N. Putilin, E.V. Antipov, O. Chmaissem and M. Marezio, Nature (London) 362 (1993) 226.

[2] A. Schilling, M. Cantoni, J.D. Guo and H.R. Ott, Nature (London) 363 (1993) 56.

[3] S.N. Putilin, E.V. Antipov and M. Marezio, Physica C212 (1993) 266.

[4] E.V. Antipov, S.M. Loureiro, C. Chaillout, J.J. Caponi, P. Bordet, J.L. Tholence, S.N. Putilin and M. Marezio, Physica C215 (1993) 1.

[5] J. Shimoyama, S. Hahakura, K. Kitazawa, K. Yamafuji and K. Kishio, Physica C224 (1994) 1.

[6] Z. Hiroi, M. Azuma, M. Takano and Y. Takeda, Physica C208 (1993) 286.

[7] K. Kishio, J. Shimoyama, Y. Kotaka and K. Yamafuji, Proc. 7th Intnl. Workshop on Critical Currents in Superconductors, Alpbach, Austria, Jan 24-27(1994); World Sci. Pub., in press.

THIS PAGE INTENTIONALLY LEFT BLANK

A New Series of Oxycarbonate Superconductors $(Cu_{0.5}C_{0.5})_mBa_{m+1}Ca_{n-1}Cu_nO_{2(m+n)+1}$

E. Takayama-Muromachi, T. Kawashima and Y. Matsui,
National Institute for Research in Inorganic Materials,
1-1 Namiki, Tsukuba, Ibaraki, 305 Japan.

We found a new series of oxycarbonate superconductors in the Ba-Ca-Cu-C-O system under high pressure of 5 GPa. Their ideal formula is $(Cu_{0.5}C_{0.5})_mBa_{m+1}Ca_{n-1}Cu_nO_{2(m+n)+1}$ ((Cu,C)-m(m+1)(n-1)n). Thus far, n=3, 4 members of the m=1 series, (Cu,C)-1223 and (Cu,C)-1234, have been prepared in bulk while n=4, 5 members, (Cu,C)-2334 and (Cu,C)-2345, have been prepared for the m=2 series. (Cu,C)-1223 shows superconductivity below 67 K while T_c's of other compounds are above 110 K. In particular, (Cu,C)-1234 has the highest T_c of 117 K.

1. Introduction

Since the first discovery of the superconductor including carbon, $(Ba,Sr)_2(Cu,C)_2O_y$ by Kinoshita and Yamada [1], various kinds of oxycarbonate superconductors have been reported; for instance, oxycarbonates based on the 123-type structure (e.g., $(Y,Sr)Sr_2(C,Cu)Cu_2O_y$ [2]), Bi-oxycarbonates (e.g., $Bi_2Sr_4Cu_2CO_3O_y$ [3]), Tl-oxycarbonates (e.g., $Tl(Sr,Ba)_4Cu_2CO_3O_y$ [4]) and Hg-oxycarbonates (e.g., $HgBa_2Sr_2Cu_2CO_3O_y$ [5]). These compounds have structures closely related to the mother superconductors, 123, Bi-2223, Tl-1223 and Hg-1223, respectively.

In this report, we discuss a new series of oxycarbonate superconductors, $(Cu_{0.5}C_{0.5})_mBa_{m+1}Ca_{n-1}Cu_nO_{2(m+n)+1}$ ((Cu,C)-m(m+1)(n-1)n) which are stable only under high pressure. The m=1 series of compounds have structures closely related to those of Hg(or Tl)-12(n-1)n [6]. The Hg (Tl) site is replaced by mixed atom of Cu and C in this series. The m=2 series have unique structures where three Ba planes are stacked in a charge reservoir block separated by the (Cu,C) ones [7].

Thus far, n=3,4 members of the m=1 series and n=4,5 members of the m=2 series have been prepared in bulk [6-7]. The highest T_c, 117 K was observed in (Cu,C)-1234 [6].

2. (Cu,C)-12(n-1)n series

The m=1 series of superconductors have been prepared under 5 GPa and 1200° C by using Ag_2O as an oxidizing agent [6]. In Fig. 1, crystal structures of the m=1 series are shown for n=3 and 4. These structures are closely related to those of Hg(orTl)-12(n-1)n, n=3 and 4, respectively. Three and four CuO_2 planes are stacked separated by the Ca planes. The Hg(or Tl) site is replaced by the (Cu,C) mixed atoms. The interesting

High Temperature Materials

Session 2 Chair: K. Kishio

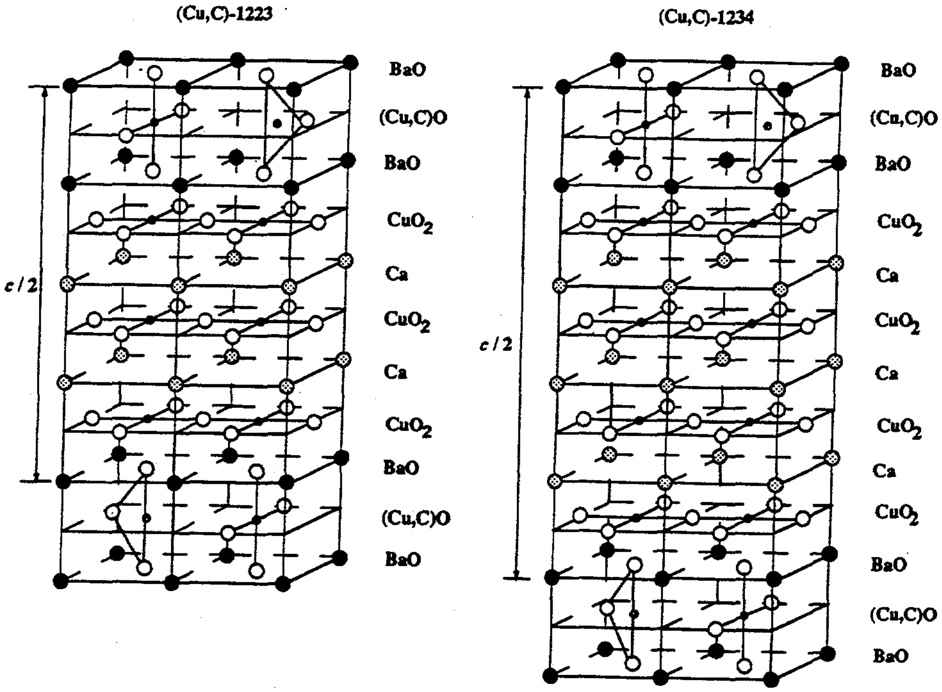

Fig.1. Structures of (Cu,C)-12(n-1)n [6].

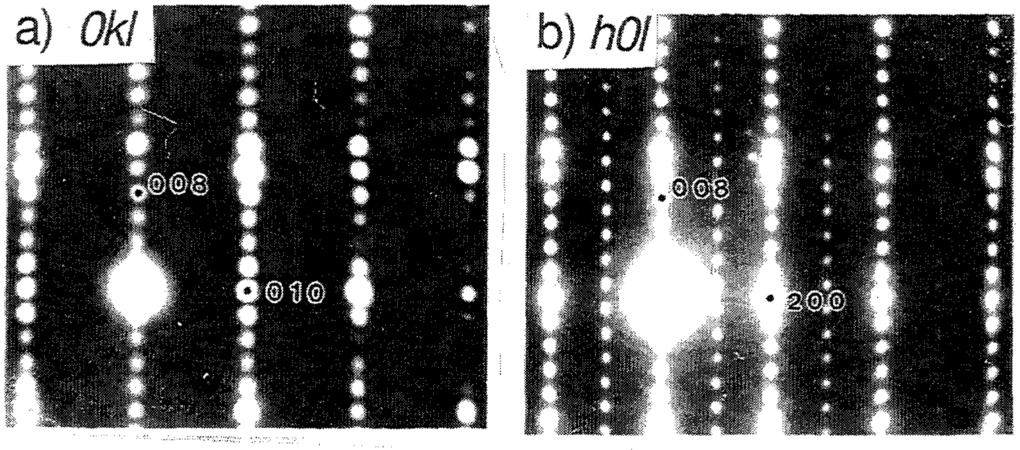

Figs.2 (a,b). Electron diffraction patterns of (Cu,C)-1234.
Indexes are given based on the orthorhombic superlattice.

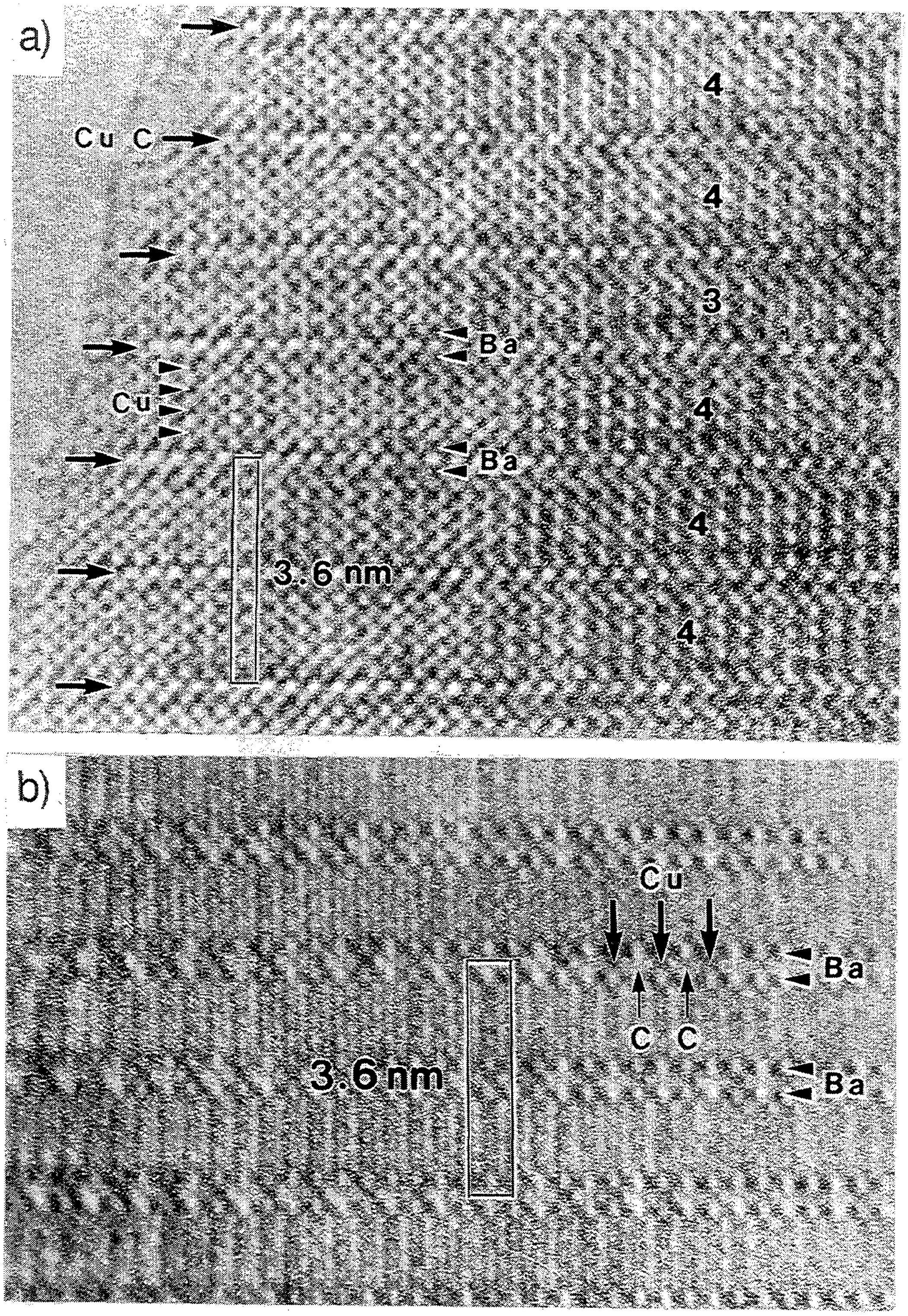

Figs.3 (a,b) Lattice images of (Cu,C)-1234.
a) projected along [100] b) along [010]

feature of the present compounds is ordering between Cu and C in the (Cu,C) plane between the Ba ones; they are placed alternatively along a the a-axis. This results in a superstructure having a_S=2a, b_S=b, c_S=2c with respect to a tetragonal subcell, a, b, c.

This Cu-C ordering was confirmed by electron microscopic observation. As an example, Figs. 2(a,b) show *0kl* and *h0l* electron diffraction patterns of (Cu,C)-1234. The patterns are compatible with the above-mentioned superstructure with the space group Bmmm. Figures 3(a,b) indicate lattice images of (Cu,C)-1234 corresponding to the diffraction patterns in Figs. 2(a,b), respectively. The (Cu,C) plane between the Ba ones consists of two types of dots in Fig. 3(b); dark and less dark dots are placed alternatively indicating the ordered arrangement, -Cu-C-Cu-C along the a-axis. The adjacent (Cu,C) planes have a different phase with respect to the Cu-C sequence, C-Cu-C-Cu, which causes 2c periodicity. Shimakawa et al. analyzed the structure of (Cu,C)-1234 by neutron powder diffraction and suggested that the Cu/C ratio in the (Cu,C) plane is not exactly 0.5/0.5 but 0.68/0.32 [8]. The partial substitution of Cu for C or mutual substitution between them in the (Cu,C) plane might occur in the present series of compounds. In addition, EPMA measurement indicated that significant substitution of Ca for the Ba site occurs in (Cu,C)-1234 [6].

In Fig. 4. DC magnetic susceptibility data are shown for (Cu,C)-1223 and 1234. The (Cu,C)-1223 phase becomes superconducting below 67 k while the (Cu,C)-1234 phase below 117 K. Kumakura et al. determined critical current densities and irreversibility fields for (Cu,C)-1223 and 1234 [9]. According to them, temperature dependencies of J_C's in a magnetic field are much smaller than that of Hg-1223 in the m=1 series of compounds. Moreover, the slopes of irreversibility lines for them are steeper than that of Hg-1223.

3. (Cu,C)-23(n-1)n series

The m=2 series of compounds have been prepared under 5 GPa and 1250° C using Ag_2O as an oxidizing agent [7]. Crystal structures of the m=2 series are shown in Fig. 5 for n=4,5. This series have unique structures where three Ba-planes are stacked in a charge reservoir block separated by the (Cu,C) planes. The Cu-C ordering in the (Cu,C) plane was confirmed by the electron microscopic observation as well as in the n=1 series [7]. The phase of the Cu-C-Cu-C sequence is the same in every (Cu,C) plane in contrast to the m=1 series which results in a superstructure, a_S=2a, b_S=b, c_S=c with respect to a tetragonal subcell, a, b, c. The m=2 series of compounds are the first examples which include three Ba planes in a charge reservoir block. This type of block seems unstable because of highly active Ba ions. In the structures in Fig. 5, every Ba ion is bounded to at least one CO_3 group. This seems key factor to stabilize the Ba ion.

It is more difficult to prepare the m=2 series than m=1 series of compounds. At the present stage, a pretty good sample have been obtained for the n=4 member but the n=5 member was prepared only as

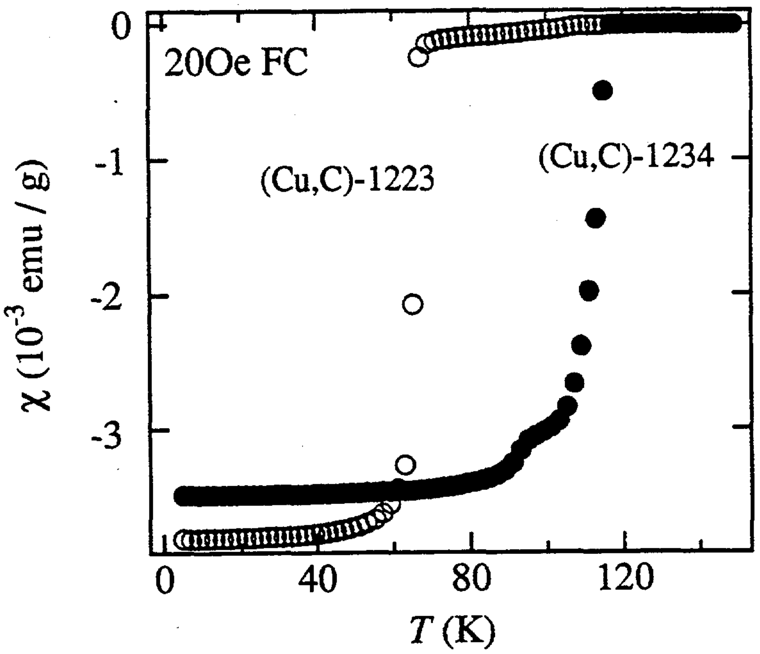

Fig. 4. DC susceptibility data for (Cu,C)-12(n-1)n [6].

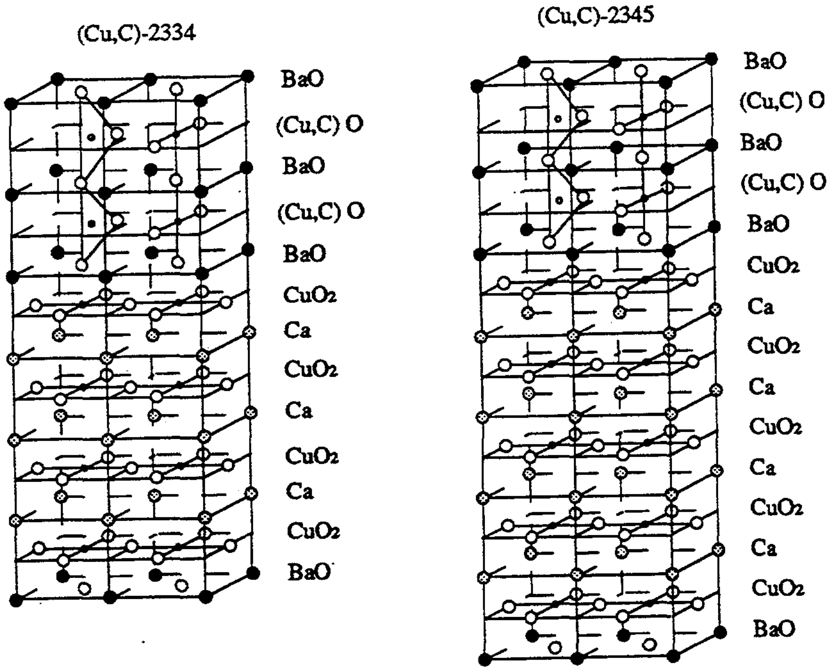

Fig. 5. Structures of (Cu,C)-23(n-1)n [7].

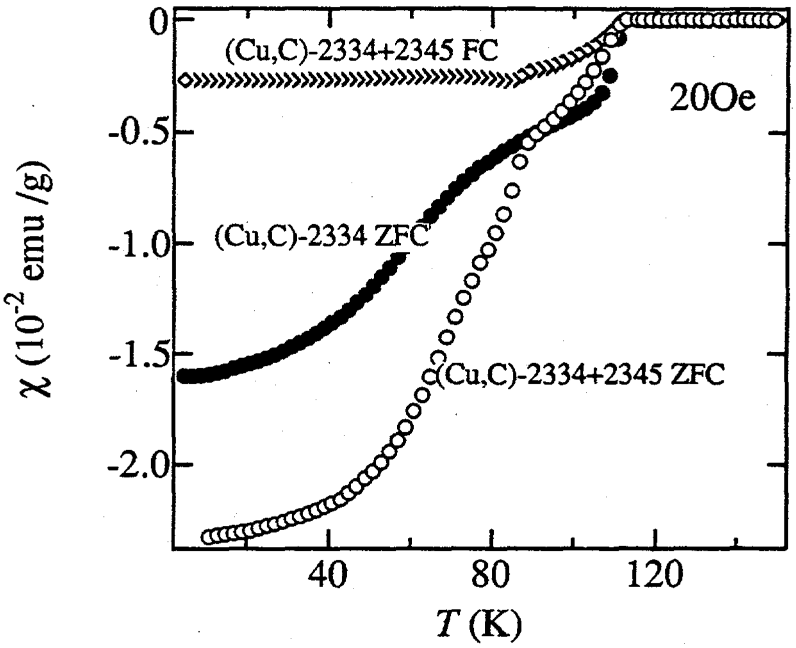

Fig. 6. DC susceptibility data for (Cu,C)-23(n-1)n [7].

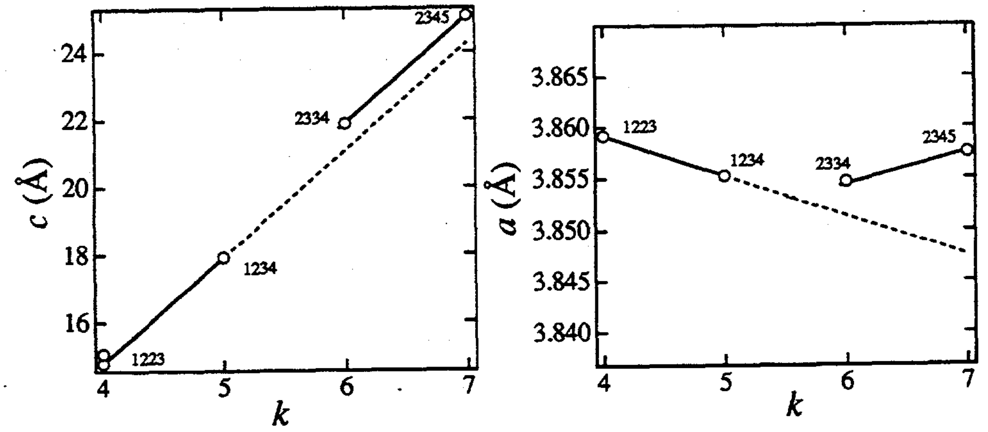

Fig. 7. Lattice parameters of (Cu,C)-m(m+1)(n-1)n [7].

mixture with the n=4 one [7]. Figure 6 shows DC magnetic susceptibility data for (Cu,C)-2334 and the mixture of (Cu,C)-2334 and 2345 [7]. Both samples show diamagnetic susceptibility below 113 K indicating that Tc of (Cu,C)-2334 is 113 K. Although we can not determine T_C of (Cu,C)-2345 definitely, it is suggested to be near 110 k since the mixture of (Cu,C)-2334 and 2345 indicated larger diamagnetic susceptibility at 5 K (see Fig. 6).

Lattice parameters of tetragonal subcells of (Cu,C)-m(m+1)(n-1)n are plotted in Fig. 7 against k, sum of (Cu,C) and Cu planes in a unit formula. The c-dimensions of the 23(n-1)n deviate upward from the straight line obtained for the 12(n-1)n series. This is probably due to larger number of Ba planes included in a subcell of (Cu,C)-23(n-1)n than in (Cu,C)-12(n-1)n. The a-axis of (Cu,C)-23(n-1)n also changes in a different manner as a function of k; it tends to increase with k while that of (Cu,C)-12(n-1)n decreases with k.

References

1. K. Kinoshita and T. Yamada, Nature, **357**, 3131 (1992).
2. Y. Miyazaki, H. Yamane, N. Ohnishi, T. Kajitani, K. Hiraga, Y. Morii, S. Funahashi and T. Hirai, Physica C **198**, 7 (1992).
3. D. Pelloquin, M. Caldes, A. Magnan, C. Michel, M. Hervieu and B. Raveau, Physica C **208**, 121 (1993).
4. F. Goutenoire, M. Hervieu, A. Maignan, C. Michel, C. Martin and B. Raveau, Physica C **210**, 359 (1993).
5. M. Uehara, S. Sahoda, H. Nakata, J. Akimitsu and Y. Matsui, Physica C **222**, 27 (1994).
6. T. Kawashima, Y. Matsui and E. Takayama-Muromachi, Physica C **224**, 69 (1994).
7. T. Kawashima, Y. Matsui and E. Takayama-Muromachi, Physica C **227**, 95 (1994).
8. Y. Shimakawa, J. D. Jorgensen, D. G. Hinks, H. Shaked, R. L. Hitterman, F. Izumi, T. Kawashima, E. Takayama-Muromachi and T. Kamiyama, to be published.
9. H. Kumakura, K. Togano, T. Kawashima and E. Takayama-Muromachi, Physica C **226**, 222 (1994).

High Pressure Synthesis and Magnetic Studies of Quasi One Dimensional Systems $Sr_{n-1}Cu_{n+1}O_{2n}$ (n = 3, 5)

M. Azuma, Z. Hiroi, M. Takano,
Institute for Chemical Research, Kyoto University, Uji, Kyoto-fu 611, Japan
and
K. Ishida and Y. Kitaoka
Department of Material Physics, Faculty of Engineering Science,
Osaka University, Toyonaka, Osaka-fu 560, Japan

ABSTRACT

$SrCu_2O_3$ and $Sr_2Cu_3O_5$ containing two-leg and three-leg S = 1/2 ladders made of antiferromagnetic Cu-O-Cu linear bonds, respectively, were synthesized at high pressure, and their crystallographic and magnetic properties were investigated. Both susceptibility and T_1 data of NMR revealed the existence of a large spin gap only for $SrCu_2O_3$. Superconductivity, which had been predicted theoretically for carrier-doped $SrCu_2O_3$ could not be realized although partial substitution of La^{3+} for Sr^{2+} seemed to be carried out successfully. Electron carriers injected seems to remain localized.

INTRODUCTION

$Sr_{n-1}Cu_{n+1}O_{2n}$ (n = 3, 5, 7...) is a homologous series of high pressure phases in which $Cu_{n+1}O_{2n}$ sheets alternate with Sr_{n-1} sheets along the c axes of their orthorhombic cells [1] as shown for the first two members $SrCu_2O_3$ and $Sr_2Cu_3O_5$ in Fig.1. Figure 2 specifically shows a $Cu_{n+1}O_{2n}$ sheet which can be obtained by shearing a regular CuO_2 sheet so that zigzag chains form periodically. In other words, the CuO_2 sheet is cut into strips (ladders) of $(n+1)/2\cdot a$ in width, each containing $(n+1)/2$ Cu ions in its width, and these strips are connected again so that the Cu ions share oxygen edges at the interface. In each strip strong antiferromagnetic

Occurrence of singlet superconductivity has thus been stressed. In contrast, phases with $n = 5, 9, 14$.. would have gapless ground states. The difference comes from whether we have an even or odd number of Cu ions in the width of a strip which they called a spin ladder with $(n-1)/2$ rungs and $(n+1)/2$ legs.

In order to find out new quantum spin systems exhibiting interesting physics including high T_c superconductivity, we have carefully synthesized by a using high pressure technique the first two compounds with $n = 3$ ($Sr_2Cu_4O_6$ or $SrCu_2O_3$) and $n = 5$ ($Sr_4Cu_6O_{10}$ or $Sr_2Cu_3O_5$) containing 2- and 3-leg ladders, respectively. To be reported here briefly are the results of magnetic susceptibility measurements revealing the presence of a large spin gap for $SrCu_2O_3$ and gapless behavior of $Sr_2Cu_3O_5$, which have been supported by ^{63}Cu NMR measurements. Partial substitution of La^{3+} for Sr^{2+} was also attempted in order to dope $SrCu_2O_3$ with electrons and make it superconducting. Lattice parameters were changed systematically by the substitution, but no trace of superconductivity was observed.

SAMPLE PREPARATION

Polycrystalline samples were prepared from mixtures of $SrCuO_2$ (the ambient pressure form), La_2O_3 and CuO in a cubic anvil type high pressure apparatus [3]. Synthesis conditions were 4.5 GPa at 1373 K and 3 GPa at 1323 K for $SrCu_2O_3$ and $Sr_2Cu_3O_5$, respectively. Samples were characterized by Powder X-ray diffraction (XRD), electron diffraction (ED) and high-resolution electron michroscopy (HREM, JEM-2000EX).

RESULTS

Figure 3 shows the HREM images and the corresponding ED patterns of $Sr_2Cu_3O_5$, in which its in-plane structure as illustrated in Fig. 2 can be seen. Two kinds of black dots are identified clearly; the large one is a Sr atom and the small one a Cu atom. In further detail, two different crystallographic sites are seen for Cu; one located on the first and the third legs of the ladders and the other on the second leg.

Figure 4 shows powder XRD patterns of $SrCu_2O_3$ and $Sr_2Cu_3O_5$. All the intense peaks could be indexed assuming the orthorhombic cells of a=3.930Å, b=11.560Å, c=3.492Å and a=3.932Å, b=19.411Å, c=3.462Å, respectively.

interactions should work through the linear Cu-O-Cu bond stretched along the *a* and *c* axes, while the interactions via 90° Cu-O-Cu bonds across the interface must be much weaker, may even be ferromagnetic [2]. Moreover, the shearing causes spin frustration by symmetry at the interface [1]. Thus, a quasi-1D $S = 1/2$ ladders with almost homogeneous intraladder antiferromagnetic interactions are realized for small-n phases and a dimensional crossover to 2D is expected with increasing n value.

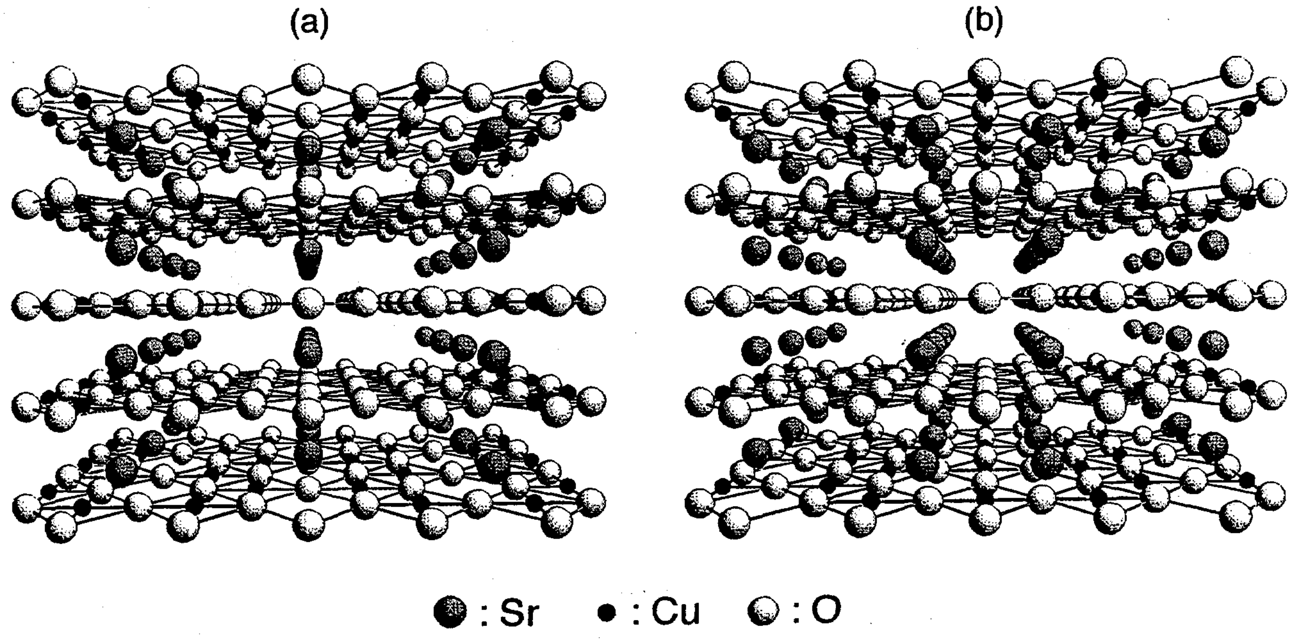

Fig. 1 Schematically illustrated structures of $SrCu_2O_3$ (a) and $Sr_2Cu_3O_5$

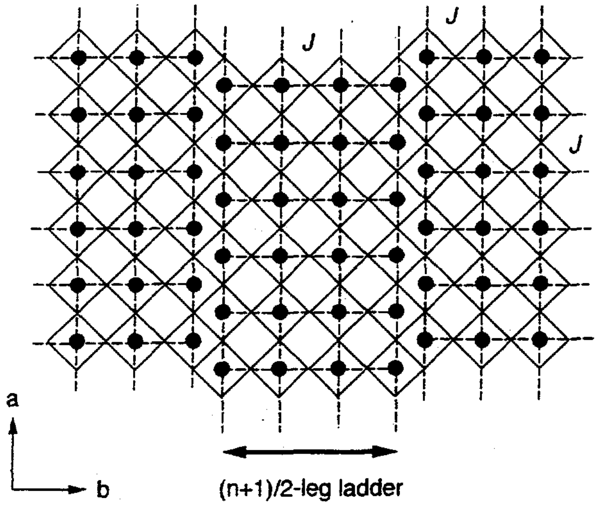

Fig. 2 Schematic drawings of the $Cu_{n+1}O_{2n}$ sheet of $Sr_{n-1}Cu_{n+1}O_{2n}$. The filled circles are Cu^{2+} ions, and O^{2-} ions exist at the corners of the squares drawn with solid lines.

Recently Rice *et al.* [2] investigated theoretically the nature of the ground states of these compounds and concluded that the stoichiometric compounds with n = 3, 7, 11... would be frustrated quantum antiferromagnets with spin liquid ground states and that the spin gap would remain after light doping with holes.

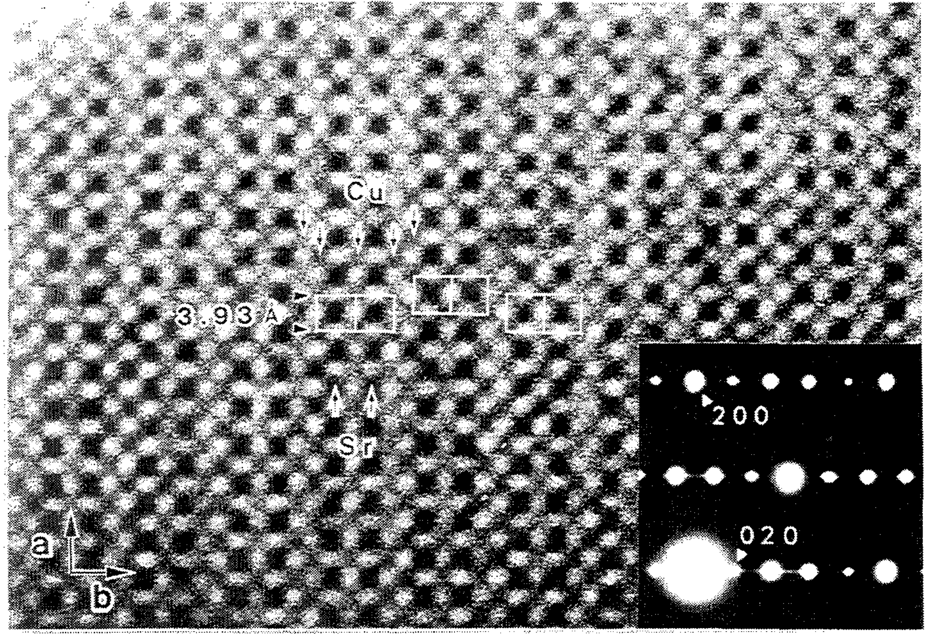

Fig. 3 High resolution electron microscopic image and the corresponding Electron diffraction patterns (inset) of $Sr_2Cu_3O_5$.

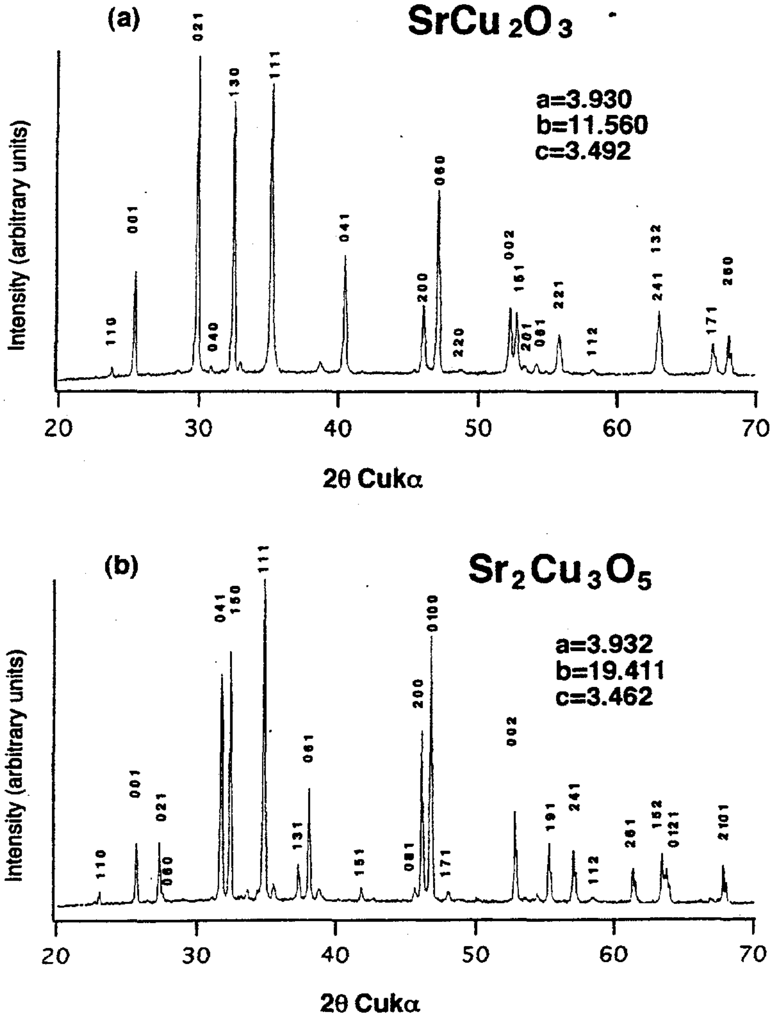

Fig. 4 Powder X-ray diffraction patterns of $SrCu_2O_3$ (a) and $Sr_2Cu_3O_5$ (b).

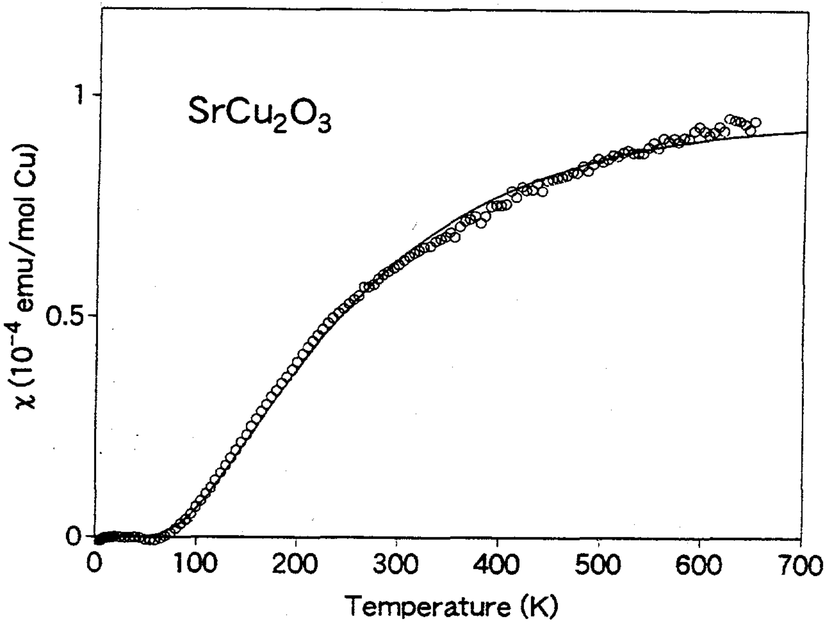

Fig.5 Temperature dependence of magnetic susceptibility of $SrCu_2O_3$ after substraction of the Curie component and the small orbital contribution. Solid line stands for the calculated susceptibility assuming a spin gap of 420 K using an equation $\chi(T) \propto T^{1/2} \exp(-\Delta / T)$ given in ref. 5.

The temperature dependence of magnetic susceptibility of $SrCu_2O_3$ is plotted in Fig. 5 after the substraction of a Curie component due to Cu^{2+} ions made free by lattice imperfections and also a small constant term due to Van Vlec paramagnetism and ionic diamagnetism [4]. The data are normalized at 1 mol of Cu for convenience of comparison with $Sr_2Cu_3O_5$. The continuous decrease of susceptibility toward zero over a wide temperature range suggests a large energy gap in the spin excitation spectrum. According to quite a recent theoretical study of the 2-leg Heisenberg ladder system, susceptibility is given as a function of temperature and the magnitude of the spin gap, Δ, with an equation

$$\chi(T) \propto T^{1/2} \cdot \exp(-\Delta / T),$$

if the intraladder interaction is homogenous and if the continuum of the first excited states has a parabolic dispersion [5]. We have performed the fitting of the obtained susceptibility data as shown in Fig. 5 with the solid line and obtained $\Delta = 420$ K.

Figure 6 shows the temperature dependence of Curie-term substracted susceptibility of $Sr_2Cu_3O_5$. The susceptibility continuously decreases with decreasing temperature but remains at a large finite value of about 3.5×10^{-5} emu/mol Cu at 0 K in contrast to the case of $SrCu_2O_3$. This suggests that the 3-leg ladders in $Sr_2Cu_3O_5$ have a gapless spin excitation spectrum as expected theoretically.

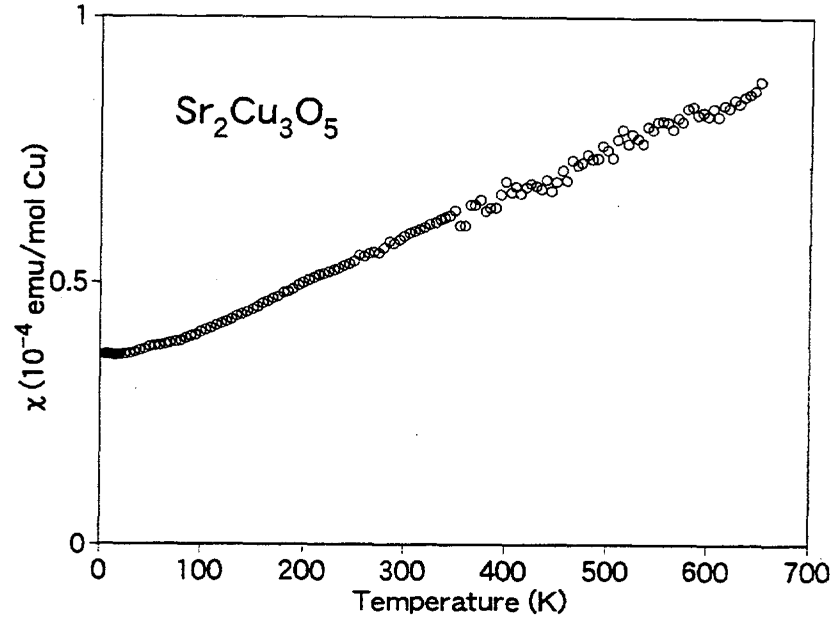

Fig. 6 Temperature dependence of magnetic susceptibility of $Sr_2Cu_3O_5$ after substruction of the Curie component from the raw data. In contrast with the case of $SrCu_2O_3$, a relatively large susceptibility remains at the lowest temperature after the correction.

A microscopic investigation by means of ^{63}Cu NMR also has revealed the existence of a spin gap in $SrCu_2O_3$[6]. A very sharp peak appeared and the Knight shift varied with temperature in parallel with χ. Interestingly, however, the Arrhenius plot of T_1 data has shown that the spin gap is 680 K as shown in Fig. 7. Fitting the T_1 data to a refined theoretical equation [5],

$$1/T_1 \propto (0.80908\text{-}\ln(0.003/T) \cdot \exp(-\Delta / T)$$

gives almost the same value of 700 K. Theoretically the spin gap is calculated to be about $J/2$ [2,5]. Although the accurate value of the intraladder antiferromagnetic exchange J is not known, it would be about 1300 K as judged from the resemblance of the ladder to the usual CuO_2 sheet with respect to the linear Cu-O-Cu bond configuration. So, the magnitude of spin gap obtained from the T_1 data is in quantitative agreement with the theoretical estimation, while the gap estimated by the susceptibility measurement is considerably smaller than the expectation. The reason is not clear at the present stage.

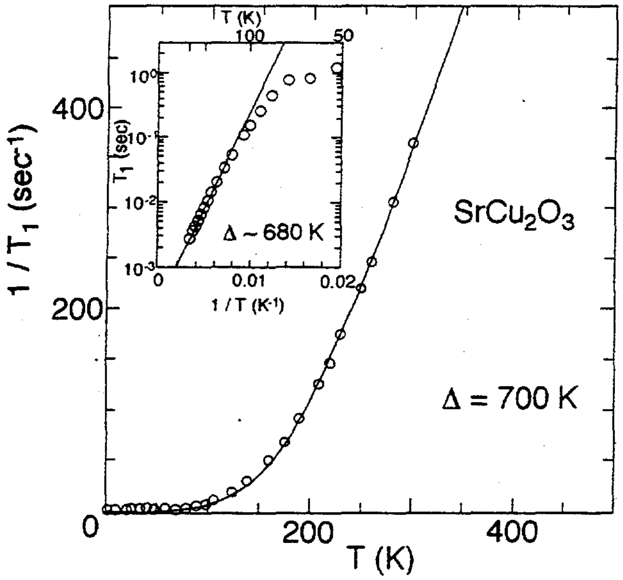

Fig 7 Temperature dependence of $1/T_1$ fitted to a refined theoretical equation assuming a spin gap of 700 K. Inset is the Arrhenius plot of T_1 of $SrCu_2O_3$ from which the magnitude of the spin gap is estimated to be 680 K.

Following Rice *et al.*'s conjecture suggesting the occurrence of superconductivity in carrier-doped $SrCu_2O_3$, we attempted to dope $SrCu_2O_3$ with electron carriers by substituting La^{3+} for Sr^{2+}. Lattice parameters of $Sr_{1-x}La_xCu_2O_3$ are plotted in Fig. 8 for the *a* and *c* axes. The length of the *c* axis shrinks with the substitution, while the *a*-parameter expands, reflecting the electrons being added into the antibonding $\sigma_{x^2-y^2}$ orbitals of the Cu_2O_3 sheet. Unfortunately, however, no trace of superconductivity was observed. Injected electrons seemed to be localized randomly.

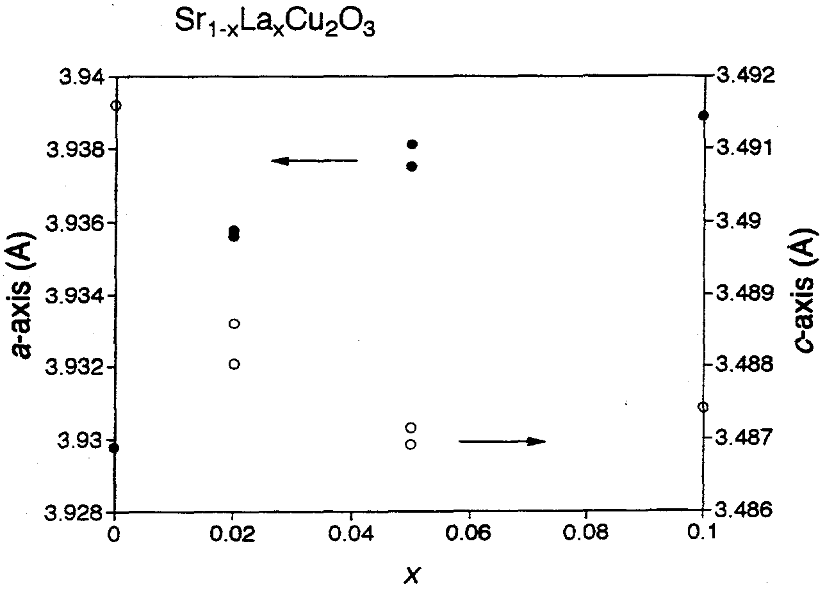

Fig. 8 Lattice parameters of $Sr_{1-x}La_xCu_2O_3$

References

[1] Z. Hiroi, M. Azuma, M. Takano and Y. Bando, J. Solid State Chem. 95 230 (1991)

[2] T. M. Rice, S. Gopalan and M. Sigrist, Europhys. Lett. 23 445 (1993);
S. Gopalan, T. M. Rice and M. Sigrist, Phys. Rev.B 49 8901 (1994);
M. Sigrist, T.M. Rice and F. C. Zhang, Phys. Rev. B 49 12058 (1994)

[3] M. Azuma, Z. Hiroi, M. Takano, Y. Bando and Y. Takeda, Nature 356 775 (1992)

[4] M. Azuma, Z, Hiroi, M. Takano, K. Ishida and Y. Kitaoka

[5] M. Troyer, H. Tsunetsugu and D. Würtz, Phys. Rev. B, in press

[6] K. Ishida, Y. Kitaoka, K. Asayama, M. Azuma, Z. Hiroi and M. Takano, submitted to J. Phys. Soc. Jpn.

INFLUENCE OF CALCIUM ON TRANSPORT PROPERTIES, BAND SPECTRUM AND SUPERCONDUCTIVITY OF $YBa_2Cu_3O_y$ AND $YBa_{1.5}La_{0.5}Cu_3O_y$.

V.E.Gasumyants[a], E.V.Vladimirskaya[a], I.B.Patrina[b]

[a]State Technical University, St.Petersburg 195257, Russia
[b]Institute of Silicate Chemistry of Russia Academy of Science, St.Petersburg, 199155, Russia

The comparative investigation of transport phenomena in $Y_{1-x}Ca_xBa_2Cu_3O_y$ ($0<x<0.25$, $6.96>y>6.87$ and $6.73<y<6.53$), $Y_{1-x}Ca_xBa_{1.5}La_{0.5}Cu_3O_y$ ($0<x<0.5$, $7.12>y>6.96$) and $YBa_{2-x}La_xCu_3O_y$ ($0<x<0.5$, $6.95<y<7.21$) systems have been carried out. The temperature dependencies of resistivity and thermopower have been measured. It was found that the S(T) dependencies take some additional features with Ca content increase. The results obtained have been analyzed on the basis of the phenomenological theory of electron transport in the case of the narrow conductive band. The main parameters of the band spectrum (the band filling with electrons degree and the total effective band width) have been determined. The dependencies of these ones from contents of substituting elements are discussed. Analyzing the results obtained simultaneously with the tendencies in oxygen content and critical temperature change we have confirmed the conclusion that the oxygen sublattice disordering has a determinant effect on band structure parameters and superconductive properties of $YBa_2Cu_3O_y$. The results obtained suggest that Ca gives rise to some peculiarities in band spectrum of this compound.

1. INTRODUCTION

An important question arising in studies of HTSC-materials is the elucidation of role and mechanism of influence of different structural elements of unit cell on superconductivity and other properties of these compounds. Influence of non-isovalent substitutions on different properties of $YBa_2Cu_3O_y$ are discussed in many papers. The common property of these substitution (in parallel with critical temperature T_c depression) is influence on oxygen content and oxygen sublattice condition as a whole. The calcium holds a distinctive position amount the substituting elements. Whereas other elements increase leads to increase of y value (Fe,Co,Al in place of Cu [1-3], La in place of Ba [4-5]), introduction of Ca decreases the one [6-7]. This tendency retains for additional substitution for Y by Ca in Y-Ba-Cu-O system with different dopants (Co→Cu [8], Al→Cu [9], La→ Ba [10]). Furthermore, in these cases the T_c value increases when compared with single substitution samples. However, the questions of band spectrum structure, of its parameters dependence on the samples composition and of connection of these parameters values with superconductive properties are still the open questions. One way to obtain samples with trended composition change. The analysis of transport phenomena in $YBa_2Cu_3O_y$ on the basis of our phenomenological theory [11] has permitted not only to account for all the specific features of temperature and concentration dependencies of transport coefficients but also to describe quantitatively their behavior as well as to determine the conductive band parameters values. As a result, we were able to follow the band spectrum transformation with oxygen content change in $YBa_2Cu_3O_y$ [11] and with iso- and non-isovalent substitution for different components of unit cell of this HTSC and to observe the correlation between band spectrum change and T_c value change [12-13]. In this paper we use our model for investigation of Ca influence on transport properties in normal phase and band spectrum transformation character in the system Y-Ba-Cu-O.

2. SAMPLES AND EXPERIMENT DETAILS

The ceramic samples investigated were prepared from high purity Y, La and Cu oxides and Ba and Ca carbonates by standard solid-state reaction for the $YBa_2Cu_3O_y$ compounds. The pellets were annealed in air three times with intermediate regrinding at temperature T=920-950°C. Then the samples were cooled slowly and were annealed in flowing oxygen at T=450°C, attended slow cooling to room temperature. Lowering of the oxygen content in the samples $Y_{1-x}Ca_xBa_2Cu_3O_y$ was achieved by annealing at T=450°C that was followed by quenching to room temperature. The oxygen content was determined by the iodometric titration method accurate to ±0.01-0.02. The X-ray analysis has revealed all the samples studied to be single phase.

The temperature dependencies of the resistivity, ρ(T), and that of the thermopower, S(T), were measured over the temperature range $T=T_c$-300K. The resistivity was measured by the standart ac four probe method with frequency and phase selection of the measurement channel. The absolute value of thermopower was determined with respect to copper electrodes and then corrected for the absolute value of the thermopower of copper. The temperature difference during the S measurements was 1-2K and was measured with a differential copper-constantan thermocouple.

3. RESULTS AND DISCUSSION

The values of oxygen content, the superconducting transition parameters and the values of thermopower at T=300K for all the samples investigated are shown in Tables 1-3. First of all, we discuss results for series 1 and 2 with single substitution. The behavior of ρ and S in normal phase has certain specific features already described in literature. The dependence ρ(T) is linear within a wide temperature range. The main features of thermopower are the weak dependencies S(T) within the wide temperature range and the smooth maximum of S(T) observed at low temperatures. However, the influence of dopant content increase on S(T) transformation is different for Ca and La. The value of S is practical constant with Ca content increase, whereas La increasing leads to significant growth of thermopower. In both cases the maximum of S(T) is shifted to higher temperatures with x (see. Fig.1, Fig.2). The T_c value decreases with dopant content increase in both series (see Table 1).

Table 1.
The oxygen content, parameters of superconductive transition and thermopower in single-substiturted samples.

x	y	T_c^m, K	T_c^o, K	S(300K), μV/K
		$Y_{1-x}Ca_xBa_2Cu_3O_y$		
0.000	6.96	92.3	90.7	-0.63
0.025	6.95	91.5	86.8	-1.48
0.050	6.93	88.2	83.3	-1.18
0.100	6.91	83.3	71.9	-1.14
0.150	6.90	79.0	71.5	-1.29
0.200	6.89	78.2	66.6	-1.24
		$YBa_{2-x}La_xCu_3O_y$		
0.00	6.95	88.2	85.4	0.78
0.05	6.98	89.8	88.8	1.12
0.10	6.99	90.2	89.5	6.32
0.20	7.03	91.5	86.9	7.67
0.30	7.10	84.2	76.8	16.63
0.40	7.14	73.3	64.2	26.35
0.50	7.21	55.7	49.7	33.98

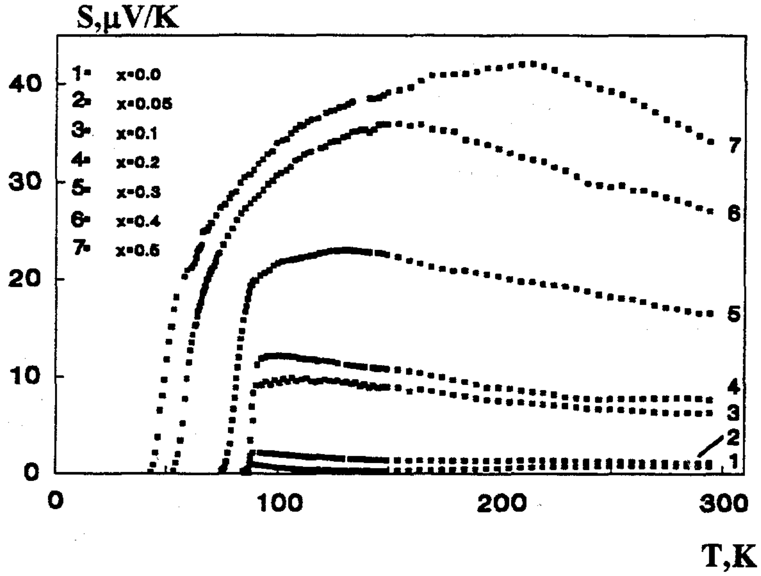

Fig.1. The thermopower vs. temperature for $YBa_{2-x}La_xCu_3O_y$.

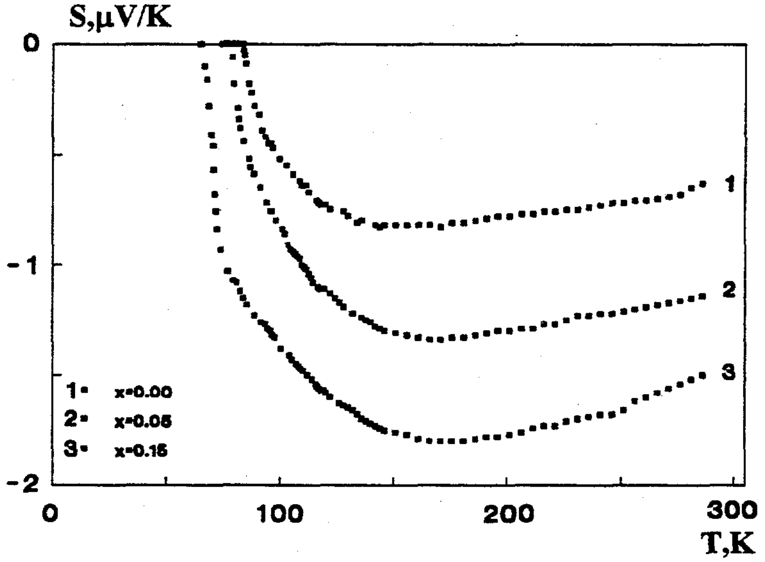

Fig.2. The thermopower vs. temperature for $Y_{1-x}Ca_xBa_2Cu_3O_y$

The results obtained have been analyzed on the basis of narrow-band model. This model assumes the transfer of charge carriers along the band whose width is much less than in usual metals or semiconductors (comparable to the k_oT value). The charge carries concentration is believed to remain constant with temperature change and is determined by the band filling degree with electrons F. This paramèter is equal to the ratio of the numbers of electrons to the numbers of states in the band. The F value determines the value and the sign of the thermopower in the region of high temperatures whenS=const(T) according with the formula:

$$S = \frac{k_o}{e} \cdot \ln \frac{F}{1-F}, \tag{1}$$

Thus, changes of F (and correspondingly, S(300K)) occurring with the deviations from the $YBa_2Cu_3O_y$ stoichiometric content (oxygen deficit increase, doping with various elements) results in changing of the conduction band parameters and the number of carriers in the band. In Ref. [11] we have shown that for describing temperature dependencies in the whole temperature range we can use the simplest approximation of density of states D(E) and differential conductivity σ(E) functions as rectangles with different widths. In this case we can obtain the analytic expressions for temperature dependencies of the transport coefficients. As this take place, contrary to resistivity and Hall coefficient the thermopower may be calculated to absolute value:

$$S = -\frac{k_o}{e} \cdot \left\{ \frac{W_\sigma^*}{\mathrm{sh} W_\sigma^*} \cdot \left[e^{-\mu^*} + \mathrm{ch} W_\sigma^* - 1 / W_\sigma^* \cdot \left(\mathrm{ch} \mu^* + \mathrm{ch} W_\sigma^* \right) \cdot \ln \frac{e^{\mu^*} + e^{W_\sigma^*}}{e^{\mu^*} + e^{-W_\sigma^*}} \right] - \mu^* \right\}, \qquad (2)$$

where: $$\mu^* \equiv \mu / k_o T = \ln \frac{\mathrm{sh}(F \cdot W_D^*)}{\mathrm{sh}\left((1-F) \cdot W_D^*\right)},$$

μ is the chemical potential, $W_D^* \equiv W_D/2k_oT$, $W_\sigma^* \equiv W_\sigma/2k_oT$, W_D is the total effective band width (the width of D(E) rectangle) and W_σ is effective width of the conductive states interval (the width of σ(E) rectangle).

The W_σ and W_D values are different. This may be due to a different nature of energy dependencies of the density of states (DOS) and the differential conductivity functions, as well as to the probable localization of the states near the band edge caused by a disordering in the lattice. In the case of $YBa_2Cu_3O_y$ with y=7 the Fermi level E_F is situated in the middle of the band near the maximum of the DOS function. In this case F=0.5 and energy parameters of the band W_D=70-90meV and W_σ=30-40meV [11]. With the oxygen content y decreasing the number of charge carriers (holes) decreases (the F value increases) which leads to the E_F displacement from the middle of the band (the DOS function maximum) to its upper edge. Also, the oxygen deficit increase is accompanied by the increase of the oxygen vacancy disordering in the lattice. According to Anderson's theory [14], this leads to the localized states share increase (in our model this corresponds to the W_σ/W_D-ratio decrease). The total band width increases in this case which causes the general drop of the DOS including $D(E_F)$. As result of this the T_c value decreases.

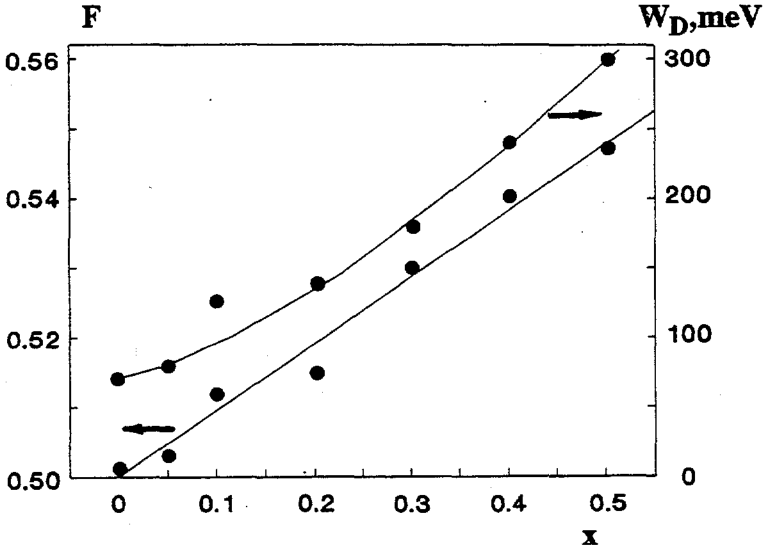

Fig.3. The band parameters vs. La content in $YBa_{2-x}La_xCu_3O_y$

Preparatory to discuss the results obtained on the basis of the model described above, one remark needs to be made. If the band filling is closed to half, the details of the band spectrum structure could influence the S(T) dependencies significantly, i.e. the approximation used becomes rough. In this reason we haven't calculated the band structure parameters for Ca-doped samples in which the

S(300K) value is closed to zero and thus F≈0.5. In this case we can make only the qualitative conclusion that the F value is practical constant and the W_D value increases with x. As to the La-doped samples (in which S(300K) value increases significantly with x) the calculated values of the main band spectrum parameters are shown in Fig.3. It can be seen that the La content increase leads to appreciable transformation of the conductive band.

The results obtained for both series with single substitution may be explained with regard to the oxygen sublattice condition change. The La^{3+} ions substitute for Ba^{2+} causing O(5) sites to become filled with oxygen in so doing the oxygen comes from both atmosphere during annealing and from neighboring cells without La. As a result, the oxygen deficiency arises in cells which don't contain La atoms. In additional, the total compensation of the excess positive charge don't take place, as result the electrons number increases (in our terms, the F value increases). In the case of Ca-doping the oxygen content decreases with x, but because Ca^{2+} ions substitute Y^{3+} increasing the holes number in the band, the increase of electrons at the expense of oxygen deficit increase is compensated. As a result the F value remains constant with Ca content increase. Thus, broadening of the band in both cases is caused by increasing of oxygen sublattice disordering degree and leads to T_c suppression. Difference of the F(x) dependencies are explained by different relationship between valences of substituting elements and substituted ones.

Table 2.
The oxygen content, parameters of superconductive transition and thermopower in $Y_{1-x}Ca_xBa_{1.5}La_{0.5}Cu_3O_y$.

x	y	T_c^m, K	T_c^0, K	S(300K), μV/K
0.0	7.22	36.6	32.0	40.49
0.1	7.19	57.9	51.7	18.98
0.2	7.13	73.0	67.9	19.19
0.3	7.08	80.6	78.9	3.34
0.4	7.01	82.4	80.2	6.19
0.5	6.96	82.5	78.9	4.23

By virtue of the fact that Ca and La influence differently on oxygen content, the investigation of the properties of the samples with double substitutions has been of our interest. It is of significance to study the transport properties of $Y_{1-x}Ca_xBa_{2-z}La_zCu_3O_y$ and to follow the band structure transformation in the case of additional substitution for Y by Ca with z value fixed when comparing with single substitution (for Ba by La) system. In this case the y value decreases with x as with single-doping by Ca samples (see Table 2). The temperature dependencies of resistivity and thermopower are shown in Fig.4 and Fig.5, the parameters of superconductive transition are given in Table 2. The Ca increase leads to decreasing of S(300K) value and increasing of the critical temperature accompanied by narrowing of superconductive transition and increasing of the slope of ρ(T) dependencies. The ρ(T) dependencies are linear except the start sample with x=0.

The following fact has engaged our attention. Whereas the ρ(T) dependencies are similar to the typical ones for Y-Ba-Cu-O system, the dependencies S(T) are modified with Ca content not quite usually. As known for the dependencies S(T) in $YBa_2Cu_3O_y$ with various oxygen content or different cations substitutions, the slope of S(T) gradually decreases with temperature in the region above S(T) maximum. In case of slight variations from stoichiometry the value of S is almost constant at the temperature range near T=300K. As illustrated in Fig.5, in the samples doped with Ca the conservation of well-pronounced maximum is accompanied by showing up of region of linear S decreasing with T above the temperature of this maximum. This suggests the doping with Ca to result in additional peculiarities appearance in band spectrum of $YBa_2Cu_3O_y$.

For explanation the S(T) dependencies obtained we have used additional assumption about slight asymmetry of the conductive band. Taking into account this fact is effected by introduction some distance ($b \cdot W_D$, where b is asymmetry parameter) between centers rectangles D(E) and σ(E). In this case in formula for thermopower (2) instead of μ we must use now (μ-b·W_D). The good agreement between the calculated and experimental dependencies of S(T) is demonstrated in Fig.5.

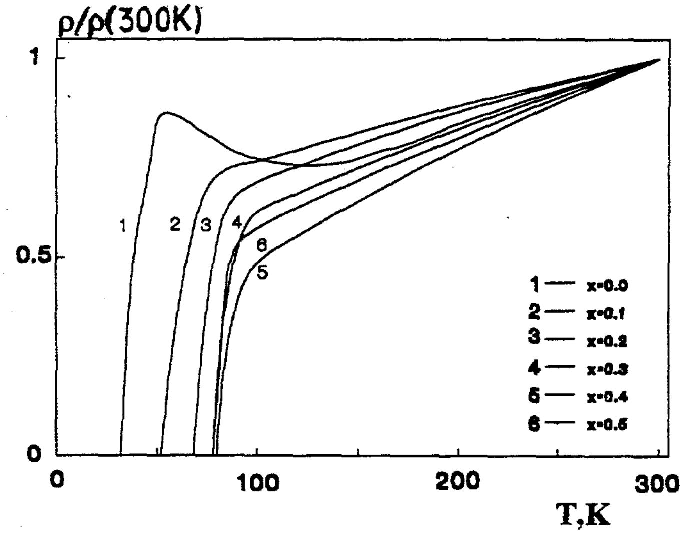

Fig.4. The resistivity vs. temperature in $Y_{1-x}Ca_xBa_{1.5}La_{0.5}Cu_3O_y$

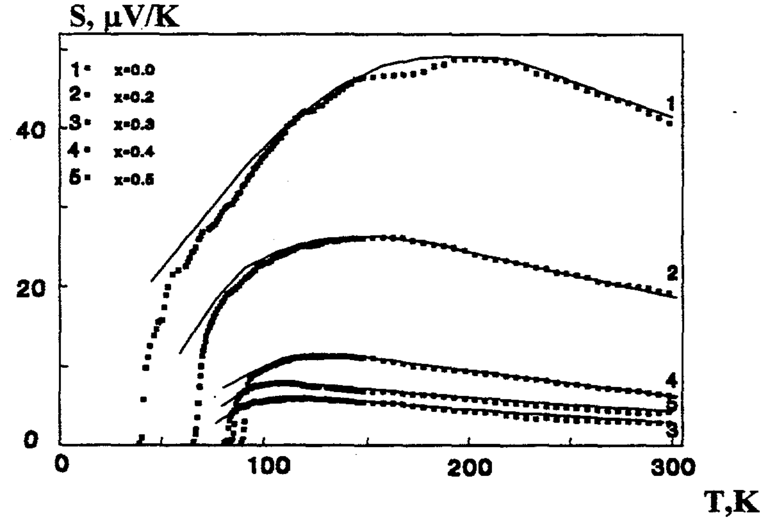

Fig.5. The thermopower vs. temperature in $Y_{1-x}Ca_xBa_{1.5}La_{0.5}Cu_3O_y$

The concentration dependencies of band structure parameters calculated are shown in Fig.6. It can be seen that the Ca content increase causes the total effective band width decreasing and reducing of F value with the slope of the W_D(x) and F(x) dependencies decreasing with x value. Thus, the trends in band spectrum parameters changing (and simultaneously in T_c value changing) are opposite to the ones observed in the systems with single substitutions described above. Nevertheless, two facts have engaged our attention. In the first place, the relation between critical temperature and band spectrum parameters is the same as in single substituted systems. It is to be noted that the practical constancy of T_c is accompanied by sligth changing of band parameters (compare Table 2 and Fig.6 for x=0.3-0.5). And in the second place, the change of all these parameters correlates with oxygen content changing. These things considered, we can explain the results obtained in the frame of our model. Additional Ca doping leads to decrease of oxygen content as compared to single substitution and the over-stoichiometric oxygen escapes from the cell (the y value closes to 7) (see Table 2). As a result the oxygen sublattice becomes more ordered which results in narrowing of the band. Simultaneously band filling degree decreases nearing to half.

Thus, the results obtained confirm the conclusion made earlier (when studying the 3d-metals substitutions for Cu [12]) about the determinant effect of oxygen sublattice condition on band spectrum parameters and superconductive properties of $YBa_2Cu_3O_y$.

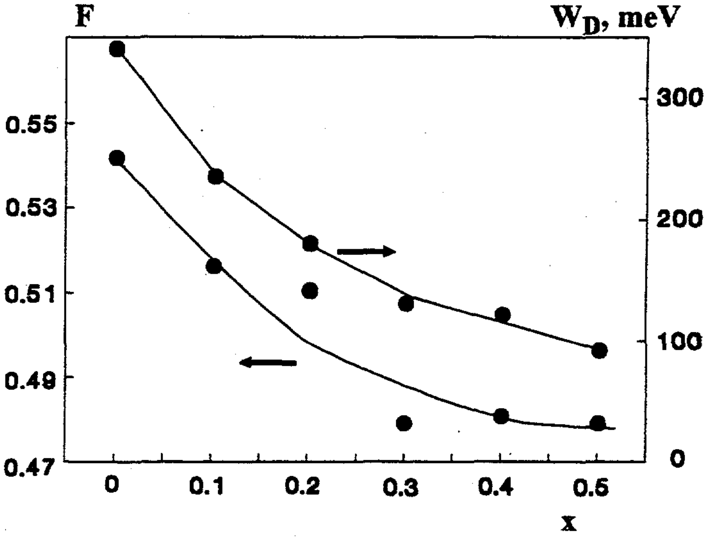

Fig.6. The band parameters vs. Ca content in $Y_{1-x}Ca_xBa_{1.5}La_{0.5}Cu_3O_y$.

For more elucidation of Ca influence on band spectrum transformation we have studied the Ca-doped samples with oxygen deficit (see Table 3). The S(T) dependencies for these samples are shown in Fig.7. The oxygen annealing gave us the possibility to obtain data which may be interpreted in the frame of our model (as indicated by Fig.7 the S values increase after annealing, i.e., the band filling increases and we can use the approximation described above). The features of S(T) dependencies revealed in the double-substitution samples hold in these ones. Besides of this the T_c value increases (see Table 3) and the F value decreases (see Fig.8) with Ca content also. As for the total effective band width our calculation show that its value remains practical constant (W_D=160-190mev). It is necessary to note that oxygen deficit in annealed Ca-doped samples increases rather significantly. According to our conception this fact must cause broadening of the band. However, if the assumption about introduction of additional Ca-states to the band is true, the combination of two effects (broadening of band and increasing of peak of Ca-states which is located in the band) can results in insignificant change of the W_D value which is the effective band width, i.e., the width of rectangle approximating the D(E) function. It can be noted that the calculated value of b parameter depends lineary with Ca content as in the samples with double substitution and the b values for both of these series fall on one trend. This confirms the assumption that it is the calcium that causes the rise of asymmetry of the band introducing additional states.

Table 3.
The oxygen content, parameters of superconductive transition and thermopower in $Y_{1-x}Ca_xBa_2Cu_3O_y$ after annealing.

x	y	T_c^m, K	T_c^o, K	S(300K), μV/K
0.000	6.73	63.7	61.1	17.8
0.025	6.72	70.8	67.9	14.0
0.050	6.70	72.0	69.7	12.4
0.075	6.68	75.1	73.1	13.3
0.100	6.66	80.0	77.3	9.4
0.150	6.58	80.5	74.2	9.3
0.200	6.53	80.9	76.6	8.0

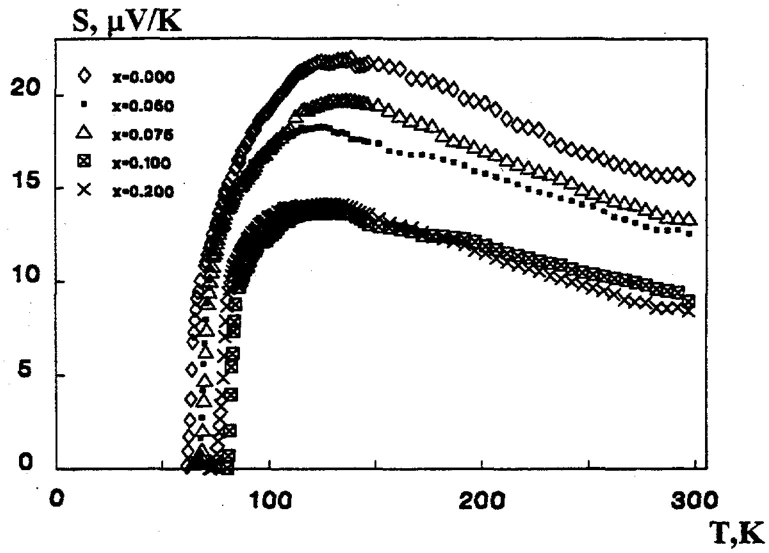

Fig.7. The thermopower vs. temperature in $Y_{1-x}Ca_xBa_2Cu_3O_y$ after annealing.

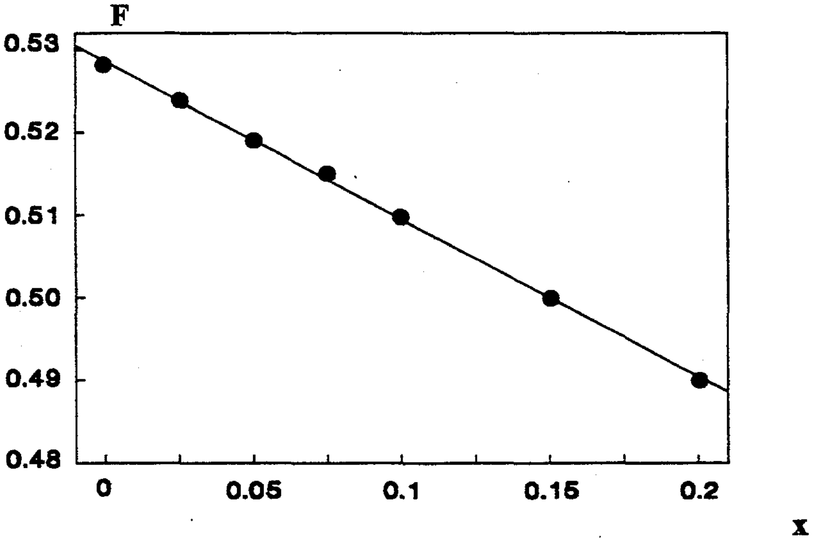

Fig.8. The degree of band filling with electrons vs. Ca content in $Y_{1-x}Ca_xBa_2Cu_3O_y$ after annealing.

The increase of T_c value with x observed in experiment can be explained by two different effects. On the one hand, the band filling nears to half with Ca content increase, i.e., the Fermi level shifts to the DOS function maximum located in the middle of the band and this causes the T_c value increase. On the other hand, the F value decreasing can be explained by arising of the additional Ca-states in the upper half of the band. In this case pinning of the Fermi level in the region of Ca-states is possible. As a result the DOS function value at Fermi level (and correspondingly the T_c value) decreases. For the final answer the question about mechanism of T_c increase observed in the Ca-doped samples the investigations of the samples with more oxygen deficit (for additional shift of Fermi level position in the start sample) is necessary.

4.CONCLUSIONS

In summary, we have performed the investigation of the transport phenomena in Ca-doped samples of the $YBa_2Cu_3O_y$ system with different oxygen content and substitution for Ba by La. The results obtained and their analysis on the basis of narrow band model allow to make the following conclusions.

1. The Ca doping leads to T_c depression in the case of near stoichiometric content and to increasing of T_c if Ca is introduced in the samples with significant deviation from stoichiometry due to oxygen deficit or substitution for Ba.

2. The temperature dependencies of thermopower in Ca-doped samples take some additional features when compared with typical ones for Y-Ba-Cu-O system.

3. The S(T) dependencies analysis on the basis of narrow band model shows that Ca doping causes the increasing of asymmetry degree of the conductive band. The most likely reason of this is additional Ca-states which are located in the region of the band.

4. The character of the critical temperature change in $YBa_2Cu_3O_y$ with dopant content increase correlates with band spectrum parameters change. The possibility of simultaneous explanation of all the experimental results obtained confirms the validity of using the narrow band model for interpretation of transport phenomena data in Y-based HTSC.

5. The conclusion about determinant effect of the extent of oxygen subsystem condition on the band spectrum parameters and critical temperature of $YBa_2Cu_3O_y$ have been confirmed.

REFERENCES

1. J.M.Tarascon et al., Phys.Rev.B, 37 (1998) 7458.
2. Y.Xu et al., Physica C, 169 (1990) 205.
3. X.Y.Zhou et al., Phys.Stat.Sol.(a), 119 (1990) K145.
4. G.V.Bazuev et al., Phys.Stat.Sol.(a), 115 (1989) 267.
5. R.Liang et al., Physica C, 157 (1989) 83.
6. M.R.Chandrahood et al., Appl.Phys.Lett., 56 (1990) 183.
7. I.Felner, Thermochimica Acta, 174 (1991) 41.
8. Y.Zhao et al., J.Phys.: Condens. Matter, 4 (1992) 2263.
9. Y.Zhao et al., Physica C, 179 (1991) 207.
10. R.P.Slater et al., Supercond.Sci.Technol., 5 (1992) 205.
11. V.E.Gasumyants et al., Sov.Superconductivity, 4 (1991) 1184.
12. V.E.Gasumyants et al., Sov.Phys.Tech.High Pres., 3 (1993)73
13. V.E.Gasumyants et al., Chinese J.Phys., 31 (1993) 999.
14. P.W.Anderson, Phys.Rev., 109 (1958) 1492.

Structure and Superconductivity in $(Bi_{0.35}Cu_{0.65})Sr_2YCu_2O_7$ and Related Materials

R.A. Jennings, S.P.Williams and C. Greaves
Superconductivity Research Group
School of Chemistry
University of Birmingham
Birmingham B15 2TT
England

The recently reported $(Bi/Cu)Sr_2YCu_2O_7$ phase has been studied by time of flight powder neutron diffraction. The proposed 1212 structure has been confirmed and refinements have shown the oxygen in the (Bi/Cu)O layer is displaced by 0.78Å from the ideal (½,½,0) site (P4/mmm space group) along {100}. Bond Valence Sum calculations have suggested oxidation states of Bi^{5+} and Cu^{2+} for the cations in the (Bi/Cu)O layers. The material is non-superconducting and all attempts to induce superconductivity have been unsuccessful. Work on the related material $(Ce/Cu)Sr_2YCu_2O_7$ has shown the ideal Ce content to be 0.5 Ce per formula unit. The introduction of Ba (10%) onto the Sr site dramatically increases phase stability and also induces superconductivity (62K).

Introduction

The discovery of high T_c superconductivity in the system Tl-Ba-Ca-Cu-O [1] was quickly followed by the identification [2-8] of two homologous series of phases with the general nominal formulae $TlBa_2Ca_{n-1}Cu_nO_{2n+3}$ (single TlO layers) and $Tl_2Ba_2Ca_{n-1}Cu_nO_{2n+4}$ (double TlO layers) with $1 \leq n \leq 5$. These phases have superconducting $Ca_{n-1}(CuO_2)_n$ layers separated by rocksalt layers.

Similarly, several bismuth compounds with double BiO layers are known and have general nominal composition $Bi_2Sr_2Ca_{n-1}Cu_nO_{2n+4}$ ($1 \leq n \leq 3$) [9,10]. However no similar materials with a BiO monolayer was known. Recently a Bi cuprate with composition $(Bi_{0.5}Cu_{0.5})Sr_2YCu_2O_7$ has been reported by Ehmann et al [11]. It was claimed that the material had the 1212 structure (Figure 1) and so would be the first reported member of the BiO monolayer series. The 1212 structure was confirmed by several other groups [12,13]. It should be noted, however, that this material is not strictly analogous to the Tl-1212 phase since it contains mixed (Bi/Cu)O layers.

Alternatively the material can be considered as a 123 (or YBCO) type structure with 1/2 Cu1 site substituted by Bi. The 1212 and 123 structures are closely related, with the 4 co-ordinate Cu 'chain' sites in 123 being replaced by approximately octahedrally co-ordinated metal ions, by movement of the oxygen in the basal plane from the face edge towards the face centre. The structure generally assumed for the Bi-1212 material is based on X-ray diffraction data with the basal oxygen confined to the face centre (1c site). Due to the insensitivity of X-ray diffraction to O atoms in the presence of heavy metals such as Bi, we have carried out a structural investigation using time of flight powder neutron diffraction on the material $(Bi_{0.35}Cu_{0.65})Sr_2YCu_2O_7$ with the objective of confirming the general structure and obtaining a more detailed description of the O position in the basal plane.

The material was reported to be non-superconducting as made, but superconductivity has been achieved using certain annealing conditions [11].

Sample Synthesis and Characterisation

High purity Y_2O_3, $SrCO_3$, CuO and Bi_2O_3 were used to make samples of composition $(Bi_xCu_{1-x})Sr_2YCu_2O_7$ for x=0.2-0.5 in 0.05 increments. The samples were heated in air at 985°C for 14hrs and then furnace cooled to room temperature. The purity of the samples was then checked by powder X-ray diffraction (Siemens D5000) with further heat treatments as required, under the same conditions, until a consistent X-ray diffraction profile was obtained. It was found that the optimum Bi content for phase stability was $(Bi_{0.35}Cu_{0.65})Sr_2YCu_2O_7$, which is in good agreement with the results of Beales et al [12]. Iodometric titrations showed the oxygen content to be 7.0

Results and Discussion

Time-of-flight neutron powder diffraction data were collected on $(Bi_{0.35}Cu_{0.65})Sr_2YCu_2O_7$ using the diffractometer POLARIS at ISIS, Rutherford Appleton Laboratory. Data in the range 0.5Å<d<2.25Å were used for the structural refinement, using the program TF15LS which is based on the Cambridge Crystallographic Subroutine Library [15,16]. The space group P4/mmm was adopted with initial atomic positions based on the idealised 1212 structure proposed by Ehmann and scattering lengths of Y=0.7750, Bi=0.8533, Sr=0.7020, Cu=0.7718 and O=0.5805 (all $x10^{-12}$cm).

Early refinements gave high temperature factors for Bi/Cu1, O1 and O4 (see Figure 1). The high temperature factor for the O1 site was consistent with the possible displacement of the O from the face centre site towards the face edge. The O1 was therefore allowed to move off this site in the [010] direction. This reduced the temperature factor and R-factors. However, since the temperature factor was still higher than expected, anisotropic temperature factors were introduced for this site. Refinement resulted in a high value for B_{22} (2.417Å^2) showing that most disorder is directed along the b-axis. This is not unexpected due to the different co-ordination preferences of the Bi and Cu cations in the adjacent Bi/Cu1 site. It has been reported by Slater and Greaves [14] that in some similar 1212 type phases the O1 site was, in fact, split into two (O1 and O1'). The structure was therefore refined with two separate O1 sites, but refinements indicated preferential occupancy of a single site, and subsequent examination assumed one O1 position with anisotropic thermal parameters. The introduction of anisotropic temperature factors for O4 resulted in a high B_{33} value which again is consistent with mixed cation occupancy of the Bi/Cu1 site. The Bi/Cu1 site was also allowed to move in the [010] direction, as had been observed in other phases, and this produced an acceptable isotropic temperature factor . Results of the final refinement are given in Table 1 and selected bond distances in Table 2.

Basic Bond Valence Sum calculations were carried out on the refined structure to obtain some insight into the oxidation states of the Cu1 and Bi. Refinements can clearly only reflect the average structure and so the results of the calculations must be viewed with some caution. Considering first the Bi-O polyhedra, since the two Bi-O4 distances are very short and alone suggest a Bi oxidation state of 3.6+, it was therefore assumed that Bi was present as Bi^{5+}. This is in agreement with Beales who proposed that chemically stable 1212 phases were generally observed when the average valency in the rocksalt layer is +3 and so a 2:1 ratio of Cu:Bi would imply Cu^{2+} and Bi^{5+}.

For simplicity the Bi/Cu1 site was constrained to its original (0,0,0) position as the displacement of the site appeared to have only a minor effect on the calculations, compared to that of the O1 displacement. Considering only the displacement of the O1, the Bi can have either a short or longer bond to O1 depending on whether the O1 is displaced towards (O1a) or away (O1b) from the Bi (Figure 2). Our calculations have demonstrated that a Bi co-ordination of 6 (with 4 short (O1a) bonds) would be consistent with an oxidation state of 5+ (Bond Valence Sum=+4.99).

In the absence of a knowledge of the detailed microstructure, even with 4 Bi-O1a bonds, the Cu stereochemistry cannot be reliably deduced. However, it is clearly impossible for the Cu to have 3 or 4 short Cu-O1 bonds. The remaining possible situations give bond valence sums of 1.4 (1 short and 3 long bonds) and 1.63 (2 short and 2 long bonds). This suggests the possibility that some of the Cu1 might be present as Cu^{1+} linearly co-ordinated to two O4 with 4 longer (3.59Å) O1b bonds not really affecting the co-ordination. Interestingly BVS calculations for the Cu2 site produce a value of +2.27 which might be consistent with this view but it must be realised that it could equally indicate simple 'overbonding' at this site [17]. Moreover, the redox properties of Bi^{5+} and Cu^{+} suggest that their coexistence within the same layer is improbable. A more likely explanation for this is that the Bi/Cu1-O4 bond actually consists of a shorter Cu-O4 bond and a longer Bi-O4 bond, with the refinement only showing the average position of the two possible O4 sites. This would be consistent with the high O4 anisotropic temperature factor, B_{33}, and would result in the true Cu oxidation state being higher than the value calculated.

More recent work focused on the related material $(Ce/Cu)Sr_2YCu_2O_7$. Using the guidelines proposed by Beales it was expected that the phase $(Ce_{0.5}Cu_{0.5})Sr_2YCu_2O_7$ would be the most stable phase. This was found to be correct although the material was still not single phase. The material was found to be non superconducting as expected and Ca doping on the Y site resulted in increased impurity phases with no change in the superconducting properties. Small amounts of Ba doping on the Sr sites dramatically improved the phase purity, with the ideal composition found to be $(Ce_{0.5}Cu_{0.5})Sr_{1.8}Ba_{0.2}YCu_2O_7$. The introduction of Ba also induced superconductivity in the material with the highest T_c observed at 62K although conditions have not yet been optimized. Further work is focusing on improving phase purity and T_c in these materials and we hope to carry out a neutron diffraction study in the near future.

Acknowledgements

We thank the Science and Engineering Research Council for financial support, including a research studentship to RAJ, and providing the neutron diffraction facilities at ISIS. We thank S.Hull and R.I.Smith for experimental assistance with the collection of neutron diffraction data

References

[1] Z.Z.Sheng and A.M.Hermann, Nature 332 (1988) 138

[2] R.M.Hazen, L.W.Finger, R.J.Angel, C.T.Prewitt, N.I.Ross, C.G.Hadidiacos, P.J.Heaney, D.R.Velben, Z.Z.Sheng, A.E.Ali and A.M.Hermann, Phys.Rev.Lett. 60 (1988) 1657

[3] C.C.Torardi, M.A.Subramanian, J.C.Calabrese, J.Gopalakrishnan, E.M.McCarron, K.J.Morrissey, T.R.Askew, R.B.Flippen, U.Chowdhry and A.W.Sleight, Phys.Rev.B38 (1988) 225

[4] C.C.Torardi, M.A.Subramanian, J.C.Calabrese, J.Gopalakrishnan, K.J.Morrissey, T.R.Askew, R.B.Flippen, U.Chowdhry and A.W.Sleight, Science 240 (1988) 631

[5] D.E.Cox, C.C.Torardi, M.A.Subramanian, J.Gopalakrishnan and A.W.Sleight, Phys.Rev.B38 (1988) 6624

[6] S.S.P.Parkin, V.Y.Lee, A.I.Nazzal, R.Savoy, R.Beyers and S.J.La Placa, Phys.Rev.Lett. 61 (1988) 750

[7] H.Ihara, R.Sugise, M.Hirabayashi, N.Terada, M.Jo, K.Hayashi, A.Negishi, M.Tokumoto, Y.Kimura and T.Shimomura, Nature 334 (1988) 510

[8] A.W.Sleight, Science 242 (1988) 1519 and references therein

[9] M.Maeda, Y.Tanaka, M.Fukutoni and T.Asano, Jpn.J.Appl.Phys 27 (1988) L209

[10] J.M.Tarascon, Y.LePage, P.Barbrox, B.G.Bagley, L.H.Greene, W.R.McKinnon, G.W.Hull, M.Giroud and D.M.Hwang, Phys.Rev.B37 (1988) 9382

[11] A.Ehmann, S.Kemmler-Sack, S.Lösch, M.Schlichenmaier, W.Wischert, P.Zoller, T.Nissel and R.P.Huebener, Physica C 1989 (1992) 1

[12] T.P.Beales, C.Dineen, S.R.Hall, M.R.Harrison and J.P.Parberry, Physica C 207 (1993) 1

[13] Q.Yitai, T.Kaibin, Y.Peidong, C.Zuyao, L.Rukang Z.Guien, Z.Yuheng and W.Nanlin, Physica C 209 (1993) 516

[14] P.R.Slater and C.Greaves, Physica C 180 (1991) 299

[15] J.C.Matthewman, P.Thompson and P.J.Brown, J.Appl.Chstallogr. 15 (1982) 167

[16] P.J.Brown and J.C.Matthewman, Rutherford Appleton Laboratory Report RAL-87-010 (1987)

[17] I.D.Brown, J.Solid State Chem. 82 (1989) 122

Table 1
Refined structural parameters for $Bi_{0.35}Cu_{0.65}Sr_2YCu_2O_7$
Estimated standard deviations are given in parentheses

ATOM	POS	X	Y	Z	B(Å^2)	UNIT CELL OCCUPANCY
Y	1d	0.5	0.5	0.5	0.50(2)	1.0
Sr	2h	0.5	0.5	0.2024(1)	1.00(2)	1.0
Cu2	2g	0.0	0.0	0.3582(1)	0.31(1)	1.0
Bi	4l	0.0	0.0730(7)	0.0	0.81(5)	0.0875
Cu1	4l	0.0	0.0730(7)	0.0	0.81(5)	0.1625
O1	4n	0.5	0.296(2)	0.0	*	0.25
O3	4i	0.5	0.0	0.3764(1)	0.64(2)	1.0
O4	2g	0.0	0.0	0.1603(2)	*	1.0

a=b=3.814(1)Å, c=11.714(3)Å; P4/mmm
R_I=6.0%, R_p=3.54%, R_{wp}=3.47%, R_{exp}=1.45%

* Anisotropic temperature factors (Å^2)

Atom	B_{11}	B_{22}	B_{33}
O1	1.8(2)	2.4(2)	1.3(2)
O4	1.40(4)	1.40(4)	1.87(8)

Table 2
Selected Bond Distances (Å)

Bi/Cu1-O1a	2.216(8)
Bi/Cu1-O1b	3.585(8)
Bi/Cu1-O4	1.877(4) [x2]
Cu2-O3	1.919(2) [x4]
Cu2-O4	2.318(3)

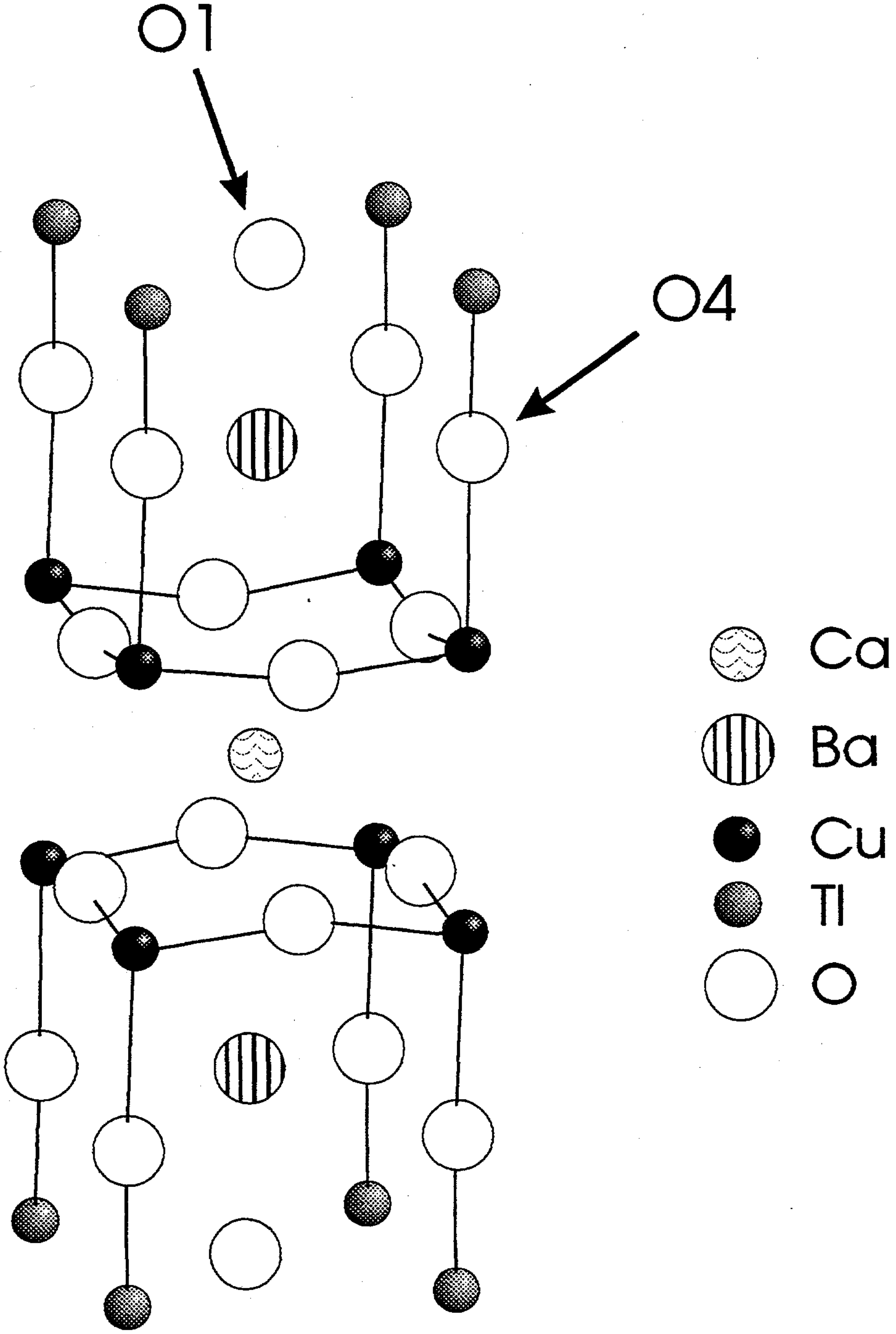

Figure 1.- The basic 1212 structure for $T1Ba_2CaCu_2O_7$.

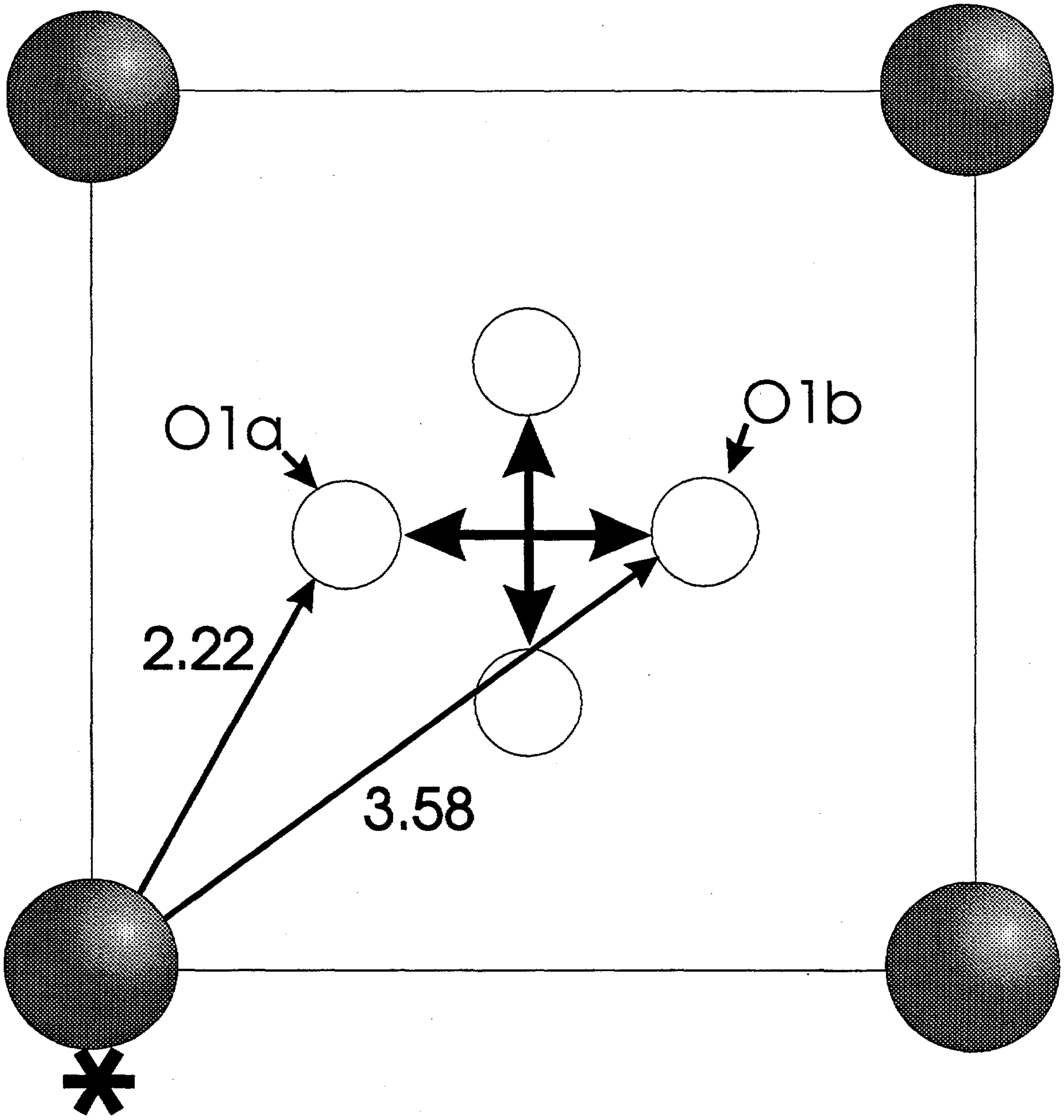

Figure 2.- The basal plane of the refined structure showing the possible positions of the O1 site with respect to the cation marked*. All bond lengths in Angstroms

STRUCTURAL, DYNAMICAL & ELECTRONIC PROPERTIES OF $CaCuO_2$

by

Bal K. Agrawal and Savitri Agrawal

Physics Department, Allahabad University,
Allahabad 211002, INDIA.

The scalar relativistic version of an accurate first principles full potential self- consistent linearized muffin tin orbital (LMTO) method has been employed for describing the physical properties of the parent system of the high_Tc oxide superconductors, i.e., CaCuO2. The presently employed modified version of the LMTO method is quite fast and goes beyond the usual LMTO_ASA method in the sense that it permits a completely general shape of the potential and the charge density. Also, in contrast to LMTO_ASA, the present method is also capable of treating distorted lattice structures accurately. The calculated values of the lattice parameters of pure CaCuO2 lie within 3% of the experimentally measured values for the Sr-doped system Ca(.86)Sr(.14)CuO(2). The computed electronic structures and the density of states is quite similar to those of the other oxide superconductors, except of their three- dimensional character because of the presence of strong coupling between the closely spaced CuO2 layers. The van Hove singularity peak appears slightly below the Fermi level and a small concentration of oxygenation /or/ substitutional doping may pin it at the Fermi level. The calculated frequencies for some symmetric frozen phonons for undoped CaCuO2 are quite near to the measured data for the Sr-doped CaCuO2.

I. INTRODUCTION

The present LMTO method is seen to produce the electronic structure, cohesive energy, lattice constants, elastic constants, phonon frequencies, mode Grüeneisen and strain parameters for the simple systems like Si, C etc [1]. Very recently, the method has been successfully applied also for the III-V and II-VI semiconducting compounds like AlAs, CdTe, GaSb, ZnSe, ZnTe, ZnS etc [2,3]. The influence of structural relaxation of the atoms on the valence-band off-set at the lattice matched interfaces of II-VI and III-V semiconductors ZnTe/GaSb(110) and the lattice mismatched interface ZnS/ZnSe(001) has been investigated [4]. Very recently the van Hove singularity scenario and hole concentrations at different pressures for the Hg-based oxide superconductors have been investigated [5].

A compound CaCuO2 is obtained if the number of CuO2 planes is allowed to increase indefinitely (n -> ∞). Thus, CaCuO2 is the infinite number of CuO2 layers limit of the above superconductors and is seen to be insulating [6]. Tc might increase with n. The n = ∞ material appears to be more difficult to dope. However, more recently (CaSr)CuO2 has been doped successfully and an electron type superconductivity has been seen [7]. In practice, the n = ∞ structure is not formed with only Ca ion on A site, a material with some Ca substitution by Sr, Ca(0.86)Sr(0.14)CuO(2) has been prepared. The Sr-mixed compound is seen to be narrow band semiconductor. For details of the LMTO method we refer to the earlier papers [1-4].

II. CALCULATION AND RESULTS

The CaCuO2 structure as shown in Fig.1 has a space group P4/mmm (D4h{i}). The atomic positions in the unit cell are Cu:(0,0,0); O(1):(.5a,0,0); O(2):(0,.5a,0); Ca:(.5a,.5a,.5c).

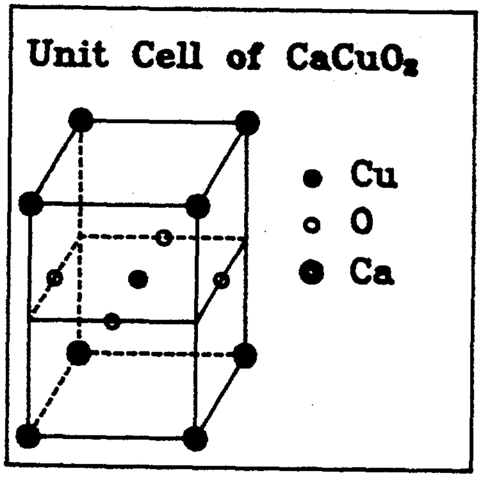

FIG.1 Unit cell for the crystal structure of CaCuO$_2$.

For the Sr-doped sample the experimental lattice parameters are a=3.86 A^{o} and c=3.2 A^{o}. The bond lengths are Cu-O(1) = Cu-O(2) = 1.93 A^{o} and Ca-O(1) = Ca-O(2) = 2.50 A^{o}.

In the present calculation, the basis employed for making expansions of the products of the LMTO envelops included functions with $l \leq 4$ and of energies -0.01, -1.0 and -2.3 Rydberg and with decays given by $\lambda^2=-1$ and -3 Rydberg. The set will include 50 functions for each atomic sphere. The local density potential of Hedin and Lundquist has been employed. An absolute convergence to better than 1.5 mRy/atom is obtained with spd basis of 22 LMTO's/atom for each atom including O. The number of atoms in unit cell were taken to be four.

The muffin tin (MT) spheres were chosen to be slightly smaller than touching and the radii for Cu, O and Ca were taken as 1.88, 1.64 and 2.99 atomic units(a.u.), respectively. The states Cu(3d,4s,4p), O(2s,2p) and Ca(3p,3d,4s) are taken as the valence band electrons. An empty sphere has been included at (0,0,.5c) in the calculation.

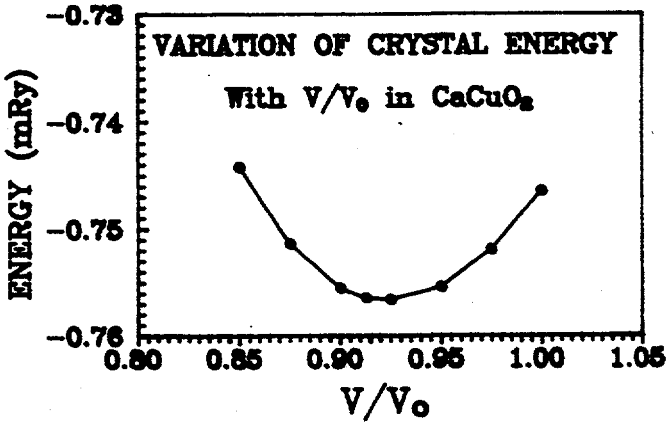

FIG.2 Variation of crystal energy (mRy) with the ratio of unit cell volumes, V_o and V as described in the text.

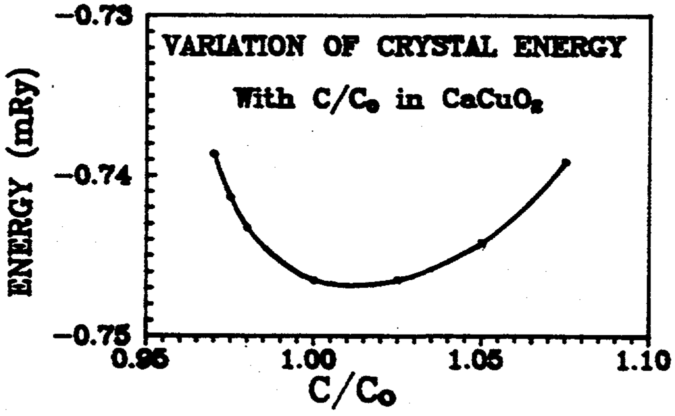

FIG.3 Energy variation with the interplaner spacing.

Variations both in the lattice parameter 'a' and the ratio c/a were investigated. The results are shown in Figs. 2 & 3, respectively. One finds energy minimum for a volume of the unit cell $V = 0.925\ V_o$ and $c/a = 1.00$, where V_o is the unit cell volume for a = 3.86 Å (in fact, these lattice parameters correspond to the experimental values for the Sr doped CaCuO2). So the values of a and c are quite close to those for Sr- doped material. The calculated value of 'c' is within 3% of the experimental value. The calculated value of bulk modulus is 1.99 Mbar.

The charge transfer from the muffin tin spheres (i.e., the difference between the atomic number and charge lying within the MT sphere) of Cu, O and Ca are 1.65, 0.56, and 0.62 electron charges, respectively. The total electron charge per unit cell outside the MT spheres is 3.39e.

(A) ELECTRONIC STRUCTURE

The calculated band structure along some symmetry directions is presented in Fig. 4. The various symmetry points of the Brillouin zone in units of $2\pi/a$ are $\Gamma(0,0,0)$; X(.5,0,0); M(.5,.5,.6); Z(0,0,.6); R(.5,0,.6)and A(.5,.5,.6). As the spacing between the two successive CuO2 layers is smaller than the intraplaner Cu-O seperation within the CuO2, the bands along the c-direction show appreciable dispersion although smaller than the dispersion seen within the x-y plane (or Cu-O2 layer). The Fermi level is set at origin of energy.

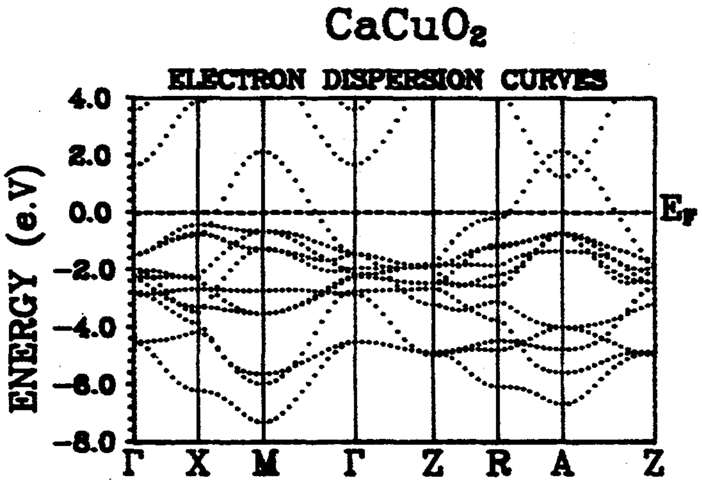

FIG.4 Dispersion curvs for the $CaCuO_2$ system.

The lowest 11 bands lying in the energy interval range of about 9 eV near and below Fermi level arise mainly from the Cu(3d) and O(2p) states. This spread ($\simeq$ 9 eV) of energy bands is similar to that calculated by Mattheiss and Hamann [8] and by Singh et al [9] using LAPW method and by Korotin an Aniscimov [10] using the LMTO-ASA method. The uppermost band crossing the Fermi level corresponds to the anti-bonding Cu-d[x^2-y^2]:O-p[x,y] states. The lower parts of the Ca(3d) bands lying above Fermi level overlap the antibonding

Cu-3d[x^2-y^2]:O-2p(x,y) sub-bands near Γ and A symmetric points.

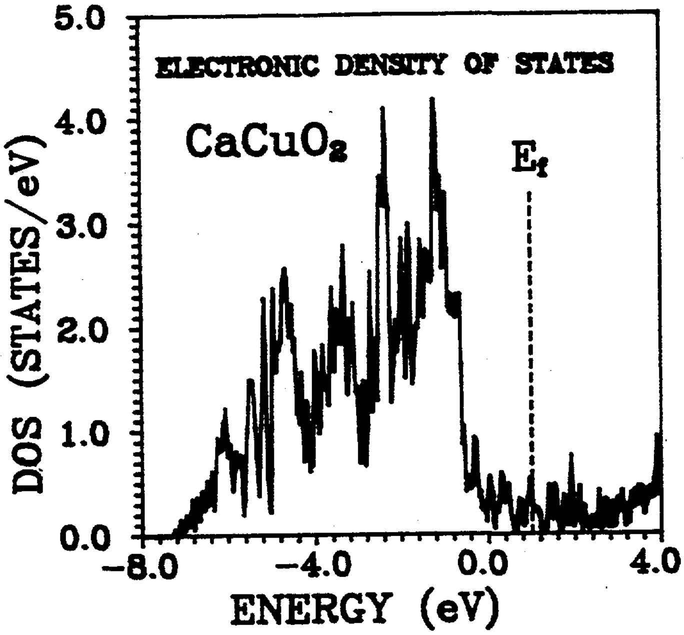

FIG.5 Total electronic DOS.

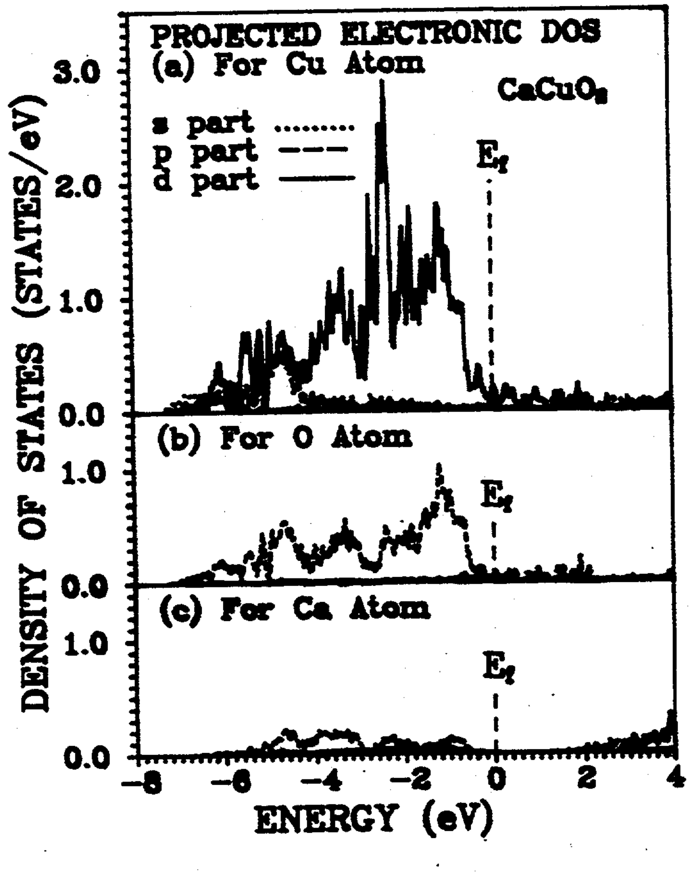

FIG.6 Projected DOS for Cu, O and Ca atoms with s, p & d orbitals contribution.

In order to see the nature of the dispersion in another plane shifted in the c - direction, we have also included in Fig. 4 the dispersion curves in the $2\pi/a[0,0,0.6]$ direction. There appear saddle points at -0.81 eV at X point and at -0.19 eV at R point.

In the calculation of the total density of states (DOS), a sampling method for 196 k points in the irreducible part of the Brillouin zone with a Gaussian energy broadening of 0.002 Ry was employed. The calculated DOS for the self - consistent calculation is shown in Fig. 5. The DOS shows the main features which are quite similar to those of the other oxide high_Tc cuprates. The projected densities at various atoms have also been shown in Fig. 6. At Fermi level, the main contributions arise from Cu(3d) and O(2p) states.

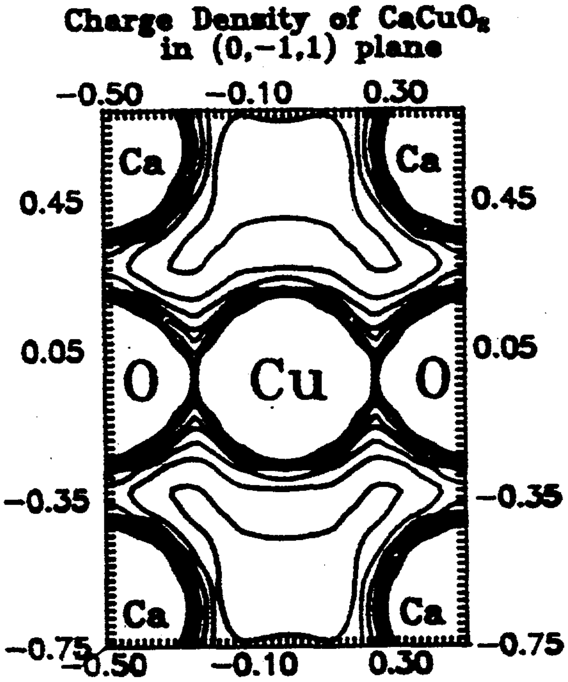

FIG.8 Valence charge density contors in the (0,-1,1) plane in interval of 0.015 $e/(a.u.)^3$ up to a maximum value of 0.12 $e/(a.u.)^3$.

The high degree of the nesting of the Fermi surface is likely to give rise to singularities in the generalized k-dependent electronic susceptibility of the two-dimensional system and may result in the electronically-driven instabilities such as the incommensurate charge or spin density waves.

B. PHONON FREQUENCIES

The variation of the internal energy of the solid with the various types of static deformations in the small displacement limit has been employed for calculating the frozen phonon frequencies at the $\Gamma(k=0)$ point of the Brillouin zone. In CaCuO2 in all, there are six optical modes out of which five are infrared active and the remaining sixth mode comprising of the out of (CuO2) plane vibrations of oxygen atoms in opposite direction is silent. The frequencies of these vibrations alongwith their eigenvectors are presented in Table I. The frequencies have been calculated by determining the harmonic force constant after fitting the energies of the distorted structure for several amplitudes with a polynomial containing terms up to third degree. In order to see the reliability of the estimates of these calculated values we have also included in the table the measured values for the Sr-doped CaCuO2. The frequencies for undoped sample are quite close to the observed values for the Sr-doped sample except for Eu mode which involves the motion of all the atoms.

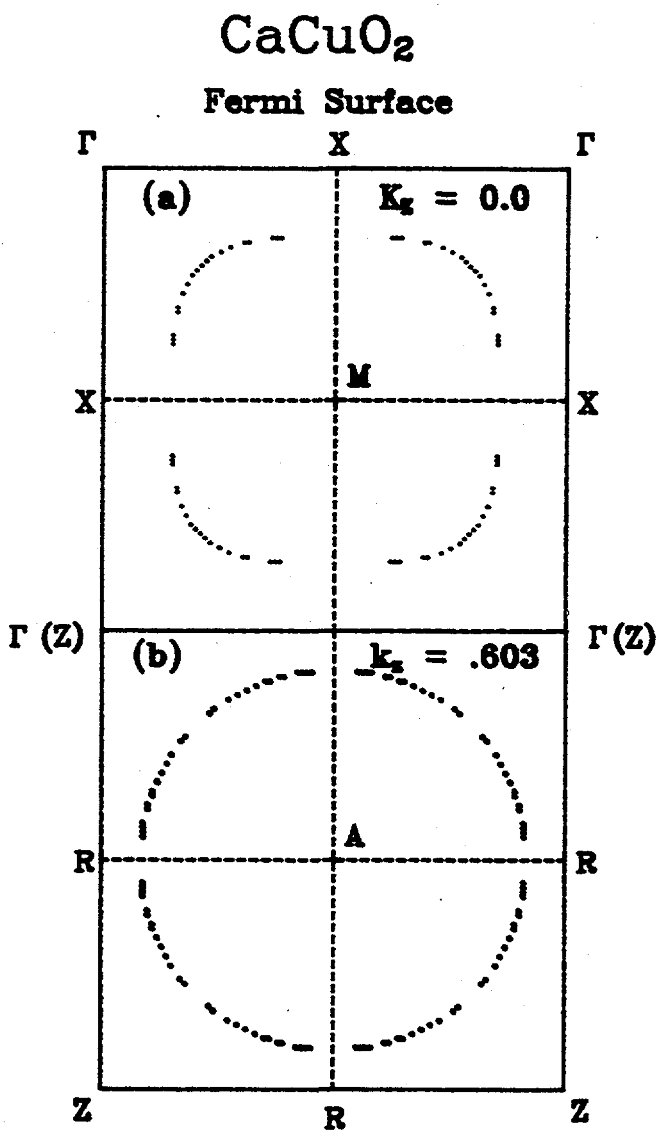

FIG.9 Cross-sections of the Fermi surface in the extended Brillouim zone scheme in two planes (a) k_z = 0.0 and (b) k_z = 0.603 for CaCuO2.

III. CONCLUSIONS :

The LMTO method which is comparatively simple and faster than the LAPW method is able to predict one electron energy spectrum of CaCuO2 quite well. Values for the bulk modulus and the frozen phonon frequencies have been otained. The phonon frequencies for the undoped CaCuO2 are quite near to those measured for the Sr-doped sample

TABLE I. Frequencies of the various phonon modes for $CaCuO_2$ in cm^{-1}.

S. No.	Mode Symmetry	Displaced Atoms	Components of atomic displacements	Calculated freq. for $CaCuO_2$	Exptl. freq. for Sr-doped CaCuO2
1.	Au	Cu, Ca	$Z_1 - Z_2$	213	186
2.	Au	O	$Z_3 - Z_4$	316	
3.	Au	Cu,O,Ca	$\begin{bmatrix} Z_1 - Z_2 \\ -Z_3 \\ -Z_4 \end{bmatrix}$	422	421 (440)
4.	Eu	Cu, Ca	$\begin{bmatrix} X_1 - Y_1 \\ -X_2 + Y_2 \end{bmatrix}$	323	230 (240)
5.	Eu	Cu,O,Ca	$\begin{bmatrix} -X_1 - Y_1 \\ -X_2 - Y_2 \\ +Y_3 - X_4 \end{bmatrix}$		306 (40)
6.	Eu	Cu, O	$\begin{bmatrix} -X_1 - Y_1 \\ +X_3 - Y_4 \end{bmatrix}$	634	597 (663)

The displacements of the various atoms are denoted by $Cu(X_1,Y_1,Z_1)$, $Ca(X_2,Y_2,Z_2)$, $O_1(X_3,Y_3,Z_3)$ and $O_2(X_4,Y_4,Z_4)$.

ACKNOWLEDGEMENTS

The financial assistance from University Grants Commission, New Delhi and Department of Science and Technology, New Delhi are acknowledged.

REFERENCES

1. M. Methfessel, Phys. Rev., B38, 1557 (1988); M. Methfessel C.O. Rodriguez and O.K. Anderson Phys. Rev., B40, 2009 (1989).
2. Bal K. Agrawal and Savitri Agrawal, Phys. Rev., B45, 8321 (1992).
3. Bal K. Agrawal, Savitri Agrawal and P.S. Yadav, preprent (1994).
4. M. Methfessel, Bal K. Agrawal & M. Scheffler, Proc. Int. Conf. of Physics of Semiconductors, 1990, Greece; Bal K. Agrawal and Savitri Agrawal, preprent, (1994).
5. Bal K. Agrawal and Savitri Agrawal, Physica C, (1994) in press; High Tc update, 1 May, (1994).
6. T. Siegrist, S.M. Zahurk, D.W. Murphy, & R.S. Roth, Nature 334, 193 (1988).
7. X. Smith et al., Nature 351, 549 (1991).
8. L.F. Mattheiss and D.R. Hamann, Phys. Rev. B40 2717 (1989).
9. D. Singh, W.E. Pickett and H. Krakacur, Physica C, 162-164, 1431 (1989).
10. M.A. Korotin and V.I. Aniscimov, Mater. Lett. 10, 28 (1990).
11. G. Burns et al, Phys. Rev. B40, 6717 (1989).

THIS PAGE INTENTIONALLY LEFT BLANK

Device Applications

Chair: Dr. Yoshifusa Wada

HIGH-PERFORMANCE PASSIVE MICROWAVE SURVEY ON JOSEPHSON JUNCTIONS

A.G.Denisov, V.N.Radzikhovsky, A.M.Kudeliya

252680, State Research Center of Superconductive
Radioelectronics "Iceberg", Kiev, Ukraine
fax: (7-044)-477-62-08

The quasi-optical generations of image of objects with their internal structure in millimeter (MM) and submillimeter (SMM) bands is one of prime problems of modern radioelectronics. The main advantage of passive MM imaging systems in comparision with visible and infrared (IR) systems is small attenuation of signals in fog, cloud, smoke, dust and other obscurants. However at a panoramic scanning of space the observation time lengthens and thereby the information processing rate become restricted. So that single-channel system cannot image in real time. Therefore we must use many radiometers in parallel to reduce the observation time. Such system must contain receiving sensors as pixels in multibeam antenna. The use of Josephson Junctions (JJ) for this purpose together with the cryoelectronic devices like GaAs FET or SQUIDS for signal amplifications after JJ is of particular interest in this case.

1. INTRODUCTION

The conception of the optic imaging systems at present is more widely employed in millimeter wave range [1-3]. Fig.1 displays attenuations of radiations in MM and SMM bands in various environments such as fog, rain, drizzle, etc, where we see relatively small attenuation of radiation in MM-wave range compared to the radiations in the infrared and visible range [4].

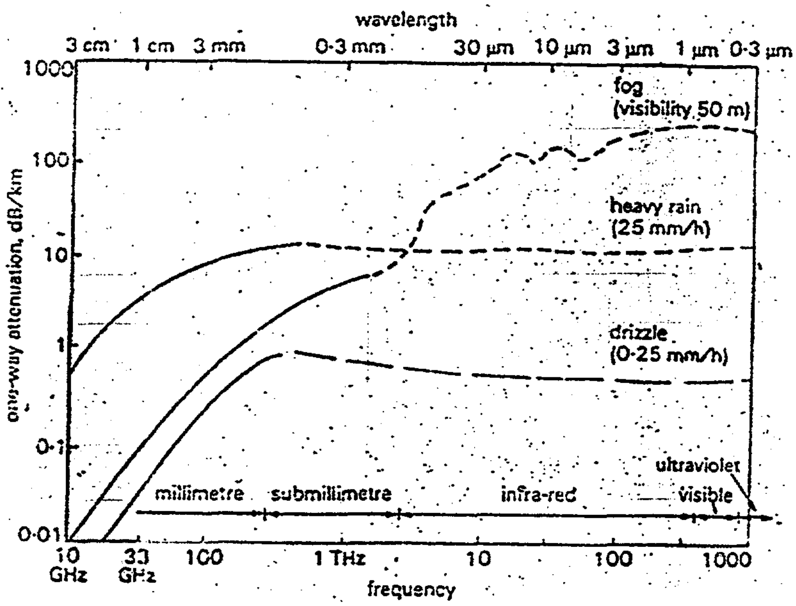

Fig. 1. Attenuations of the radiations in various wavebands for different environments

The problem of development of devices for obtaining images of objects in the optical and IR bands has practically been solved both physically and technologically. A number of physical and technical difficulties, howerer, arise in MM and SMM bands, first of all because at the corresponding radiation frequencies the quantum energy is low and becomes lower than the photoeffect threshold. Due to this, bringing these bands to a practical use calls for developing basically new techniques and sensors for reception and detection of the radiation.

At the same time the developing of new future microwave systems must be more at the base of idea of ecologically pure devices without any artificial radiations or with small radiated power. In some cases the passive many elements and multifrequency systems of the artificial vision (including stereo) are principal or competive for employing [5].

There have been substantial progresses in MM technics, including radiometric systems, due to the availability of high-quality, small-sized elements of the conventional types such as Shottky diodes, FET's, Gunn oscillators, etc, with the fluctuational sensitivity of the uncooled radiometer being better than 0.04 K at signal averaging time of 1 s. The sizes of radiometric modules produced by "Iceberg" in the "tranparent windows" at 8 mm and 3 mm wave bands are about 70x40x20 mm^3 or in a tube with the diameter about 20 mm. In principal there may be future decision concerning the diminishing of radiometer but as for the matrix must be another principal idea for doing manyelement systems. It is desirable that this system must be analyzed in terms of the sensitivity, dynamic range, simplicity, frequency bands, size and mass as well as of the electromagnetic compatibility and of feasibility of the use of the integral technology for their fabrication.

The development of a radiometer as an elementary sensor (cell) of a multielement matrix is practically feasible with the using of three types of receiving devices: amplifiers, frequency converters and microwave detectors.

According to experimental and theoretical analysis performed in "Iceberg" the use of JJ in the self-pumping mode [6], which is one of the varieties of the heterodyne detection, is particular interest in this case.

2. ARRAY OF SENSORS.

The array of the receiving sensors is the main functional block of the multichannel passive imager. The number of the sensors and its sensitivity determines the efficiency of systems in the whole. Matrix of JJ with down convertion to the intermediate frequency Ga FET amplifier or SQUID [7,2] at the detector output yields a level of sensitivity not worse than 0.01 K.

This obviates the need for an external heterodyne, since the oscillation of the junction itself is employed and there exists the possibility of the JJ tuning to the frequency of the signal being received in accordance with the expression describing the nonstationary Josephson effect [8]:

$$2eV = \hbar\omega ,$$

where e and $\hbar$ are fundamental constants, V is the voltage across the JJ, and ω - the frequency of the oscillation generated by JJ.

As shown by the analisis [6], the equivalent temperature of the noise of such a receiver (T_s) is given by expression:

$$T_s = T_{in} + T_j + \frac{T_{ifa} \cdot L}{2\sqrt{\frac{\Delta\Gamma - f_{if}}{\Delta f_{if}}}}$$

where T_j - is the effective noise temperature of the Josephson generation, T_{in}- is the noise temperature due to background radiation; L - is the power loss at the frequency conversion in the JJ; f_{if}, Δf_{if} and T_{ifa} are respectively the central frequency, the amplification band, and the noise temperature of the intermediate frequency amplifier at the detector output, and $\Delta\Gamma$ - is the Josephson oscillation bandwidth.

The estimation of parameters being expected in accordance with [7] at a cooling temperature of about 20÷30 K and $T_{ifa} \leqslant 20$ K; $T_j \approx 60$ K, $\Delta\Gamma \approx 20$ GHz, $f_{if} \approx 4$ GHz, $\Delta f_{if} \geqslant 700$ MHz and $T_{in} \approx 20$ K (only the path loss) with the use of generally-accepted theories [8] and account of modern experiments [9] yields the fluctuational sensitivity value at a level not worse than 0.01 K (0.005 K). This value is quite adequate for solving of most problems.

In practice, the technical realization of such system may be performed at the base of the various types of the matching with antenna system depending on the real tasks and on the area coverage [10, 11, 12]. There are may by LTSA (Linearly Tapered Slot Antenna) [10] or an integrated-circuit antenna array [11] which was planned for analogy items in radar technics with multibeam antenna.

It should be noted that the problem of the microwave modulator (or beam chopper) which is principal but nonadvantagable device for the radiometer scheme and especially in case of matrix system may be decided by the another method in case of JJ sensors. Modulator can be removed from the entrance before the JJ according to the possibility of using the pilot-signal regime of radiometer scheme or the regime with the modulation of working point of JJ which was examined in [9]. In case of integrated-circuit antenna for the receiving sensor built on JJ there may be used the second

JJ as a generator for controlling signal. This JJ can be performed from the opposite side (to the entrance signal) of the substrate. At the fig.2

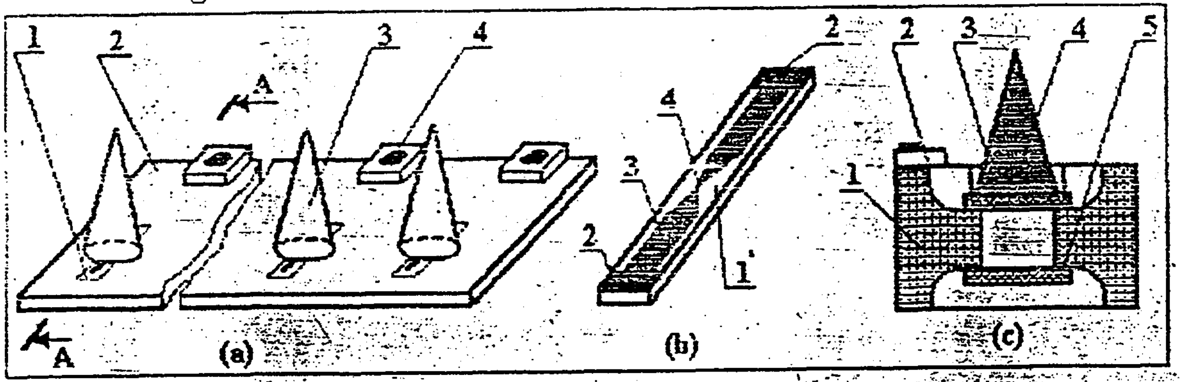

Fig. 2 The receiving module
a) 1 - the detector JJ; 2 - the copper plate; 3 - the matching cone; 4 - the SQUID sensor or a matching transformer
b) the Josephson element: 1 - the substrate (sapphire); 2 - the bonding pad-Cu; 3 - a HTSC film; 4 - weak coupling
c) 1 - the copper plate; 2 - the SQUID sensor or a matching transformer; 3 - the matching cone; 4 - the detector JJ; 5 - the generator JJ

are presented the possible decision of this construction which was designed in "ICEBERG".

CONCLUSION

So, the using of JJ for imaging systems can do the advantage of good sensitivity, exclusion of the special local oscillators and modulators. Besides this there exists the possibility of the electronic tuning to the frequency of the signal being received [13].

REFERENCES

1. B.Vowinkel, J.K.Peltonen, W.Reinert, K.Gryner, B.Aumiller. Airborne Imaging System Using a Cryogenic 90 GHz Receiver. IEEE Trans on MTT, 1981, vol.MTT-29, N 6, p.535

2. D.P.Osterman, P.Marr, H.Dang, C.T.Yao, M.Radparvar. Superconducting Infrared Detector Arrays With Integrated Processing Circuitry. IEEE Trans on Magn. 1991, vol.27, N 2, p.2681.

3. R.Davidheiser. Analog use of Superconducting Microelectronics Nears. MSN, 1982, Oct.,p.101.

4. V.N.Esepkina, D.V.Korolikov, Y.N.Pariysky. Radiotelescopes and Radiometers, Edition "Nayka", Moscow, 1972.

5. R.Appelby, D.Gleed, R.Anderton. High-performance passive millimeter-wave imaging. Optical engeneering 1993, June, vol.32, N 6, p.1370.

6. A.Denisov, V.Gaevskiy, L.Gassanov, S.Kusenkov, L.Nazarenko. Study of the Operation of a Josephson Down-Converter in Self-Pumping Mode. Soviet Journal of Communications Technology and Electronics, 1985, vol.30, N 9, p.33.

7. A.Denisov, V.Radzikhovskiy. Specific Features of Using Josephson Junctions for Radiometric Reception. 27th All-USSR Conference "Radioastronomic Equipment", Erevan, 1985, Oct.10-12.

8. K.Lukharev, B.Ul'rikh. Systems with Josephson Contacts. Edition "Moscow State University", Moscow, 1978.

9. A.Denisov, V.Makhov. On the Use of Josephson Junctions in Self-Pumped Mode, High-Temperature Superconductor Technologies, 179 Meeting of Electrochemical Society, Inc., The Sheraton Washington Hotel, 1989, May 5-10.

10. S.Yngvesson. MMW Radio-Astronomical Imaging Instrumentation. MSN, 1988, December, p.74.

11. P.Tong, D.Neikirk, R.Young, W.Pebles, N.Lihmann, D.Rutledge. Imaging Polarimeter Arrays for near-Millimeter Waves. IEEE Trans on MTT, 1984, vol. MTT-32, N 5, p.507.

12. F.Lalezari, C.Massey, D.Hunter Millimeter-Wave Tactical/Small-Aperture Antennas. MSN, 1988, December, p.41.

13. V.Gaevskiy, A.Denisov. Noise Temperature of Josephson Frequency Converter Down in Self-Pumping Mode. Pis'ma v ZhTF, 1984, vol.10, N 11, p.697.

JOSEPHSON FREQUENCY METER FOR MILLIMETER AND SUBMILLIMETER WAVELENGTHS.

S.E.Anischenko, S.Y.Larkin, V.I.Chaikovsky, P.V.Khabayev, V.V.Kamyshin
State Research Center "Fonon", 37, Pobedy Ave., KPI, Kiev, 252056 Ukraine.

1. INTRODUCTION

Frequency measurements of electromagnetic oscillations of millimeter and submillimeter wavebands with frequency growth due to a number of reasons become more and more difficult. First, these frequencies are considered to be cutoff for semiconductor converting devices and one has to use optical measurement methods instead of traditional ones with frequency transfer. Second, resonance measurement methods are characterized by using relatively narrow bands and optical ones are limited in frequency and time resolution due to the limited range and velocity of movement of their mechanical elements as well as the efficiency of these optical techniques decreases with the increase of wavelength due to diffraction losses. That requires the apriori information on the radiation frequency band of the source involved. Method of measuring frequency of harmonic microwave signals in millimeter and submillimeter wavebands based on the ac Josephson effect in superconducting contacts is devoid of all the above drawbacks. This approach offers a number of major advantages over the more traditional measurement methods, that is the one based on frequency conversion, resonance and interferometric techniques. It can be characterized by high potential accuracy, wide range of frequencies measured, prompt measurement and the opportunity to obtain panoramic display of the results as well as full automation of the measuring process.

2. THEORY

All known frequency measurements methods using the ac Josephson effect are mainly based on the major relationship binding the frequency of the external electromagnetic radiation Ω with the voltage V_Ω across the Josephson junction:

$$\Omega = 2e\, V_\Omega / \hbar \qquad (1)$$

This specific feature has the form of a Shapiro step on the voltage-current curve (V-I curve), i.e. the voltage across the junction is remaining constant with the biasing current that is varying in the sync zone. From this point on let us call this part of the V-I curve a "Special feature existence" zone. Thus, functionally, the frequency measurement procedure of the monochromatic signal that is disturbing the Josephson junction reduces to the coordinate estimation of a "special feature existence" zone on the V-I curve.

In practice the pattern of measuring the frequency of monoharmonic signals based on the ac Josephson effect described above can be carried out using different techniques. Let the external disturbance be described by the expression for the current amplitude:

$$I = A \cos \Omega t \qquad (2)$$

Let us introduce for convenience the current peak value of the disturbing external source normalized in current:

$$A_\Omega = A / 2I \qquad (3)$$

Then, the V-I curve of the Josephson junction being irradiated by the described signal can be presented as follows [1]:

$$V = V_\Omega + \begin{cases} 0, & \text{for } |I - I_\Omega| < A_\Omega \\ \operatorname{sign}(I - I_\Omega) R_d \left[(I - I_\Omega)^2 - A_\Omega^2 \right]^{1/2}, & \text{for } |I - I_\Omega| \ge A_\Omega \end{cases} \qquad (4)$$

where V_Ω is a bias voltage across the junction which produces the coincidence of the Josephson oscillation frequency ω_J with the frequency of the external signal Ω, I_Ω is a hypothetical current of the junction corresponding to the voltage V_Ω without incident radiation; R_d is a dynamic resistance. At this, beyond the "special feature existence" zone the V-I curve of irradiated junction is monotonically approaching the curve of the non-irradiated one which is splitting the discontinuous section into two equal parts at the point with the coordinates (I_Ω, V_Ω) . Let us call this point a "central point" of the "special feature existence" zone on the V-I curve. It should be pointed out that the expression (4) does not take into account the effect of the junction fluctuations as the peak value of the induced current is assumed to be far in excess of the current amplitude of the natural fluctuations. This inclusion of fluctuations when analyzing the V-I curve leads to the quadratic smoothing of the hyperbolic sections.

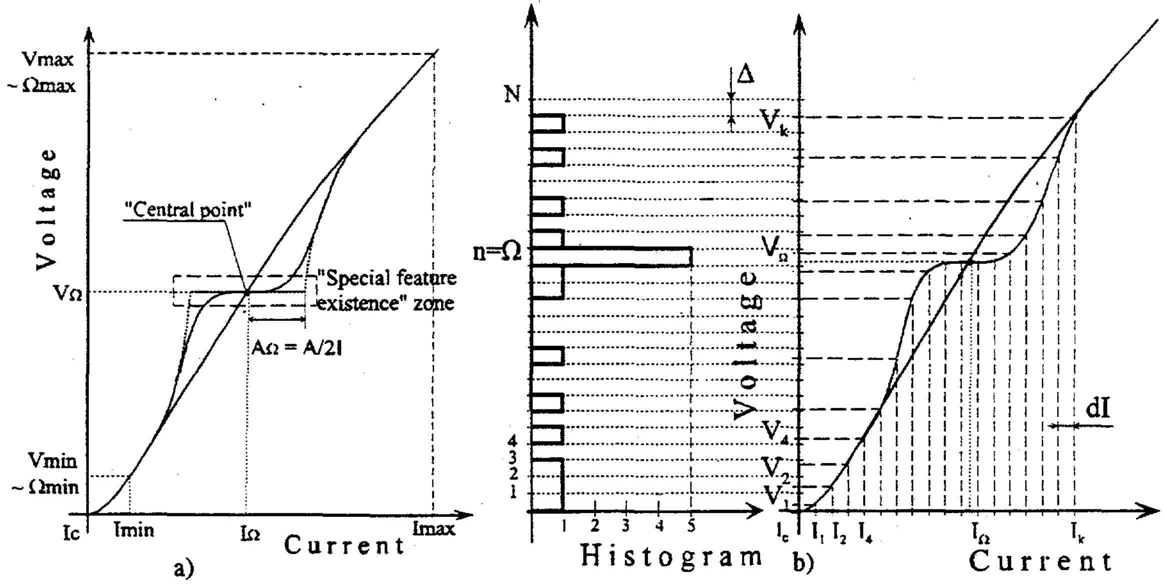

Fig.1. a) Schematical illustration of both V-I curves with and without incident radiation in the coordinate system displaced to the point $(I_c, 0)$;

b) Procedure of forming the histogram P_n.

Fig. 1a schematically displays the diagrams of both V-I curves with and without incident radiation in the coordinate system displaced to the point (I_c, 0). In this figure the V-I curve of the non-irradiated junction is linearly approximated. Analyzing a shape of the V-I curve displayed in Fig.1 and described by expression (4) the frequency measuring procedure can be roughly presented as the procedure of identifying the "special feature existence" zone with the subsequent determination of the central point coordinates. The advantages of the frequency measurement technique, based on the ac Josephson effect, are the best seen during digital registration and functional processing of the disturbed V-I curve with a certain rational algorithm. For this purpose it is necessary to carry out the quantization of the biasing current and to represent the V-I curve as the latticed function that is in shape of the finite sequence of discrete counts in the prescribed system of nodes and with the prescribed quantization increment of their instantaneous values. The counts for the V-I curve are represented on the set of nodes (see Fig.1b): $v = f(i) \rightarrow \{v_k\}$, $k \in K$.

In our previous paper [2] we offered the frequency measurement algorithm based on the analysis of the first differences of the V-I curve of irradiated Josephson junction. The present paper suggests for consideration the algorithm forming the histogram of the count's sequence of this curve. In this case the rationality criterion is marked by several features:

- information productivity or possibility of insuring measurement accuracy approaching limiting values;

- functional simplicity allowing one-increment processing procedure;
- minimization of the computation time and expenses;
- possibility of panoramic displaying the results in the real time scale.

Finalizing the theoretical analysis it should be pointed out the important restriction for the amplitude of the external effect that defines the application scope of the above approaches. The signal measured is considered to be a low-power signal on carrying out the following inequality:

$$A << I_c * \Omega^2 / \Omega^2_c \qquad (5)$$

where I_c is a critical current of the junction; Ω_c is a characteristic frequency. This restriction breaks down when the frequency band is higher than Ω_c but the junction sensitivity sharply falls off.

3. TECHNIQUE

To carry out digital processing technique for the V-I curve it is necessary to have the discrete image of it by setting the discrete current counts, dI (see Fig.1b). The value of the elementary current count influence upon the performance of the algorithm and evidently should be chosen as minimum as it could be. Evidently to identify a Shapiro step it is necessary that the minimum size of discrete count dI_{min} be related to minimum-discernible disturbance of $A_{\Omega min}$ as: $A_{\Omega min} = 3dI_{min}$. Furthermore, the amplitude of the external effect should at least three times exceeded the intrinsic noise of the Josephson junction (when no external noise exist). It follows that:

$$dI_{min} \approx 10\, I_f \approx 10\sqrt{\frac{4k_B T}{R}\frac{R^2_{d\,max}}{R^2}} \qquad (6)$$

where I_f is a fluctuating current of the junction; R is a normal resistance; R_{dmax} is a maximum dynamic resistance of the non-radiated junction for the frequency band being analyzed.

For processing the discrete image of the V-I curve of the irradiated Josephson junction and terminating the coordinates of the central point of the "special feature" we use the algorithm that forms the histogram of the V-I curve. To identify the "special feature existence" zone on the V-I curve the algorithm mentioned provides the criterion of equation of all count ordinates of the V-I curve which are attributed to the Shapiro step. The V-I curve of non-irradiated junction is a monotonically increasing function. Its discrete representation is equivalent to carrying out the inequality $V_{k+1} > V_k$ on the hole set of nodes $\{V_k\}$. There exists the final window Δ (see Fig.1b) of the uniform splitting of the interval for the possible values of the V-I curve. As this takes place, not more than one count of the V-I curve should correspond to each splitting window Δ_n (or the window limited by levels of $n*\Delta$ и $(n+1)*\Delta$ out of $\{V_k\}$). At this, some number P, that is equal to the quantity of counts thrown into the specified splitting interval is taken the value to: 1 or 0. It is sufficient for the minimum value out of the set of first differences $d_k^{(A)}$ for the V-I curve of the non-irradiated junction:

$$d_k^{(A)} = V_{k+1}^{(A)} - V_k^{(A)}\ , \quad \inf\{d_k^{(A)}\} > \Delta \qquad (7)$$

The V-I curve of the irradiated junction is characterized by inherence of the "special feature existence" zone including more than 2 counts that are equal to each other:

$$V_k = V_{k+1}\ , \text{ for } K_{min} \le K \le K_{max} \qquad (8)$$

where the limits of zone are determined by the following relationships:

$$K_{min} = \text{fix}\,(K_\Omega - 0.5P)$$
$$K_{max} = \text{fix}\,(K_\Omega + 0.5P) \qquad (9)$$

where K_Ω is the abscissa dimensionless index of the "special feature" central point. Then more than 2 counts ($P > 2$) of the V-I curve get into the window Δ_n with index $n = \Omega$ covering the "special feature existence" zone. Having completed the registration procedure for the quantity of counts P_n captured by each window out of the continuous set, a certain latticed function $\{P_n\}$ is formed (see Fig.1b). The hole interval of possible values of ordinates for the V-I curve is spanned in the process. This function or histogram takes the value of 0 or 1 in all the nodes except $n = \Omega$ node. The window of it spans the "special feature existence" zone. There are 2 counts or more ($P > 2$) within this node and in this manner it is easy to identify the "special feature existence" zone on this indicator. The dimensionless integer index $n = \Omega$ (i.e. the dimensionless abscissa of the histogram overshoot) is easily converted into ordinate V_Ω of the "special feature" in accordance with the following rule:

$$n^*\Delta \le V_\Omega \le (n+1)^*\Delta, \qquad (10)$$

where $\Delta \sim dI_{min}$ is a window (i.e. the established size of the interval or the splitting increment for the position of existence of the V-I curve registered counts $\{V_k\}$. Value of voltage V_Ω determined in a such way can be easily recalculated into the desired frequency Ω of the incident radiation according to Eq. (1).

Besides measurement of the frequency Ω, the result of histogram construction enables comparing value P_n with peak $2A_\Omega$ of the "special feature existence" zone in terms of the current interval dI. By this means value P_n at $n = N$ is a measure of intensity of the incident power for amplitudes A_Ω limited by inequality (5)

$$2A_\Omega = P_n^*dI \qquad (11)$$

There exists a limit for the reasonable size reduction of window Δ for the histogram P_n. It approximately corresponds to the equation of the window size Δ and the interval dV of the amplitude quantization of the registered counts. The choice of size Δ less than interval dV does not lead to the reduction in error of the measurement of the ordinate of the "special feature" central point V_Ω. The reason is that the registration error of the estimated value V_Ω as a result of the finite length of its digital representation makes itself evident and comes on to dominate. As the interval dV is proportional to the discrete count dI the window size Δ is bound with frequency of the current quantization. Finally, the window size Δ can be presented as follows:

$$\inf\{d_k^{(A)}\} \le \Delta \le dV \qquad (12)$$

So, the algorithm of measuring frequency of incident radiation with the use of histogram analysis incorporates a sequence of the following steps:

1. Registration of sequence of V-I counts of the Josephson junction without incident radiation $\{V_k^{(A)}\} \leftrightarrow \{I_k^{(A)}\}$. At this, frequency of current quantization dI is being determined in accordance with Eq. (6). The number of registered counts K of discrete V-I curve is defined by a current peak and quantization interval for overlapping the working interval of voltages $V_{min}...V_{max}$: $K = (I_{max} - I_{min}) / dI$.
2. Obtaining a file of the first differences $\{d_k^{(A)}\}$ according to Eq. (7)
3. Determination of the minimum value out of the file $\inf\{d_k^{(A)}\}$ as well as the window size of histogram Δ according to Eq. (12).
4. Registration of the counts sequence of V-I curve in case of incident radiation.
5. Selection of the V-I curve section bearing information by means of recalculation of the boundary conditions of the measured frequency band Ω_{min} ... Ω_{max} using Eq. (1) into lower and upper boundaries of the interval $\inf\{V_k\}$ and $\sup\{V_k\}$. Determination of the number of intervals (i.e. windows) N of the histogram formed:

$$N = (\mathrm{fix}[\sup\{V_k\} - \inf\{V_k\}]) / \Delta \qquad (13)$$

6. Formation of the histogram $\{P_n\}$ for the selected counts of the V-I curve.
7. Conversion of node arguments of the histogram into the frequency Ω_n.
8. Registration of arguments of the histogram overshoots as the frequency estimations of the harmonics making up an incident radiation.

4. EXPERIMENTAL RESULTS

In the course of the experiment the task was directed to the evaluation of the simulation model of the method and its comparison with the real results obtained with the experimental set-up. Fig.2 presents a block diagram of the experimental set-up described in [3]. As the Josephson junction the low temperature niobium edge contact with the following parameters was utilized: the normal resistance is about 1 Ohm; the critical current is 0.4 ma; the junction area is 0.5 μm^2.

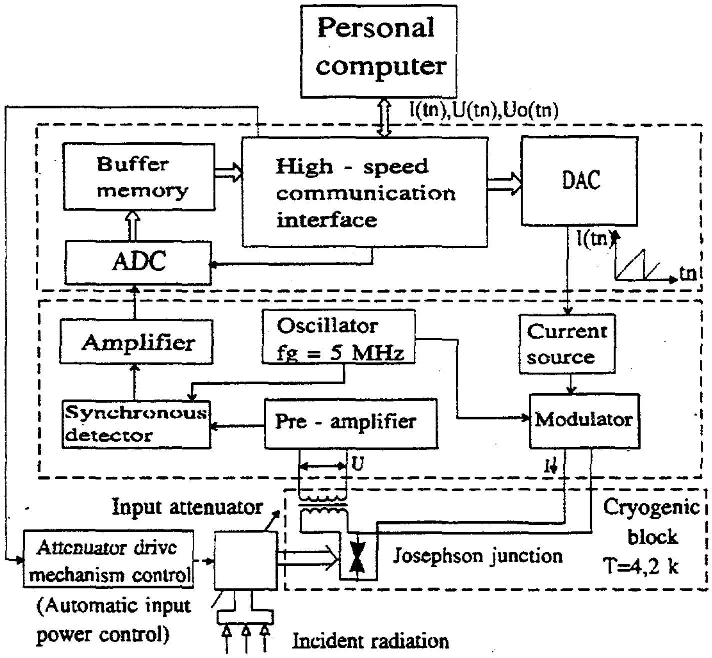

Fig.2. Block diagram of the experimental set-up.

Fig.3 shows the V-I curve of the Josephson junction simulated on a computer. The radiation frequency was chosen to be 60 GHz and the fragment of the junction V-I curve corresponds to the classic theoretical behavior in the neighborhood of the "special feature existence" zone. The software allows to get the idealized histogram that is consistent with such representation. Fig.4 also gives the simulation results without taking into account the fluctuations influence. They refer to the minimum amplitude signal allowed. The response size perfectly corresponds to three points along the sweep tone of the V-I curve. Fig.5 illustrates the behaviour of the model under the condition of strong external induction. The histogram can confirm that the method is stable to external parasitic sources. Fig.6 displays the fragment of the real V-I curve of the Josephson junction irradiated by 140 GHz oscillator. The line width of the intrinsic Josephson oscillation constitutes 190 MHz. The line width of the oscillation source was certified with a filter and runs to 1,3 GHz that corresponds to the histogram obtained on an experimental set-up. Thus, the experimental set-up and software developed allow to get 300 MHz frequency resolution, at this, the line width of the intrinsic oscillation being 200 MHz. Fig.7 presents the results of a more complex experiment. The Josephson junction was exposed to the influence of three oscillators with different frequencies: f_1 = 135 GHz with generation line width of

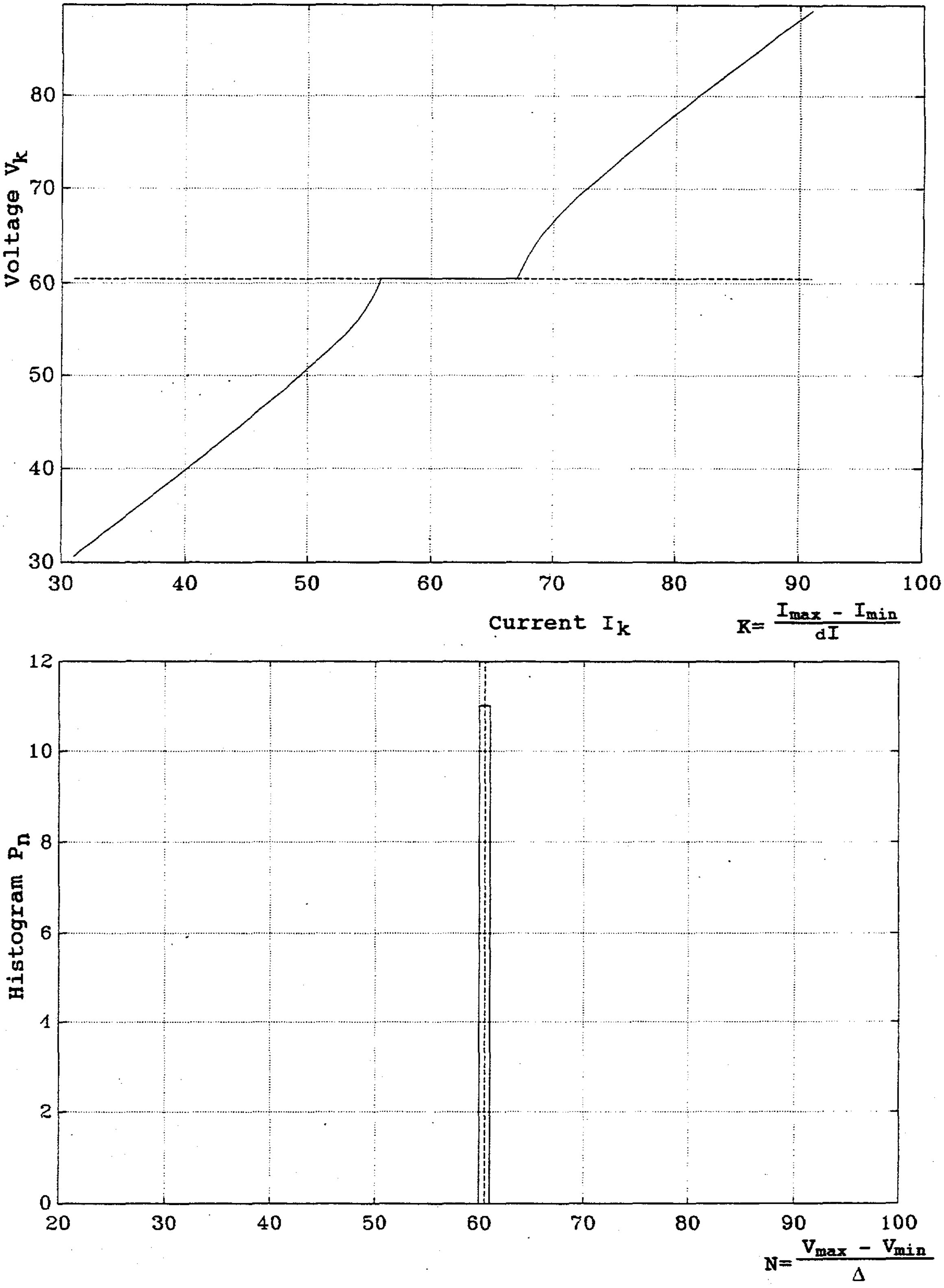

Fig.3 The fragment of the V-I curve of the Josephson junction simulated on a computer and the results of the experiments in the form of a histogram for the radiation frequency chosen to be 60 GHz.

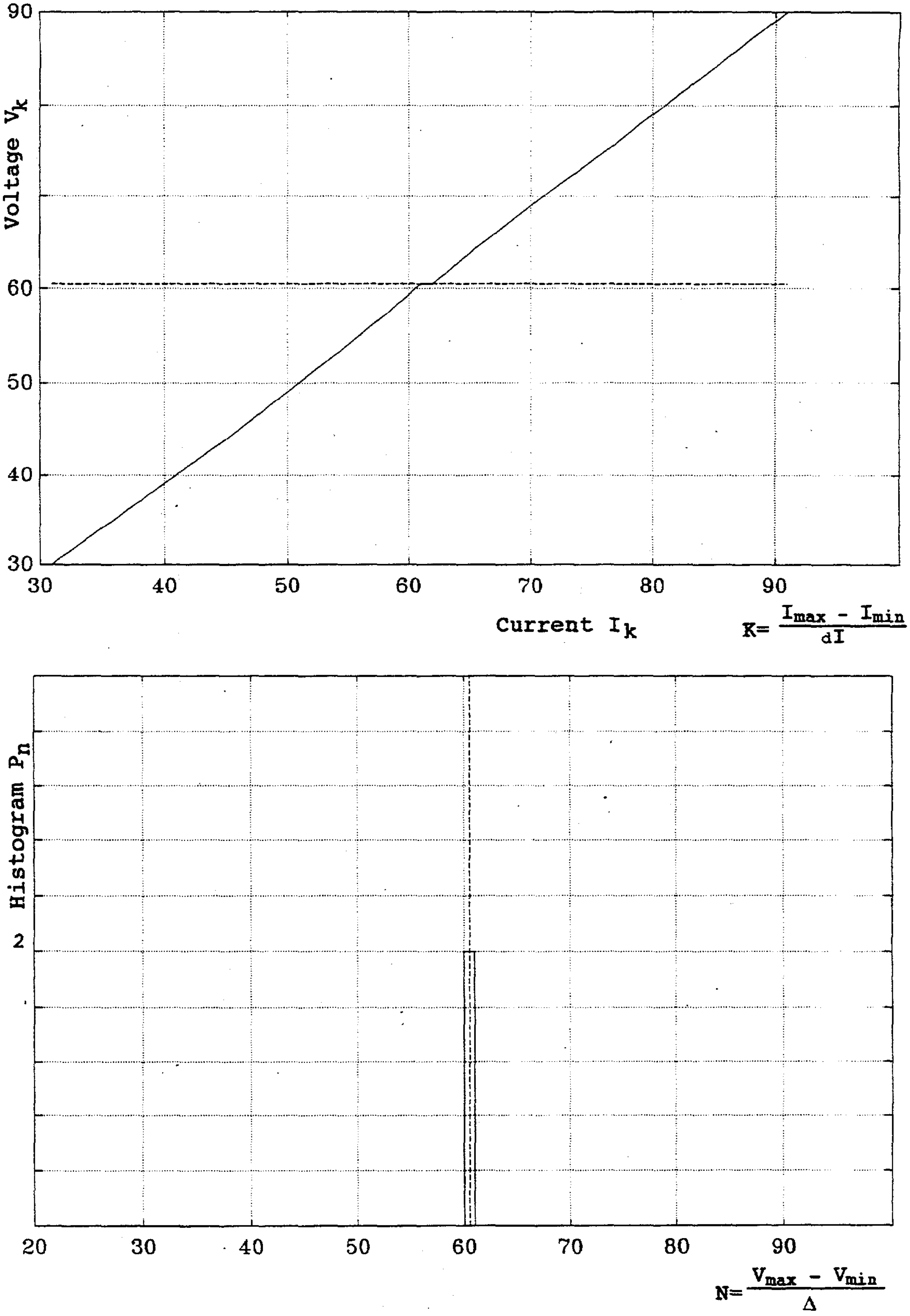

Fig.4. The results simulated on a computer for the experiments of obtaining a histogram for the signal of 60 GHz with minimum amplitude allowed and without fluctuations influence.

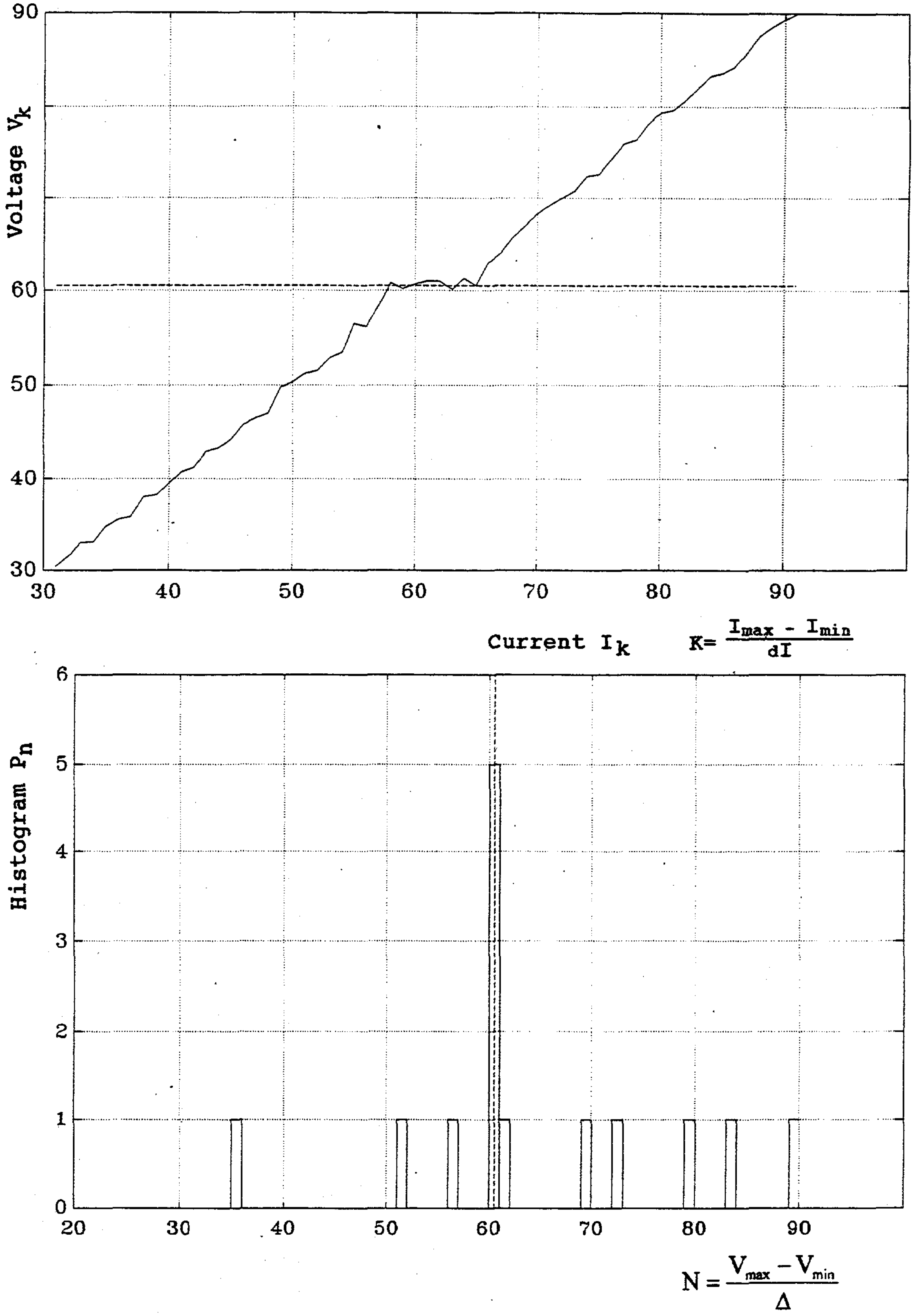

Fig.5. The behaviour of the computer model for the signal of 60 GHz under the condition of strong external induction. The histogram confirms that the method is stable to external parasitic sources.

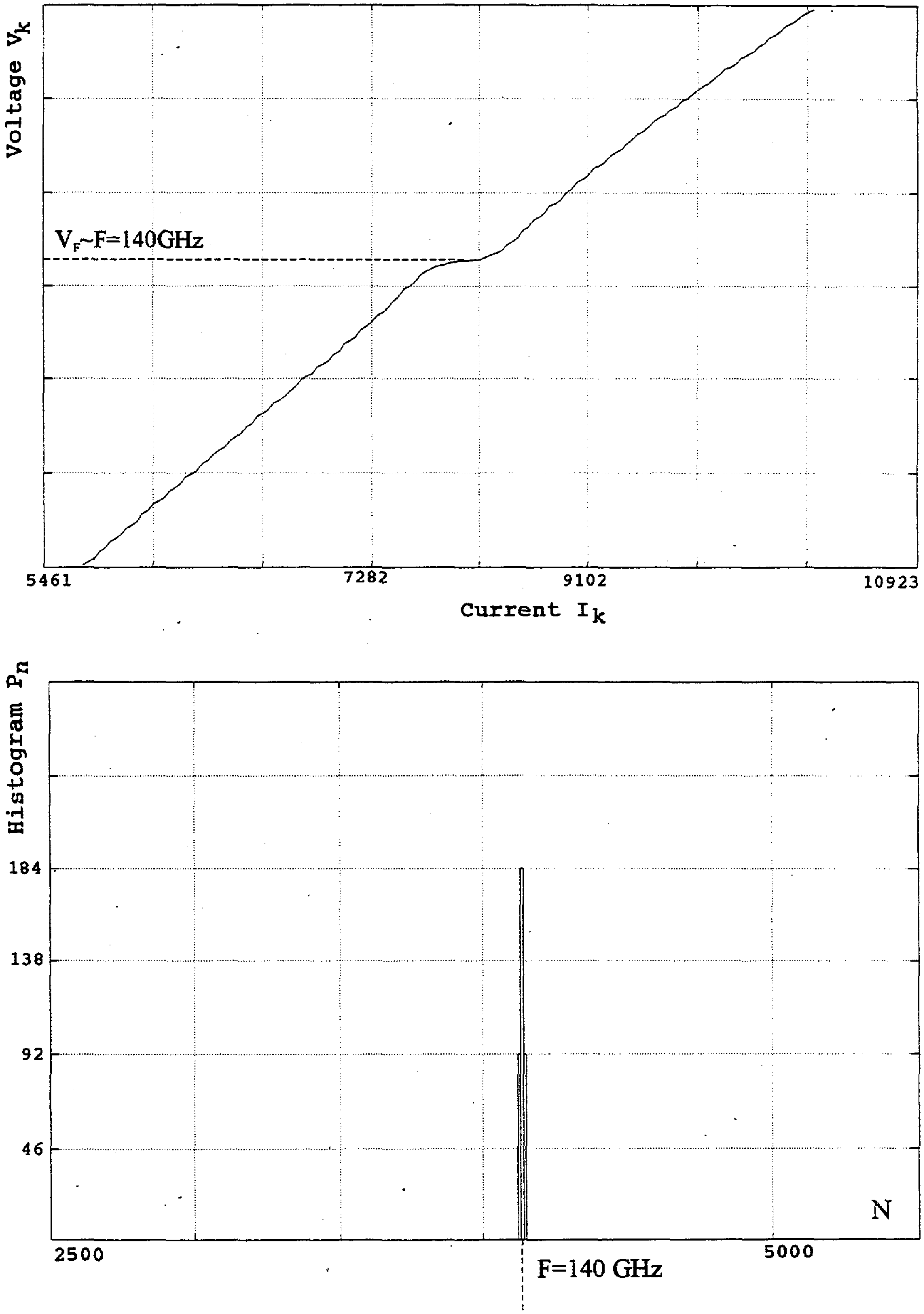

Fig.6. A fragment of the real V-I curve of the Josephson junction irradiated by 140 GHz oscillator and the corresponding histogram as a result of frequency measurement.

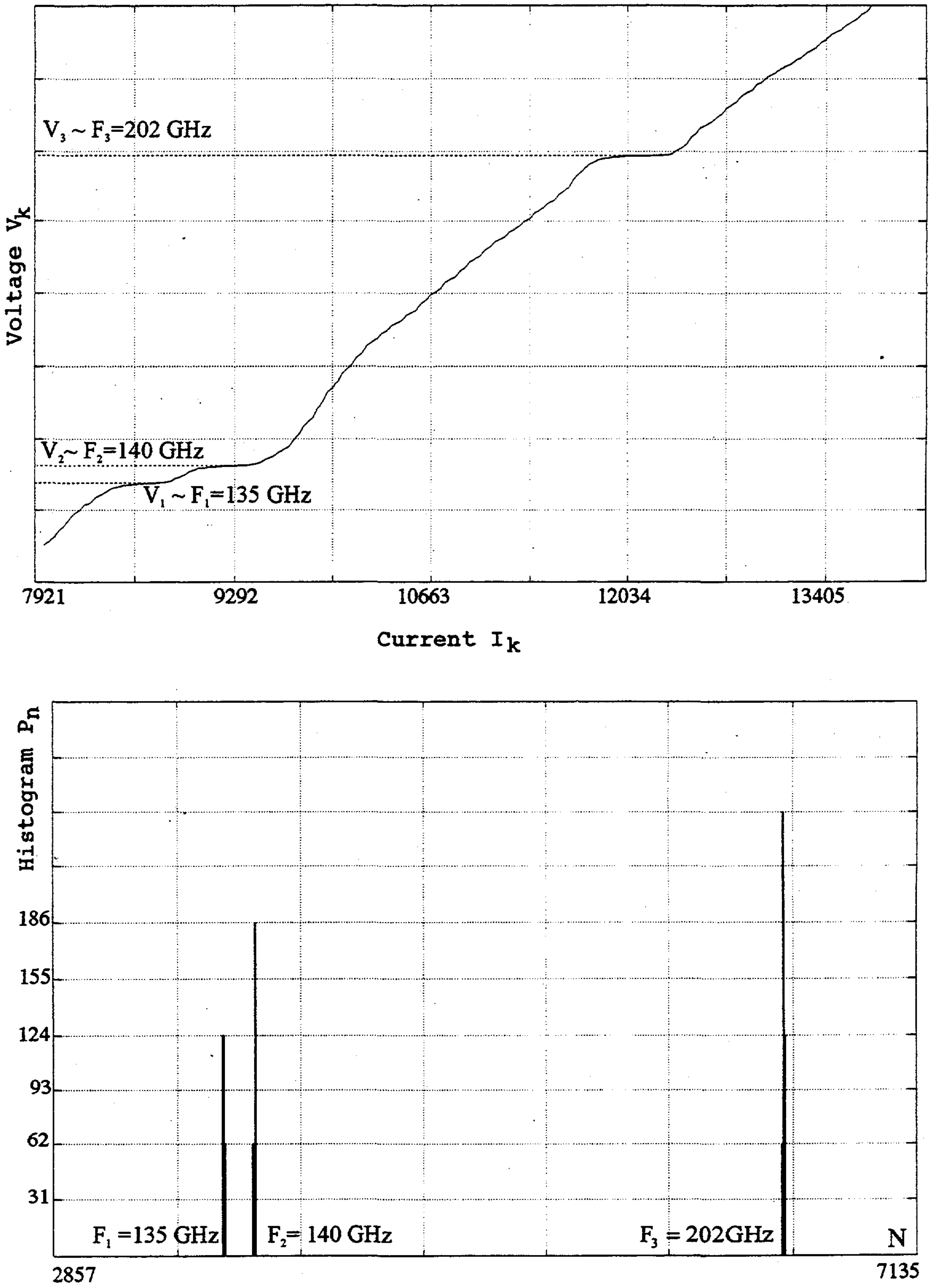

Fig. 7. A fragment of the real V-I curve of the Josephson junction irradiated by the complex polyharmonic signal and the corresponding histogram as a result of frequency measurement.

Δf_1 = 500 MHz, f_2 = 140 GHz with Δf_2 = 1,3 GHz and f_3 =200 GHz with Δf_3 = 2 GHz. The histogram depicts the conditions of the experiment with high accuracy (not worse than 10^{-4} of relative units to the accuracy of the evaluation of the average source frequency). The amplitude of the lab sources was measured with the use of standard power meters and controlled by way of introducing attenuation into the microwave transmission line in accordance with block-diagram given in the technical specifications of the experimental set-up. The analysis of the determination of the microwave signal amplitude according to the histogram shows that in conformity with theoretical background and on carrying out the inequality (5) the response value of the Josephson junction is practically proportional to the square root of the external radiation power. At this, the less is the amplitude of the external source influence and its frequency related to the typical frequency of the Josephson junction, the closer this dependence is to the linear form. It takes 1 sec to make analysis and display the results. This time can be minimized at least one order higher without any loss for the accuracy of measurements with the use of high-speed DAC/ADC of the corresponding number of bits.

We would like to finalize that the proposed technique related to the panoramic analysis of the frequency composition of microwave signals and the equipment involved can be used:

- in radio engineering research of various microwave radiation sources;
- radioastronomy and navigation;
- for specific task on radio provision.

REFERENCES

[1] K.K.Likharev, B.T.Ulrich. Systems with Josephson contacts. Moscow State University Publishing House, 1978.

[2] S.E.Anischenko, S.Y.Larkin, P.V.Khabayev. "Methods of frequency measurements of microwave signals of MM- and SubMM- wave bands with the use of the ac Josephson effect", Pros. SPIE 2104, pp. 273- 276, 1993.

[3] S.E.Anischenko, S.Y.Larkin, V.V.Kamyshin. "Microwave wideband frequencymeter using Josephson junctions", Pros. SPIE 2250, pp. 281- 282, 1994.

JOSEPHSON JUNCTION SPECTRUM ANALYZER FOR MILLIMETER AND SUBMILLIMETER WAVELENGTHS

S.Y.Larkin, S.E.Anischenko, P.V.Khabayev.
State Research Center "Fonon". 37, Pobedy Ave., KPI, Kiev, 252056 Ukraine.

ABSTRACT

A prototype of the Josephson-effect spectrum analyzer developed for the millimeter-wave band is described. The measurement results for spectra obtained in the frequency band from 50 to 250 GHz are presented.

INTRODUCTION

Spectroscopic studies in millimeter-wave and submillimeter-wave bands are faced a lot of problems when the techniques initially developed for lower or higher frequencies are applied in this intermediate spectral band. On the one hand, the efficiency of heterodyne RF mixing technique decreases rapidly with the decrease of wavelength and this technique also fails to provide continuos measurements in the whole band. On the other hand, the measurements of more continuos spectra can be carried out by extending the optical techniques using diffraction gratings and Michelson interferometers to millimeter-wave band, but the efficiency of these optical techniques decreases with the increase of wavelength due to diffraction losses .

A new spectroscopic technique based on the AC Josephson effect in superconducting junctions was proposed earlier [1,2} and developed afterwards [3] and some experiments were done to estimate the applicability of this technique in general spectroscopic measurements of submillimeter-wave and millimeter-wave radiation. In this technique a frequency scanning is accomplished by changing the voltage on the junction and fast spectral measurements are in principle possible by the technique. These features are very attractive for the high-speed millimeter-wave spectra in the frequency band of 30-300 GHz and should be analyzed with rather moderate spectral resolution of 2 GHz but with characteristic time interval about 10 ms.

THEORY

When weak electromagnetic radiation with the spectral distribution of intensity S(f) is applied to the Josephson junction, its current-voltage curve (I-V curve) is changed (Fig.1a). When the Josephson junction is described by the resistively-shunted-junction (RSJ) model, the difference $\Delta I(V)=I(V)-I_0(V)$ between the current values with and without incident radiation is shown to be related with the radiation spectrum by the Hilbert transform [1]:

$$S(f) \cong K\int_{-\infty}^{+\infty}\frac{g(u)du}{u - hf/2eV} \qquad (1)$$

where $g(V)=k*\Delta I(V)*I(V)*V$ is the response function (Fig.1b).

Thus, the spectral analysis consists of two parts: at first one should measure the I-V curves of the Josephson junction both with and without incident radiation and then apply the Hilbert transform to measured response function g(V). A spectral line for the 70 GHz monochromatic signal obtained with the use of Hilbert transform is shown in Fig.1c. The operational principle in some respect is similar to that of the Fourier-transform-spectroscopy. The main difference between two techniques lies in the following: for the Hilbert-transform- spectroscopy, the first integral transformation of spectrum into electric signal occurs directly in the solid-state detector, but in the FTS this transformation takes place in the detector-comprising optico-mechanical interferometer. This difference results in some advantages of the HT spectroscopy as compared with the FT spectroscopy: a potentiality of the high- speed spectroscopy is one of them.

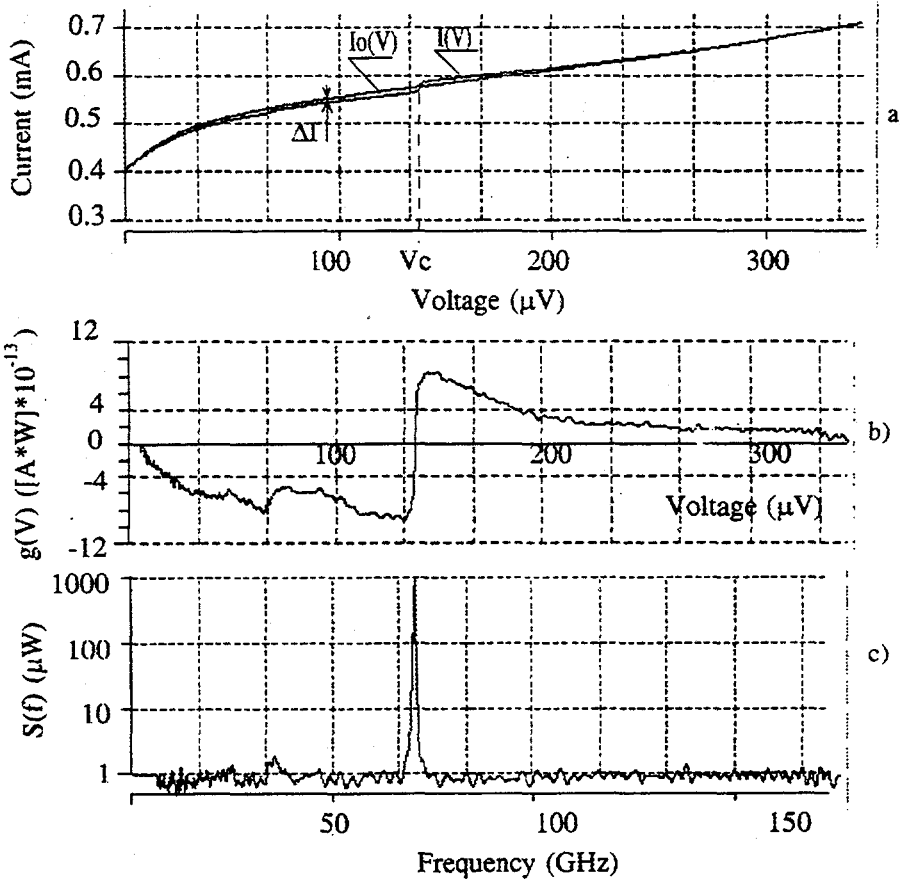

Fig.1. Spectral measurements of 70 GHz monochromatic signal

The main advantage of this technique is due to its possibility to provide the wide-band (about a decade) millimeter measurements using only one measuring channel.

The following restriction for this spectroscopic method should be mentioned. This method rests on the assumption that the amplitude of the current induced in the junction is comparable to the amplitude of the fluctuating current i_f. In this case a response of the junction can be expressed as [4]

$$resp = \frac{\overline{v} - \overline{v}^{(A)}}{a^2(\Omega)} = \frac{1}{8\overline{v}^2}\mathrm{Re}\frac{1}{\delta - j\gamma} \qquad (2)$$

where: $\overline{v}$ and $\overline{v}^{(A)}$ are respectively the voltages on the Josephson junction with and without incident radiation; $a(\Omega)$ is the amplitude of the induced current; $\Omega = 2e\overline{v}/\hbar$ is the frequency of the incident radiation; $\delta = \overline{v} - \omega$ is a mistuning for the Josephson frequency ω; γ is a parameter characterizing fluctuations of the junction.

Analytically the response of the junction may be given as [1]:

$$\Delta i(\bar{v},\Omega)=\frac{a^2(\Omega)}{8\bar{i}\bar{v}}\left[\frac{\bar{v}+\Omega}{(\bar{v}+\Omega)^2+\gamma^2}+\frac{\bar{v}-\Omega}{(\bar{v}-\Omega)^2+\gamma^2}\right] \tag{3}$$

The next conclusion follows herefrom. The inherent fluctuations of the Josephson junction bring into existence the quadratic change of shape of its I-V curve under weak incident radiation. That is to say that this change is proportional to square of the induced current amplitude $a^2(\Omega)$. What this means is that at first in case of weak radiation there appear a feature in shape of a bend in the I-V curve instead of the Shapiro step. This feature or a response of the Josephson junction is governed by the equation [4]:

$$resp=\frac{1}{8\bar{v}^2}\mathrm{Re}\left[\frac{1}{\omega-\bar{v}-j\gamma}-\frac{1}{\omega-\bar{v}+j\gamma}\right] \tag{4}$$

Fig.2 shows different shapes of feature of the I-V curve under changing the incident power of the harmonic radiation. From this figure we notice that within the feature region the dynamic resistance of irradiated junction varies through a range:

$$0\le R_d\le R_d^{(A)} \tag{5}$$

where $R_d\cong 0$ is consistent with the Shapiro step; $R_d^{(A)}$ is a dynamic resistance of the Josephson junction without incident radiation.

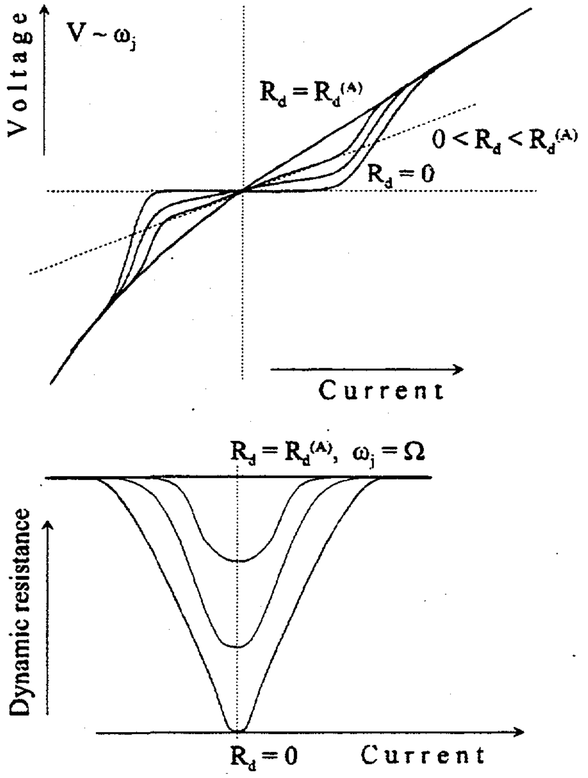

Fig.2. The dynamic resistance dependence of the incident power of harmonic radiation in the neighbourhood of the central poinr of the feature zone.

The implication of this analysis we use for the development of the Josephson spectrometer is that a dynamic range of the incident power is limited at the top. The induced current amplitude may not exceed a fixed quantity wherein the dynamic resistance is equal to 0. A practical implementation of this restriction is carried out by analyzing the dynamic resistance in every point of the I-V curve within a corresponding frequency range and attenuation of the incident power if the dynamic resistance becomes equal to 0.

EXPERIMENTAL SET-UP

Fig.3 shows a block diagram of the experimental set-up. The set-up consists of four main units:

1. A Cryogenic block.
2. An Analog signal processing unit.
3. A high speed communications interface with the quick DAC and ADC.
4. A quasi-optical microwave transmission line.

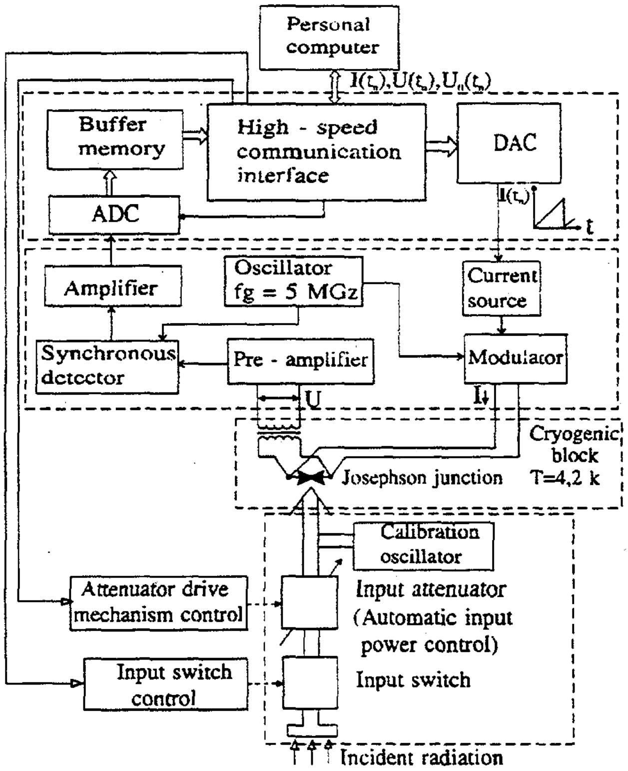

Fig.3. Block diagram of the experimental set-up.

The spectrum analyzer performance is controlled by the personal computer. Operating software for measuring the spectra depends on signal type. When studying the determinate processes the I-V curve measurements are followed by signal spectrum recovery at once. The recovery time is no more than 20 s. The spectrum calibration with respect to the frequency and power is performed by the calibrating signal which frequency is beyond the frequency range being under consideration. When quick-changed random signals such as the microwave radiation of the thermonuclear plasma are analyzed a set of the I-V curves is taken and stored in the computer memory. The time is taken for one I-V curve to be measured does not exceed 20 μs. After stopping the signal action or a required number of the I-V curves are measured, the computer recovers the slide-spectra followed by their storage in memory.

The 14-bit DAC is controlled by the computer via the high-speed communications interface. The DAC in combination with the current source forms the current ramp $I(t_n)$ as a bias of the junction operating point. The shape of the junction response voltage $U(t_n)$ is similar to its I-V curve. This signal is amplified and sampled by the high-speed 16-bit ADC. To reduce noise the analog signals are processed at 5 MHz modulation frequency. A transformer that has a helium level of cooling is used for matching the low-resistive Josephson junction (R_n is about 1 Ohm) with the amplifier input resistance. The measured response signal is stored in a buffer memory for the time when the successive I-V measurements are made, then it is directed into the computer via the high-speed communications interface.

The spectrum is obtained by a personal computer in accordance with Eq.1 having extracted the experimental data $I(t_n)$, $V_o(t_n)$, $V(t_n)$ from its memory and using the canonical discrete Hilbert transform algorithm.

From Eq. (1) and the equations attending its derivation it follows that the canonical algorithm for Hilbert-spectroscopy prescribes execution of seven successive steps:

Step 1. Input of the sequence of counts y_2, representing the I-V curve $y_2=f(x)$ of the junction disturbed by the external microwave signal.

Step 2. Input of the sequence of counts y_1, representing the basic I-V curve $y_1=f(x)$ of the screened junction.

Step 3. Formation of the inverted sequence z_2, representing the inverted I-V curve $z_2=g(y_2)$ of the disturbed junction.

Step 4. Formation of the inverted sequence z_1, representing the inverted basic I-V curve $z_1=g(y_1)$.

Step 5. Formation of the coloring function wgh(x) equal to element-by-element product of the inverted basic I-V curve by the sequence of the independent variable y counts (the segment of the natural set of numbers).

Step 6. Formation of the difference function $dz=z_2-z_1$ and its coloring to yield the form dlt=dzx*wtgh suitable for transformation.

Step 7. Execution of the Hilbert transform of the coloring difference function with the transformation core size specified by the operator.

The final transformation product forms the equidistant sequence of counts of the estimated signal energy spectrum for the irradiated junction under the test determination of I-V values $y_2=f(x)$.

It should be noted that the synthesized canonical form of the Hilbert spectroscopy algorithm can be used with both non-coherent and monochromatic signals under the test conditions. For the latter, the algorithm is realized by passing Step 5 and Step 6 that foresee the difference function coloring to equalize the non-uniformity of the Josephson junction sensitivity over the operating frequency band.

Fig. 4 shows a block-schematic diagram of the microwave transmission-line. When designing this system we made a choice of the quasi-optical components due to existence of some basic problems. They are:

- wide range of frequencies being investigated, from 50 to 350 GHz;
- high frequency resolution that is about 2 GHz;
- linearity of an amplitude-frequency characteristic (bandpass flatness no more than 2 dB);
- difficulty to match the high waveguide resistance with the low resistance of the Josephson junction over a wide frequency band.

The hollow square metal-dielectric waveguide with appropriate electromagnetic focusing is utilized as a system for radiation channeling from the input antenna to the Josephson junction. The input switch and attenuator provided with the personal computer control are employed to adjust the incident power at the Josephson junction and to take measure I-V curves of irradiated junction. The designed microwave unit allows the following parameters to be realized in the frequency range from 50 to 400 GHz:

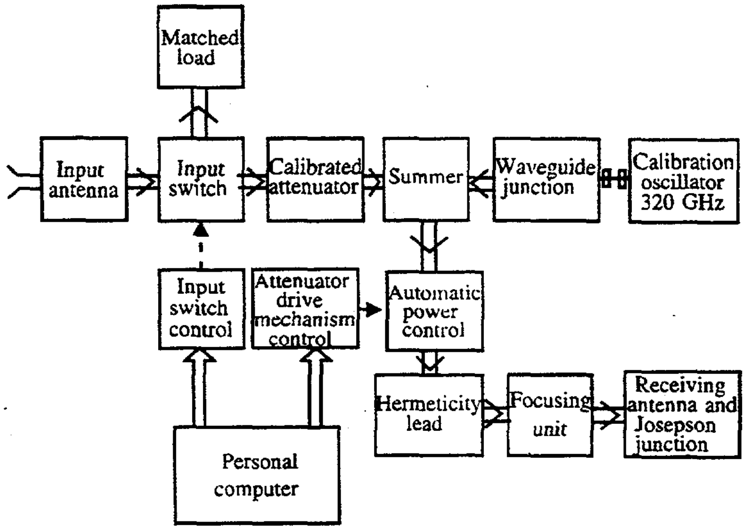

Fig.4. Block schematic diagram of the quasi-optical microwave transmission line.

- bandpass flatness of the amplitude-frequency characteristic is no more than 2 dB;
- longitudinal losses along 1.5 m are no more than 0.6 dB/m;
- attenuation at the low frequency range margin is no more than 6 dB;
- adjusting level for the input power is 50 dB.

The high-stability calibrating oscillator with the input power of 1 μW at a frequency of 320 GHz is incorporated into the microwave transmission line via the directional coupler for calibrating the spectrum analyzer during the measurement process.

Designed microwave transmission line has some advantages over the other cryogenic microwave systems. The cryogenic receiver manufactured on the basis of it allows to work with any transport Dewar flasks and simplifies procedure of preparing the cryogenic block to the measurements. The time interval for this procedure is about 2 minutes.

The matching structure was developed to match the best the low impedance Josephson junction with an impedance of the metal-dielectric waveguide within the wide frequency range [3]. This structure (see Fig. 5) consists of the planar tapered V-antenna, the impedance transformer and planar integrated low temperature niobium junction, was properly calculated and the necessary layout was designed. The antenna feed-point impedance is adjusted to the junction normal resistance of about 1 Ohm by the multi-layered structure consisting of the broadband taper between a quasi-coplanar strip line and a parallel plate line. The substrate material is a sapphire. The main parameters of the Josephson junction are:

- normal resistance is 0.5 ...1.5 Ohm;
- critical current is 0.2 ... 0.4 ma;
- junction area is about 0.5 μm^2.

The I-V curve for unperturbed junction (see Fig.6) is not similar to that of the Josephson junction in RSJ model but nevertheless Josephson behavior is observed for the frequencies within the band from 30 to 500 GHz.

The multi-layered structure appears to be a disadvantage because it is too hard to manufacture such high-temperature samples with the two-step junction or bicrystal junction that answer the best the resistively-shunted-junction model. Another disadvantage of the multi-layered structure consists in poor correspondence of the weak superconductivity mechanism to the restively-shunted-junction model that is a basis of our methodological approaches due to high capacitance of the junction.

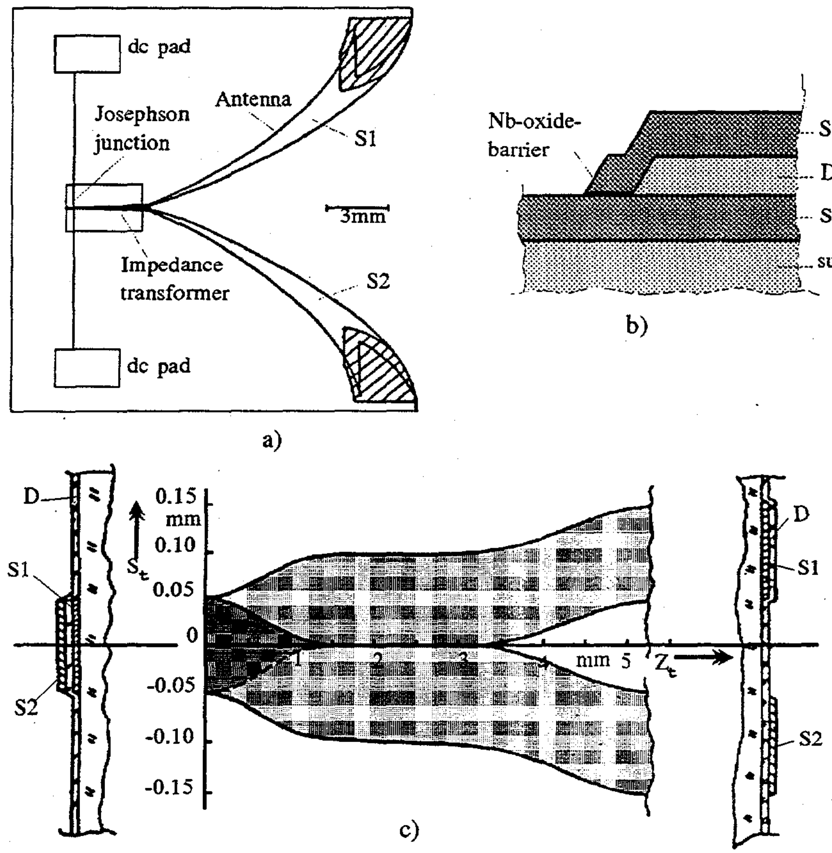

a)

b)

c)

Fig.5. a) Layout of the broad-band receiving antenna with the Josephson junction;
b) Structure of the Josephson junction;
c) Layout of the broadband impedance transformer.

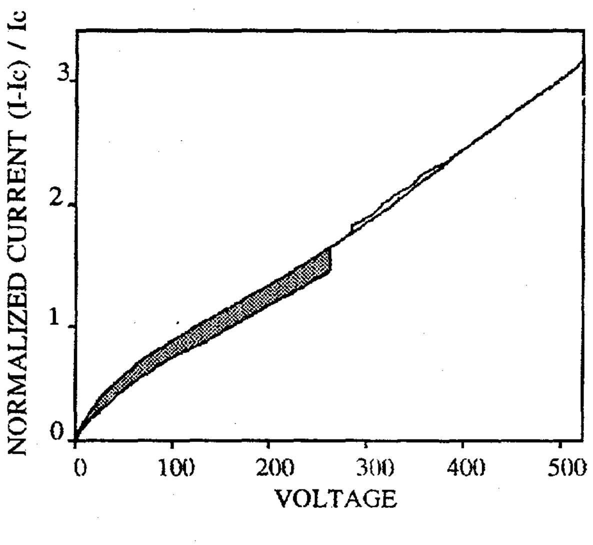

Fig.6. I-V curves of the Josephson junction with and without incident radiation.

RESULTS

The set-up described above allowed the analysis of the complex line spectra to be performed over the frequencies from 40 to 250 GHz with the frequency resolution being not worse than 2 GHz and the sensitivity being not less than 10^{-13} W/√Hz.

The most characteristic results have been obtained when complex polyharmonic signals were passed to the spectrum analyzer input.

Fig. 7 shows the signal spectrum taken from the Josephson junction co-irradiated by the non-coherent laboratory back-ward-wave oscillators. The output power levels of the oscillators are from 0.01 to 1 mW. Therefore the attenuation level was adjusted more than 30 dB to reach the dynamic range of the junction. The frequency resolution is about 2 GHz.

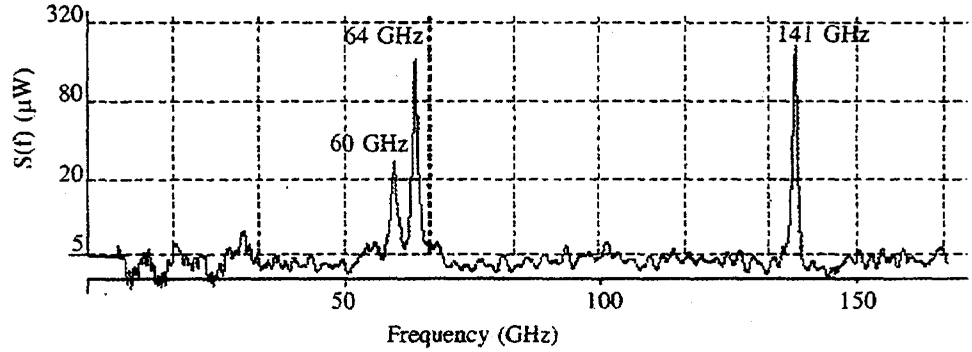

Fig.7. Spectral measurements of mixed three monochromatic signals.

Fig. 8 presents the spectrum of five non-coherent laboratory back-ward-wave oscillators.

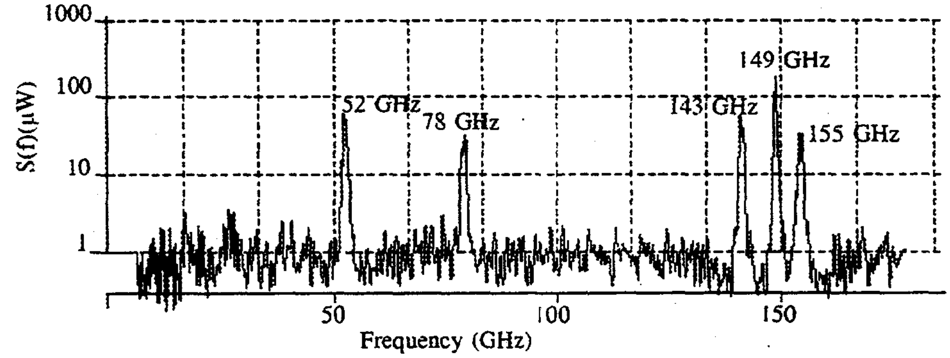

Fig.8. Spectral measurements of mixed five monochromatic signals.

Fig. 9 shows the signal spectrum obtained from the 9 GHz driving oscillator with the 14 times avalanche diode multiplier. Inspection of the spectrum reveals that its structure is vertical lines with pronounced fundamental frequency f_m = 126 GHz and several lateral harmonics separated by 9 GHz.

The incident power at the fundamental frequency f_m exceeds the dynamic range for the specimens of this type. Therefore, the lateral harmonics which frequencies are less than f_m, are poorly observed. This is confirmed by the I-V curve of the Josephson junction irradiatedby the avalanche diode oscillator signal with the vertical line spectrum (see Fig.6). From Fig.9 it is evident that a significant nonlinearity in the initial part of the

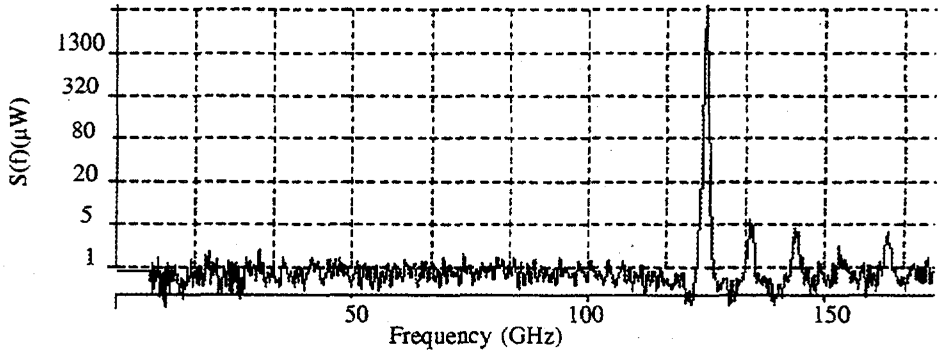

Fig.9. Spectrum of the signal obtained from the 9 GHz driving oscillator with the 14 times avalanche diode multiplier.

I-V curve leads to both the effect of the junction response signal from the frequency fm upon those from the frequencies that are less than fm (dashed area), and limitation of the dynamic power range up to 20 dB.

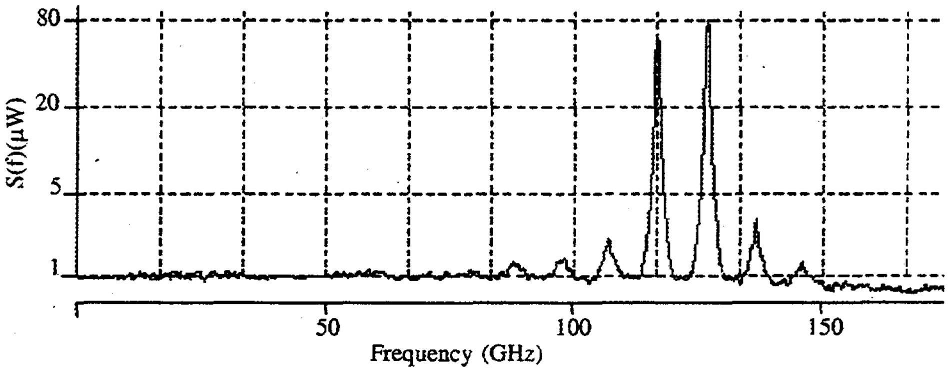

Fig.10. See text.

Fig. 10 shows the signal spectrum obtained from the same oscillator but with the notch-filter for the fundamental harmonic. In this case a dynamic range of the junction is not exceeded and the spectrum obtained really corresponds to the factual one.

REFERENCES

[1] Yu.Ya.Divin,O.Yu.Polyanski,A.Ya.Schulman. Incoherent radiation spectroscopy by means of the Josephson effect, Sov. Tech. Phys. Lett., 1980, 6, 454-455.

[2] Yu.Ya.Divin,O.Yu.Polyanski,A.Ya.Schulman. Incoherent radiation spectroscopy based on ac Josephson effect, IEEE Trans.Magnetics.,1983, 19, 613-615.

[3] J.H.Hinken et al. Computer-controlled mm- & submm-wave Josephson spectrometer with planar integrated front end. Pros. 18th Europ.Microwave Conf.,1988, 177-182.

[4] K.K.Likharev, B.T.Ulrich. Systems with Josephson Contacts. Moscow: Moscow State University Publishing House, 1978.

Non-Destructive Testing (NDT) of Metal Cracks Using a High Tc rf-SQUID and Eddy Current Method

D. F. Lu, Chang-xin Fan, J. Z. Ruan

Midwest Superconductivity Inc.
Lawrence, KS 66049

S. G. Han, K. W. Wong, G. F. Sun

Department of Physics and Astronomy
University of Kansas
Lawrence, KS 66045

Abstract

A SQUID is the most sensitive device to detect change in magnetic field. A non-destructive testing (NDT) device using high temperature SQUIDs and eddy current method will be much more sensitive than those currently used eddy current systems, yet much cheaper than one with low temperature SQUIDs. In this paper, we present our study of such a NDT device using a high temperature superconducting rf-SQUID as a gradiometer sensor. The result clearly demonstrates the expected sensitivity of the system, and indicates the feasibility of building a portable HTS SQUID NDT device with the help from cryocooler industry. Such a NDT device will have a significant impact on metal corrosion or crack detection technology.

INTRODUCTION

It has been known for almost thirty years since its discovery that a Superconducting QUantum Interference Device (SQUID) is the most sensitive instrument for the measurement of change in magnetic flux, and if used in non-destructive testing (NDT) of materials, it can offer unprecedented sensitivity. It also offers a wide range of frequency response (DC to 10 kHz), which is very important to NDT with eddy current method since low frequency electromagnetic field has a large skin depth and can penetrate deep through a conductor. It was the work of Weinstock and Nisenoff [1] that revealed the first page of such an investigation, in which they demonstrated using a low temperature superconducting (LTS) SQUID that simulated cracks could be detected in ferromagnetic and nonferromagnetic pipes by observing the magnetic field associated with flaws. Thereafter, several research groups joined in to explore this new technology. A LTS SQUID has been used in laboratories for the detection of ferromagnetic rods and plates [2], corrosion in pipes [3,4], naval mines [5], to name a few examples. However, its application in NDT has been proven to be rather difficult to implement. Along with others, the foremost reason is the requirement of a LTS SQUID for liquid helium, which seems not practical for field applications. Hence, the LTS SQUID NDT technology has not been commercially adopted.

The discovery of high temperature superconductors has once again aroused people's enthusiasm for using a SQUID in non-destructive testing in the near future. A high temperature superconducting (HTS) SQUID has the required sensitivity, yet it is capable of working at liquid nitrogen temperature, which is far more advantageous to liquid helium for field applications. The advances in cryocooler industry make it feasible to place a HTS SQUID sensor in a portable cryocooler. Thus, a HTS SQUID magnetometer or gradiometer has a great potential to satisfy all the four requirements needed in a commercial NDT device, namely: sensitivity, penetration depth, spatial resolution, and device portability. Many efforts have been made to take advantage of HTS SQUIDs. Various types of HTS thin film SQUID magnetometers and gradiometers have been studied [6,7,8,9]. In this paper, we report a different approach we have been using from all previous researches. We proposed [10,11] that a two-hole rf-SQUID be used directly as a gradiometer sensor. In doing so, we eliminate the need for high temperature superconducting flux transformer coils that the conventional design requires. More importantly, we have demonstrated experimentally that this idea works well. Our SQUID has the desired sensitivity, and is capable of working in a noisy environment without magnetic shielding.

EXPERIMENTAL SETUP

The principle is quite simple. It is easy to show that it is the magnetic flux that is measured with a single hole rf-SQUID, but the difference in magnetic fluxes between the holes that is measured with a two-hole rf-SQUID. Suppose that the two holes are aligned in the x direction, with their axes parallel with the z direction, the output voltage of the measuring system, V_{out}, is proportional to the difference of Φ_1 and Φ_2, the magnetic fluxes through the two holes, respectively. If the area A of the two holes are the same, the flux difference $\Phi_1 - \Phi_2$ is then proportional to the mean magnetic field difference $\Delta B_Z = (\Phi_1 - \Phi_2)/A$. The distance between the two holes, Δx, is the base line length over which the magnetic field gradient $\Delta B_z / \Delta x$ is averaged. Hence it is a natural first order gradiometer. It is insensitive to ambient field interference, yet sensitive to the difference in field between the two holes. Thus it is suitable for NDT field applications since it can eliminate the disturbances from the environment where sources are relatively far from the sensor such that fields generated can be considered uniform over the size of the sensor.

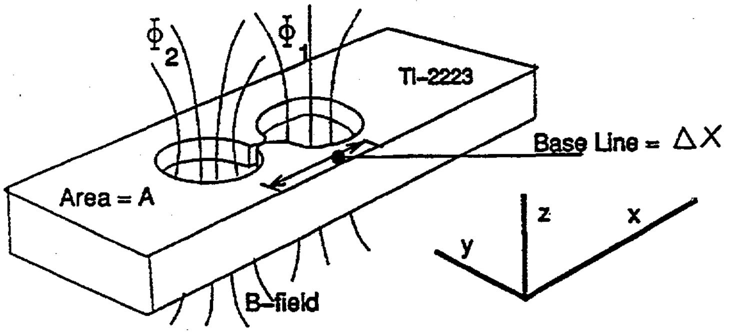

Fig. 1 A double-hole rf-SQUID used as a gradiometer sensor.

Our two-hole rf-SQUID is fabricated on a 3 mm thick Tl-2223 pellet. Two parallel holes of 1 mm in diameter are drilled such that the distance between their centers is 2 mm. A straight thin slot is carved between the holes using a 0.2 mm wire saw until a thin bridge remains right in the middle between the holes. The bridge is then cut carefully until a clear rf-SQUID transfer function pattern is observed [12]. A coil of sixty turns, made from #36 copper wire of about 0.8 mm diameter is inserted into one of the holes. A capacitor of 220 pF is connected in parallel to the coil to form a resonant tank circuit. Finally, model 330 SQUID electronics manufactured by BTi. Inc. and its RF head operating at 19 MHz are used as the measuring equipment. It is experimentally proven that we can operate our HTS rf-SQUID successfully without magnetic shielding, except for the minor shielding from the stainless steel wall of our dewar. Our study also shows that the SQUID has the sensitivity of $10^{-11}\mathrm{T}/2\mathrm{mm}/\sqrt{\mathrm{Hz}}$.

The apparatus used in our NDT experiment is illustrated in Fig. 2. A liquid nitrogen Dewar with a long thin tail made of stainless steel is used. The rf-SQUID is placed near the bottom of the tail, as close to its bottom as possible since the magnetic field decreases dramatically as the distance between the sensor and the source, in our case the cracks, increases. The test samples we use are aluminum alloy (6061-T6) slabs,

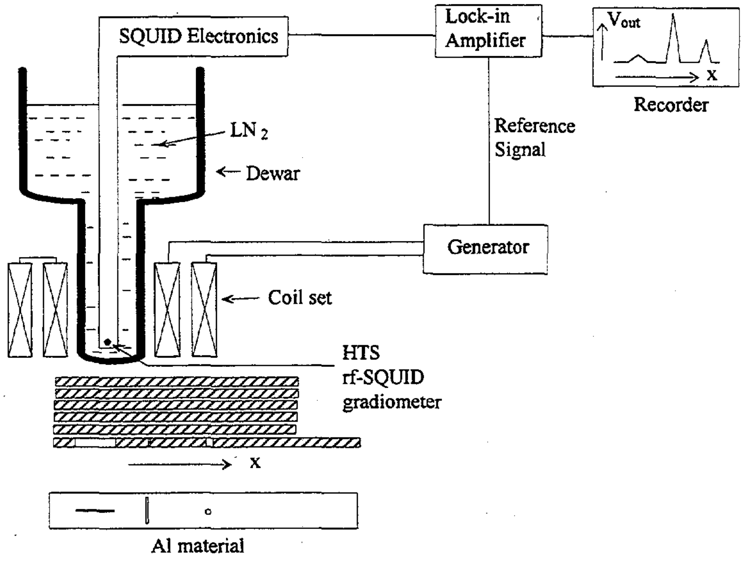

Fig. 2 Sketch of experimental setup

1/8" thick and 2" wide. Several mock cracks of different sizes and shapes are cut in a sample at the bottom of the stack as shown in the figure. This sample is then covered by several pieces of aluminum slabs that do not have defects, and they are pulled slowly under the Dewar tail by a step motor.

In this paper, we adopt the eddy current method. It is very similar to the conventional eddy current method, except that the sensor now is a SQUID that is much more sensitive than coils used in the conventional method. The advantage of this method is that no physical contact with the sample is needed. This may be very important if somehow the conducting sample is covered by other non-conducting materials such as paint, cloth, etc. The eddy current method also offers the benefit that the field can be concentrated on only a small part of the sample depending on the size of exciting coils. Thus, there is less restraint on the size of the sample than that for the applied current [10]. To induce eddy current in the sample, two exciting coils are wound and fastened co-axially to the flange on the Dewar tail. The coils are connected in series such that the field at their axes, where the sensor is placed, is very small. The two coils can be moved along their axes for further fine adjustment. Due to the size of the Dewar tail, the diameters of the coils are 1.35" and 3", respectively, which set a limit on the resolution of the system.

In our experiment, the symmetry of the two-hole SQUID is only about 98%, thus leading to a relatively large noise reception. The spectrum of the environmental noise measured by the not-perfectly-symmetric two-holes rf-SQUID shows that the main contributions to noises are from power lines and its harmonics. It also shows minima at 30 Hz and several other frequencies. To eliminate this large environmental noise, we utilize the large dynamic reserve feature of the SQUID system and feed the signal of the SQUID system into a lock-in amplifier for singling out and amplifying the signal that has the same frequency as the supplied field. Then the signal is plotted on a x-y recorder or a computer. If there is no defects in the sample, we would expect a straight horizontal line. However, if there is a crack, a change in field or its gradient would be detected and a peak is generated on the plot. This is the simple illustration of how it works.

EXPERIMENTAL RESULTS

Our first experiment is done with the detection of cracks in aluminum slabs. Several thin slots are cut through a piece of aluminum plate. The lengths of the three slots are: 1-1/2", 1/4", and 1", respectively from left to right as shown in Fig. 3. The width is 1/16" for all the slots. This sample is now covered by 1/2" thick solid aluminum alloy plate, and is displaced 1" from the sensor. The gradiometer sensor is aligned in such a way that the line passing the centers of the two holes is in parallel with the direction of motion. A current of 0.5 mA and 30 Hz is supplied to the set of coils. Fig. 3 clearly demonstrates the sensing capability of our SQUID gradiometer in the presence of environmental interference. Notice that

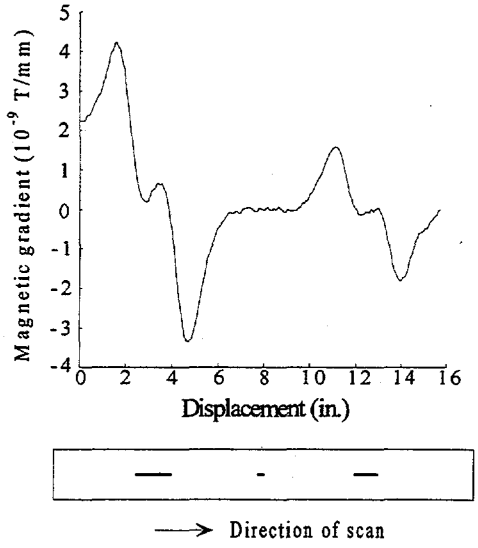

Fig. 3 Test result of crack detection.

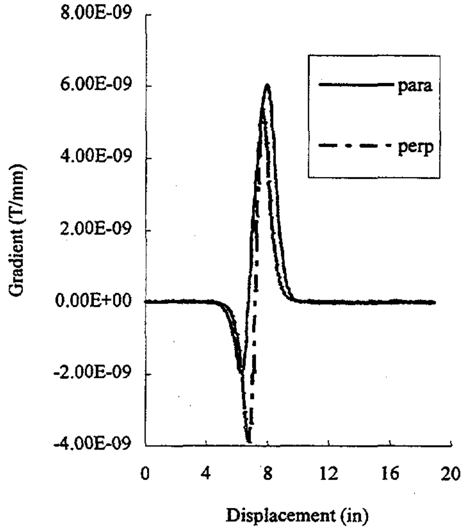

Fig. 4 Test result of metal presence

there is no magnetic shielding at all; the SQUID is exposed to the external interference. Nevertheless, the signal response is clean and sensitive in general. From the figure, we see clearly the effects of two large cracks (1" and 1-1/2" long). The signals observed clearly shows that the changes in magnetic gradient, in the order of nT/mm, are detected due to the presence of these cracks. However, in this particular test, the smaller crack in the sample does not generate a big enough signals for our system to detect. This is due to the limitation on the resolution of the system as we discussed in the last section. Because of the large sizes of the coils, the field generated does not produce a sharp contrast in a small region. The field cannot be concentrated on a small area to generate a large gradient at the small crack that our sensor is able to measure. This will be solved in our future experiments.

We can also use our SQUID NDT device as a metal detector. Fig. 4 is a plot of detection of the presence of a small piece of aluminum. The size of the piece is 2"×1/2"×1/8". The sample to sensor distance is 1/2", and the sample is not covered any more. In this test, we supply a current of 4.5 mA, 160 Hz to the coil set. We pass the sample underneath the Dewar tail, with its long side parallel with and then perpendicular to the direction of motion. The sensor is still aligned with the direction of motion. The results are shown in the plot and the shape of the curves is expected. It first has a negative peak and then a positive peak. It is interesting to notice that no matter how the sample travels, the amplitude of the signal change and the displacement over which the signal changes are almost the same. For example, the signal changes between position 5 inch and 9 inch on this plot. There is only a slight difference in these positions between the two curves. The peak to peak amplitude of the two curves are almost the same, about 8 nT/mm. This is again due to the poor resolution of the current system.

One of the applications as a metal detector is to detect the distribution of metal objects buried in non-conducting objects, such as re-bars in a piece of concrete. Fig. 5 (a) shows the picture of a piece of such a concrete block, with its front view on the left and the rear view on the right. The concrete is 4" in diameter and 1 foot long. Re-bars of different sizes are randomly buried, with their ends exposed to the surface. The current we supply here is 1 mA and 30 Hz. We scan its side surface and the result is shown in Fig. 5 (b) using a contour plot. Correspondence between the re-bars and the field distribution is immediately shown. The center part of the plot reflect the rear side of the block with only one big spot, while the parts on the left and right, when combined, show the cluster of re-bars at the front. It clearly indicates that the re-bars at the front have a elongated distribution, and its shape shows several maxima where the re-bars are exposed to the surface. By the way, this plot is a plot of field, not gradient. The reason is that our two-hole SQUID

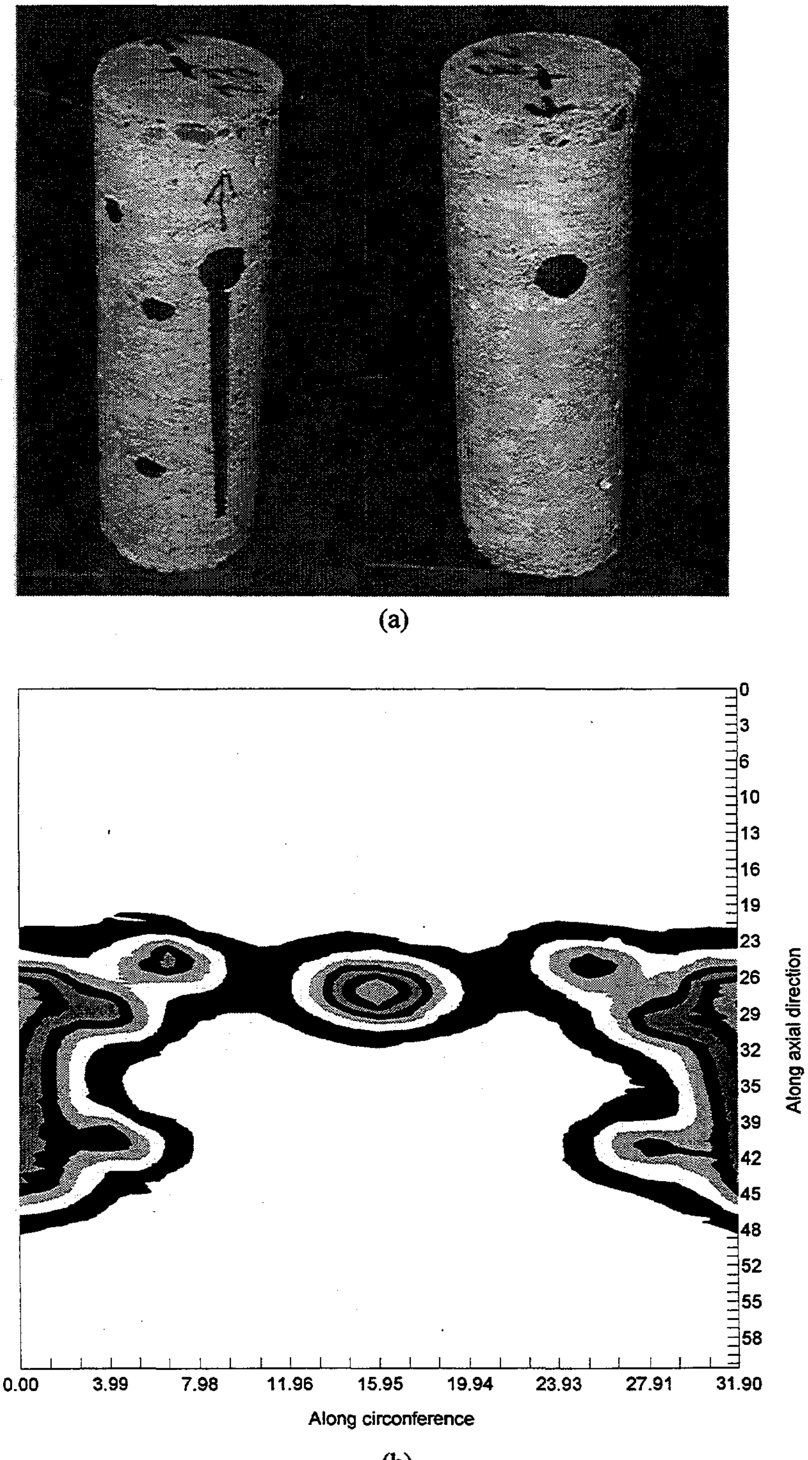

(a)

(b)

Fig. 5 (a) Photo of a piece of concrete block with re-bars. The front view is on the left and the rear view on the right. Deep dark areas indicate exposure of re-bars. (b) Contour plot of side surface scan of the concrete. Dimensions are in centimeters.

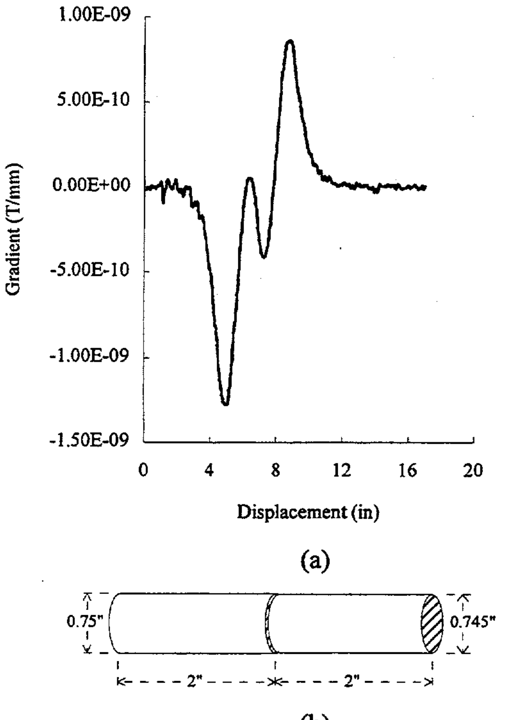

(a)

(b)

Fig. 6 Corrosion test result.

is not perfectly symmetric as we discussed above. Thus certain amount of field signal will be measured. Since re-bars are ferromagnetic materials, their field is so strong that we have to move the SQUID sensor far from it. The distance between the sensor and the surface of the block is about 1-1/2". Thus the field there, even only 2% appears in the SQUID, is much stronger than its gradient so that field is detected instead. We accept this fact and use the gradiometer as a magnetometer in this test. The advantage of doing this is that environmental noise is already eliminated.

Can we detect corrosion? Yes. Again due to the size of coils, we choose a relatively big piece of brass bar with a diameter of 3/4" and length of 4". Half of the brass bar is corroded with nitric acid vapor. The thickness of the corrosion is only about 0.005". We pass the corroded bar under the SQUID sensor with its length parallel to the direction of motion. The distance between the sensor and the top of the surface is 1/2" and the current supplied is 8 mA and 33 Hz. If it were a uniform long bar, we would expect a curve similar to those in Fig. 4, with no turning back in the middle. However, because of the corrosion, there is a sudden change in thickness and in sample to sensor distance in the middle of the sample. Therefore, a sudden drop in signal happens as it seems to meet another new piece of metal.

In conclusion, we have demonstrated the usage of a HTS rf-SQUID in NDT. Our system, working at liquid nitrogen temperature, does not require any special magnetic shields, nor does it need superconducting transformer coils. Thus, the difficulties associated with making a HTS transformer coil, especially a gradiometer coil, are avoided. The most important feature of our system is its high sensitivity and its ability to measure low frequency signals, which can be utilized to inspect cracks buried deeply inside a conductor. The advance in cryocooler technology makes it very possible to build a portable, practical NDT device. We will work on further improvement of its resolution and portability.

We acknowledge the supports of Midwest Superconductivity Inc. We would also like to thank Profs. Joe Lee, Carl Kurt, and Ray Moore, Department of Transportation, University of Kansas for preparing us with the concrete block.

REFERENCES:

1 H. Weinstock and M. Nisenoff, *SQUID '85, Proceedings of the Third International Conference on Superconducting QUantum Devices*, H. D. Hahlbohm and H. Lubbig, eds., de Gruyter, Berlin, 843 (1985)

2 R. J. P. Bain, G. B. Donaldson, S. Evanson, and G. Hayward, *SQUID '85, Proceedings of the Third International Conference on Superconducting QUantum Devices*, H. D. Hahlbohm and H. Lubbig, eds., de Gruyter, Berlin, 841 (1985)

3 J. C. Murphy, G. Hartong, and R. F. Cohen, *J. Electrochem. Soc.* **135(2)**, 310 (1988)

4 J. C. Murphy, R. Srinivasan, and R. S. Lillard, *Review of Progress in QNDE*, D. D. Thompson and D. E. Chimenti, eds., **8b**, 2149, (Plenum, NY 1989)

5 P. V. Czipott and W. N. Podney, *IEEE Trans. on Mag.* **Mag-25**, 1204 (1989)

6 R. Kromann, J. J. Kingston, A. H. Miklich, L. T. Sagdahl, and John Clarke, *Appl. Phys. Lett.* **63**, 559 (1993).

7 L.P. Lee, K. Char, M.S. Colclough, and G. Zaharchuk, *Appl. Phys. Lett.* **59**, 3051 (1991).

8 B. Oh, R. H. Koch, W. J. Gallagher, R.P. Robertazzi, and W. Eidelloth *Appl. Phys. Lett.* **59**, 123 (1991).

9 M. N. Keene, S. W. Goodyear, N. G. Chew, R. G. Humphreys, J. S. Satchell, J. A. Edwards, and K. Lander, *Appl. Phys. Lett.* **64**, 366 (1994).

10 Chang-xin Fan, D. F. Lu, K. W. Wong, Y. Xin, B. Xu, N. S. Alzayed, M. Chester, and D. E. Knapp., *Cryogenics*, in press.

11 Naser S. Alzayed, Chang-xin Fan, D. F. Lu, K. W. Wong, Marvin Chester, and David E. Knapp, *IEEE Trans. on Appl. Superconductivity*, **4**, 81 (1994).

12 S. Harrop, C.E. Gough, M.N. Keene and C.M. Muirhead, *Physica C* **153-155**, 1411 (1988).

HIGH TEMPERATURE SUPERCONDUCTORS APPLICATIONS IN TELECOMMUNICATIONS*

A. Anil Kumar, Jiang Li and Ming Fang Zhang

Center for Materials, Microdesign & Microfabrication
and
Department of Electrical Engineering
Prairie View A&M University
Prairie View, Texas 77446-0397
e-mail: akumar@pvcea.pvamu.edu

ABSTRACT

The purpose of this paper is twofold: (i) to discuss high temperature superconductors with specific reference to their employment in telecommunications applications; and (ii) to discuss a few of the limitations of the normally employed two-fluid model. While the debate on the actual usage of high temperature superconductors in the design of electronic and telecommunications devices - obvious advantages versus practical difficulties - needs to be settled in the near future, it is of great interest to investigate the parameters and the assumptions that will be employed in such designs. This paper deals with the issue of providing the microwave design engineer with performance data for such superconducting waveguides. The values of conductivity and surface resistance, which are the primary determining factors of a waveguide performance, are computed based on the two-fluid model. A comparison between two models - a theoretical one in terms of microscopic parameters (termed Model A) and an experimental fit in terms of macroscopic parameters (termed Model B) - shows the limitations and the resulting ambiguities of the two-fluid model at high frequencies and at temperatures close to the transition temperature. The validity of the two-fluid model is then discussed. Our preliminary results show that the electrical transport description in the normal and superconducting phases as they are formulated in the two-fluid model needs to be modified to incorporate the new and special features of high temperature superconductors. Parameters describing the waveguide performance - conductivity, surface resistance and attenuation constant - will be computed. Potential applications in communications networks and large scale integrated circuits will be discussed. Some of the ongoing work will be reported. In particular, a brief proposal is made to investigate of the effects of electromagnetic interference and the concomitant notion of electromagnetic compatibility (EMI/EMC) of high T_c superconductors.

Research supported by a grant from the Texas Higher Education Coordinating Board's Advanced Technology Program, Project # 010366-215

INTRODUCTION

With the high temperature superconducting materials becoming increasingly available, the interest in their applications in microwave telecommunications is on the rise [1-9]. While the debate on their actual usage in the design of electronic and telecommunications devices - obvious advantages versus practical difficulties - is still active, it is of great interest to investigate the parameters that will be employed in such designs [10,11].

This paper addresses the issue of high-T_c superconducting materials for telecommunications applications. More specifically, it focuses on the design of waveguides using high-T_c superconducting materials. The performance of a waveguide is described by the parameters such as the surface resistance of the guide wall, signal attenuation and power loss, maximum carrying frequency and bandwidth, maximum transmitted power and dynamic range. Most of these parameters are determined by the properties of the material of which the waveguide is made. High-T_c superconducting materials provide good material properties for these parameters but they also provide certain bounds for the improvement of the performance of waveguides. In this paper, the parameters are investigated with existing theory for high-T_c superconducting materials. They provide us with a better comprehension of the underlying models - their usefulness and their limitations.

Because of these advantages, and with the high-T_c superconducting materials available, recent years have seen a substantial increase in the attempts to employ high temperature superconductors in microwave telecommunications applications. The high-T_c superconductors have been used in many kinds of microwave devices such as resonators, filters, delay lines, couplers, antennas, waveguides, striplines, transmission lines, detectors, mixers, switches, oscillators, digital interconnects, wires, etc.

The main objective of this paper is to discuss some relevant parameters of the high T_c superconductors from the viewpoint of design of microwave telecommunications devices. As with any new materials a careful look at the fundamental assumptions behind the models employed should precede their actual application. The emphasis of this paper and of the discussions presented is not the exploration of fundamental theories (though a few suggestions as to their modification will be made) but the employment of existing concepts and models as applied to waveguides. More specifically we study the implications to the waveguide design based on the two-fluid model. The main intention is provide the microwave engineer with performance data available (in terms of material parameters) for different waveguide configurations - rectangular and cylindrical, in particular.

BRIEF DISCUSSION OF THE TWO-FLUID MODEL

The high temperature superconducting materials are inherently different from their low-temperature counterparts in that they are copper-oxide materials, as opposed to metallic conductors. A remarkable consequence of the high transition temperatures of the copper-oxide superconductors is a marked increase in the energy gap frequency and critical current density, as well as a decrease in the cooling price. While the research efforts continue vigorously, at present there is no acceptable microscopic or phenomenological theory explaining the high T_c phenomenon. In the absence of such a theory, the two-fluid model seems to have served a reasonable starting point in the literature.

The two-fluid model was first introduced to provide a phenomenological description of superconductivity, in analogy with that postulated for liquid helium phase transition. In this model, the total current is assumed to be made up of a combination of normal electrons and superconducting electron pair concentration. The normal electron component is assumed to satisfy the weak scattering transport limit, while the superconducting electron pair transport is assumed to be collision-free. The movement of super-conducting and the normal electrons is expressed by the following transport equations [12]:

$$m\frac{d\bar{v}_s}{dt} = -q\bar{E} \tag{1}$$

and

$$m\frac{d\langle\bar{v}_n\rangle}{dt} + m\frac{\langle\bar{v}_n\rangle}{\tau_n} = -q\bar{E}, \tag{2}$$

In the above equations, $\bar{v}_s$ is the velocity of the electron pairs, $\langle\bar{v}_n\rangle$ is the average velocity of the normal electrons, and m and q are the mass and charge of a single electron, respectively. The total current density is given by:

$$\begin{aligned} J &= J_s + J_n, \\ J_s &= -n_s q\bar{v}_s, \\ J_n &= -n_n q\langle\bar{v}_n\rangle, \\ n &= n_n + n_s. \end{aligned} \tag{3}$$

In Equations 3, the various quantities have the obvious connotation: n is the total electron concentration; and n_n and n_s are the concentrations of normal electrons and superconducting electrons, and J_n, J_s are the corresponding current densities, respectively. n_n and n_s are assumed to obey the following expressions:

$$n_s = n\left[1-\left(\frac{T}{T_c}\right)^4\right], \tag{4}$$

and

$$n_n = n\left(\frac{T}{T_c}\right)^4 \tag{5}$$

where T_c is the critical temperature of the superconducting material.

PARAMETERS OF INTEREST - SURFACE RESISTANCE AND ATTENUATION

Surface Resistance, R_s:

The surface resistance is one of the most important parameters which determine the performance of high-T_c superconducting materials in the microwave telecommunication applications. The reason for this is that the waveguide performance related parameters such as the signal attenuation a, the power loss P_L, noise and signal dispersion depend on R_s. The Q factor of a resonator also depends on R_s.

With a complex conductivity, the surface resistance of a high-T_C superconductor R_S can be written as

$$R_s = \mathrm{Re}\sqrt{\frac{j\omega\mu_0}{\sigma}} = \mathrm{Re}\sqrt{j\omega\mu_0\frac{\sigma_1 + j\sigma_2}{\sigma_1^2 + \sigma_2^2}} \tag{6}$$

Attenuation, α:

The attenuation of a waveguide can be obtained once the surface resistance is given.

For a rectangular waveguide operating in the TE_{10} mode, the attenuation a is expressed by

$$\alpha = \frac{R_s}{b\eta\sqrt{1-\left(\frac{f_c}{f}\right)^2}}\left[1+\frac{2b}{a}\left(\frac{f_c}{f}\right)^2\right]. \tag{7}$$

The corresponding equation for the cylindrical waveguide operating in TE_{11} mode is

$$\alpha = \frac{R_s}{a\eta\sqrt{1-\left(\frac{f_c}{f}\right)^2}}\left[\left(\frac{f_c}{f}\right)^2 + 0.420\right], \tag{8}$$

where a and b are the dimensions of the rectangular waveguide in Equation 7 and a is the radius in Equation 8.

MODELS OF COMPUTATIONS

The quantities computed are:

- conductivity s
- surface resistance R_s
- attenuation constant α

In the literature, two different models within the two-fluid approximation seem to be used. One is a **microscopic approach (Model A)** [Mei & Liang], and the other is an **experimental fit (Model B)** [Tewksbury et al.].

Model A [Mei and Liang]:
The conductivity of the superconducting material is expressed in terms of microscopic parameters [12]:

$$\sigma = \frac{n_n q^2 \tau_n}{m(1+\omega^2 \tau_n^2)} - j\left(\frac{n_s q^2}{m\omega} + \frac{n_n q^2 \omega^2 \tau_n^2}{m\omega(1+\omega^2 \tau_n^2)} \right), \tag{9}$$

where τ_n is the relaxation time.

Model B [Tewksbury, et al.]:
Another approach is the experimental fit to the two-fluid model is based on the experimental data [6]

The conductivity is computed in terms of the macroscopic measurable parameters from

$$\sigma = \sigma_n \left(\frac{T}{T_c} \right)^4 - j \frac{1}{\omega \mu_0 \lambda^2(T)} \tag{10}$$

where σ_n is the normal conductivity of the material. $\lambda(T)$ is the effective penetration depth and can be found from the equation 11, where $\lambda(0)$, the effective penetration depth at temperature $T = 0$, is an experimentally measurable quantity.

$$\lambda(T) = \frac{\lambda(0)}{\sqrt{1 - \left(\frac{T}{T_c} \right)^4}} . \tag{11}$$

RESULTS AND DISCUSSION

From a majority of the literature surveyed by us, we found that a consistent set of parametric values does not seem to exist for any given superconductor. To obtain typical values of the various quantities of interest, the following numerical values have been chosen [7].

T_c=70K, τ_n=2.66¥10^{-13}s, $\lambda(0)$=10^{-7}m , σ_n=10^5 /W m,, n = 1 0^{22}/(cm)^3 , T_c=70K
τ_n=2.66¥10^{-13}s, Model A: $\sigma = \sigma_{ar} - j\sigma_{ai}$ Model B: $\sigma = \sigma_{br} - j\sigma_{bi}$

σ vs. T

Figures 1 and 2 summarize the plots of the conductivity - real and imaginary parts from equation 9 versus temperature. σ_{rn} (sigma.a22 in the figure) and σ_{in} (sigma.a1 in the figure) are the real and imaginary parts of the conductivity contributed by the normal electrons and σ_{is} (sigma.a21 in the figure), imaginary part, is the contribution from the superconducting electrons. Our calculations show that when the temperature is lower than $0.5T_c$, the major contribution to the conductivity comes from the superconducting electrons. But as the temperature increases, the part of the conductivity due to normal electrons can no longer be neglected.

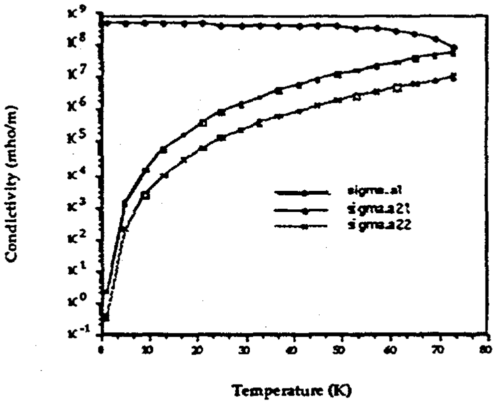

Fig. 1 Conductivity of the superconducting materials $\sigma = \sigma_{rn} - j(\sigma_{is} + \sigma_{in})$

As can be seen, the assumption made, viz., $n_n << n_s$, is not valid beyond T = 0.6 T_c. Figure 2 summarizes the plots of the conductivity versus temperature from the two approaches.

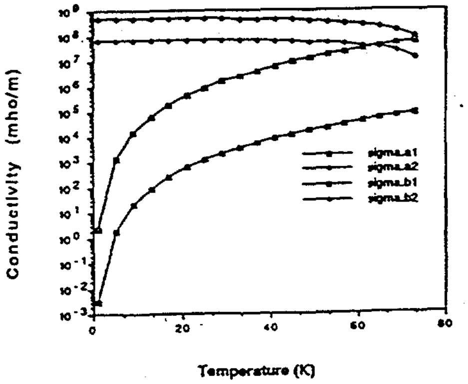

Fig. 2 Comparison of the conductivity obtained from Model A and Model B

R_S* *vs. frequency

Figure 3 shows the variation of R_S with the frequency. The surface resistance, while seemingly constant at low temperatures, does increase at higher temperatures.

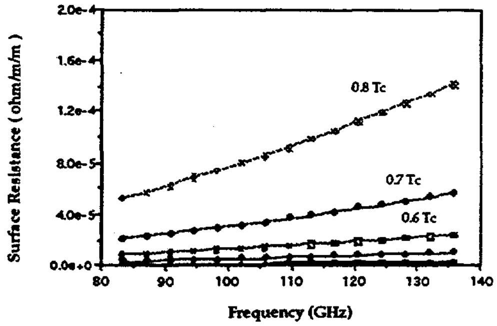

Fig. 3 Surface Resistance R_S of the High-T_C Superconducting Material at Temperatures Ranging from 0.4 T_c to 0.8 T_c

α vs. frequency

Figure 4 shows the attenuation in a superconducting waveguide. The parameters chosen for the rectangular waveguide operating in TE_{10} mode is a=2b=2mm, f_c=75GHz, and for the cylindrical waveguide operating in the TE_{11} mode, a=1.172mm , f_c=75GHz.

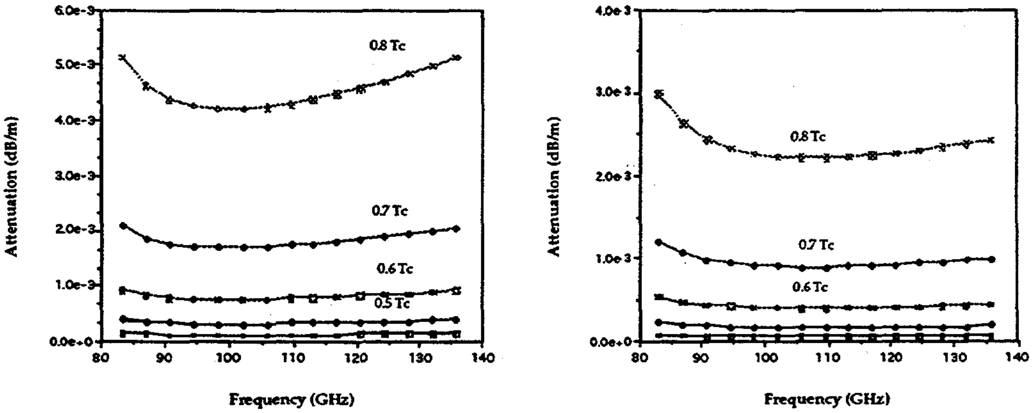

(a) Rectangular waveguide (b) Cylindrical waveguide.

Fig. 4 The attenuation of the superconducting waveguides

Figure 5 shows the difference of the attenuation of rectangular and cylindrical waveguide modes from superconducting (at temperature 0.8 T_c) and normal material.

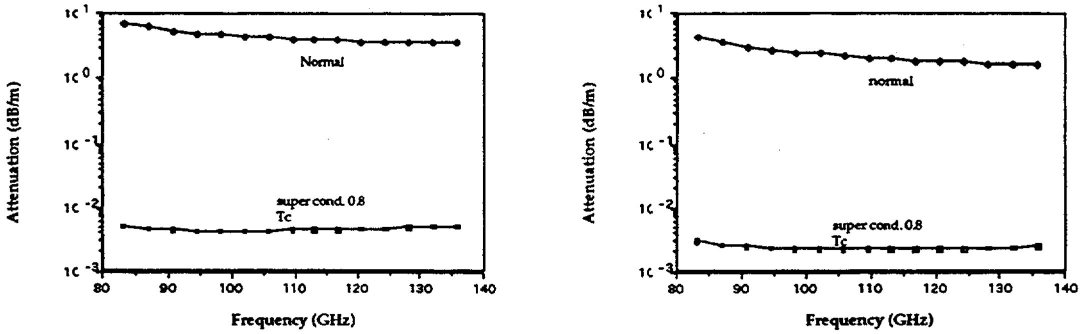

(a) Rectangular waveguide (b) Cylindrical waveguide

Fig. 5 Attenuation of the superconducting ($T=0.8T_c$) and normal waveguides

The results show that as the temperature increases, the dependence of the waveguide parameters on the frequency is more prominent at higher temperatures.

As we can see from the above calculations, some parameters have to be chosen before the conductivity can be calculated. Even though both approaches are based on the two-fluid model, there is a lack of common basis for the choice of the parameter, this constitutes another difficulty in calculating the conductivity of the superconducting material employing the existing two-fluid model. Our calculations show that although there is no common basis for the choice of the conductivity calculations, the trend of variation of the σ with temperature is similar.

As can be seen, the values of σ obtained are different. At the very least, this seems to point to a certain non-trivial ambiguity that is present in these types of overly phenomenological approaches.

RECOMMENDATIONS FOR IMPROVEMENTS

As seen from the computations, two aspects seem to be clear:

- the usual approximation made in the two-fluid model - relative smallness of the normal electron concentration with respect to the superconducting electron pair concentration - is questionable at temperatures higher than about 0.6 T_C. Also, the collision-free nature of the superconducting component transport cannot be correct, since there does exist a maximum current at a given temperature; and
- within the two-fluid model, there seem to be differences in terms of the computed parametric values, leading to ambiguities in the choice of appropriate value for the design parameters for the waveguides.

The modifications that seem necessary are:

- a more accurate (velocity-limiting) mechanism for the superconducting current component;

- a more physically acceptable mechanism for transport for electrons in the normal state - the two-fluid model assumes the usual diffusive, weak scattering transport; and

- a consistent set of values for microscopic parameters that are used in the design process of superconducting devices.

ONGOING WORK

Several generalizations and related aspects are being addressed in our group:

- modification of the two-fluid model to include:
    - a more accurate description of the transport process for the normal component σ_n; and
    - a physically admissible "velocity saturation mechanism" for the superconducting component σ_s;
- computation of power transmitted and received and the associated dynamic range and bit error rate;
- development of a comprehensive object-oriented database for high T_c superconductors;
- development of an "intelligent design system" for design of superconducting waveguides; and
- development of a circuit simulation program for superconducting circuits.

EMI/EMC OF SUPERCONDUCTING CIRCUITS -A PROPOSAL

This brief section addresses the issue of electromagnetic interference (EMI) and electromagnetic compatibility (EMC) as applied to high T_c superconducting elements and circuits. The intrinsic damping due to electrical resistance in a normal circuit accounts for a major portion of the system EMC. In superconducting circuits, however, such a resistance is close to zero, so that new approaches are needed to determine the conditions under which a system is said to possess a certain minimum degree of electromagnetic compatibility.

Traditionally, the standard approach to the control of electromagnetic effects has been to build the system first, measure the EMI problems and then fix them in a largely empirical way. Our contention is that such a control should be incorporated at the design level. More precisely, the approach taken should be somewhat parallel to that taken during the development of VLSI design, namely that the designers have computer-derived design rules and design-checking programs that give advance warning of problem areas before anything is actually built. Our main goal here consists of seeking to establish such a well-defined procedure for the case of EMI-related problems, viz., minimize EM emissions and susceptibility to external emissions which maximize EM compatibility.

CONCLUSIONS

This paper reported part of the research conducted by our group on the application of existing models and concepts to the design of microwave telecommunications devices. The major conclusions were that: some of the approximations involved in the usual waveguide design are not valid at high frequencies and temperatures close to the transition temperature; and the two-fluid model needs non-trivial modifications for accurate applicability to a real high T_c superconductor.

ACKNOWLEDGMENTS

The research reported in this paper has been conducted under the support of a grant from the Texas Higher Education Coordinating Board's Advanced Technology Program, Project #010366-215. Partial support in terms of a summer support for Dr. Li and some computer support was provided by the Center for Materials, Microdesign and Microfabrication, and the Laboratory for Radiation Studies, Dr. Thomas N. Fogarty, Director.

REFERENCES

1. Richard W Ralston, "Microwave Applications of Superconducting Electronics," *Supercond. Sci. Technol.* 4, pp. 386-392, 1991.
2. W. G. Lyons *et al.*, "High-Temperature Superconductive Passive Microwave Devices," *IEEE MTT-S Digest.* pp. 1227-1230, 1991.
3. Katsumi Suzuki *et al.*, "High T_c superconductor microwave resonators and filters," *Applied Superconductivity*, vol. 1, Nos 10-12, pp. 1575-1593, 1993.
4. Michael K. Skrehot and Kai Chang, "A New Resistance Measurement Technique Applicable to High-Temperature Superconducting materials at Microwave Frequencies," *IEEE Transactions On Microwave Theory And techniques*, vol. 38, No. 4, pp.434-437, Apr. 1990.
5. Randy Simon, "High-Tc Thin films and Electronic Devices," *Physics Today*, pp. 64-70, June 1991.
6. Pierre Hartemann, "Effective and Intrinsic Surface Impedances of High-Tc Superconducting Thin Films", *IEEE Transactions On Applied Superconductivity*, vol. 2, No. 4, pp. 228-235, Dec. 1992.
7. Kack H. Winters, Christopher Rose, "High-T_c Superconductor Waveguides: Theory and Applications", *IEEE Transactions on Microwave Theory and Techniques*, Vol. 39, No. 4, Apr. 1991.
8. Gerald Burns, *High-Temperature superconductivity* , Academic Press Inc., 1992
9. S.M. El-Ghazaly, R.B. Hammond and T. Itoh, "Analysis of Superconducting Microwave Structures: Application to Microstrip Lines" *IEEE Transactions On Microwave Theory And Techniques*, vol.40, No. 3, pp. 499-508, Mar. 1992.
10. Robert B. Hammond, "Designing With Superconductors," *IEEE Spectrum*, pp. 35-39, Apr. 1993.
11. S.K. Tewksbury, L.A. Hornak and M. Hatamian, "High Tc Superconductors For Digital System Interconnections," *Solid-State Electronics*, Vol. 32, No. 11, pp. 947-959, 1989.
12. Kenneth K. Mei and Guo-chun Liang, "Electromagnetic of Superconductors," *IEEE Transactions On Microwave Theory And Techniques*, vol.39, No. 9, pp. 1545-1552, Sept. 1991.

HTS THIN FILMS: PASSIVE MICROWAVE COMPONENTS AND SYSTEMS INTEGRATION ISSUES

F. A. Miranda, C. M. Chorey[1], and K. B. Bhasin
National Aeronautics and Space Administration
Lewis Research Center, Cleveland, OH. 44135

ABSTRACT

The excellent microwave properties of the High-Temperature-Superconductors (HTS) have been amply demonstrated in the laboratory by techniques such as resonant cavity, power transmission and microstrip resonator measurements. The low loss and high Q passive structures made possible with HTS, present attractive options for applications in commercial, military and space-based systems. However, to readily insert HTS into these systems improvement is needed in such areas as repeatability in the deposition and processing of the HTS films, metal-contact formation, wire bonding, and overall film endurance to fabrication and assembly procedures. In this paper we present data compiled in our lab which illustrate many of the problems associated with these issues. Much of this data were obtained in the production of a space qualified hybrid receiver-downconverter module for the Naval Research Laboratory's High Temperature Superconductivity Space Experiment II (HTSSE-II). Examples of variations observed in starting films and finished circuits will be presented. It is shown that under identical processing the properties of the HTS films can degrade to varying extents. Finally, we present data on ohmic contacts and factors affecting their adhesion to HTS films, strength of wire bonds made to such contacts, and aging effects.

I. INTRODUCTION

The desirable properties and potential benefits of the high-temperature-superconductors (HTS) have been well established [1]. Numerous published papers on both the basic properties of the materials and their application in prototype circuits have demonstrated that significant improvement can be made in certain components and systems by including HTS [2-4]. As efforts continue towards the inclusion of HTS-based circuits in working systems, attention is turning to issues regarding the quality and reliability of the HTS components. These include uniformity and repeatability of the starting HTS films and substrates, stability of the material through processing and assembly, formation of ohmic contacts to the HTS films and the ability to bond reliably to these contacts. Gauging the quality of a given HTS component or process is a subjective matter dependent upon the intended application and operating environment. While components are routinely produced for laboratory demonstrations and experiments, the more stringent demands of components for real systems require a higher level of material and processing control.

The Naval Research Laboratory's High Temperature Superconductivity Space Experiment II (HTSSE-II) has recently provided an opportunity to assess the ability of current HTS technology

---

[1] NYMA Inc., 20001 Aerospace Parkway, Cleveland, OH., 44142

to produce components for a space qualified sub-system. For HTSSE-II a hybrid semiconductor-superconductor microwave receiver-downconverter was designed and assembled with a level of space qualification conforming to a class 'D' space experiment [5]. This qualification process followed MIL-STD-883 and covered basic issues such as shock and vibration, bond pull strength, die shear strength and hermiticity. Basic concerns such as these are of interest in any systems application.

The topics covered in this paper relate primarily to the quality and durability of the HTS films and devices as they are subjected to the various fabrication and assembly steps necessary to produce a packaged device. We present data on the uniformity of the starting material and the resultant spread in the material's properties as it is subjected to the various processing and assembly steps. Also, we examine the ohmic contacts to the HTS material in terms of the adhesion to the HTS material, the strength of wire bonds made to those contacts and the contact resistivity (ρ_c). The data presented here are not the result of a systematic study but rather are observations recorded in the course of producing the HTSSE-II module in our laboratory. Hence, aspects of this work may not be fully complete. It is hoped, though, that the material covered here will provide a guide to the further development of HTS devices for practical systems.

II. HTS FILM UNIFORMITY/REPEATABILITY

As HTS moves towards insertion into practical systems, uniformity of the components is of major importance; HTS devices must have repeatable and predictable properties. The demands are especially stringent for superconducting devices as many of the applications are in highly frequency selective, high 'Q' components such as narrow band filters or oscillators where variations of a few percent can have significant impact on the desired device characteristics. Variations in the final performance of a device can arise from many sources. Some obvious factors are the dielectric properties of the substrate or the physical dimensions of the structures such as the etched line widths and substrate thickness tolerances. For HTS the properties of the electrical conductor, the actual superconducting film, are also of importance, affecting the device performance through factors such as the T_c, the microwave losses and the internal inductance of the superconducting lines. While the quality of commercially available films has improved, the variations routinely found are of the order of several percent. For example, Table 1.a shows the measured T_c's from several unprocessed magnetron sputtered films. It is seen that even for pieces from a single wafer (samples 1-4) there is a spread in T_c of several degrees amounting to $\sim 2\%$ variation. Variations of the same order are found when comparing T_c's of wafers produced in the same chamber (samples 5,6). Similar variations are observed in films produced by other growth techniques such as laser ablation, as noted in table 1.b.

The piece to piece variation can be seen in the microwave properties as well. Table 2 and Figure 1 show the T_c's and measured Q's from five ring resonators patterned from laser ablated films. Despite the high values and small spread of the T_c's exhibited by these films there is a significant spread in the unloaded Q's as well as a variation in the resonant frequency at 77 K. All resonators showed measurable Q's up to 90 K suggesting that any possible Tc degradation during processing was very small. Since the processing was the same for these samples, it may be suggested that the observed film-to-film variation of the unloaded Q's is determined by the morphological and structural properties (i.e., grain boundaries, vacancies, surface roughness, etc) of the particular film.

In addition to what may be inherent differences in the HTS film properties, degradations (as measured by T_c) were observed for some films as they were processed into circuits. As a means of monitoring this, films typically 2500-3500 Å thick on 20 mil thick $LaAlO_3$ substrates were obtained from commercial vendors. Films grown both by laser ablation and off-axis magnetron sputtering were investigated. A four-point-probe technique was used to measure the T_c of the films as received and at intermediate steps as the films were processed into test patterns. After the initial T_c measurements (no processing involved), the following process steps were investigated:

(1) Pattern etching:
  a. Clean sample's surface: 5 min. in acetone in ultrasonic cleaner, followed by 5 min. in ethanol in ultrasonic cleaner and blow dry with nitrogen gas (GN_2).
  b. Spin coat positive photoresist (AZ4210); softbake at 90°C for 30 min.
  c. Expose (1.5 min at 20 mW/cm^2) and immerse in developer (4:1 H_2O:AZ400K developer) for 2.5 min. with constant agitation; rinse in deionized (DI) water and blow dry in GN_2.
  d. Etch samples:
    i. In diluted H_3PO_4 (H_2O:H_3PO_4) 100:1 concentration; cool solution to room temperature; etch for 20 sec.; remove, rinse, and blow dry; re-etch as required in 10 sec. intervals.

    or:

    ii. Etch as above in saturated EDTA.
  e. Strip photoresist:
    i. Soak in acetone 5 min.
    ii. soak in methanol 5 min.
  f. Perform T_c measurements.

(2) Contact deposition:
  a. Spin on positive photoresist (AZ4210); softbake at 70°C for 30 min.
  b. Expose at 20 mW/cm^2 and soak in chlorobenzene for 10 min. at 23°C; blow dry in GN_2; bake for 5 min.
  c. Develop contact pattern (using Shipley CD-30 Developer); Solution temperature 25±1°C; develop for ~2.5 min. with constant agitation; rinse in DI water and blow dry in GN_2.
  d. Perform O_2 plasma (50 W rf) cleaning for 30 sec.
  e. E-beam evaporate: 1000 Å silver followed by 1500 Å of gold.
  f. Liftoff: soak in acetone, 5 min.; soak in methanol, 5 min.; blow dry in GN_2.

(3) Contact anneal:
  a. Purge tube furnace with 5 SLM of O_2; insert sample at 200°C; ramp temperature at 20°C/min. to 425°C in 5 SLM O_2.

b. Reduce O_2 flow to 1 SLM and hold sample at 425°C for 50 min. Cool slowly to 200°C at 1 SLM O_2; remove sample from furnace at $T \leq 200°C$.
c. Perform T_c measurements.

In addition to the above processing steps, the integration of individual HTS-based components into the complete HTSSE-II receiver required some additional processing steps. The first process cured a silver-based epoxy used to attach semiconductor die to the superconducting circuit, this epoxy and heat curing was also separately used to attach the complete HTS circuit to a metal (gold plated KOVAR) sub-carrier. The second process was a vacuum bake-out used to drive off adsorbed moisture immediately prior to the hermetic sealing of the receiver package.

(4) Epoxy cure cycle treatment:
  a. Heat in air at 150°C for 1 hr.
  b. Perform T_c measurements.

(5) Vacuum bake-out:
  a. Heat under vacuum (< 10 mtorr) at 100°C for 24 hr.
  b. Perform T_c measurements.

Figure 2 shows a chart of T_c following the processing steps as observed for laser ablated (LA) and magnetron sputtered (MS) YBCO thin films. For the laser ablated samples the T_c did not change appreciably as a function of the processing steps, although a small drop in T_c (less than 1 K) was observed for the sample etched with H_3PO_4 after the annealing in oxygen. These two samples belonged to the same wafer and their behavior suggest that samples with T_c's $\geq$90 K are less sensitive to processing. The sputtered samples exhibited a greater sensitivity to processing and showed a wider variation in T_c degradation. Samples with similar T_c's at step 1 and 2 show different behavior with respect to processing during the remaining processing steps (e.g., MS1 and MS2). It is also apparent that for the magnetron sputtered samples step 3 appears to be a "turning-point" with regards to their T_c values. The annealing step was further investigated by subjecting unprocessed (i.e. unetched, unmetallized) films to the annealing cycle and monitoring the T_c. The results of this test are shown in table 1.a and show a great sensitivity and apparent random variability of the sample T_c to annealing. This behavior was characteristic of many of the magnetron sputtered and, to a lesser extent, of the laser ablated samples examined in our laboratory.

III. OHMIC CONTACTS

Another area important for HTS applications is the formation of ohmic contacts with low contact resistivity, good adhesion and characteristics which allow the formation of strong wire bonds. In producing the HTSSE II circuits, the strength of wire bonds made to the ohmic contacts were found to be highly dependent on the process used to produce the contacts. Wire bond strengths were determined by conducting pull tests as outlined in MIL-STD-883 and were performed for 0.7 mil gold wire and 1 X 2 mil gold ribbon. In general, the procedure necessary to produce a quality contact depended upon the deposition method used to produce the HTS film, i.e. depended upon if the film was produced by laser ablation or magnetron sputtering. For magnetron sputtered samples, the following "types" of contacts were studied:

(1) Type-1:
  a. E-beam evaporation of 1000 Å of silver followed by 1500 Å of gold.
  b. Annealing at 425°C in O_2 for 50 min.; cool to room temperature in flowing O_2.

(2) Type-2:
  a. O_2 plasma cleaning, 50 W, 1 min.
  b. E-beam evaporation of 1000 Å silver followed by 4000 Å of gold.
  c. Annealing; same as for type 1.

(3) Type-3:
  a. O_2 plasma cleaning, 50 W, 1 min.
  b. E-beam evaporation of 500 Å silver followed by 4000 Å of gold.
  c. Annealing; same as for types 1 and 2.

Results of the pull tests are shown in Figs. 3 (1 X 2 mil ribbon) and 4 (0.7 mil wire). The results show increasing pull strengths from contact type 1 to type 3, with only type 3 consistently showing strengths which meet MIL-STD-883. The increasing bond strength correlates with the decreasing fraction of silver in the contact metallization. The original rationalization for depositing silver was to lower the contact resistance. However, these tests indicate that the silver has a negative effect on the bond strength.

Similar studies were done with samples deposited by laser ablation to determine the effect of cleaning the HTS surface prior to deposition of the contact metallization. Three processes for cleaning the surface of the contact area were compared: a surface etch using dilute hydrofluoric acid, a surface etch using diluted phosphoric acid, and an oxygen plasma discharge clean.

(1) Process-1:
  a. Dip in $HF:H_2O$ 1:10 for 10 sec.; rinse in DI water and blow dry in GN_2.
  b. E-beam evaporate 500 Å of silver followed by 4000 Å of gold.
  c. Anneal in O_2 at 425°C for 50 min; cool to room temperature in flowing O_2.

(2) Process-2:
  a. Dip in $H_3PO_4:H_2O$ 1:100 for 4 sec.; rinse in DI water and blow dry in GN_2.
  b. Same type of metallization and annealing conditions as in process-1.

(3) Process-3:
  a. O_2 plasma cleaning, 100 W, 1 min.
  b. Sputtering, 40 milliamps, 25 sec. (removed approximately 200 Å of YBCO).
  c. E-beam evaporation of either, (i) 4000 Å of gold or (ii) 500 Å of silver followed by 4000 Å of gold.
  d. same annealing conditions as in (1) and (2).

Pull tests of 1x2 mil gold ribbon bonds on these samples produced widely different results. Contacts produced by processes (1) and (2) resulted in pull strengths below 2 grams for all bonds. Contacts made using process (3) had better pull strengths as shown in Fig 5. Two observations are made from these tests. First, cleaning of the HTS surface by the wet etchant process was extremely detrimental to the pull strength. (Similar results were observed in early tests on magnetron sputtered films: very poor pull strengths for surfaces cleaned with a phosphoric acid etch). Second, for contacts produced by process 3, the pure gold contacts have better pull strength than the silver-gold ones again illustrating the negative effect of silver on the contact pull strength. A three-point-probe technique was used to measure the contact resistance (ρ_c) for these contacts; $\rho_c=2.8\times10^{-6}$ Ω-cm^2 and $\rho_c=9.1\times10^{-6}$ Ω-cm^2 were measured for the gold contacts at 10 K and 77 K, respectively. For the silver-gold contacts $\rho_c=1.3\times10^{-6}$ Ω-cm^2 for both 10 K and 77 K. These values are consistent with those reported by others [6].

Two other contact types were examined during the HTSSE II project. The first was a sputtered contact consisting of 250 nm of silver followed by 250 nm of gold. Initial tests made when the samples arrived in our laboratory showed moderate pull strengths for both 0.7 mil gold wire bonds ($\geq$2 g) and for 1 X 2 mil gold ribbon bonds (~10-16 g). In subsequent tests made after ~ 3 months of storage in a dry box the 0.7 mil wires could not be bonded to the contacts. The 1 X 2 mil ribbons bonded as before and showed similar pull strengths as the initial tests. Auger analysis was performed on these contacts and instead of a layered gold/silver structure the contact metallizations were found to be intermixed and a uniform mixture of gold and silver from the top surface to the HTS interface. Since the 0.7 mil gold wire has a much smaller bonding area, its bond strength is much more sensitive to the surface properties. It is speculated that the silver at the surface of the contact may be oxidized and prevent the formation of a strong bond. The second contact examined was a pure gold in-situ deposited contact fabricated at JPL's Microdevices Laboratory [5]. The bonding properties of these contacts were very good (~18-20 g), consistently producing pull strengths far in excess of the MIL-STD minimum values.

CONCLUSIONS

In this paper we have presented data on some of the processing issues of HTS thin films faced during our work with HTS-based components for the HTSSE-II experiment. It was observed that not only films deposited by different methods but also those deposited by the same technique can show variations in their initial properties (as evaluated by T_c). These initial variations between samples broaden as the HTS films are processed and assembled into components with the result that finished devices rarely have identical performance. We studied, also, several contact processing techniques with the intent to identify a process producing low contact resistance as well as good bond strength. The presence of silver in the contact metallization was found to have a negative effect on the bonding properties of the ohmic contacts. Surfaces cleaned with a plasma discharge showed better mechanical properties than those cleaned with either a hydrofluoric or phosphoric acid etch. The best contacts, in terms of bonding strength and repeatability, were pure gold contacts deposited in-situ. In view of the data presented here we believe that despite all the successful HTS-based components demonstrated so far there is still work to be done aimed at improving the uniformity, repeatability and robustness of these materials so that their excellent electrical properties can be fully exploited in real microwave components and systems.

REFERENCES

[1] Miranda, F. A., Gordon, W. L., Bhasin, K. B., Heinen, V. O., and Warner, J. D., "Microwave Properties of $YBa_2Cu_3O_{7-\delta}$ High-Transition-Temperature-Superconducting Thin Films Measured by the Power Transmission Method," *J. Appl. Phys.*, **70**, pp. 5450-5462 (1991).

[2] Jackson, C. M. and Bhasin, K. B.:"High-Temperature Superconductivity for Satellite Communication Applications," in "High-T_c Microwave Superconductors and Applications," *Proc. SPIE* **2156**, pp. 21-26 (1994).

[3] "Special Issue on Superconductive Microwave Devices and Circuits," *Micro. and Opt. Tech. Lett.*, **6**, (1993).

[4] "High-T_c Microwave Superconductors and Applications," Hammond, R. B. and Withers, R. S., eds., *Proc. SPIE*, **2156**, (1994).

[5] Javadi, H. H. S., et al., "Low-Noise Hybrid Superconductor/Semiconductor 7.4 GHz Receiver/Downconverter for NASA Space Applications," *Proc. SPIE* **2156**, pp. 101-106 (1994).

[6] Dreuth, H. and Dederichs, H.:"Evaluation of Low Resistance Contacts on $YBa_2Cu_3O_7$ Thin Films Using the Transmission Line Model," *Supercond. Sci. Technol.*, **6**, pp. 464-468 (1993).

Table 1.a

Tc Variations Before and After Annealing for Unpatterned and Nonmetallized YBCO on $LaAlO_3$ Thin Films*

Sample	Wafer	Initial Tc (K)	Intercept[a]	Final Tc (K)	Intercept
1	Wafer 1	87.0	0.163	59	0.306
2	Wafer 1	90.8	0.046	74	0.250
3	Wafer 1	90.8	0.046	85.5	0.224
4	Wafer 1	88.0	0.138	<87	0.250
5	Wafer 2	>89.5	-0.016	>89.7	0.067
6	Wafer 3	>89.5	-0.046	>89.7	0.019

a) Intercept with ordinate axis representing $(R/R_{max}) \times 10$, R=resistance.

*) Films were deposited by magnetron sputtering.

Table 1.b

Tc Variation for Unpatterned and Nonmetallized Laser Ablated YBCO on $LaAlO_3$ Thin Films

Sample	Batch	Tc (K)	Sample	Batch	Tc (K)
1	1	90.47	10	1	88.71
2	1	90.58	11	1	90.42
3	1	90.69	12	1	89.91
4	1	89.41	13	1	90.61
5	1	89.66	14	2	87.67
6	1	89.71	15	2	88.42
7	1	89.35	16	3	88.83
8	1	90.13	17	3	89.69
9	1	90.90	18	3	89.50

Table 2

Tc and Q Data for Double Sided Laser Ablated YBCO on $LaAlO_3$ Thin Films

Sample #	Conductor Level	Tc (K)	Q (@77K)	f (GHz)
294	Strip	91.55	5040	8.407
	Ground Plane	90.24		
295	Strip	91.19	3005	8.404
	Ground Plane	91.11		
296	Strip	91.48	1077	8.420
	Ground Plane	91.29		
297	Strip	91.13	2483	8.419
	Ground Plane	90.52		
298	Strip	91.18	2273	8.417
	Ground Plane	90.70		

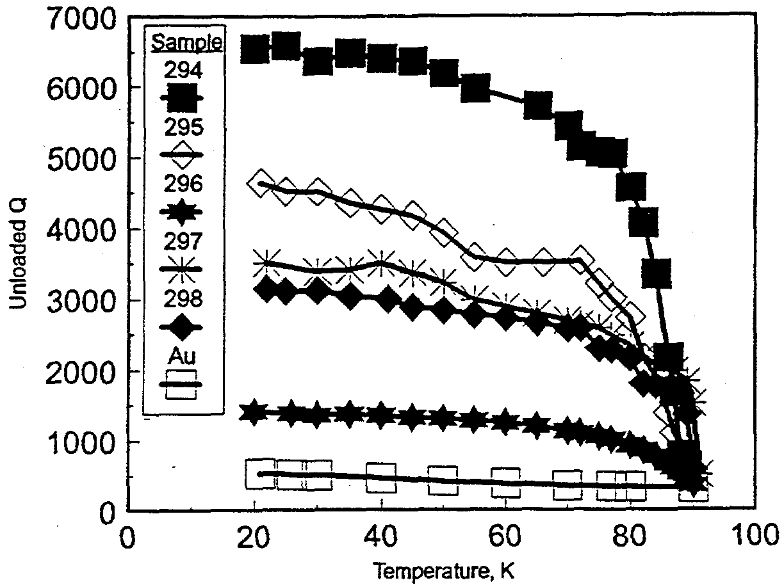

Fig 1. Unloaded quality factor (Q) versus temperature for 8.4 GHz ring resonators etched on laser ablated YBCO on $LaAlO_3$.

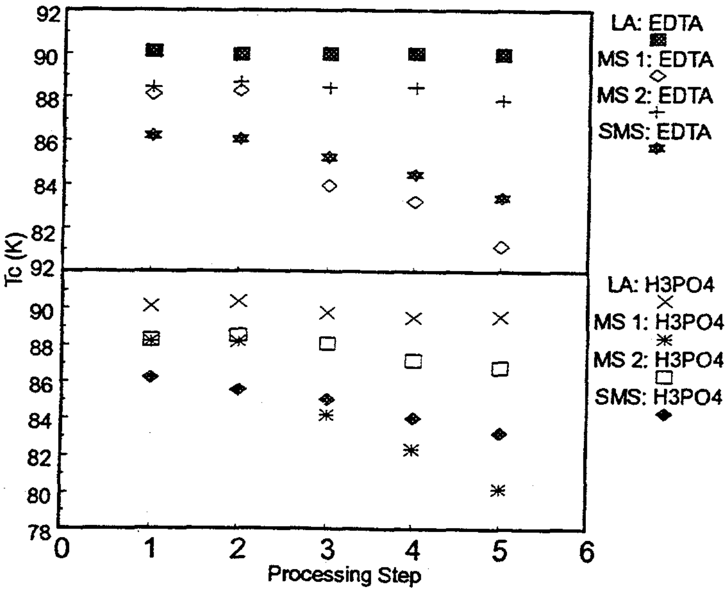

Fig 2. T_c versus processing steps for laser ablated (LA), magnetron sputtered (MS) and "smooth" magnetron sputtered (SMS) YBCO thin films on $LaAlO_3$. The processing steps are: 1) As received 2) wet etching (either with EDTA or H_3PO_4, 3) contact deposition and annealing, 4) epoxy cure cycle, 5) vacuum bake-out.

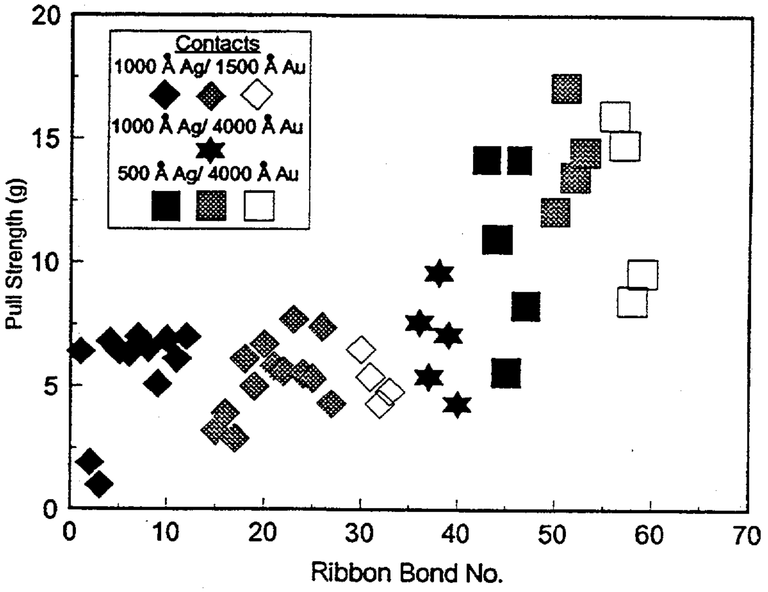

Fig 3. 1x2 mil gold ribbon bond pull strengths for magnetron sputtered samples of YBCO; each shading type corresponds to a different sample.

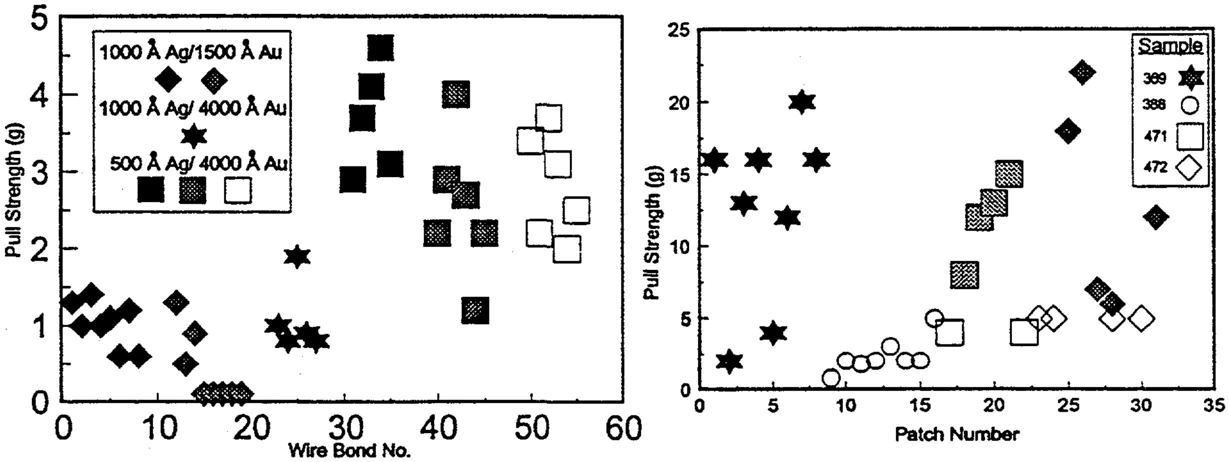

Fig 4. 0.7 mil diameter gold wire bond pull strengths for sputtered YBCO thin films; each shading type corresponds to a different sample.

Fig 5. 1x2 mil gold ribbon pull strengths for laser ablated YBCO thin films. Empty symbols are Au/Ag contacts and solid symbols are Au contacts.

THIS PAGE INTENTIONALLY LEFT BLANK

Wire Fabrication

Chair: Dr. K. C. Goretta

DEVELOPMENT OF PRACTICAL HIGH TEMPERATURE SUPERCONDUCTING WIRE FOR ELECTRIC POWER APPLICATIONS

Robert A. Hawsey, Program Manager
Oak Ridge National Laboratory
PO Box 2008
Oak Ridge, Tennessee 37831-6040

Robert S. Sokolowski , Program Manager, and Pradeep Haldar, Senior Engineer
Intermagnetics General Corporation
PO Box 461
Latham, New York 12110-0461

Leszek R. Motowidlo, HTS Group Leader
IGC Advanced Superconductors
1875 Thomaston Avenue
Waterbury, Connecticut 06704

Abstract

The technology of high temperature superconductivity has gone from beyond mere scientific curiosity into the manufacturing environment. Single lengths of multifilamentary wire are now produced that are over 200 meters long and that carry over 13 amperes at 77 K. Short-sample critical current densities approach 5×10^4 A/cm^2 at 77 K. Conductor requirements such as high critical current density in a magnetic field, strain-tolerant sheathing materials, and other engineering properties are addressed. A new process for fabricating round BSCCO-2212 wire has produced wires with critical current densities as high as 165,000 A/cm^2 at 4.2 K and 53,000 A/cm^2 at 40 K. This process eliminates the costly, multiple pressing and rolling steps that are commonly used to develop texture in the wires. New multifilamentary wires with strengthened sheathing materials have shown improved yield strengths up to a factor of five better than those made with pure silver. Many electric power devices require the wire to be formed into coils for production of strong magnetic fields. Requirements for coils and magnets for electric power applications are described.

Introduction

Since the discovery of the rare-earth-doped oxide, or high temperature, superconductors, private companies have been developing wires and cables for energy-related applications.[1] Wires under development contain bismuth-based

---

2212 and 2223 phase materials and the new thallium powder. The largest market for low critical temperature wire continues to be for medical imaging and high energy physics experiments. However, new markets are developing for high temperature superconducting wires due to reduced refrigeration and capital equipment costs associated with operating electric power equipment at temperatures above 20 K (see Fig. 1).

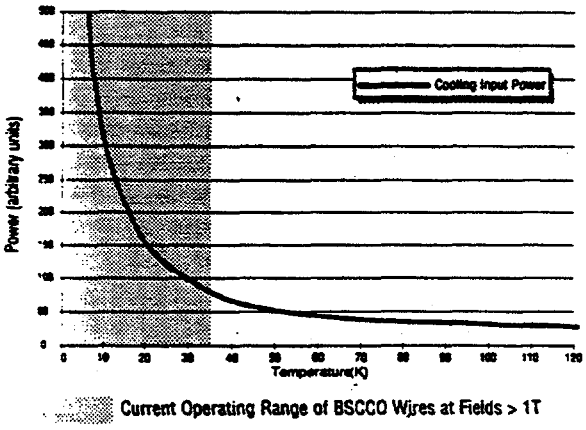

Fig. 1. Refrigeration power requirements vs operating temperature.

Private companies have now developed oxide superconducting powder processes and wire fabricated from the powders as well as prototype components for electric power applications. Such applications include electric motors and generators, transmission lines, fault current limiters, and current limiting reactors and inductors.

Superconducting Wire Development

Silver-sheathed wires are made using a powder-in-tube technique.[2]

Powders are placed into hollow cylinders of silver or silver alloys, sealed, and then processed using a powder-specific series of heat treatments and deformation steps to yield the final, superconducting phase assemblage as well as the desired final form of the wire. Wires may be produced in either flat "ribbon," or tape form (the same final shape used to produce some low-temperature Nb_3Sn wire) or left in a conventional round shape. An optical photomicrograph of the cross section of a 37-filament, 215-m-long tape is shown in Fig. 2.

This wire carries 13 amps at 77 K and has a core critical current density (J_c) of 10,000 A/cm^2. A monofilament wire of the same phase assemblage carried 20 amps at 77 K. As shown in Fig. 3, there is presently more controlled uniformity in critical current over the wire length with the multifilamentary wires. In addition, short (<1 m) lengths of prototype wires now routinely carry nearly 50,000 A/cm^2 at 77 K. The BSCCO-2223 phase, however, will have limitations for high-field applications at liquid nitrogen temperatures due to flux motion. This limitation can become severe for flat tapes used in large coils where there may be a large component of the magnetic field in the direction perpendicular to the plane of the tape. Because of these anisotropy effects, and because the round conductors may offer advantages for use with ac current, several companies are exploring the use of round, multifilamentary BSCCO-2212 superconductors for applications below 40 K.

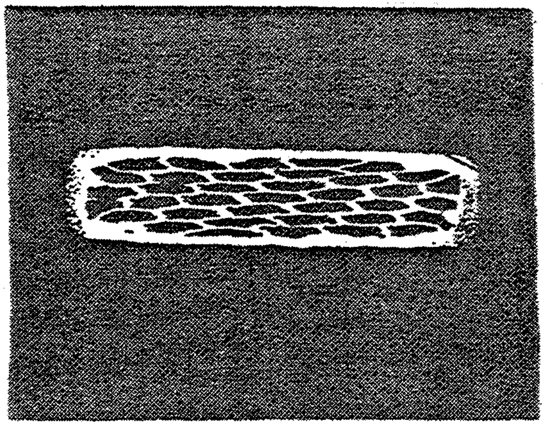

Fig. 2. Optical photomicrograph of mulitfilament BSCCO-2223 wire after heat treatment. There are 37 filaments of 45-µm thickness.

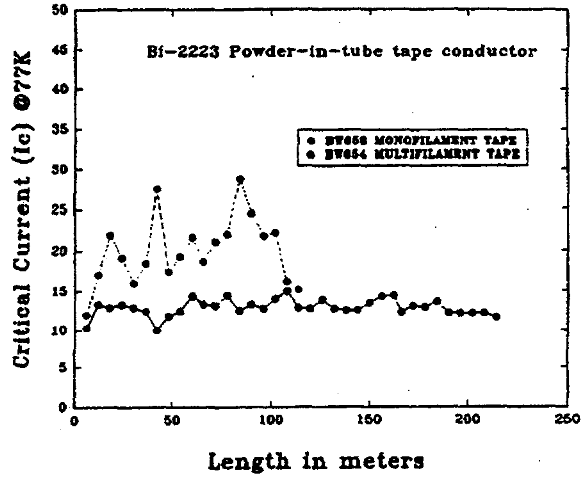

Fig. 3. Variation in critical current density over length for multifilamentary (solid line). and monofilamentary (dashed line) wires.

Round wires show promise

Marketability of the wire, a key concern for any wire manufacturer, can be enhanced by reducing manufacturing steps and by improving material properties over long lengths. Short twist pitch lengths are desirable to enable low-loss operation in the presence of ac current or time-varying magnetic fields as may be present in rotating machinery. Round, multifilament wire processed by the powder-in-tube process is inherently well-suited to the manufacture of long cable lengths. In this case, the superconducting properties are developed through a melt process rather than a roll and sinter operation typical of flat tapes. Fig. 4 shows the microstructure of a 259-filament BSCCO-2212 round wire that carries 165,000 A/cm^2 at 4.2 K. The J_c increases with decreasing filament diameter, with the highest J_c occuring in round wires with 11-µm-size filaments.[3] A summary of typical critical current densities in powder-in-tube wires is shown in Fig. 5.

The Energy Applications

National laboratories have teamed with U. S. industry to enable development of energy applications for the high temperature superconducting wire. Some teaming arrangements take the form of cooperative agreements, which involve no exchange of funding but provide private companies the unique facilities and skilled scientists and engineers necessary for wire development. The national laboratories have active research and development activities under way in most of the energy applications of superconductors, and these partnerships support the goals of each organization.

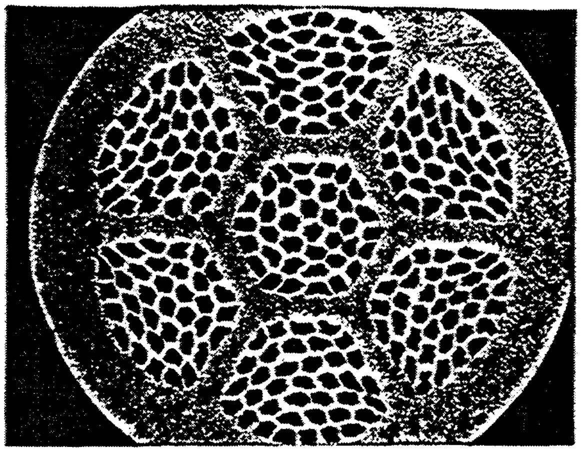

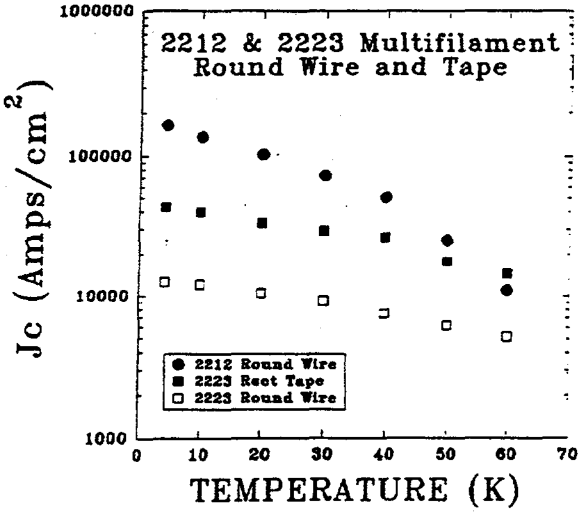

Fig. 4. Optical photomicrograph of 259-filament BSCCO-2212 round wire (before heat treating) with 16-μm average filament width. Wire diameter is 0.05 cm.

Fig. 5. Critical current density as a function of operating temperature for round and tape-form multifilamentary conductors.

High temperature superconductors are being developed for applications such as fault current limiters[4], current downleads,[5] magnetic bearings for energy storage systems,[6-8] motors,[9,10] and generators.[11] Application of the wires has also been suggested for inductors for switching power supplies[12] and for transformers.[13] At least one group has developed a motor/generator concept with stationary superconducting magnets[14] to simplify the cooling system. A good overview of the potential applications of high temperature superconductors in the power area may be found in several of the references.[1, 15]

<u>Wire and Magnet Performance Requirements</u>

Wires must be capable of enduring bending strains of at least 0.2% for most energy applications. One means to increase the strain tolerance of wires and tapes is to strengthen the silver sheath. This sheath becomes work-hardened after the deformations and heat treatments required to produce the wire. A promising technique for strain enhancement is to add aluminum oxide (Al_2O_3) to the silver. As shown in Fig. 6, such dispersion-hardened sheathing can increase the yield strength of the wires by a factor of five.

Coils and magnets must have high overall winding critical current densities, acceptable strain, electrical, and thermal properties, and low joint resistance between lengths of wire.[16] The losses must be minimized in the presence of ac

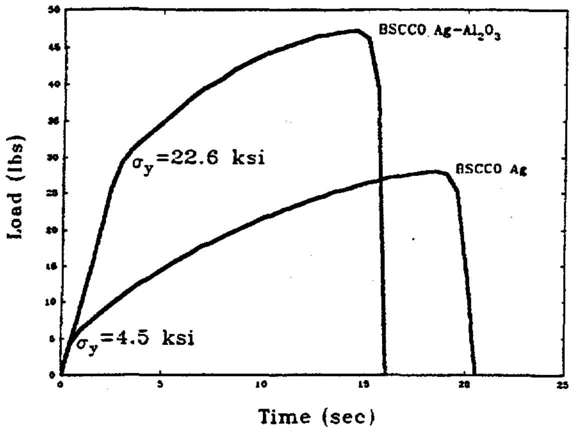

Fig. 6. Effect of Al_2O_3 addition to silver sheath for powder-in-tube wires.

currents or other sources of time-varying magnetic fields, and detection and magnet protection systems must be provided for in the event of a quench. Although quench propagation velocities are expected to be low, normal zone voltages will be adequate to allow detection of normal zones before the conductor overheats.[17]

While early magnets were fabricated using a "wind-and-react" technique,[2] most recent magnets are now made with pre-reacted wire. These magnets required the developmentof efficient react-and-wind fabrication approaches, with low-temperature insulation and epoxy impregnation techniques to maintain the wire's superconducting properties. Record performance for a high temperature superconducting magnet was achieved using a stack of ten pancake coils and three co-wound tapes per pancake (Fig. 7). In a 1-in. bore, the coil produced a field of 2.6 T at 4.2 K and 1.8 T at the relatively warm temperature of boiling neon (27 K).[18] This magnet also produced a record 1.0 T at 4.2 K with a 20-T background field.

Cost Targets

Estimates for the desired cost of the high temperature superconducting wire vary depending on the application and the expected life-cycle costs of the equipment compared to traditional, non-superconducting, or low temperature superconducting versions of that same equipment. For the rotating machinery applications, wire manufacturers have suggested cost targets in the $5-10/kA-m range. Power applications in which the superconductor remains stationary, such as fault current limiters or transmission cables, may command a premium of 2-10 times this cost. By comparison, NbTi wire may be purchased for as little as $1.50/kA-m, depending on the wire specifications, and Nb_3Sn tape is typically $4-8/kA-m, again depending on wire performance.

Early commercialization expected

Some of the earliest commercial prototypes for high temperature superconductors will come from power applications that have less stringent field requirements compared to the large rotating machines. These applications, which include

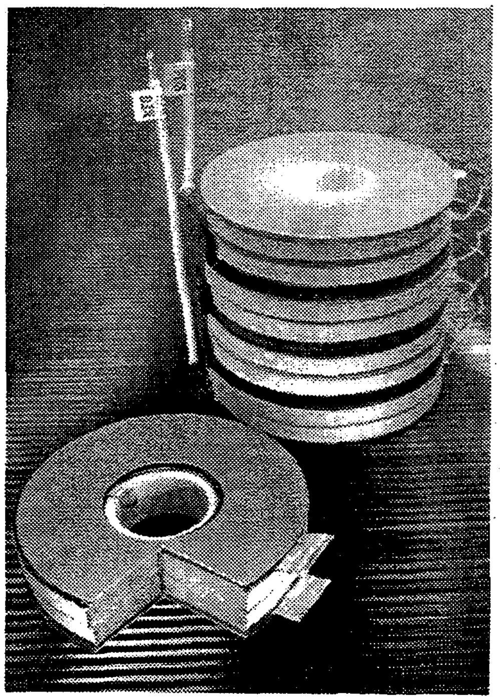

Fig. 7. Prototype high temperature superconducting magnet showing construction similar to world-record 2.6-T magnet (4.2 K). Coil consists of a four-high stack of double pancake modules.

fault current limiters, inductors and transformers, and transmission lines will see full commercial service within the next 5-8 years with continued progress in wire development.

The energy applications that require strong magnetic fields, such as motors and generators, also continue to be developed in the United States and abroad. The U. S. Department of Energy's Superconductivity Partnership Initiative is providing cost-shared contracts to three industry teams. The teams will develop a 100-hp prototype motor, the design and coils for a 100-MVA generator, and a prototype fault current limiter. Electric utility participation on the teams will assure a customer focus on the part of the systems developers and the national laboratories. Development of full commercial products is expected to occur during the next 7-9 years.

Summary

A summary of the wire performance requirements for four different energy applications of high temperature superconductors is shown in Table 1.[19] Wire is being developed with the requisite current-carrying performance at intermediate temperatures to enable early prototype equipment to be designed and fabricated. Cost and manufacturing issues are being addressed by producing round wires with superior electrical transport properties and with great potential for use in ac current and field applications. Strengthened sheathing has been developed to improve the strain tolerance of the wires. Numerous new markets are expected to develop in the electric equipment industry as a result of the development of high temperature superconducting wires.

Table 1. Performance requirements for high temperature superconducting wire

Electric power application	J_c (A/cm^2)	Field (T)	T_{op} (K)	I_c (A)	Wire length (m)	Strain (%)	Bend radius (m)
Fault-current limiter	10^4-10^5	1-3	20-77	10^3-10^4	100	0.2	0.1
Large motor (1000 hp)	10^5	4-5	20-77	500	1000	0.2-0.3	0.05
Generator (100 MVA)	5×10^4	5	20-50	1000	2000	0.2	0.1
Transmission cable	10^4-10^5	<0.2	77	25-30[a]	100	0.4	2

[a] Current in individual wire. Cable will have 100 or more parallel wires.

Acknowledgements

This work was based in part on work performed at the Oak Ridge National Laboratory (ORNL), managed by Martin Marietta Energy Systems, Inc. for the U.S. Department of Energy under contract DE-AC05-84OR21400. The work at ORNL was supported by the U. S. Department of Energy's Office of Energy Management: Superconductivity Program for Electric Power Systems. This work was also partially supported by the U.S. Department of Energy through the SBIR program under grant number DE-FG02-92ER81461.

References

1. D. Von Dollen et al., Energy Applications of High-Temperature Superconductors—A Progress Report, report #TR-101635, Electric Power Research Institute, Palo Alto, California (July 1992).

2. P. Haldar et al., "Fabrication and Properties of High-T_c Tapes and Coils Made from Silver-Clad Bi-2223 Superconductors," paper #CY-6, Cryogenic Engineering Conference, Albuquerque, NM (July 1993).

3. L. R. Motowidlo, G. Galinski, G. Ozeryansky, and E. E. Hellstrom, "The Dependence of J_c on Filament Diameter in Round Multifilament Ag-Sheathed $Bi_2Sr_2Ca_1Cu_2O_x$ Wires Processed in O_2," submitted to Appl. Phys. Lett.

4. T. Verhaege et al., "Experimental 7.2 kV_{rms}/1 kA_{rms}/3 kA_{peak} Current Limiter System," IEEE Trans. Appl. Superc., Vol. 3, No.1, pp. 574-77 (March 1993).

5. J. R. Hull, "High-temperature Superconducting Current Leads," IEEE Trans. Appl. Superc., Vol. 3, No.1, pp. 869-875 (March 1993).

6. C. K. McMichael et al., "Practical Adaptation in Bulk Superconducting Magnetic Bearing Applications," Appl. Phys. Lett., Vol. 60, No. 15, pp. 1983-85 (13 April 1992).

7. R. Weinstein et al., "Progress in J_c, Pinning, and Grain Size, for Trapped Field Magnets," Proc. 6th Int. Symp. on Superc., Hiroshima, Japan (October 1993).

8. M. Okano, "Superconducting Bearings," ISTEC Journal, Vol. 5, No. 3, pp. 28-3 (1992).

9. P. Tixador, C. Berriaud, and Y. Brunet, "Superconducting Permanent Magnet Motor Design and First Tests," IEEE Trans. Appl. Superc., Vol. 3, No. 1, pp. 381-84 (March 1993).

10. C. H. Joshi and R. F. Schiferl, "Design and Fabrication of High Temperature Superconducting Field Coils for a Demonstration DC Motor," IEEE Trans. Appl. Superc., Vol. 3, No. 1, pp. 373-76 (March 1993).

11. C. E. Oberly et al., "Progress Toward Megawatt Class Superconducting Generators which Operate at Greater Than 20 Kelvin," paper #CF-07, Cryogenic Engineering Conference, Albuquerque, NM (July 1993).

12. E. Schempp and C. Russo, "Applications of High-temperature Superconducting Coils as Inductors in Switching Power Supplies," IEEE Trans. Appl. Superc., Vol. 3, No. 1, pp. 563-65 (March 1993).

13. J. A. Dirks et al., High Temperature Superconducting Transformer Performance, Cost, and Market Evaluation, report #PNL-7318, Pacific Northwest Laboratory, Richland, WA (September 1993).

14. J. W. McKeever et al., "Operation of a Test Bed Axial-Gap Brushless DC Rotor with a Superconducting Stator," paper #CF-6, Cryogenic Engineering Conference, Albuquerque, NM (July 1993).

15. T. Sacks, "Super reality- superconductors in power engineering," Electrical Review, Vol. 225, No. 5, pp. 24-6 (March 1992).

16. G. Ries, "Magnet Technology and Conductor Design with High Temperature Superconductors," Cryogenics, Vol. 33, No. 6, pp. 609-14 (June 1993).

17. L. Dresner, " Stability and protection of Ag/BSCCO magnets operated in the 20-40 K range," Cryogenics, Vol. 33, No. 9, pp. 900-09 (September 1993).

18. P. Haldar, et al., from a paper presented at the 6th Inter. Symp. on Superc., Hiroshima, Japan, (October 1993).

19. R. D. Blaugher, "U. S. Technological Competitive Position," proceedings of the U. S. DOE Wire Development Workshop, St. Petersburg, Florida, February 16-17, 1994 (to be published).

MECHANICAL PROPERTIES OF HIGH–TEMPERATURE SUPERCONDUCTING WIRES

K. C. Goretta, J. A. Cluff, J. Joo, M. T. Lanagan, J. P. Singh,
and N. Vasanthamohan

Argonne National Laboratory, Argonne, Illinois 60439 USA

Y. Xin and K. W. Wong

Midwest Superconductivity, Inc., Lawrence, KS 66049 USA

ABSTRACT

Bending strength, fracture toughness, and elastic modulus data were acquired for $YBa_2Cu_3O_x$, $Bi_2Sr_2CaCu_2O_x$, $(Bi,Pb)_2Sr_2Ca_2Cu_3O_x$, and $Tl_2Ba_2Ca_2Cu_3O_x$ bars. These data and thermal expansion coefficients strongly suggest that the maximum possible tensile strain without fracture of bulk tapes or wires is ≈0.2%. In Ag–clad conductors, residual stresses will be of limited benefit, but fractures produced by larger strains can be accommodated by shunting current through the Ag.

INTRODUCTION

Large–scale application of high–temperature superconductors requires high critical current (I_c) and critical current density (J_c). In addition, the superconductors must also exhibit mechanical reliability and chemical and cryogenic stability.[1] In this paper, mechanical property data are summarized for Ag, $YBa_2Cu_3O_x$ (Y-123), $Bi_2Sr_2CaCu_2O_x$ (Bi-2212), $(Bi,Pb)_2Sr_2Ca_2Cu_3O_x$ (Bi-2223), and $TlBa_2Ca_2Cu_3O_x$ (Tl-2223) and implications on wire performance are assessed.

EXPERIMENTAL METHODS

The Ag was 99.9% pure and was purchased as 6.35-mm-diameter rods.[2] The Y-123 powder was synthesized by solid-state reaction at reduced O_2 pressure,[3] and bulk bars were fabricated by cold-pressing and sintering in O_2; in some cases, Ag particles were added.[4,5] The Bi-2212 powder was $Bi_2Sr_{1.7}CaCu_2O_x$ that was consolidated into dense, highly textured forms by sinter forging.[6,7] The Bi-2223 was $Bi_{1.8}Pb_{0.4}Sr_2Ca_2Cu_3O_x$ that also was consolidated by sinter forging.[7-9]

The Tl-2223 powder was prepared as $Tl_2Ba_2Ca_2Cu_3O_x$ from reagent-grade oxides and carbonates. Pellets were cold-pressed and then heated in O_2 at a rate of 1°C/min to 895°C and held for 10 h. The furnace was cooled at 1°C/min to 650°C, held for 5 h, and then turned off, and the pellets were cooled to room temperature. X-ray diffraction revealed that the pellets were highly phase pure.[10]

Geometric densities and microstructures were obtained for all specimens. Elastic-modulus (E) data were obtained from the literature[11-14] or measured by ultrasonic methods.[6]

Strength tests were conducted on bars approximately 3 x 3 x 25 mm. The bars were tested in four-point flexure at a loading rate of 1.27 mm/min. Fracture toughness (K) values were determined by the single-edge notched beam method.[15] The test bars were similar to the bars used for strength testing and were loaded in three-point bending at a rate of 1.27 mm/min. K was calculated from the equation

$$K = 3\,P\,L\,Y\,(C)^{0.5} / B\,W^2\ , \tag{1}$$

where P is the load at fracture, L is the support span (14–19 mm for these tests), Y is a constant related to specimen geometry,[15] C is the notch depth, B is the specimen width, and W is the specimen height.

RESULTS AND DISCUSSION

Data for E, strength (σ), and K are shown in Table 1. The values quoted were taken from materials of high phase purity and density (ρ). The Tl-1223 data are new and were obtained from specimens that were ≈ 88% dense. By available mathematical approximations, these values can be related to those of more dense materials.[16,17]

The data set for Y-123 was taken from dense, nearly randomly oriented polycrystals. The Bi-based specimens, except the Bi-2223 specimen used to determine E, were highly textured. The Tl-2223 exhibited little texture, but also was less dense than the other specimens. Photomicrographs of representative microstructures, obtained by either optical microscopy or scanning electron microscopy (SEM), are shown in Fig. 1. Of all of the specimens, only the Bi-2223 used for σ and E testing exhibited appreciable phase impurity: ≈10% total of Bi-2212 and alkaline-earth cuprates were present.[9]

The Vickers hardness of the Tl-2223 was 2.9 GPa, which is closer to that of Y-123 than of the Bi-based materials.[6,20] Based on the similarity of microstructure, hardness, and modulus, it appears that the mechanical properties of the Tl-based superconductors will be close to those of Y-123.

Table 1. Summary of mechanical-property data and approximate specimen densities for Ag, Y-123, Bi-2212, Bi-2223, and Tl-2223.

Material	ρ (g/cm^3)	E (GPa)	σ (MPa)	K (MPa$\sqrt{m}$)	References
Ag	10.6	77	200*	—	18
Y-123	6.3	148	230	1.5–2.0	4,12,19
Bi-2212	6.5	118, 44**	150	3.0	9,14
Bi-2223	6.4	82	150	3.0	9,11
Tl-2223	6.0	101	—	1.2	This work

* Value for average yield stress.

** Values are for highly textured specimens and represent the a-b plane and c-axis direction.

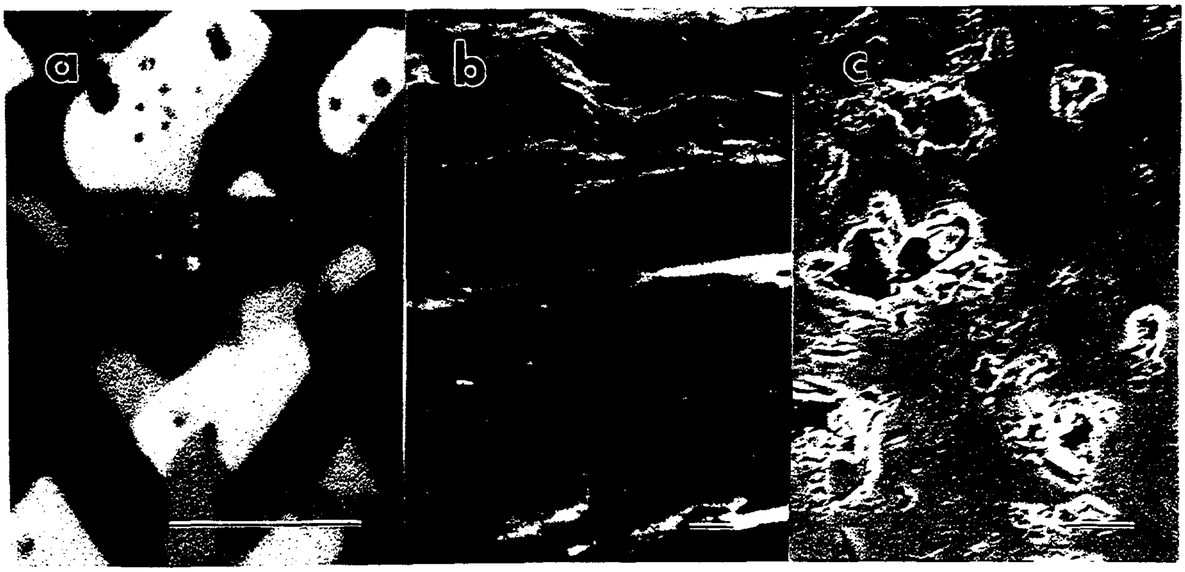

Figure 1. Representative microstructures: (a) optical image of Y-123, (b) SEM image of Bi-2212 fracture surface, and (c) SEM image of Tl-2223; bars = 10 μm.

Although further improvements in strength and fracture toughness can be expected, possibly through creation of composite structures,[21] the values in Table 1 are likely to be close to those of commercial bulk superconductors. These properties define the limits of flexibility of wires and tapes. For any wire or tape of thickness 2t, the bending radius R is defined as[22]

$$\sigma = (t/R)E \; . \tag{2}$$

For a typical strength of ≈200 MPa and a typical modulus of ≈120 GPa, the strain to failure is < 0.2%, but, for sufficiently thin conductors, the allowable bending radius can be quite small.

The presence of an Ag sheath or of Ag in the core substantially complicates predictions of overall strength and flexibility. The thermal expansion coefficient of Ag is higher than the average value for any of the high-temperature superconductors.[18,23-26] Therefore, a favorable residual stress state would be expected in a superconductor/Ag composite. In fact, increases in strength of ≈10% have been observed for Y-123/Ag particulate composites.[5,27] Ag is also less stiff than the superconductors, and thus particulate composites can have lower elastic moduli than the corresponding monolithic material.[28] However, the effect on modulus for a 15% Ag core was only ≈15%. Thus, even with higher strength and lower stiffness, the flexibility of a superconductor/Ag composite is likely to improve by no more than ≈25%. The limit on strain would still be ≈0.2%.

For powder-in-tube tapes, several investigators report strains reaching at least ≈0.5% before J_c is significantly degraded.[29-33] A possible explanation for the high strain tolerance is that favorable residual stresses are imparted by the Ag sheath. Recent neutron-diffraction measurements of residual strains in Ag-clad Bi-2223 tapes cast serious doubt on that possibility. It was found that for highly textured tapes the directions in the Bi-2223 near the c-axis were indeed in a compressive stress state, but the a-b plane was in residual tension.[34] Fracture will occur perpendicular to the a-b plane; thus residual stresses induced by the Ag sheath are deleterious.

A more likely explanation for the apparent strain tolerance of Ag-clad conductors is that current can shunt through the Ag where cracks are present and reenter the superconductor once it is past the crack. A mathematical model of this effect was published recently.[35] The model indicated that, if the resistivity of the superconductor/Ag interface is sufficiently low relative to that of Ag, nearly all of the current will return to the superconductor from the Ag. The resistivity of pure Ag at 77 K is ≈0.3 μΩ-cm;[36] thus, it is quite reasonable that the current will return to the superconductor. Generation of 1 μV of voltage may thus require several transverse cracks.

SUMMARY

The basic mechanical properties of all high–temperature superconductors are similar. Bi-2212 and B-2223 are slightly softer than the others, and the Bi-based conductors are much more easily textured. The maximum strain that these ceramics can sustain is ≈0.2%. Ag particles can improve strain tolerance by ≈25% at most, but Ag sheaths may impart unfavorable residual stresses. The apparent strain tolerance of Ag-clad wires is probably due to current shunting through the Ag sheath at cracks.

ACKNOWLEDGMENTS

This work was supported by the U.S. Department of Energy (DOE), Energy Efficiency and Renewable Energy, as part of a DOE program to develop electric power technology, under Contract W–31–109–Eng–38; and Midwest Superconductivity, Inc. The efforts of N. V. were performed in partial fulfillment of the requirements for the Ph.D. degree from the Illinois Institute of Technology, Chicago.

REFERENCES

1. T. Nakahara, in World Congress on Superconductivity, C. G. Burnham and R. D. Kane, ed. (World Scientific, Singapore, 1988) p. 88.
2. C.-T. Wu, M. J. McGuire, G. A. Risch, R. B. Poeppel, K. C. Goretta, H. M. Herro, and S. Danyluk, in 2nd World Congress on Superconductivity, C. G. Burnham, ed. (World Scientific, Singapore, 1992) p. 370.
3. U. Balachandran, R. B. Poeppel, J. E. Emerson, S. A. Johnson, M. T. Lanagan, C. A. Youngdahl, D. Shi, K. C. Goretta, and N. G. Eror, Mater. Lett. 8, 454 (1989).
4. K. C. Goretta, N. Chen, M. T. Lanagan, W. Wu, J. P. Singh, R. A. Olson, J. L. Routbort, and R. B. Poeppel, in Advances in Powder Metallurgy & Particulate Materials – 1992, Volume 8 (Metal Powder Industries Federation, Princeton, NJ, 1992) p. 271.
5. J. P. Singh, J. Joo, T. Warzynski, and R. B. Poeppel, J. Mater. Res. 8, 1226 (1993).
6. C.-Y. Chu, J. L. Routbort, N. Chen, A. C. Biondo, D. S. Kupperman, and K. C. Goretta, Supercond. Sci. Technol. 5, 306 (1992).
7. K. C. Goretta, M. E. Loomans, L. J. Martin, J. Joo, R. B. Poeppel, and N. Chen, Supercond. Sci. Technol. 6, 282 (1993).
8. S. E. Dorris, B. C. Prorok, M. T. Lanagan, S. Sinha, and R. B. Poeppel, Physica C 212, 66 (1993).
9. L. J. Martin, K. C. Goretta, J. Joo, J. P. Singh, S. R. Olson, S. Wasylenko, R. B. Poeppel, and N. Chen, Mater. Lett. 17, 232 (1993).
10. Y. Xin, B. R. Xu, S. Nasrazadni, W. S. He, D. F. Lu, G. F. Sun, K. W. Wong, and D. Knapp, J. Mater. Res. 9, 1672 (1994).
11. H. M. Ledbetter, S. A. Kim, R. B. Goldfarb, and K. Togano, Phys. Rev B 39, 9689 (1989).
12. H. Ledbetter, J. Mater. Res. 7, 2905 (1992).
13. J. Dominec, Supercond. Sci. Technol. 6, 153 (1993).
14. F. Chang, P. J. Ford, G. A. Saunders, J. Li, D. P. Almond, B. Chapman, M. Cankurtaran, R. B. Poeppel, and K. C. Goretta, Supercond. Sci. Technol. 6, 484 (1993).
15. W. F. Brown, Jr. and J. E. Srawley, in Plane Strain Crack Toughness Testing of High Strength Metallic Materials – ASTM STP 410 (ASTM, Philadelphia, 1967) p. 12.

16. A. S. Wagh, R. B. Poeppel, and J. P. Singh, J. Mater. Sci. 26, 3862 (1991).
17. A. S. Wagh, J. P. Singh, and R. B. Poeppel, J. Mater. Sci. 28, 3589 (1993).
18. CRC Handbook of Chemistry and Physics (CRC Press, Boca Raton, FL, 1989).
19. K. C. Goretta, M. L. Kullberg, D. Bär, G. A. Risch, and J. L. Routbort, Supercond. Sci. Technol. 4, 544 (1991).
20. A. Goyal, P. D. Funkenbusch, D. M. Kroeger, and S. J. Burns, J. Appl. Phys. 71, 2363 (1992).
21. J. P. Singh, H. J. Leu, R. B. Poeppel, E. Van Voorhees, G. T. Goudey, K. Winsley, and D. Shi, J. Appl. Phys. 66, 3154 (1989).
22. K. C. Goretta, J. T. Dusek, J. P. Singh, M. T. Lanagan, U. Balachandran, S. E. Dorris, and R. B. Peoppel, in World Congress on Superconductivity, C. G. Burnham, ed. (World Scientific, Singapore, 1988) p. 311.
23. T. Hashimoto, K. Fueki, A. Kishi, T. Azumi, and H. Koinuma, Jpn. J. Appl. Phys. 27, L214 (1988).
24. R. H. Arendt, M. F. Garbauskas, C. A. Meyer, F. J. Rotella, J. D. Jorgensen, and R. L. Hitterman, Physica C 182, 73 (1991).
25. R. H. Arendt, M. F. Garbauskas, C. A. Meyer, F. J. Rotella, J. D. Jorgensen, and R. L. Hitterman, Physica C 194, 397 (1992).
26. M. Mouallem-Bahout, J. Gaudé, G. Calvarin, J.-R. Gavarri, and C. Carel, Mater. Lett. 18, 181 (1994).
27. D. S. Kupperman, J. P. Singh, J. Faber, Jr., and R. L. Hitterman, J. Appl. Phys. 66, 3396 (1989).
28. M. Cankurtaran and G. A. Saunders, Supercond. Sci. Technol. 5, 529 (1992).
29. S. Jin and J. E. Graebner, Mater. Sci. Eng. B7, 243 (1991).
30. T. A. Miller, J. E. Ostenson, Q. Li, L. A. Schwartzkopf, D. K. Finnemore, J. Righi, R. A. Gleixner, and D. Zeigler, Appl. Phys. Lett. 58, 2159 (1991).
31. J. W. Ekin, D. K. Finnemore, Q. Li, J. Tenbrink, and W. Carter, Appl. Phys. Lett. 61, 858 (1992).
32. J. P. Singh, J. Joo, N. Vasanthamohan, and R. B. Poeppel, J. Mater. Res. 8, 2458 (1993).
33. S. Ochiai, K. Hayashi, and K. Osamura, Cryogenics 33, 976 (1993).
34. D. S. Kupperman, Argonne National Laboratory, unpublished results (1994).
35. Y. S. Cha, M. T. Lanagan, K. E. Gray, V. Z. Jankus, and Y. Fang, Appl. Supercond. 2, 47 (1994).
36. R. A. Matula, J. Phys. Chem. 8, 1147 (1979).

PROGRESS IN DEVELOPMENT OF TAPES AND MAGNETS MADE FROM Bi-2223 SUPERCONDUCTORS

U. Balachandran and A. N. Iyer
Energy Technology Division
Argonne National Laboratory
Argonne, IL 60439

P. Haldar and J. G. Hoehn, Jr.,
Intermagnetics General Corporation
Latham, NY 12110

L. R. Motowidlo
IGC Advanced Superconductors, Inc.
Waterbury, CT 06704

Abstract

Long lengths of $(Bi,Pb)_2Sr_2Ca_2Cu_3O_x$ tapes made by powder-in-tube processing have been wound into coils. Performance of the coils has been measured at temperatures of 4.2 to 77 K, and microstructures have been examined by X-ray diffraction and electron microscopy and then related to superconducting properties. A summary of recent results and an overview of future goals are presented.

Introduction

Powder-in-tube (PIT) processing has been used by several research groups to obtain very high critical current density (J_c) in short lengths of Ag-clad Bi-Sr-Ca-Cu-O (BSCCO) superconductors. Sato et al. and Yamada et al. reported J_c values of 5.4×10^4 A/cm^2 and 3.3×10^4 A/cm^2, respectively, at 77 K and zero applied field. The NKT Research Center in Denmark reported J_c values as high as 6.9×10^4 A/cm^2.[1-9] Because the J_c values of BSCCO tapes at 4.2 K and in high magnetic fields are significantly higher than those of low-T_c superconductors such as NbTi and Nb_3Sn, BSCCO can be used to replace presently used low-T_c superconductors. Additionally, BSCCO conductors can be used well beyond the temperature and field capability of low-T_c superconductors. The success in short-length tapes has not only helped researchers better understand the PIT process, but has also encouraged them to develop techniques for fabricating long lengths of robust conductors.

The high J_c values of BSCCO tapes can be attributed to the strong c-axis orientation of its grains. Good grain alignment improves intergrain connectivity, thereby increasing the current–carrying capacity of the material. Alignment and texturing of the BSCCO grains can be obtained very easily by the PIT process, compared to various other conventional techniques such as sinter forging, hot isostatic processing, and jelly roll.[3-4,8,10-11] At 77 K, the transport properties of conventionally consolidated and sintered BSCCO samples are very low. On the other hand, tapes fabricated by the PIT process seem to exhibit very high J_cs.[1,8-12] The silver sheath used in the PIT process provides good thermal, mechanical, and electrical stability. Additionally, because the PIT process is analogous to the current manufacturing technology for fabricating low-T_c superconductors, it can be very easily modified to fabricate high-T_c superconductors at the industrial level.

The high–J_c values mentioned above were obtained by subjecting the short-length tapes to a series of uniaxial–pressing and heat–treatment schedules. Potential applications of high-T_c superconductors include power transmission cables, current leads, motors, generators, magnetic resonance imaging (MRI), and superconducting magnetic energy storage (SMES) systems. Most of these applications require that long lengths of robust and flexible conductors, with uniform and reproducible properties, be manufactured.[5,8,12-14] Because it is impossible to meet these goals with uniaxial pressing, considerable effort is being expended to overcome this problem. Employing a two-step rolling and heat-treatment procedure, Intermagnetics General Corporation and Argonne National Laboratory successfully fabricated long lengths of Ag-clad BSCCO conductors. These tapes were cowound into prototype pancake-shaped coils by the "wind-and-react" approach. Test magnets were then fabricated by stacking the pancake coils and connecting them in series. The coils and magnets have been characterized at various temperatures and magnetic fields.

During fabrication and service, the tapes are subjected to significant axial and bending stresses. Additionally, the temperature gradient and magnetic field generated induces additional stresses in the material. These factors could lead to degraded transport properties. Because the mechanical properties of Ag are inadequate to withstand all stresses, considerable effort is being focused on improving the strain tolerance of the tapes.[15-22] Techniques such as addition of Ag to the superconducting powder, use of alloy sheath material such as AlNiMg and Ag-Al_2O_3 as an alternative to Ag, and fabrication of multifilament conductors have been used to improve the mechanical characteristics of the Ag-clad BSCCO tapes.[1,17-22]

Singh et al. reported that strain tolerance of the tape can be improved, without much loss in J_c, by addition of Ag to the superconducting core. They observed that for a 1.2% applied strain, 90% of the original J_c was retained in the BSCCO-Ag composite, compared to only 40% in the monolithic tape.[17] Although the role of Ag is not yet fully understood, it is known to reduce the melting temperature and alter the reaction kinetics of the superconductor core. Additionally, it helps to prevent crack growth and assists in the texturing of the superconductor grains.[11] Sato et al. developed a 1296-filament BSCCO superconducting wire with a much better strain tolerance (1.2%) than that of monocore tapes (0.2%).[1] Dou et al. studied the mechanical properties of monocore and multifilament conductors containing 19 filaments. The critical bend strain and tensile strain of the multifilament conductor was found to be 0.8% and 0.65%, respectively, compared to 0.2% for the monocore conductor.[19] Intermagnetics General Corporation fabricated a 61-filament BSCCO-2212 conductor with sheathing of both pure Ag and Ag-Al_2O_3. Using the principle of dispersion strengthening, they obtained improved mechanical properties in the sheath material.[18,22] This paper discusses some of the issues of fabrication and characterization of long lengths of mono- and multifilament Ag-clad BSCCO conductors.

Experimental Procedure

The precursor powder for the PIT process was obtained by the solid-state reaction of high-purity oxides and carbonates of Bi, Pb, Sr, Ca, and Cu. The powders were mixed and calcined at ≈800-850°C for ≈50 h. To obtain a more homogeneous powder, intermittent grinding was employed during the calcination stage. For some of the best results, the cation ratio was Bi:Pb:Sr:Ca:Cu = 1.8:0.4:2:2.2:3. The powders were then packed into high-purity Ag tubes by mechanical agitation. The tubes were swaged, drawn through a series of dies to a final diameter of ≈2 mm, and then rolled at the rate of about 10% reduction per pass to a final thickness of ≈0.1 mm. Short lengths of tape were cut and subjected to a series of thermomechanical treatments consisting of uniaxial pressing and heat treatment. Several parameters are involved in the PIT process, including powder composition, homogeneity, reduction ratio, heat–treatment temperature, time, and atmosphere. All should be carefully controlled in order to obtain the desired properties.

Although very high J_c has been obtained in short-length tapes by uniaxial pressing, the process is not useful for fabricating long length conductors. A more practical approach such as rolling is required. Using two-step rolling and intermediate and final heat treatments, we have manufactured long lengths of Ag-clad BSCCO conductors. Conductors up to several meters in length (30 to 100 m) and as thin as ≈0.1 mm have been processed. Pancake-shaped coils were formed by the "wind-and-react" approach, wherein the tape is first cowound on an alumina former and then heat treated. Ceramic insulation was used to separate each turn in the coil. Test magnets were fabricated by stacking together and connecting in series a set of the pancake-shaped coils. The magnets were characterized at 4.2, 27, and 77 K in background fields up to 20 T.

For the multifilament conductors, several sections of monocore Ag-clad conductors were assembled into a second Ag tube with an outer diameter (OD) of 12.70 mm and an inner diameter (ID) of 9.36 mm. Using a drawing schedule similar to that used for monocore conductor, we drew the tubes to a diameter of ≈2.5 mm. Finally, with a special shape-forming technique, the tubes were rolled into tapes with a final thickness of ≈0.5 mm. Multifilament BSCCO-2212 conductors have also been fabricated using Ag and Ag-Al_2O_3 as the sheath material. The conductor tapes were first heat treated at 885°C for ≈0.3 h, followed by slow cooling to 850°C. The tapes were held at this temperature for ≈111 h. The multifilament conductor with Ag-Al_2O_3 sheathing was given periodic annealings at ≈350°C to relieve work-hardening of the sheath.

Results and Discussion

Short-length samples that had been subjected to a series of uniaxial-pressing and heat–treatment schedules exhibited J_c values of $>4 \times 10^4$ A/cm^2 at 77 K and zero-applied field, and 2×10^5 A/cm^2 at 4.2 K and zero-applied field. Haldar et al. showed that by increasing the superconducting fraction of the BSCCO tapes, the current–carrying capacity of the tapes can be enhanced considerably.[12] In addition to J_c measurement, the short samples were characterized by X-ray diffraction and scanning electron microscopy. Qualitative analysis of J_c as a function of number of thermomechanical treatments reveals that J_c initially increases, reaches a peak, and then finally decreases. This variation has been reported by several groups and has been attributed to the variation in degree of texturing and local inhomogeneities present in the tape.[23-25] The short tapes have been characterized at various temperatures and applied magnetic field. Figure 1 shows J_c, as a function of applied field up to 3 T, at 77 K and at pumped liquid nitrogen temperature (64 K). These measurements were made at Brookhaven National Laboratory. At 64 K, J_c in the field parallel to the tape surface increased by one order of magnitude at 2 T over that at 77 K.

We fabricated long conductors (≈30-70 m), wound them into pancake-shaped coils, and tested the coils. J_c values were ≈60-80% of the short rolled samples at 77 K. The difference in J_c values between the short and long conductors can be attributed to inhomogeneities and microcracks along the length of the tapes. Additionally, the coils are subjected to large self-fields

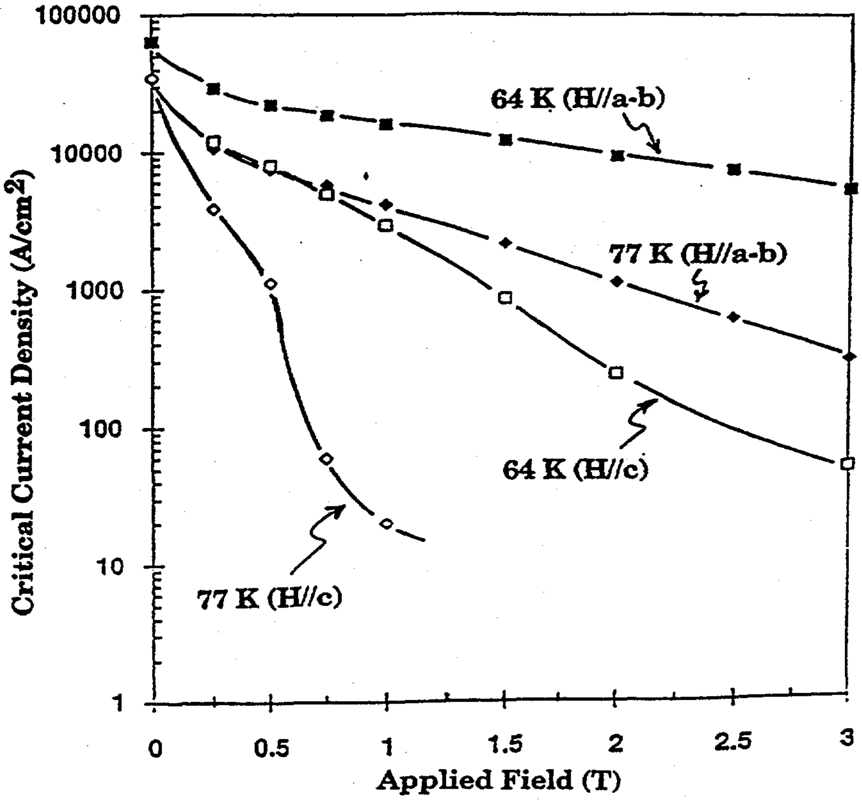

Fig. 1. Critical current density, as a function of applied magnetic field, of short samples at liquid nitrogen (77 K) and pumped liquid nitrogen (64 K) temperatures.

during testing, whereas the short tapes do not generate much self-field. A test magnet was fabricated by stacking together and connecting in series 10 pancake coils, each containing three 16–m lengths of BSCCO-2223 conductor. Total length of the conductor used in the magnet was ≈480 m. The magnet was characterized at 4.2, 27, and 77 K. At 77 K, the maximum field generated was 0.36 T, while at 27 and 4.2 K it was 1.8 and 2.6 T, respectively. Figure 2 shows another test magnet fabricated with eight double–pancake coils, each containing three 16–m lengths of BSCCO conductors. Total length of the conductor was 768 m. Figure 3 shows the characteristics of this magnet at 4.2 and 27 K, in background fields up to 20 T. The magnet generated a field of ≈1 T in a background field of 20 T at 4.2 K. These results are very encouraging because they show not only the robustness of the high-T_c superconductor magnet but also that it can generate substantial field in a very high background field. The results also show that the high-T_c coil can be used as an insert to generate a very high field in a hybrid magnet containing low-T_c superconductors. Additionally, the high-T_c magnet can be used to meet the stringent requirements of field–sensitive applications such as MRIs.

Multifilament conductors containing 37 filaments of up to 230 m in length have also been fabricated. Figure 4 shows I_c as a function of length; the consistent results demonstrate the considerable improvement in development of multifilament conductors. J_c of a multifilament BSCCO-2212, with Ag-Al_2O_3 as the sheath material, was ≈1-3 x 10^3 A/cm^2 at 77 K, 4.5 x 10^4 A/cm^2 at 4.2 K and zero applied field, and 2.5 x 10^4 A/cm^2 at 4.2 K and 12 T. The tensile properties of the BSCCO-2212/Ag and BSCCO-2212/Ag-Al_2O_3 have also been studied. Figure 5 shows the stress/time relationship of the yield strength of multifilament conductors. At room temperature, yield strength of the Ag–Al_2O_3–sheathed BSCCO-2212 was greater by a factor of 4 than that of Ag–sheathed BSCCO. These results indicate that long lengths of multifilament conductors with improved mechanical properties can be fabricated with alternative sheathing material.

Summary

By carefully controlling the various parameters involved in the PIT process, we have obtained very high J_cs in Ag-clad BSCCO superconductors. Pancake–shaped coils and test magnets have been fabricated from long–length conductors and characterized at various temperatures and magnetic

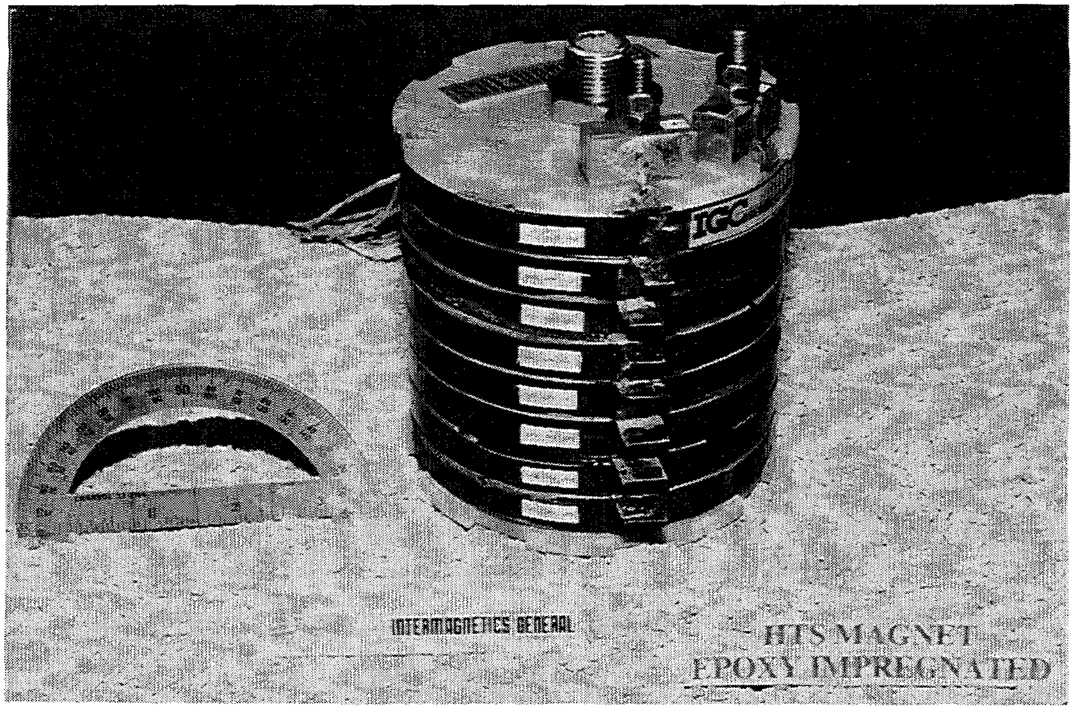

Fig. 2. Test magnet assembled by stacking eight double–pancake coils in series.

fields. The results indicate that devices capable of operating at higher temperatures and magnetic fields could now be fabricated from high-T_c superconductors. The issue of conductor strain tolerance has also been addressed.

Acknowledgments

The work at Argonne National Laboratory, and part of the work at IGC is supported by the U.S. Department of Energy (DOE), Energy Efficiency and Renewable Energy, as part of a DOE program to develop electric power technology, under Contract W-31-109-Eng-38; work at IGC is also supported by the DOE SBIR Program Phase II work, conducted under Contract DE-FG02-92-ER81461. The authors thank Y. Iwasa of the Francis Bitter National Magnet Laboratory at the Massachusetts Institute of Technology, and M. Suenaga of Brookhaven National Laboratory, for the low-temperature and high-field measurements.

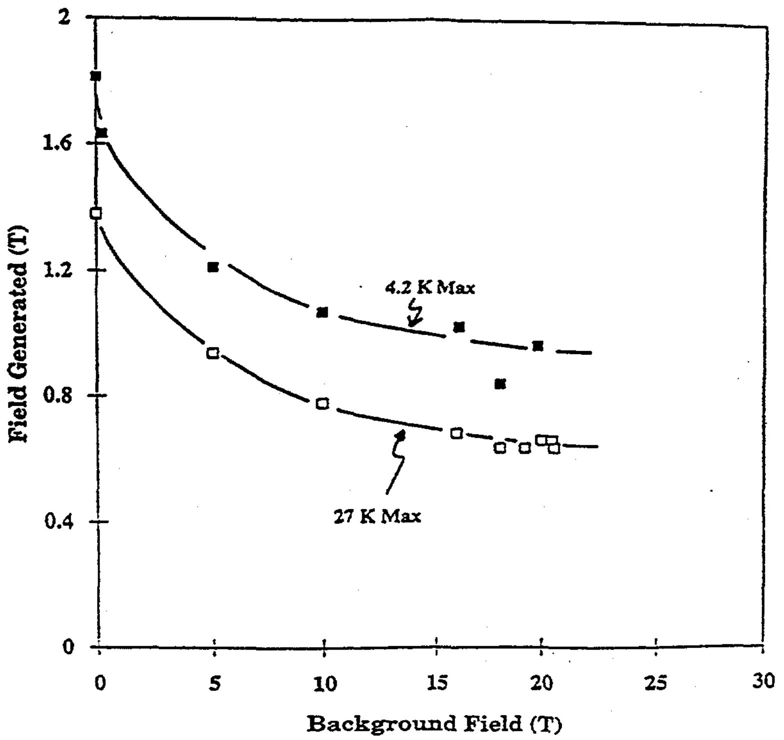

Fig. 3. Field generated by high–T_c magnet vs. background field at 4.2 and 27 K.

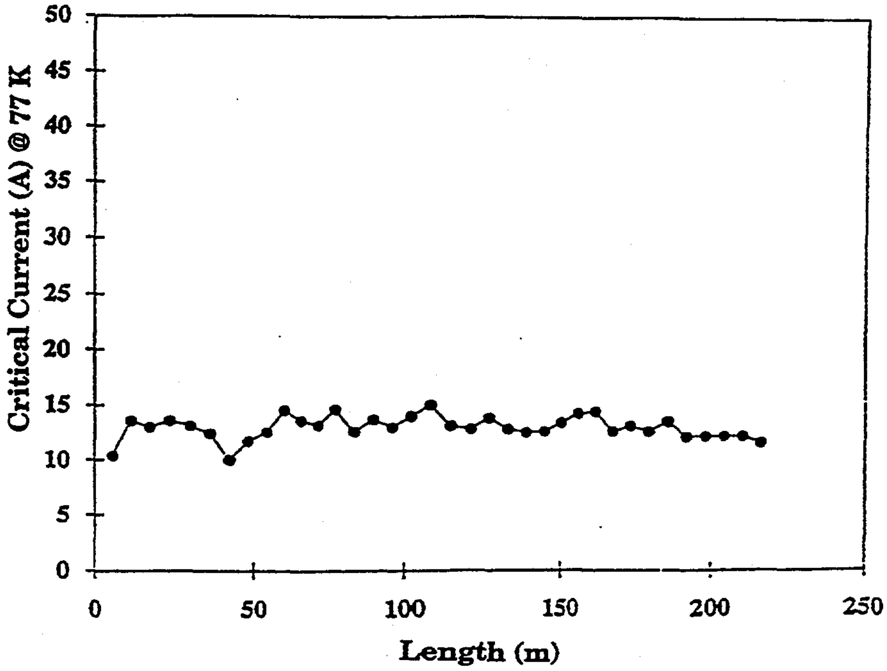

Fig. 4. I_c at 77 K of multifilament conductor containing 37 filaments.

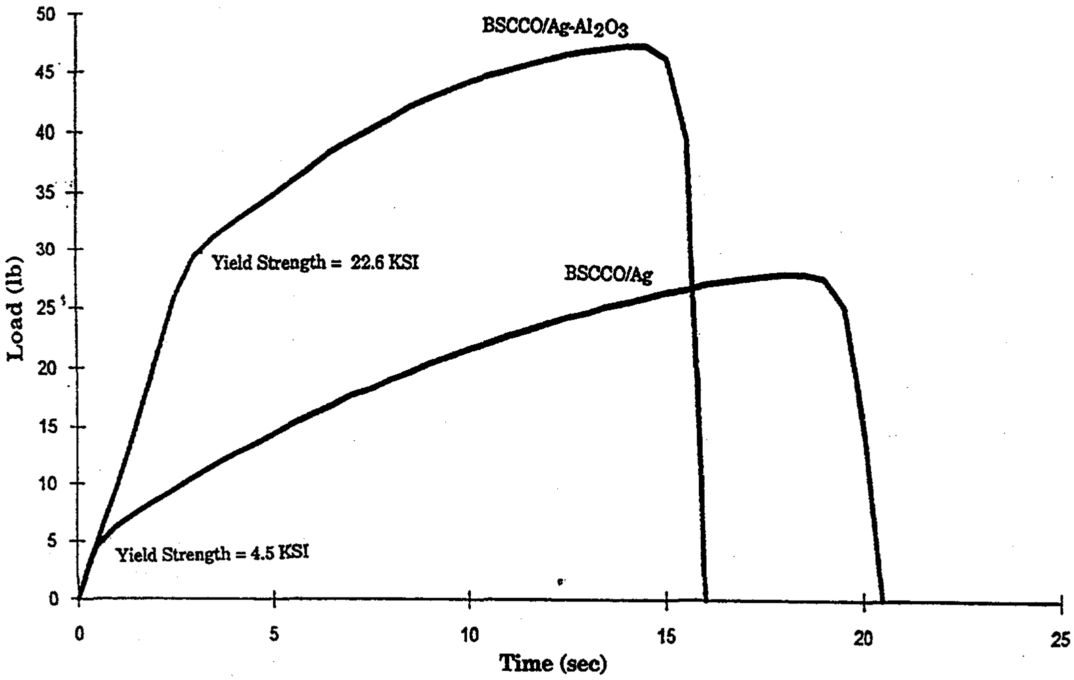

Fig. 5. Stress/time curves of BSCCO–2212/Ag and BSCCO–2212/Ag–Al_2O_3 multifilament conductors.

References

1. K. Sato, T. Hikata, H. Mukai, M. Ueyama, N. Shibuta, T. Kato, T. Masuda, M. Nagata, K. Iwata, and T. Mitsui, "High-J_c Silver-Sheathed Bi-Based Superconducting Wires," IEEE Trans. Mag., **27** 1991, 1231-1238.
2. Y. Yamada, B. Obst, and R. Flukiger, "Microstructural Study of Bi(2223)/Ag Tapes with J_c (77 K, 0 T) Values up to 3.3 x 10^4 A/cm^2," Supercond. Sci. Technol., **4** 1991, 165-171.
3. K. H. Sandhage, G. N. Riley, Jr., and W. L. Carter, "Critical Issues in the OPIT Processing of High-J_c BSCCO Superconductors," J. Metals, **43** (1991) 21-25.
4. E. E. Hellstrom, "Important Considerations for Processing of Bi-Based High-Temperature Superconducting Tapes and Films for Bulk Applications," MRS Bulletin, **XVII** 1992, 45-51.
5. R. Flukiger, B. Hensel, A. Jeremie, A. Perin, and J. C. Grivel, "Processing of Classical and High T_c Superconducting Wires," Appl. Supercond., **1** 1993, 709-723.

6. K. Heine, J. Tenbrink, and M. Thoner, “High-Field Critical Current Densities in $Bi_2Sr_2Ca_1Cu_2O_{8+x}$/Ag Wires,” Appl. Phys. Lett., **55** 1989, 2441-2443.
7. T. Hikata, K. Sato, and H. Hitotsuyanagi, “Ag-Sheathed Bi-Pb-Sr-Ca-Cu-O Superconducting Wires with High Critical Current-Density,” Jpn. J. Appl. Phys., **28** 1989, L82-L84.
8. S. Jin, "Processing of Long Lengths of Superconductors," U. Balachandran, E. W. Collings, and A. Goyal, eds., The Minerals, Metals & Materials Society, 1994, 3-12.
9. R. Flukiger et al., "High Critical Current Densities in Bi(2223)/Ag Tapes," Supercond. Sci. Technol., **5** 1992, S61-68.
10. S. X. Dou and H. K. Liu, "Ag-Sheathed Bi(Pb)SrCaCuO Superconducting Tapes," Supercond. Sci. Technol., **6** 1993, 297-314.
11. U. Balachandran, A. N. Iyer, P. Haldar, and L. R. Motowidlo, "Processing and Properties of Commercially Viable High-T_c Bi-2223 Tapes and Coils Fabricated by the Powder-In-Tube Technique," J. Metals, **45** 1993, 54-57.
12. P. Haldar, J. G. Hoehn, Jr., L. R. Motowidlo, and U. Balachandran, "Processing of Long Lengths of Superconductors," U. Balachandran, E. W. Collings, and A. Goyal, eds., The Minerals, Metals & Materials Society, 1994, 23-30.
13. C. H. Rosner, M. S. Walker, P. Haldar, and L. R. Motowidlo, “Status of HTS Superconductors: Progress in Improving Transport Critical Current Densities in HTS Bi-2223 Tapes and Coils,” Cryogenics, **32** 1992, 940-948
14. J. Tenbrink, M. Wilhelm, K. Heine, and H. Krauth, "Development of High-T_c Superconductor Wires for Magnet Applications," IEEE Trans. Magn., **27** 1991, 1239-1246.
15. J. W. Ekin, "Materials at Low Temperatures," R. P. Reed and A. F. Clark, eds., American Society for Metals (1983), 494-496.
16. G. Reis, "Magnet Technology and Conductor Design with High Temperature Superconductors," Cryogenics, **33** 1993, 609-614.
17. J. P. Singh, J. Joo, N. Vasanthamohan, and R. B. Poeppel, "Role of Ag Additions in the Microstructural Development, Strain Tolerance, and Critical Current Density of Ag-Sheathed BSCCO Superconducting Tapes," J. Mater. Res., **8** 1993, 2458-2464.
18. L. R. Motowidlo, “High Strength Mono and Multifilament 2212 BSCCO Superconductors for High Field Applications,” DOE Final Rept. No. DE-FG02-92ER81461, Jan. 1993. Also presented at MRS Spring Meeting, San Fransisco, CA, April 12-16 (1993).

19. S. X. Dou, Y. C. Guo, J. Yau, and H. K. Liu, "Effect of Interfacial Layers on the Mechanical Properties of Ag-Clad Bi-Based Superconducting Composite Tapes," Supercond. Sci. Technol., **6** 1993, 195-198.
20. S. X. Dou, H. K. Liu, Y. C. Guo, C. C. Sorrell, and P. Munroe, "Flexible Superconducting Ag-clad Bi-Pb-Sr-Ca-Cu-O Wires," Physica C, **185-189** 1991, 2493-2496.
21. T. A. Miller, J. E. Ostenson, Q. Li, L. A. Schwartzkopf, D. K. Finnemore, J. Righi, R. A. Gleixner, and D. Zeigler, "Strain Tolerant Microfilamentary Conductors of $Bi_2Sr_2CaCu_2O_{8-\delta}$," Appl. Phys. Lett., **58** 1991, 2159-2161.
22. U. Balachandran, A. N. Iyer, P. Haldar, J. G. Hoehn, Jr., L. R. Motowidlo, and G. Galinski, "Recent Issues in Fabrication of High-T_c Magnets and Long-Length Multifilament Conductors," Applied Superconductivity (1994, in press).
23. A. N. Iyer, U. Balachandran, P. Haldar, J. G. Hoehn, Jr., and L. R. Motowidlo, "Processing of Long Lengths of Superconductors," U. Balachandran, E. W. Collings, and A. Goyal, eds., The Minerals, Metals & Materials Society, 1994, 13-22.
24. J. Joo, J. P. Singh, and R. B. Poeppel, "Effects of thermomechanical treatment on phase development and properties of Ag-sheathed Bi(Pb)-Sr-Ca-Cu-O superconducting tapes," Supercond. Sci. Technol., **6** 1993, 421-428.
25. R. Flukiger, T. Graf, M. Decroux, C. Groth, and Y. Yamada, "Critical Currents in Ag Sheathed Tapes of the 2223-phase in (Bi,Pb)-Sr-Ca-Cu-O," IEEE Trans. Mag., **27** 1991, 1258-1263.

HIGH TEMPERATURE SUPERCONDUCTORS AS A TECHNOLOGICAL DISCONTINUITY IN THE POWER CABLE INDUSTRY.

T P Beales and J S McCormack

BICC Cables Ltd, Superconductivity Group, Hedgeley Road,
Hebburn, Tyne and Wear NE31 1XR, England.

ABSTRACT

The advent of superconductivity above 77 K represents to the power cable industry a technological discontinuity analogous to that seen in the copper telecommunications industry by the arrival of optical fibres. This phenomenon is discussed along with technical criteria and performance targets needed for high temperature superconducting wire to have an economic impact in transmission cables.

1. TECHNOLOGICAL DISCONTINUITIES: A COMPARISON

Analysis of the emergence of high temperature superconductivity in the cable industry has strong parallels with that already seen for optical fibres [1]. Both innovations represent a discontinuity in which a known technology can be displaced by a new process which is superior in at least one performance criteria. This presents both new opportunities for business but is also a threat to established markets and careful management of the technological change with adoption of appropriate technological strategies is required for commercial success [2,3].

Utterback and Kim have defined technological discontinuities invading stable businesses as four basic types [4]. Type 1 can be described as a Product-Process discontinuity which involves a brand new product and manufacturing process. An example of this is the introduction of transistors to replace vacuum tubes in the electronics industry. Type 2 is a Product discontinuity where a new product using similar or existing manufacturing skills replaces an existing one. An example is the replacement of components with discrete transistors by integrated circuits. Type 3 is the Process discontinuity where an old product is made using a new manufacturing route. An example is the replacement of open hearth furnace by oxygen processing in steel making. Type 4 is the Process-Product in which an existing product is made by a radical new manufacturing route which totally changes the companies' manufacturing. An example of this is the introduction of quartz watches over clockwork products.

High temperature superconductivity can be defined as a totally new product *vis à vis* copper wire. The manufacturing methods used to form high temperature superconductors from MOCVD to powder-in-tube are established manufacturing routes in industries as diverse as semiconductors to fire-proof cabling but not in an established electro-ceramic superconductor industry. We can define high temperature superconductivity as a type 1 case ie a Product-Process discontinuity which is the most difficult type to manage successfully. Each of the industry players will regard this transition as being different in magnitude and scope and will enter into it carrying a different technological baggage. This will affect their psychology of perception as to the threats and opportunities of high temperature superconductors.

Using the analogy with the development of optical fibres we can group the industry players into five categories based on each companies technology background in telecommunications or power industry for the case of optical fibres and high temperature superconductivity respectively. Group 1 is the outsiders, typically materials manufacturers. In telecommunications these were companies like Corning, Du Pont, Hereas and Pilkington, in electrical transmission they are Du Pont, ICI, Hoechst, Merck etc. Group 2 are the service industries. In telecommunications these were AT&T, GTE, GPO and in power transmission these are US utilities, National Power in the UK, EDF in France and ENEL in Italy. Group 3 are the cable manufacturers which in telecommunications were Times Wire and Cable, Belden, General Cable, BICC, Pirelli and GEC and in Power transmission are BICC, Pirelli, Siemens, Alcatel, Sumitomo. Group 4 can be classed as traditional companies which for the telecom case were the illumination fibre companies such as American Optical Corp and Galileo and in superconductivity are the conventional superconductor companies such as Oxford Instruments, IGC and Furukawa. The final category Group 5 are start-up companies. In telecoms these were companies like Spectran, Fibronics and Valtec and in superconductivity are represented by companies such as American Superconductor Corp.

In optical fibres of the five groups above, the ones who perceived the smallest product-process discontinuity were the first to move. Companies like Corning had relevant R&D expertise in glass technology and so the transition for them was smaller than for companies like Times Wire and

Cable who did not. The most radical innovations in optical fibres came from groups 1 and 5. In high temperature superconductivity, close parallels are being observed and the most successful alliances for power cables are likely to be cablemakers allied to a non-cablemaker who perceives a small technological discontinuity in the introduction of high temperature superconductors.

2. SUPERCONDUCTING CABLES

The market for power cables is a large one, in the UK alone for low and high power cables the market size is above £ 13,000 million [5]. Studies and prototypes in the 1960s and 1970s using niobium alloys targeted superconductivity having an impact on the high power end of the transmission network. This is serviced by supertension cables which can be defined as a cable which operates with a conductor above ambient temperature at an operating voltage of 132 kV and power rating of 300 MVA and above. In this design heat flows out from the conductor to the external ambient and the conductors are subject to thermal expansion forces. The cable may need to be force cooled by using oil or gas down a central duct. We can compare this with a superconducting cable which has a conductor far below ambient and so has a net heat flow from the ambient to the conductor, requiring an insulation layer, and is always force-cooled. The operating voltage is not as well defined yet but is certain to be lower than for a conventional cable. For conventional cables at levels of 1 GVA the heat generated in a supertension cable may be as high as 2×10^5 Wkm^{-1} making force-cooling inevitable and therefore a superconducting design an attractive alternative. Low temperature superconducting cables were and are uneconomical except at power levels higher than needed (3-5 GVA) [6,7].

The advent of the new ceramic high temperature superconductors changed the operating temperature of a superconducting cable and the situation was reviewed once again in the hope that the reduced refrigeration costs may alter the economics of superconducting cable installation. Also in the interim period between low and high temperature superconducting cables, environmental aspects regarding siting of overhead lines and right-of-way issues in congested urban areas have become prominent. In this aspect a superconducting cable has advantages in (i) no soil contamination from oil leaks (ii) thermal insulation superconducting cables do not affect surface vegetation, (iii) for the same power a superconducting cable is smaller than a conventional cable occupying less land, (iv) external magnetic fields can in principle be eliminated in a superconducting cable and (v) there is a low fire risk with a superconducting cable.

3. TECHNICAL REQUIREMENTS FOR SUPERCONDUCTING TAPES IN CABLES

The technical challenge for high temperature superconducting cables remains in the fabrication of the superconductor itself. The past work on helium-cooled cables has solved many of the problems with cooling and design and advances in dielectrics since the 1960s have answered many questions regarding suitability at cryogenic temperatures.

Techno-economic studies of the performance requirements for high temperature superconducting wires to be economical in transmission cables have taken place in Europe [8], Japan [9] and the USA [10]. The European study concentrated in two areas (i) a newly installed high power cable at 1 to 3 GVA optimised for maximum efficiency and (ii) a medium power rated cable of 0.5 GVA optimised for maximised efficiency at a fixed diameter. In this study, the values for an economical breakthrough for transmission cost (expressed in MVA per km) of the critical current density of the superconductor wire would need to be 2×10^9 Am^{-2} at 77 K and self-field [11]. For the three oxide superconductor systems these Jc values have been reached using thin film deposition techniques. However, problems with scale-up to long lengths seem to be very problematical for techniques used. The most promising for making long lengths of viable conductor seem to be techniques such as Doctor Blade [12] and powder-in-tube [13]. The jury is out on the thallium containing compounds at present but high Jc values of 9×10^8 Am^{-2} have recently been reported using a spray pyrolysis technique [14] which could be envisaged to be easily scaled up to longer lengths.

By far the greatest effect on economics is the Tc value and if this can be increased even nearer to room temperature then the breakeven point becomes much lower. Recent reports on a Tc value of 250 K in the bismuth-containing cuprate system may prove to be another breakthrough in this area [15].

In the absence of any new breakthrough in Tc, the system most likely to be used in a cable system appears to be the (Bi,Pb)-2223 system with a Tc of 108 K and operable at 77 K in a high current low-field application like a transmission cable. This material is also amenable to powder-in-tube manufacture, a well-known technique industrially and relatively cheap for a high-tec operation and already 1 km wires are being made [16]. The powder-in-tube technique is also preferred as it allows a degree of mechanical integrity to the superconductor either by increasing the number of filaments or by alloying the silver with another metal such as magnesium [17] showing bend strains up to 0.2 %. Ac losses in filaments have also been found to be acceptable for ac cable operation at 50 - 60 Hz using a braided multistrand approach [18].

So the technical objectives for the implementation of high temperature superconducting wires in operational transmission cable systems appear to be close to being achieved. There are many factors that influence this. One analysis has been to calculate the cost of the superconductor using a powder-in-tube process with "bulk" powder values and estimating associated conductor losses.

Fig 1 shows a graph of the calculated transmission cost in units of ecu $kW^{-1}km^{-1}$ against the cost of producing the conductor for cables in units of ecu $kA^{-1}m^{-1}$. These costs are for the optimised high power cable in the European study [11]. For clarity these have been simplified in this graph to show three cases with Jc values of 1×10^9, 1.5×10^8 and 0.5×10^8 Am^{-2} respectively. These results are compared to a single core oil-filled cable 400 kV, 1000 MVA rating (solid line). The most interesting fact found by relating the conductor costs in units of ecu $kA^{-1}m^{-1}$ is that a breakeven Jc can be estimated for a range of wire properties and operating conditions. These results show that for conductor costs below 100 ecu $kA^{-1}m^{-1}$ the transmission costs are dominated by the ancillary equipment such as installation and coolers etc. For values near to 1000 ecu $kA^{-1}m^{-1}$ the wire would constitute near to 60 - 70 % of the cost of the cable, while at values near to 10 ecu $kA^{-1}m^{-1}$ the wire would be less than 5 % of the total cost of the cable.

Fig 2 shows a plot of operating Jc in Am^{-2} against the cost of the conductor in ecu $kA^{-1}m^{-1}$ for the optimised high power cable at a rating of 1000 MVA and the replacement medium power superconducting cable operating at 400 MVA *compared with the equivalent copper cable system.* The European study [11] found that there were three factors in high temperature superconducting wire manufacture that may influence the use of the product in cables:

1. Advances in the critical current density toward 10^9 Am^{-2} for a process that can be scaled to industrial production

such as powder-in-tube. This would tend to move the graphs up the y axis in Fig 2.

2. Process route economies that reduce the overall cost of production for the superconductor tape ie reduction of processing time of the (Bi,Pb)-2223 tape for example. This would move the curves to lower conductor cost values along the x axis in Fig 2.

3. Identification of new products that could benefit from the technology as it know exists. Such an approach is the EPRI-cable to retro-fit pipe-type cables [10]. This has the effect of moving the two curves closer together in Fig 2.

Fig 3 is a further representative breakdown which shows the conductor Jc in Am^{-2} versus the absolute cost per unit length of the conductor in $kA^{-1}m^{-1}$. This was taken to be a typical monocore tape of the type made in most laboratories by rolling or pressing with dimensions of 2 mm x 50 μm. It was also assumed that a factor of 2.5 in the ratio of superconductor cross-section to current density to allow for uneven current distribution. These curves give a good idea of the actual manufacturing costs needed for a high temperature superconducting tape to be economical in power cable systems.

4. CONCLUSIONS

High temperature superconductors represent a technological discontinuity in the power cable industry and a potential threat to the high power supertension cable area especially.

Technical requirements of powder-in-tube samples are nearer the specification required for economical operation at 77 K.

The best performance so far of these wires is in the order of 6×10^8 Am^{-2} for short pressed samples, and in long lengths (100 m +) this has been shown to be 1 to 2×10^8 Am^{-2}. These values are close to the Jc(operational) values needed for transmission cables which typical one would expect to be near 50 % Jc at 77 K, 0 T. The European cablemakers view is that an operational Jc for a new optimised high power cable would be 2×10^8 Am^{-2} for a wire price of 60 ecu $kA^{-1}m^{-1}$ and for a retrofit medium power fixed diameter cable the same Jc would need wire price of 400 $kA^{-1}m^{-1}$ making it an attractive first solution for high temperature superconducting cables.

REFERENCES

[1] J M Senior and T E Ray, Int J Technology Management, 5(1), 71 (1990).

[2] J A Alic and R R Miller, Int J Technology Management, 4(6), 653 (1989).

[3] C Watanabe and A Kanaya in Proc 3rd International Superconductivity Industry Summit, Oxford, 18-20 May 1994.

[4] J M Utterback and L Kim in " The Management of Productivity and Technology in Manufacturing", Ed: P R Kleindofer, Pub: Plenum Press (1986).

[5] W C Atkinson and F E Ellis "Electricity distribution - asset replacement considerations", Electron & Power, (1987).

[6] G Bogner in "NATO Advances in Superconductivity: Superconducting Machines", Ed by S Foner and B B Schwartz, Chapt 7, 401, Plenum Press NY (1981).

[7] D R Edwards, Proc IEE, 135, 9 (1988).

[8] Report of the EEC on "Applications of HTSC materials with reference to power cables", JOULE contract No JOUE 0050-GB (1992).

[9] In "Feasibility Studies in Application Fields of Superconductivity", Executive Summary Report of ISTEC, Japan (March 1990).

[10] J S Engelhardt, D Von Dollen and R Samm, AIP Conf Proc no 251, 692 (1992).

[11] P Metra, S P Ashworth, R J Slaughter and E M Hughes in Proc of IEE 3rd International Conference on "Power Cables and Accessories 10 kV - 500 kV", London, UK (1993).

[12] R Hornung, H-W Neumuller, L Rockford and G Tomandl in Proc EUCAS, page 633, Ed H C Freyhardt, Pub DGM Informationsgesellschaft, Göttingen, Germany, October 4-9 (1993). ISBN 3-88355-107-X

[13] K Sato, Physics World, 37, July 1992.

[14] T Yuasa, T J Doi, T Ozawa and K Higashiyama in Proc "1994 International Workshop on Superconductivity", Kyoto, Japan, page 273. Pub: ISTEC, Japan (1994).

[15] M Lagües, X Xie, H Tebbji, X Xu, V Mairet, C Hatterer, C Beuran and C Deville-Cavellin, Science, 262, 1850 (1993).

[16] T Hikata, K Muranaka, S Kobayashi, J Fujikami, M Ueyama, T Kato, T Kaneko, H Mukai, K Ohkura, N Shibuta and K Sato in Proc "1994 International Workshop on Superconductivity", Kyoto, Japan, page 69. Pub: ISTEC, Japan (1994).

[17] H Krauth, J Tenbrink, H-W Neumuller, M Wilhelm, K Fischer, M Schubert, W Goldacker and J Keßler in Proc EUCAS, page 147, Ed H C Freyhardt, Pub DGM Informationsgesellschaft, Göttingen, Germany, October 4-9 (1993). ISBN 3-88355-107-X

[18] J J Gannon Jr, P Metra and G Vellego in Proc "1994 International Workshop on Superconductivity", Kyoto, Japan, page 73. Pub: ISTEC, Japan (1994).

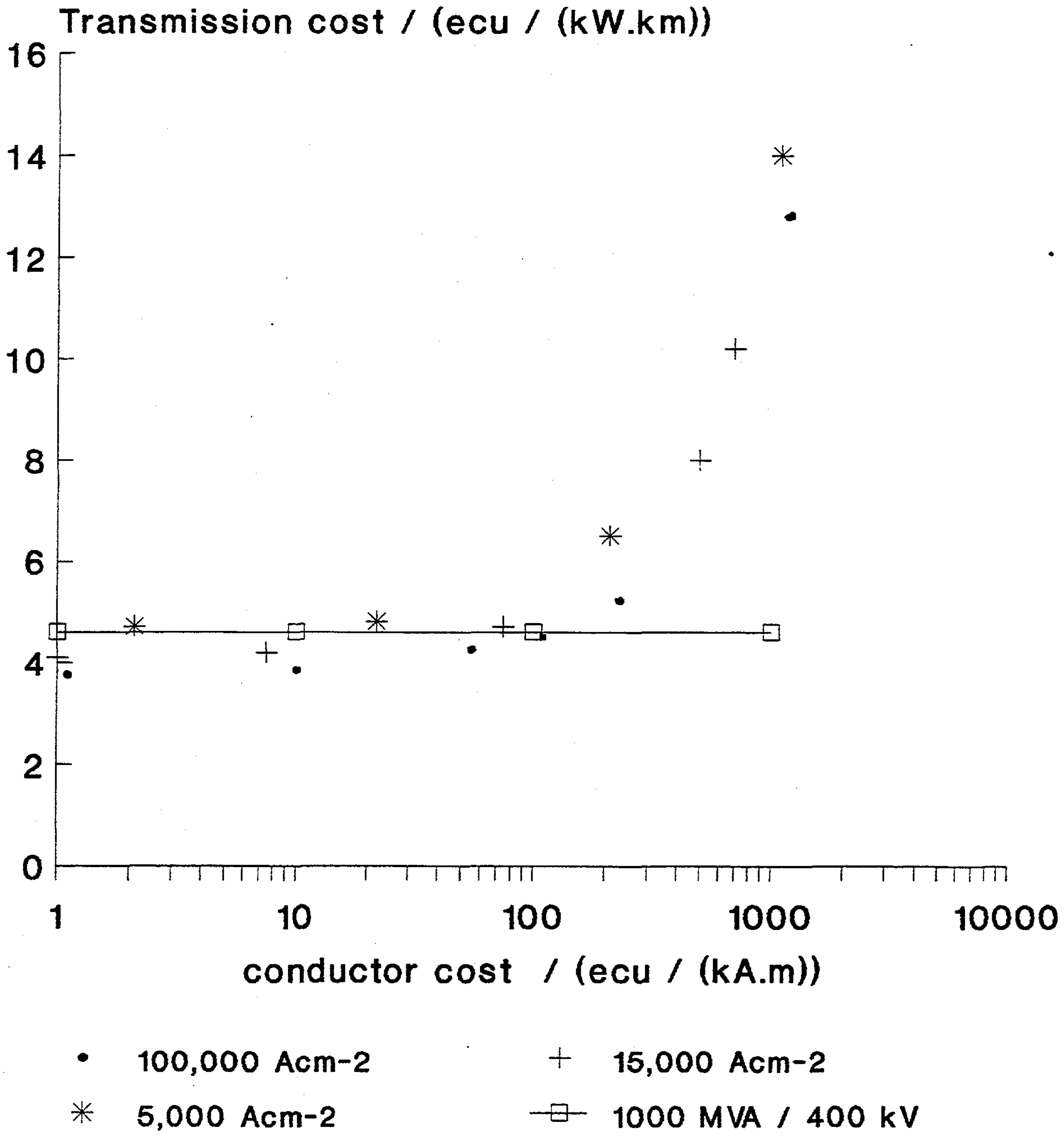

FIG 1 a graph of the calculated transmission cost in units of ecu $kW^{-1}km^{-1}$ against the cost of producing the conductor for cables in units of ecu $kA^{-1}m^{-1}$. These costs are for the optimised high power cable in the European study [11].

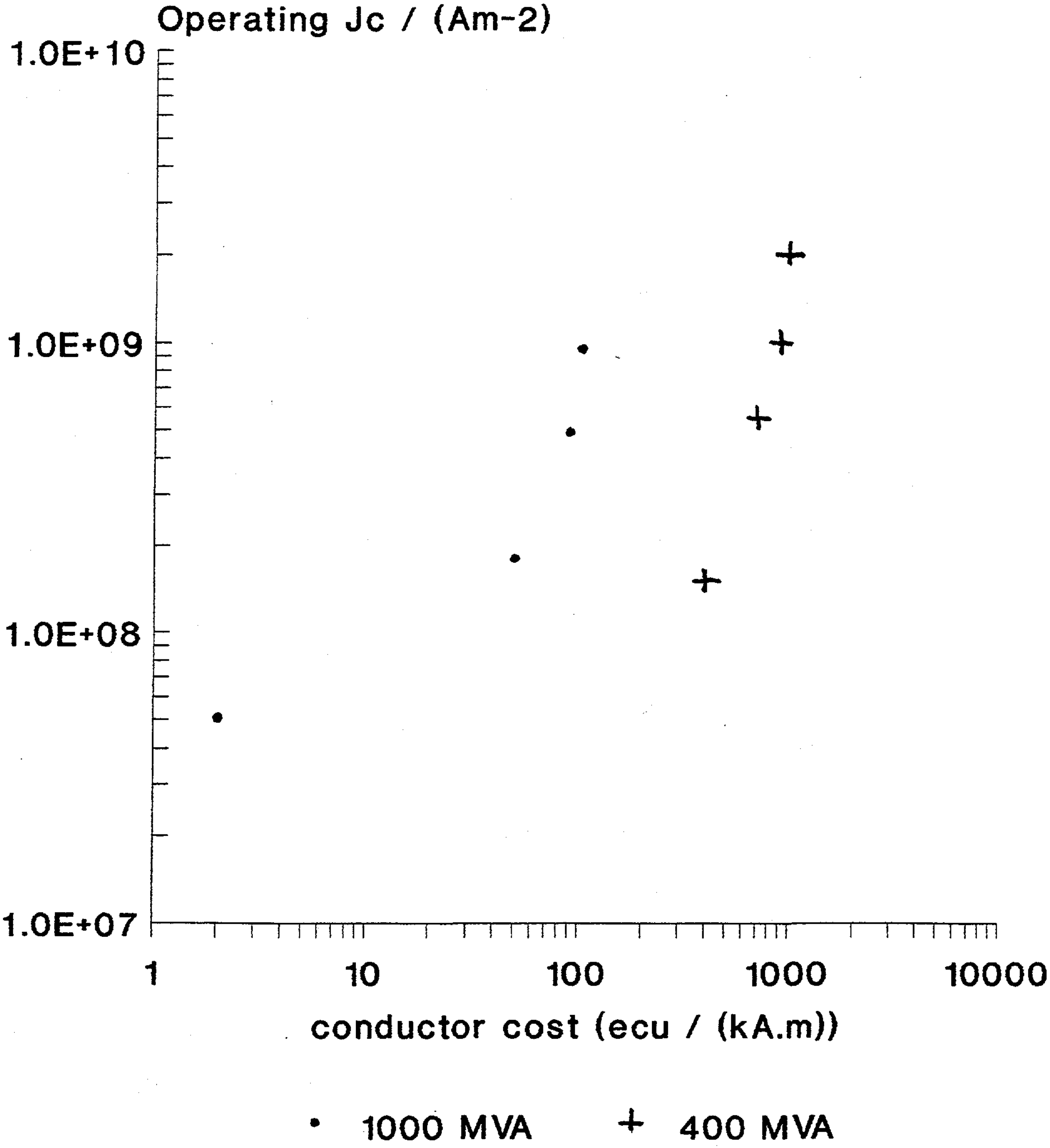

FIG 2 a plot of operating Jc in Am^{-2} against the cost of the conductor in ecu kA^{-1}m^{-1} for the optimised high power cable at a rating of 1000 MVA and the replacement medium power superconducting cable operating at 400 MVA *compared with the equivalent copper cable system.*

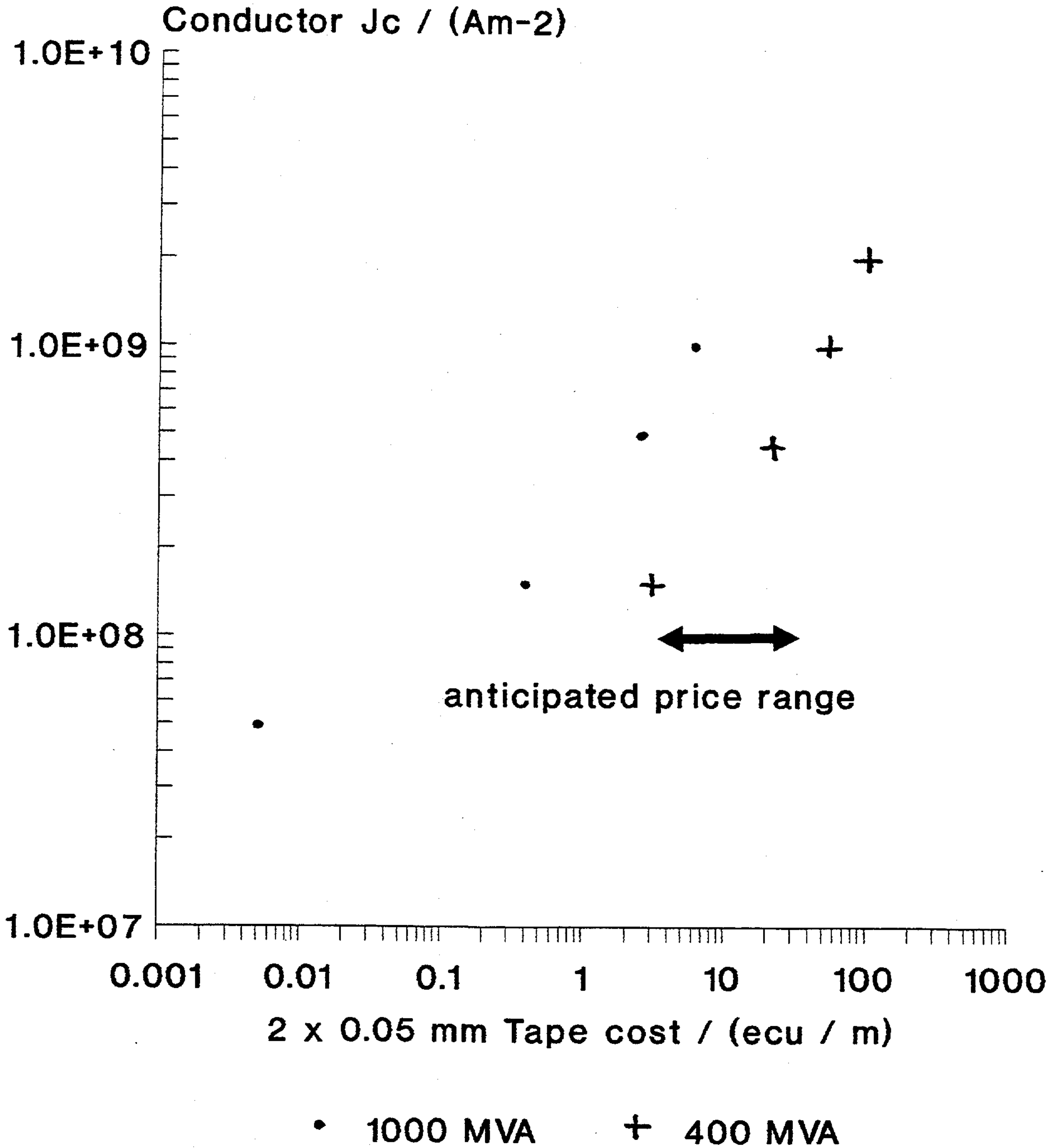

FIG 3 the conductor Jc in Am^{-2} versus the absolute cost per unit length of the conductor in $kA^{-1}m^{-1}$ - (2 mm x 50 μm conductor).

Improvement of Critical Current Density in Thallium-Based $(Tl,Bi)Sr_{1.6}Ba_{0.4}Ca_2Cu_3O_x$ Superconductors

Z. F. Ren, C. A. Wang, and J. H. Wang
Superconductive Materials Laboratory
State University of New York at Buffalo, Amherst, NY 14260

D. J. Miller
Materials Science Division, Argonne National Laboratory
Argonne, IL 60439

K. C. Goretta
Energy Technology Division, Argonne National Laboratory
Argonne, IL 60439

Abstract

Epitaxial $(Tl,Bi)Sr_{1.6}Ba_{0.4}Ca_2Cu_3O_x$ ((Tl,Bi)-1223) thin films on (100) single crystal $LaAlO_3$ substrates were synthesized by a two-step procedure. Phase development, microstructure, and relationships between film and substrate were studied by X-ray diffraction (XRD), scanning electron microscopy (SEM), and transmission electron microscopy (TEM). Resistance versus temperature, zero-field-cooled and field-cooled magnetization, and transport critical current density (J_c) were measured. The zero-resistance temperature was 105—111 K. J_c at 77 K and zero field was $> 2 \times 10^6$ A/cm^2. The films exhibited good flux pinning properties.

Introduction

An important step in understanding of flux pinning in high-T_c superconductors was the prediction by Kim et al. that flux pinning should improve as the layers between Cu-O planes become thinner [1]. The model of Kim et al. stimulated interest in Tl-based 1212 and 1223 superconductors because of their thin insulating layers relative to Tl-2212, Tl-2223, Bi-2212, and Bi-2223 types. Tl-1212 and Tl-1223 tapes with J_c to 2×10^4 A/cm^2 at 77 K and zero field have been fabricated by the powder-in-tube method [2-18]. However, attempts at further improvement have met with little success, in spite of the worldwide effort, due mainly to weak-link problems. The transport J_c of these tape samples often decreased by a factor of 20 at 77 K as the external magnetic field was raised from 0 to 0.2 T [10].

The intrinsic flux pinning properties of the bulk samples was quite good: for example, J_c decreased only by a factor of 3 at 77 K as the field was increased from 0.2 to 5.5 T. The best bulk samples are probably the thick films reported by General Electric [19-21], and Tl-1223 tapes electrodeposited on metallic silver and annealed in a two-zone furnace [22]; however, weak links continue to be a serious problem in these samples. Thin films are well known to have high transport J_c and excellent flux pinning at 77 K. We have, therefore, directed our efforts toward the fabrication of Tl-based 1223 thin films. We have successfully made epitaxial (Tl, Bi)$Sr_{1.6}Ba_{0.4}Ca_2Cu_3O_x$ ((Tl,Bi)-1223) thin films with high J_c in magnetic field for the first time [23]. In this paper, we report on microstructural development and superconductivity as functions of temperature and heat treatment.

Experimental Details

The films were prepared by laser ablation. A pellet of composition $Tl_{0.95}Bi_{0.22}Sr_{1.6}Ba_{0.4}Ca_2Cu_3O_x$ was prepared by pressing an intimate mixture of 0.475 Tl_2O_3 + 0.11 Bi_2O_3 + $Sr_{1.6}Ba_{0.4}Ca_2Cu_3O_x$ in a 1.28 cm die at a pressure of 150 MPa. The pellet was placed between gold plates, wrapped in silver foil, sintered in air at 870–900°C for 3–5 h, cooled, and then pulverized. The source pellet for film fabrication was made by mixing 1 FW of the above powder with 0.475 FW Tl_2O_3 and 0.4 FW CaO, and pressing at 750 MPa in the 1.28 cm die. Laser ablation was conducted at 120 mJ/pulse, 21 KV, and 2–10 pulse/s; substrate temperature was 300–500°C. Films were deposited on (100) single-crystalline $LaAlO_3$. The resulting films were placed between $Tl_{0.95}Bi_{0.22}Sr_{1.6}Ba_{0.4}Ca_2Cu_3O_x$ pellets and set on a gold plate. This assembly was wrapped in silver foil with a plenum space, and heated in air at 840–870°C for 25–60 min.

The phase structure and mosaic distribution of the films were measured by 2θ scans and rocking curves. The relationship between the film and substrate was determined by both X-ray ϕ scans and TEM. Microstructures were characterized by SEM, energy dispersive spectroscopy (EDS), and TEM. Magnetization versus temperature was measured by DC SQUID. DC zero-resistance temperature (T_c) and transport J_c were measured by standard four-probe methods. Films were 1 μm thick and were patterned into 90 x 200 μm microbridges by photolithography. Four silver contacts were deposited onto each film. Measurements of $J_c(H)$ were performed in a DC SQUID, with the magnetic field aligned perpendicular to film c-axes.

Results and Discussion

1. Phase development: Figure 1a shows the morphology of the precursor films; Figs. 1b and 1c show the annealed films. The precursor films consisted of uniform small particles. Although the ablation source was Tl-rich ($Tl_{1.8}Bi_{0.22}Sr_{1.6}Ba_{0.4}Ca_2Cu_3O_x$), the content of Tl in the precursor was substoichiometric (Table 1). There were many more acicular grains in Fig. 1b than in Fig. 1c. These grains were found to have a-axis orientation. The

Table 1. Average composition of precursor and annealed films.

	Tl	Bi	Sr	Ba	Ca	Cu
Precursor	0.7	0.2	1.6	0.3	2.7	2.5
Annealed film 1	0.7	0.2	1.6	0.4	2.3	2.8
Annealed film 2	0.7	0.2	1.6	0.2	2.8	2.5

average composition, determined by EDS, of the annealed films with fewer acicular grains was 0.9/1.9/2.3/2.9, which was close to stoichiometric 1223. The films with more acicular grains had an average composition of 0.9/1/8/2.8/2.5, further from the ideal stoichiometry.

Annealing temperature was a key parameter for 1223 phase development. At low temperature (820°C), we obtained only 1212 phase. As the temperature increased, the 1223 phase gradually formed (Fig. 2). At 840°C, the sample consisted of 1223 and 1212 phases. Although the 1223 phase was dominant, the XRD peaks of 1212 phase were still strong (shown by the relative intensity of the (004) peak of 1212 vs. that of the (005) peak of the 1223, and of the (005) peak of the 1212 to the (006) peak of the 1223). At 860°C, the peaks of 1212 phase were barely distinguishable.

Another key parameter for 1223 phase development was annealing duration. Samples were heated at 860°C for different lengths of time. For short time at temperature, 1212 formed (Fig. 3). For longer annealing times, more and more 1223 phase formed. After 60 min, the 1212 phase completely transformed into 1223. Rocking curves of the (006) peak of the 1223 were examined for several films. The typical full width at half maximum (FWHM) was 0.365°, which is comparable with high-quality $YBa_2Cu_3O_x$ films. We concluded that the optimal annealing temperature and time were 860°C and 60 min, respectively.

2. Microstructure and Orientation: From the XRD patterns, it was clear that the films were highly phase pure and c-axis oriented. We investigated the epitaxy between film and substrate by both X-ray ϕ scans and TEM. To determine the in-plane orientation between the (Tl,Bi)-1223 film and $LaAlO_3$ substrate, we measured ϕ scans of the (103) film reflection and the (222) substrate reflection (Fig. 4). The [100] axis of (Tl, Bi)-1223 overlapped with the [100] of $LaAlO_3$. This epitaxial growth is reasonable because the lattice mismatch between [100] of (Tl, Bi)-1223 and [100] of LaAlO is only 0.5%.

Figure 5a shows a typical area of the epitaxial film and a misoriented grain. This misoriented grain could be either intrinsic or caused by sample preparation. Figure 5b shows dislocations within the film near the interface.

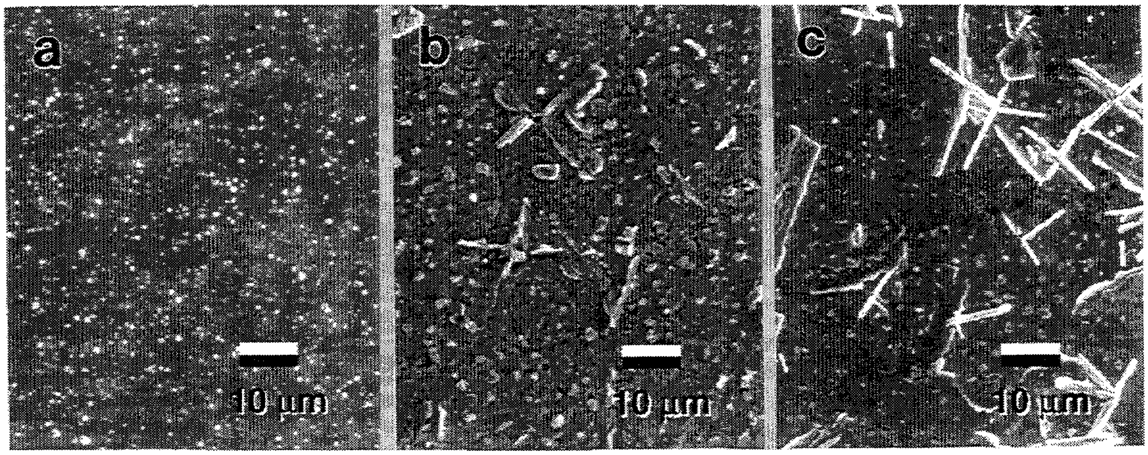

Fig. 1. SEM photomicrographs of precursor and annealed films.

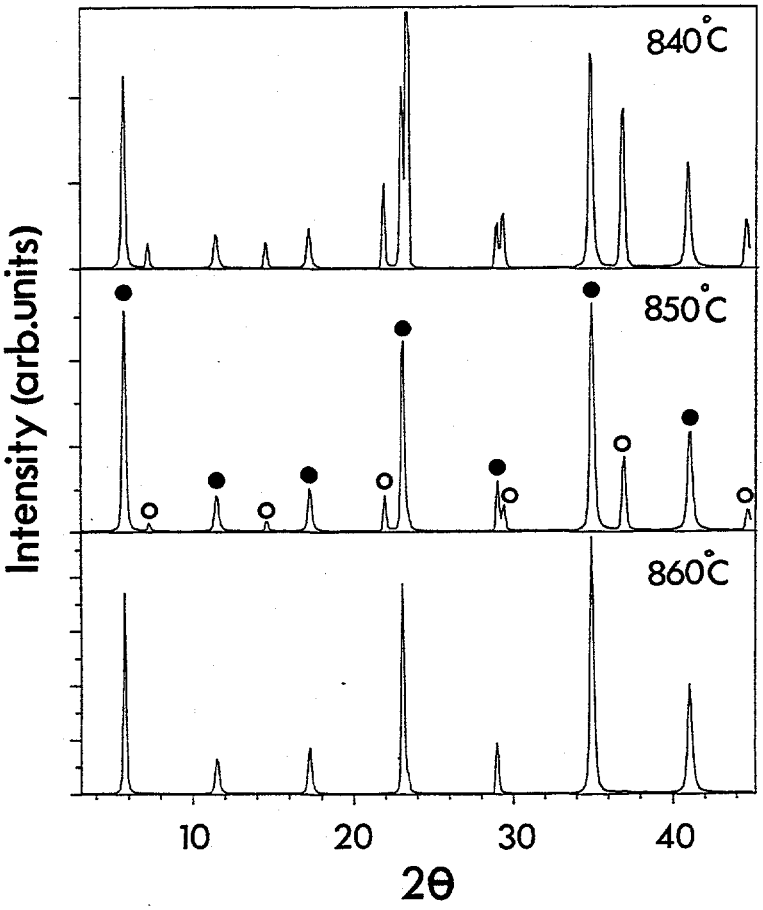

Fig. 2. XRD plots of films annealed as shown; only (*00l*) peaks are present; (Tl,Bi)-1223 marked by filled circle, (Tl,Bi)-1212 by open circle.

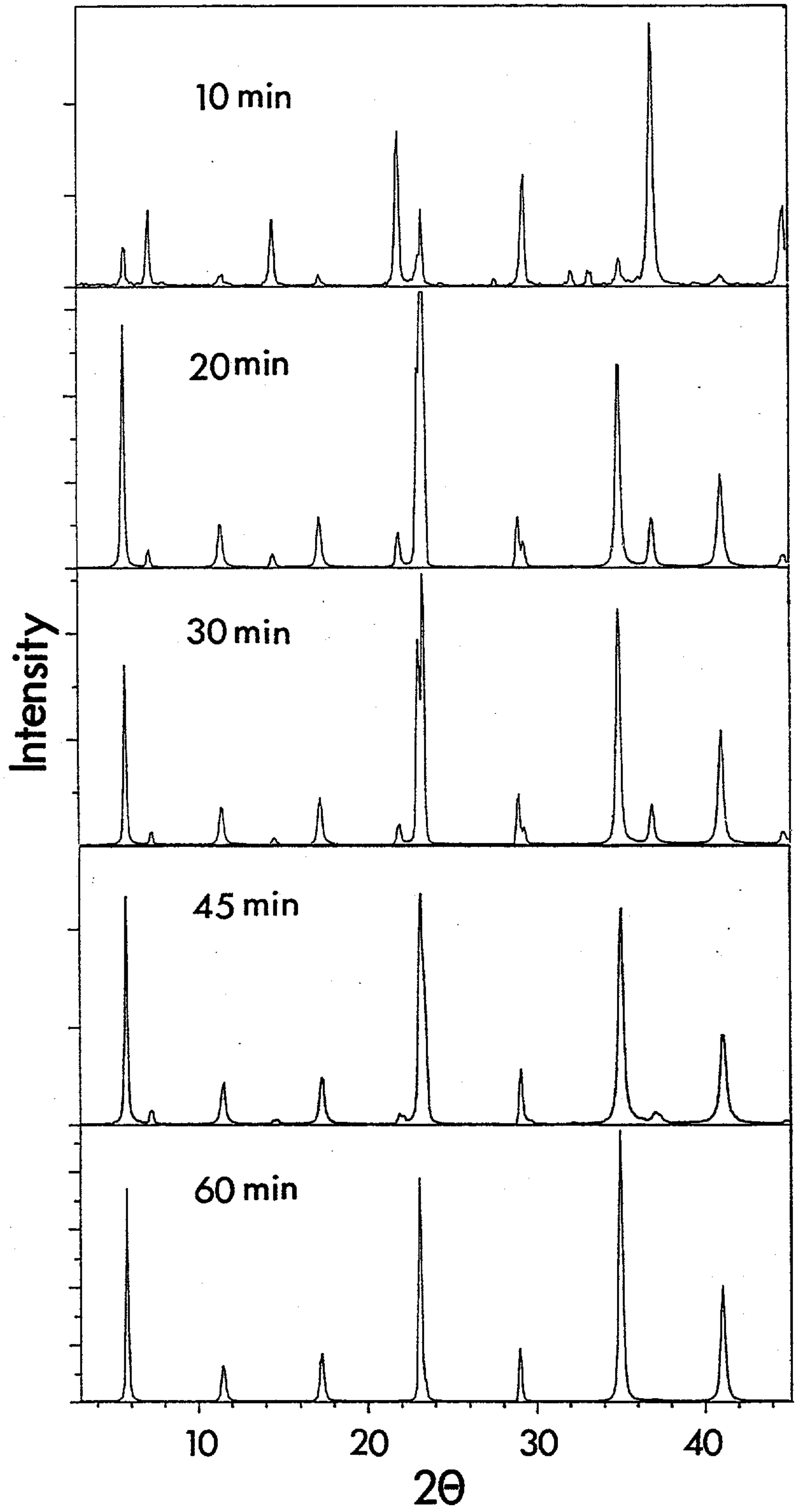

Fig. 3. XRD plots of (Tl,Bi)-1223 films annealed at 860°C in air.

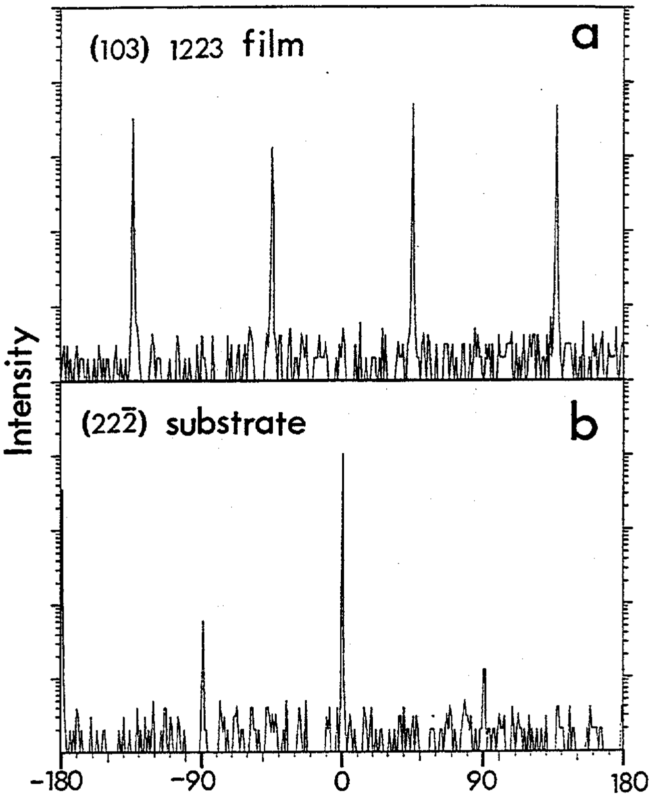

Fig. 4. XRD ϕ scans of (a) (Tl,Bi)-1223 film and (b) $LaAlO_3$ substrate.

Figure 6a is a high-resolution image of the interface. A semi-periodic contrast and a few small defects were observed. The contrast was due to strain caused by the lattice mismatch between the film single-crystal substrate. Figure 6b shows a thin layer near the interface containing dislocations and a region above the layer containing many stacking faults. There was a slight rotation between the two areas, as confirmed by convergent-beam electron diffraction.

3. Superconductivity: Figure 7 shows two typical T_c curves. T_c was 105–111 K, and depended on phase purity. For many measurements, we found that samples with pure Tl-1223 phase had T_c of 105–107 K (Fig. 7a), whereas films with a little 1212 phase had a higher T_c of $\approx$ 111 K (Fig. 7b). This phenomenon has yet to be clearly understood.

Figure 8 shows typical zero-field-cooled (ZFC) and field-cooled (FC) magnetization curves measured at 20 G with the field parallel to the c-axis of the (Tl,Bi)-1223 film. The transition onset was 105 K, which was lower than the DC zero resistance of 107 K. If we assume flux exclusion was 100% at the lowest measured temperature of the ZFC curve, the flux expulsion measured by FC would be $\approx$ 3%, which would reflect highly incomplete flux expulsion. Incomplete flux expulsion could originate for several possible reasons: flux pinning, the Ebner-Stroud superconduction glass model, or less than full superconductivity of sample [24]. The last two causes require presence of

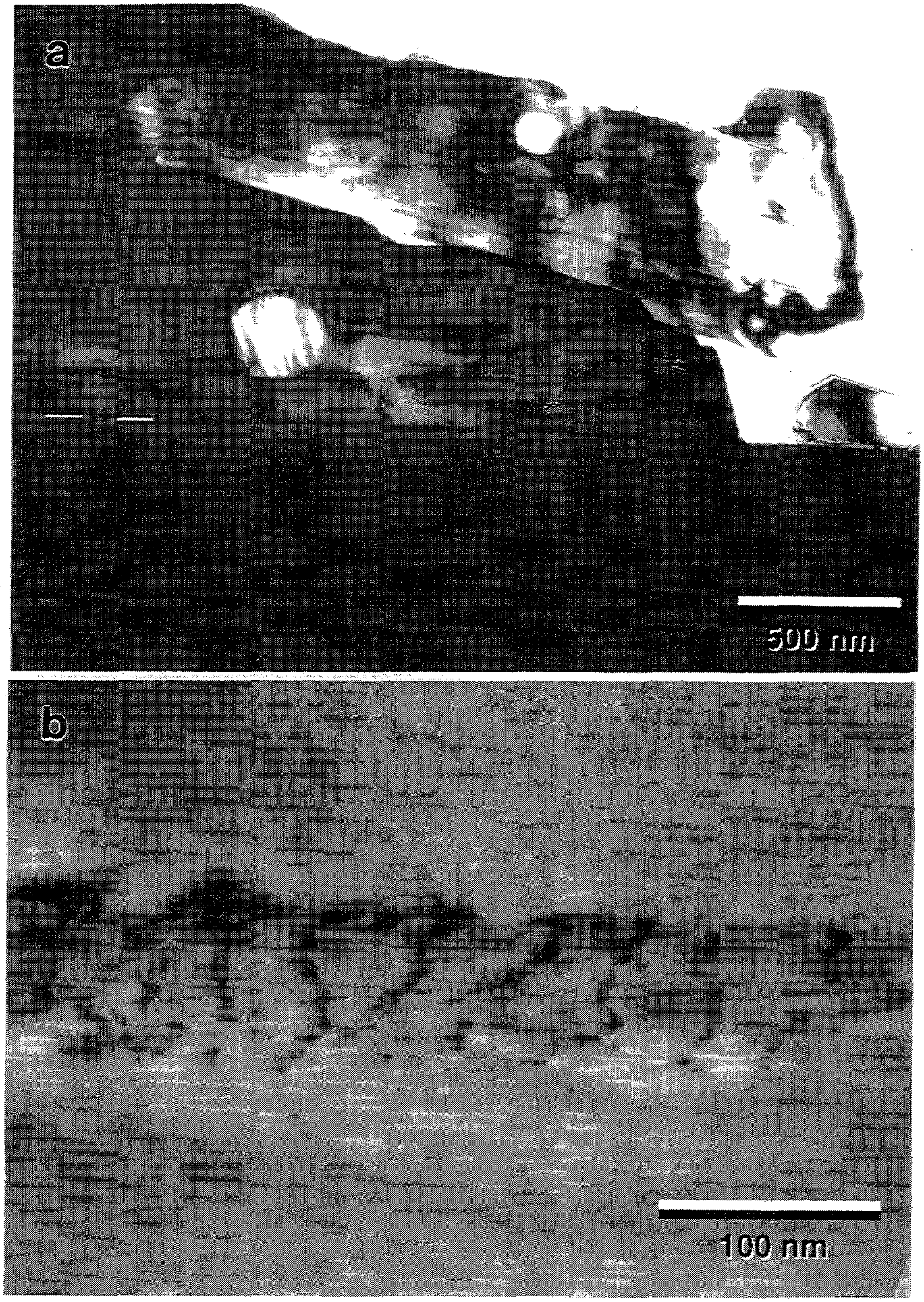

Fig. 5. TEM photomicrograph of (a) typical area of epitaxially grown (Tl,Bi)-1223 film and (b) dislocations in film at $LaAlO_3$ interface.

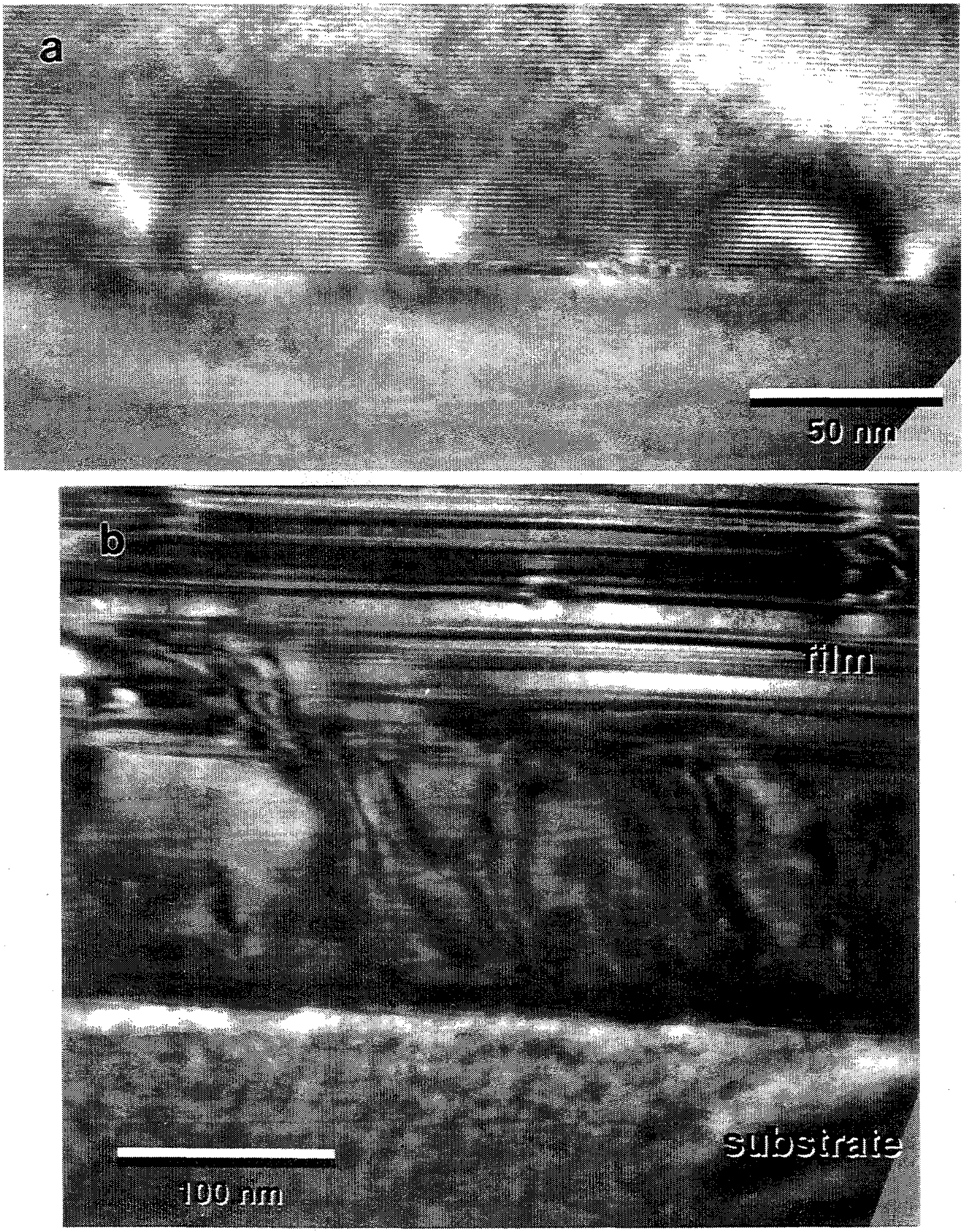

Fig. 6. High-resolution TEM photomicrographs of (a) semi-periodic lattice strain caused by lattice mismatch between (Tl,Bi)-1223 film and $LaAlO_3$ interface and (b) dislocations near interface.

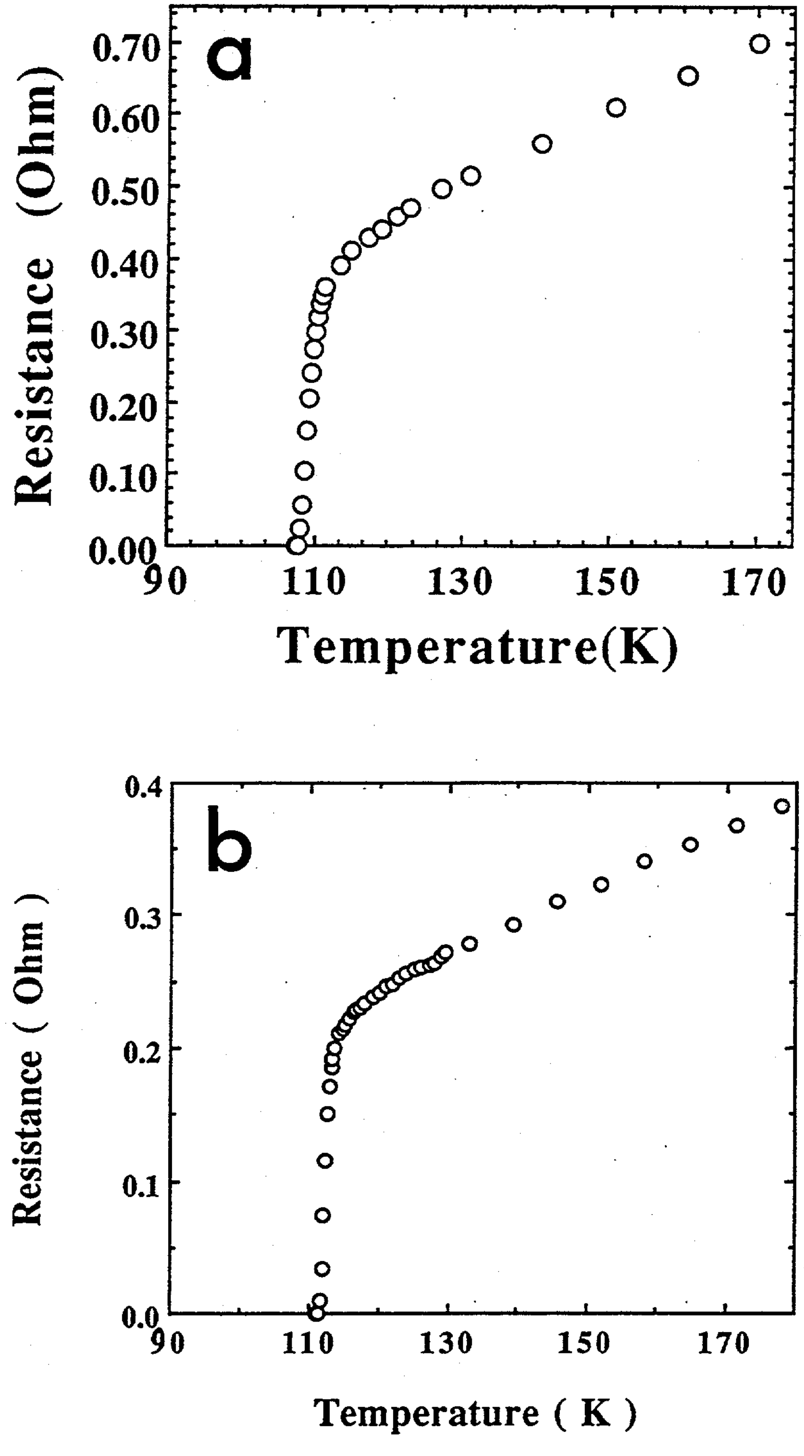

Fig. 7. Typical resistance vs. temperature curves for (a) films with a little (Tl,Bi)-1212 and (b) pure (Tl,Bi)-1223 films.

weak links. The transport J_c data discussed below indicate the absence of significant weak links in our films and suggest that the observed incomplete flux expulsion is due to strong flux pinning.

Defects such as twin boundaries [25] and a-axis oriented plates [26] have been observed to be effective pinning centers, in addition to the intrinsic pinning between Cu-O layers [27]. Several defects in our films that may perhaps be partly responsible for good flux pinning were observed by TEM.

The results of $J_c(H)$ measurements are shown in Fig. 9. The insert shows the clear J_c–H relationship at low magnetic field. At 67 K, J_c did not decrease from 0 to 0.1 T, and, surprisingly, there was a small increase below 200 G. At 87 K, an obvious increase was observed, and then J_c decreased for $H > 0.1$ T. At 77 K and 5.5 T, J_c was 5×10^5 A/cm^2. At 87 K and 5.5 T, J_c remained $> 10^5$ A/cm^2. Because of the limited chamber size in the SQUID, to date we have managed to measure J_c with H perpendicular to c-axis only. The J_c–H dependence for H parallel to c-axis is now being studied.

Conclusions

$(Tl,Bi)Sr_{1.6}Ba_{0.4}Ca_2Cu_3O_x$ films were epitaxially grown on (100) $LaAlO_3$ single crystals. Both c-axis and a–b-axis alignment were achieved. T_c was 105–111 K and depended on phase purity. Samples with some 1212 phase had T_c of ≈ 111K; phase-pure samples had T_c of ≈ 105–107 K. J_c at 77 K and zero field reached 2×10^6 A/cm^2 when measured on a 1 μm thick, 90 μm wide, 200 μm long microbridge. J_c was 5×10^5 A/cm^2 with a 5.5 T magnetic field applied perpendicular to the c-axis.

Acknowledgments

We thank many colleagues at NYSIS for their help in this work: D. T. Shaw, S. Patel, and F. Yang in laser ablation; E. Narumi in XRD, P. Liu and Z. Chen in determining film thickness; H. S. Kwok and W. Shen in patterning the films; D. Petrov in SQUID measurements; and M. N. Pitsakis, G. Sagerman, and M. Michalski for sitting up the J_c equipment. This work was supported by the New York State Energy Development Authority and the U.S. Department of Energy (DOE), Offices of Energy Efficiency and Renewable Energy, as part of a DOE program to develop electric power technology, and Basic Energy Sciences (Materials Sciences), under Contract W-31-109-Eng-38. Microstructural characterization was carried out in the Electron Microscopy Center at Argonne National Laboratory.

References

1. D. H. Kim, K. E. Gray, R. T. Kampwirth, J. C. Smith, D. S. Richeson, T. J. Marks, J. H. Kang, J. Talvacchio, and M. Eddy, Physica C **177** (1991) 431.
2. M. A. Subramanian, C. C. Torardi, J. Gopalakrishnan, P. L. Gai, J. C. Calabrese, T. R. Askew, R. B. Flippen, and A. W. Sleight, Science **242** (1988) 249.

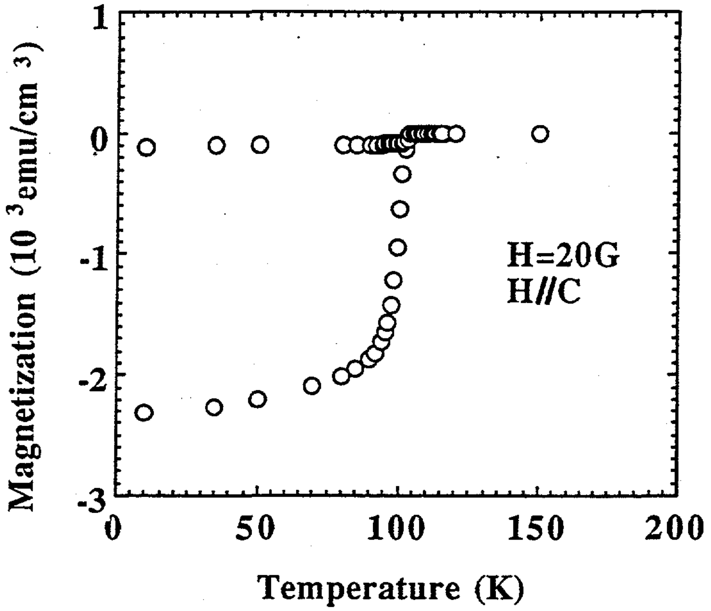

Fig. 8. Zero-field-cooled (ZFC) and field-cooled (FC) magnetization of (Tl,Bi)-1223 film measured in field of 20 G.

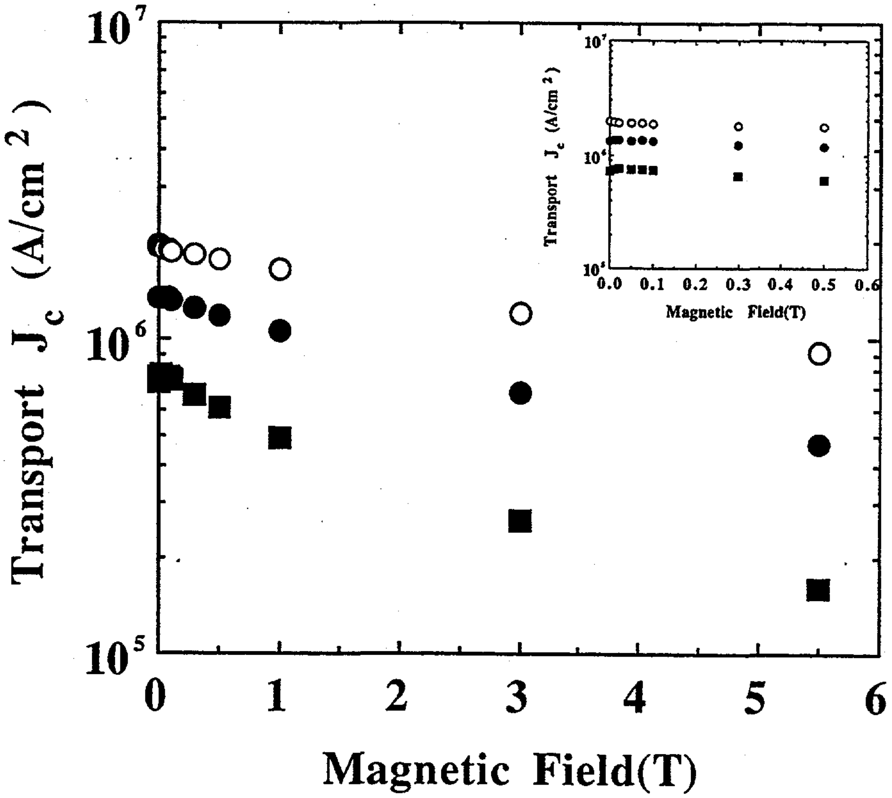

Fig. 9. Relationship between transport J_c and field with H perpendicular to c axis: 67 K (open circles, 77 K (filled circles, and 87 K (filled square).

3. O. Inoue, S. Adachi, and S. Kawashima, Jpn. J. Appl. Phys. **29** (1989) L1167.
4. Y. Torii, H. Takei, and K. Tada, Jpn. J. Appl. Phys. **29** (1989) L2192.
5. O. Inoue, S. Adachi, and S. Kawashima, Jpn. J. Appl. Phys. **29** (1990) L763.
6. Y. Torii, H. Kugai, H. Takei, and K. Tada, Jpn. J. Appl. Phys., 29 (1990) 952.
7. T. Kamo, T. Doi, A. Soeta, T. Yuasa, N. Inoue, K. Aihara, and S. P. Matsuda, Appl. Phys. Lett. **59** (1991) 3186.
8. T. Doi, M. Okada, A. Soeta, T. Yuasa, K. Aihara, T. Kamo, and S. P. Matsuda, Physica C **183** (1991) 67.
9. B. A. Glowacki and S. P. Ashworth, Physica C **200** (1992) 140.
10. Z. F. Ren and J. H. Wang, Appl. Phys. Lett. **61** (1992) 1715.
11. K. C. Goretta, C.-T. Wu, M. T. Lanagan, M. A. Boling, D. Shi, D. J. Miller, N. Chen, W. G. Hanewald, S. Senguta, Z. Wang, and R. B. Poeppel, Mater. Res. Soc. Symp. Proc. **275** (1992) 813.
12. D. E. Peterson, P. G. Wahlbeck. M. P. Maley, J. O. Willis, P. J. Kung, J. Y. Coulter, K. V. Salazar, D. S. Phillips, J. F. Bingert, E. J. Peterson, and W. L. Hults, Physica C **199** (1992) 161.
13. R. S. Liu, D. N. Zheng, J. W. Loram, K. A. Mirza, A. M. Campbell, and P. P. Edwards, Appl. Phys. Lett. **60** (1992) 1019.
14. Z. F. Ren and J. H. Wang, Appl. Phys. Lett. **62** (1993) 3025.
15. Z. F. Ren and J. H. Wang, Physica C **216** (1993) 199.
16. M. R. Presland, J. L. Tallon, N. E. Flower, R. G. Buckley, A. Mawdsley, M. P. Staines, and M. G. Fee, Cryogenics **33** (1993) 502.
17. Z. F. Ren, J. H. Wang, D. J. Miller, and K. C. Goretta, Physica C, in press.
18. D. J. Miller, J. G. Hu, Z. F. Ren, Q. Hong, and J. H. Wang, J. Electron. Mater., in press.
19. J. A. DeLuca, M. F. Garbauskas, R. B. Bolon, J. G. McMullen, W. E. Balz, and P. L. Karas, J. Mater. Res. **6** (1991) 1415.
20. J. E. Tkaczyk, J. A. DeLuca, P. L. Karas, P. J. Bednarczyk, M. F. Garbauskas, R. H. Arendt, K. W. Lay, and J. S. Moodera, Appl. Phys. Lett. **61** (1992) 610.
21. J. A. DeLuca, P. L. Karas, J. E. Tkaczyk, P. J. Bednarczyk, M. F. Garbauskas, C. L. Briant, and D. B. Sorensen, Physica C **205** (1993) 21.
22. R. N. Bhattacharya, A. Duda, D. S. Ginley, J. A. DeLuca, Z. F. Ren, C. A. Wang, and J. H. Wang, Physica C, in press.
23. Z. F. Ren, C. A. Wang, and J. H. Wang, Appl. Phys. Lett., July 11 issue (1994).
24. A. P. Malozemoff, pp. 77-134, in “Physical properties of high temperature superconductors I” ed. D. M. Ginsberg, World Scientific, 1989.
25. G. J. Dolan, G. V. Chandrashekhar, T. R. Dinger, C. Field, and F. Holtzberg, Phys. Rev. Lett. **62** (1989) 827.
26. H. Fuke, H. Yoshino, M. Yamazaki, T. D. Thanh, S. Nakamura, K. Ando, and Y. Kobayashi, Appl. Phys. Lett. **60** (1992) 2686.
27. M. Tachiki and S. Takahashi, Sol. St. Commun. **70** (1989) 291.

THIS PAGE INTENTIONALLY LEFT BLANK

Granular Superconductors

Chair: Prof. Manu S. Multani

Introduction of Artificial Pinning Centres in „$Bi_2Sr_2CaCu_2O_8$“ Ceramics

P. Majewski, S. Elschner*, H. Bestgen*, and F. Aldinger

Max-Planck-Institut für Metallforschung, D-70569 Stuttgart, FRG, and
* Hoechst AG, D-65926 Frankfurt am Main, FRG

Abstract

Considering the phase equilibrium diagram of the system Bi_2O_3-SrO-CaO-CuO, single phase „$Bi_2Sr_2CaCu_2O_8$“ ceramics have been transformed by a simple annealing procedure into multi phase samples. The transformation results in the formation of second phases and in an increase of the intra grain critical current density at 1 T of five times. This increase is believed to express improved pinning properties of the superconducting crystals. The prepared pinning centres are believed to be e.g. coherent precipitates (Guinier-Preston-zones) within the superconducting crystals.

1. Introduction

"$Bi_2Sr_2CaCu_2O_8$" (2212 phase, Tc 94 K) and "$(Bi,Pb)_2Sr_2Ca_2Cu_3O_{10}$" (2223 phase, Tc = 110 K) exhibit weak internal pinning at temperatures above 20 K resulting in a decrease of the critical current density of about two orders of magnitude in an applied magnetic field of up to 2 T [1-5]. Therefore, an application of these materials in devices under magnetic fields is still not possible yet. Effective pinning centres are assumed to may not exceed about 10 nm [6,7]. Therefore, in this article a processing route is presented resulting in superconducting bulk ceramics with very fine (« 1 μm) precipitates of second phases and enhanced pinning properties using temperature dependent solubility lines. In addition, the microstructure of the prepared samples has been studied in order to clarify the nature of the produced pinning centres.

2. Experimental

Samples with the composition $Bi_{2.18}Sr_{1.7}Ca_{1.3}Cu_2O_{8+d}$ using Bi_2O_3, PbO, $SrCO_3$, $CaCO_3$ and CuO as starting material (purity 99 %) were prepared. The mixed and ground powders were calcined at 750 °C and 800 °C for 24 h and pressed into cylindrical pellets (15 mm long and 4 mm in diameter, 625 MPa). The pellets were sintered at 820 °C in air for 90 h with intermediate grinding and pressing, furnace cooled and subsequently annealed at 885 °C for 10, 15, 22.5, 25, 30, 37.5, 45, 60, 180 and 360 minutes (Fig. 1). Finally, the samples were air quenched on a copper plate.

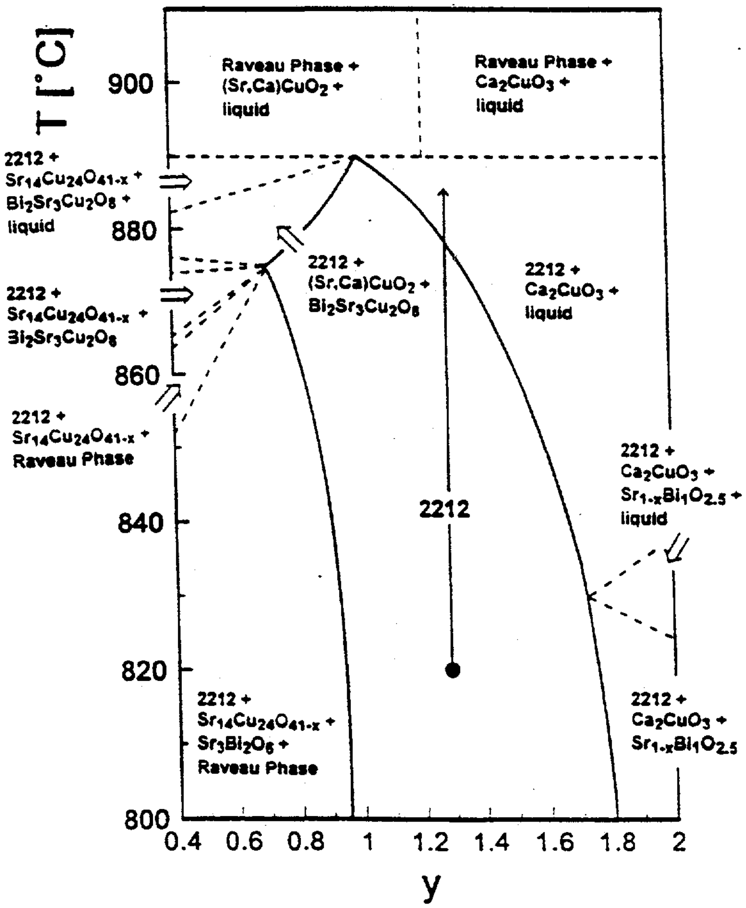

Fig. 1: Temperature vs. Ca content [8] including the performed annealing step to precipitate Ca_2CuO_3 + liquid.

The critical current densities of the pellets have been obtained by measuring of the magnetic susceptibility at 30 K up to 1 T and calculating J_c from these data using Bean's model [9]. The magnetic susceptibility has been measured at 30 K, as at this temperature an increase of the pinning properties is expected to become most obvious. The second phase content of the samples have been determined by optical and electron microscopy. The critical temperatures (onset) of the pellets have been determined by AC susceptibility measurements. Phase identification has been performed using electron microscopy with energy dispersive x-ray analysis (EDX), optical microscopy using polarized light, x-ray diffraction (CuKα_1, XRD) and transmission electron microscopy (TEM).

3. Results

The as-sintered 2212 samples are single phase (> 99 vol.-%) refering x-ray analysis, as well as, electron and optical microscopy. According to the phase equilibria, the annealing of the samples results in the formation of Ca_2CuO_3 and liquid (Fig. 2 and 3) combined with a reduction of the Ca content of the 2212 phase.

Fig. 4 shows the susceptibility vs. temperature plots of a starting sample and the 30 min post annealed sample. It is seen that the critical temperatures T_c of the samples and the trend of the susceptibility lines have not be changed significantly by the post annealing ($\Delta T_c \approx 5$ K). The graphic analysis (Fig. 5) shows that the

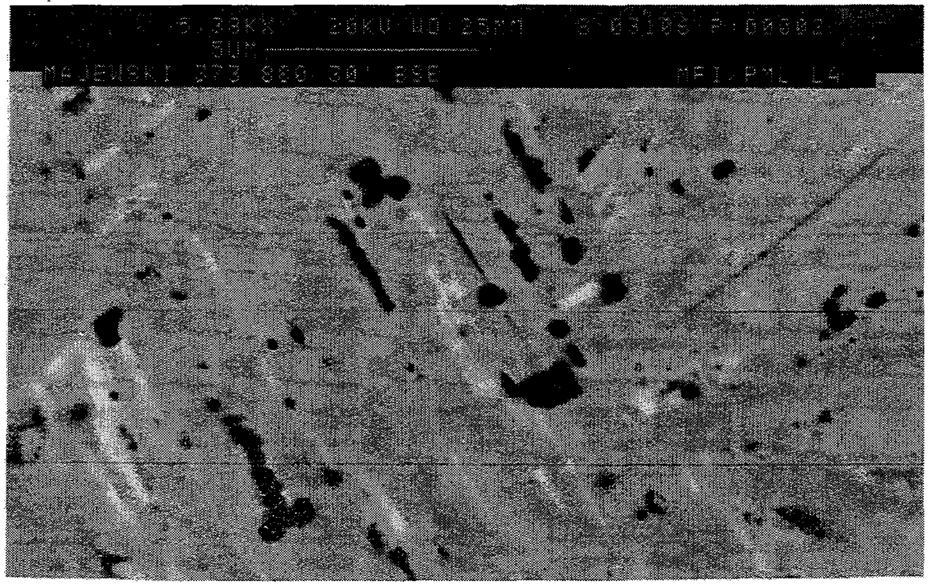

Fig. 2: SEM/BSE image of the 30 min annealed sample. Black: Ca_2CuO_3 precipitates, grey: 2212 phase, white: liquid.

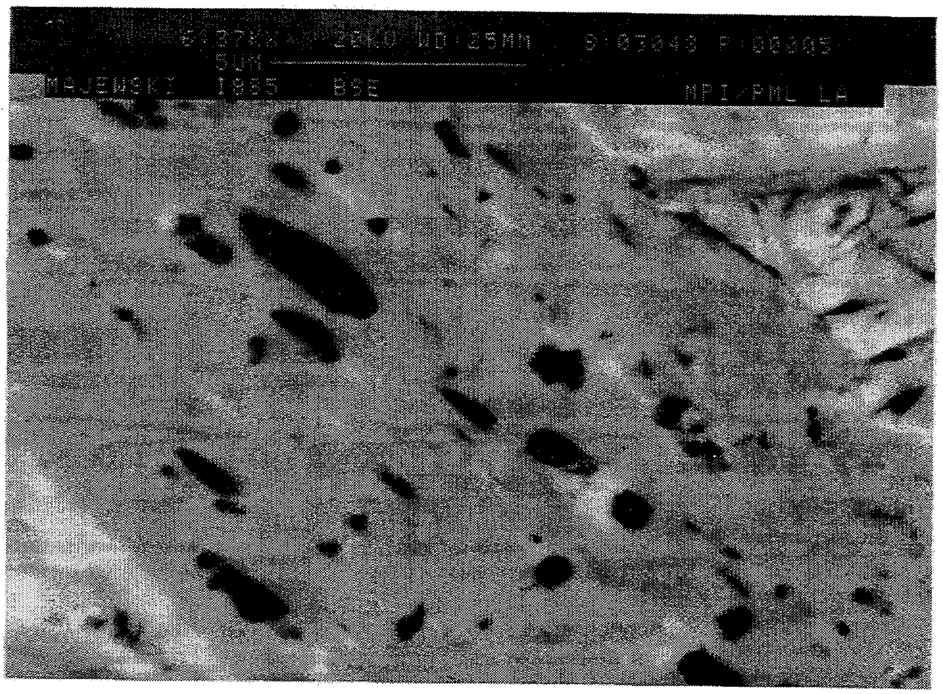

Fig. 3: SEM/BSE image of the 60 min annealed sample. Description see Fig. 2.

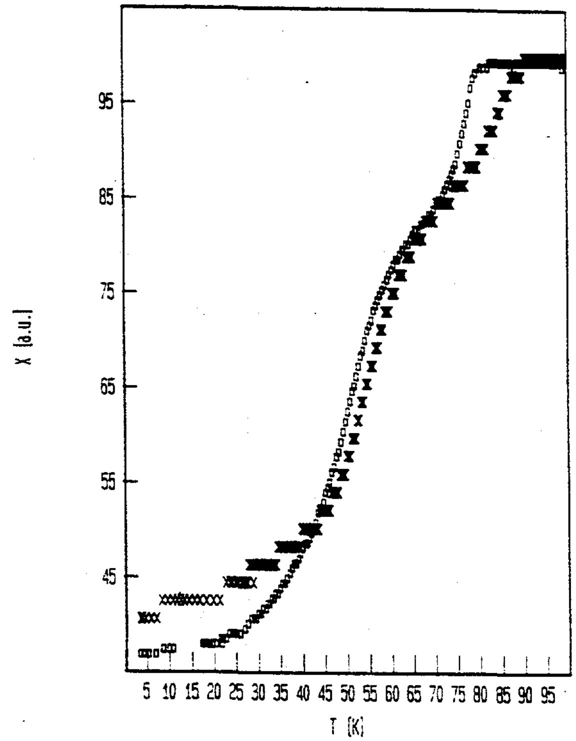

Fig. 4: Susceptibility vs. temperature plot of the starting samples (corsses) and the 30 min annealed samples (triangles).

$J_{c(1T)}/J_{c(0t)}$ values which represent the pinning force exhibit a distinct maximum at an annealing time of about 20 min. With increasing and decreasing annealing time the values decrease. The J_c vs. B plot of the starting samples and the 15 min annealed sample are depicted in Fig. 6. The samples have a J_c of 4000 A/cm^2 at zero magnetic field.

Fig. 7 shows the grain size distribution curves of the Ca_2CuO_3 precipitates of different samples. It is clearly seen that the grain size of the precipitates increases with increasing annealing time. Precipitates smaller than 100 nm have not been determined due to the resolution of the electron microscope. To overcome this drawback TEM-studies of the starting sample and the 15 and 30 min annealed samples have been performed. Nevertheless, even using the TEM precipitates with a grain size smaller than about 100 nm have not found. In addition, the size of the liquid precipitates which form unregularly shaped streaks also exceeds 10 nm.

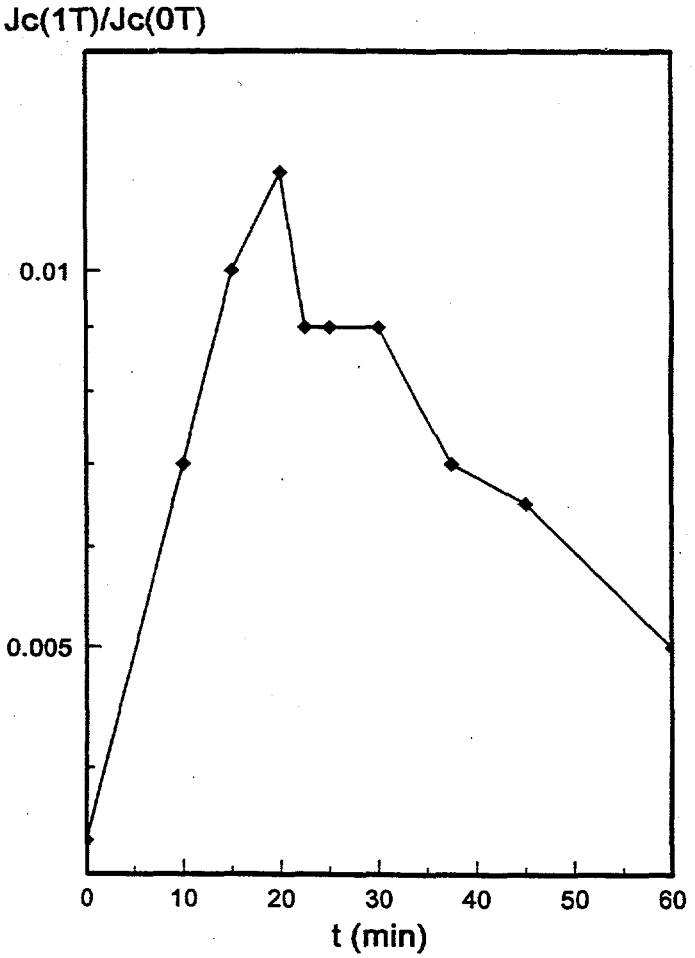

Fig. 5: $J_{c(1T)}/J_{c(0T)}$ at 30 K vs. the post annealing time of the samples.

Fig. 8 shows the mean grain size of the samples vs. the square rout of the annealing time revealing a linear dependence which suggests a diffusion controlled growth of the precipitates. Considering this diagram, it is clearly seen that a mean grain size of the precipitates of about 10 nm can be maintained at annealing times of only about 1 min. However, considering Fig. 5 a significant shift of the pinning properties can not be expected for a annealing time of only 1 min.

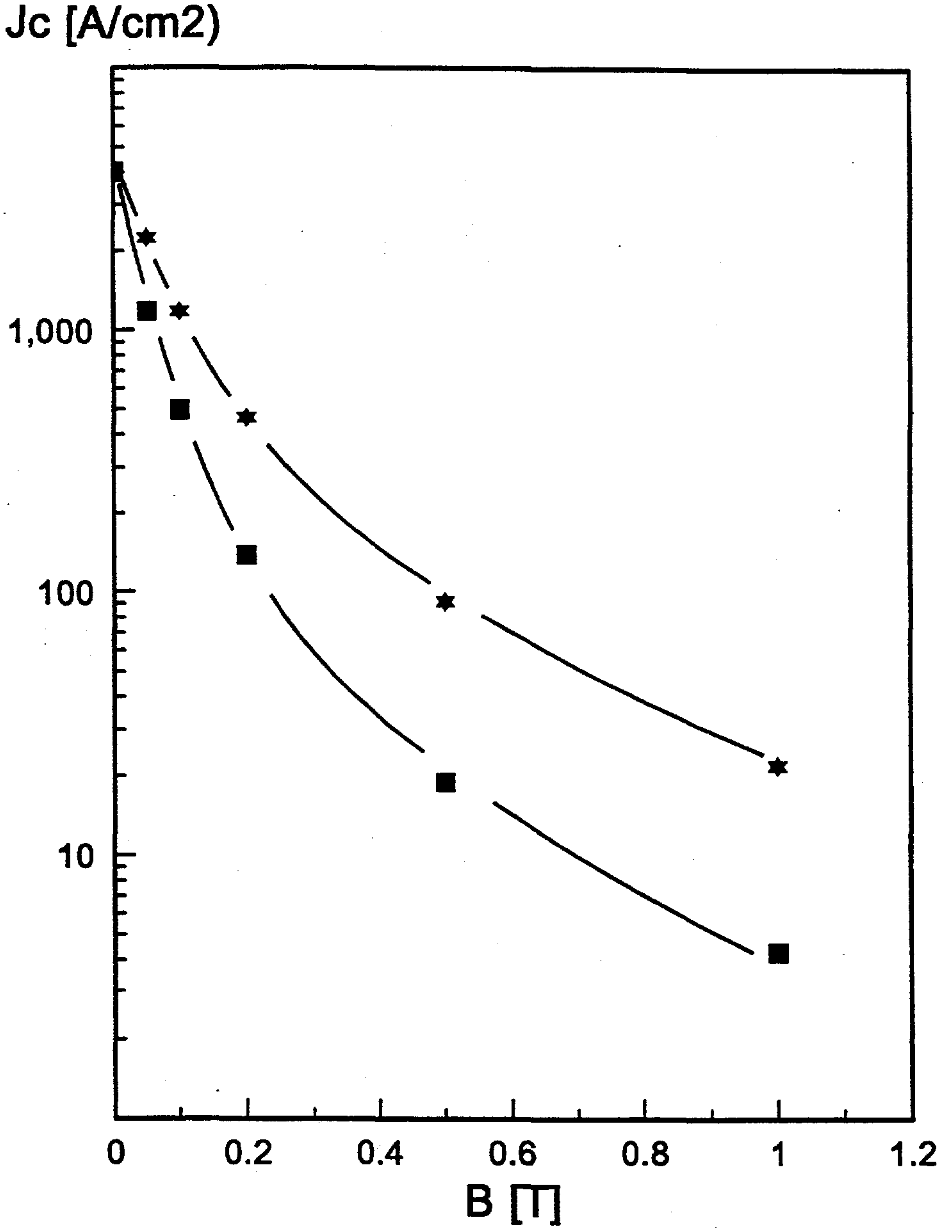

Fig. 6: J_c vs. the applied magnetic field of the starting sample (squares) and the 15 min annealed sample (stars). T = 30 K.

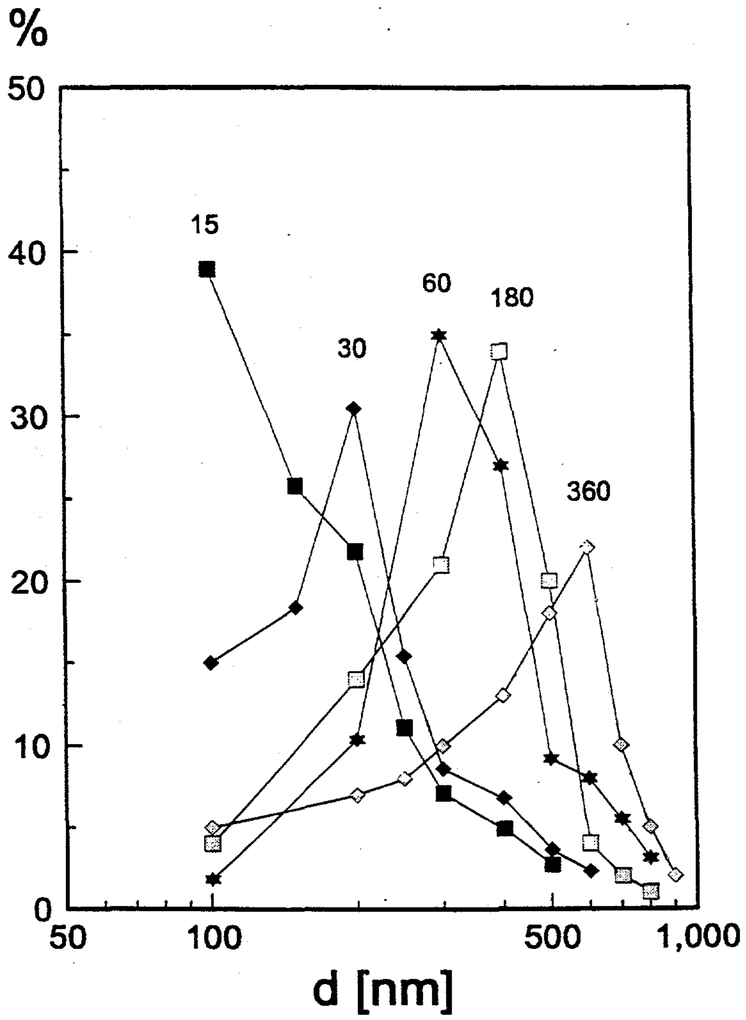

Fig. 7: Grain size distribution lines of the Ca_2CuO_3 precipitates. The values at the lines indicate the post annealing time (min).

The results of the analysis of the XRD-pattern of the samples are shown in Fig. 9, where the full width at half maximum of different reflections of the 2212 phase are plotted vs. the duration of the post annealing. The full width at half maximum of all considered reflections show a maximum at the 15 and 30 min annealed samples, which suggest an inceased lattice distortion of the 2212 crystals of these samples. In addition, TEM studies of the microstructure of the 15 and 30 min annealed samples and the starting sample show that the annealed samples exhibits an significantly higher density of dislocation of about 5×10^9 cm^{-2} compared to the starting samples. In addition, it is remarkable that the dislocation lines are concentrated at the a-b-planes of the crystals (Fig. 10).

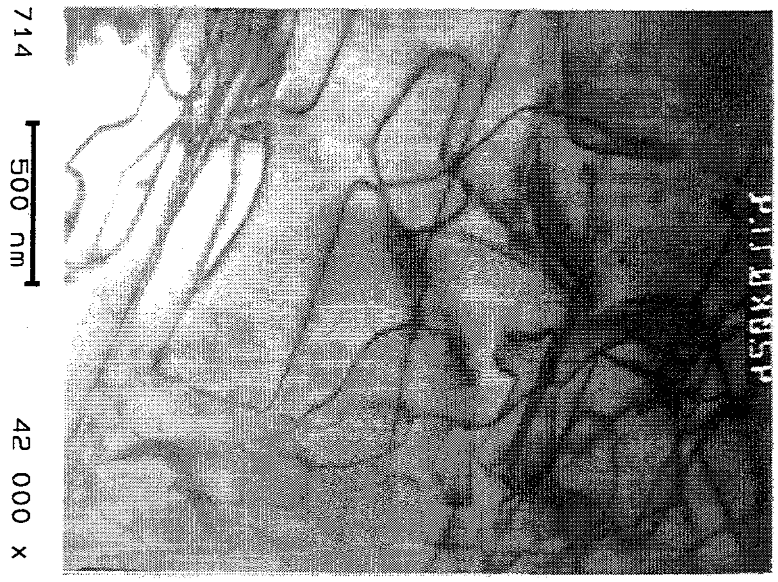

Fig. 10: TEM image of the a-b-plane of a 2212 crystal of the 30 min annealed sample.

4. Discussion and Conclusions

The increase of the J_c at magnetic fields above 0.1 T with annealing shows a strong evidence for the improvement of the pinning properties of such samples by the precipitation of second phases. The decrease of the pinning effect with increasing annealing time might be due to coarsening of the second phases. However, the grain size of the Ca_2CuO_3 precipitates significantly exceeds 10 nm and therefore, it can be concluded that the precipitates are not effective pinning centres, if at all.

It has to be taken into account that besides the possible effect of such second phases the increased pinning can also be caused by defects in the 2212 phase itself resulting from the phase transformation due to the reactions:

$$2212\text{ (Ca rich)} \Leftrightarrow 2212\text{ (lower Ca content)} + Ca_2CuO_3 + \text{liquid}$$

Such defects could be e.g. lattice distortions which may act as pinning centres. In this case, the observed decrease of J_c with increasing annealing time could be explained by the defect healing.

A strong evidence for the existence of an increased amount of lattice distortions e.g. coherent precipitates within the post annealed samples is the increased value of the full width at half maximum of different reflexes of the 2212 phase of the 15 and 30 min annealed samples and the higher density of dislocation lines of the annealed samples compared to the as sintered sample.

Considering this facts, it is extremly remarkable that especially these samples exhibits the highest increase of the pinning properties. Therefore, the increased pinning properties of the 15 to 30 min post annealed samples is believed to be caused by an increased amount of lattice distortions e.g. coherent precipitates (Guinier-Preston-zones) within the 2212 crsytals due to the precipitation of Ca_2CuO_3 and liquid. The Ca_2CuO_3 and liquid precipitates observed within these samples are believed to be too large to act as pinning centres.

5. Reference

1] H. Krauth, K. Heine, J. Tenbrink, High-Temperature Superconductors - Materials Aspects, Ed.: H.C. Freyhardt, R. Flükiger, M. Peuckert, DGM, Oberursel, FRG, 1991, 29.

2] K. Togano, H. Kumakura, H. Maeda, J. Kase, Chemistry of High Temperature Superconductors, Ed.: C.N.R. Rao, World Scientific, London, 1991, 399.

3] J. Bock, S. Elschner, E. Preisler, Adv. in Superconductivity III, Editors: K. Kajimura, H. Hayakawa, Proc. ISS 1990, Sendai, Springer Verlag, Tokyo, 1991, 797.

4] S.X. Dou, H.K. Liu, Supercond. Sci. Technol., **6** (1993), 297.

5] U. Balachandran, A.N. Iyver, P. Haldar, L.R. Motowidlo, J. of Mater., **45** (1993), 54.

6] J. Boiko, P. Majewski, F. Aldinger, Zeitschrift f. Metallkde, **85** (1994), 100.

7] E.H. Brandt, Physica C, **195** (1992), 1.

8] P. Majewski, H.-L. Su, B. Hettich, Adv. Mater., **4** (1992), 508.

9] C.P. Bean, Phys. Rev. Lett., **8** (1962), 250.

Tape Casting and Partial Melting of Bi-2212 Thick Films

D. Buhl, Th. Lang, B. Heeb and L.J. Gauckler
Nichtmetallische Werkstoffe, ETH Zürich, Sonneggstr. 5, CH-8092 Zürich, Switzerland

Abstract

To produce Bi-2212 thick films with high critical current densities tape casting and partial melting is a promising fabrication method. Bi-2212 powder and organic additives were mixed into a slurry and tape casted onto glass by the doctor blade tape casting process. The films were cut from the green tape and partially molten on Ag foils during heat treatment.

We obtained almost single-phase and well-textured films over the whole thickness of 20 µm. The orientation of the (a,b)-plane of the grains was parallel to the substrate with a misalignment of less than 6 °. At 77K/0T a critical current density of 15'000 A/cm^2 was reached in films of the dimension 1cm x 2cm x 20µm (1µV/cm criterion, resistively measured). At 4K/0T the highest value was 350'000 A/cm^2 (1nV/cm criterion, magnetically measured).

Introduction

For applications in electrical engineering, superconducting devices with macroscopic dimensions are required. This asks for other fabrication techniques and processing parameters than for thin films, sputtered polycrystalline films or single crystals. According to today's knowledge textured polycrystalline material is suitable for operations of large currents.

Melt-processing of Bi-2212 produces a dense, almost single-phase microstructure with no weak-link behavior [1]. The appropriate superconducting properties (T_c, T_{irr}, j_c) are achieved by controlling the processing parameters during melting, solidification and post annealing [2]. Particularly the critical current density can be further increased in thick films by grain alignment.

Kase et al. [3] first reported that tape casting and partial melting is a promising method to fabricate highly textured Bi-2212 thick films on Ag-substrates up to 10 µm thickness. Improvements of their processing lead to high critical current densities up to 3.2 x 10^4 A/cm^2 (77K/0T) and 5.9 x 10^5 A/cm^2 (4.2K/0T) [4].

The exact controlling of the processing parameters for partial melting and annealing is crucial, since the single-phase region is a function of temperature, oxygen partial pressure and cation stoichiometry [4] and an aligned microstructure is achieved only by the appropriate cooling [5].

Today, the applications of Bi-2212 thick films tend to low temperatures and high transport currents. Reproducable high critical current densities of thick films at 77K without

Ag as a parallel conductor are scarcely reported yet. The relation between properties and microstructure has not been clarified yet.

In this paper, we report processing procedures to fabricate textured Bi-2212 thick films on Ag-substrates by tape casting via the partial melting route. Emphasis is laid on the parameters enhancing the critical current densities and their reproducibility at 77K, as well as on the correlation between the properties and the microstructures of the tapes.

Experimental

Powder calzination

The starting materials (Bi_2O_3, $SrCO_3$, $CaCO_3$, Cu0) were weighed in the desired stoichiometry of $Bi_{2.2}Sr_{2.05}Ca_{0.95}Cu_2O_x$ which is in the centre of the single-phase region of Bi-2212. The powder was calcined at temperatures from 750 to 820 °C for 24 to 72 hours with intermediate grindings. This resulted in a powder consisting mainly of Bi-2212 containing small amounts Bi-2201 and Bi-free 014x24 as secondary phases. The grain size of the powder was smaller than 32 µm.

Tape casting

The Bi-2212 powder was mixed with organic additives into a non-toxic slurry. The organic formulation consisted of solvent (ethanol), dispersant (triolein), plasticizer (polyethylene glycol and phtalic acid ester) and binder (polyvinyl butyral). The slurry was milled for 4 hours, degassed and cast into tapes by the doctor blade tape casting process. The green tapes were 1.5 m long and 15 cm wide. The thickness of the tapes was 100 µm and shrank to 50 µm during drying. Samples of the desired shapes were cut from the green tape, put on silver foils (50 µm thick) and subjected to the heat treatment. The thickness of the tapes after the heat treatment was 20 µm.

Heat treatment

The heat treatment consisted of 4 main steps. First, the organic additives used for the tape casting process were burned out by heating slowly to 500 °C and holding there for 10 hours. The second, crucial step was the partial melting. The samples were heated at 40 °C/h to the maximum temperature (870 - 890 °C) and then cooled down with 5 °C/h to the annealing temperature of 850 °C. During this step the material was densified, the grains were aligned and the Bi-2212 phase formed. This part of the heat treatment was done in O_2 or air. The third step was the annealing of the samples at 850 °C in O_2 . This is known to influence both, microstructure and properties, of Bi-2212 ceramics.The last step after cooling down to room temperature was a reduction treatment at temperaturers below 600 °C in flowing N_2 ($p(O_2) < 10^{-3}$ atm) to adjust the oxygen content of the samples.

The processing parameters of the heat treatment were varied to investigate the influence of the processing on the properties and the microstructure. The maximum temperature was changed in small steps from clearly below the (870 °C) to high above the solidus temperature (895 °C). Additionally, the partial melting was done in air adjusting the temperatures to the lower solidus temperature (minus 20 °C compared to O_2). The annealing at 850 °C in O_2 was prolonged up to 100 hours. The reduction treatment was done at different temperatures between 400 and 600 °C in N_2 for 2 to 25 hours.

Sample characterization

To determine the superconducting properties the samples were magnetically measured by vibrating sample magnetometer (VSM) and AC-susceptometer. The critical temperature and the irreversibility temperature were determined by extrapolation of the reversible and the irreversible magnetization (VSM) or the real and the imaginary part of the susceptibility(AC). The critical current density was calculated from the width of the hystersis loop of M(H) (VSM). As we never found any granularity in melt-processed Bi-2212, ΔM is purely due to macroscopic intergranular currents [7]. It was measured from 4 to 90 K. Additionally, the critical transport current and its dependence on applied magnetic fields was measured resistively by the four-point dc method. The microstructure was investigated by light microscopy, X-ray diffraction analysis with CuK_α radiation and Si as internal standard, and scanning electron microscopy. Chemical compositions of phases were determined by energy dispersive X-ray diffraction.

Results and discussion

a) Microstructure

The thickness of the final Bi-2212 layer is approximately 1/3 of the green tape thickness. Fig.1 shows the fractured cross-section of a melt processed tape with the oxide thickness of 20 µm. The highly aligned microstructure, which is formed during the slow cooling from the partially molten state, is attributed to the Ag substrate and the low oxide layer thickness < 30 µm. The Bi-2212 layer is composed of stacks of plate-like grains with the aspect ratio exceeding 50. The XRD patterns confirm the good texture of the films; only the *(00l)* reflections of the Bi-2212 phase are observed (inset in fig.2). The misalignment of the grains is estimated from rocking curves of XRD measurements to be < 6° (fig.2).

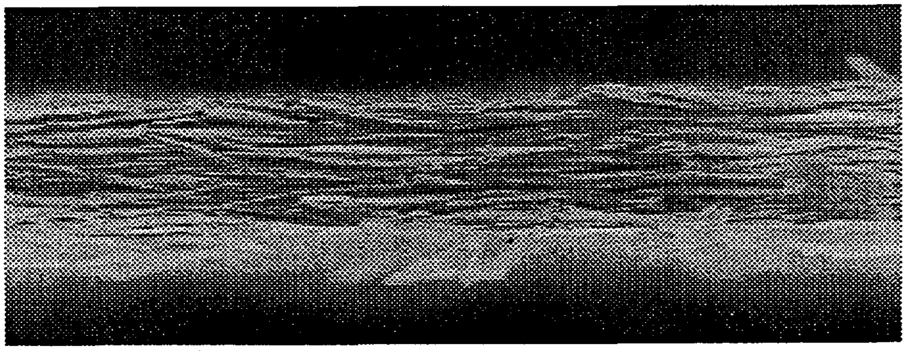

Fig.1 cross-section of a partially molten Bi-2212 thick film with a homogenous thickness of 20µm.

Influence of maximum processing temperature

Fig. 2 shows as well the strong influence of the maximum processing temperature on the phase composition of the thick films. Partial melting 5 °C above the solidus temperature results in nearly single-phase Bi-2212. The secondary phases are the one-layer Bi-2201, the Bi-free phase of the stoichiometry $Sr_{14-x}Ca_xCu_{24}O_y$ and the Cu-free phase $Bi_3Sr_4Ca_3O_z$. Partial melting 10 °C above the solidus temperature increases the amount of secondary phases. Increasing the maximum processing temperature to 15 °C above the solidus temperature increases the amount of secondary phases. The Bi-2201 phase becomes the main phase besides 2212 grains with a high density of 2201-intergrowths. From the asymmetric broadening of the *(008)* and *(0012)* reflections of the Bi-2212 phase the amount of these intergrowths can be calculated [8].

Light microscopy investigations show that the Bi-free 014x24 phase has the shape of needles, independent of the processing temperature. For processing temperatures more than 10 °C above the solidus temperature the length of the needles grows from less than 20 µm to over 200 µm. The Cu-free 3430 phase appears as cubes (length < 5 µm) for processing temperatures lower than 10 °C above solidus. At higher temperatures, large stalks of 3430 (length > 200 µm) are visible.

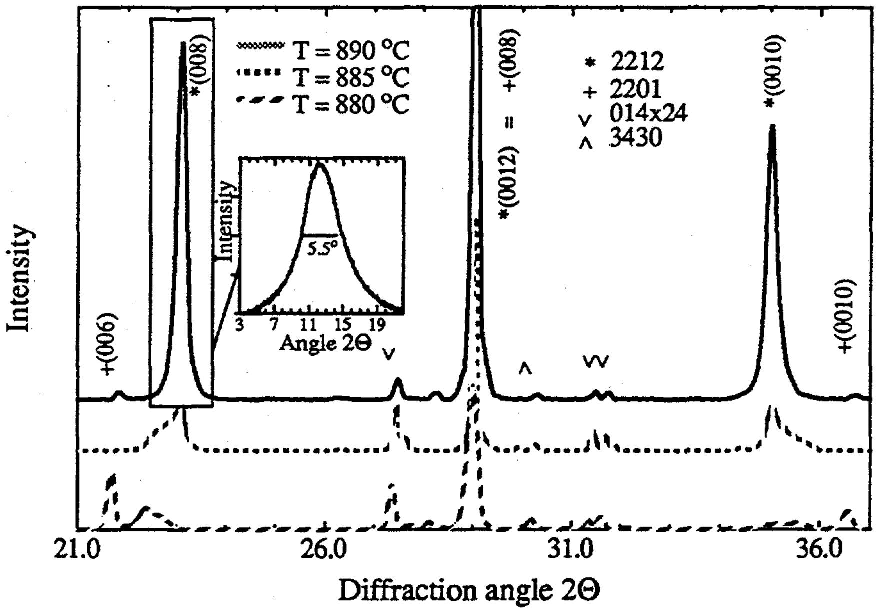

Fig.2 XRD patterns of Bi-2212 thick films with diffrent maximum processing temperatures. The inset shows a rocking curve of the (008)-reflection of the Bi-2212 phase.

Influence of annealing

The Cu-free and the Bi-free phases are the solid phases of the peritectic melting. On cooling, they react with the liquid to form Bi-2201 or Bi-2212. In contrast to bulk material, where the 2201 phase forms first and is transformed to the 2212 phase during annealing at 850 °C in O_2 by liquid/solid and solid/solid reactions [9], the Bi-2212 phase in thick films is the primary phase, formed by controlling the maximum processing temperature in the narrow temperature range of 3 - 8 °C above the solidus temperature. Partial melting above this temperature leads to large amounts of secondary phases which cannot be dissolved by annealing. The transformation from Bi-2201 to Bi-2212 remains incomplete and the amount of the Bi-free and Cu-free phases is hardly decreased. The different behavior of bulk and thick films is attributed to the different lengths of the oxygen diffusion paths. In bulk the remaining oxygen deficiency after partial melting controls the phase formation, whereas in thick films the oxygen uptake is much faster. Therefore, the cations influence the phase formation, leading to the direct crystallization of Bi-2212, if the volume fraction of the 3430-phase remains small.

b) Properties

The superconducting properties (T_c, T_{irr}, j_c) are strongly influenced by the processing parameters. An optimized heat treatment schedule leads to a critical temperature T_c = 92K, an irreversibility temperature T_{irr} = 88K, a critical current density j_c = 18000 A/cm^2 at 77K/0T and j_c = 350000 A/cm^2 at 10K/0T (1µV/cm-criterion) in 20 µm thick films. Critical transport currents up to 30A (corresponding to j_c = 15'000 A/cm^2) were measured resistively in samples of 1cm x 2cm x 20µm size. Fig. 3 illustrates that applied magnetic fields strongly decrease the critical current density depending on the orientation of the external fields. Only the component perpendicular to the (a,b)-plane of the 2212-grains decreases j_c. The I-V characteristics of the thick films obey a power law $V \sim I^{\alpha}$ (fig.4) with a smaller exponent α than found in bulk material at 77K [11]. The α measured at 77K is dependent on the external field. This confirms other results going more into the theory [12].

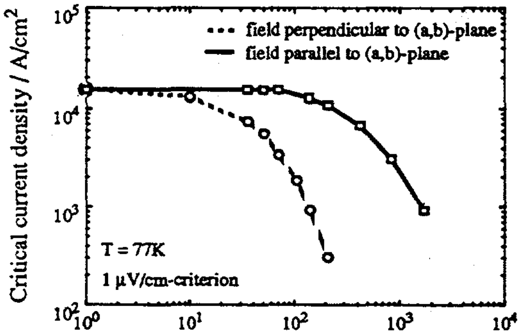

Fig.3 Critical current densities for applied magnetic fields at 77K.

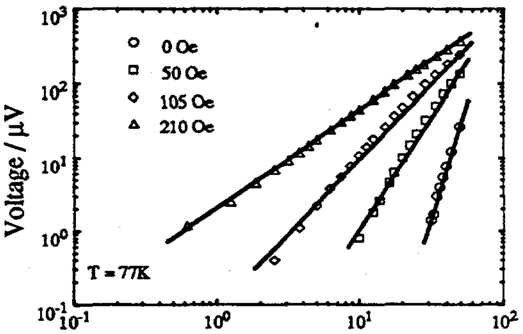

Fig. 4 I-V characteristics for Bi-2212 thick films. at 77K.

Influence of maximum processing temperature

In fig. 5 the critical current densities determined at 77K/0T are shown as a function of the maximum temperature. Maximum j_c are obtained only in the narrow range of 876 ± 3 °C as maximum temperature. The inset of fig.5 shows that different maximum temperatures shift the j_c-T curve parallel to higher or lower values without a remarkable change in the shape of the curves. This indicates that j_c is controlled by the same parameter over the whole temperature range from 10 to 77K. We therefore suggest that this behavior can be attributed to the connectivity of the current leading paths, rather than to pinning or granularity.

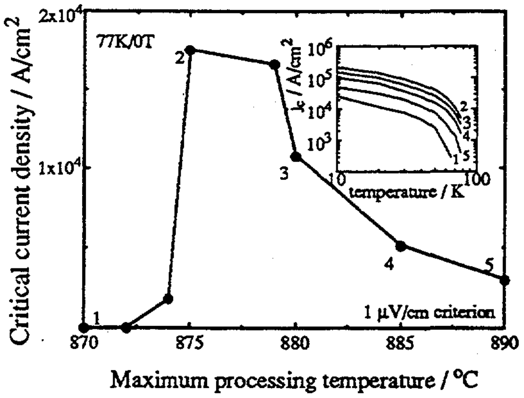

Fig.5 Critical current densities for different maximum processing temperatures at 77K. The inset shows the critical current densities from 10 to 85K.

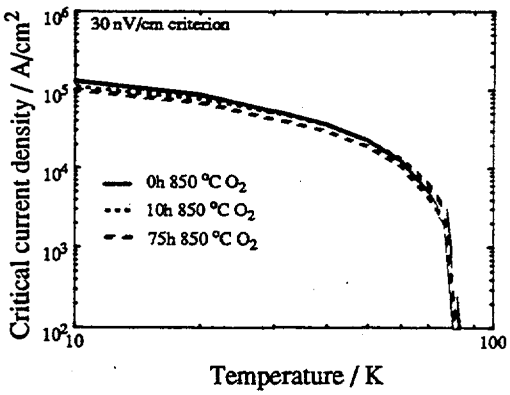

Fig.6 Critical current densities for different annealing time periods at 77K.

Influence of annealing

Samples processed at 876 °C were annealed at 850 °C in O_2 for different time periods. The critical current densities were equal over the whole temperature range from 10 to 85K for annealing 0, 10 and 75 hours (fig.6). Thus, annealing in the single-phase region at 850 °C in O_2 does not increase further the critical current density if the sample was partially molten within the optimum processing window.

In addition, samples with different maximum processing temperatures were measured before and after annealing for 50 hours (inset of fig. 5). The critical current densities did not change at all. Thus, annealing in the single-phase region at 850 °C in O_2 does not compensate the loss of critical current density caused by partial melting outside of the optimum processing temperature range. These observations are in good agreement with the analysis of the microstructures showing that the volume fraction of the secondary phases was not reduced by annealing.

Influence of processing atmosphere

Fig.7 shows that the shape of the j_c-T curve of samples processed in air is different from those processed in O_2. At low temperatures the critical current densities are the same but at higher temperatures the values for air-processed samples are lower. The microstructures of the samples have to be analysed more carefully to see wether different microstructures cause this different behavior for higher temperatures. So far, XRD-patterns show less 2201-intergrowths in 2212-grains in air-processed samples.

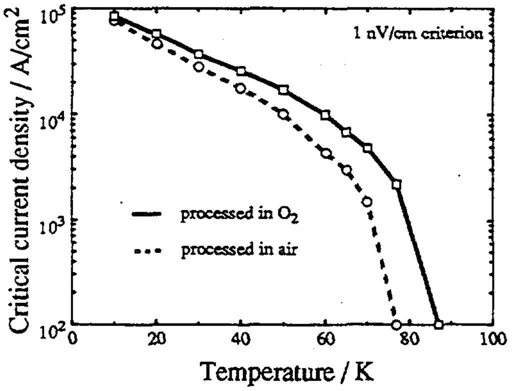

Fig.7 Critical current density for samples processed in air and O_2 from 10 to 85K.

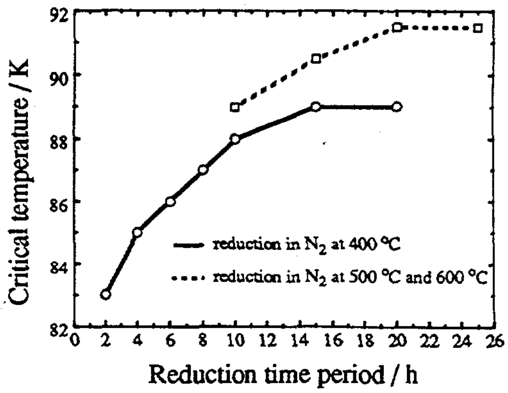

Fig.8 Critical temperature for different reduction time periods and temperatures.

Influence of reduction treatment

Reducing the samples at temperatures below 600 °C in N_2 adjusts the oxygen content without affecting the microstructure. It shifts the critical temperature T_c and the irreversibility temperature T_{irr} to higher values and thus increases j_c at 77K. Fig. 8 shows that annealing for 20 hours at temperatures between 500 and 600 °C optimizes T_c, T_{irr} and j_c at 77K.

Summary

Highly aligned Bi-2212 thick films were prepared by tape casting and partial melting on Ag-substrates. The maximum heat treatment temperature was found to be the most important processing parameter for microstructure and properties. It has to be controlled within 5 to 10 °C above the onset of the peritectic melting to minimize the amount of secondary phases and to maximize the critical current density at 4 and 77K. Annealing at 850 °C in O_2 did not change the critical current densities at all and the volume fraction of the secondary phases was not significantly reduced.

Thus the amount of the secondary phases is strongly correlated to the critical current density. Additionally, the connectivity of the current leading paths is the limiting factor over the whole temperature range rather than pinning or granularity.

References

1 W. Paul and Th. Baumann, Physica C, 175 (1992) 102.

2 B. Heeb, S. Oesch, P. Bohac and L.J. Gauckler, J. Mat. Res., 7 [11] (1992) 2948.

3 J. Kase, N. Irisawa, T. Morimoto, K. Togano, H. Kumakura, D.R. Dietderich and H. Maeda, Appl. Phys. Lett.56 [10] (1990) 970.

4 J. Shimoyama, N. Tomita, T. Morimoto, H. Ktaguchi, H. Kumakura, K. Togano, H. Maeda, K. Nomura and M. Seido, Jpn. J. Appl. Phys., 31 (1992) 1328.

5 P. Majewski, B. Hettich, N. Rüffer and F. Aldinger, J. of El. Mat., 22 [10] (1993) 1259.

6 W. Zhang and E. Hellström, Physica C, 218 (1993) 141.

7 W. Paul, B. Heeb, Th. Baumann, M. Guidolin and L.J. Gauckler, MRS Symp. Proc.275 Pittsburgh (1992) 383.

8 H. Heinrich, Ph.D. Thesis ETH Zurich No. 10760 (1994).

9 B. Heeb and L.J. Gauckler, H. Heinrich and G. Kostorz, J. Mat. Res., 8 [9] (1993) 2170.

10 Th. Schweizer, R. Müller and L.J. Gauckler, Physica C, 225 (1994) 143.

11 W. Paul and J.P. Meier, Physica C, 205 (1993) 240.

12 E. Zeldov, N.M. Amer, G. Koren, A. Gulpa, M.W. McElfresh and R.j. Gambino, Appl. Phys. Lett., 56 [7] (1990) 680.

Effect of Microwave-Enhanced Superconductivity in $YBa_2Cu_3O_7$ Bi-crystalline Grain Boundary Weak-links

C. M. Fu, C. M. Chen, H. C. Lin, K. H. Wu, J. Y. Juang, T. M. Uen, and Y. S. Gou

Institute of Electrophysics, National Chiao-Tung University, Taiwan, R. O. C.

Abstract

We have studied systematically the effect of microwave irradiation on the temperature dependent resistivity *R(T)* and the current-voltage (*I-V*) characteristics of $YBa_2Cu_3O_{7-x}$ (*YBCO*) bicrystalline grain boundary weak-links (GBWLs), with grain boundary of three different tilt angles. The superconducting transition temperature, T_c, has significant enhancement upon microwave irradiation. The microwave enhanced T_c is increased as a function of incident microwave power, but limited to an optimum power level. The GBWLs of 45° tilt boundary has shown to be most sensitive to the microwave irradiation power, and the GBWLs of 36.8° tilt boundary has displayed a moderate response. In contrast, no enhancement of T_c was observed in the GBWLs of 24° tilt boundary, as well as in the uniform films. Under the microwave irradiation, the *R(T)* dependence is hysteretic as the transition taken from superconducting state to normal state and vice versa. Mechanisms associated with the redistribution of nonequilibrium quasiparticles under microwave irradiation are discussed.

1. Introduction

The enhancement of superconductivity by microwave irradiation has been observed in a wide range of conventional superconductors and structures made thereof [1-9]. The fascinating phenomena of microwave induced enhancements of superconductivity has excited a considerable amount of investigations to find the operating mechanisms.

Eliashberg and colleagues [13] proposed the first microscopic theory to link the microwave-enhanced effects to the nonequilibrium processes of the quasiparticles induced by the electromagnetic fields. At finite temperatures, some of the quasiparticles are excited from the low-lying energy state near the edge of the energy gap to the higher-energy states and reach to a new nonequilibrium steady state. Since the low-lying quasiparticles are more effective in inhibiting paring correlation than the higher energy ones, with the total number of quasiparticles being preserved, the microwave induced redistribution of excited quasiparticles would lead to an increase of the energy gap. As a consequence, the critical temperature and the critical current are enhanced, in agreement with the BCS theorem. Later, calculation by Chang and Scalapino has shown that [14] not only the redistribution of quasiparticles causes the gap enhancement, but a net decrease in the total number of quasiparticles plays an important role. Aslamazov and Larkin have pointed out that [15], the nonequilibrium state occurs locally and the resultant enhancement is associated with gap oscillations in the weakly-coupled regions. Only if the constriction size, *a*, is smaller than coherence length (ξ) but larger than a characteristic length $\eta = \xi(T)(1-T/T_c)^{1/4}$, there is superconductivity enhancement. They showed that the effective cooling of electrons trapped in the region of the contact which has a lower value of the gap may result in an increase of critical current.

We report in the article, for the first time to our knowledge, the microwave-enhanced superconducting transition temperature in $YBa_2Cu_3O_{7-x}$ (YBCO) grain boundary weak-links (GBWL), with grain boundary of various tilt angles. The experimental results have demostrated significant enhancement of superconducting transition temperature ($\Delta T_C > 2$ K as compared to a few tens of mK obtained in conventional superconductors) when the GBWL's were irradiated by an $f = 12.4$ GHz microwave with appropriate incident powers. The GBWLs of 45° tilt boundary has shown to be most sensitive to the microwave irradiation power, and the GBWLs of 36.8° tilt boundary has displayed a moderate response. On the contrast, the GBWLs of 24° tilt boundary as well as the uniform film have shown no enhancement on the T_C. Mechanisms associated with the redistribution of nonequilibrium quasiparticles under microwave irradiation will be discussed. We note that the present observations are fundamentally different from the enhancements manifested by the photoinduced hole doping effects, recently reported in under-optimized HTSC systems [16].

2. Experimental

The $YBa_2Cu_3O_{7-x}$ grain boundary weak-links studied in this work were fabricated from the YBCO epitaxial films deposited onto the $SrTiO_3$ bicrystal substrates by KrF excimer pulsed laser. There different misorientation angle of $SrTiO_3$ bicrystal substrates was used. The details of the thin film deposition conditions has been described previously[17]. Briefly, the substrate temperature was held at 770°C using a CW CO_2 laser as the heating source. The oxygen partial pressure was kept in the range of 0.2-0.3 Torr during deposition with a laser energy density of 2-4 J/cm^2 and a repetition rate of 3-5 Hz. At the end of deposition, the CO_2 laser is shut off, resulting in a fast quench from 770°C to room temperature by taking less than 1 minute. The films obtained are nearly perfect *c*-axis oriented in crystalline structure.

The weak-link bridge was patterned by photolithography into a geometry of 20 μm in width, 1200 Å in thickness and 60 μm in length of two voltage electrodes crossing boundary. The standard four-probe arrangement was used to determine the electrical behavior of the YBCO weak-links. To improve the contact resistance, gold pads were evaporated on the contact electrodes. The sample was mounted to sample holder which was cooled in the closed cycle system. The pulsed current method was applied to prevent heating from long time running in the normal state, which may suppress the critical values. The microwave energy is irradiated to the sample via an antenna, with a fixed frequency of 12.4 GHz. Careful shielding of the thermometer and electrical circuit was ensured to prevent the microwave heating on thermometers and the pick-up voltage in a feedback circuit which may result in a lower bath temperature. No temperature change (within a resolution of ± 0.03K) was observed even when the maximum output power up to 18dBm was applied.

3. Results and Discussion

Fig. 1 shows the $R(T)$ dependence of the transition from the superconducting to normal state (S → N) of a GBWLs of 36.8° tilt boundary. As shown in Fig. 1, the critical superconducting transitions are shifted to higher temperatures under appropriate microwave power, with the main features of normal state resistance not affected by the microwave irradiation. Further, the enhancement appears to be dependent on the incident microwave power and reaches the maximum at an optimal power P_{opt}. At incident power $P > P_{opt}$ the transition cease to shift to higher temperatures and moves back to lower temperatures. The numerical value given here for P is labeled for the output power from microwave generator. One might compare this result with those observed photoinduced T_c enhancement in under-optimized HTSC systems [16]. What is immediately noted is that the microwave-induced T_c enhancement can only be observed during GBWLs are being irradiated by microwave,

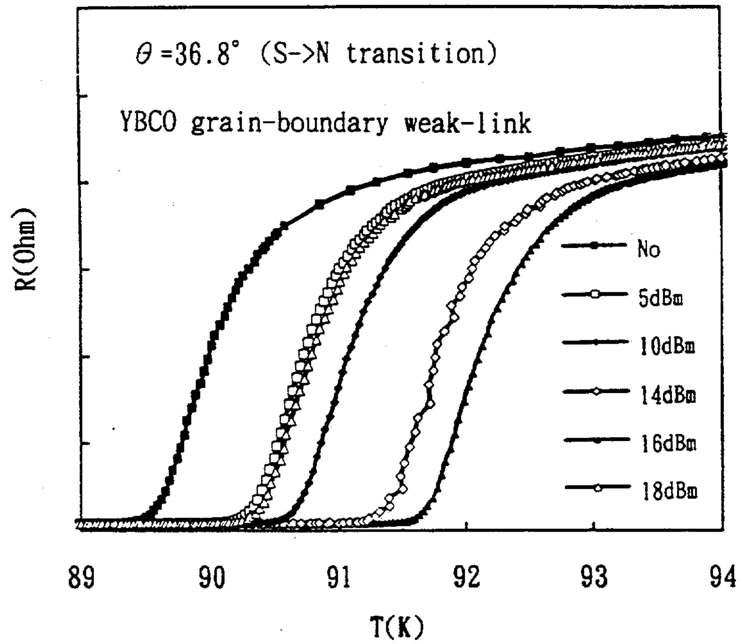

Fig. 1: The temperature dependent resistance, $R(T)$, of YBCO grain boundary weak-links under microwave irradiation in a variety of powers levels.

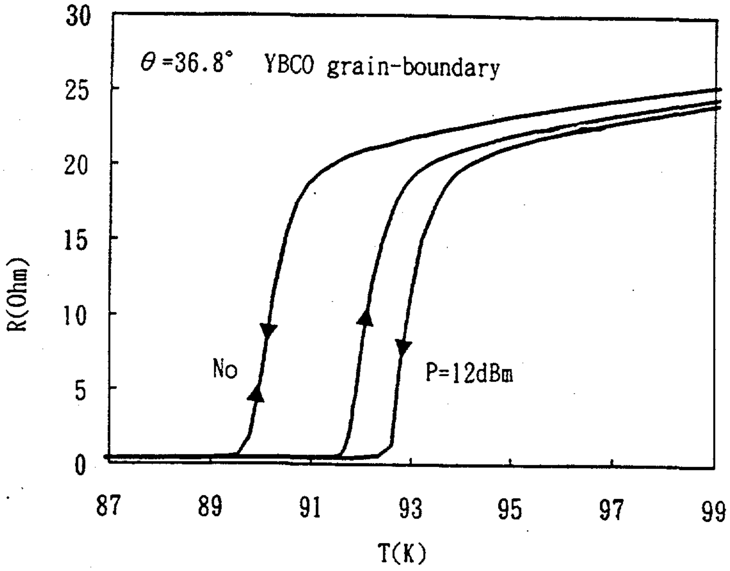

Fig. 2: The plot of the temperature hysteresis effect of the *R(T)* behavior under microwave irradiation.

while the photoinduced T_c enhancement remains persistent when the illumination was turned off.

As shown in Fig.1, the resistance near the superconducting transition is also significantly reduced. The *R(T)* curve deviating from usual normal state linearity was much more pronounced with increasing incident power and reaches the maximum value at P_{opt}, though the deviations are already evident for high T_c cruprates in the absence of microwave irradiation. Moreover, as incident power $P > P_{opt}$ the deviations were suppressed. The fact that the power dependence of both the T_c enhancement and excess-conductance changes in accordance with each other indicates the underlying physical mechanisms giving rise to the phenomena must be closely related. One might associate the T_c enhancement and excess-conductance as simply due to thermal fluctuations. However, according to the fluctuation theory, the enhancement of superconducting transition temperature originating from fluctuations should not exceed the "bulk" value of the system. Apparently, herein, the interpretation simply by fluctuations does not agree with the "large" T_c enhancement observed in our GBWL samples.

As shown in Fig. 2, the critical transitions under microwave irradiation are hysteretic, with the transition from normal state to superconducting state (N → S) occuring at higher temperatures than that of the S → N ones. We have checked the same measurements with no external microwave applied and no transition hysteresis were evident. Thus the results should be entirely originating from the microwave-induced effects. In Fig. 3, we summarize the power dependence of T_c enhancement of two different cases. Where the T_c is defined as the temperature at which 5 % of the normal state resistance remains. The T_C defined in this way is apt to the main transition of the microbridge, to be distinguished from the T_{CO} encountered with phase slippage effect, as will be described later. As can be seen immediately, the typical T_C enhancements (≈3K at optimal case) obtained here is remarkable, as compared to the values of a few tens of mK to 100 mK typically observed in conventional superconductors. The fact that the microwave-enhanced T_C's are all well above the equilibrium value of the system, again, indicates that conventional fluctuation theorem alone is inadequate to explain the results.

The mechanism that might be able to account for the T_C enhancement in YBCO grain boundary weak-links is the microwave-induced nonequilibrium dynamics of the redistributed quasiparticles derived for similar phenomena observed in conventional superconductors [2-9]. The essence of this theoretical scenario was that the redistributed quasiparticles in high-lying energy states, driven by the microwave field, have higher recombination rate, resulting in a more effective pairing, and could effectively increase a net reduction in the quasiparticle density. This, in turn, increase the averaged magnitude of the superconducting energy gap, leading to enhancements of both T_C and excess-conductance, in consistence with the results observed here.

In the framework of the nonequilibrium quasiparticle dynamics, the transition hysteresis is explainable as: more energy is required to break up "well-ordered" pair from cool side [1]. As a consequence, the transition from S → N should be characterized by an abrupt jump as indeed usually being observed. Such a signature, however, is hardly evident in the present case. Thus, in order to understand the intriguing results observed, we propose here a qualitative interpretation based on the notion of fluctuation-aided nonequilibrium quasiparticle redistribution. Here, the ever-existent fluctuations are regarded as the background needed for the realization of microwave-triggered quasiparticle redistribution. Within the context of this crude

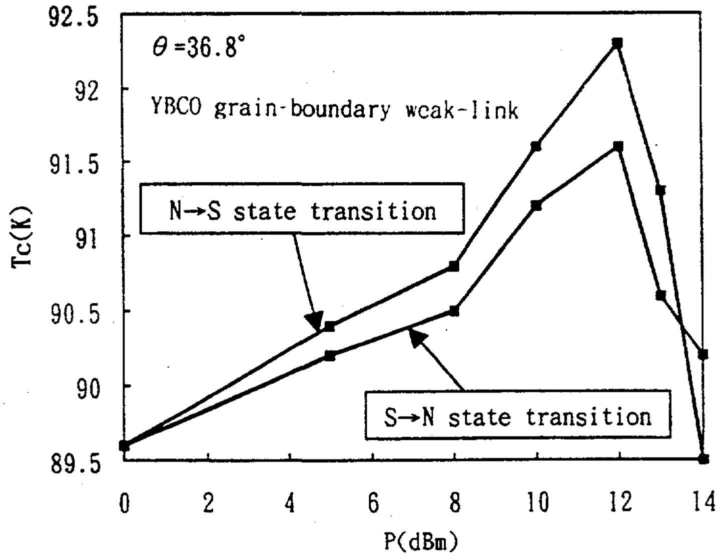

Fig.3: The microwave power dependence of T_C enhancement, for the resistive transition from normal (*N*) to superconducting (*S*) state (*N* → *S*) and (*S* → *N*).

picture, a qualitatively consistent interpretation for all the results presented here can be obtained as follows. In the circumstances, the Cooper pairs in the superconducting state below T_C are much well-defined, making it hard to turn on quasiparticle excitations by the driving microwaves, even with the same extent of fluctuation background assumed. On the other hand, when the temperature is approaching T_C from the normal state region, the fluctuating quasiparticles are very easy to be excited and re-distributed. As a result, the T_C enhancement occurs at higher temperature in N → S transition than that of S → N one's. The functional dependence of $\Delta T_C(P)$ (see Fig.3) may also lend further support to the above argument.

To further elucidate the mechanisms underlying these phenomena other peculiar features originating from microwave irradiation were investigated systematically. Perhaps the most important one to be noted is that the enhancement can only be realized when cross boundary configuration were practiced. No microwave-induced enhancement was observed in intra-regions despite of the fact that essentially the same bridge dimensions in the same films were used. This strongly suggests that the microwave induced enhancement occurs only in weak-links and not in homogeneous regions. It is contradicting to the experimental results observed in conventional superconductors as asserted by Eliashberg's theory, of which microwave enhancement of superconductivity can exist in a 'uniform structure' only. As have been pointed out by Aslamazov and Larkin that [15], the nonequilibrium state occurs locally and the resultant enhancement is associated with gap oscillations in the weakly-coupled regions. Only if the constriction size, a, is smaller than coherence length (ξ) but larger than a characteristic length $\eta = \xi(T)(1-T/T_C)^{1/4}$, there is superconductivity enhancement. In order to interpret the results of no enhancement of I_C at $T \approx T_C$, the constraint of $\xi > a > \eta = \xi(T)(1-T/T_C)^{1/4}$ is needed to be regarded.

Furthermore, we have performed studies on the GBWLs of 24° and 45° tilt boundary, respectively. Fig.4 shows the effect of the microwave power on the $R(T)$ behavior of a GBWLs of 45° tilt boundary, measured as the transition taken from the superconducting to normal state (S → N). We notice that, as revealed in Fig.4, the transitions can be shifted to an optimal higher temperature upon a microwave power comparative lower than that for optimal case in GBWLs of 36.8° 's. Moreover, when incident power $P > P_{opt}$ the enhancement is ceased and the transition systematically drops back to lower temperatures as P increased. In contrast, the GBWLs of 24° tilt boundary is insensitive to the microwave irradiation, as shown in Fig.5. It corroborates that no enhancement effect upon microwave irradiation was also observed in case of the uniform film.

The relation between tilt angles of GBWL's and the sensitivity of $\Delta T_C(P)$ is summarized as follows. To the microwave power, the GBWLs of 45° tilt boundary are seen to be the most sensive, the 36.8° 's displays moderrate respone, and the 24° 's is inert. This implies a correlation between GBWLs junction properties and the microwave enhancement of superconductivity. A systematic study on this scheme is

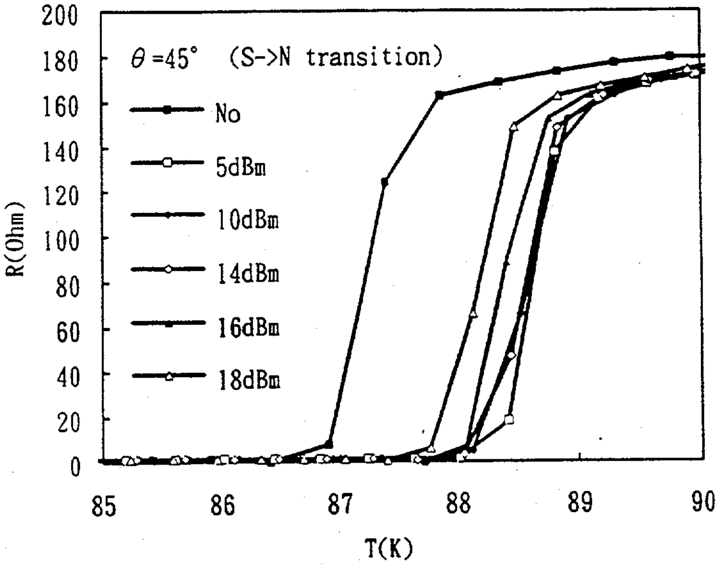

Fig. 4: The $R(T)$ curve of YBCO grain boundary weak-links of 45° tilt boundary under microwave irradiation in a variety of powers levels.

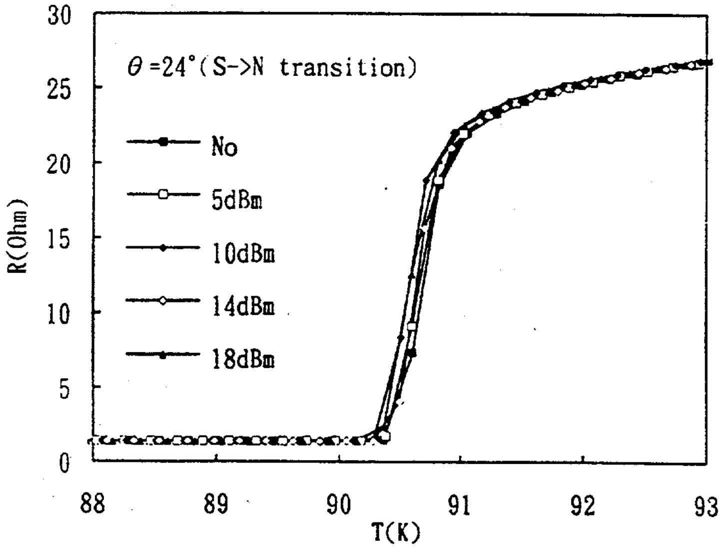

Fig. 5: The $R(T)$ curve of YBCO grain boundary weak-links of 24° tilt boundary. No enhancement is observed under under microwave power levels.

under progress, to ascertain to what extent of the physical constraint in GBWLs play a role for the observation of T_C enhancement under microwave irradiation.

In conventional superconductors, the observation of T_C enhancement was always accompanied with observations of enhancement in I_C and energy gap in the *I-V* characteristics. To check if, indeed, similar effects occur in the YBCO weak-link, we have performed the *I-V* measurements at a variety of fixed temperatures and incident powers. For the temperature range $T < T_{CO}$, the experimental results showed that under the microwave irradiation the I_C was depressed, accompanying with current steps in the *I-V* characteristics. That is, no enhancement of I_C was observed in the YBCO weak-links. However, when the *I-V* measurements were performed at $T \approx 0.99T_{CO}$, shape of V(I) curve changed from parabolic to hyperbolic with an invaried ohmic linearity at higher current part, indicating an opening of energy gap. Detailed descriptions of the particular features is given in Ref[20].

In ending, we would like to emphasize that the microwave induced enhancement of superconducting properties was observed repeatedly for at least 3~ 4 runs each in three weak-links.

4. Conclusion

In conclusion, we have presented the microwave induced enhancement of superconductivity in YBCO grain-boundary weak-links; in which remarkable enhancement of T_C were observed. The temperature dependent resistance curves shows anomalous hysteresis behavior as the transition taken from superconducting state to normal state and vice versa. Compared the microwave enhanced $\Delta T_C(P)$, the strength of sensitivity of three different tilt anglar GBWLs upon the microwave irradiation have shown a systematic variations: the GBWLs of 45° tilt boundary is most sensitive, the 36.8° 's displays a moderrate respone, and the 24° 's is inert to the microwave powers. The correlation between GBWLs junction properties and the microwave enhancement of superconductivity implies the geometrical constraint is needed to be regared for the enhancement effect. Mechanisms associated with the redistribution of nonequilibrium quasiparticles under microwave irradiation is being worked out.

Acknowledgements :

We would like to thank Prof. C.C. Tsuei, Prof. C.C. Chi, Prof. T. J. Watson Yang, Prof. V.V. Moshchalkov, Prof. Y. Bruynseraede, Prof. A. Gilabert for helpful discussions. C. M. Fu was supported by the National Science Council (NSC) of Republic of China. This work is supported by the National Science Council of Republic of China No. NSC82-0212-M009-002 and NSC83-0212-M009-022.

References:

1. For an extensive review, see 'Nonequilibrium superconductivity', edited by D. N. Langenberg and A. I. Larkin, North-Holland Publishing, (1986).
2. T. M. Klapwijk and J. E. Mooij, Physica **81B**, 132 (1976); T. M. Klapwijk, J. N. van der Bergh, and J. E. Mooij, J. Low Temp. Phys. **26**, 385 (1977).
3. B. R. Fjordboge, T. D. Clark, and P. E. Lindelof, Phys. Rev. Lett. **37**, 1302 (1976).
4. J. A. Pals and J. Dobben, Phys. Rev. B **20**, 935 (1979).
5. James T. Hall, Louis B. Holdeman, and Robert J. Soulen, Jr. Phys. Rev. Lett., **43**, 1011 (1980)
6. Yu. I. Latyshev and F. Ya. Nad', JETP **44**, 1136 (1976).
7. A. H. Dayem and J. J. Wiegand, Phys. Rev. **155**, 419 (1967).
8. A. F. G. Wyatt, *et.al.* Phys. Rev. Lett. **16**, 1166 (1966).
9. B. I. Ivlev, *et.al.* J. Low Temp. Phys. **10**, 449 (1973). Elishberg
10. T. K. Hunt, Phys. Rev. **177**, 749 (1977); T. K. Hunt, and J. E. Mercereau, Phys. Rev. Lett., **18**, 551 (1967).
11. V. M. Dmitriev, E. V. Khristenko, and S. Shapiro, Fiz. Kond. Sost., **28**, 3 (1973).
12. P. E. Lindelof, Solid State Comm., **18**, 283 (1976).
13. G. M. Eliashberg, Sov. Phys. JETP **34**, 668 (1972).
14. J. J. Chang and D. J. Scalapino, J. Low Temp. Phys. **29**, 477 (1977); **31**, 2 (1978).
15. L. G. Aslamazov, and A. I. Larkin, JETP, **47**, 1136 (1978).
16. G. Nieva, E. Osquiguil, J. Guimpel, M. Maenhoudt, B. Wuyts, Y. Bruynseraede, M. B. Maple, and I. K. Schuller, Phys. Rev. B **46**, 14249 (1992).
17. K. H. Wu, C. L. Lee, J. Y. Juang, T. M. Uen, and Y. S. Gou, Appl. Phys. Lett. **58**, 1089 (1991).
18. R. Gross, Physica C **180**, 235 (1991).
19. D. Winkler, et.al., Phys. Rev. Lett., **72**, 1260 (1994).
20. C. M. Fu, et. al. submitted to Phy. Rev. Lett.

Effects of Oxygen Stoichiometry on the Scaling Behaviors of $YBa_2Cu_3O_x$ Grain Boundary Weak-Links

K. H. Wu, C. M. Fu*, W. J. Jeng, J.Y. Juang, T. M. Uen, and Y.S. Gou

Institute of Electrophysics, National Chiao-Tung University, Taiwan, R.O.C.

Abstract

The effects of oxygen stoichiometry on the transport properties of the pulsed laser deposited $YBa_2Cu_3O_x$ bicrystalline grain boundary weak-link junctions were studied. It is found that not only the cross boundary resistive transition foot structure can be manipulated repeatedly with oxygen annealing processes but the junction behaviors are also altered in accordance. In the fully oxygenated state i.e with $x = 7.0$ in $YBa_2Cu_3O_x$ stoichiometry, the junction critical current exhibits a power of 2 scaling behavior with temperature. In contrast, when annealed in the conditions of oxygen-deficient state (e.g with $x = 6.9$ in $YBa_2Cu_3O_x$ stoichiometry) the junction critical current switches to a linear temperature dependence behavior. The results are tentatively attributed to the modification of the structure in the boundary area upon oxygen annealing, which, in turn, will affect the effective dimension of the geometrically constrained weak-link bridges. The detailed discussion on the responsible physical mechanisms as well as the implications of the present results on device applications will be given.

1. Introduction

Since the first demonstration of Dimos et al. [1], the YBCO bicrystalline grain boundary weak-link (GBWL) junctions have become one of the most extensively studied fields in high T_c superconductivity researches. From the practical application point of view, such an extensive effort makes the GBWL the most successful structure in superconducting electronic devices realized to-date [2-6]. Even for the step-edge type junction devices developed later with the aid of rapidly maturing deposition techniques [7-9], the basic physics involved were all, at least to some extent, originated from the understanding acquired through the studies on GBWLs. However, despite the successes obtained along this line, there exist many fundamental issues to be clarified. For instance, the low frequency *1/f* noise exhibited in most superconducting quantum interference devices (SQUID) made of GBWLs were tremendous and were believed to be due to either the trapping and detrapping processes of charges situated at the localized states existing in oxygen-depleted regions of about 1 nm thick near the grain boundaries or due to the motion of fluxons trapped in the boundary area. On the other hand, in the step-edge type junctions, the critical current-normal resistance product (I_cR_n product), which determines the detection sensitivity of the devices, were usually too low as compared to the predicted superconducting energy of gaps of the materials [10-13]. As a result, a thorough understanding on the nature the GBWLs and to find a way of manipulating their properties in a fully controllable manner are undoubtedly the most important task to be surmounted if further improvements in devices of this kind are considered.

In this paper, we report on the transport properties of YBCO bicrystalline GBWLs deposited *in-situ* onto $SrTiO_3$ bicrystal substrates with various grain misorientations by pulsed laser deposition technique. It was found that by using a novel annealing process to precisely control the stoichiometry of the whole structure, not only the structure of the resistive transition tails (appears when the applied current was across the junction) but the scaling behaviors of the junction critical current as a function of temperature were all able to be altered in a repeatable manner, indicating a fundamental change in the nature of the GBWLs occurred. In the fully oxygenated state *i.e.* with x = 7.0 in $YBa_2Cu_3O_x$ stoichiometry, where the T_c's of the films remote from boundary areas were all above 90 K indicative of high quality films were obtained, the junction critical current exhibits a 3/2 power scaling behavior with temperature. In contrast, when annealed in the conditions of oxygen-deficient state (e.g . with x = 6.9 in $YBa_2Cu_3O_x$ stoichiometry) the junction critical current switches to a linear temperature dependence behavior. The physical mechanisms responsible for the observed switchovers are tentatively attributed to the modification of the effective dimension of the geometrically constrained weak-link bridges during oxygen annealing. More important is that such switchover behaviors were in fully controllable fashion and were dependent only the annealing conditions applied. Since the actual nature of the junction is what determines the all important Josephson effects to be utilized in device manufacturing, the results obtained in the present study are considered significant not only in the understanding of the fundamental physical mechanisms involved but also have important implications from the practical point of views.

2. Experimental

The bicrystalline YBCO films used in this study were deposited *in-situ* onto the $SrTiO_3$ bicrystal substrates with a tilt grain boundary angle of 36.8° by KrF excimer laser. The deposition conditions have been reported in detail previously [14]. Briefly, the substrate temperature was held at 770° C using a CW CO_2 laser as the heating source. The oxygen partial pressure was kept in the range of 0.2-0.3 Torr during deposition with a laser energy density of 2-4 J/cm^2 and a repetition rate of 3-5 Hz. It is noted that it took less than 1 minute to cool the films down to room temperature by the present process. Usually, the films thus obtained are all having rather smooth surface morphology with $T_{co} \sim 90$ K and nearly perfect c-axis oriented crystalline structure.

In order to define the junction properly, the bicrystalline YBCO films were all patterned into bridge-type configuration, as depicted in Fig. 1, by standard photolithography processes. It is noted that the patterning processes, though involving some acid etching, do not affect the quality of the films noticeably. In Fig. 1, the leads were arranged in way such that both intra-boundary and inter-boundary properties of the same films would be measured and compared. To avoid possible heating effects, which may become crucial in later measurements, gold pads were deposited on each connecting lead and then annealed in oxygen to reduce the contact resistance.

For oxygen stoichiometry control, the thorough equilibrium data of Gallagher et al. [15] were used as a standard reference in setting appropriate annealing conditions. In our practice, samples were sealed in a quartz tube with proper oxygen partial pressures and then the whole assembly was then placed into a tube furnace hold at an appropriate temperature, typically in the range of between 370 ℃ and 470 ℃. Since the whole system was essentially at thermodynamical equilibrium, the oxygen content was thus determined thereby. To make further check the full resistive transition *R(T)* behaviors were compared with those of Ohkubo et al. [16] and Ossandon et al. [17] for samples with different presumed oxygen stoichiometries. It was found that the two independent methods gave rather consistent results, indicating we are indeed obtaining the right oxygen stoichiometry by using the present annealing scheme. All the samples, when

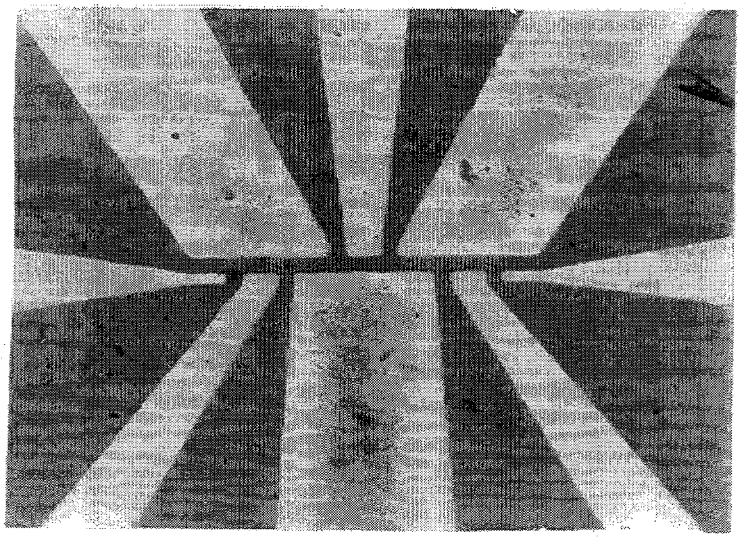

Fig. 1: The optical picture showing the typical geometrical configuration of the grain boundary weak-link junctions formed on YBCO films deposited on bicrystalline $SrTiO_3$ substrates. The arrow shows the location of the grain boundary.

irradiated with microwave with frequency of ~ 12GHz, showed clear current steps at correct voltages in the cross-boundary current-voltage (*I-V*) characteristics, indicating that the GBWLs are indeed Josephson junctions in nature. It is, however, very difficult to distinguish the nature of the junctions directly from the steps appearing in I-V characteristics alone, as the manifestations of Josephson effects are, essentially, indistinguishable for SIS and SNS junctions. Thus, other steps have to be taken to further elucidate the subtle effects of oxygen stoichiometries.

3. Results and Discussion

Figure 2 shows, as an example, the effects of changing oxygen stoichiometry on the *R*(*T*) transition of one of the GBWLs studied. It is emphasized that the behaviors shown here are completely reversible and fully controllable. That is, depending on the particular annealing condition given, the *R*(*T*) behaviors shown in Fig. 2 are unique for each condition applied. We have checked this for at least four cycles and found that the uniqueness remains essentially unchanged. As can be seen in Fig. 2, there are several features to be noted. The foot structures shown in Fig. 2 are only observable when the current is applied across the bicrystal grain boundary and does not appear when the current was limited in the intra-boundary regions. Thus it can be considered only arise from the effects of the boundary and not from inhomogenity of the films. Furthermore, the foot structure as well as the whole *R*(*T*) curve, as depicted clearly by the three conditions given here, change significantly when the oxygen stoichiometry varies, indicative of overall change in oxygen stoichiometry during annealing processes. This

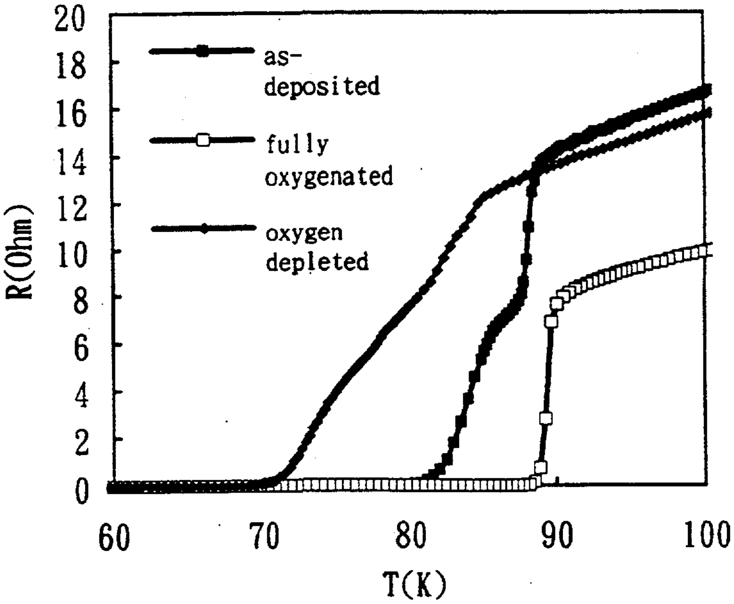

Fig. 2: The typical cross boundary *R*(*T*) behaviors exhibited by the same GBWL under three different annealing conditions. Three curves depict the as-deposited, fully oxygenated and oxygen-deficient cases, respectively.

is not surprising as has been pointed out earlier [14, 16-17]. The diffusion of oxygen in YBCO films is at least comparable with that in sintered porous bulk samples and it is easy to acquire equilibrium oxygenation states. Consequently, the depression and enhancement in T_c as compared to the as-deposited case are due to overall oxygenation states. The normal state resistance further indicates the effects of annealing in promoting atomic rearrangement and, hence, in eliminating crystalline defects. In our deposition process, the films were all quenched directly from deposition temperatures within a matter of tens of seconds and no intermediate oxygen annealing and slow cooling was involved [14]. Thus, relatively defective structure is expected. This explains why even with higher T_c's as compared to the oxygen deficient case the normal state resistance is higher. The situation, nonetheless, should not affect the general behaviors to be discussed in the following.

Perhaps, the most important feature that is of interest here is the foot structure in $R(T)$ curves. As is clearly demonstrated in Fig. 2, in the fully oxygenated condition, though the foot structure has been suppressed significantly as compared to the other two conditions, it is still existent. As has been mentioned earlier, this is a direct consequence of weak-link behavior. Otherwise, similar effects should also be observable in intra-boundary region. An alternative explanation of such foot structure in $R(T)$ transition was attributed to the fluxon creep effects, first proposed by Tinkham [18]. However, since there were Josephson effects routinely observed in these GBWL's together with the fact that it only appeared when cross boundary properties were measured, the mechanism responsible for the foot structure is believed to be a manifestation of order parameter phase slippage across the boundary instead of being due to flux creep effects. With this in mind, we have proceeded to measure the temperature scaling behavior of the junction critical current to try to delineate the nature of the GBWL's, especially how it would be altered with the change of oxygen stoichiometry.

Figure 3 shows the characteristics of the current-voltage (I-V), which display the overall I-V features can be described by the RSJ model. We have extented our I-V measurements to a linear region and then extrapolate back from the linear region to the zero voltage state to determine I_c. The results thus obtained were then plotted as a function of reduced temperature, define as $t = T/T_c$, and is shown in Fig. 4. For the full oxygenated junction the I_c shows an $I_c \sim (1-t)^{1.98}$ behavior, Fig. 4(a). Such a temperature dependence, is consistent with quadratic dependence (*i.e.* $I_c \sim (1-t)^2$) expected for an SNS proximity effect tunnel junction. Alternatively, one might suggest that it is may comparable to a $(1-t)^{1.5}$ results observed in superconducting whiskers and long bridges, however. Thus, it seems that the present GBWL structures are more likely to be geometrically constrained bridges rather than direct tunnel junctions. In contrast to that described above, for junctions annealed in oxygen-deficient conditions (*e.g.* $x = 6.9$), the $I_c(T)$ exhibits an $I_c \sim (1-t)^{0.93}$ behavior, as shown in Fig. 4(b). Since the nearly linear temperature dependence of junction I_c can be either interpreted as a result of SIS Josephson behavior or direct consequence of a short bridge constriction, the results are to be discussed further.

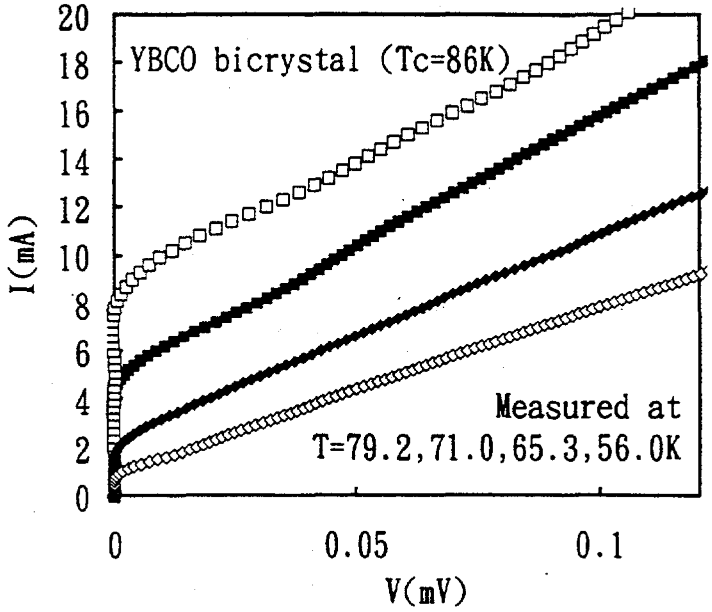

Fig. 3: The characteristics of the *I-V* of a fully oxygenated YBCO GBWL's.

According to Ambegaokar and Baratoff [19], in an SIS Josephson junction, the critical current as a function of temperature is expressed as:

$$I_c(T) = I_o[\Delta(T)/\Delta(0)]\ tanh[\Delta(T)/2k_B T], \qquad (1)$$

with $I_o = \pi\ \Delta(0)/2eR_n$ representing the zero-temperature critical current. Expression (1) can be further reduced to

$$I_c(T) \sim 1/4\ \{I_o[2\Delta(0)/k_B T_c]\ \}[1-(T/T_c)], \qquad (2)$$

for temperatures very close to T_c and taking the usual BCS expression $\Delta(T) = \Delta(0)$ $[1-(T/T_c)]^{1/2}$ for the superconducting energy gap. Although, it gives the required linear temperature dependence for the observed results, the fact that the observed linear $I_c(T)$ is evidently extended to a region well below where expression (2) is applicable and whether the gap energy is BCS-like or not is still a matter of debate [20, 21], it seems not physically plausible to assume that it is indeed the case. On the other hand, as compared to the results shown in Fig. 4(a), the present case should also be considered as a consequence of geometrical constraint alternation due to oxygen lodgment and dislodgment during annealing. In the fully oxygenated state homogeneous distribution of the much needed oxygen is expected to be fulfilled, thus the whole boundary can be considered as a single weak-link and hence gives rise to a long bridge behavior. On the contrary, in the oxygen deficient condition, localized short bridges are likely to exist due to defective nature of the grain boundaries. By attributing the switching behaviors in $I_c(T)$ scaling of the GBWL's not only the

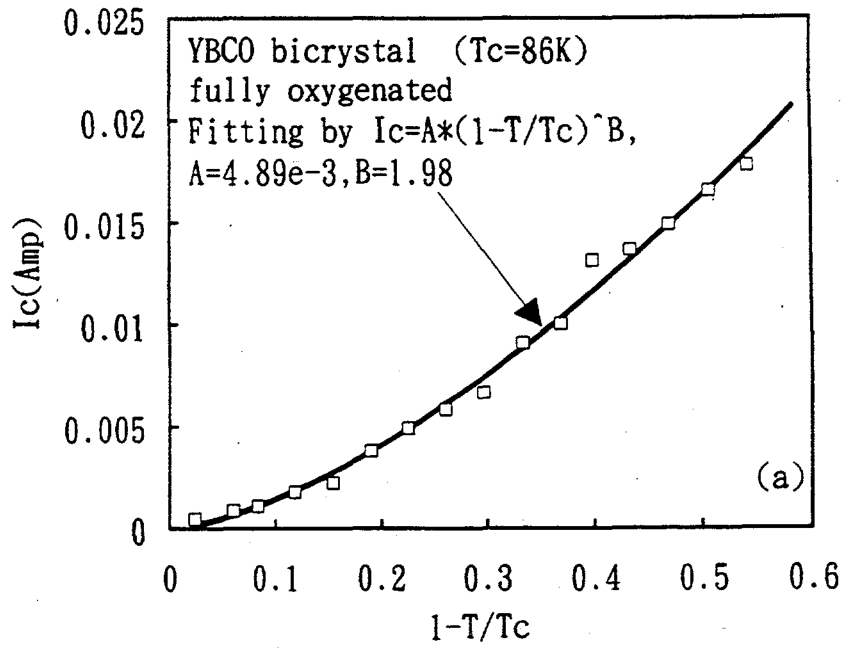

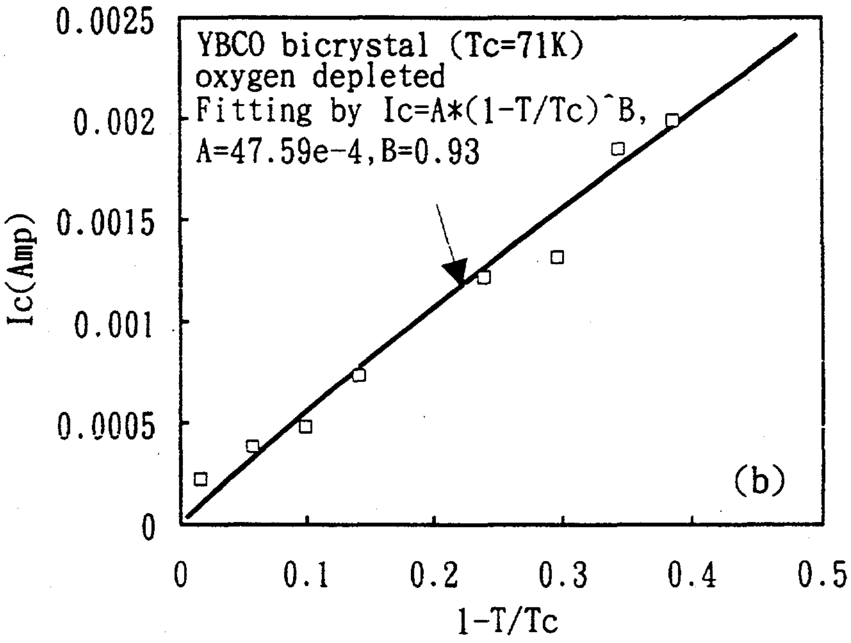

Fig. 4(a): The temperature dependence of the critical current I_C ploted as a function of $(1\text{-}t)$ for the fully oxygenated YBCO GBWL's, showing a power of nearly 1.98 behavior for geometrically constrained long bridge characteristics.

Fig. 4(b): Similar plot as in (a) for the oxygen-deficient YBCO GBWL's, demostrating a near linear temperature dependence, a characteristic of geometrically constrained short bridge weak-links.

observed experimental results can be explained in a rather consistent fashion but also on a physically more plausible basis. Certainly the validity of the above assessments has to rely on more detailed microstructural studies of the bicrystalline films to give direct supporting evidences. Nevertheless, the present experiment has, undoubtedly, not only provided a powerful probe to investigate the fundamental electronic properties of these practically important device structure but also has made a further step on the designing of applications.

4. Conclusion

In summary, we have presented a novel technique in controlling the oxygen stoichiometry and investigated its effects on the transport properties of the pulsed laser deposited YBCO bicrystalline GBWL structures. It has been observed that, by precisely manipulating the oxygen stoichiometry the $I_C(T)$ behaviors of the GBWL's exhibit a switchover from the SNS behavior tends to be SIS type, as for fully oxygenated state is de-oxidated to be an oxygen-deficient situation. Alternative may be given as an switchover from a geometrically constrained long bridge weak-link for fully oxygenated state to a short bridges for oxygen-deficient situations. The results are tentatively attributed to the defect structure rearrangements induced by the lodgment and dislodgment of oxygen during the annealing processes.

Acknowledgement:

This work was supported by the National Science Council of Taiwan, R.O.C., under grant #: NSC82-0212-M009-002 and NSC83-0212-M009-022.

References:

*Author to be correspondent

1. D. Dimos, P. Chaudhari, J. Mannhart, and F.K. Legoues, Phys. Rev. Lett. 61, 219 (1988).
2. J. Mannhart, P. Chauhari, D. Dimos, C.C. Tsuei, and T.R. Mcguire, Phys. Rev. Lett. 61, 2476 (1988).
3. R.H. Koch, C.P. Umbach, G.J. Clark, P. Chauhdrai, and R.B. Laibowitz, Appl. Phys. Lett. 51, 200 (1987).
4. R. Gross, P. Chauhdrai, K. Kawasaki, M.B. Ketchen, and A. Gupta, Appl. Phys. Lett. 57, 727 (1990).
5. J. Gao, W.A.M. Aarnink, G.J. Gerritsma, and H. Rogalla, Physica C171, 126 (1990).
6. D.K. Chin and T. Van Duzer, Appl. Phys. Lett. 58, 753 (1991).
7. M.S. DiIorio, S. Yoshizumi, K.-Y. Yang, J. Zhang, and M. Moung, Appl. Phys. Lett. 58, 2552 (1991).

8. R.H. Ono, J.A. Beall, M.W. Cromar, T.E. Harvey, M.E. Johansson, C.D. Reinysema, and D.A. Rudman, Appl. Phys. Lett. 59, 1126 (1991).
9. K. Enpuku, J. Udomoto, T. Kisu, A. Erami, Y. Kuromizu, and K. Yoshida, Jpn. J. Appl. Phys. 30, L1121 (1991).
10. B.D. Huut, M.C. Foote, and L.J. Bajuk, Appl. Phys. Lett. 59, 982 (1991).
11. J. Gao, Yu. Boguslavskij, B.B.G. Klopman, D. Tersptra, G.J. Gerritsma, and H. Rogalla, Appl. Phys. Lett. 59, 2754 (1991).
12. S.E. Romaine, P.M. Mankiewich, W.J. Skocpol, and E. Westerwick, Appl. Phys. Lett. 59, 2603 (1991).
13. M.J. Zani, J.A. Luine, R.W. Simon, and R.A. Davidheiser, Appl. Phys. Lett. 59, 234 (1991).
14. K.H. Wu, J.Y. Juang, C.L. Lee, T.C. Lai, T.M. Uen, Y.S. Gou, S.L. Tu, S.J. Yang, and S.E. Hsu, Physica C195, 241 (1992).
15. T.B. Lindemer, J.F. Hunley, J.E. Gates, A.L. Sutton, J. Brynestad, C.R. Hubbard, and P.K. Gallagher, J. Am. Ceram. Soc. 72, 1775 (1989).
16. M. Ohkubo, T. Kachi, and T. Hioki, J. Appl. Phys. 68, 1782 (1990).
17. J.G. Ossandon, J.R. Thompson, D.K. Christen, B.C. Sales, H.R. Kerchner, J.O. Thomson, Y.R. Sun, K.W. Lay, and J.E. Tkaczyk, Phys. Rev. B 45, 12534 (1992).
18. M. Tinkham, Helv. Physica Acta 61, 443 (1988); Phys. Rev. Lett. 61, 1658 (1988).
19. V. Ambegoakar and A. Baratoff, Phys. Rev. lett. 10, 486 (1963); 11, 104 (1963).
20. T. Hasegawa, M. Nantoh, and K. Kitazawa, Jpn. J. Appl. Phys. 30, L276 (1991).
21. M.L. Chu, H.L. Chang, C. Wang, J.Y. Juang, T.M. Uen, and Y.S. Gou, Appl. Phys. Lett. 59, 1123 (1991).

Effect of Particle Size and Particle Size Distribution on Physical Characteristics, Morphology and Crystal Structure of Explosively Compacted High-Tc Superconductors

I. Kotsis, M. Enisz, D. Oravetz, A. Szalay*
University of Veszprém, Hungary
*Metalltech Ltd. Budapest, Hungary

ABSTRACT

A superconductor, of composition $Y(Ba,K,Na)_2Cu_3O_x/F_y$ and a composite, of composition $Y(Ba,K,Na)_2Cu_3O_x/F_y + Ag$, with changing K, Na and F content, but a constant silver content (Ag = 10 mass per cent) was prepared using a single heat treatment. The resulting material was ground in a corundum lined mill, separated to particle size fractions of 0-40 µm, 0-63 µm and 63-900 µm and explosively compacted, using an explosive pressure of 10^4 MPa and a subsequent heat treatment. Best results were obtained with the 63-900 µm fraction of composition $Y(Ba_{1,95}K_{0,01})Cu_3O_xF_{0,05}/Ag$: porosity < 0.01 cm^3/g and current density 2800 A/cm^2 at 77 K.

INTRODUCTION

The raw material, synthesized for explosive compaction was a superconducting solid solution, of composition $YBa_2Cu_3O_{7-\Delta}$, with Ba-ions partly replaced by alkali ions, and oxygen ions by fluoride ions. In some of the experiments a superconductor/silver composite was used.

According to I-Wei Chen [1] superconducting properties are less affected by oxygen content and sintering parameters if alkalis are substituted for barium.

Nedkov and Dragieva [2] studied superconductors, of general composition $Y_{1-0.2x}Ba_{2-0.2x}M_xCu_3O_{7-\Delta}$, where M = Li, K, Na, and found that with increasing sintering temperature the shape of the magnetic susceptibility vs. temperature plot is changed as contrasted to pure $YBa_2Cu_3O_7$. The most striking change was shown in case of K-doped sample. As the density of samples was also changed, in the order of nondoped > K > Na > Li, their obvious explanation was that doping ions occupy a part of lattice vacancies. The comparative XPS investigation of the K-containing and nondoped samples showed an increased number of trivalent copper ions, to be explained with the transformation of

$$Cu^{2+} + Ba^{2+} = K^{+} + Cu^{3+} \qquad [3]$$

Nedkov and co-workers [4] tried another possibility too: to replace even copper by alkalis (K^+, Na^+, Li^+) in superconducting ceramics. The change in the valency state of copper can be described by the formula

$$Y^{3+}Ba_2^{2+}M_x^{+}Cu_{3.5-2x}^{2+}Cu_x^{3+}O_{7-\Delta}^{2-}$$

Superconducting crystals increase in size as a consequence of alkali substitution for Ba^{2+} ions (2.5 mol.%), even in case of identical heat treatment (Enisz, Kotsis, [5]). This tendency increases in the order of Na < K.

$YBa_2Cu_3O_7F$ and $YBa_2Cu_3O_6F_2$ should be mentioned among fluoride-containing superconductors [6, 7, 8]. These have been prepared by solid state reactions, from BaF_2, CuF_2 and YF_3 showing a slight improvement of Tc and other superconducting properties. If, however, the $YBa_2Cu_3O_{7-\Delta}$ phase is thermally treated at 300 ^oC in NF_3 gas, then only the Meissner effect is improved considerably.

The joint partial replacement of Ba^{2+} ions by Na^+ and K^+, and of oxygen ions by fluoride ions (Kotsis and Enisz [9]) result in an increase of Tc (by 6-10 K), of bulk density and of critical current density.

$YBa_2Cu_3O_{7-\Delta}$/Ag composites were designed primarily for HIP technology (Hendrix, Borofka [10, 11]), showing that the incorporation of silver brings improvements in workability; besides that the composite is denser, has a higher critical current density and even its soldering properties are improved. Silver is present primarily as a metal in this composite. A superconductor, of composition $YBaAg_3O_x$ (Tc = 50 K) is also known. A partial replacement of copper by silver in $YBaCu_3O_{7-\Delta}$ superconductors results in the formation of a multiphase material, simultaneously with a decreased Tc.

EXPERIMENTAL

Aim:

Preparation of a composite substance, of composition $Y(Ba,K,Na)_2Cu_3O_xF_y$ + Ag which can be well shaped with explosive compacting, and its density, critical current density and solderability enables practical application.

Materials:

The following raw materials were used: Y_2O_3 (purity 99.99%, surface area 18.1 sq. m/g (Merck); $Ba(OH)_2.8H_2O$; CuO (surface area 18.4 sq. m/g, prepared by a 500 ^oC/1h heat treatment of basic copper carbonate,

$CuCO_3.Cu(OH)_2.nH_2O$); $KF.2H_2O$; NaF; and $AgNO_3$. All chemicals were of r.g.purity.

Weighed batches of dry raw materials were shaped into pressed pellets (dia 25 mm, high 3 mm), and fired in an electric kiln in oxygen (15 dm^3/h flow velocity). Heating and cooling rate was 300 $^oC/h$. The pressure used was 25 MPa.

Equipment:

The pore volume of heat treated samples was measured by a Carlo Erba type mercury porosimeter.

The phase composition of the heat treated samples was determined by X-ray diffraction analysis. These measurements were carried out by means of a Philips-1825 type instrument. The lattice parameters were calculated by a regression analysis of data corrected for systematic error.

Magnetic susceptibility was measured in Brucker's device according to Faraday's principle.

Critical current density was investigated with the system consisting of a Solartron-Schlumberger 7071 type voltmeter and a DC Power Supply current generator.

The microstructure of the heat treated samples was examined by a JEOL JSM 50A type scanning electron microscope.

RESULTS

Results are summarized in Table 1. The second column shows calculated compositions of the batches, the third the actual chemical composition of fired samples.

Table 1. Composition of batches and fired samples
(Fired samples contain 10% (m/m) Ag)

Designation	Calculated composition of batch	Composition of fired sample
KF	$Y(Ba_{1.95}K_{0.05})Cu_3O_xF_{0.05}$	$Y(Ba_{1.95}K_{0.02})Cu_3O_xF_{0.05}$
KF/Ag	$Y(Ba_{1.95}K_{0.05})Cu_3O_xF_{0.05}/Ag$	$Y(Ba_{1.95}K_{0.01})Cu_3O_xF_{0.05}/Ag$
NaF	$Y(Ba_{1.9}Na_{0.1})Cu_3O_xF_{0.1}$	$Y(Ba_{1.9}Na_{0.1})Cu_3O_xF_{0.1}$
NaF/Ag	$Y(Ba_{1.9}Na_{0.1})Cu_3O_xF_{0.1}/Ag$	$Y(Ba_{1.9}Na_{0.07})Cu_3O_xF_{0.1}/Ag$
NaKF	$Y(Ba_{1.9}Na_{0.05}K_{0.05})Cu_3O_xF_{0.1}$	$Y(Ba_{1.90}Na_{0.05}K_{0.02})Cu_3O_xF_{0.1}$
NaKF/Ag	$Y(Ba_{1.9}Na_{0.05}K_{0.05})Cu_3O_xF_{0.1}/Ag$	$Y(Ba_{1.90}Na_{0.03}K_{0.01})Cu_3O_xF_{0.1}/Ag$

Investigation results clearly show that no fluoride losses occur during heat treatment; alkali ions, however, behave in a different way. In silver-free samples, the Na quantity remains unchanged after firing, while the K quantity is reduced by two-thirds; in silver-containing samples, both Na and K are reduced during firing.

Those pellets were selected for further investigation which show favorable $\kappa = f(T)$ characteristics (Fig. 2). As well seen in the figure, a minimum change of the plot, in the presence of silver, is shown by samples containing K-ions.

Fig. 3 shows that the presence of silver, according to XRD patterns, changes the ratios of other crystalline phases. Approx. 5 % (m/m) CuO, $BaCuO_2$ and Y_2BaCuO_5 can be seen, besides approx. 85 % (m/m) orthorhombic superconducting phase and approx. 10 % (m/m) silver phase.

Porosity of fired pellets is shown in Table 2. In this table total porosity (ΣV_p), porosity over 7500 nm (r >7500 nm V_p) and porosity below 7500 nm are shown; in the latter case, pore size distribution is indicated too. Here "*r*" means pore radius, while "*R%*" the quantity of the pores > *r*, expressed in % (V/V).

Table 2. Porosity of sintered KF and KF/Ag samples

Designation	ΣV_p (cm^3/g)	V_p (cm^3/g) ↓	↓		
		r >7500 nm	*r* < 7500 nm	*r* (nm)	*R%*
KF	0.2570	0.1159	0.1411 {	1500	73
				1250	83
				682	93
				183	100
KF/Ag	0.0612	0.0462	0.0150 {	1250	73
				682	83
				183	91
				150	100

As well seen in Table 2., the porosity of the KF sample is decreased to its quarter upon the addition of 10 % Ag. The volume ratio of pores > 7,5 μm radius increases from 45 % to 75 %, while that of <7,5 μm decreases from 55 % to 25 %, with a simultaneous decrease of pore sizes.

Samples in pellet form were ground in a corundum mill and the ground product separated to particle size fractions 0-40 μm, 0-63 μm and 63-900 μm. These fractions were then explosively compacted in the device shown in Fig. 1. By increasing explosive pressure from 10^3 MPa to 10^4 MPa, the surface of crystals became destructed (fraction 0 - 40 μm, sample KF) as seen in the polished surface electron micrograph (Fig. 4.). Table 3. summarizes the porosities of explosively compacted samples (explosive pressure = 10^4 MPa).

Table 3. Porosity of explosively compacted samples

Designation	Particle size range (μm)	Total porosity (cm^3/g) ΣV_p after explosive compaction
KF	0 - 40	0.05
	0 - 63	0.0375
	63 - 900	0.0322
KF/Ag	0 - 40	0.0306
	0 - 63	0.0282
	63 - 900	0.0203

The comparison of porosities clearly shows that highest density can be achieved of the 63 - 900 μm fraction of sample KF/Ag: this is only one third of the same sintered, and only 1/13 part of the silver-free sintered sample.

Fig. 5. clearly shows that the decrease of porosity causes only little changes in the susceptibility vs. temperature plot in case of the KF and KF/Ag samples. In explosively compacted samples critical current density increases with decreasing porosity, to reach a highest value of 800 A/cm^2 at 77 K. The porosity can be reduced to a value of < 0.01 cm^3/g using a subsequent heat treatment (850 °C, 10 h, 15 dm^3 oxygen/h). This increased the critical current density up to 2800 A/cm^2 at 77 K. Figs. 6., 7. show SEM micrographs of the fracture surfaces of sintered KF and KF/Ag samples; the similar micrograph of the explosively compacted, 63 - 900 μm sample is shown in Fig. 8. It is striking that average crystal size in Fig. 8. is smaller than individual crystal size in Fig. 7. All this means that explosive shock separates relatively coarse particles, glued either via a bond phase or a boundary phase to yield a favorable, dense steric arrangement. A disintegration of particles takes place too, albeit to a lesser extent only.

As a result of subsequent heat treatment the particle size increased (Fig. 9.) besides decreasing of porosity causing a higher value of critical current density.

CONCLUSIONS

- The heat treatment of $Y(Ba,K,Na)_2Cu_3O_xF_y$-based superconducting ceramics does not decrease the Na and F content of the batch, while the K content is reduced to 1/3 of the original.
- The heat treatment of a composite containing 90 % (m/m) $Y(Ba,K,Na)_2Cu_3O_xF_y$ and 10 % (m/m) Ag results in the constancy of F, a

decrease of K to 1/5 of its original value and a decrease of Na by 30 - 35 % (m/m).

- The minimum amount of explosive pressure to reach a satisfactory density is 10^4 MPa, in case of $Y(Ba,K)_2Cu_3O_xF_y$ and $Y(Ba,K)_2Cu_3O_xF_y/Ag$ samples.
- The density of the product can be affected to a high extent by changing the particle size of the starting material.
  - The silver-containing composite gives higher density.
  - Density of final samples shows the order of 0 - 40 μm < 0 - 63 μm < 63 - 900 μm.
- Best result achieved in this series of experiments: critical current density = 2800 A/cm^2 at 77 K, porosity < 0.01 cm^3/g, using a $Y(Ba,K)_2Cu_3O_xF_y$ + Ag (90 + 10 % m/m) composite, 63 - 900 μm fraction, 10^4 MPa explosive pressure and a subsequent heat treatment.

REFERENCES

[1] I-Wei Chen, S. Keating, C.Y. Keating, X. Wu, J. Xu, P.E. Reyes-Morel, T.Y. Tien: Adv. Cer. Mat. 2, 3B (1987) 457-470

[2] I. Dragieva, I. Nedkov: IEEE, Trans. Magn. Mag., 26 (5) (1990)

[3] I. Felner: Thermochimica Acta, 174 (1991) 41-69.

[4] I. Nedkov, I. Iliev, S. Tinchev, M. Taslakov, V. Kojucharov: Supercond. Sci. Technol. 1 (1989) 324-325.

[5] M. Enisz, I. Kotsis, T. Korim, D. Oravetz, É. Kristóf: Relation between the physical properties and microstructure of the high-T_c $YBa_2Cu_3O_x$-based ceramic superconductors containing K^+ and Na^+ ions. 7th CIMTEC, Satellite Symp. Triest 2-5 July (1990), 135.

[6] J.S. Kim, J.S. Swinnea, A. Manthiram, H. Steinfink: Solid State Commun. 66 (1987) 287.

[7] K. Kobayashi: J. Am. Ceram. Soc. 73 (1) (1990) 146-147.

[8] A.G. Klimenko, V. Ye. Fedorov: Thermochimica Acta 174 (1991) 71-83

[9] I. Kotsis, M. Enisz: Effect of Alkali fluoride additives on the properties of superconductors of the system Y-Ba-Cu-O, 8th SIMCER Int. Symp. on Ceramics, Rimini 9-14 Nov. (1992), Proceedings of the Conference

[10] B.C. Hendrix, T. Abe, J.C. Borofka, P-C Wang, J.K. Tien: J. Am. Ceram. Soc. 76 (4) (1993) 1008-1010.

[11] J.C. Borofka, B.C. Hendrix, A.J. Attarwala, J.K. Tien: J. Am. Ceram. Soc, 76 (4) (1993) 1011-1016.]

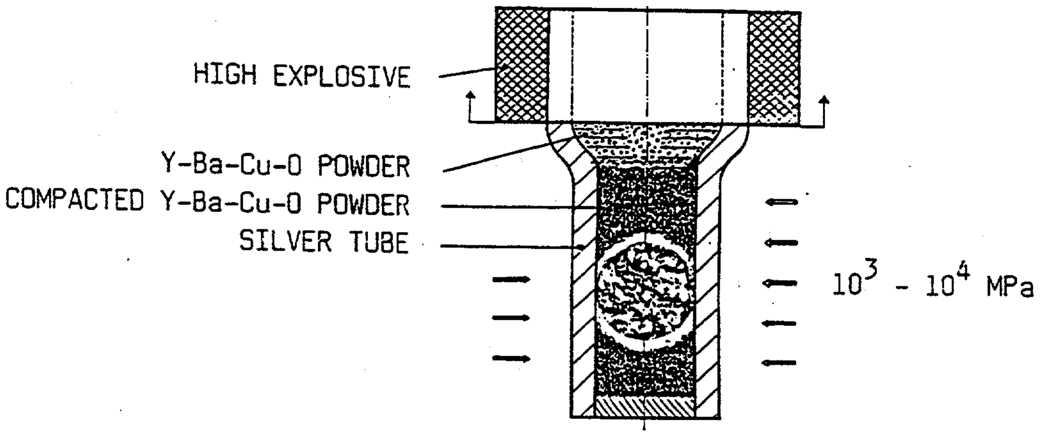

Fig. 1. Scheme of explosive powder compaction

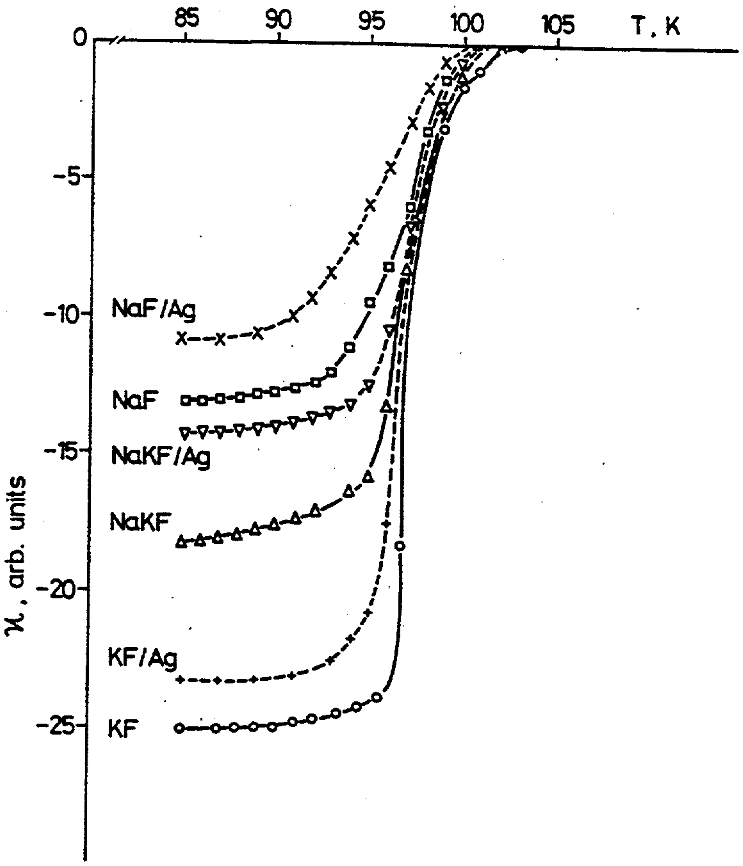

Fig. 2. κ = f(T) for superconducting pellets (B = 1 tesla)

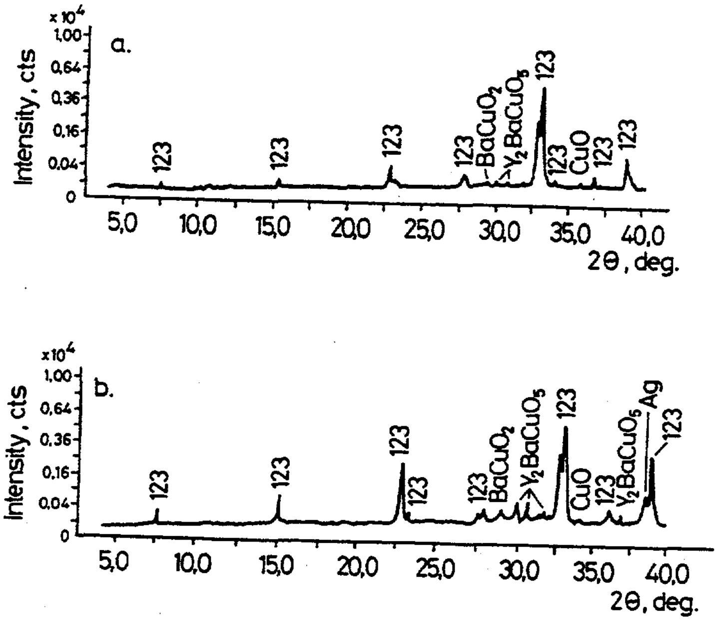

Fig. 3. X-ray diffraction patterns of KF (a) and KF/Ag (b) pellets

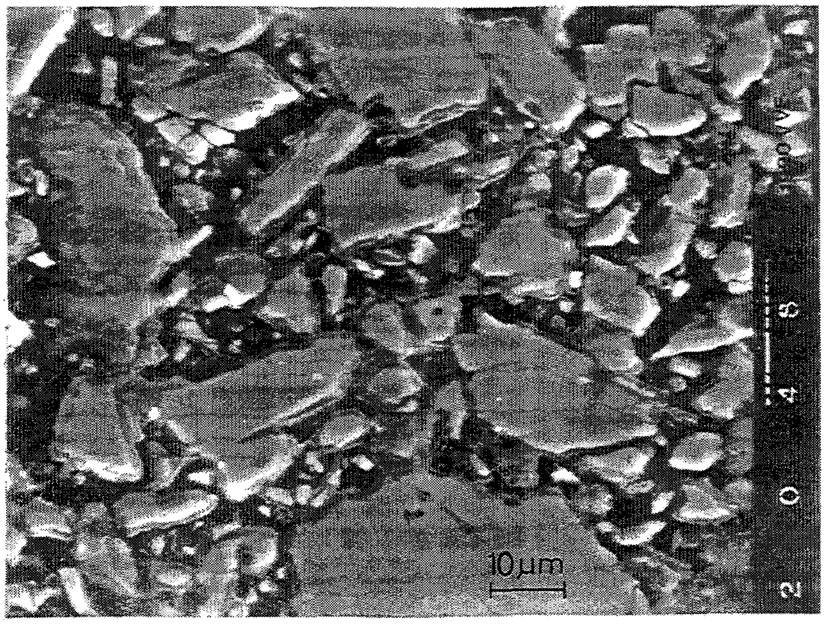

Fig. 4. Polisched surface of an explosively compacted sample

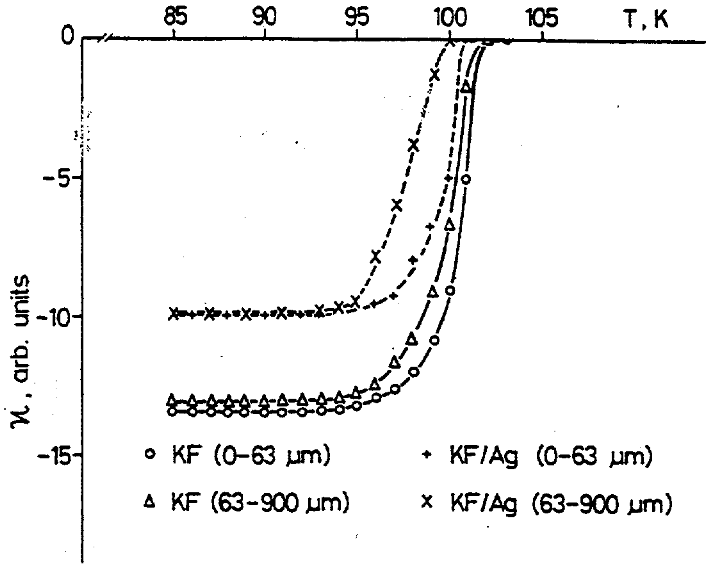

Fig. 5. κ = f(T) for explosively compacted samples (B = 1 tesla)

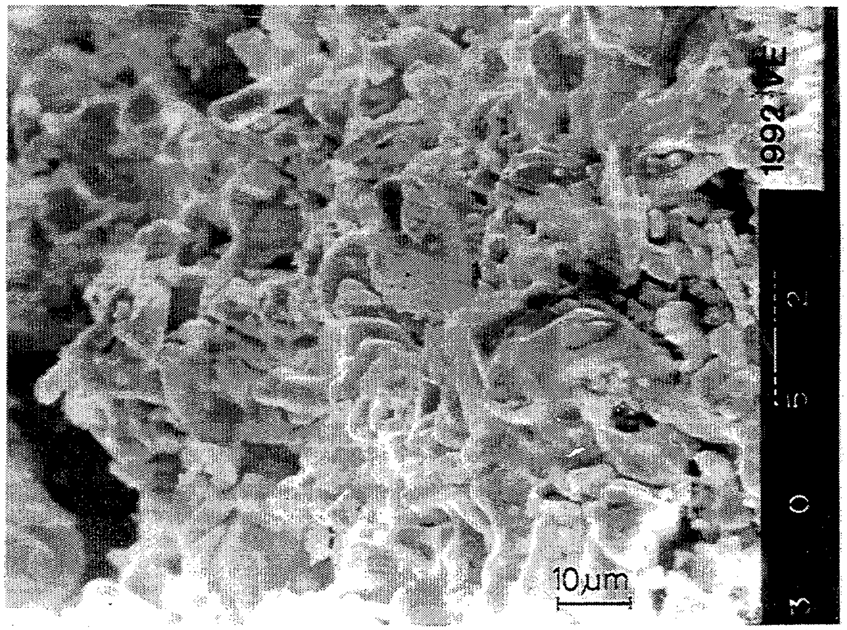

Fig. 6. Fracture surface of the sintered KF sample

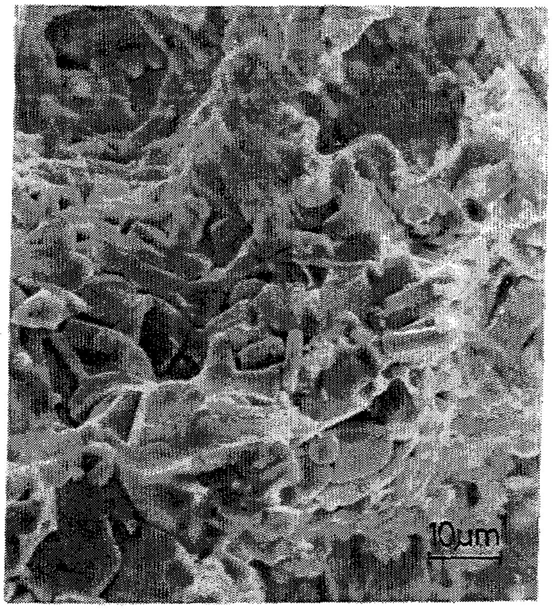

Fig. 7. Fracture surface of the sintered KF/Ag sample

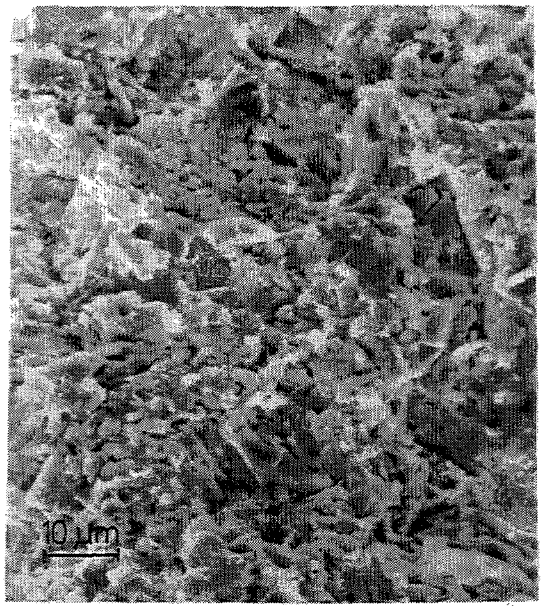

Fig. 8. Fracture surface of the explosively compacted, 63-900 µm KF/Ag sample

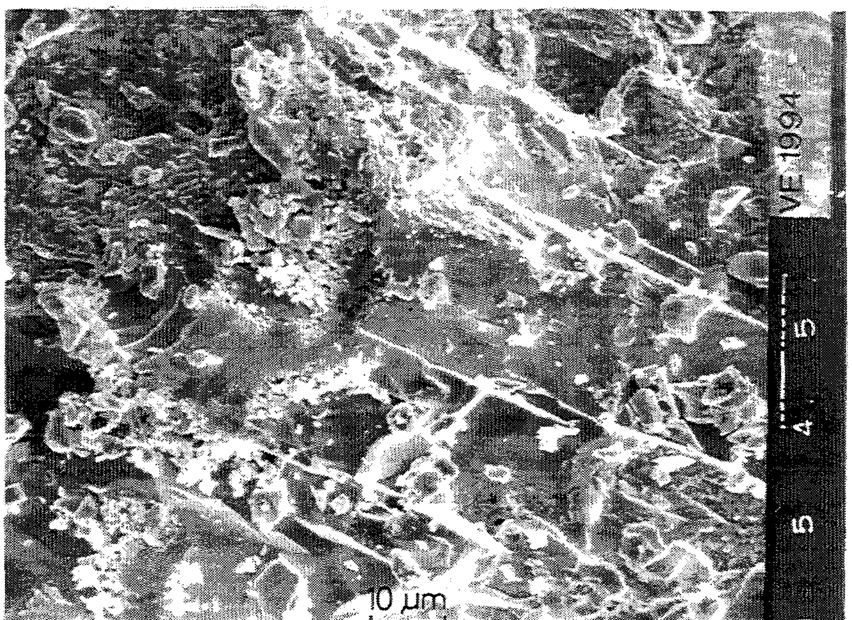

Fig. 9. Fracture surface of the explosively compacted KF/Ag sample after subsequent heat treatment

PERCOLATION EFFECT IN THICK FILM SUPERCONDUCTORS

(Using a Bi(Pb)SrCaCuO based paste to prepare a superconducting planar transformer)

Róbert Sali - dr.Gábor Harsányi
Technical University of Budapest , Department of Electronics Technology
1521 Budapest, Hungary ,Tel : (361) 181-1520   Fax : (361) 166-6808

SUMMARY

A thick film superconductor paste has been developed to study the properties of granulated superconductor materials, to observe the percolation effect and to confirm the theory of the conducting mechanism in the superconducting thick films. This paste was also applied to make a superconducting planar transformer. Due to high T_C and advantageous current density properties the base of the paste was chosen to be of Bi(Pb)SrCaCuO system. For contacts a conventional Ag/Pt paste was used.

The critical temperature of the samples were between 110 K and 115 K depending on the printed layer thickness. The critical current density -at the boiling temperature of the liquid He- was between 200 - 300 A/cm^2. The R(T) and V(I) functions were measured with different parameters. The results of the measurements have confirmed the theory of conducting mechanism in the material. The percolation structure model has been built and described.

As an application, a superconducting planar thick film transformer was planned and produced. Ten windings of the transformer were printed on one side of the alumina substrate and one winding was printed on the other side. The coupling between the two sides was possible through the substrate. The samples did not need special drying and firing parameters. After the preparation, the properties of the transformer were measured. The efficiency and the losses were determined. Finally, some fundamental advantages and problems of the process were discussed.

1. INTRODUCTION

In recent years, various methods were applied to prepare superconductor materials. The screen - printing film technology is one of the rarely applied methods, however it can be performed using conventional substrates and it needs only cheap polycrystalline materials. In Hungary a good manufacturing process was developed to make a high T_C superconductor paste, which does not need special drying and firing parameters. Using the paste, the process is fully compatible with the traditional thick film technology. Thus, the superconductor electronic elements made with this technology can be connected to other thick-film electronic elements and two dimensional layouts of complicated shape can be prepared.[1]

2. STRUCTURE OF THE MATERIAL

The base of the paste is the Bi(Pb)SrCaCuO system. This type of superconductor material has a granulated structure. In this structure, the typical grain size is between 0.5 to 10 μm. The couplings between the individual grains generate a 3 dimensional - net, resulting in superconduction. The name of these couplings, because of their superconductor-insulator-superconductor structure, is "Josephson transitions" and the name of the net is "Josephson - net". Mészáros et al [2] have observed, that the composition of the surface of the grains is different from the inside of the grains. The surface area is richer in copper and poorer in oxygen than the bulk. This difference may cause the relatively low critical current density of the samples.

3. SAMPLE PREPARATION

The samples were prepared on 96 % alumina substrates by the method described by Besenyei et al [3]. During the preparation of the paste, the grain size was measured on the basic powder. Firstly, more than 30 percent of the sample consisted of grain-size 10 - 50 μm. This average size was still not satisfactory for the conducting mechanism, so a manual grinding was applied to decrease the size of grains. Secondly, the grain size distribution was better then in the first case because the average size was about 5 μm.

After the grain size measurements, a printable paste was produced from the basic powder. Samples were printed with 200 mesh screen (the swap off was 1.8 mm) and dried for 10 minutes at 150 °C in air. The superconductor layer was fired in a Johnson -Wattkins furnace with a normal temperature profile, where T_{max} was 850°C. For contacts, a general purpose Ag/Pt conductor paste was applied. In the case of contact layers the maximum firing temperature was 800°C and the atmosphere was air, too. The thickness of fired layers were 20 and 38 μm.

4. RESULTS AND DISCUSSION

The electric field in the superconductors depends on the current density (J), on the external magnetic field (B_{ext}) and on the temperature (T). However, the value of the magnetic field (B) is determined not only by the external magnetic field, but also by the so called "magnetic prehistory" of the samples. Before the application of the paste, we wanted to know the electrical properties of the superconductor samples. So, we performed the following measurements by using contacts as shows in Fig.1:

1. R - T function $V=V(T)$, $B_{ext}=const$, $I=const$
2. I - V function $V=V(I)$, $B_{ext}=const$, $T=const$
3. B - V function $V=V(B)$, $I=const$, $T=const$

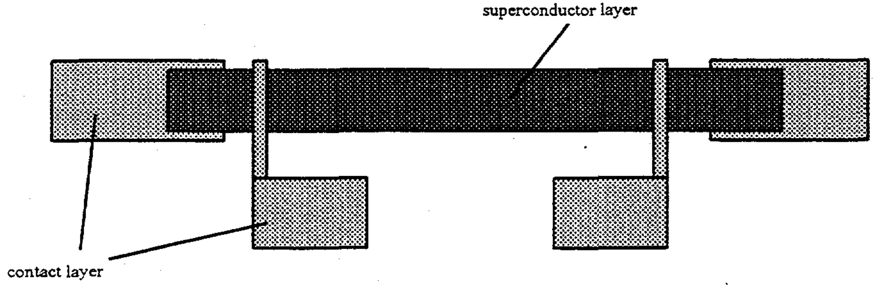

Fig.1 Layout of four-contact method

4.1. The R - T functions

These functions are important characteristic of the superconducting materials, because the T_C can read from the graphs and the graphs show the different ways of the conducting mechanism. Fig.2.a shows two graphs : One corresponds to the one-layer sample, the other to the two-layer sample. One can observe, that the resistance of the two-layer sample is less than the one-layer, but the T_C-s are equal. Thus, the T_C which can be read from the graphs is about 115 K.

Fig.2.b shows the results of measurements with three different current values from 0.05 mA to 0.5 mA by decades. The graphs confirmed the theory of the conducting mechanism. They show a significant difference only in the case of $T<T_C$. The reason may be the grainy structure of the material. The graphs can be divided into two parts according to the way of conducting mechanism;

-in the case of $T>T_C$, almost only the individual grains conduct and their critical current density is larger than the critical current density of the inter - grain Josephson - transitions. Thus, the three graphs coincide;
-in the case of $T<T_C$, the inter - grain Josephson - transitions determine the critical current of the samples. This current is less than the critical current of the grains, so a difference between the measuring currents appears on the graphs.

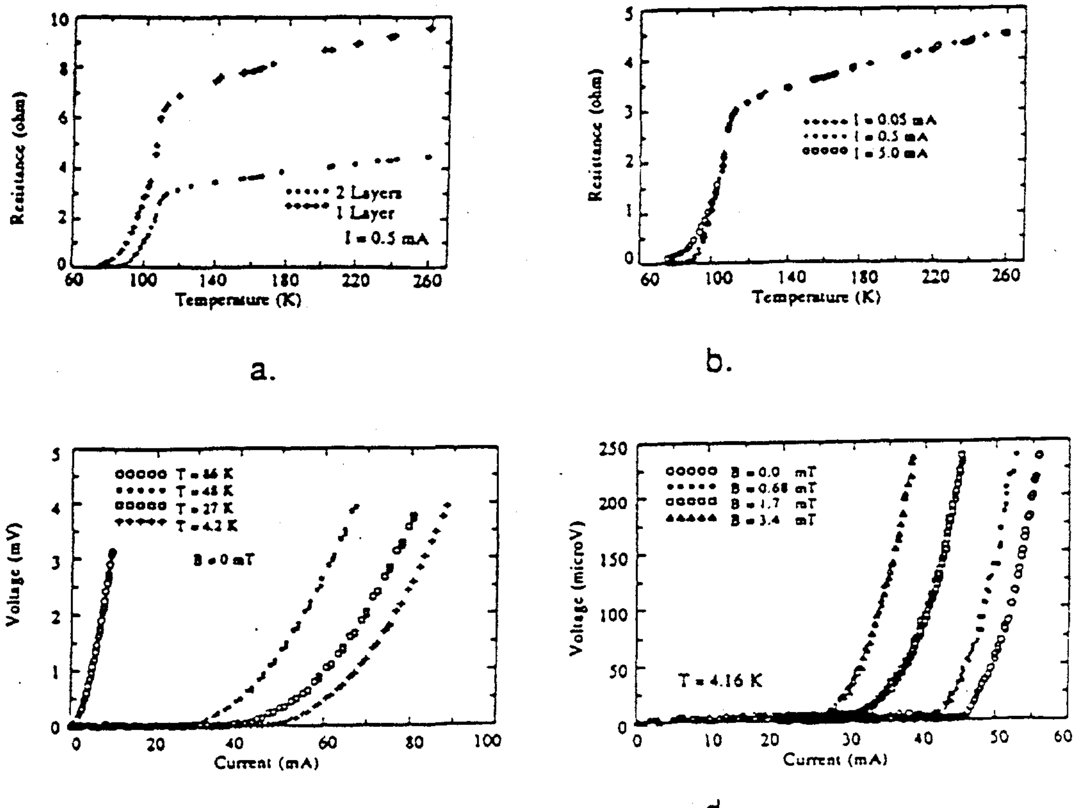

a. b.

c. d.

Fig.2 Measurement results by using four-contact method:
a-b. R-T functions; c-d. V-I functions;

4.2. The V- I functions

The graphs shown in Fig.2.c are the V - I functions with T as a parameter, when T ranges from 4.2 K to 86 K and the value of external magnetic field is zero. Significant difference was registered only at T=86 K. Here, the critical current density decreased drastically and the sample resistance increased rapidly to a relatively high level. The reason of this deviation is the low critical current of inter-grain Josephson-transitions.

The V - I function with B as a parameter was measured at constant T=4.2 K temperature. Fig.2.d clearly shows that the external magnetic field works against the superconduction. The value of the critical current decreased significantly with increased of the value of the external magnetic field.

From the results, the so-called "percolation model" can be built up. It means: the 3D-bar ceramic superconductor consists of many individual grains. These grains joint to each other with Josephson-transitions and the grains with the transitions form a weak-coupled net. This 3D-net is the percolation structure. Fig.3 shows a piece of superconductor material in 2D, where the grains and the percolation paths can be observed. During measurements, the most important observation was that the external magnetic field penetrates into the grains -decreasing the critical current density of the samples before its value reaches the value of the critical magnetic field of the superconductor (H_C). The reason of this phenomena may be that a so-called "Josephson-flux" starts to grow between the grains.

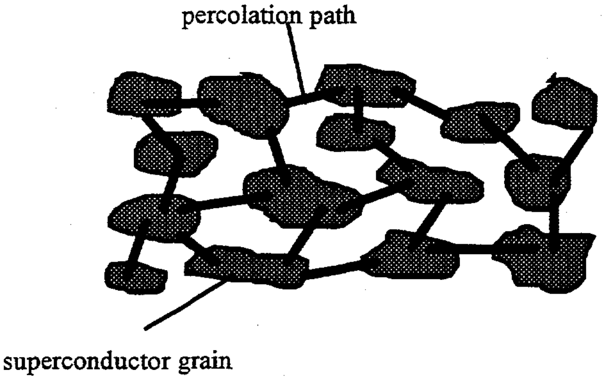

Fig.3 Percolation paths in the superconductor

5. THE PLANAR TRANSFORMER

Finally, a realised superconductor planar transformer is described. The properties of the superconductor layers of the transformer were the same as we stated above. Our aims were as follows;

- to transform the voltage from a higher level to a lower level, where the response is true to the original form;
- to realise a good electrical isolation between the two sides of the transformer.

According to the stated rules above, ten windings of the transformer were printed on one side of the 96 % purity alumina substrate and one winding was printed on the other side as shown in Fig.4. Transformer parameters were as follows [4]:

-Internal diameter	10 mm
-Outside diameter	40 mm
-Width of primary turns	1 mm
-Width of secondary winding turn	15 mm

The samples were prepared with the same drying, firing and printing parameters as we have described previously, but the primary and the secondary superconductor layers of the transformer were fired at the same time. It was a big problem to give the same atmosphere and the same temperature profile to both layers on two sides. Number of the printed layers were 1 or 2 on each side of the substrates. On the secondary side of the transformer the width of the winding was different from the width of the primary windigs. The reason of this layout design was that we wanted a good coupling between the two sides. It was very interesting, that the fully non-magnetic substrate can cause a satisfactory coupling.

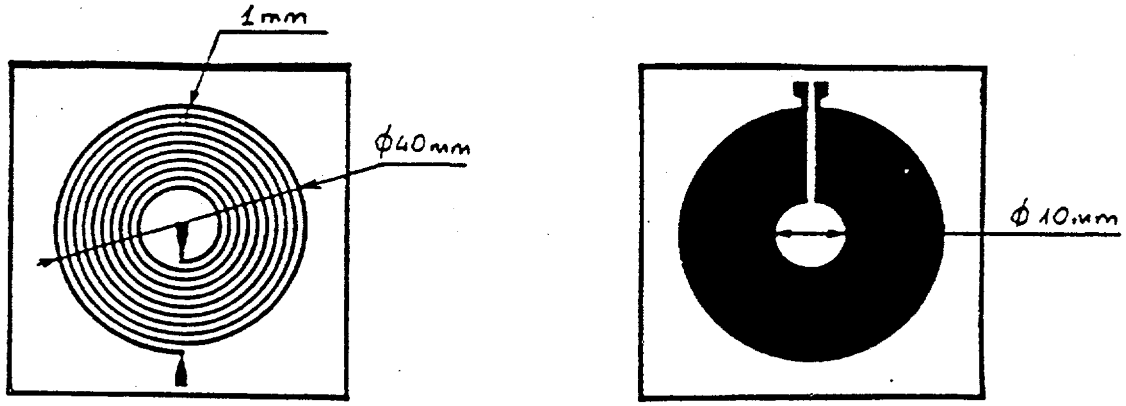

Primary side

Secondary side

Fig.4 Layout of the planar transformer

5.1. Measurements on the transformer

In the first part of the measurements we wanted to make certain of the superconduction on each side of the transformer. Thus, we performed the simple four - contact measuring on both sides of the samples. The results were very interesting, because we could find the abrupt resistance - changing, but the value of the resistance did not reach zero. There are two possible different explanation of this phenomena;

-because of the two-side firing technology, the samples are not able to reach the superconducting state and they have a finite resistance;

-the samples would be able to reach the superconducting state, if the transformer had only one side. We suppose, that the throw-out magnetic field of the non-measured side of the sample (which is in superconducting state too) may destroy the superconduction of the measured side. This influence prevents the samples from reaching the superconducting state.

In the second part of the measurements the superconductor transformer was measured in normal and in cooled (superconducting) state. At last the measurement results of the superconductor samples were compared with another transformer which was made of a general purpose Ag/Pt conducting paste. The measurements were performed with three different input signals (square-, triangle- and sine functions). We gave to the samples 2.2 V peak-to-peak voltage and examined the output voltage with oscilloscope. The efficiency (η) and the losses (δ) were defined:

$$\eta=\frac{V_{outreal}}{V_{outideal}} \quad (1.) \qquad\qquad \delta = 1-\eta \quad (2.)$$

where $U_{outreal}$ was the value of the measured voltage on the secondary side and $U_{outideal}$ was the value of the input voltage divided by the coupling factor (n=10). Thus, the efficiency and the losses could be calculated based on the results. The frequency of the input signals was chosen as a parameter from 10 kHz to 2 MHz.

. Table 1. shows the measurement results of a two-layer superconductor sample in normal state. We observed, that the transmission of the square- and the triangle functions was not satisfactory because these functions were differentiated by the sample. The transmission of the sine function was faithful to the original form in all frequency - region. Thus, later the sine input signal was chosen to be the main input signal. The maximum efficiency was calculated at 1.9 and 2 MHz, its value was 79%.

Table 1. Measurement results in non-superconducting state

Frequency (kHz)	Response of 2-layer sample (mV)	Efficiency (%)	Losses (%)
10	8	4	96
100	51	23	77
1000	130	59	41
1300	145	66	34
1600	165	75	25
1900	175	79	21
2000	175	79	21

We wanted to measure the one-layer samples too, but after the firing these samples became useless, because the relative thin superconductor layer was not continuous.

Table 2. shows the measurement results of the previous two-layer superconductor transformer in the superconducting state. The main input signal was the sine function with different frequencies from 10 kHz to 2 MHz. One can observe, that the efficiency was better - above 1 MHz - than we measured in the normal state. The maximum efficiency was calculated at 1.9 and 2 MHz, its value was 89 %. The increased efficiency value might be caused by the abrupt resistance decreasing.

Table 3. shows the measurement results of a two-layer planar transformer made of general used Ag/Pt paste. This device had got a very low efficiency and high losses. It started to transform only at 1 MHz, but it had got a big advantage: It worked with 20 V peak-to-peak input voltage too.

Table 2. Measurement results in superconducting state

Frequency (kHz)	Response of 2-layer sample (mV)	Efficiency (%)	Losses (%)
10	6	3	97
60	30	14	86
100	48	22	78
600	120	55	45
1000	150	68	32
1300	170	77	23
1600	180	82	18
1900	195	89	11
2000	195	89	11

Table 3. Measurement results of a traditional thick-film transformer

Frequency (kHz)	Response of the sample (mV)	Efficiency (%)	Losses (%)
100	0	0	100
600	0	0	100
1000	60	27	73
1300	80	36	64
1600	80	36	64
1900	90	41	59
2000	100	45	59

6. CONCLUSIONS

The produced paste correctly showed the special properties of the high T_C superconducting ceramics. This paste could be printed well and easily, it did not need special drying and firing methods and parameters. The measurement results of the R-T functions and the percolation effect confirmed the theory of the conducting mechanism in the superconducting thick films.

A superconductor middle- and high- frequency planar transformer was fabricated and tested. This transformer operated satisfactory in the MHz region. It was compared to a normal planar transformer and the results were given. The greatest problem of the transformer was caused by the grainy structure of the superconductor material. In this type of superconductor the boards of grains as a Josephson - transitions are not able to put up higher power. Thus, the conduction mechanism gives a limit of using and the value of the input signal of the transformer was relatively low, 2.2 V. The maximum critical current density was 10^3 A/cm^2 as opposed to the 10^6 A/cm^2 ideal value.

The way of improvement is to decrease the size of the grains in order to increase the value of the critical current density.

7. ACKNOWLEDGEMENTS

The authors wish to express their thanks to E.Besenyei, P.Arató and F.Wéber from Research Institute for Technical Physics of the Hungarian Academy of Sciences for their help of producing the paste, to S.Mészáros, K.Vad and G.Halász from Institute of Nuclear Research, Debrecen for their help of measuring of the samples. A special thank is to V.Kolonits, B.Hidasi, B.Kovács and I.Németh from the Technical University of Budapest for their useful advice.

REFERENCES

[1] S.Mészáros-K.Vad, "Jósnô" research and development program, Research Institute for Technical Physics of the Hungarian Academy of Science (1991)

[2] S.Mészáros,K.Vad,G.Halász,F.J.Kedves,Sz.Balanyi,"Investigation of the coupling mechanism between superconducting grains in high T_c superconductors" Physica C 167, 1990

[3] E.Besenyei,G.Katona,P.Arató,A.Kele, "The effect of heat treatment on the superconducting properties of Bi-Sr-Ca-Cu thick films on alumina substrates", Supercond.Sci.Technology, vol.2,1989 IOP Publishing Ltd.

[4] P.G.Barnwell, Custom Interconnect LTD, Whithurch, Hants, England, A.Shippen, K.Williams, Kingston Polytechnic, Kingston Surrey, England, "High frequency transformers using thick film technology" ,1990

LINE GROUP TECHNIQUES IN DESCRIPTION OF THE STRUCTURAL PHASE TRANSITIONS IN SOME SUPERCONDUCTORS

Cs. Mészáros(1), Á.Bálint(2) and J.Bánkuti(1)

(1) Department for Low Temperature Physics, Roland Eötvös University,
Budapest, Hungary
(2) Department of Chemistry and Biochemistry, University of Agricultural
Sciences, Gödöllő, Hungary

ABSTRACT

The main features of the theory of line groups, and their irreducible representations are briefly discussed, as well as the most important applications of them. A new approach in the general symmetry analysis of the modulated systems is presented. It is shown, that the line group formalism could be a very effective tool in the examination of the structural phase transitions in High Temperature Superconductors. As an example, the material $YBa_2Cu_3O_{7-x}$ is discussed briefly.

INTRODUCTION

The geometrical symmetries of a system possessing periodicity in one dimension form a line group by definition. The line groups were first derived by Hermann [1], and 75 line groups were found with "crystallographic character". Omitting the detailed discussion of the intermediate steps in the development of the line group theory is mentioned the X-ray structure analysis of polymers [2] based on this theory. The line group theory is the base for the Fourier-Bessel synthesis of structural investigations of polymers, as well as the Schönfliess' theory in the structural investigations of *3D* crystals. This paper presents and adopts completely the formalism and notation of the line groups, described and later repeatedly exploited by Vujičić et al [3-6]. It has been proved, that all of the innumerable line groups can be gathered into thirteen families containing "non-crystallographical" symmetry transformations among the group elements, too. There is a crucial difference between the derivation of the line groups and the space groups of the ordinary, *3D* crystals. In the case of the line groups, the possible symmetries of the motif (monomer - in the case of polymers), is examined leaving invariant the main axis of the system, too. While in the construction of the space groups of *3D* crystals the symmetry relations between the possible translations in the crystal and the point group-symmetries of the unit cell (and not of the molecule!) are studied. Thus the usefulness and the advantage of the line group formalism is obvious: starting from the ***quantum-mechanical description of the motif***, there is a valuable tool to examine the electron (or spin-) density functions in the condensed matter. Such a Q1D subsystems have been examined in detail in some well-known superconductors [7]. Besides, there are some interesting results, which also show that the modulation of the crystal structure could be very interesting in the examination of the High Temperature Superconductivity Phenomena [8]. In this paper we show, that the line group formalism is very appropriate for the description of the modulation. The new thermodynamical methods [9] would also give valuable contributions in these investigations.

1. SUBGROUP STRUCTURE AND IRREDUCIBLE REPRESENTATIONS OF LINE GROUPS

1.1. Subgroup structure

Recognizing the line groups being the subgroups of the Euclidean group, the use of the usual Koster symbol for the general line group element [3] is convenient:

$$\underline{\mathbf{L}} \ni (R \mid v+t);\ v \in [0,1),\ t \in Z \qquad (1)$$

The line group elements in their orthogonal part possess the elements R_i, which constitute the *isogonal point group* $\underline{\mathbf{P}}$, $|\underline{\mathbf{P}}| = N_p$. $\underline{\mathbf{P}}$ is always an axial point group when one deals with line groups. There are two types of point and line groups. Namely, if the point group $\underline{\mathbf{P}}$ contains an element R^-, which reverses the direction of the main axis, then it will be denoted as $\underline{\mathbf{P}}^-$, which has the following subgroup structure:

$$\underline{\mathbf{P}}^- = \underline{\mathbf{P}}^+ + R^- \underline{\mathbf{P}}^+ \qquad (2)$$

i.e. $\underline{\mathbf{P}}^+$ is an index-two invariant subgroup in $\underline{\mathbf{P}}^-$. Similarly, all the line groups are $\underline{\mathbf{L}}^+$ or $\underline{\mathbf{L}}^-$ type, depending on the type of isogonal point group. The list of all line groups is completed by use of the concept of the generalized semi-direct product of the line groups [3].

1.2. Irreducible representations

In the short description of the irreducible representations we use the technique and notation presented in [4-5]. The general formula for the irreducible representation of the $\underline{\mathbf{L}}^+$ type line group element can be written as:

$${}_kD_m(R \mid v+t) = D_m(R)\exp[ik(v+t)a] \qquad (3)$$

i.e. it is built up from the irreducible representations of $\underline{\mathbf{P}}$ and $\underline{\mathbf{T}}$. The irreducible representations of $\underline{\mathbf{P}}$ and $\underline{\mathbf{T}}$ are labelled by indices m and k, respectively ($k \in (-\pi/a, \pi/a]$). With the matrices ${}_k\boldsymbol{D}_m(\underline{\mathbf{L}}^+)$, the irreducible representations of $\underline{\mathbf{L}}^-$ can be obtained by *induction* technique [4],[12].

2. SOME APPLICATIONS OF LINE GROUP FORMALISM IN CONDENSED MATTER PHYSICS

There are some remarkable results, which show the power and the usefulness of the line group formalism. It is well-known in the mathematical crystallography, that the non-symmorphic space groups of 3D crystals are not factorized yet in the sense of the product of its subgroups [10]. The algorithms developed in the elaboration of the abstract line group theory would be also useful in the solving of this important crystallographic problem [11].

With the addition of the time-reversal symmetry to geometrical symmetry transformations of the line group, the ***magnetic line groups*** tabulated in [6] can be obtained. This result is completely analogous to the derivation of Heesch-Shubnikov point-, and space-groups (see for example in [12]). The irreducible representations of the magnetic line groups have also been derived and tabulated already and completely can be found in [13-14].

A general discussion of the normal modes of *Q1D* systems as well as the complete classification of the orbits of the line groups is given in [15]. There is another important result in the same paper: the classical Jahn-Teller theorem is generalized to the case of systems, whose symmetry groups are line groups.

The line group formalism was introduced in the structural investigation of modulated crystals in our earlier paper [16]. It was shown, in the Landau power expansion of thermodynamic potential (for description of the phase transitions, in which modulated structures could appear), that the terms concerning translational invariance are exactly line group invariants.

This thermodynamical analysis gave us the following geometrical result: let the function $\rho(\vec{r})$ be the electron (or spin-) density function with the ordinary space-group symmetry, and let $f(\vec{r})$ be the modulation function in one particular direction only. The function $f(\vec{r})$ must be invariant under the symmetry transformations of the supersymmetry - which is a particular line group. Thus, to describe the scattering experiments and to obtain the adequate structure factors of the modulated structures we have the formula:

$$F_{\mathrm{mod}}(S) = \mathscr{F}\{f(\vec{r}) * \rho(\vec{r})\} = \mathscr{F}\{f(\vec{r})\} \cdot F(S) \ , \tag{4}$$

where the sign * denotes the convolution operation, instead of the usual expression $F(S) = \mathscr{F}\{\rho(\vec{r})\}$ applied for ordinary structures. It is convenient and customary [2] to use cylindrical coordinates in this calculation of the modulated structure factor. In the fully developed form, formula (4) can be written as:

$$F_l(R,\Psi,lc^*) = \sum_j \sum_n fj\, J_n(2\pi r_j R) \exp\left[i\left(n\left(\Psi + \frac{\pi}{2}\right) - n\psi_j + 2\pi l \frac{z_j}{c}\right)\right] \tag{5}$$

This description de facto implies the following factorization of the symmetry group $\underline{\mathbf{G}}_S$ of the modulated crystals:

$$\underline{\mathbf{G}}_S = \underline{\mathbf{G}} \circ \underline{\mathbf{G}}_M \ (\text{ or } \underline{\mathbf{G}}_S = \underline{\mathbf{G}}_M \circ \underline{\mathbf{G}}) \tag{6}$$

In this formula $\underline{\mathbf{G}}$ means the space group according to Schönfliess, while $\underline{\mathbf{G}}_M$ denotes symmetry group, which describes the modulation of the structure. $\underline{\mathbf{G}}_M$ could be a line group, but the nature of the product $\circ$ is not clear yet (i.e. when it is a weak-direct, a semi-direct or a direct product [6] of the subgroups, which constitute the full group) and it requires further group-theoretical investigations concerning the general problem of the orthogonal invariance in the modulated systems. This investigation in progress gives the result will be applied in the examination of structural phase transitions in liquid crystals, as well as in the complete classification of them. Moreover, this approach would be very useful in the investigation of the crucial properties of the heavy-fermion superconductor UPt_3, because some interesting results [17] show clearly the possibility of influence of incommensurate modulation of the crystal structure on the superconductivity in such a systems.

The suitability of the presented formalism can be accepted for the structural investigation of High Temperature Superconductors (*HTSC*), too. There are many experimental results, which show, that some of the *HTSC* materials also have modulated structures [18-20]. The technique proposed in [16] would provide crucial results in the symmetry analysis of the structures of these superconductors. Moreover, the advantage of the line group technique is obvious in the investigation of the structural phase transitions in *HTSC*-s. For such investigations we also have fully elaborated techniques based on the line group theory. The polar-vector and axial-vector representations of line groups are also well-known and presented in [21]. Connecting the line group formalism with Ascher's epikernel technique [22], Damnjanović showed, [23-24], that the reduction of symmetry during the continuous phase transition of some *3D* crystals can be studied equally well using line groups. Recently, this method has been developed for the phase transitions without translation lost, i.e. for the equitranslational phase transitions only. The extension to the general case is also possible [11]. As it is well-known [22], the phase transitions with $\mathbf{k}=0$ can be described as equitranslational phase transitions i.e. one should deal with the irreducible representations of point groups only:

$$\mathrm{D}_m(\mathrm{R}) \equiv {}_k\mathrm{D}_m(\mathrm{R} \mid \mathrm{v}+\mathrm{t}) \tag{7}$$

The procedure is the following: let $\underline{\mathbf{L}}_0$ be one line group and let $\underline{\mathbf{L}}_1$ be one of its equitranslational epikernels concerning irreducible representation ${}_k\boldsymbol{D}_m(\underline{\mathbf{L}}_0)$. Then, if $\underline{\mathbf{P}}_1$ is the isogonal point group of $\underline{\mathbf{L}}_1$, then it is also an epikernel of $\underline{\mathbf{P}}_0$, corresponding to the representation $\boldsymbol{D}_m(\underline{\mathbf{P}}_0)$. In this case an epikernel $\underline{\mathbf{P}}_1$ of $\underline{\mathbf{P}}_0$ belongs to each equitranslational epikernel $\underline{\mathbf{L}}_1$ of $\underline{\mathbf{L}}_0$, and $\underline{\mathbf{P}}_1$ is the isogonal point group of $\underline{\mathbf{L}}_1$. Obviously, the described line group-epikernel formalism (*LEF*) is a very suited technique for description of the tetragonal-orthorhombic structural phase transition in $YBa_2Cu_3O_{7-x}$. Using some results of the phenomenological description of this phase transition based on Landau's theory [25] and on group-subgroup technique [26], we have enough information for application of the *LEF*. Namely, it is shown in [25], that the primary order parameter for this transition is the quantity $\eta = n_b - n_a$, i.e. the difference between oxygen atom rate along b and a axes, respectively. It is pointed out in both [25] and [26], that the above mentioned phase transition is exactly equitranslational. Thus, the order parameter η also could be treated by *LEF* and this method would provide a valuable new method to describe the oxygen atom ordering, which is believed to be crucial in the examination of the High Temperature Superconductivity mechanism. Namely, the irreducible representation relevant for this phase transition denoted by $\boldsymbol{B_{1g}}$ in [25] can be identified as $\boldsymbol{B_1}^+$ in the tables given in [24]. At first, we give in Table 1. the adequate space- ($\underline{G}_i$) and point groups ($\underline{P}_i$) (i=0 and 1 for the high- and low-symmetry phase, respectively).

Table 1.* Space and point groups of high (tetragonal) and low temperature (orthorombic) phase

	Space Group	Point Group
High Temperature Phase ($\underline{G}_o$,$\underline{P}_o$)	P4/mmm (D_{4h}^1)	4/mmm (D_{4h})
Low Temperature Phase ($\underline{G}_1$,$\underline{P}_1$)	Pmmm (D_{2h}^1)	mmm (D_{2h})

*The Schönfliess symbols are given in brackets.

The symmetry analysis based on the above mentioned epikernel-technique gives the results, presented in Table 2. Thus, we have two line groups as the possible equi-translational epikernels and also two strictly determined ***supersymmetries*** for description of the ordering ***of oxygen atoms***. Then, formula (5) gives also possibility to calculate the intensity spectra in the diffuse X-ray scattering and for the direct comparison of such a results with the already existing profiles (see for example the adequate references in [20]). The new results concerning the general problem of the scattering processes from a *real* superlattices [27], as well as the suited available experimental data [28-30] provide possibilities for doing such a calculations.

Table 2. The maximal *Q1D* subsystems in $YBa_2Cu_3O_{7-x}$ and the adequate equitranslational epikernels in the low temperature phase according to B_1^+:

	Line Groups		
High Temperature Phase Line groups as maximal subgroups	$\underline{L}(4)/mmm$	$\underline{L}(4)/mcc$	$\underline{L}(4)_2/mcc$
Low Temperature Phase The equitranslational epikernels	$\underline{L}(\bar{4})/2m$	$\underline{L}(\bar{4})/2c$	$\underline{L}(\bar{4})/2c$

CONCLUSIONS

The line group formalism provides a very effective tool in the symmetry analysis of different *Q1D* (sub-)systems in the condensed matter. Due to their obvious suitness, the line group techniques could penetrate into many recently developing areas, which are exactly in the front of the condensed matter physics and it could provide some valuable new results. The superconductivity is expected to be an especially fruitful topic.

REFERENCES:

1. C.Hermann: Z.Kristallogr. **69**, (1928) 250
2. B.K.Vainshtein: ***Diffraction of X-rays by chain molecules***
   Amsterdam: *Elsevier* **(1966)**
3. M.Vujičić, I.B.Božović and F.Herbut:
   J.Phys.A: Math.Gen. **10**, (1977) 1271
4. I.B.Božović, M.Vujičić and F.Herbut:
   J.Phys.A: Math.Gen. **11**, (1978) 2133
5. I.B.Božović and M.Vujičić:
   J.Phys.A: Math.Gen.**14**, (1981) 777
6. M.Damnjanović and M.Vujičić: Phys.Rev.**B 25**, (1982) 6987
7. I.Kirschner and K.Sajó: J. Low Temp. Phys. **35**, (1982) 235
8. A.C.Bódi, I.Kirschner and S.Leppävuori:
   Phys.Lett. **A 158**, (1991) 318
9. I.Kirschner: Sensors and Actuators **A 41**, (1994) 622
10. J.P.Elliot-P.G.Dawber: ***Symmetry in Physics Vol.2.***
    London: *McMillan* **(1979)**
11. M.Damnjanović: private communication (1992)

12. C.J.Bradley and A.P.Cracknell:
The mathematical theory of symmetry in solids
Oxford: *Clarendon Press* **(1972)**
13. M.Damnjanović, I.Milošević and M.Vujičić:
Phys.Rev.**B 39**, (1989) 4610
14. M.Damnjanović and I.Milošević:
Phys.Rev.**B 43**, (1991) 13482
15. I.Milošević and M.Damnjanović:
Phys.Rev.**B 47**, (1993) 7805
16. Cs.Mészáros and J.Bánkuti:
Phys.Stat.Sol.(b) **183**, (1994) 73
17. V.P.Mineev: JETP Lett. **57 10** (1993), 659
18. T.Kármán, E.Lähderanta, S.Leppävuori, R.Laiho, I.Halász, I.Dódony, G.Zsolt, T.Porjesz, A.Uusimäki, I.Kirschner and Gy.Kovács : Z.Phys **B 78**, (1990) 169
19. I.Kirschner, S.Leppävuori, A.C.Bódi, A.Uusimäki and I.I.Dódony:
Appl.Supercond. **1** (1993), 1721
20. Y.Zhu and J.M.Cowley: Phil.Mag.**A 69** (1994), 397
21. M.Damnjanović: Phys.Lett. **A 14** (1981), 1055
22. E.Ascher: J.Phys.**C**: Solid.State.Phys.**10**, (1977) 1365
23. M.Damnjanović:
J.Phys.**C**: Solid.State.Phys.**14**, (1981) 4185
24. M.Damnjanović:
J.Phys.**C**: Solid.State.Phys.**15**, (1982) 2321
25. V.Dvorák: Phys.Stat.Sol. (b) **151**, K23 (1989)
26. A.Q.He, G.W.Qiao and H.Q.Ye: Physica **C 204**, (1992) 85
27. V.I.Punegov and K.M.Pavlov: Kristallografiya **38**, (1993) 34
28. I.Halász, I.Kirschner, T.Porjesz, Gy.Kovács, T.Kármán, G.Zsolt, Cs.Sükösd, N. S.-Rozlosnik, and J.Kürti: Physica **C 153**, (1988) 379
29. I.Halász, V.Fülöp, I.Kirschner and T.Porjesz:
Journ.Cryst.Growth **91**, (1988) 91
30. I.Halász, A.Rockenbauer, I.Kirschner and T.Porjesz:
Journ.Supercond. **1**, (1988) 451

Posters

Macroscopic and Bulk - Controlled Elastic Modes in an Interaction of Interstitial Alcali Metal Cations within a Face-Centered Cubic Crystalline Fullerine

Valentine A. Tatarenko, Constantin L. Tsysman,
Yelena T. Oltarzhevskaya

Department of Solid State Theory (06) at the Institute for Metal Physics;
36 Academician Vernadsky Blvd, Kiev-142, 252180 Ukraine

Tel.:(+7) 044 4440530
Fax.:(+7) 044 4442561

The calculations in a majority of previous works for the fulleride (AqC_{60}) crystals were performed within the framework of the rigid-lattice model, neglecting the distoration relaxation of the host fullerene (C_{60}) crystal caused by the interstitial alkali-metal (A) cations. However, an each cation is a source of a static distoration field, and the resulting field is a superposition of such fields generated by all cations. This is a reason why the host-crystal distortions depend on the A-cations configurations, i.e. on a type of a spatial bulk distribution of interstitial cations.

~~The given~~ This paper seeks to find a functional relation between the amplitudes of the doping-induced structure-distortion waves and of statistic concentration ones. A semiphenomenological model is constructed here within the scope of statistical-thermodynamic treatment and using the lattice-statistics simulation method(*). In this model the effects due to the presence of q solute A cations over available interstices (per unit cell) on the statistic inherent reorientation and/ or displacements of the solvent molecules from the "average-lattice" sites" as well as on the lattice parameter a of the elastically-anysotropic "cubic" C_{60} crystal are taken into account .

The (indirect) "strain-induced" interaction between the interstitial A cations "by means of the host crystal ", as any dipole--dipole-like interaction, is highly directionally anisotropic and long-range. That is why the (*macroscopic*) total volume-dependent energy of the single-crystalline fulleride AqC_{60} becomes a functional of boundary conditions, i.e. a shape and a spatial-orientations variants of a product phase, and that modifies the Gibbs statistical thermodynamics of the martensitic-like constant-composition transformation of the C_{60} lattice upon a further doping by A atoms from the pristine FCC structure to the BCT one within experimentally determined phases manifesting themselves in different properties for doing a conductivity. With an aid of a proposed interstitialcy model it may be possible to overcome such an obstacle in the analytic thermodynamycal treatment of data from the electron-diffraction and TEM studies of abnormalities associated with *A*-cationic redistribution's in the FCC-fullerene-derived *Ag* C_{60} phase. Although such a phase is expected to be insulating at low doping levels (q< <3), it is clear that an understanding the origin of this crystalline structure and its interplay with A-doped fullerides based on the BCT fullerene (or on the SC one) will have important consequences for an ongoing process of an unveiling the bulk high-Tc-superconductivity origin as well as the pair-formation mechanism, which are dependent on a spatial arrangement of *A* cations.

As a result of numerical analysis of the nonanalytic wave-vector dependence of the Fourier components $\hat{E}_{AA}(\mathbf{k})$ of spatial-dispersion energies of the *bulk-controlled* “strain-induced” interaction between the *A* cation within the scope of the quasi-harmonic approximation of the C_{60}-crystal natural vibrations, the absolute minimum value of these quantities exists at the singular central point $\Gamma(\mathbf{k=0})$ of the FCC-C60-crystal first Brillouin zone and is equal to the (negative) total energy $\hat{E}_{AA}(0)$ of the “strain-induced” interaction (“attraction”) between one chosen octahedral a cation and the rest of them within the intercalation crystalline compound *Aq*C60, if the intrinsic elastic moduli (in the Voigt designations) of the “pure” C_{60} crystal are C_{11}= 22.7, C_{12}= 9.8, C_{44}= 12.3 (in GPa) (**), and its lattice parameter is a*0*=a(q=0)= 14.04 A. Figure 1 shows the predicted arrangement of dispersion curves for $\hat{E}_{AA}(\mathbf{k})$ (in units of the square of concentration coefficient of the linear FCC-C60-lattice dilatation due to dissolving *A* atoms, L2) in high-symmetry directions in the Brillouin zone.

Besides, for example, the values of the A-A “pairwise” “strain-induced” interaction energies E1,E2,...,E6 for the 1st, 2nd, ...6th octahedral-interstitial coordination spheres in the real space respectively are in the -28.3:8.0:-8.6:-1.3:5.6:2.3 ratio, i.e. such a “strain-induced” interaction energy has a substantially nonmonotonic(“quasi-oscillating) dependence on an intercationic distance (see Fig. 2).

The absolute thermodynamical instability of a homogeneous solid solution of *A* cations in C_{60} crystal with respect to arbitrary infinitesimal concentration fluctuations (heterogeneity's) as a precursor effect associated with the possible spinodal-decoposition reaction in the *A* cations subsystem may be considered in view of the above-mentioned behavior of the characteristic function $\hat{E}_{AA}(\mathbf{k})$ in the vicinity of reciprocal-lattice points $\mathbf{\Gamma}$ (i.e. the instability range in **k**-space), when no the fully-screened electrostatic A-A intercationic interaction exists. (According to Ref> (***), at the early stage of spinodal decomposition, amplitudes of all concentration waves whose wave vectors belong to the instability range about **k**=0 will increase exponentially.)

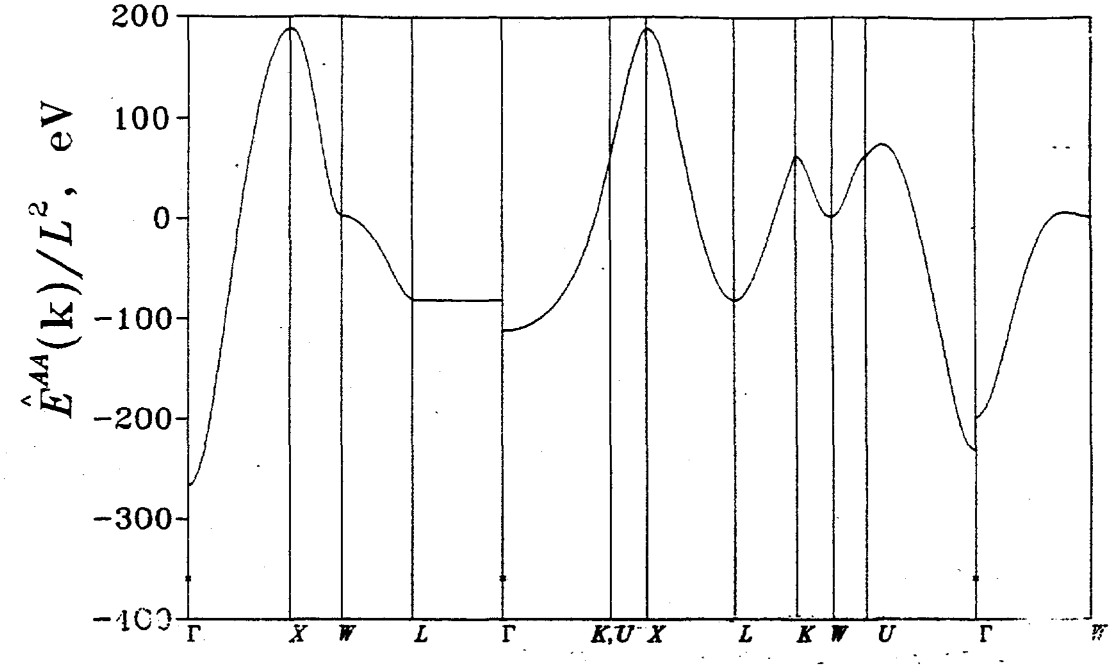
$\hat{E}^{AA}(\mathrm{k})/L^2$, eV
200
100
0
−100
−200
−300
−400
Γ
X
W
L
Γ
K,U
X
L
K
W
U
Γ
W

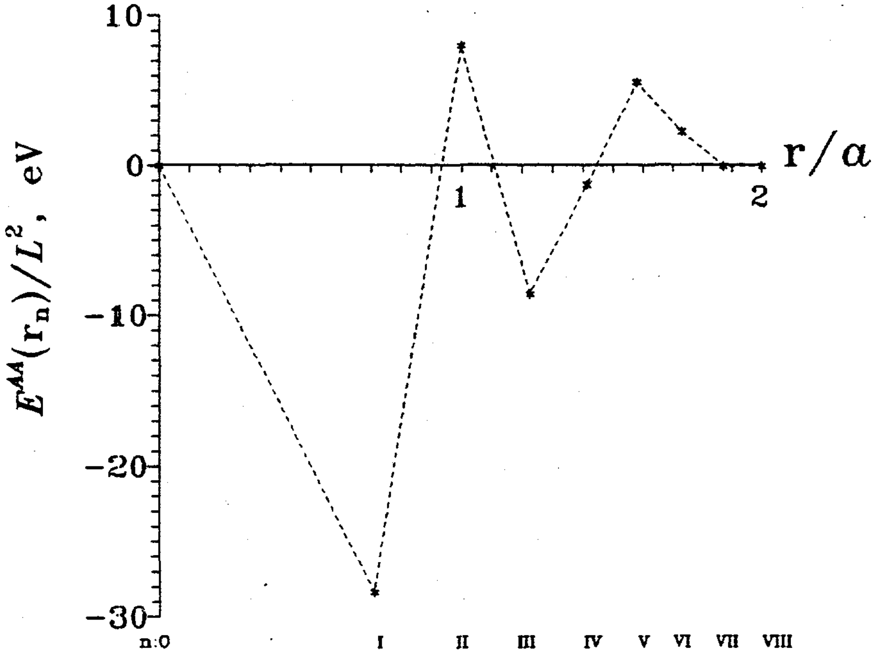
$E^{AA}(\mathrm{r_n})/L^2$, eV
10
0
−10
−20
−30
r/α
1
2
n:0
I
II
III
IV
V
VI
VII
VIII

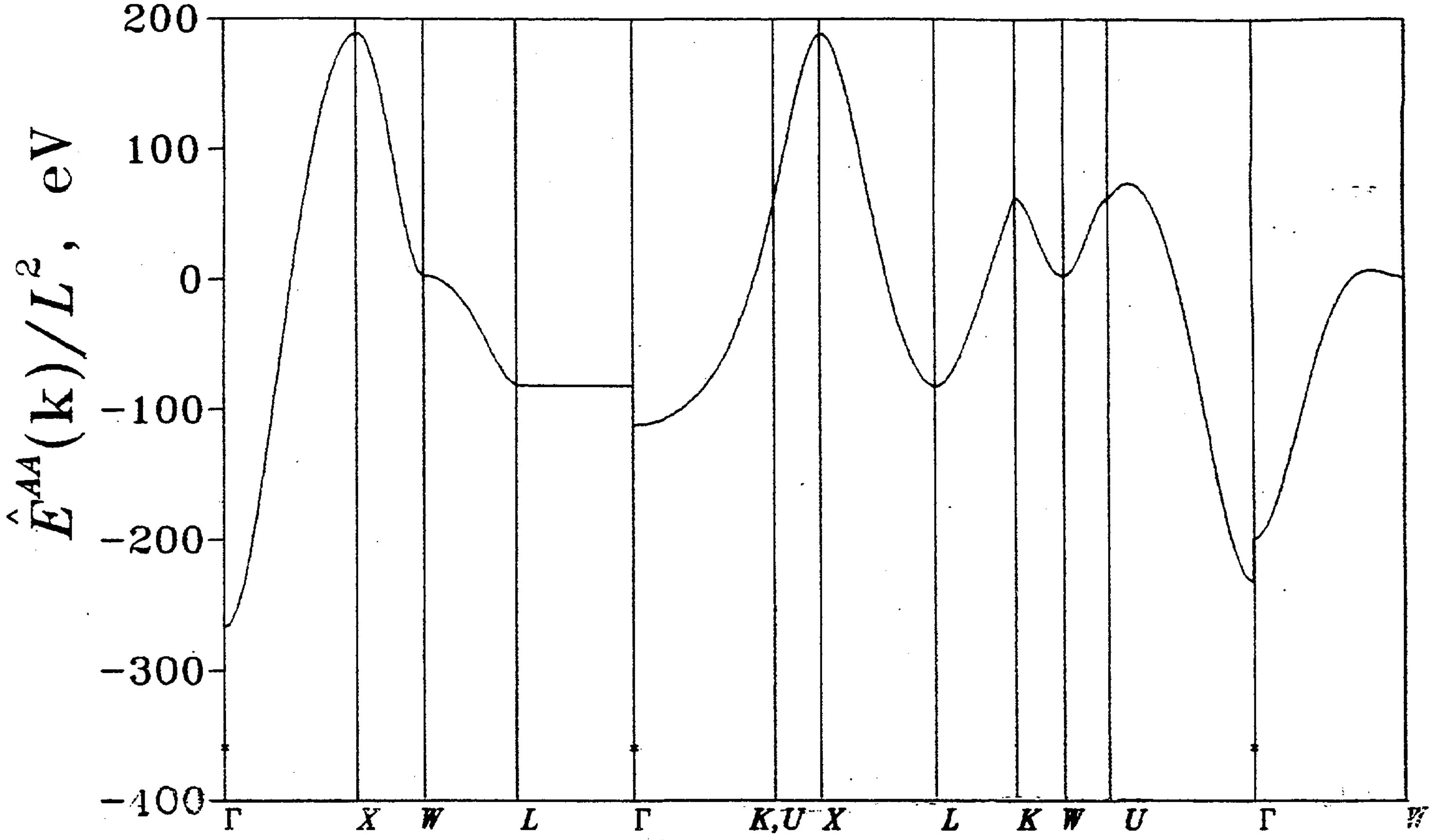
$\hat{E}^{AA}(\mathrm{k})/L^2$, eV
200
100
0
−100
−200
−300
−400
Γ
X
W
L
Γ
K,U
X
L
K
W
U
Γ
W

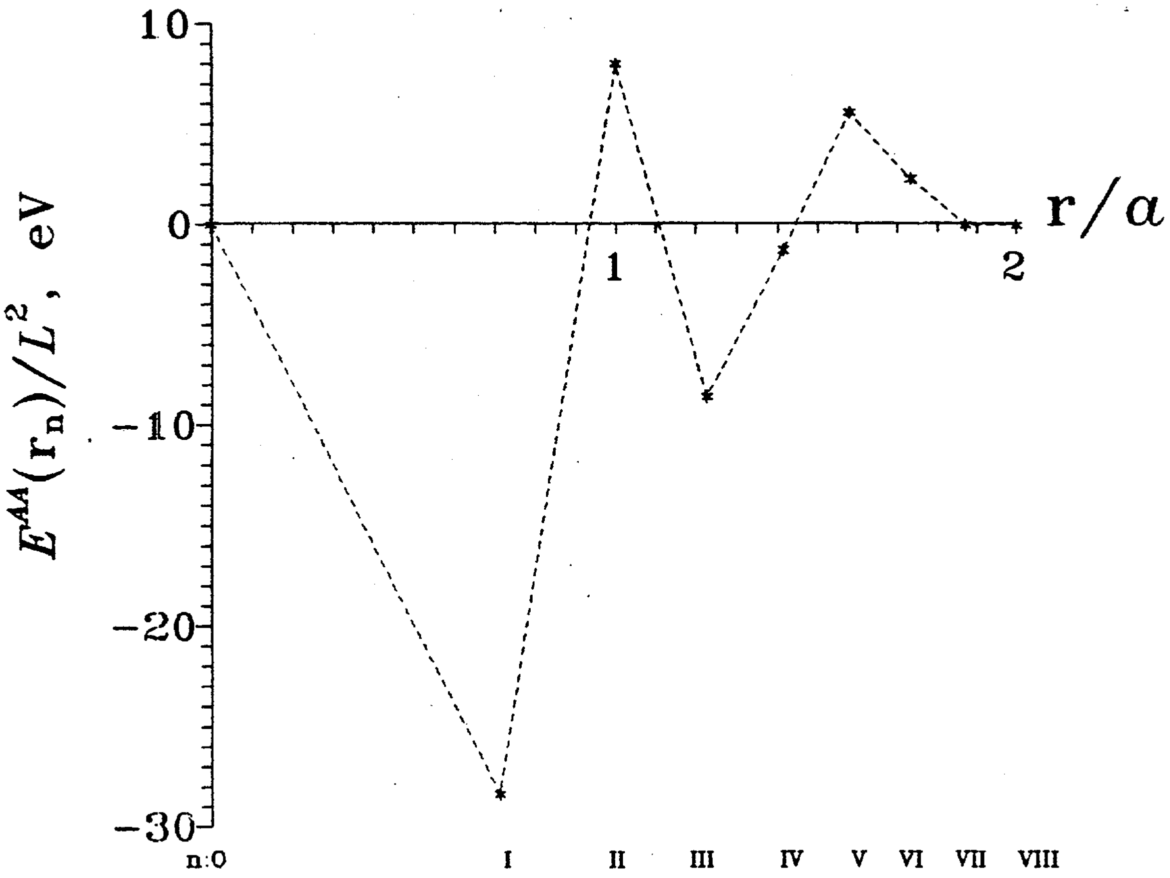
$E^{AA}(\mathrm{r_n})/L^2$, eV
10
0
−10
−20
−30
r/a
1
2
n:0
I
II
III
IV
V
VI
VII
VIII

Thallium 2223 High Tc Superconductor in a silver matrix and its magnetic shielding, hermal cycle and time aging properties

X. Fei, W.S. He, A. Havenhill, Z.Q. Ying, Y. Xin, N. Alzayed, and K.K. Wong.
Midwest Superconductivity Inc.

Y. Guo, D. Reichle, and M. S. P. Lucas
Kansas State University

ABSTRACT

Superconducting $Tl_2Ba_2Ca_2Cu_3O_{10}$ (Tl2223) was ground to powder. Mixture with silver powder (0--80% weight) and press to desired shape. After proper annealing, one can get good silver-content Tl2223 bulk superconductor. It is time-stable and has good superconducting property as same as pure Tl2223. It also has better mechnical property and far better thermal cycle property than pure Tl2223.

I. INTRODUCTION

From pratical view, one hope bulk superconductor has good superconducting property, good machnical preperty, time-stable, and good thermal cycle property (one cycle means rapidly temperature change 25°c --> liquid nitrogen --> 25°c).

Unfortunately, pure Tl2223 does not have all above mention properties. It has good superconducting property and it is time stable. But, its mechnical preperty is not good. It is not easy to form it. Its thermal cycle property is bad. After a few thermal cycle, it loses transport superconductivity.

For pratical application, need to improve its mechnical property and thermal cycle property.

Tl2223 superconductor in silver matrix can give better mechnical property and far better thermal cycle property than pure Tl2223 and still give good superconducting property.

We have made some high Tc superconducting shielding devices using this kind of material two years ago. By thermal cycle test and time aging test, we can say Tl2223 with 10%--80% weight silver is good superconducting engineering material.

II. SAMPLE PREPARATION

Synthesizing $Tl_2Ba_2Ca_2Cu_3O_{10}$ raw superconducting material

Tl_2O_3 (>99%), BaO_2 or BaO (>95%), CaO(>99%), and CuO(>99%) with the molar ratio of cations of 2:2:2:3 are mixed and ground in an agate mortar. Then the ground powder is pelletized in a die with a hydraulic press at an applied pressure of about 7000kg/cm^2. The pellets are then placed in a tubular alumina crucible and covered with an alumina plug. The crucible with contents is placed in a tube furnace; The power turned on and the temperature of the furnace raised to about 895°c at an ascending rate of 20 degrees per minute. The samples are heated at 895°c for 50 hours and then cooled within the furnace at a descending rate of 1 degree per minute to 600°c. Finally the furnace is turned off and the samples cooled to room temperature within the furnace. Oxygen is flowing in the furnace during sintering.

Fabrication of Ag-content Tl2223 superconducting cylinder

The pellet of raw superconducting $Tl_2Ba_2Ca_2Cu_3O_{10}$ is then broken and pulverized to a particle size of 1-5 microns. The ground powder is then mixed uniformly with silver powder (99.9% purity, 0.7-1.3 microns particle size) with the weight percentages of Ag:0, 10, 20, 40, 60, 80, 100. The mixed powders are then pressed into cylinders which are then annealed in a tube furnace. Oxygen is flowing in the furnace tube during the annealing . The temperature of the furnace is raised from room temperature to 790-820°c at a rate of 0.5 - 1 degree per minute and then maintained at this temperature for 30 hours. The furnace temperature is then reduced at a rate of 1-2 degrees per minute to 200°c, at which point the cylinders are then removed from the furance.

About two years ago (May--July, 92), we made several Tl2223 cylinder with 10%, 20%, 40%, 60% weight silver. A few months later, we made cylinder with 0%, 80%, 100% silver for comparison.

Sample dimensions and weights as following:

SAMPLE NUMBER	#1	#2	#3	#4	#5	#6	#7
SILVER CONTENT (%)	0	10	20	40	60	80	100
INNER DIAMETER (mm)	14.7	10.0	10.0	10.0	10.0	10.0	10.0
OUTER DIAMETER (mm)	24.5	25.0	25.0	25.0	25.0	23.0	25.0
HEIGHT (mm)	68.0	30.0	25.0	22.0	20.0	25.0	26.0
WEIGHT (g)	112	60	60	59	60	79	79

III. TEST

We use Fig.1 measurement system to measure magnetic shieding attenuation of cylinder samples.

Then all samples underwent thermal cycle. After every 20 cycles, measure shielding attenuation again. As the first batch of test, total 61 thermal cycles were done.

Each thermal cycle is following: Rapidly immerse sample in liquid nitrogen for about 5 minutes, take out and put in open air. So, a lot of frost first and then water condense on surface of sample. When sample reachs room temperature again and dry, immerse it in liquid nitrogen again. As you see, the thermal cycle is very harsh test.

After all samples were in open air for more than one and a half year, all underwent another 50 thermal cycles, then measure shielding attenuation again.

Then, another 50 cycles thermal cycles. Now, this test is continuing.

IV. RESULT AND DISCUSSION

All test results are shown in fig. 2 - 9. At beginning, all samples are good. Magnetic shielding attenuations are 70-90 db at f=60 Hz.

After 20 thermal cycles, pure Tl2223 (no Ag) sample lost its magnetic shielding property. All silver-content samples are still good.

The first batch of thermal cycle test is 60 cycles. All silver-content samples are still good after 61 cycles

In fact, when superconductor is rapidly colding and warming, it rapidly expands and contracts. For pure Tl2223, all grains are hard ceramic. So, contacts between grains are hard to hard. When expansion and contraction, hard to hard contact produces very high stress and it causes many microcracks inside. After several thermal cycles, there are so many microcracks inside that all transport paths are cut off. So, there is no screen current and lost magnetic shielding property.

When add silver into pure superconductor, silver locats between superconducting grains. So, many contacts between grains are soft. Less microcracks are produced during thermal cycles. So, Ag-content superductor has good thermal cycle property.

According to above analysis, low Ag-content sample produces more microcracks than high Ag-content sample during one thermal cycle. So, if we continue to do thermal cycle test more and more, low Ag-content sample will loss its shielding property more early than high Ag-content sample. Test result proved it.

After all samples were in open air for 1 1/2 years, we did thermal cycle test again. The second batch of test is 50 thermal cycles. After 50 cycles, measure shielding attenuation again. Test results are:

a. 10% Ag sample was dead, lost its shielding proporty.

b. Other high Ag-content samples with Ag-content more than 10% are still good.

The results agree with above analysis. The results also mean that Ag-content Tl2223 superconductor is time stable.

V. INCREASE MAGNETIC SHIELDING EFFECT

The all Ag-content samples of the first batch are very short. they have low length diamenter rate (L/d see Fig. 10).

H=2L
d-inner dia.

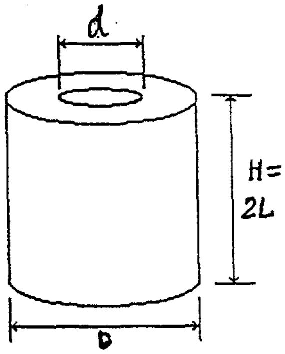

Fig. 10. Sample's shape

All L/d are = 1 - 1.5

For more high magnetic shielding attenuation, need to increase critical current density Jc of superconductor, L/d value and more thick of wall.

We have fabricated more longer cylinder:

10% Ag + 90% Tl2223, ID=9.7mm, OD=19.1mm, L=89mm;
20% Ag + 80% Tl2223, ID=9.8mm, OD=19.0mm, L=88mm.
The first one reached 132 db attenuation;
The second one reached 126 db attenuation.
The effect of increasing length is shown in Fig. 11.
Inside field dependence of applied field is shown in Fig. 12.

VI. CONCLUSION

Ag-content Tl2223 is a good superconducting engineering material. It is time-stable and good superconducting property as same as pure Tl2223. It has better mechnical property and far better thermal cycle property than pure Tl2223.

References

1.J.Wang and M. Sayer, "Low frequency magnetic shielding of $YBa_2Cu_3O_{7-}$:Ag_x high temperature superconductors," Cryogenics 1993 Vol 33, No 12

2. Ramesh chandra, A.K. Gupta, and others, "Fabrication and characterization of High Tc Superconducting magnetic shield," IEEE Trans. on Magn. Vol.25, No.2, 1991.

3. J.O. Wellis, M.E. Mchenry, M.P. Maley and H. Sheibrerg, "Magnetic shielding by superconducting Y-Ba-Cu-O hollow cylinders," IEEE Trans. on Magn. Vol.25, No.2, 1991.

4. H. Matsuba, A. Yahara, and D. Irisawa, "Magnetic shielding properties of HTc Superconductor," supercond. Sci. and Technol. 5 (1992)

5. M. Masale, N.C. Constantinon, and D.r. Tilley "The critical field of a hollow type-II superconducting cylinder," Supercond. Sci. and Technol. 6(1993)

6. R. Miilller, G. Fuchs, A. Grahl and A. Kohler "Magnetic shielding properties of $YBa_2Cu_3O_{7-x}$ tubes" Supercond. Sci. and Technol. 8(1993)

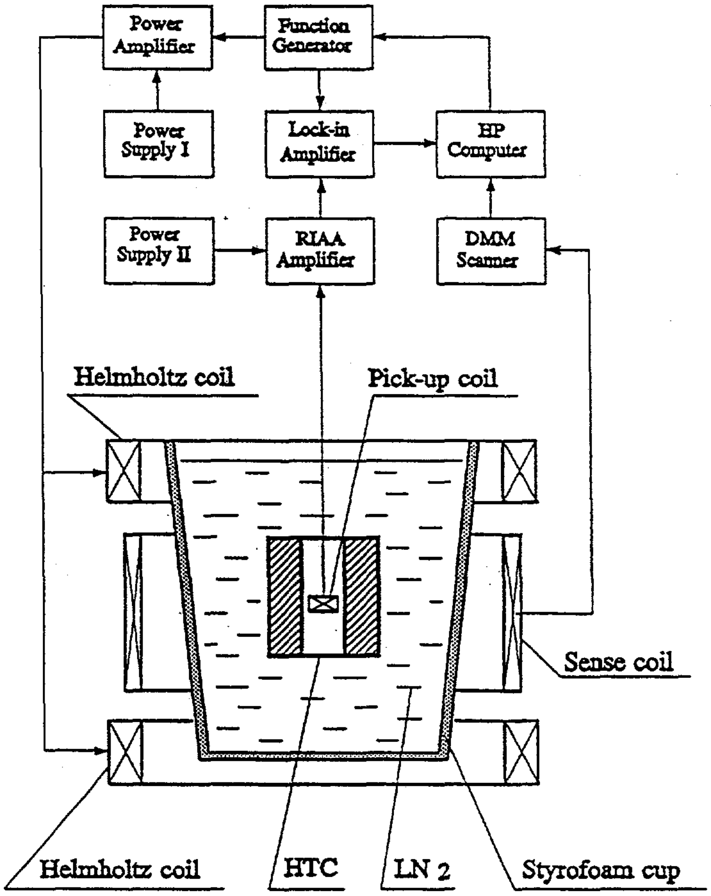

Fig. 1. Measurement System Diagram

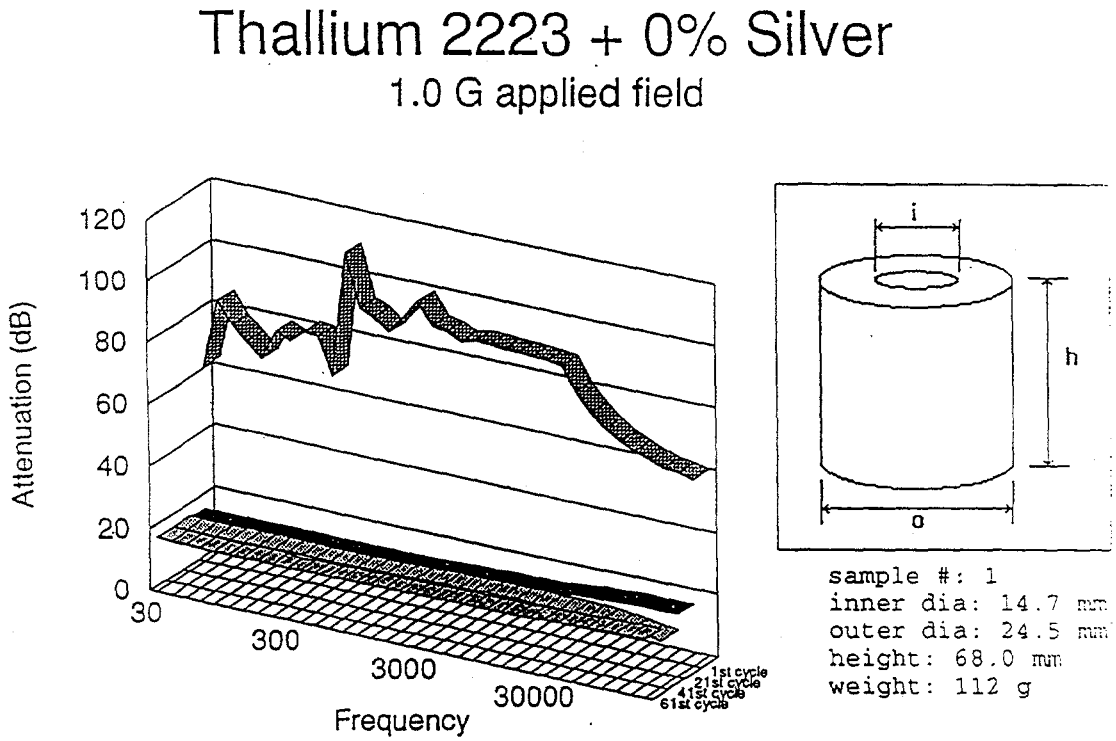

Thallium 2223 + 0% Silver

1.0 G applied field

sample #: 1
inner dia: 14.7 mm
outer dia: 24.5 mm
height: 68.0 mm
weight: 112 g

Fig.2. Magnetic field attenuation as a function of frequency for Thallium 2223 tube with 0% added silver. The magnetic field was applied parallel to the tube axis. The graphs show measurements made during the 1st, 21st, 41st and 61st cycles between room temperature and 77.3 K.

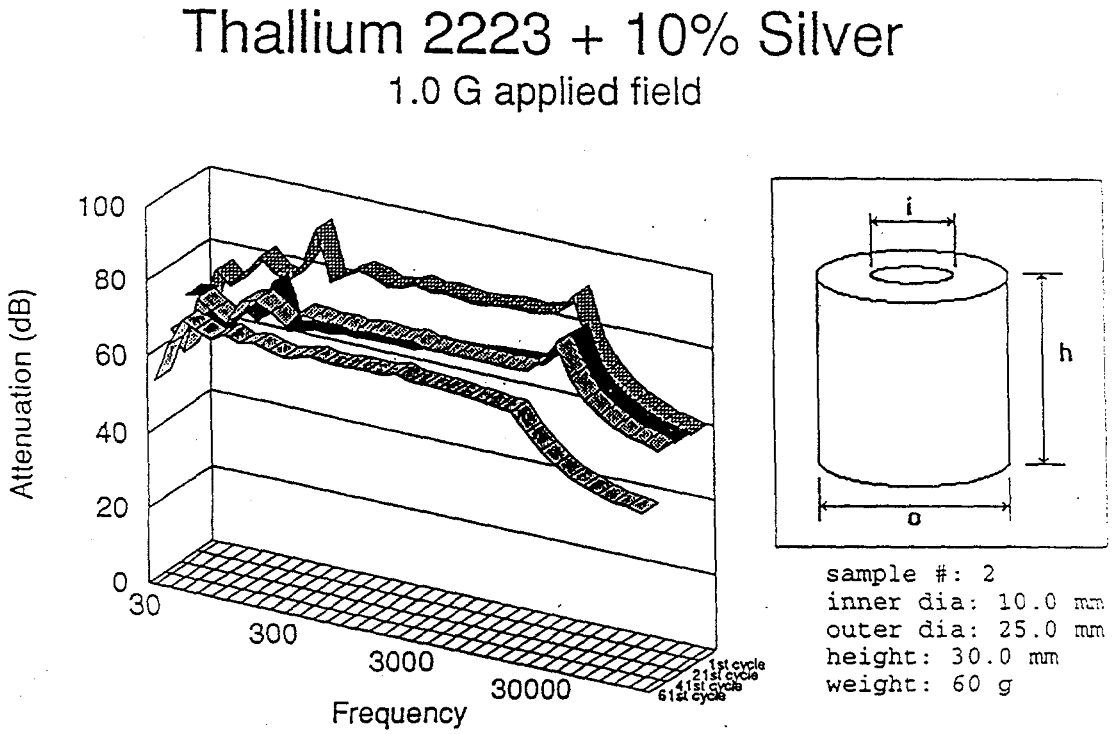

Thallium 2223 + 10% Silver

1.0 G applied field

sample #: 2
inner dia: 10.0 mm
outer dia: 25.0 mm
height: 30.0 mm
weight: 60 g

Fig.3. Magnetic field attenuation as a function of frequency for Thallium 2223 tube with 10% added silver by weight. The magnetic field was applied parallel to the tube axis. The graphs show measurements made during the 1st, 21st, 41st and 61st cycles between room temperature and 77.3 K.

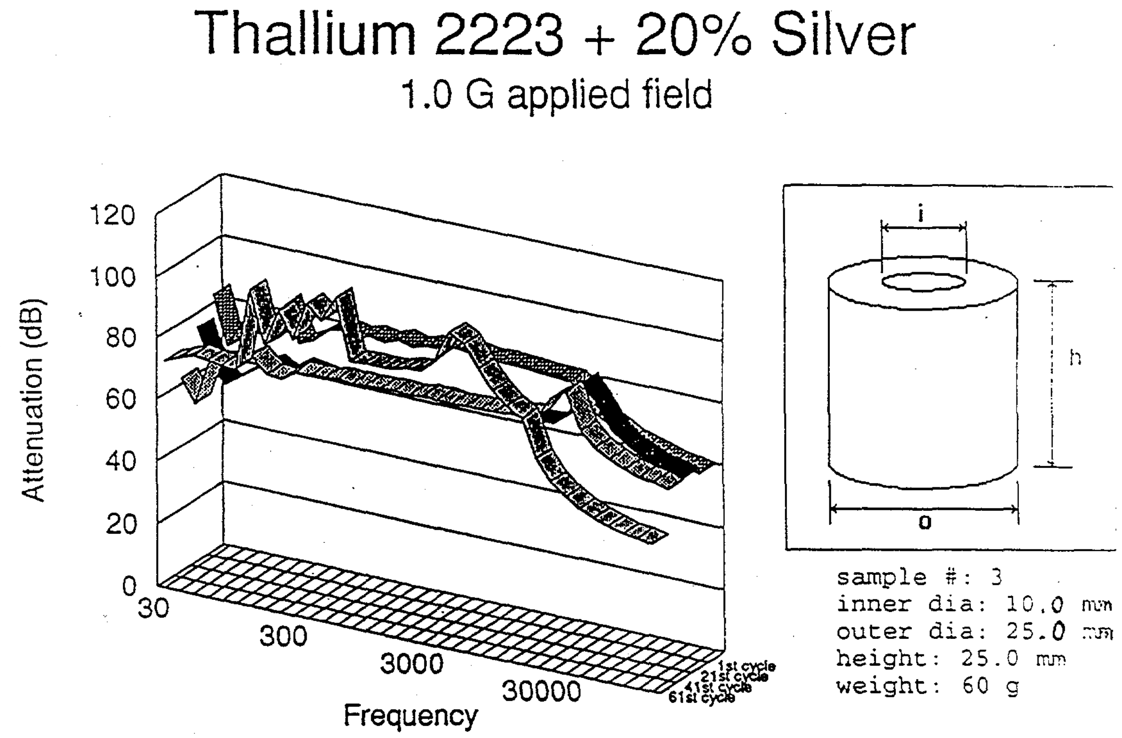

sample #: 3
inner dia: 10.0 mm
outer dia: 25.0 mm
height: 25.0 mm
weight: 60 g

Fig. 4 Magnetic field attenuation as a function of frequency for Thallium 2223 tube with 20% added silver by weight. The magnetic field was applied parallel to the tube axis. The graphs show measurements made during the 1st, 21st, 41st and 61st cycles between room temperature and 77.3 K.

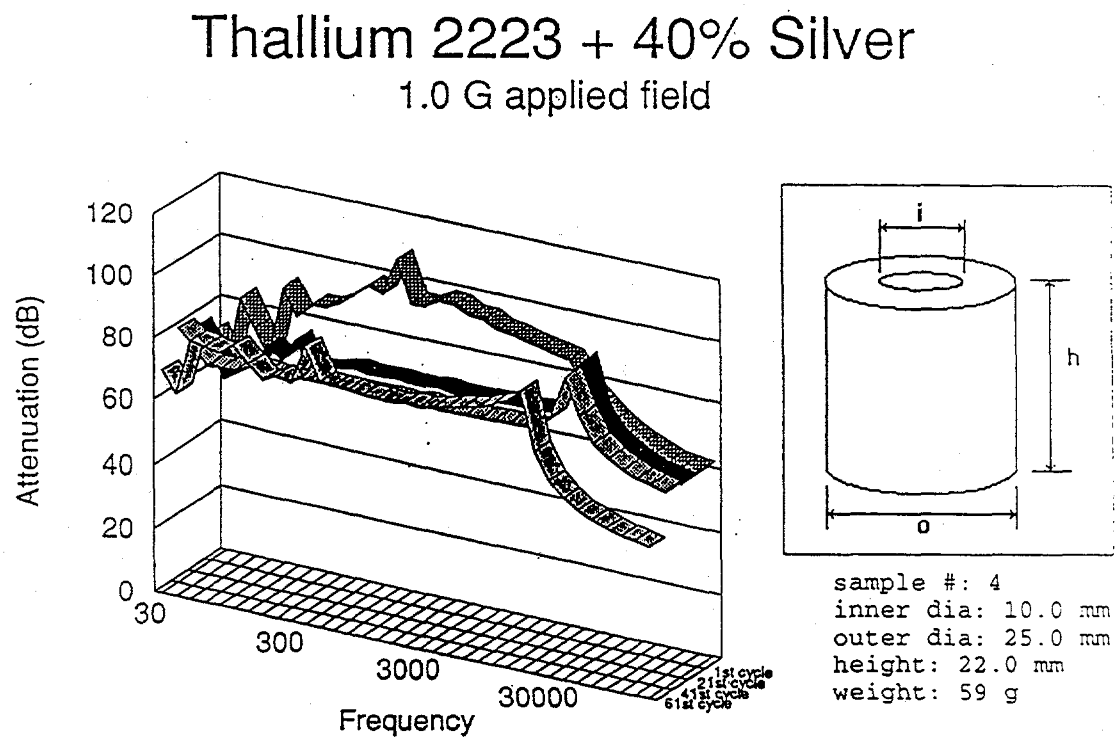

sample #: 4
inner dia: 10.0 mm
outer dia: 25.0 mm
height: 22.0 mm
weight: 59 g

Fig. 5. Magnetic field attenuation as a function of frequency for Thallium 2223 tube with 40% added silver by weight. The magnetic field was applied parallel to the tube axis. The graphs show measurements made during the 1st, 21st, 41st and 61st cycles between room temperature and 77.3 K.

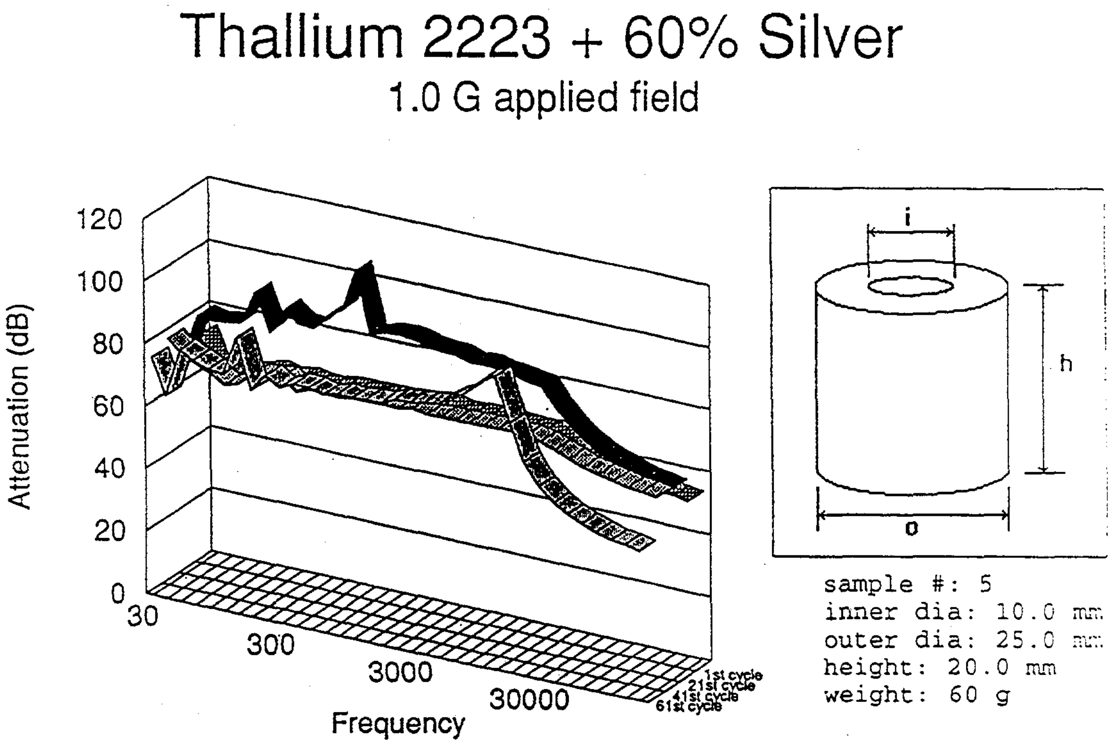
Thallium 2223 + 60% Silver

1.0 G applied field

sample #: 5
inner dia: 10.0 mm
outer dia: 25.0 mm
height: 20.0 mm
weight: 60 g

Fig. 6 . Magnetic field attenuation as a function of frequency for Thallium 2223 tube with 60% added silver by weight. The magnetic field was applied parallel to the tube axis. The graphs show measurements made during the 1st, 21st, 41st and 61st cycles between room temperature and 77.3 K.

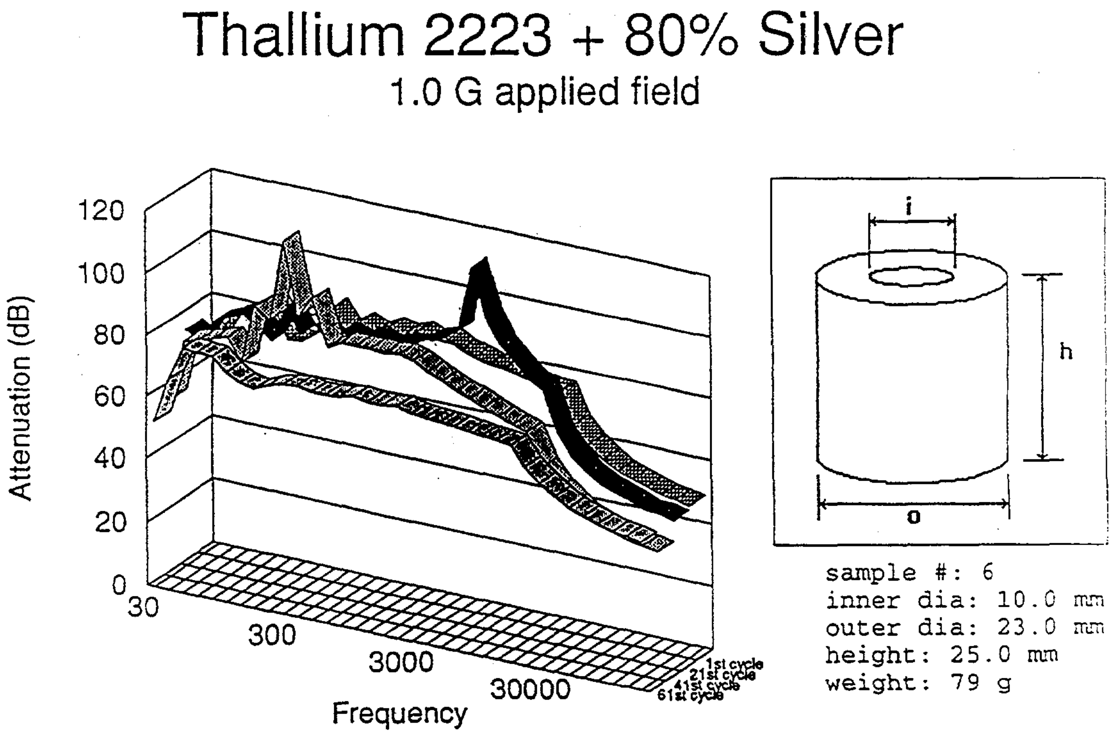
Thallium 2223 + 80% Silver

1.0 G applied field

sample #: 6
inner dia: 10.0 mm
outer dia: 23.0 mm
height: 25.0 mm
weight: 79 g

Fig. 7 . Magnetic field attenuation as a function of frequency for Thallium 2223 tube with 80% added silver by weight. The magnetic field was applied parallel to the tube axis. The graphs show measurements made during the 1st, 21st, 41st and 61st cycles between room temperature and 77.3 K.

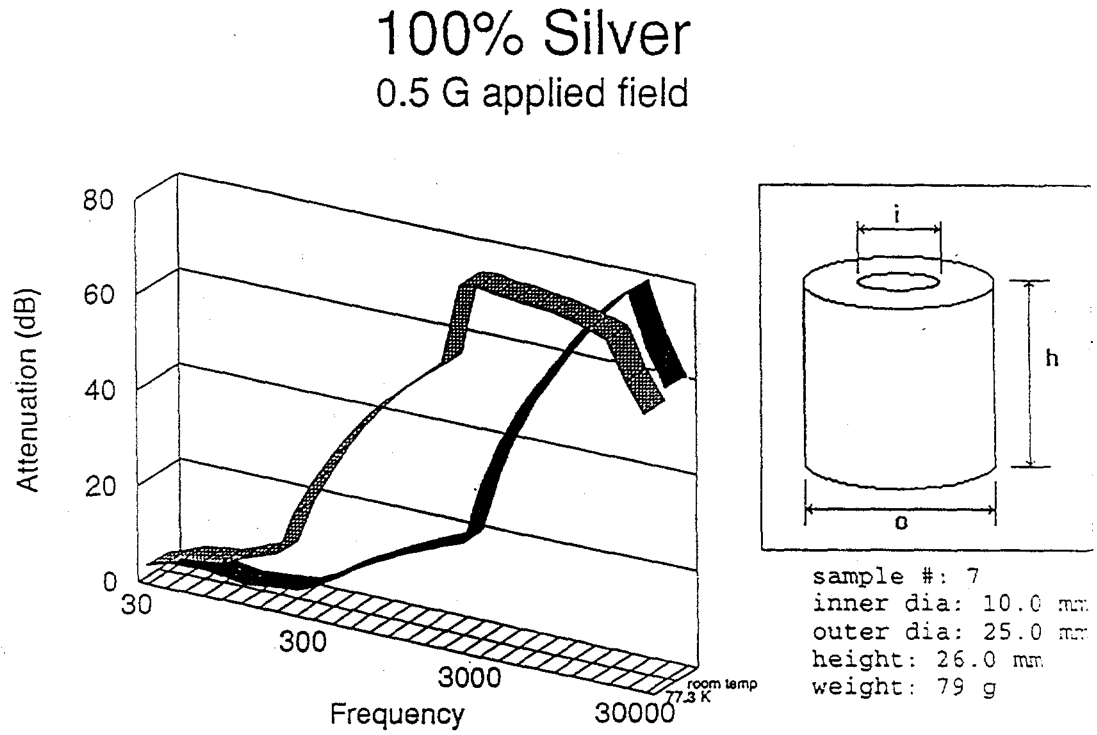

Fig. 8. Magnetic field attenuation as a function of frequency for a pure silver tube. The magnetic field was applied parallel to the tube axis. The graphs shows measurements made at room temperature and 77.3 K.

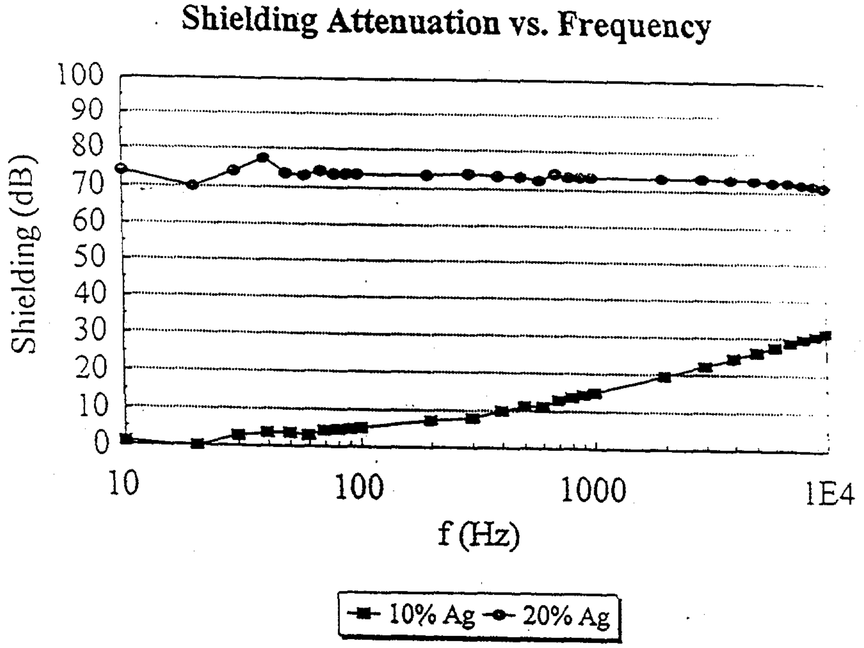

Fig. 9. Results of test after 1 1/2 year in open air, another 50 thermal cycles, and total 111 thermal cycles
10% Ag sample is dead and others are OK

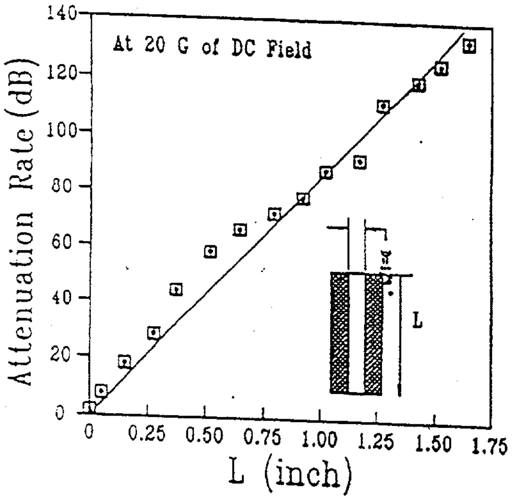

(B) Attenuation measurement

Figure 11

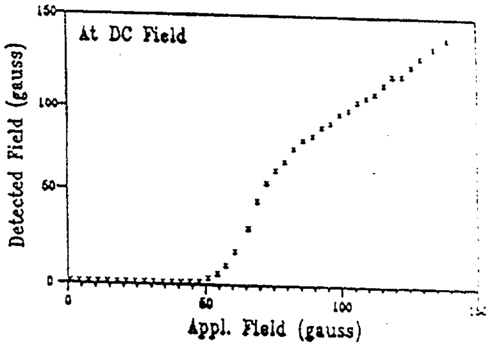

(A) Critical field measurement

Figure 12

The Role of Silver in the Processing and Properties of Bi-2212

Th. Lang, B. Heeb, D. Buhl and L.J. Gauckler

Nichtmetallische Werkstoffe, ETH Zürich, Sonneggstrasse 5, CH-8092 Zürich

Abstract

The influence of the silver content and the oxygen partial pressure on the solidus temperature and the weight loss during melting of $Bi_2Sr_2Ca_1Cu_2O_x$ has been examined by means of DTA and TGA. By decreasing the oxygen partial pressure the solidus is lowered (e.g. $\Delta T=59°C$ by decreasing pO_2 from 1 atm to 0.001 atm) and the weight loss is increased. The addition of silver causes two effects: (a) the solidus is further decreased (e.g. 2wt% Ag lower $T_{solidus}$ by up to 25°C, depending on the oxygen partial pressure), (b) the weight loss during melting is reduced.

Thick films (10-20 μm in thickness) with 0 and 5 wt% silver and bulk samples with 0 and 2.7 wt% silver were melt processed in flowing oxygen on a silver substrate in the DTA, allowing the observation of the melting process and a good temperature control. The critical current densities are vigorously dependent on the maximum processing temperature. The highest j_c in thick films (8000 A/cm^2 at 77 K, 0 T) was reached by melting 7°C above the solidus temperature. The silver addition shows no significant effect on the processing parameters or the superconducting properties.

The highest j_c for bulk samples (1 mm in thickness) was obtained by partial melting at 900°C or 880°C, depending on the silver content of the powder (0 or 2.7 wt%). The j_c of the samples is slightly enhanced from 1800 A/cm^2 (at 77 K, 0 T) to 2000 A/cm^2 by the silver addition.

To be able to reach at least 80% of the maximum critical current density, the temperature has to be controlled in a window of 5°C for thick films and 17°C for bulk samples.

Introduction

Silver is of great importance for the preparation of superconducting Bi-Sr-Ca-Cu-oxide, because of several advantageous properties: (a) It was found to be nonpoisonous to the superconducting properties of Bi-2212 [1-3], (b) Silver shows a high oxygen diffusivity [2-5] so that the oxygen uptake through a silver sheath is possible, (c) Bi-2212 tapes melt processed on silver are highly a/b textured [6-10], (d) Silver lowers the processing temperatures of Bi-2212 thick films [11], (e) its ductility enables the production of tapes and wires through a powder-in-tube process [12], still providing a sufficient mechanical stabilization.

These reasons make silver the preferred material to surround the Bi-Sr-Ca-Cu-O compound, especially when the samples are prepared by a process involving a reactive liquid phase. Such a process is the partial melting process, which was shown to be suitable to reach high critical current densities in Bi-2212 thick films [13-14] and bulk samples [15-16]. Therefore, it is interesting to know how the silver substrate or a silver addition influences the processing parameters of such compounds.

The aim of this study was to evaluate the influence of silver additions on the solidus temperature and the weight loss during melting of Bi-2212 and to examine the influence of the maximum processing temperature during the partial melting on the critical current density of thick films and bulk samples.

Experimental

a. Powder preparation

Powders with the stoichiometry $Bi_2Sr_2Ca_1Cu_2O_x$ and $Bi_{2.2}Sr_{2.05}Ca_{0.95}Cu_2O_x$ were prepared by the standard calcination process. The appropriate amounts of Bi_2O_3[A], $SrCO_3$[B], $CaCO_3$[C] and CuO[D] were mixed and calcined in MgO- or Ag-crucibles at 750°C, 800°C and 820°C with intermediate grindings. Finally they were pressed into pellets, sintered for 150 h at 850°C in air and ground again. XRD measurements showed the powders to be nearly single phase.

Mixtures of Bi-2212 with silver (0-15.4 wt%) were prepared by adding appropriate amounts of Ag_2O powder[E], mixing for 3 h in a ball mill and decomposing the silver oxide at 600°C. After this treatment the silver was distributed homogeneously over the whole batch as metallic particles with diameters of a few µm.

The melting behavior of Bi-2212 with silver additions up to 15.4 wt% was investigated by means of *differential-thermal-analysis* (DTA) and *thermal-gravimetry* (TGA). 100 mg of Bi-2212 powder with different Ag contents were heated in Al_2O_3 crucibles with 5°/min to 1000°C in three different atmospheres: (a) oxygen[F] (pO_2=1 atm), (b) air (pO_2=0.21 atm), (c) nitrogen[F] ($pO_2 \approx 0.001$ atm).

b. Sample preparation

Thick films

The thick films were prepared by drying a butanol suspension of Bi-2212 (cation-ratio 2.2:2.05:0.95:2) with 0 and 5 wt% silver in silver forms. The partial melting of these samples was carried out in the DTA.

[A] PCF, 99.9% purity

[B] Solvay Barium Strontium GmbH, >99.9%

[C] Solvay Barium Strontium GmbH, >99.9%

[D] Cerac Inc., >99.8%

[E] Fluka Chemika, >99.0%

[F] Pan Gas, technical grade

The heat treatment consisted of the following steps:

- heating with 1°/min to T_{max} ($868°C \leq T_{max} \leq 897°C$)
- cooling to 850°C with 5°/h
- cooling to room temperature with 5°/min

The whole heat treatment was done in flowing oxygen.

To adjust the oxygen content of the Bi-2212 and therefore the T_c, the films were post-annealed in flowing nitrogen ($pO_2 \approx 0.001$ atm) at temperatures below 600°C. The final thickness of the films was 10-20 µm, the diameter 11 mm.

Bulk

Bulk samples with a diameter of 13 mm and a final thickness of 1 mm were prepared by pressing the Bi-2212 powder (cation ratio 2.2:2.05:0.95:2) with 0 and 2.7 wt% Ag uniaxially into silver cups with a pressure of 150 MPa. This silver amount was chosen, because it was measured after processing a Bi-2212 pellet without Ag addition by the partial melting process on a Ag substrate to be uptaken by the superconductor from the substrate.

The heat treatment for bulk samples differed from the one for thick films and consisted of the following steps:

- heating with 1°/min to T_{max} ($865°C \leq T_{max} \leq 918°C$)
- holding T_{max} for 2 h
- cooling to 850°C with 40°/h
- annealing at 850°C for 12 h
- cooling to room temperature with 5°/min

This part of the heat treatment was performed in the DTA. In order to reach an almost single phase microstructure [17], the samples were post-annealed for 72 h at 850°C. Both, the melting and the annealing were done in flowing oxygen. To control the oxygen stoichiometry and therefore the T_c of the samples, the atmosphere was switched to nitrogen ($pO_2 \approx 0.001$ atm) at 700°C during cooling to room temperature.

c. Characterization

The measurements of the critical current densities were performed in an AC magnetometer at f=4-10 Hz using the 1 µV/cm criterion. The samples were immersed in a bath of liquid nitrogen during the measurement. The current densities were calculated using the width of the measured M(H) loops.

Results and Discussion

a. DTA/TGA measurements

Figure 1 shows the dependence of the solidus temperature $T_{solidus}$ of Bi-2212 on the silver content at three different oxygen partial pressures. Besides the well known fact, that the melting is shifted towards lower temperatures for decreasing oxygen partial pressures, the measurements show a drop of the solidus with silver additions for all oxygen partial pressures. In oxygen as well as in air, $T_{solidus}$ reaches a minimum at approximately 2 wt% Ag addition. Silver contents of more than 5 wt% lead to no further change. The maximum temperature drop due to the silver is reduced with decreasing oxygen partial pressures and comes to 25°C in oxygen, 20°C in air and 10°C in nitrogen.

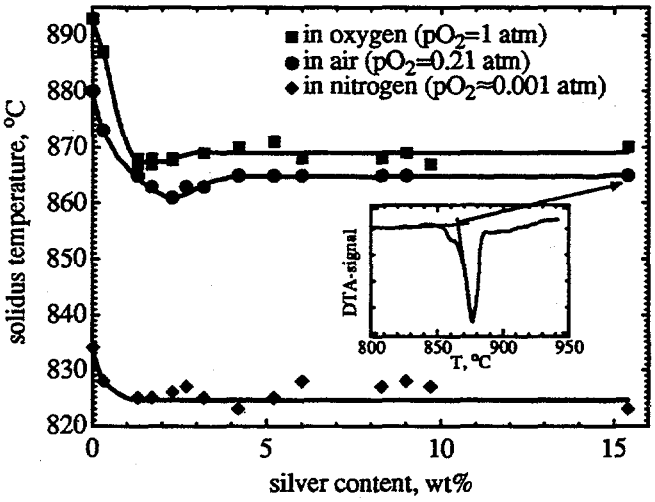

Fig. 1: Influence of silver addition and oxygen partial pressure on the solidus temperature of Bi-2212. The inset shows how the solidus temperatures were determined from the DTA data.

During melting, Bi-2212 releases oxygen to the atmosphere, leading to a loss of weight. Figure 2 shows the TGA curves of Bi-2212 without any added silver at three different oxygen partial pressures (1, 0.21 and 0.001 atm). A strong weight loss is observed as soon as the solidus temperature is exceeded. It is obvious, that the Bi-2212 releases more oxygen in low oxygen containing atmospheres. At pO_2≈0.001 atm the weight loss comes to 1.5 wt% of the initial amount of powder, at pO_2=1 atm it is about 1 wt%. The kink in the TGA measurement in oxygen, which was observed in all measurements in this atmosphere with varying evidence, cannot be explained ultimatively. It may be related to the formation and decomposition of a solid phase, which is stable only at higher oxygen partial presssures (e.g. the 0$\underline{14}$x$\underline{24}$ phase), during the peritectic melting.

The loss of oxygen during melting is found to be dependent on the silver content of the Bi-2212 powder, as shown in figure 3, where the weight loss of the oxide in the temperature range between the solidus temperature $T_{solidus}$ and ($T_{solidus}$+100°C) is plotted as a function of the silver content. Here again the behavior in three different oxygen partial pressures is investigated. Despite the scattering of the measurements, a trend towards lower weight losses with increasing silver contents is visible. This effect being pO_2-dependent is most pronounced in oxygen (pO_2=1 atm) and least in nitrogen (pO_2≈0.001 atm). Kanai *et al* [18] presume the Ag to be liquid at the partial melting temperatures in the presence of Bi-2212, and the liquid metal to accomodate released oxygen in the melt process. Taking into account that the oxygen solubility of liquid Ag is enhanced with increasing oxygen partial pressure, the results obtained in this work confirm their assumption.

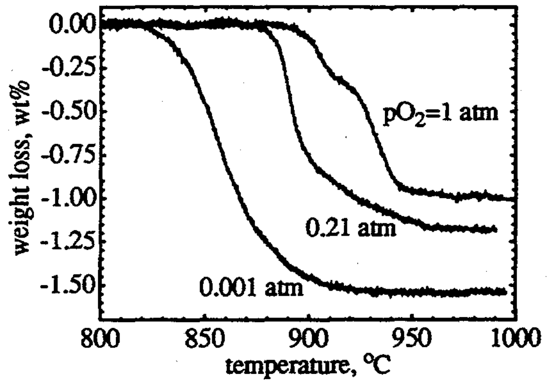

Fig. 2: TGA curves of Bi-2212 without silver additions showing the weight loss during melting. The solidus temperatures (determined from the DTA data), are 834°C, 880°C and 893°C for the measurement at pO_2=0.001 atm, 0.21 atm and 1 atm, respectively.

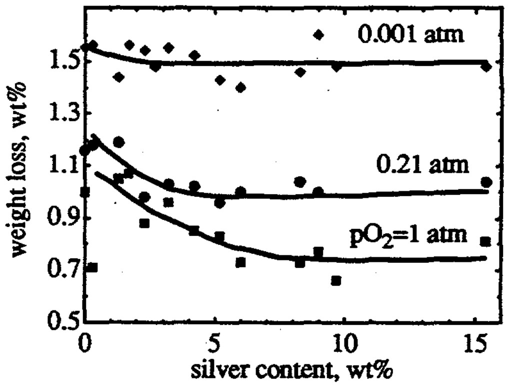

Fig. 3: Weight loss of Bi-2212 as a function of the silver content and the oxygen partial pressure in the temperature range $T_{solidus}$ to ($T_{solidus}$+100°C).

b. Partial melting of Bi-2212 thick films

The maximum processing temperature during the partial melting strongly influences the superconducting properties of Bi-2212. Figure 4 shows the dependence of the critical current density (at 77 K, 0 T; 1μV/cm-criterion) on the maximum temperature during the heat treatment combined with a typical DTA curve of a Bi-2212 thick film on a silver substrate. The DTA data reveal a solidus temperature of 873°C, being significantly lower than the measured 886°C for the powder in Al_2O_3 crucibles. Therefore, the Ag substrate influences the melting behavior of the Bi-2212 thick film considerably.

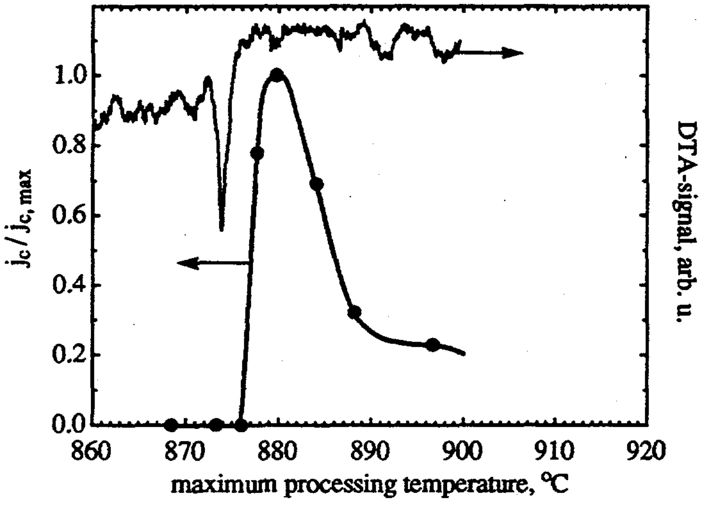

Fig. 4: Influence of the maximum processing temperature on the critical current density of Bi-2212 thick films.
The upper left curve shows the DTA peak of the melting of a film.

The critical current densities of the thick films show a narrow maximum at about 880°C, corresponding to 7°C above the solidus temperature. If T_{max} is chosen below or only a little above the solidus ($T_{max} \leq 876$°C), no or not enough liquid phase is produced to densify the sample. By processing the thick film at a temperature exceeding the solidus more than 15°C, coarse secondary phases lead to a decrease of j_c. Therefore, to reach high critical current densities in thick films the processing temperature has to be controlled within 5°C.

The j_c of thick films is very sensitive on the heat treatment or, more precisely, on the temperature difference between the melting of the sample and the maximum processing temperature. Thus, it is not possible to declare a specific T_{max} to be the best to produce high j_c thick films, because $T_{solidus}$ is influenced by many parameters: the atmosphere, the substrate material, doping elements, powder stoichiometry and so on. A thick film on a MgO substrate heat treated with T_{max}=880°C (the most promising temperature to produce thick films on silver) would not show high critical current densities, because the $T_{solidus}$ of Bi-2212 on magnesia is about 886°C and, therefore, no liquid phase would appear to densify the material. In consideration of these facts, it is more reasonable to regard $\Delta T = T_{max} - T_{solidus}$ and not T_{max} as crucial processing parameter.

Figure 5 shows the result of the same experiment as above but carried out with 5 wt% silver added samples in comparison with the results without silver addition. The maximum j_c of both, silver free and silver added Bi-2212, is the same (8000 A/cm^2 at 77 K, 0 T). However the curve for the silver added samples is shifted slightly towards lower temperatures. The width of the processing window promoting high j_c remains unchanged.

Since no major difference in the $j_c(T_{max})$ behavior of pure and Ag added Bi-2212 thick films is observed, we conclude that the film thickness of 10-20 µm and the high diffusivity found for silver in Bi-2212 [19] allow chemical interactions between the superconductor and the substrate. Thus, there is no significant difference in the solidus temperature of thick films whether the silver is present as substrate or added to the powder.

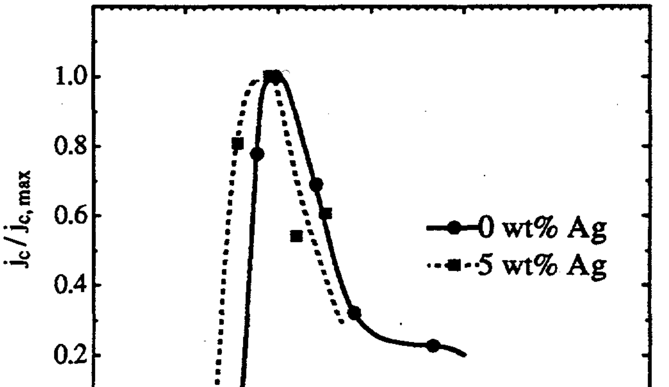

Fig. 5: Dependence of j_c on the maximum process temperature of thick films with 0 and 5 wt% silver. The maximum j_c for both samples is 8000 A/cm^2 (77 K, 0 T; 1µV/cm-criterion)

c. Partial melting of bulk samples

A typical DTA curve and the critical current densities in dependence of the maximum temperature T_{max} of the pure Bi-2212 bulk samples are plotted in figure 6. The DTA curve shows two major peaks (marked as 1 and 2). The low temperature peak (1) is attributed to the melting of the Bi-2212 at the interface with the silver. Peak 2 represents the melting of the rest of the sample, which is not in contact with the silver substrate. It agrees well with the $T_{solidus}$ of Bi-2212 in Al_2O_3 crucibles.

As shown before for Bi-2212 thick films, the critical current densities depend on T_{max}, having a maximum of 1800 A/cm^2 (at 77 K, 0 T) at 900°C. This temperature exceeds the solidus temperature of the pellet (marked as T_s in figure 6) by 12°C. The temperature window to produce bulk samples with a high j_c is markedly broader than for thick films.

The melting behavior of the bulk sample clearly shows, that it can be considered to be composed of a silver influenced region close to the substrate and the bulk, which is not affected by the silver substrate. To achive high critical current densities, the optimum processing temperature has to be adjusted to the melting of the ***bulk***. Since the Ag substrate does not influence this part of the sample, the temperature lays as high as 900°C. Lowering T_{max} in order to adjust it to the melting of the interface is detrimental for the densification of the sample. The amount of liquid is insufficient leading to a porous microstructure with low j_c. However, the high processing temperature is unvavorable for the microstructure and properties of the Ag affected interface (c.f. figure 4). The interface is overheated, contains a high amount of secondary phases and does not contribute distinctively to the current density of the whole sample. This is particularly undesirable because the interface is the most textured part of the sample [16] with a good current carrying potential.

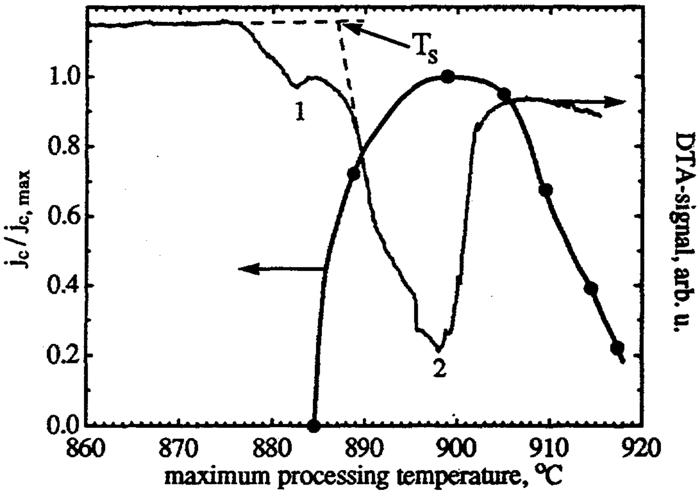

Fig. 6: Influence of the maximum processing temperature on the critical current density of Bi-2212 bulk samples in silver crucibles.
The second curve is a typical DTA measurement of such a sample, where two distinct peaks can be seen. Their origin is explained in the text.

The overheating of the interface should be avoided using silver doped Bi-2212 powder. In this case the interface of the pellet being in contact with the silver substrate does not melt at lower temperatures than the rest of the sample. The DTA curve of a pellet with 2.7 wt% Ag shows only one peak with an onset temperature of 864°C, confirming the homogenous melting of the entire sample. Figure 7 compares the results of the j_c measurements of the Ag-added and the Ag-free samples as a function of the processing temperature. The Ag addition shifts the dome significantly towards lower temperatures (ΔT=10-15°C) and enhances the maximum current density from 1800 A/cm^2 without silver to 2000 A/cm^2 in the silver containing samples. The optimum processing temperature for Ag added bulk (880°C) lays in the range of the temperatures leading to high critical current densities of thick films. Therefore, it is adjusted to the melting of the *bulk and the interface* leading to excellent phase purity of the entire sample and an enhanced j_c (77 K).

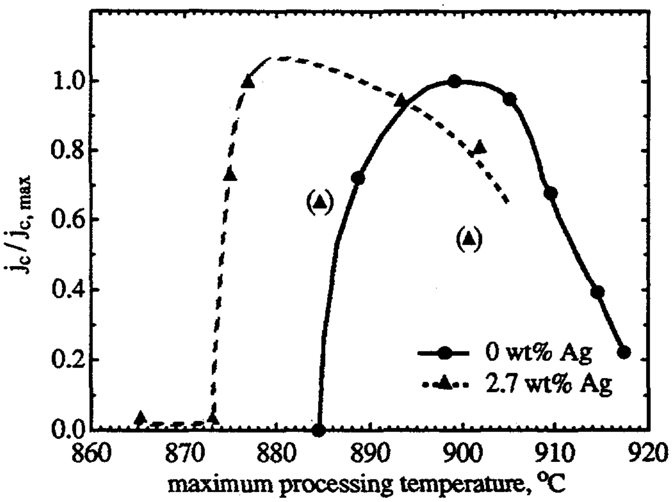

Fig. 7: Dependence of j_c (77 K, 0 T) on the maximum processing temperature of bulk samples with 0 or 2.7 wt% Ag. The maximum critical current densities are 1800 A/cm^2 for the silber free and 2000 A/cm^2 for the silver added samples.
The points in brackets result from samples, which lost some of the liquid phase during the melt processing through the silver substrate.

To explain the enhancement of j_c (77 K) due to the Ag addition, we can make a simple calculation with the following assumptions: The Ag/Bi-2212 interface is regarded as well-textured thick film with a thickness of 20 µm and j_c of 10^4 A/cm^2 for T_{max}=880°C and of 1800 A/cm^2 for T_{max}=900°C. The thickness of the bulk should be 980 µm, its j_c 1800 A/cm^2. It is now possible to compare the critical current density of a sample with an overheated interface (T_{max}=900°C) and a sample with a good interface (T_{max}=880°C). It results, that by keeping the processing temperature low enough to reach an interface free of secondary phases and therefore high local j_c, the j_c of the entire sample can be enhanced by about 10%. This indeed is the increase measured in this work by adding silver to the Bi-2212 powder and by processing at lower temperatures.

Summary

The melting behavior of Bi-2212 with silver additions up to 15.4 wt% in different oxygen partial pressures was inverstigated by means of DTA and TGA. The results show, that the addition of 2 wt% Ag lowers the solidus of Bi-2212 by up to 25°C, depending on the atmosphere. Silver contents exceeding 5 wt% cause no further change of $T_{solidus}$. The weight loss during melting, which is related to a oxygen loss of the compound, is decreased by melting in high oxygen partial pressures and by adding silver.

Thick films (d=10-20 µm) and bulk samples (d=1 mm) with and without silver additions were melt processed on silver substrates in the DTA. In thick films, the highest j_c was reached by melting 7°C above the solidus temperature of the film ($T_{solidus}$=873°C). The critical current density depends strongly on the maximum process tempearture, which has to be controlled within a window of about 5°C. An addition of 5 wt% Ag to the thick film lowers the process temperatures slightly (2°C) and does not enhance j_c. The physical properties of the thick films are mainly influenced by the silver substrate and, therefore, additional silver has hardly any further effects.

Bulk samples show a broader dependence of j_c on the maximum process temperature than the thick films. Temperature variations of ±7°C still lead to a high j_c (>80% of $j_{c,max}$). The addition of 2.7 wt% silver leads to significantly lower processing temperatures and an enhancement of the critical current density. The enhancement is attributed to the improved microstructure of the Ag/Bi-2212 interface.

Acknowledgments

The authors gratefully acknowledge the financial support of the Schweizer Nationalfonds (NFP 30).

References

[1] S. Jin, R.C. Sherwood, T.H. Tiefel, G.W. Kammlott, R.A. Fastnacht, M.E. Davis, S.M. Zahurak, Appl. Phys. Lett. **52** (19) 1628-30 (1988).

[2] M.-S. Oh, Q.F. Liu, W. Misiolek, A. Rodrigues, B. Avitzur, M.R. Notis, J. Am. Ceram. Soc. **72** (11) 2142-7 (1989).

[3] N. Savvides, A. Katsaros, S.X. Dou, Physica C **179** 361-8 (1991).

[4] B.R. Weinberger, L. Lynds, D.M. Potrepka, D.B. Snow, C.T. Burila, H.E. Eton, Jr., R. Cipolli, Physica C **161** 91-104 (1989).

[5] R.A. Outlaw, S.N. Sankaran, G.B. Hoflund, M.R. Davidson, J. Mater. Res. **3** (6) 1378-84 (1988).

[6] J. Kase, N. Irisawa, T. Morimoto, K. Togano, H. Kumakura, D.R. Dietderich, H. Maeda, Appl. Phys. Lett. **56** (10) 970-2 (1990).

[7] N.-W. Neumueller, H. Assmann, B. Kress, G. Ries, Adv. in Superconductivity IV, Eds. H. Hayakawa and N. Koshizuka, Springer Tokyo, 553-8 (1992).

[8] T. Hasegawa, H. Kobayashi, H. Kumakura, H. Kitaguchi, K. Togano, Adv. in Superconductivity V, Eds. Y. Bando and H. Yamauchi, Springer Tokyo, 737-40 (1993).

[9] W. Zhang, A. Pashitski, E.E. Hellstrom, Proc. of the 6th annual Conference on Superconductivity and Applications, Buffalo NY, USA, Sept. 15-17 (1992).

[10] B. Heeb, D. Buhl, Th. Lang, L.J. Gauckler, Proc. of Materials Week '93, Pittsburgh PA, USA, October 17-21 (1993).

[11] D.R. Dietderich, B. Ullmann, H.C. Freyhardt, J. Kase, H. Kumakura, K. Togano, H. Maeda, Jpn. J. Appl. Phys. **29** (7) L1100-3 (1990).

[12] Y. Yamada, M. Satou, S. Murase, Adv. in Superconductivity V, Eds. Y. Bando and H. Yamauchi, Springer Tokyo, 717-20 (1993).

[13] J. Shimoyama, N. Tomita, T. Morimoto, H. Kitaguchi, H. Kumakura, K. Togano, H. Maeda, K. Nomura, M. Seido, Jpn. J. Appl. Phys. **31** (9B) L1328-31 (1992).

[14] D. Buhl, Th. Lang, B. Heeb, L.J. Gauckler, submitted to Proc. of 4th World Congress on Superconductivity, Orlando FL, USA, June 27-July 1 (1994).

[15] Th. Baumann, G. Kemmler, P. Kluge-Weiss, Proc. of 7th Int. Workshop on Crit. Currents in Superconductivity, Alpbach, Austria, Jan. 24-27 (1994).

[16] B. Heeb, L.J. Gauckler, submitted to Proc. of 4th World Congress on Superconductivity, Orlando FL, USA, June 27-July 1 (1994).

[17] B. Heeb, L.J. Gauckler, H. Heinrich, G. Kostorz, J. Mater. Res. **8** (9) 2170-6 (1993).

[18] T. Kanai, T. Kamo, Supercond. Sci. Technol. **6** 510-3 (1993).

[19] Y. Fang, J.L. Routbort, J. Appl. Phys. **75** (1) 210-5 (1994).

A STUDY ON THE SUPERCONDUCTING PROPERTIES OF $YBa_2Cu_{3-X}Nb_XO_Y$ THIN FILMS

S.Srinivas and A.K.Bhatnagar
School of Physics, Univ. of Hyderabad, Hyderabad-500134, India
and
R.Pinto, S.P.Pai, P.R.Apte, S.C.Purandare and C.P.D'Souza
Solid State Electronics Group, T.I.F.R., Bombay -400 005. India

ABSTRACT

Effect of Niobium substitution at the copper site in $YBa_2Cu_3O_{7-x}$ was studied in thin film form. The films were deposited by laser ablation technique using the targets of the $YBa_2Cu_{3-x}Nb_xO_y$ where x = 0.0, 0.025, 0.05, 0.1, 0.2, 0.4, 0.8 and 1.0 under identical deposition conditions on $SrTiO_3$ <100> substrates. Films were characterized by XRD, resistivity, I-V and J_C measurements. Films made from x = 0.025 and 0.05 concentrations of Nb substituted targets showed relatively improved superconducting properties compared to that of undoped films. The best J_C realized for x = 0.025 Nb concentration was 1.8×10^6 A/cm^2 and for 0.05 Nb concentration it was 3.2×10^6 A/cm^2 at 77K. However, degradation of the superconducting properties, with the increase of $x \geq 0.1$ Nb concentration and drastic suppression and complete loss of superconductivity was noticed for $x \geq 0.4$. The growth of impurity phase YBa_2NbO_6 for x = 0.1 and above of Nb concentration was noticed from XRD patterns. However, the site occupancy of Nb could not be confirmed from these studies.

INTRODUCTION

Recent research trends in high temperature superconductivity(HTSC) have aimed at the improvement of superconducting properties by substitution or addition of other elements. However, substitution at Cu sites of HTSC compound has resulted in drastic degradation of superconducting properties [1-3]. The superconducting properties of $YBa_2Cu_3O_{7-x}$(YBCO) have revealed that the Cu-O plane and chain assembly is primarily responsible for the superconductivity and the main contribution to the density of states at the fermi level comes from the copper 3d and the oxygen 2p hybridization states. Hence, many researchers thought that the substitution for Cu by transition metals should produce substantial changes in the superconducting properties. The substitution of Nb in bulk has shown [4,5] that Nb substitution has not made any substantial improvement in the superconducting properties of YBCO, however it has shown improvement in mechanical properties. Moreover, substitution of Nb and Ta at Cu1 site in YBCO system has been confirmed by neutron diffraction analysis [10]. In the present study we report the superconducting properties of Nb substituted ($YBa_2Cu_{3-x}Nb_xO_y$) thin films.

EXPERIMENTAL

The targets for pulsed laser deposition (PLD) were prepared in the nominal stoichiometric compositions $YBa_2Cu_{3-x}Nb_xO_y$ where x = 0.0, 0.025, 0.05, 0.10, 0.2, 0.4, 0.8 and 1 using high pure chemicals. Thin films were made from the above targets using a Lambda Physik 301:KrF 248 nm excimer laser and a 300nm focal length quartz lens for beam focusing with a pulse width of 25 ns and a 1-10 Hz variable frequency. The target to substrate distance was maintained constant at 4.5cm, at a substrate temperature of 700°C and in an oxygen partial pressure of 200 mTorr. Thin films of 2000 A thickness of the above mentioned targets were deposited on $SrTiO_3$ <100> substrate under identical deposition conditions for comparison. Films were characterized by

XRD, SEM, four probe electrical resistivity and I-V characteristics and critical current density J_c measurements were done on 20μm and 1mm long microbridges.

RESULTS AND DISCUSSIONS

The XRD patterns have shown c-axis oriented films (fig.1) and with the increase of Nb concentration growth of a secondary phase YBa_2NbO_6 [6]has been identified. The transition temperatures for x = 0.0, 0.025, 0.05 are around 89K, 89.2K and 89.6K respectively. The critical current densities are 1.2 x 10^6 A/cm^2 1.8x 10^6 A/cm^2 and 3.2x 10^6 A/cm^2 respectively. D.Kumar et al [7] have reported that the nature of grain boundaries in undoped and doped films can be studied using a model proposed by De. Gennes[8] and Clarke[9]. As per this model, the slope of the $\sqrt{J_c}$ vs T_c -T will give a measure of the grain boundary domain thickness. When the slope is large, it indicates perfect alignment of grains and hence reduction of weak links which results in good quality film. From fig.2b, it is evident that the slope of Nb substituted films for the concentrations 0.025 and 0.05 is larger compared with undoped YBCO film. Our scanning electron micrographs have also resulted in featureless grain structure which may be due to the perfect alignment of grains during the growth process, however, particulates still exist (fig.4). The possible explanation for the improvement of critical current densities may be due to the fact that substitution of Nb (for lower concentrations only) at Cu1 sites in the basal plane, introduces extra oxygen at the vacant O5 which results in the change of oxygen coordination of the Cu1 cation from planar to octahedral coordination [11].

With the increase in Nb concentration for x ≥ 0.1 degradation and complete loss of superconductivity has been observed (fig 2a). It is due to the stabilization of YBa_2NbO_6 phase at higher concentrations. However, it has been realized that substitution of Nb up to x = 0.05 for Cu will improve the microstructural and superconducting properties of YBCO thin films compared to undoped YBCO films deposited under identical conditions.

CONCLUSIONS

The effect of Nb substitution for Cu on the superconducting properties of YBCO thin films has been investigated. It is noticed that no significant change in the orthorhombcity of the crystal structure or in T_c has been observed in YBCO thin films for Nb substitution up to $x = 0.05$ concentration, however, increase in J_c up to $x = 0.05$ of Nb concentration compared to that of undoped YBCO thin films has been realized. Degradation of superconducting properties and complete loss of superconductivity with the increase of Nb concentration confirm that Nb substitution has not made any substantial improvement on the superconducting properties even though it exists in +5 valance state. It can not be concluded from this study that whether Nb has substituted for Cu in YBCO lattice. A more detailed study is needed.

ACKNOWLEDGEMENTS :

One of the authors <SS> is thankful to University Grants Commission, INDIA for financial support and <AKB> is thankful to Council of Scientific and Industrial Research (CSIR) India, for High T_c Superconductivity research support. Authors would like to thank Dr M.S.R. Rao for useful discussions.

REFERENCES :

1. Gang Xiao, F.H. Strelty, A.Gavain, Y.W.Du and C.L. Chien : Phys. Rev. B 35(1987) 8782.
2. M.S.Islam. and Baetzold : Phys. Rev. B. 40(1989) 10926.
3. S.B.Ogale, M.Vedavyas, G.S.T.Bendre and S.M. Kanetkar : Appl. Phys . Lett. 61(1992) 2105.
4. M.Kuwabara and N.Kusaka : Jpn. J. Appl. Phys 27(1988) L1504.
5. Suresha N.G., Higo.S, Hakuraku.Y, Otawa.T, Honjo.Y and Ogushi.T : Int. J. Mod. Phys. B2(1988) 435.
6. Paulouse K.V., Koshy. J and Damodaran A.D.: Jpn. J. Appl

Phys.30(1991) L458.

7. D.Kumar et al : Appl. Phys. Lett. 62(1993) 3522.
8. P.G.DeGennes : Rev. Mod. Phys. 36(1964) 225.
9. J. Clarke : Proc. R. S. London A 308(1969) 447.
10. C.Greaves and P.R.Slater : Physica C161 (1989) 245.
11. Rey M.J., Dehaudt P.H., and Joubert J. : Physica C 167(1990) 162.

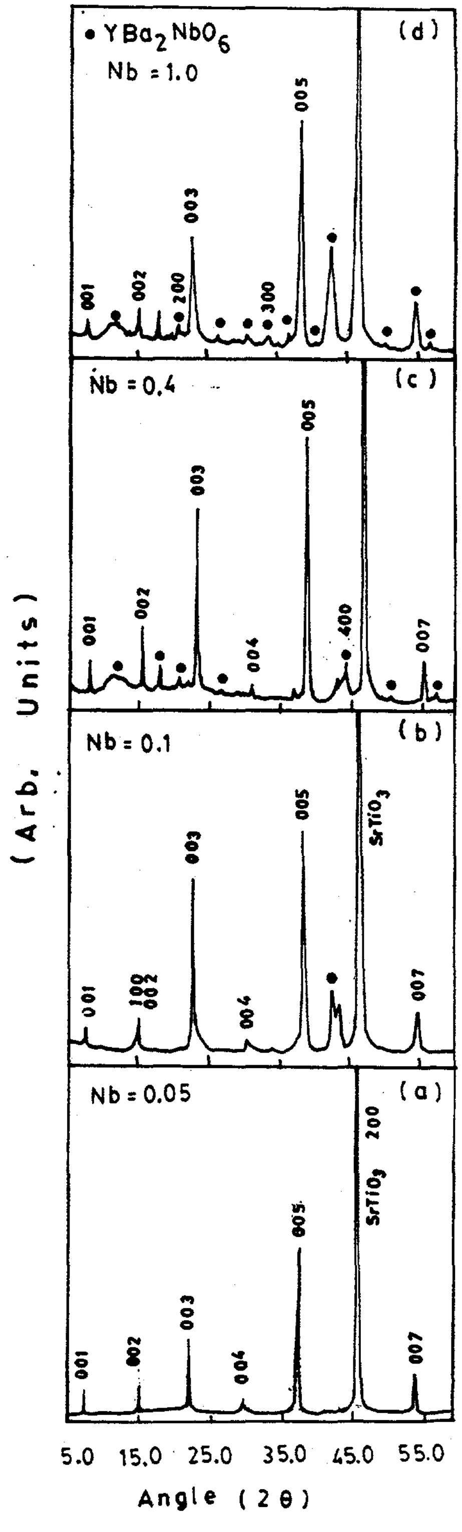

Figure 1.- X-Ray diffraction pattern of Nb substituted films.

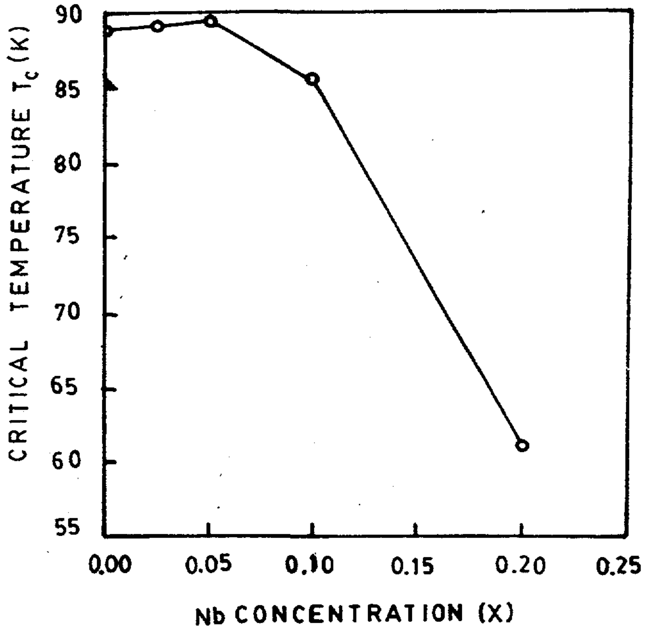

Figure 2.-Nb concentration (x) vs critical temperature (T_C) of the Nb substituted thin films.

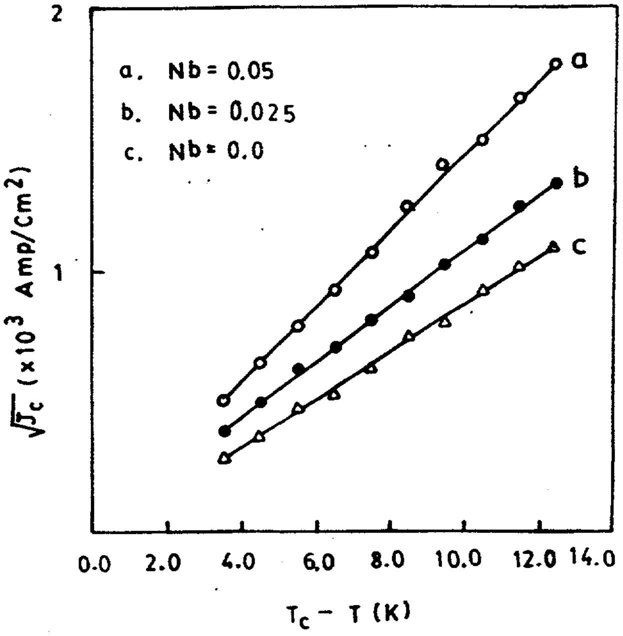

Figure 3.- T_C-T vs $\sqrt{Jc}$ of Nb substituted and undoped YBCO thin films.

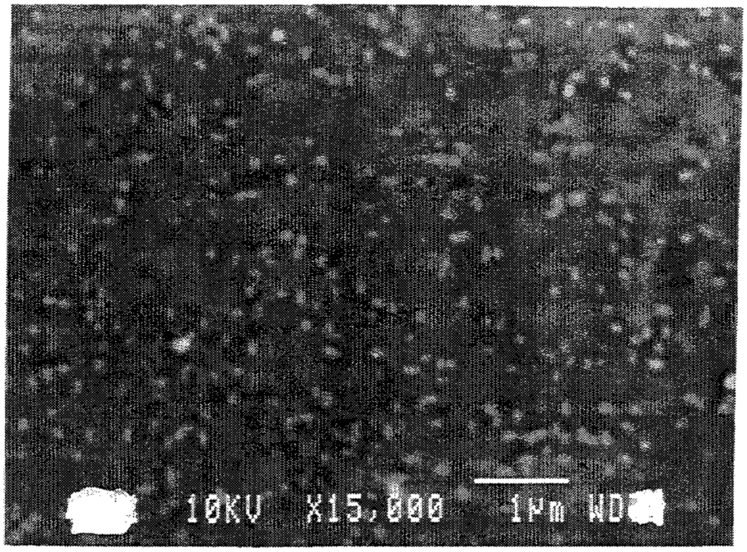

Figure 4.- Scanning electron micrograph of 0.05 concentration of Nb substituted film.

GROWTH AND MICRO STRUCTURAL STUDIES ON YITTRIA STABILIZED ZIRCONIA (YSZ) AND STRONTIUM TITANATE(STO) BUFFER LAYERS

S.SRINIVAS*, R.PINTO, S.P.PAI, C.P.D'SOUZA, P.R.APTE, D.KUMAR,
S.C.PURANDARE AND A.K.BHATNAGAR*
SOLID STATE ELECTRONICS GROUP, TIFR, BOMBAY-400 005, INIDA.
* SCHOOL OF PHYSICS, UNIV.OF HYDERABAD, HYDERABAD-500134, INDIA.

ABSTRACT

Microstructure of Yittria Stabilized Zirconia (YSZ) and Strontium Titanate (STO) of radio frequency magnetron sputtered buffer layers was studied at various sputtering conditions on Si<100>, Sapphire and $LaAlO_3$<100> substrates. The effect of substrate temperatures upto 800 C and sputtering gas pressures in the range of 50 mTorr. of growth conditions was studied. The buffer layers of YSZ and STO showed a strong tendency for columnar structure with variation growth conditions. The buffer layers of YSZ and STO showed <h00> orientation. The tendency for columnar growth was observed above 15 mTorr sputtering gas pressure and at high substrate temparatures. Post annealing of these films in oxygen atmosphere reduced the oxygen deficiency and strain generated during growth of the films. Strong c-axis oriented superconducting $YBa_2Cu_3O_{7-x}$ (YBCO) thin films were obtained on these buffer layers using pulsed laser ablation technque. YBCO films deposited on multilayers of YSZ and STO were shown to have better superconducting properties.

INTRODUCTION

There have been many reports on the deposition of high quality $YBa_2Cu_3O_{7-x}$ (YBCO) thin films on Si and Sapphire substrates using buffer layers. It has been well established that the use of buffer layer makes it possible to deposit thin superconducting films on a variety of substrates which otherwise are not suited because of the chemical reactivity with the superconducting thin film [1-4]. The most desirable properties of a buffer layer are a) to act as an effective barrier against inter diffusion, b) to improve lattice match between supeconducting film and substrate and c) to withstand for thermal cycling stresses. Yittria Stabilized Zirconia (YSZ) which satisfies the above criteria is widely used as buffer layer on Si and Sapphire. On the otherhand, $SrTiO_3$ <100> (STO) which has a good lattice match with YBCO can also act as a buffer layer on the above mentioned substrates.

H.Schmidth etal [5] have discussed the insitu growth of YSZ thin films using RF magnetron sputtering technique. Sputtering is a versatile technique for obtaining good quality epitaxial thin films as well as large area depositions with good uniformity. However, very few research reports are available on STO buffer layers [6]. For better understanding on the growth conditions of YSZ and STO buffer layers a detailed study about the preparatory conditions for reproducible results is needed .

EXPERIMENTAL

A diode RF magnetron sputtering system (NORDICO 2000) was used to grow buffer layers on Si<100> sapphire and $LaAlO_3$<100> substrates. The YSZ (10% Yittria) and STO sputtering targets were of 99.9% pure (10cm dia obtained from Cerac.Inc., USA). Si wafers were degreased followed by etching with 6:1 mixture of high purity HF and deionised water for removing the native oxide layer on Si. Other substrates were cleaned by usual methods. Using CT-8 Cryotorr cryopump(CTI) the chamber was pumped upto a base pressure of 1x 10^{-7} Torr in all our experiments. A halogen lamp was used to heat the substrates upto 800°C. Thickness of the films was measured after deposition using surface profilometer (stylus).

Films were deposited at room temperature(RT), 600°C, 700°C and 800°C. Studies also were made on buffer layers in different sputtering gas environments (pure Ar, Ar + O_2 mix gas and pure oxygen). STO layers were deposited at 700°C and 750°C. Films were characterized by XRD and SEM. A set of films were post annealed at 800°C - 1000°C. YBCO thin films were deposited on these buffer layers and growth conditions were optimized by using pulsed laser deposition (PLD) techinque [7]. Microstructural studies were done on the fractured Si<100> substrates.

RESULTS AND DISCUSSION

1. Optimum deposition conditions for YSZ buffer layers :

For obtaining reproducible results and high quality oriented films, we have observed that irrespective of the nature of substrate, 24 - 30 mTorr Ar +O_2 gas mixture (in the ratio 9:1) and 800°C substrate temparature are the best conditions. We have realized that it is difficult to produce <hoo> oriented thin films of YSZ on Si substrates as reoxidization of Si surface is unavoidable in sputtering technique. However, the films deposited on Sapphire, $LaAlO_3$ substrates yielded <hoo>oriented films. [Fig. 1,2, 3.]. A set of YSZ films deposited on various substrates are post annealed and YBCO thin films have been deposited on these substrates with optimized conditions. Post annealed films resulted with good crystalline quality with single phase. YBCO thin film deposited on polycrystalline buffer layer (deposited at 600° C and post annealed at 850° C) has yielded 80 -84 K and on <hoo> oriented YSZ film has yielded 86 -88K reproducibly on Sapphire substrate.

2. $SrTiO_3$ buffer layers :

The optimum deposition conditions for STO buffer layers on Si and Sapphire are 700° C and 15 -20 mTorr sputtering gas pressure (Ar+ O_2 in 9:1 ratio). However, we couldn't achieve highly <hoo>oriented STO films on Sapphire or Si due to lattice mismatch between STO and the substrates. Since, $LaAlO_3$ has good lattice match with STO, we have deposited STO on LAO <100> substrate and have obtained highly <hoo> oriented films using the above sputtering conditions. This clearly indicates the importance of lattice match for depositing <hoo> oriented films. However, we could achieve oriented STO films on YSZ buffered sapphire substrate which is due to the lattice match between YSZ and $SrTiO_3$. YBCO thin films are deposited on these buffer layers which have yielded reproducible T_c values in the range 85K-88K.

3. Microstructure of Buffer layers.

It has been pointed out by R.Pinto [8] et al that in the case of MgO films that coloumnr growth is a common phenomenon above 15 mTorr sputtering gas pressure. Similar columnar growth has been realized in the case of YSZ and STO buffer layers above 15m Torr sputtering gas pressure. Our scanning electron micrographs (fig.4) have confirmed this observation on fractured Si surfaces.

CONCLUSIONS

We have realized the effect of growth conditions on the microstructural properties of YSZ and STO thin films on Si, Sapphire and $LaAlO_3$ substrates. We have optimized the growth conditions of buffer layers for reproducible results. The microstructural studies of YSZ and STO films on Si<100> substrate have revealed a tendency for coloumnar growth above 15 mTorr. It is noticed that even with polycrystalline YSZ buffer layers it is possible to get highly c-axis oriented YBCO superconducting thin films.

ACKNOWLEDGEMENTS :

One of us <SS> wants to thank UGC New Delhi for financial support and we would like to thank Dr M.S.R.Rao for useful discussions.

REFERENCES :

1. J.W. Lee, A.K. Stamper M. Migluolo, D.W. Geve, and D.E.Laughlin : J. Appl. Phys. 64(1988) 6502.
2. D.K. Fork, et al : App. Phys. Lett. 57(1990) 1137.
3. K. Char N. Newman, S.M. Garrison R.W. Bartor, R.C. Taber, S.S. Laderman and R.D. Jacowitz :Appl Phys Lett 57(1990) 407.
4. A.Inam et al Solid State Tech. Feb(1990) 113.
5. H. Schmidth K. Hradil, G. Gieres, W. Hosler and O Eibl : Physica C 180(1991) 34
6. Jeffery et al : Appl. Phys. Lett. 60(1992) 3180.
7. R.Pinto et al : Physica C 196(1992) 264.
8. R.Pinto et al : J.Vac. Sci.Technology A90(1991) 2670.

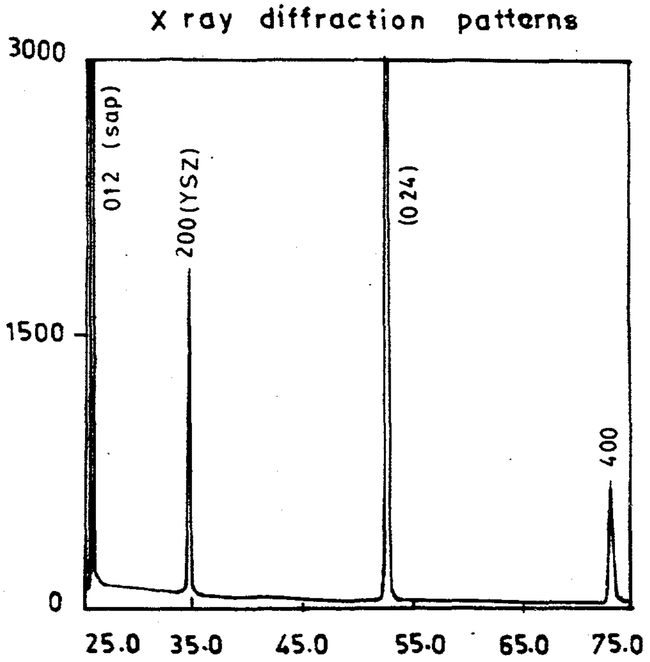

Figure 1.a)- XRD pattern of YSZ buffer layer on Sapphire substrate deposited 800° C and 25 mTorr sputtering gas pressure.

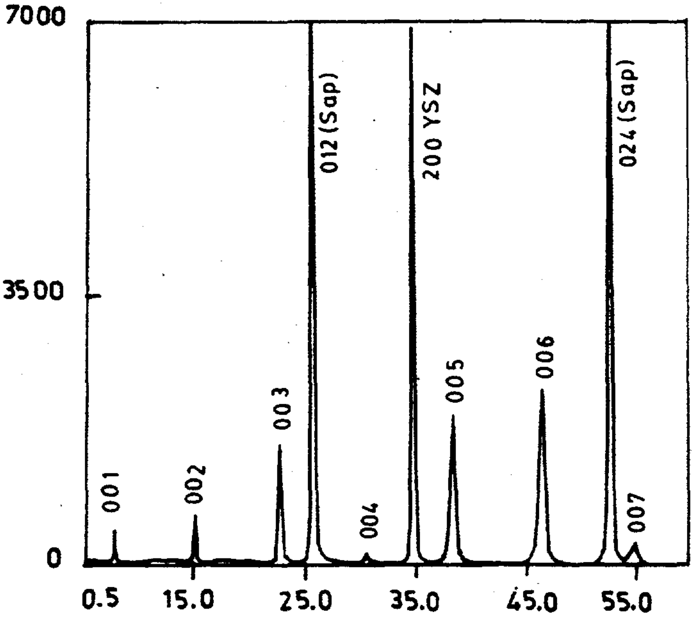

b)- XRD pattern of YBCO on YSZ buffered on SI <100>

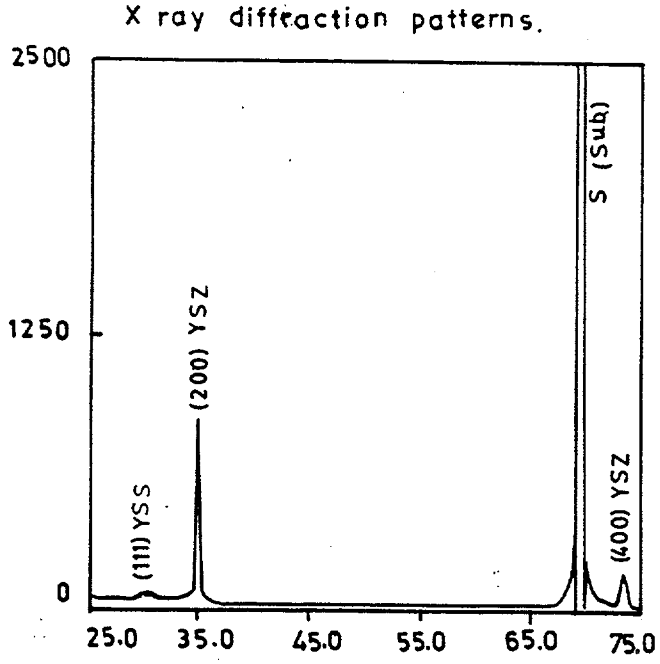

Figure 2.a)- XRD pattern of YSZ buffer on SI <100> deposited at 800° C and 30 mTorr sputtering gas pressure.

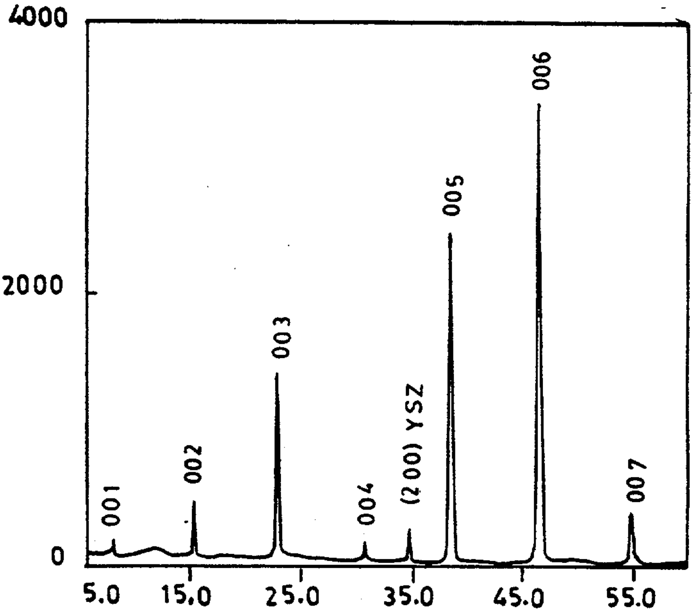

b)- XRD patter of YBCO on YSZ buffered si <100>.

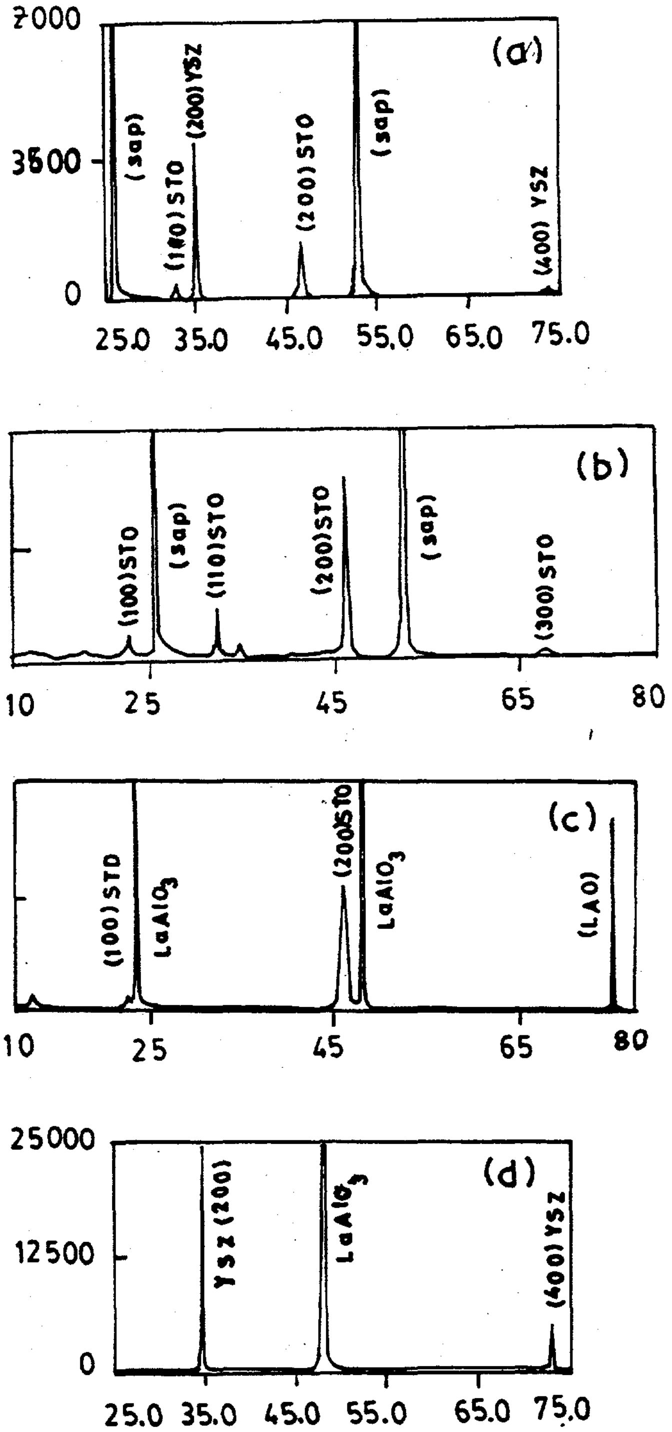

Figure 3.a)- XRD patter of STO film on YSZ buffered Sapphire substrated deposited at 700° C and 20 mTorr sputtering gas pressure.

b)- XRD pattern of STO film on Sapphire substrate deposited at 700° C mTorr sputtering gas pressure.

c)- XRD pattern of STO buffer layer on $LaA10_3$ substrate deposited at 700° C and 20 mTorr sputtering gas pressure.

d)- XRD pattern of YSZ thin film on $LA1O_3$ substrate deposited at 700° C and 20 mTorr sputtering gas pressure.

(a.)

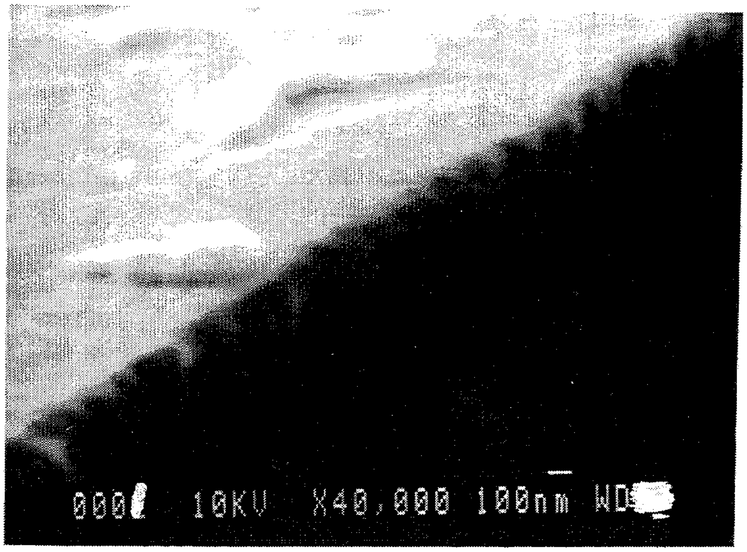

(b.)

Figure 4.- Scanning electron micrographs which shows the columnar growth for
a) YSZ film on Si substrate deposited at 25 mTorr.
b) STO layer on SI substrate deposited at 20 mTorr.

Index

INDEX